



# University of HUDDERSFIELD

## University of Huddersfield Repository

Sendanayake Achchige, Isuru

Novel Geometric Modelling and Aerodynamic Characterisation Methodology for Truck-Trailer Vehicles

### Original Citation

Sendanayake Achchige, Isuru (2018) Novel Geometric Modelling and Aerodynamic Characterisation Methodology for Truck-Trailer Vehicles. Doctoral thesis, School of Computing and Engineering.

This version is available at <http://eprints.hud.ac.uk/id/eprint/34983/>

The University Repository is a digital collection of the research output of the University, available on Open Access. Copyright and Moral Rights for the items on this site are retained by the individual author and/or other copyright owners. Users may access full items free of charge; copies of full text items generally can be reproduced, displayed or performed and given to third parties in any format or medium for personal research or study, educational or not-for-profit purposes without prior permission or charge, provided:

- The authors, title and full bibliographic details is credited in any copy;
- A hyperlink and/or URL is included for the original metadata page; and
- The content is not changed in any way.

For more information, including our policy and submission procedure, please contact the Repository Team at: [E.mailbox@hud.ac.uk](mailto:E.mailbox@hud.ac.uk).

<http://eprints.hud.ac.uk/>

NOVEL GEOMETRIC MODELLING AND  
AERODYNAMIC CHARACTERISATION  
METHODOLOGY FOR TRUCK-TRAILER VEHICLES

---

ISURU SENDANAYAKE ACHCHIGE

A THESIS SUBMITTED IN PARTIAL FULFILMENT OF THE REQUIREMENTS FOR THE  
DEGREE OF DOCTOR OF PHILOSOPHY AT THE UNIVERSITY OF HUDDERSFIELD

School of Computing and Engineering

University of Huddersfield

UK

June 2018



# PUBLICATIONS ARISEN FROM THESIS

---

- (1) Malviya, V., Asim, T., Sendanayake, I., & Mishra, R. (2018). Development of a Novel Characterisation Methodology for the Aerodynamic Coefficients of a Tractor–Trailer Unit Based on Relative Flow Angles and Vehicle Dimensions. *Arabian Journal for Science and Engineering*, 1-19.

Dr. Vihar Malviya, a former PhD student in my research group, produced the first draft version of this research paper. Since I have joined the research group, numerous meetings were held with the supervisory team and with their ideas and contributions, the paper has completely changed from the initial draft version which Dr. Malviya had produced. I have contributed to the above mentioned research paper since the very beginning by setting up and conducting numerical simulations; collating, analysing and presenting data; as well as being actively involved in the write-up process. I was also involved in the process of developing the semi-empirical prediction models to determine the aerodynamic coefficients of a tractor-trailer unit. This paper was produced as a result of the work outlined and carried out in chapter 4 of this thesis.

- (2) Sendanayake, I., Asim, T., & Mishra, R. (2017). Development of novel vehicle design modelling functions for quantifying vehicles' shapes. *International Journal of Research, Science, Technology & Management*, 7(2), 26-31.

Author has contributed to the above mentioned research paper by carrying out the literature review and identifying the niche; setting up and conducting numerical simulations; collating, analysing and presenting data; as well as being actively involved in the write-up process. The technique of using the shape functions to carry out geometric modelling of a truck-trailer model was published on this research paper. This paper was produced as a result of the work outlined in geometric modelling of a truck-trailer unit carried out in chapters 4 and 5 of this thesis.



# ABSTRACT

---

With the ever increasing consumer goods demand and increasing e-commerce sector, seeing truck-trailers dominate today's roads and motorways is no strange sight. The large surface areas coupled with high operational speeds means these heavy goods vehicles produce high resistive forces, hence consuming significantly more fuel in comparison to an average family car. With increasing fuel costs truck-trailer designers are challenged to build more fuel efficient vehicles while still providing maximum cargo space. In order to be in motion, truck-trailer units must be able to overcome resistive forces such as aerodynamic drag, rolling and gravitational resistance, drivetrain resistance etc. With aerodynamic drag being the biggest resistive force at higher velocities, shape optimisation of truck-trailer units has proven to be the most effective and efficient method of making these vehicles more aerodynamic and hence, more fuel efficient. Boundary layer separation at sharp edges causes flow disturbance and creates negative pressure regions, which create more drag. By increasing the curvature of an edge the boundary layer separation can be minimised. By optimising the shape of a truck-trailer unit, the overall aerodynamic drag can be reduced.

The following study utilises modern computational techniques such as computational fluid dynamics (CFD) to closely examine the effects of the aerodynamic performance of the truck-trailer unit. The local and global variations in the flow parameters have been studied. Various truck-trailer configurations with changing dimensional parameters such as overall length, height and width was studied along with the geometrical shape parameters using both qualitative and quantitative analytical techniques. The obtained data and the conclusions drawn from the studies were used to develop a parametric model in order to introduce a novel aerodynamic prediction tool, which is expected to aid the truck-trailer design process.

The first aim of this study is the development of a mathematical model to predict aerodynamic forces on a truck-trailer and at a range of crosswind angles. Initially a 2D outline was generated, followed by a 3D wireframe and a solid CAD model of the truck-trailer. Validation proved that the developed geometric modelling methodology and the numerical setup was accurate. A detailed qualitative and quantitative critical analysis had been carried out to understand the flow structure and behaviour of pressure and velocity fields. Qualitative analysis was used to describe the pressure and velocity distribution in the vicinity of truck-trailer surfaces at various crosswind

angles. Quantitative analysis had been carried out using the coefficient of pressure to study the effect of change in height and length at both, straight headwind and crosswind scenarios. The outcome confirmed the possibility to streamline the design process for truck-trailer units by a means of developing and employing a geometric modelling tool.

The second aim is the development of a mathematical model to predict aerodynamic forces based on truck-trailer shape parameters and straight headwind. In this case, four new shape coefficients have been introduced, namely, B1, B2, B5, B6. These shape coefficients are capable of independently altering the shape of the truck and trailer geometries. Each B coefficient had been defined by three levels: 0.01, 0.05, and 0.1. Given this, 81 configurations had been obtained. Qualitative analysis had been carried out to investigate the variations of velocity magnitude and coefficient of pressure in vicinity of and on the key surfaces. Also, quantitative analysis had been carried out using axial flow velocity, coefficient of pressure and variations in aerodynamic forces to capture the effects of changing B coefficients. The second semi-empirical prediction model has been developed to accurately predict the aerodynamic drag, lift and side force coefficients when provided with the respective B1, B2, B5 and B6 shape coefficients at straight headwind scenario.

The third facet of the work is development of a mathematical model to predict aerodynamic forces based on truck-trailer shape parameters at various cross wind conditions from  $15^\circ$  to  $90^\circ$  in increments of  $15^\circ$ . This combination had been used to analyse the change in aerodynamic flow field characteristics. Qualitative analysis had been carried out to investigate the variations of velocity magnitude contour, velocity magnitude streamlines and coefficient of pressure contour at various crosswind flow profiles. Also, quantitative analysis had been carried out for each changing B coefficient at each crosswind profile. The coefficient of pressure had been analysed to determine the pressure asymmetry on windward and leeward sides. Additionally, forces experienced by each of the key surfaces had been investigated to determine the contribution to the overall aerodynamic forces. This final semi-empirical prediction model incorporates the effect of change in length, height and width, with change in shape coefficients and crosswinds, to predict the respective aerodynamic force coefficients.

# DECLARATION

---

- The author of this thesis (including any appendices and/or schedules to this thesis) owns any copyright in it (the “Copyright”) and he has given The University of Huddersfield the right to use such Copyright for any administrative, promotional, educational and/or teaching purposes.
- Copies of this thesis, either in full or in extracts, may be made only in accordance with the regulations of the University Library. Details of these regulations may be obtained from the Librarian. This page must form part of any such copies made.
- The ownership of any patents, designs, trademarks and any and all other intellectual property rights except for the Copyright (the “Intellectual Property Rights”) and any reproductions of copyright works, for example graphs and tables (“Reproductions”), which may be described in this thesis, may not be owned by the author and may be owned by third parties. Such Intellectual Property Rights and Reproductions cannot and must not be made available for use without the prior written permission of the owner(s) of the relevant Intellectual Property Rights and/or Reproductions.



# Dedication

*I dedicate this thesis to my parents,*

*Piyasena Sendanayake and Anula Tennakoon,*

*whose love, support and example laid the foundations for the discipline*

*and application required to complete this work.*

# ACKNOWLEDGEMENTS

---

First and foremost, I would like to express my gratitude and appreciation to Prof. Rakesh Mishra for offering me the opportunity to carry out this research, providing support and guidance. I would also like to express my gratitude for Dr. Taimoor Asim for his constant support and guidance throughout my research journey. I would also like to acknowledge Dr. Suman Pradhan for his support and guidance.

I am eternally grateful for my parents Mr. Piyasena Sendanayake and Dr. Anula Tennakoon for all the help, support and advise during this process. They have sacrificed much, enabling me to follow my dreams and achieve my goals, leading me to where I am today. I am very grateful to my brother Savith Sendanayake, for being the best brother anyone can ever have. He was always there through thick and thin every step of the way with constant encouragement, motivation and support.

A special thanks to my best friend, Karina Zala, for her constant support and motivation throughout this process. It was a pleasure to share this journey with her including those sleepless nights. She has been the light in my dark times throughout my PhD journey.

I would like to thank my colleagues, with a special thanks to Sree Nirjhor Kaystha for all his advice, suggestions and support whenever it was required.

Finally, I would like to thank many others whom I have met in this journey and have supported me even with a word of encouragement.

# TABLE OF CONTENTS

---

1. CHAPTER 1 .....	1
1.1 Introduction into the UK Transportation Industry .....	2
1.2 Heavy Commercial Vehicles.....	4
1.3 Dimensional Restrictions of Truck-Trailer Units both in Europe and in UK .....	6
1.4 Fuel Efficiency for Truck-Trailer Units .....	7
1.5 Resistive Forces Acting on Truck-Trailer Units .....	7
1.6 Flow around a truck-trailer model.....	13
1.6.1 Active Flow Control Devices.....	15
1.6.2 Passive Flow Control Devices .....	16
1.7 Effect of Shape on truck-trailer aerodynamics.....	17
1.8 Effects of crosswinds on truck-trailer units.....	19
1.9 Overview of Vehicle Modelling and Design Process .....	21
1.9.1 Performance Based Design Considerations .....	22
1.9.2 Short comings in conventional Experimental and CFD based design methods .....	23
1.9.3 Potential for Mathematical Vehicle Design and Optimisation .....	24
1.9.4 Parametric Design Process.....	25
1.10 Motivation .....	28
1.11 Research Aims.....	30
2. CHAPTER 2 .....	31
2.1 Geometrical modelling techniques for road vehicle design optimisation .....	32
2.1.1 Summary of Literature regarding Geometrical Modelling Techniques.....	39
2.2 Effect of Truck-Trailer Dimensions and Shape on Aerodynamic Forces .....	40

2.2.1	Use of Passive Add-On Devices to alter the Truck-Trailer Shape .....	45
2.2.2	Summary of Literature regarding Effect of Truck-Trailer Dimensions and Shape on Aerodynamic Forces.....	49
2.3	Effect of Crosswinds on Truck-Trailer Aerodynamic Forces .....	50
2.3.1	Summary of Literature regarding Effect of Crosswinds on Aerodynamic Forces acting on a Truck-Trailer Unit.....	54
2.4	Scope of Research .....	55
2.5	Research Objectives .....	56
3.	CHAPTER 3 .....	58
3.1	Numerical Methodology .....	59
3.2	Pre-Processing Stage of CFD.....	59
3.2.1	Geometry Stage for Generic Truck-Trailer.....	60
3.2.2	Flow domain, Discretisation (meshing) and Mesh Independence Study.....	61
3.3	Solver Execution .....	64
3.3.1	Conservation of Mass .....	65
3.3.2	Conservation of Momentum .....	65
3.3.3	Turbulence modelling.....	68
3.3.4	Boundary Conditions .....	68
3.3.5	Solution methods setup.....	69
3.3.6	Convergence Criteria .....	69
3.4	Post-processing.....	70
3.5	Scope of the Numerical Investigations.....	71
4.	CHAPTER 4 .....	72
4.1	Introduction into Geometric Modelling .....	73
4.2	Applicable Mathematical Techniques for Geometric Modelling.....	74

4.2.1 Vectors ..... 74

4.2.2 Matrix Methods..... 75

4.2.3 Polynomial Interpolation ..... 75

4.2.4 Mathematical Vehicle Modelling Using Shape Functions ..... 76

4.3 2D Representation of the Baseline Truck-Trailer Unit ..... 78

4.4 Solid Modelling of Baseline Truck-Trailer Model ..... 84

4.5 3D Representation of the Baseline Truck-Trailer Unit ..... 85

4.6 Validation of the CFD Code and Proposed Design Methodology ..... 86

4.7 Validation of the Proposed Design Methodology using the Baseline Truck-Trailer Model. .... 88

4.7.1 Pressure Distribution on Key Surfaces of the Baseline Truck-Trailer Unit ..... 88

4.7.2 Pressure Distribution on the Front Face of the Truck..... 89

4.7.3 Pressure Distribution on the Rear Face of the Truck ..... 90

4.7.4 Pressure Distribution on the Front Face of the Trailer ..... 91

4.7.5 Pressure Distribution on the Rear Face of the Trailer..... 92

4.7.6 Velocity Distribution Around the Baseline Truck-Trailer Unit..... 93

4.8 Effect of crosswinds on the Pressure Distribution on Key Surfaces of the Truck-Trailer Unit 98

4.8.1 Pressure Distribution on the Front Face of the Truck..... 99

4.8.2 Pressure Distribution on the Rear Face of the Truck ..... 101

4.8.3 Pressure Distribution on the Front Face of the Trailer ..... 102

4.8.4 Pressure Distribution on the Rear Face of the Trailer..... 104

4.8.5 Pressure Distribution on the Windward Face of the Vehicle..... 106

4.8.6 Velocity Distribution on the Leeward Side of the Baseline Truck-Trailer Unit at Crosswinds..... 109

4.9 Flow Field Characteristics at Varying Trailer Heights. .... 111

4.10 Flow Field Characteristics at Varying Trailer Lengths..... 116

4.11 Overall Variation of Aerodynamic Forces with the Effect of Truck-Trailer Dimensions and Crosswind Angles..... 120

    4.11.1 Effect of Truck-Trailer Height on Aerodynamic Forces at Various Crosswind Flow Profiles 121

    4.11.2 Effect of Truck-Trailer Length on Aerodynamic Forces at Various Crosswind Flow Profiles 124

4.12 Development of Semi-Empirical Prediction Models for the Aerodynamic Coefficients of a Truck-Trailer Unit..... 127

    4.12.1 Developing the Drag Coefficient Equation..... 128

    4.12.2 Developing the Lift Coefficient Equation..... 134

    4.12.3 Developing the Side Coefficient Equation ..... 139

    4.12.4 Further Validation of the Proposed Prediction Techniques ..... 146

4.13 Summary ..... 147

5. CHAPTER 5 ..... 149

    5.1 Mathematical Modelling Technique to Modifying Truck-Trailer Shapes ..... 150

    5.2 2D Representation of the Baseline Truck-Trailer Unit ..... 151

    5.3 3D Representation of the Baseline Truck-Trailer Unit ..... 152

    5.4 Full Factorial Truck-Trailer Unit Design Configurations ..... 153

    5.5 Effect of B1 on the truck-trailer unit aerodynamic characteristics ..... 153

        5.5.1. Velocity Distribution around the Truck-Trailer Unit with Changing B1 Values. 154

        5.5.2. Pressure Distribution around the Truck-Trailer Unit with Changing B1 Values. 161

        5.5.3. Pressure Distribution on the Truck-Trailer Unit with Changing B1 Values ..... 162

        5.5.4. Effects of Changing B1 Values on Aerodynamic Forces ..... 164

5.6	Effect of B2 on the truck-trailer unit aerodynamic characteristics .....	166
5.6.1.	Velocity Distribution around the Truck-Trailer Unit with Changing B2 Values.	166
5.6.2.	Pressure Distribution around the Truck-Trailer Unit with Changing B2 Values.	173
5.6.3.	Effects of Changing B2 Values on Aerodynamic Forces .....	176
5.7	Effect of B5 on the truck-trailer unit aerodynamic characteristics .....	178
5.7.1	Velocity Distribution around the Truck-Trailer Unit with Changing B5 Values .	178
5.7.2	Pressure Distribution around the Truck-Trailer Unit with Changing B5 Values.	185
5.7.3	Effects of Changing B5 Values on Aerodynamic Forces .....	189
5.8	Effect of B6 on the truck-trailer unit aerodynamic characteristics .....	190
5.8.1	Velocity Distribution around the Truck-Trailer Unit with Changing B6 Values .	191
5.8.2	Pressure Distribution around the Truck-Trailer Unit with Changing B6 Values.	199
5.8.3	Effects of Changing B6 Values on Aerodynamic Forces .....	201
5.9	Optimum Truck-Trailer Model .....	203
5.10	Development of Semi-Empirical Prediction Models for Drag and Lift Aerodynamic Coefficients for Changing Truck-Trailer Shapes .....	210
5.10.1	Developing the Drag Coefficient Equation.....	211
5.10.2	Developing the Lift Coefficient Equation.....	215
5.11	Summary .....	219
6.	CHAPTER 6 .....	220
6.1	Introduction into the effect of crosswinds on the truck-trailer unit.....	221
6.2	Flow field in the vicinity of a Truck-trailer unit at crosswinds.....	221
6.3	Effect of B1 on the truck-trailer unit performance under crosswinds.....	226
6.4	Effect of B2 on the truck-trailer unit performance under crosswinds.....	232
6.5	Effect of B5 on the truck-trailer unit performance under crosswinds.....	237
6.6	Effect of B6 on the truck-trailer unit performance under crosswinds.....	242

6.7	Pressure variations on windward, top and leeward surfaces of truck-trailer unit with changing B coefficient at a constant crosswind angle of 60° .....	247
6.8	The Aerodynamic Forces Experienced by Truck-Trailer Models with Varying B Coefficients and Crosswind Angles. ....	256
6.9	Development of Semi-Empirical Prediction Models for Drag, Lift and Side Aerodynamic Coefficients considering Shapes Effects at Varying Crosswind Angles .....	261
6.9.1	Developing the Drag Coefficient Equation.....	261
6.9.2	Developing the Lift Coefficient Equation.....	267
6.9.3	Developing the Side Coefficient Equation .....	273
6.10	Summary .....	278
7.	CHAPTER 7 .....	280
7.1	Research Problem Synopsis .....	281
7.2	Research Aims and Achievements.....	282
7.3	Thesis Conclusions.....	284
7.4	Thesis Contribution .....	290
7.5	Recommendation for Future Work .....	291
	REFERENCES .....	293
	APPENDICES .....	305
	A-1 Full Factorial Geometrical Configurations .....	305

# LIST OF FIGURES

---

Figure 1.1 Domestic goods moved by mode 1990 to 2010, Great Britain [1].....	3
Figure 1.2 Goods moved by Articulated and Rigid vehicles in UK between 1990 and 2010 [1] ..	4
Figure 1.3 Generic single deck truck-trailer unit and a double deck truck-trailer unit.....	5
Figure 1.4 Horsepower required to overcome the aerodynamic drag and rolling friction as a function of travel speed for a typical Class 8 truck-trailer [4] .....	9
Figure 1.5 Main resistive force acting against a moving Heavy goods vehicle [3].....	10
Figure 1.6 Influence of drag on fuel consumption of a 40ton truck-trailer unit [6] .....	10
Figure 1.7 Aerodynamic forces acting on a vehicle .....	12
Figure 1.8 Velocity gradient in the boundary layer (a) and flow separation from a curved wall (b) [7].....	13
Figure 1.9 Typical air flow patterns around a non-aerodynamic truck-trailer unit [1].....	14
Figure 1.10 A truck-trailer unit with a MSBC device located at the top edge of the trailer unit [21].....	16
Figure 1.11 Pressure distribution around a generic truck-trailer unit [33] .....	18
Figure 1.12 Example of a teardrop shaped inspired trailer design expected to reduce drag force [33].....	19
Figure 1.13 Overturned truck-trailer vehicle under strong crosswinds. ....	20
Figure 1.14 Three types of crosswind caused vehicle accidents Batista [35].....	21
Figure 1.15 Vehicle design process [36].....	22
Figure 1.16 Different search and optimisation techniques [39].....	25
Figure 1.17 Schematic representation of the whole optimisation scheme.....	26
Figure 1.18 Roof shape representation using a quadratic Bézier curve. Outlined control polygon is also plotted. Red dots refer to control points [40].....	27
Figure 1.19 Roof shape representation using a quadratic Bézier curve. Outlined control polygon is also plotted. Red dots refer to control points [40].....	28
Figure 2.1 Box model category.....	32
Figure 2.2 Vehicle Geometry: Configuration Boxes. ....	33
Figure 2.3 The pickup vehicle in the morphing process. ....	34
Figure 2.4 The design parameters and the morph boxes around the vehicle model. ....	35

Figure 2.5 The design variables and levels and the 3D car model used for the study.....	36
Figure 2.6 Standard template model generated using ASD for this study.....	37
Figure 2.7 Upper and lower limits of Middle Roof Z (a) and Windscreen Top Z (b) design parameters.....	38
Figure 2.8 Handles correspond to D_A design alteration.....	39
Figure 2.9 Energy consumed to overcome drag for ground, air, and water vehicles .....	40
Figure 2.10 Simplified truck-trailer model used for wind tunnel experiments by Allan [76] .....	41
Figure 2.11 Velocity streamlines on top of the truck-trailer model projected along the symmetry plane. (a) Model 1 (small gap width, sharp edges). (b) Model 2 (small gap width, round edges). .....	42
Figure 2.12 The trailer unit with square edges (a) and the trailer unit with rounded edges (b)....	43
Figure 2.13 Drag force reduction for ten different truck-trailer models with varying payload spaces (a) and the flow velocity for baseline truck-trailer and the optimised truck-trailer model A (b).....	44
Figure 2.14 The fuel reduction percentage vs drag reduction percentage for different operation conditions for 40,000 kg and 20,000kg truck-trailer models.....	48
Figure 2.15 The side force coefficient with respect to yaw angle. ....	50
Figure 2.16 The side force coefficient with respect to yaw angle. ....	51
Figure 2.17 base pressure variations with the yaw angle.....	52
Figure 2.18 Drag coefficient for various configurations of add-on fuel saving devices. ....	53
Figure 2.19 Percentage decrease of drag force over baseline model, for each add-on device under varying yaw conditions. ....	54
Figure 3.1 Dimensions for the baseline truck-trailer unit.....	60
Figure 3.2 The DAF CF400 truck model with the Don-Bur trailer unit.....	61
Figure 3.3 Mesh with inner section contained finer elements and the outer section consisted of much coarser elements.....	63
Figure 3.4 Mesh Independence test results.....	64
Figure 4.1 Vehicle model with box sections [43].....	76
Figure 4.2 Modelling function for external shapes [43] .....	77
Figure 4.3 Sections of a truck-trailer unit .....	79
Figure 4.4 Very first profile of the truck unit .....	80

Figure 4.5 Section profiles on the YZ plane, positioned along the x direction to represent the truck (a), bridge (b) and the trailer unit (c). .....	80
Figure 4.6 The generated 3D wireframe structure for a complete truck-trailer model. ....	82
Figure 4.7 Profiles of the complete truck-trailer unit with wheelbase. ....	82
Figure 4.8 Complete truck trailer profile including the wheel base generated using the shape function equations. ....	83
Figure 4.9 Profiles of the truck-trailer unit .....	84
Figure 4.10 CAD model of the baseline truck-trailer model with a 15.28m length and 4.4m trailer height. ....	85
Figure 4.11 The baseline truck-trailer configuration with a total length of 15.28m and a height of 4.4m. ....	86
Figure 4.12 Comparison of aerodynamic coefficients at various yaw angles (a) Side coefficient ( $C_s$ ) (b) Lift coefficient ( $C_L$ ) .....	87
Figure 4.13 Distribution of coefficient of pressure ( $C_P$ ) on the front face of the truck unit with a 15.28m trailer length and 4.4m height. ....	90
Figure 4.14 Distribution of coefficient of pressure ( $C_P$ ) on the rear face of the truck unit with a 15.28m trailer length and 4.4m height. ....	91
Figure 4.15 Distribution of coefficient of pressure ( $C_P$ ) on the front face of the trailer unit with a 15.28m trailer length and 4.4m height. ....	92
Figure 4.16 Distribution of coefficient of pressure ( $C_P$ ) on the rear face of the trailer unit with a 15.28m trailer length and 4.4m height. ....	93
Figure 4.17 Velocity fields around the baseline truck-trailer unit 15.28m long (Side view) .....	94
Figure 4.18 Velocity fields around the baseline truck-trailer unit 15.28m long (Top view) .....	95
Figure 4.19 Velocity magnitude displayed in XY-planes along the trailer unit .....	95
Figure 4.20 The streamline patterns of the flow field in the front section of the baseline truck-trailer vicinity and in the gap region .....	96
Figure 4.21 Streamline patterns of the flow field at the rear of the baseline truck-trailer model. ....	97
Figure 4.22 Formation of relative wind velocity with respect to the vehicle by considering the wind velocity $V_w$ , velocity of the truck-trailer unit $V_v$ , direction of the wind $\alpha$ , wind velocity relative to truck-trailer $V_r$ and the yaw flow angle $\psi$ . ....	98

Figure 4.23 Variations in coefficient of pressure ( $C_P$ ) on the front face of the 15.28m truck unit when the trailer height is 4.4m at yaw flow angles ( $\psi$ ) of (a) $0^\circ$ (b) $30^\circ$ (c) $60^\circ$ (d) $90^\circ$ . .....	100
Figure 4.24 Variations in coefficient of pressure ( $C_P$ ) on the rear face of the 15.28m truck unit when the trailer height is 4.4m at flow angles ( $\psi$ ) of (a) $0^\circ$ (b) $30^\circ$ (c) $60^\circ$ (d) $90^\circ$ . .....	102
Figure 4.25 Variations in coefficient of pressure ( $C_P$ ) on the front face of the 15.28m trailer unit when the trailer height is 4.4m at flow angles ( $\psi$ ) of (a) $0^\circ$ (b) $30^\circ$ (c) $60^\circ$ (d) $90^\circ$ . .....	103
Figure 4.26 Variations in coefficient of pressure ( $C_P$ ) on the rear face of the 15.28m trailer unit when the trailer height is 4.4m at flow angles ( $\psi$ ) of (a) $0^\circ$ (b) $30^\circ$ (c) $60^\circ$ (d) $90^\circ$ . .....	105
Figure 4.27 Variations in coefficient of pressure on the left face of the truck-trailer unit at a relative flow angle ( $\psi$ ) of (a) $0^\circ$ (b) $30^\circ$ (c) $60^\circ$ (d) $90^\circ$ . .....	108
Figure 4.28 The streamlines along the baseline truck-trailer cross section at 7.64m from the front truck face when $\psi = 0^\circ$ (a), $\psi = 30^\circ$ (b), $\psi = 60^\circ$ (c) and $\psi = 90^\circ$ (d).....	110
Figure 4.29 Truck-trailer geometry with 36 data points .....	111
Figure 4.30 Variation in pressure coefficient on the front truck surface with varying trailer heights. ....	113
Figure 4.31 Variation in pressure coefficient on the rear truck surface with varying trailer heights .....	114
Figure 4.32 Variation in pressure coefficient on the front trailer surface with varying trailer heights .....	115
Figure 4.33 Variation in pressure coefficient on the rear trailer surface with varying trailer heights .....	116
Figure 4.34 Variation in pressure coefficient on the front truck surface with varying trailer lengths .....	117
Figure 4.35 Variation in pressure coefficient on the rear truck surface with varying trailer lengths .....	118
Figure 4.36 Variation in pressure coefficient on the front trailer surface with varying trailer lengths .....	119
Figure 4.37 Variation in pressure coefficient on the rear trailer surface with varying trailer. ...	120
Figure 4.38 Drag force experienced by 15.28m truck-trailer configuration at 4.4m, 4.6m and 4.8m trailer heights at changing yaw angles. ....	122

Figure 4.39 Lift force experienced by 15.28m truck-trailer configuration at 4.4m, 4.6m and 4.8m trailer heights at changing yaw angles. ....	123
Figure 4.40 Side force experienced by 15.28m truck-trailer configuration at 4.4m, 4.6m and 4.8m trailer heights at changing yaw angles. ....	124
Figure 4.41 Drag force experienced by 4.4m high truck-trailer configuration at 15.28m, 15.78m and 16.28 trailer lengths at changing yaw angles. ....	125
Figure 4.42 Lift force experienced by 4.4m high truck-trailer configuration at 15.28m, 15.78m and 16.28 trailer lengths at changing yaw angles. ....	126
Figure 4.43 Side force experienced by 4.4m high truck-trailer configuration at 15.28m, 15.78m and 16.28 trailer lengths at changing yaw angles. ....	127
Figure 4.44 The drag coefficient for truck-trailer models with changing maximum heights changing maximum lengths at 0° yaw angle. ....	130
Figure 4.45 The drag coefficient for truck-trailer models with changing maximum heights, when length is 15.28m for 15°(a), 45°(b) and 75°(c) crosswind flow, 15.78m for 15°(d), 45°(e) and 75°(f) crosswind flow and 16.28m length for 15°(g), 45°(h) and 75°(i) crosswind flow.....	131
Figure 4.46 The drag coefficient for truck-trailer models with changing maximum lengths, when height is 4.4m for 15°(a), 45°(b) and 75°(c) crosswind flow, 4.6m for 15°(d), 45°(e) and 75°(f) crosswind flow and 4.8m length for 15°(g), 45°(h) and 75°(i) crosswind flow. ....	132
Figure 4.47 Correlation between aerodynamic drag coefficient measured from CFD and calculated by the new methodology for various vehicle geometries and relative flow angles. ...	134
Figure 4.48 The lift coefficient for truck-trailer models with changing maximum heights (a) and changing maximum lengths (b) at 0° yaw angle.....	135
Figure 4.49 The lift coefficient for truck-trailer models with changing maximum heights, when length is 15.28m for 15°(a), 45°(b) and 75°(c) crosswind flow, 15.78m for 15°(d), 45°(e) and 75°(f) crosswind flow and 16.28m length for 15°(g), 45°(h) and 75°(i) crosswind flow.....	136
Figure 4.50 The lift coefficient for truck-trailer models with changing maximum lengths, when height is 4.4m for 15°(a), 45°(b) and 75°(c) crosswind flow, 4.6m for 15°(d), 45°(e) and 75°(f) crosswind flow and 4.8m length for 15°(g), 45°(h) and 75°(i) crosswind flow. ....	137
Figure 4.51 Correlation between aerodynamic lift coefficient measured from CFD and calculated by the new methodology for various vehicle geometries and relative flow angles. ....	139

Figure 4.52 Side force coefficient $15^\circ$ , $45^\circ$ and $75^\circ$ yaw angles for 4.4m, 4.6m and 4.8m high truck-trailer units at (a) 15.28m, (b) 15.78m and (c) 16.28m lengths.....	141
Figure 4.53 Side force coefficient $15^\circ$ , $45^\circ$ and $75^\circ$ yaw angles for 15.28m, 15.78m and 16.28m long truck-trailer units at (a) 4.4m, (b) 4.6m and (c) 4.8m heights. ....	142
Figure 4.54 The side force coefficient for truck-trailer models with changing maximum heights, when length is 15.28m for $15^\circ$ (a), $45^\circ$ (b) and $75^\circ$ (c) crosswind flow, 15.78m for $15^\circ$ (d), $45^\circ$ (e) and $75^\circ$ (f) crosswind flow and 16.28m length for $15^\circ$ (g), $45^\circ$ (h) and $75^\circ$ (i) crosswind flow....	143
Figure 4.55 The side coefficient for truck-trailer models with changing maximum lengths, when height is 4.4m for $15^\circ$ (a), $45^\circ$ (b) and $75^\circ$ (c) crosswind flow, 4.6m for $15^\circ$ (d), $45^\circ$ (e) and $75^\circ$ (f) crosswind flow and 4.8m length for $15^\circ$ (g), $45^\circ$ (h) and $75^\circ$ (i) crosswind flow. ....	144
Figure 4.56 Correlation between aerodynamic side force coefficient measured from CFD and calculated by the new methodology for various vehicle geometries and relative flow angles... ..	145
Figure 5.1 Baseline truck-trailer model when $\{B1, B2, B5, B6\} = 0$ (a) and when $\{B1, B2, B5, B6\} = 0.1$ (b).....	151
Figure 5.2 Varying B1 and B2 coefficient of 0.01, 0.05, 0.1 to obtain changing truck shapes (a-b) and varying B5 and B6 coefficient of 0.01, 0.05, 0.1 to obtain changing trailer shapes (c-d) ...	152
Figure 5.3 The generated 3D wireframe structure for a complete truck-trailer model with shape alterations.....	153
Figure 5.4 Truck-trailer unit with changing B1 coefficients (a) $B1 = 0.01$ (b) $B1 = 0.05$ (c) $B1 = 0.1$ .....	154
Figure 5.5 Velocity fields around the Truck-trailer units with changing B1 coefficients. ....	155
Figure 5.6 Data line locations around the top leading edge of the truck unit when $B1 = 0.1$ ....	156
Figure 5.7 The x direction velocity plotted along the data line $L1_F$ .....	157
Figure 5.8 The x direction velocity plotted along the data lines $L2_{BL}$ (left) and $L6_{BR}$ (right) ....	158
Figure 5.9 The x direction velocity plotted along the data line $L3_{TL}$ (left) and $L5_{TR}$ (right) .....	159
Figure 5.10 The x direction velocity plotted along the data line $L4_T$ .....	159
Figure 5.11 Axial flow velocity profiles at various distances from the top leading edge of the truck unit when $B1 = 0.01$ .....	160
Figure 5.12 Axial flow velocity profiles at various distances from the top leading edge of the truck unit when $B1 = 0.1$ .....	161

Figure 5.13 Coefficient of pressure around the Truck-trailer units with changing B1 coefficients. .....	162
Figure 5.14 Coordinate $\eta$ is used to plot pressure coefficient around the truck-trailer unit along the symmetry line starting at bottom front truck face and ending at bottom rear trailer face. ...	163
Figure 5.15 The pressure coefficient ( $C_p$ ) plotted over the truck-trailer unit along the symmetry line with changing B1 coefficients. ....	164
Figure 5.16 The drag force (a), lift force (b) and side force (c) coefficients for the truck-trailer geometry when $B1 = 0.01$ , $B1 = 0.05$ and $B1 = 0.1$ at straight headwind.....	165
Figure 5.17 Velocity fields around the Truck-trailer units with changing B2 coefficients. ....	167
Figure 5.18 Data line locations around the top trailing edge of the truck unit when $B2 = 0.1$ ...	168
Figure 5.19 The x direction velocity plotted along the data line L7 <sub>R</sub> .....	169
Figure 5.20 The x direction velocity plotted along the data lines L8 <sub>BL</sub> (left) and L12 <sub>BR</sub> (right)	170
Figure 5.21 The x direction velocity plotted along the data lines L9 <sub>TL</sub> (left) and L11 <sub>TR</sub> (right)	171
Figure 5.22 The x direction velocity plotted along the data line L10 <sub>T</sub> .....	172
Figure 5.23 Axial flow velocity profiles at various distances from the top leading edge of the truck unit when $B2 = 0.01$ (a) and $B2 = 0.1$ (b).....	173
Figure 5.24 Coefficient of pressure around the Truck-trailer units with changing B2 coefficients. .....	174
Figure 5.25 The pressure coefficient ( $C_p$ ) plotted over the truck-trailer unit along the symmetry line for changing B2 coefficients. ....	176
Figure 5.26 The drag force (a), lift force (b) and side force (c) coefficients for the truck-trailer geometry when $B2 = 0.01$ , $B2 = 0.05$ and $B2 = 0.1$ at straight headwind.....	177
Figure 5.27 Velocity fields around the Truck-trailer units with changing B5 coefficients. ....	179
Figure 5.28 Data line locations around the top leading edge of the trailer unit when $B5 = 0.1$ .	180
Figure 5.29 The x direction velocity plotted along the data line L13 <sub>F</sub> .....	181
Figure 5.30 The x direction velocity plotted along the data lines L14 <sub>BL</sub> (left) and L18 <sub>BR</sub> (right) .....	182
Figure 5.31 The x direction velocity plotted along the data lines L15 <sub>TL</sub> (left) and L17 <sub>TR</sub> (right) .....	183
Figure 5.32 The x direction velocity plotted along the data line L16 <sub>T</sub> . ....	184

Figure 5.33 Axial flow velocity profiles at various distances from the top leading edge of the trailer unit when $B5 = 0.01$ (a) and $B5 = 0.1$ (b). .....	185
Figure 5.34 Coefficient of pressure around the Truck-trailer units with changing $B5$ coefficients. ....	187
Figure 5.35 The pressure coefficient ( $C_p$ ) plotted over the truck-trailer unit along the symmetry line for changing $B5$ coefficients.....	189
Figure 5.36 The drag force (a), lift force (b) and side force (c) coefficients for the truck-trailer geometry when $B5 = 0.01$ , $B5 = 0.05$ and $B5 = 0.1$ at straight headwind.....	190
Figure 5.37 Velocity fields around the Truck-trailer units with changing $B6$ coefficients. ....	192
Figure 5.38 Data line locations around the top leading edge of the trailer unit when $B6 = 0.1$ . ....	193
Figure 5.39 The x direction velocity plotted along the data line L19 <sub>R</sub> . ....	194
Figure 5.40 The x direction velocity plotted along the data lines L20 <sub>BL</sub> (left) and L24 <sub>BR</sub> (right) .....	195
Figure 5.41 The x direction velocity plotted along the data lines L21 <sub>TL</sub> (left) and L23 <sub>TR</sub> (right) .....	196
Figure 5.42 The x direction velocity plotted along the data line L22 <sub>T</sub> . ....	197
Figure 5.43 Axial flow velocity profiles at various distances from the top leading edge of the trailer unit when $B6 = 0.01$ (a) and $B6 = 0.1$ (b). ....	198
Figure 5.44 Coefficient of pressure around the truck-trailer units with changing $B6$ coefficients. (a) $B6 = 0.01$ (b) $B6 = 0.05$ (c) $B6 = 0.1$ . ....	200
Figure 5.45 The pressure coefficient ( $C_p$ ) plotted over the truck-trailer unit along the symmetry line for changing $B6$ coefficients.....	201
Figure 5.46 The drag force (a), lift force (b) and side force (c) coefficients for the truck-trailer geometry when $B6 = 0.01$ , $B6 = 0.05$ and $B6 = 0.1$ at straight headwind.....	202
Figure 5.47 Variations in drag force for various truck-trailer combinations with varying $B1$ , $B2$ , $B5$ and $B6$ coefficients.....	203
Figure 5.48 Pressure Coefficient of the (a) minimum drag model on the Truck-Front surface (b) maximum drag model of the Truck-Front surface (c) minimum drag model of the Truck-Rear surface (d) maximum drag model of the Truck-Rear surface.....	206

Figure 5.49 Pressure Coefficient of the (a) minimum drag model on the Trailer-Front surface (b) maximum drag model of the Trailer-Front surface (c) minimum drag model of the Trailer-Rear surface (d) maximum drag model of the Trailer-Rear surface. ....	208
Figure 5.50 The pressure coefficient ( $C_p$ ) plotted over the truck-trailer unit along the symmetry line for minimum and maximum drag truck-trailer models.....	210
Figure 5.51 The drag force coefficients for the truck-trailer geometry for changing B coefficients.....	213
Figure 5.52 Correlation between aerodynamic drag force coefficient measured from CFD and calculated by the new methodology for various truck-trailer geometries.....	214
Figure 5.53 Lift force coefficients of the truck-trailer geometry with changing B coefficients to (a) 0.01; (b) 0.05; (c) 0.1 .....	217
Figure 5.54 Correlation between aerodynamic drag force coefficient measured from CFD and calculated by the proposed prediction methodology for various truck-trailer geometries. ....	218
Figure 6.1 Variations in flow velocity in the vicinity of the truck-trailer model at yaw flow angles ( $\psi$ ) of (a) $30^\circ$ (b) $60^\circ$ and (c) $90^\circ$ .....	223
Figure 6.2 Velocity streamlines on the leeward side of the truck-trailer model at yaw flow angles ( $\psi$ ) of (a) $30^\circ$ (b) $60^\circ$ and (c) $90^\circ$ .....	225
Figure 6.3 Variations in coefficient of pressure ( $C_p$ ) on the front face of the truck unit with $B_1 = 0.01$ (left) and $B_1 = 0.1$ (right), where $\psi = 30^\circ$ (top); $\psi = 60^\circ$ (middle); $\psi = 90^\circ$ (bottom). ....	227
Figure 6.4 The data lines (Highlighted) position on either side of truck front surface which will be used to extract average pressure coefficient data. ....	229
Figure 6.5 The average pressure coefficient on the truck front surface for $B_1 = 0.01$ and $B_1 = 0.1$ models from $\psi = 15^\circ$ to $\psi = 90^\circ$ . ....	230
Figure 6.6 The force acting on the truck front surface in the positive X direction (a) positive Y direction (b) and positive Z direction (c) for $B_1 = 0.01$ and $B_1 = 0.1$ models from $\psi = 15^\circ$ to $\psi = 90^\circ$ .....	232
Figure 6.7 Variations in coefficient of pressure ( $C_p$ ) on the rear face of the truck unit with $B_2 = 0.01$ (left) and $B_2 = 0.1$ (right), where $\psi = 30^\circ$ (top); $\psi = 60^\circ$ (middle); $\psi = 90^\circ$ (bottom). ....	234
Figure 6.8 The average pressure coefficient on the truck rear surface for $B_2 = 0.01$ and $B_2 = 0.1$ models from $\psi = 15^\circ$ to $\psi = 90^\circ$ .....	235

Figure 6.9 The force acting on the truck rear surface in the positive X direction (a) positive Y direction (b) and positive Z direction (c) for B2 = 0.01 and B2 = 0.1 models from $\psi = 15^\circ$ to $\psi = 90^\circ$ .....	237
Figure 6.10 Variations in coefficient of pressure (CP) on the front face of the trailer unit with B5 = 0.01 (left) and B5 = 0.1 (right), where crosswind flow is $30^\circ$ (top); $60^\circ$ (middle); $90^\circ$ (bottom). .....	239
Figure 6.11 The average pressure coefficient on the trailer front surface for B5 = 0.01 and B5 = 0.1 models from $\psi = 15^\circ$ to $\psi = 90^\circ$ . .....	241
Figure 6.12 The force acting on the trailer front surface in the positive X direction (a) positive Y direction (b) and positive Z direction (c) for B5 = 0.01 and B5 = 0.1 models from $\psi = 15^\circ$ to $\psi = 90^\circ$ . .....	242
Figure 6.13 Variations in coefficient of pressure (CP) on the rear face of the trailer unit with B6 = 0.01 (left) and B6 = 0.1 (right), where crosswind flow is $30^\circ$ (top); $60^\circ$ (middle); $90^\circ$ (bottom). .....	244
Figure 6.14 The average pressure coefficient on the trailer front surface for B6 = 0.01 and B6 = 0.1 models from $\psi = 15^\circ$ to $\psi = 90^\circ$ . .....	246
Figure 6.15 The force acting on the trailer rear surface in the positive X direction (a) positive Y direction (b) and positive Z direction (c) for B6 = 0.01 and B6 = 0.1 models from $\psi = 15^\circ$ to $\psi = 90^\circ$ .....	<b>Error! Bookmark not defined.</b>
Figure 6.16 Variations in coefficient of pressure ( $C_p$ ) on windward side of the truck-trailer unit with changing B profiles. (a) B1, B2, B5, B6 = 0.01 (b) B1 = 0.1, (c) B2 = 0.1, (d) B5 = 0.1, (e) B6 = 0.1 at $\psi = 60^\circ$ .....	249
Figure 6.17 Variations in coefficient of pressure ( $C_p$ ) on top surface of the truck-trailer unit with changing B profiles. (a) B1, B2, B5, B6 = 0.01 (b) B1 = 0.1, (c) B2 = 0.1, (d) B5 = 0.1, (e) B6 = 0.1 at $\psi = 60^\circ$ . .....	251
Figure 6.18 Variations in coefficient of pressure ( $C_p$ ) on leeward surface of the truck-trailer unit with changing B profiles. (a) B1, B2, B5, B6 = 0.01 (b) B1 = 0.1, (c) B2 = 0.1, (d) B5 = 0.1, (e) B6 = 0.1 at $\psi = 60^\circ$ . .....	253
Figure 6.19 The force acting on the windward vehicle surface in the positive Z direction for B1, B2, B5, B6 = 0.01, B1 = 0.1, B2 = 0.1, B5 = 0.1, B6 = 0.1 models, from $\psi = 15^\circ$ to $\psi = 90^\circ$ . .	255

Figure 6.20 The force acting on the leeward vehicle surface in the positive Z direction for B1, B2, B5, B6 = 0.01, B1 = 0.1, B2 = 0.1, B5 = 0.1, B6 = 0.1 models, from $\psi = 15^\circ$ to $\psi = 90^\circ$ . .	256
Figure 6.21 Truck-trailer drag force acting for various B1, B2, B5, B6 configurations with varying magnitudes from $\psi = 15^\circ$ to $\psi = 90^\circ$ . .....	257
Figure 6.22 Truck-trailer lift force acting on various B1, B2, B5, B6, configurations with varying magnitudes from $\psi = 15^\circ$ to $\psi = 90^\circ$ . .....	259
Figure 6.23 Truck-trailer side force acting on various B1, B2, B5, B6, configurations with varying magnitudes from $\psi = 15^\circ$ to $\psi = 90^\circ$ . .....	260
Figure 6.24 Drag force coefficient for varying (a) B1, (b) B2, (c) B5 and (d) B6 shape coefficients at $15^\circ$ yaw angle. ....	262
Figure 6.25 Drag force coefficient for varying (a) B1, (b) B2, (c) B5 and (d) B6 shape coefficients at $45^\circ$ yaw angle. ....	263
Figure 6.26 Drag force coefficient for varying (a) B1, (b) B2, (c) B5 and (d) B6 shape coefficients at $75^\circ$ yaw angle. ....	264
Figure 6.27 Correlation between aerodynamic drag force coefficient measured from CFD and calculated by the proposed prediction methodology for various truck-trailer geometries. ....	267
Figure 6.28 Lift Force Coefficient for varying (a) B1, (b) B2, (c) B5 and (d) B6 shape coefficients at $15^\circ$ yaw angle. ....	268
Figure 6.29 Lift Force Coefficient for varying (a) B1, (b) B2, (c) B5 and (d) B6 shape coefficients at $45^\circ$ yaw angle. ....	269
Figure 6.30 Lift Force Coefficient for varying (a) B1, (b) B2, (c) B5 and (d) B6 shape coefficients at $75^\circ$ yaw angle. ....	270
Figure 6.31 Correlation between aerodynamic lift force coefficient measured from CFD and calculated by the proposed prediction methodology for various truck-trailer geometries. ....	272
Figure 6.32 Side force coefficient for varying (a) B1, (b) B2, (c) B5 and (d) B6 shape coefficients at $15^\circ$ yaw angle. ....	274
Figure 6.33 Side force coefficient for varying (a) B1, (b) B2, (c) B5 and (d) B6 shape coefficients at $45^\circ$ yaw angle. ....	275
Figure 6.34 Side force coefficient for varying (a) B1, (b) B2, (c) B5 and (d) B6 shape coefficients at $75^\circ$ yaw angle. ....	276

Figure 6.35 Correlation between aerodynamic side force coefficient measured from CFD and calculated by the proposed prediction methodology for various truck-trailer geometries. .... 278

# LIST OF TABLES

---

Table 1.1 Commercial vehicle categories by weight .....	3
Table 1.2 Parametric limitations of the truck-trailer units .....	6
Table 3.1 Domain independency .....	62
Table 4.1 Further validation of drag force coefficient (a), lift force coefficient (b), side force coefficient (c) using CFD and prediction model.....	146
Table 5.1 Variations in drag force for various truck-trailer combinations with varying B1, B2, B5 and B6 coefficients .....	204

# NOMENCLATURE

---

$B_1$	n/a	Shape Coefficient – Truck front edge
$B_2$	n/a	Shape Coefficient – Truck trailing edge
$B_3$	n/a	Shape Coefficient – Bridge front edge
$B_4$	n/a	Shape Coefficient – Bridge rear edge
$B_5$	n/a	Shape Coefficient – Trailer front edge
$B_6$	n/a	Shape Coefficient – Trailer rear edge
$C_D$	n/a	Drag force coefficient
$F_D$	N	Drag force
$\rho$	kg/m <sup>3</sup>	Flow density
$V_\infty$	m/s	Free stream flow velocity
$A$	m <sup>2</sup>	Projected frontal area
$C_L$	n/a	Lift force coefficient
$F_L$	N	Lift force
$C_S$	n/a	Side force coefficient
$F_S$	N	Side force
$l_w$	m	Wheel base length
$V$	m/s	Vehicle speed
$V_r$	m/s	Wind velocity relative to vehicle
$G_{base}$	n/a	Baseline shape
$f_i$	n/a	Shape function
$w_i$	n/a	Weighting factor
$n$	n/a	Bézier curve degree
$\psi$	Degrees	Yaw angle
$k$	Joule	Turbulence kinetic energy
$\omega$	1/s	Specific rate of dissipation (K into thermal energy)
$\varepsilon$	m <sup>2</sup> /s <sup>3</sup>	Rate of dissipation of turbulence energy
$H$	m	Height of the profile
$K$	n/a	Vertical position of start and end points of wheels

$r$	m	Wheel radius
$x$	m	Length dimension
$W_c$	n/a	Wheel centroid position
$C_p$	n/a	Coefficient of pressure
$P$	Pascal	Local static pressure
$P_\infty$	Pascal	Static pressure at free-stream location
$V_w$	m/s	Wind velocity
$V_v$	m/s	Velocity of truck-trailer unit
$\alpha$	Degrees	Direction of wind
$l$	m	Truck-trailer length
$h$	m	Truck-trailer height
$w$	m	Truck-trailer width
$C_{D0}$	n/a	Drag coefficient corresponding to zero degree flow angle
$L_{BL}$	n/a	Bottom left line
$L_F$	n/a	Front line
$L_{BR}$	n/a	Bottom right line
$L_T$	n/a	Top line
$L_{TL}$	n/a	Top left line
$L_{TR}$	n/a	Top right line

# CHAPTER 1

## INTRODUCTION

---

Truck-trailer units are primarily used as a key component within the transportation industries around the world. The large surface areas coupled with high operational speeds have forced the heavy goods vehicles to become prone to producing high resistive forces, hence consuming more fuel. The possibilities of making truck-trailer units more aerodynamic and economical have been looked at by various researchers over the years, making considerable progress. The scope of shape alterations of truck-trailer units is rather limited due to cargo capacity and dimensional constrictions. Aerodynamic add-on devices have been employed over the past century attaining success in making truck-trailer units more fuel efficient and have become popular in the industry. The shape optimisation of truck-trailer units remains the most effective and efficient method for making these vehicles more fuel efficient and hence more economical. This chapter provides an insight into truck-trailer industry and the adverse resistive forces acting on truck-trailer units. Also, the current measures that are in place to make the truck-trailers more aerodynamic are discussed along with the various shape optimisation methods and parameters that could be used to optimise the shape of these vehicles.

## 1.1 Introduction into the UK Transportation Industry

Goods transportation sector in the United Kingdom is supported by well-structured Rail, Road and water networks. Transportation was revolutionised in the United Kingdom in the 18<sup>th</sup> century with the opening of the first major railway from Liverpool to Manchester, and by 1840s, there was a huge surge in building the railways. Most cities were connected in the United Kingdom by railways, making the goods transportation more convenient.

Post 19<sup>th</sup> century, UK saw a significant growth in production and goods transportation due to the industrial revolution. In 1953, 89 billion tonne kilometres of goods were moved in the UK, with the rail transportation accountable for more than 42% share while road transportation was lagging behind with only 36%. However, by 2002 the amount of goods moved had seen a rapid increase and had almost trebled having moved 254 billion tonne kilometres. Moreover, by 2002 the rail transportation had seen a rapid decline of usage having only transported 7.5% of goods. On the other hand, road transportation has moved to 62% of goods transportation and has become the main source of inland goods transportation in the UK [1].

The statistics of goods moved in the UK by various transportation modes from 1990 to 2010 are depicted in Figure 1.1. It is evident that by 1990, road transportation has become the major mode of transportation in UK. The goods moved in 2010 is almost at the same level as in 1990 due to the economic turbulence created by the recession. Since 2010, the economy and manufacturing industries have recovered from the economic recession. Therefore, an increased amount of goods haulage is expected in the future.

The road transport industry in the UK consists of both single bodied small delivery vehicles and multiple axial, multiple bodied articulated vehicles. These are further classified into categories based on the weight of the vehicles. Table 1.1 summarises the commercial vehicles' categories used by road transportation industry in the UK. Out of these two main categories, articulated vehicles are responsible for long distance goods transportation. According to the Department for Transport's statistics, articulated truck-trailer units move the most amount of goods throughout the UK.

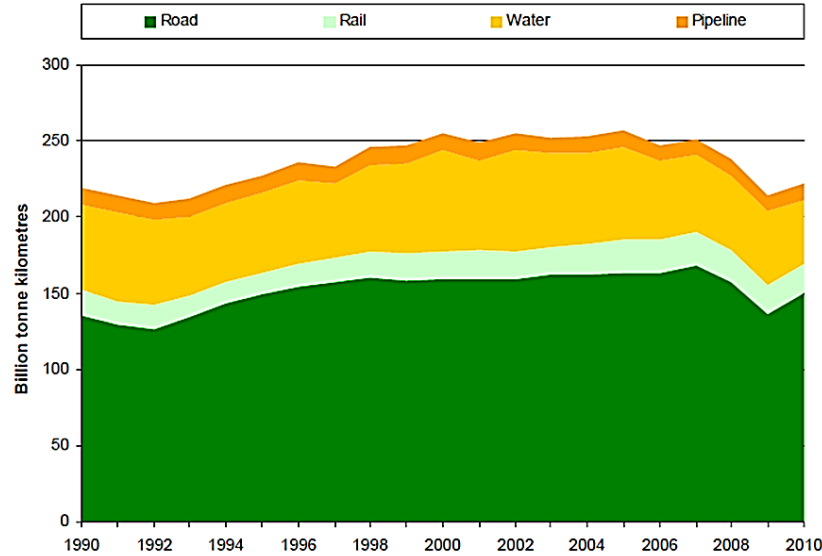


Figure 1.1 Domestic goods moved by mode 1990 to 2010, Great Britain [1]

Table 1.1 Commercial vehicle categories by weight

<b>Rigid Vehicles</b>	<b>Articulated Vehicles</b>
Over 3.5T to 7.5T	Over 3.5T to 33T
Over 7.5T to 17T	Over 33T
Over 17T to 25T	
Over 25T	
T = Tonne	

The graph shown in Figure 1.2 displays the amount of goods moved by articulated vehicles and rigid vehicles from 1990 until 2010 in the UK. Upon examining the graph, it is clear that since 1990, articulated vehicles had moved most amount of commodities throughout the UK. A drop in the usage of articulated vehicles can be seen after 2007 and this could most certainly be due to the economic recession. However, after the year 2009, there is a sharp increase in the number of articulated vehicles used to transport goods compared to the rigid vehicles. Heavy commercial vehicles sector dominates the road transportation industry and has become one of the key components of modern day freight transportation industry. In present day, truck-trailer units move about 83% of the total freight tonnage that accounts for 4.8 million tonnes of goods each day in the UK.

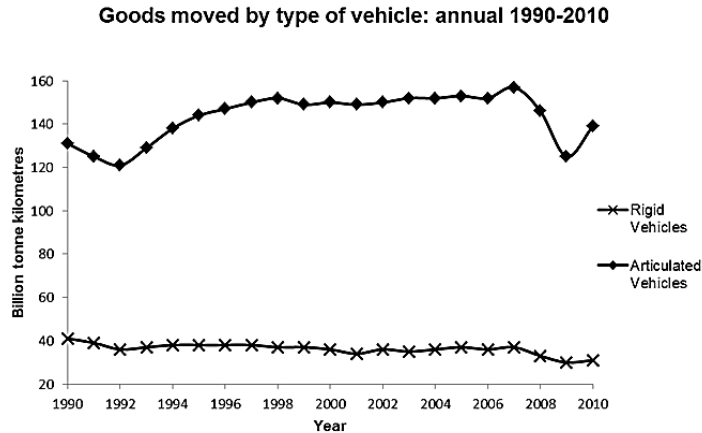


Figure 1.2 Goods moved by Articulated and Rigid vehicles in UK between 1990 and 2010 [1]

## 1.2 Heavy Commercial Vehicles

Modern day heavy commercial vehicles are fitted with powerful engines that enable them to pull heavy loads with ease, along with the large bluff bodied trailer units in order to transport maximum amount of cargo from one place to another. A truck unit attached to a trailer unit is often called a semi-trailer truck unit, or in this study, a truck-trailer unit.

Over the last couple of decades, the heavy commercial vehicles' sector has changed from having rigid vehicle units to having more flexible articulated truck-trailer units. This transition happened most likely to avoid a number of operational implications. Heavy commercial vehicles are naturally longer than any other road vehicle. Therefore, the manoeuvrability of the vehicle is an extremely important factor. The conventional vehicles with rigid trailers were fixed to the truck unit whereas the articulated semi-trailers have the turning point near the king pin. Furthermore, they can be coupled and un-coupled in a short space of time. So, various truck units can be used to transport the goods while causing minimum disturbance to the goods in the trailer units.

Single deck trailer units are the most common type of truck-trailer configuration and they are more commonly used in mainland Europe due to the 4.0m height restriction. Single deck trailer units are mainly being used to transport heavy cargo loads due to their rigid body and low centre of gravity. The maximum length, height and the width of the single deck trailer units are restricted to 16.2m, 4.0m and 2.6m respectively. Compared to double-deck trailer units, the load

carrying capacity of single-deck trailers are clearly limited. However, due to small frontal areas, they produce less interference to the oncoming flow and therefore have better aerodynamic characteristics over double-deck trailers.

Over the last couple of years, the double-deck truck-trailer configurations have become a common sight in UK transportation network. Maximum height of double-deck trailers has been increased up to 4.9m in the United Kingdom. Double-deck trailers allow the transport companies to gain extra vertical cubic space allowing them to transport double the amount of goods in a single trailer unit while staying within the legal weight limits. This distribution in load permits a more efficient goods distribution while reducing the fuel consumption and therefore exhaust gas emissions per tonne of goods delivered. A truck-trailer unit in tandem with a single and double deck trailer unit is shown in Figure 1.3.



Figure 1.3 Generic single deck truck-trailer unit and a double deck truck-trailer unit

It is worth noting that there is very limited amount of data available on double-deck trailer fuel consumption compared with generic single-deck trailer units. Due to the increased frontal area, it can be assumed that the double-deck trailers are less aerodynamically efficient compared to the single-deck trailer units. According to a study conducted by Lawrence David Ltd and MIRA in

2004 [2], increasing the trailer height from 4m to 4.875m had resulted in a 5-6% increase in truck-trailer fuel consumption. Nevertheless, more research is required in order to clearly understand the aerodynamic implications of using double-deck trailers.

### 1.3 Dimensional Restrictions of Truck-Trailer Units both in Europe and in UK

Truck-trailer manufacturers are always under pressure from freight companies to design and build trailer units that are capable of carrying maximum amount of cargo. However, factors such as operational restrictions and legislation mean that there is a very limited scope of changing the dimensions of trailer designs significantly. This in turn makes it difficult to produce heavy goods commercial vehicles that are more economical to operate.

The key design restrictions of truck-trailer units are quite simple and straightforward. Various countries impose various regulations and legislation on parametric limitations of truck-trailer designs. The parametric limitations that are applicable to UK and Europe are depicted in Table 1.2.

Table 1.2 Parametric limitations of the truck-trailer units

Parameter	Truck-trailer unit
Maximum Width	2.6m
Maximum Length	16.5m (In United Kingdom and Ireland )
	18.0m (In Italy)
	19.0m (In Australia)
	21.55m (In Canada)
Maximum Height	4.0m (In Europe)
	4.9m (In United Kingdom)
Maximum distance between kingpin and rear	12m
Maximum distance from kingpin to any point on the front	2.04m
Maximum gross weight	26,000kg (3 axles)
	38,000kg (4 axles )
	40,000kg (5 axles)
	45,000kg (6 axles)

The design restrictions displayed in Table 1.2 mean that key truck-trailer geometrical dimensions cannot be changed in order to make them more economical. Therefore, the truck-trailer designers have to operate within these limitations to produce streamlined truck-trailer units while not compromising on haulage capacity or crossing legal boundaries.

## **1.4 Fuel Efficiency for Truck-Trailer Units**

Around 1950's and 1960's, the global economies were growing rapidly and hence, the low and virtually non-fluctuating fuel prices had made fuel a key component that controls the global economy. The first fuel crisis the world faced befallen around 45 years ago in 1973, when the Organization of the Petroleum Exporting Countries (OPEC) decided to increase the fuel prices significantly. This decision had a significant adverse effect on transportation industries and the ripple effect was reverberated throughout the world leading economies. This situation encouraged the truck-trailer industry to research and produce more streamlined, hence more fuel efficient, vehicles to maintain profitable operation. Nowadays, the global focus is shifting towards reducing overall emissions, impact of greenhouse gases on the climate and the environment. The target of EU 20-20-20 energy and climate change policy [3] focused on reducing the greenhouses gases by 20%, energy consumption by 20% and utilising renewable energy sources to obtain 20% of the energy requirement. Because of these issues, the focus today has shifted from achieving higher speeds to conserving more energy and reducing the carbon footprint in the truck-trailer industry. This feat can only be achieved by producing more aerodynamically efficient and streamlined truck-trailer units. In order to do so, it is vital to first understand the various resistive forces acting on the truck-trailer units.

## **1.5 Resistive Forces Acting on Truck-Trailer Units**

The fuel consumed by a truck-trailer unit is converted into mechanical power by the engine and is used to generate a tractive force at the wheels. This tractive force must overcome all the resistive forces acting on the vehicle in order to sustain steady-state motion. The operating fuel economy of truck-trailer units depend on number of factors such as:

- Aerodynamic resistance - Resistance from pressure drag and skin friction drag causes the engine to work harder in order to move the vehicle forward.
- Characteristics of the engine - Engine capacity, age, wear etc. are some of the main factors that affect the fuel economy.
- Weight of the vehicle - Size of the vehicle and how much load is being transported affects the fuel consumption.
- Rolling resistance - Wear and tear and air pressure on tires can increase rolling resistance and increase fuel consumption.
- Transmission characteristics - A slipping clutch, four-wheel drive system or general wear within the transmission setup affect the fuel consumption.
- Driving cycle (conditions) - Driving short distances and using mountainous roads increase fuel consumption.
- Driver behaviour - Speeding, rapid acceleration and poor planning ahead are some of the factors that affect the fuel economy.

The truck-trailer units must overcome the resistive forces mentioned above to move forward. The aerodynamic drag force and the rolling resistance are the two most dominant resistive forces. At lower vehicle speeds, the rolling resistance is the most dominant force resisting a vehicle's forward motion. However, as the vehicle speed increases, the aerodynamic drag becomes the most dominant resistive force. The drag force increases proportionally with the square of the vehicle's speed.

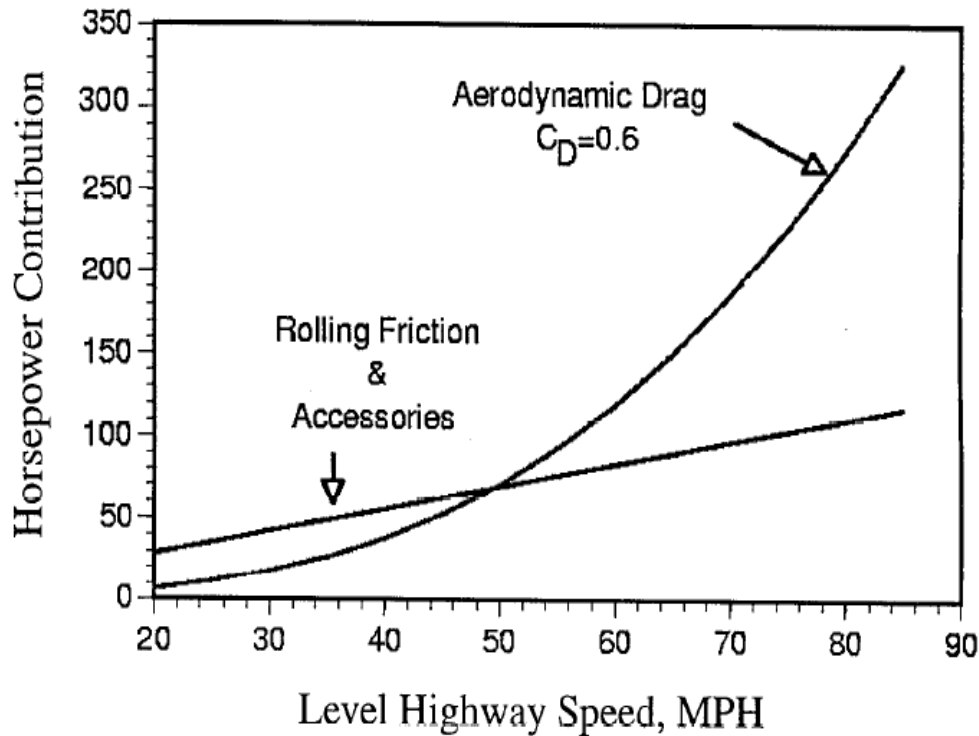


Figure 1.4 Horsepower required to overcome the aerodynamic drag and rolling friction as a function of travel speed for a typical Class 8 truck-trailer [4]

Figure 1.4 illustrates the required amount of horse power to overcome aerodynamic drag and rolling resistance as a function of speed for a class 8 truck-trailer unit with an associated drag coefficient of 0.6. The data shown in figure 1.4 was obtained by Rose et al [4] in 1999 and it is claimed that at a speed of 70mph, around 65% of the total energy generated by the engine is used to overcome the aerodynamic drag force. So, above the 50mph threshold aerodynamic drag becomes the most prominent resistive force acting on truck-trailer unit and most of the energy produced by the engine will be used to overcome this resistive force.

Figure 1.5 depicts the proportion of fuel needed to overcome the drag force, rolling resistance and the drive train losses. At normal cruising conditions the aerodynamic drag force is the most prominent resistive force accounting for over 50% of the resistance to motion. Around 40% of fuel is required to overcome the rolling resistance and around 5% to 7% of the fuel is used to overcome the drive train losses. By looking at Figure 1.5, immediately it is evident that the aerodynamic drag force greatly influences the fuel consumption of a heavy goods vehicle.

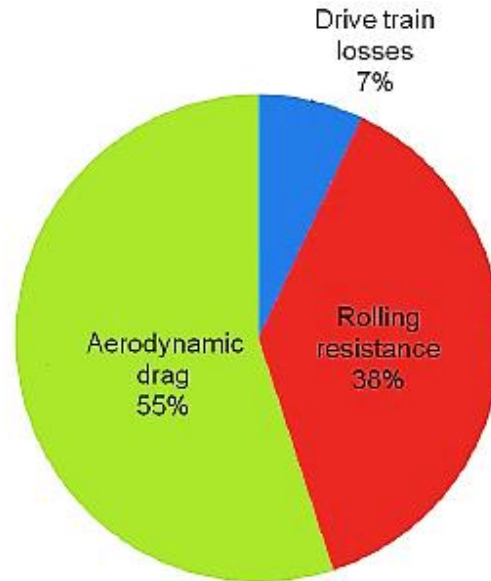


Figure 1.5 Main resistive force acting against a moving Heavy goods vehicle [3]

In Figure 1.6 the fuel saving data given are based on overall consumption in real conditions and various route profiles were taken into consideration and along with the idealized level road driving.

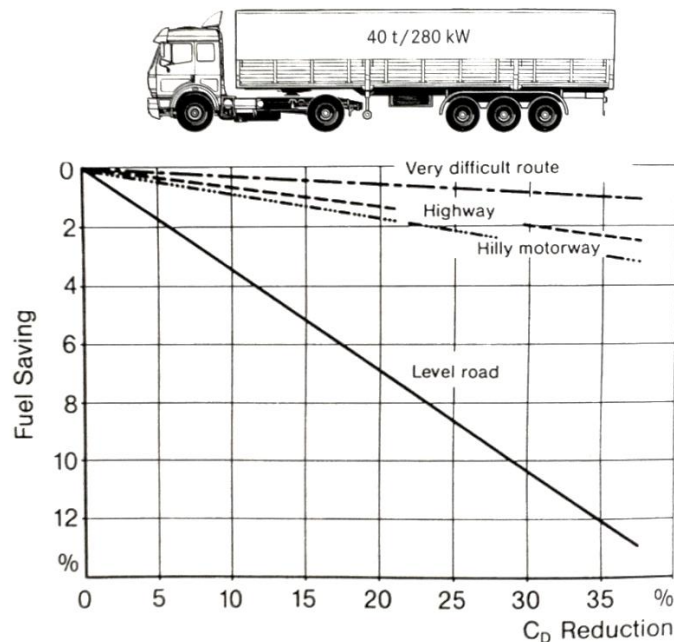


Figure 1.6 Influence of drag on fuel consumption of a 40ton truck-trailer unit [6]

Aerodynamic drag force acting on the truck-trailer unit is a resistive force that acts in the opposite direction when moving through air. The total aerodynamic drag force experienced by the truck-trailer unit is the sum of pressure and frictional forces. For truck-trailer units, the primary drag force is the pressure drag generated by wake regions. The pressure drag is defined as the net rearward drag force generated due to relatively low pressure areas at the rear portion of the vehicle with respect to relatively high pressure areas at the front of the vehicle. This highlights the importance of making the truck-trailer units more aerodynamic and streamlined to reduce pressure drag component [6] [92].

Figure 1.7 below depicts the aerodynamic forces acting on a truck-trailer vehicle. Once the total drag force is obtained it is possible to calculate the drag force coefficient. It is a dimensionless quantity and a useful parameter when comparing the aerodynamic efficiency of various vehicle designs regardless of the operating speed and the size.

$$C_D = \frac{F_D}{\frac{1}{2} \rho V_\infty^2 A} \quad (1-3)$$

Here,  $F_D$  denotes for drag force,  $\frac{1}{2} \rho V_\infty^2$  is the dynamic pressure and  $A$  is the projected frontal area of the truck-trailer unit.

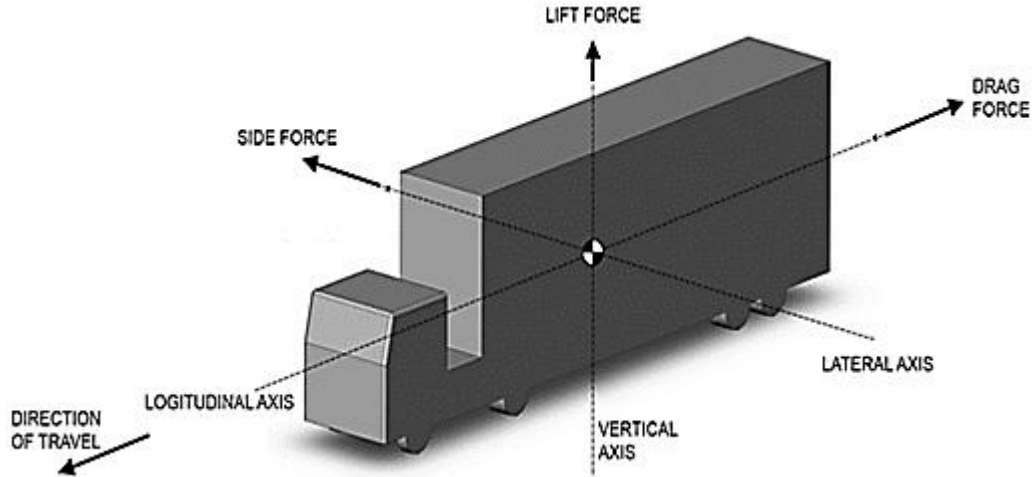


Figure 1.7 Aerodynamic forces acting on a vehicle

Coefficients of these forces can be calculated using the same analogy as the drag force coefficient.

$$\text{Lift force coefficient} \quad C_L = \frac{F_L}{\frac{1}{2} \rho V_\infty^2 A} \quad (1-4)$$

$$\text{Side force coefficient} \quad C_S = \frac{F_S}{\frac{1}{2} \rho V_\infty^2 A} \quad (1-5)$$

Where,  $F_D$ ,  $F_L$  and  $F_S$  is drag force, lift force and side force respectively where the projected frontal area of the vehicle is denoted by  $A$  [6].

By rearranging equation 1-3, it is possible to obtain the expression for the drag force. The drag force is defined as follows

$$F_D = \frac{1}{2} \rho V_\infty^2 C_D A \quad (1-6)$$

The headwind and tailwind plays a significant role of ambient wind resulting in modification of equation 1-6 as follows

$$F_D = \frac{1}{2} \rho (V + V_r)^2 C_D A \quad (1-7)$$

Where,  $V$  is the vehicle speed and  $V_r$  is the wind velocity relative to vehicle.

## 1.6 Flow around a truck-trailer model

The air flow is expected to separate at the sharp edges around a truck-trailer unit before re-attaching towards the rear of the vehicle. If the former case is true, the viscous effects of the flow will be limited to thin layer of air flow close to the vehicle surface. This thin flow layer is known as the boundary layer. The flow velocity near the surface is zero and gradually increases away from the surface joining the free stream flow velocity away from the vehicle as shown from the Figure 1.8 below.

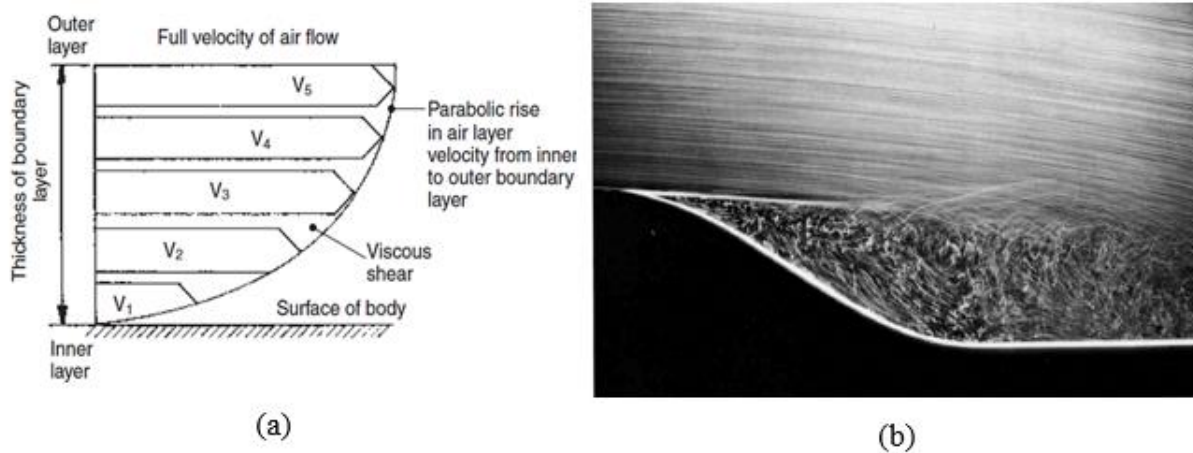


Figure 1.8 Velocity gradient in the boundary layer (a) and flow separation from a curved wall (b) [7]

The positive pressure gradient in the direction of the flow encourages the flow separation by slowing down the boundary layer. The drastic changes in the vehicle surfaces such as leaning away from the flow increases the flow separation [7, 8, 92]. In the case of truck-trailer units, the flow separates around the truck and the trailer leading edges generating viscous wake regions behind the truck and the trailer units. The position of flow separation is also dictated by the flow characteristics within the boundary layer. The flow phenomenon around the truck-trailer units are rather complex and the separation and reattachment of the air flow is expected to take place at various positions along the surfaces.

Moreover, flow often separates away at multiple locations on a bluff bodied vehicle such as a truck-trailer unit. The separation will significantly alter the pressure distribution around the

truck-trailer unit as this will give rise to substantially low pressure regions at the rear of truck and trailer unit. These low pressure areas are also known as wake regions where low velocities and low pressures exist. The net pressure drag could be calculated by integrating the force components along the direction of the flow.

Air tends to flow from high pressure regions to a low pressure regions and this pressure difference creates a force in the direction of the flow. This is called the pressure drag and this is considered to be the most significant contributor to the overall drag force experienced by a truck-trailer unit. By designing streamlined truck-trailer units, it is possible to reduce the pressure drag acting on the vehicle. However, implementing drastic design changes on truck-trailers are extremely difficult due to legal and operational restrictions.

Figure 1.9 illustrates the basic air flow patterns around a truck-trailer unit. From the Figure it is possible to see that the flow separates above and around the truck unit impinging on the front of the trailer unit and again separating around the top-front end of the trailer unit and at the back of the trailer unit. This separation phenomenon generates high turbulence flow, which in turns produces pocket regions of wake flow where low velocity flow and low pressure regions exist.

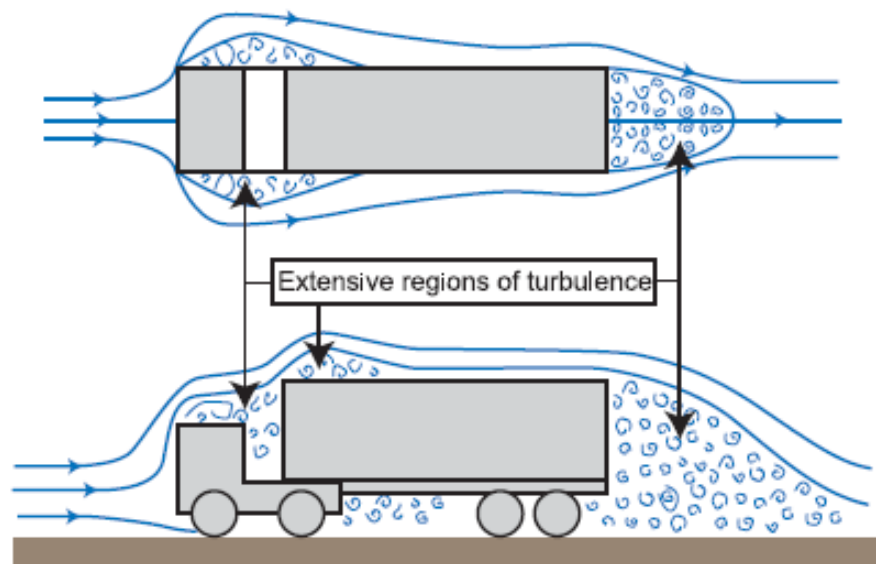


Figure 1.9 Typical air flow patterns around a non-aerodynamic truck-trailer unit [1]

The total drag force acting on a truck-trailer unit is also contributed by the low pressure inside the gap region between the truck and the trailer unit. If this gap was small, both the rear face of the truck unit and the front face of the trailer unit would have roughly the same pressure hence the forces produced will cancel out. However, in this study the truck-trailer gap will be maintained at a constant length. As discussed previously, there are number of limitations and regulations to meet when it comes to optimising the design of truck-trailer units. Firstly, they should be able to carry maximum amount of cargo, hence the trailer units need to be as spacious as possible while adhering to the design regulations. The ability of the truck unit to turn relative to the trailer means that a sufficient gap should be maintained between the truck and the trailer.

These design limitations paved the way for externally mounted drag reducing devices to become popular in the heavy good vehicle industry within a very short time period. At present, there are number of different add-on devices in the market. Each add-on device is designed and used to treat a specific flow area of a truck-trailer unit. For example, the truck roof fairing is used to deflect the flow over the truck to the top of the trailer. Moreover, the side skirts are designed to stop the flow entering underneath the trailer and to maintain an undisturbed, fast moving underbody flow profile.

### **1.6.1 Active Flow Control Devices**

Active flow control devices work by using a secondary energy source to function such as compressed air or an electric motor. These devices are rarely used in the industry due to high installing and maintenance costs. Alvarez et al [10] and Favre [11] first used a running belt on the upper surface of an aerofoil and discovered that this delays the boundary layer separation at the leading edge of the aerofoil. Singh et al [12] has carried out some studies to look into the feasibility of applying this method into truck-trailer units. The results indicated a reduction in aerodynamic drag force. MSBC (moving surface boundary-layer controller) device consists of a rotating cylinder fixed at the front-top edge of a trailer unit rotating in the stream wise direction. Having this rotating cylinder at the leading edge of the trailer unit minimised flow separation by injecting kinetic energy to the flow by recovering the velocity lost due to dissipation of kinetic energy of the flow. Studies conducted by Modi et al [13, 14,15] and Malviya et al [16] support

the theory of MSBC devices being able to decrease the drag value from 6% up to 23%. The most drag reduction was produced as a result of using material with surface roughness of grade 40. In addition, it is also reported that if splined cylinders were used it is possible to reduce drag by up to 35% [17]. Robson and Ahmed [18] successfully employed a rotating ventilator technique which proved beneficial in terms reducing drag while not having an adverse impact on cargo space. Buckley and Marks [19] utilised the engine cooling airflow as a blowing and suction mechanism to successfully increase the pressure in the wake region to reduce the drag force. Agarwal [20] has refined the techniques used by Buckley and Marks by injecting a powerful jet of air using an oscillatory jet actuator device to further reduce the drag. A truck-trailer model with a MSBC device is shown in Figure 1.10.

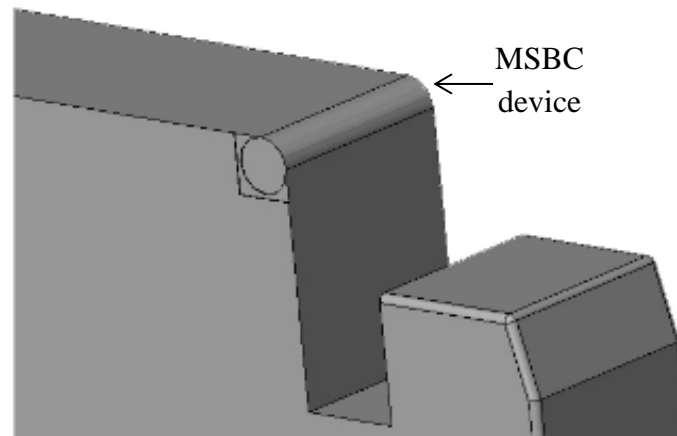


Figure 1.10 A truck-trailer unit with a MSBC device located at the top edge of the trailer unit  
[21]

## 1.6.2 Passive Flow Control Devices

Passive flow control devices operate by changing the oncoming flow profiles using their shapes. They are the most widely used type of add-on devices for truck-trailer units and are commonly used in almost all truck-trailer configurations that currently operate in the UK. These are much cheaper to manufacture and install compared with active flow control devices and often come with no running/maintenance costs. There are many types of passive add-on devices and some of the most commonly used devices are listed below.

1. Truck roof fairing – A device that is mounted on top of the truck to direct oncoming flow smoothly over to the trailer unit.
2. Corner vanes – Devices that are mounted on either side of the truck unit to direct the oncoming flow along either side of the truck-trailer unit.
3. Side skirts – A device mounted at the bottom of the trailer unit to attain smooth flow under the truck-trailer unit.
4. Truck-trailer gap seals – A device that eliminates crossflow through the truck-trailer gap at high crosswind angles.

By using these devices, it is possible to make the truck-trailers more streamlined and hence reduce the flow separation, ultimately reducing aerodynamic drag force. This in turn will reduce the fuel consumption and lower the truck-trailer emissions. Krishna and Ram [22], Jing et al [23], Marks et al [24], Bavraktar [25] and Das et al [26] have carried out research on the effects of cab roof fairing devices on truck-trailer unit aerodynamic characteristics. Various cab roof fairing sizes and shapes were used to identify the most effective configuration. Dominy [27] and Wang et al [28] has studied the optimum position of the cab roof deflector with respect to the trailer height. It was found that, cab roof fairing devices were extremely effective in minimizing flow separation, hence reducing drag force. Ali and Mahmood [29] and Chowdhury [30] have investigated the use of a combination of add-on devices including base flap and splitter plate devices as well as front fairing, side skirting and gap filling methods which resulted in significant reduction in drag.

## **1.7 Effect of Shape on truck-trailer aerodynamics**

There is a direct correlation between the force acting on an object and its shape. This was pioneered first in the motorsport sector where the need for more speed resulted in exploiting all possible avenues. It was not long until designers discovered the concepts of drag, lift and side force and learned the significant impact the shape of a vehicle has on these forces. As a result, the vehicle shapes in motorsport have been highly streamlined to produce less drag and lift forces. Hucho and Sovran [31] further iterated this by stating that nature's own tear drop exhibits

the most aerodynamically evolved shape, smooth sloping lines. The same applies to truck-trailer units, however this means a compromise has to be made between the ‘cuboid’ storage space and the extent of aerodynamic shaping. This has been further explored by Cooper [32] where the influence of the truck, trailer shape and yaw angle on resulting drag force was analysed in detail. In summary, the studies show that blunt, sharp edged bodies result in high aerodynamic drag which is due to flow separation and reversal giving rise to turbulent zones. The pressure distribution of a generic truck-trailer unit is depicted in Figure 1.11 where the low pressure due to separation is evident. It was discovered as the shape of the truck was modified by changing the blunt edges into smooth curves the aerodynamic drag was drastically reduced. The possibility of add-on modifications which ultimately alter the shape of truck or trailer were also found to reduce the drag. However, these mechanisms require fine tuning and regular attention and maintenance to obtain the best results.

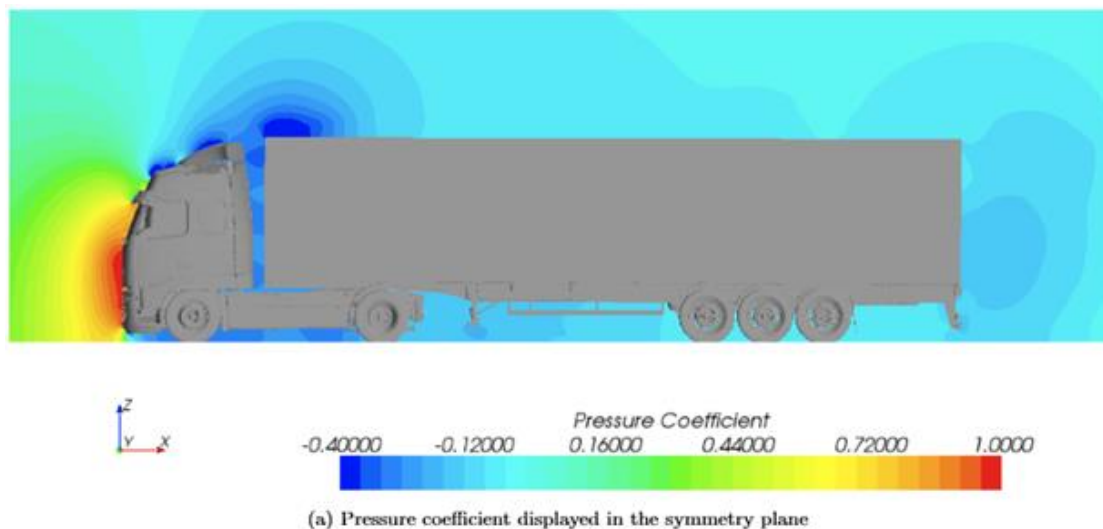


Figure 1.11 Pressure distribution around a generic truck-trailer unit [33]

Changing the shape of the trailer as well as other changes such as base drop, gap elimination, wheel covers prove to reduce overall drag acting on the truck trailer [33]. Figure 1.12 below presents a teardrop shaped trailer. The theory being, having smooth curved surfaces without gaps discourages flow separation, which reduces turbulent flow. Furthermore, wind flow from 2 yaw angles have been tested ( $0^\circ$  and  $5^\circ$ ). One trend that was noticed in these studies was that, they all attempt to discuss all possible solutions such as shape alterations, add-on modifications, flow direction and driving conditions etc. This prevents the study from being able to look into any one

solution in great depth to truly optimise that particular solution. For example, in order to gain a deeper understanding of how the flow interacts with shape alterations, exploring a range of magnitudes for the curvature at different locations would be beneficial. Also, it has been noticed most attention has gravitated towards the trailer whereas, different combinations of truck shape alterations have not been analysed. It would also be interesting to understand how the truck-trailer as a complete unit performs with varying shape modifications between truck and trailer, hence being able to find the most effective combination.

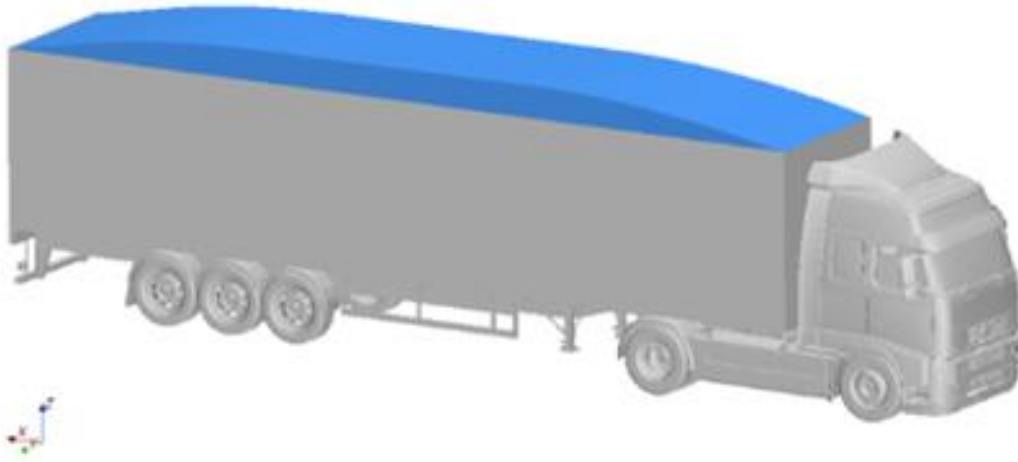


Figure 1.12 Example of a teardrop shaped inspired trailer design expected to reduce drag force [33]

## 1.8 Effects of crosswinds on truck-trailer units

The crosswinds impinging on high sided, bluff bodied truck-trailer units are known to cause stability concerns and significantly raise the safety risks. Figure 1.13 below shows a photo of an overturned lorry under similar circumstances. The crosswind force component acts in the perpendicular direction to the vehicle motion. The effects of crosswinds are known to increase when the truck-trailers are travelling through open areas such as bridges and planes. During strong crosswinds the lateral aerodynamic forces and lift force combines to increase the rolling moment about the low pressure leeward side of the vehicle. The load of the vehicle is considered to be the main stabilising factor under crosswinds. Truck-trailer overturning accidents due to crosswinds was reported to be the most common according to Coleman and Baker [34]. Purely

due to significant adverse effects possessed by crosswinds, it is considered a vital factor in truck-trailer aerodynamic studies.



Figure 1.13 Overturned truck-trailer vehicle under strong crosswinds.

Taking into account the sheer size/weight of an average truck-trailer vehicle, any type of accident has great potential to cause harm in a large scale to other road users, buildings and general public and environment. In addition, crosswinds present problems to the drivers by making it extremely tricky to operate the vehicle at any speed, at times road authorities denying access to truck-trailers on certain areas due to elevated risk. Therefore, it is imperative to understand how crosswinds interact with a moving truck-trailer.

Batista [35] explores different scenarios of how crosswinds can affect a moving vehicle. Figure 1.14 below shows three possible scenarios of crosswinds affecting a moving vehicle. Due to the superior height of a truck-trailer compared to the average road vehicle the most susceptible mode for truck-trailers is rollover. Rollover occurs when the contact force on the wheels reduces to zero. Respectively, when all wheels reach the friction limit and when one of axles of the vehicle reach the friction limit causes sideslip and rotation.

Moreover, it would be interesting to observe and understand how crosswind affects a truck-trailer. The most obvious observation would be that crosswind perpendicular to the truck-trailer would increase the overall the drag force on the vehicle. However, the same cannot be said in confidence regarding crosswind acting at a specified angle other than perpendicular. The flow field alterations and force spectrum at various crosswind angles would be beneficial to understand. In addition, understanding how the shape of the vehicle interacts with crosswind is equally important, in order to understand the stability and address various safety concerns.

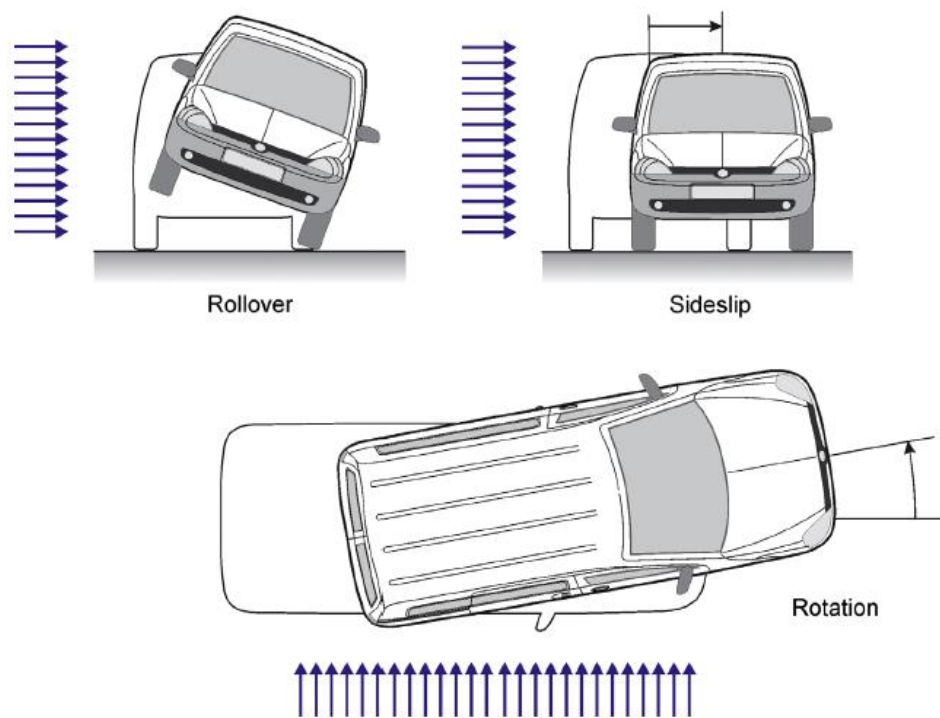


Figure 1.14 Three types of crosswind caused vehicle accidents Batista [35]

## 1.9 Overview of Vehicle Modelling and Design Process

The traditional vehicle design process starts with a number of sketches drawn by the designers on a drawing board, followed by a full scale clay model of the vehicle. This model will be used to test and evaluate the performance of various design concepts and ideas under consideration. Early in the process, the aerodynamic targets will be set to ensure that the performance criteria

can be achieved. Then the scaled models of the vehicle will be used to streamline and further refine the shape of the vehicle using wind tunnel tests in order to produce a sound conceptual design. The designers can obtain accurate data and reproduce test conditions similar to road conditions, but the number of geometric configurations and design variables associated with the initial design stage of vehicle design makes the initial design process very costly and both intensively time and resource consuming. Furthermore, the traditional design process has changed remarkably with the availability of Computer Aided Design (CAD) software combined with high performance computers. This has transformed the traditional process of hand drawn sketches and clay models. Instead, new methods have been applied such as CAD sketching and 3D modelling of the CAD software which have improved vastly over the years. Moreover, the availability of Computational Fluid Dynamics (CFD) software containing relatively accurate and comprehensively tested turbulence models are being used widely to simulate the fluid flow fields around the road vehicles. This has taken the work-load off the wind tunnels to a certain extent while cutting down the costs, time and resources required. A typical vehicle design process is illustrated in Figure 1.15. After the evaluation process, the design will be further improved by ‘CAD Design, Prototype and Evaluation’ steps being iteratively repeated until an optimised design is achieved.

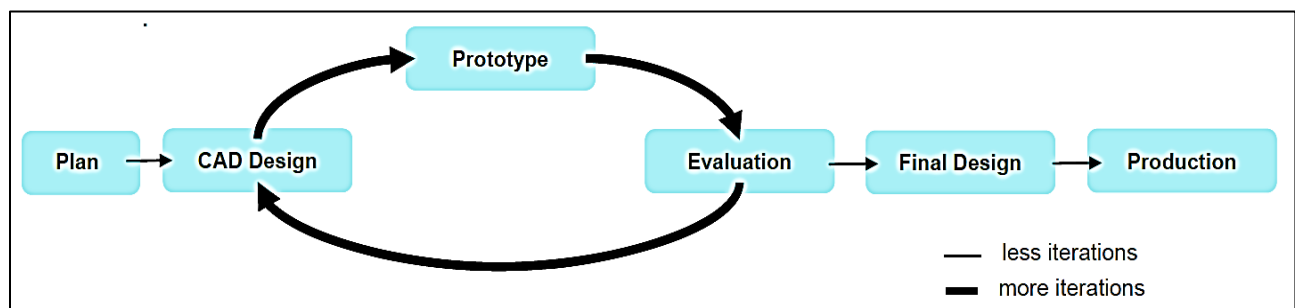


Figure 1.15 Vehicle design process [36]

### 1.9.1 Performance Based Design Considerations

Aerodynamicists are actively involved throughout the vehicle design process. They optimise vehicle performance, maximum speed, and fuel economy, while assisting designers to shape vehicles. The vehicle shape requires moving air to be directed towards the engine and brakes for

cooling purposes, while minimising wind noise and providing maximum comfort to passengers. Furthermore, it is vital to ensure that the designed vehicle is aerodynamically stable under both high speeds and various crosswind conditions. The process for aerodynamic optimisation involves reducing drag force, providing a fuel efficient design. Therefore, shape optimisation for low drag has become an essential part of the overall vehicle design process.

The aerodynamic optimisation process is considered as an extremely important and integrated aspect of vehicle development process. In the case of truck-trailer units, the design process is legally restricted to a pre-defined design space with a fixed height and a width. Therefore, the aerodynamicists must achieve the best possible truck-trailer unit design within set design limits.

### **1.9.2 Shortcomings in conventional Experimental and CFD based design methods**

Over the years CFD has emerged as an alternative for experimental methods in the sector of road vehicle design and development. This trend is driven mainly due to economic reasons where the costs of running and maintaining wind tunnels, equipment, and personnel, has limited them mainly to research facilities. In contrast to this, CFD has emerged as a relatively low cost (20%-40% reduction over wind tunnels [37]), accurate and widely recognised tool and rapidly decreasing computational costs has further increased the appeal for CFD. The experimental set ups are widely being used as a validation tool for CFD setups or towards the end of the design process only on the optimum designs. For an instant, CFD was being used to significantly reduce the number of wind tunnel tests which was required to design Boeing 777 and 787 aircrafts [38]. Albeit the relatively low cost compared to wind tunnel testing, the general operating costs of CFD techniques seemed to be quite high. Personnel costs and the infrastructure costs including computing power and software licences are seen as major drawbacks of CFD. The design optimisation using CFD is expected to be an iterative method where number of vehicle models will be generated and tested. This is known to be highly time and resource consuming. In order to have a low cost design methodology, the use of mathematical means such as geometric modelling methods and aerodynamic force prediction tools could be coupled to eliminate the need for multiple models and number of simulations to obtain an optimum model.

### 1.9.3 Potential for Mathematical Vehicle Design and Optimisation

The vehicle design optimisation process is still known to be expensive and time consuming. In comparison with traditional design methods, today's advanced computation power and software only makes the process relatively cheap. The optimisation can be either single-objective or multi-objective. The latter method of optimisation simultaneously deals with two or more conflicting objectives with respect to a set of certain constraints. In case of a truck-trailer unit, both these strategies could be used to carry out the optimisation process depending on the number of objective functions.

According to Bandyopadhyay and Saha [39], different optimisation techniques that are being used widely can be largely classified into three categories as listed below

- Calculus-based techniques
- Enumerative techniques
- Random techniques

Calculus-based methods, also known as numerical methods, use a set of necessary and sufficient conditions and these must be satisfied by the solution of the optimisation problem. Calculus-based methods can be subdivided into two categories as indirect and direct methods.

Enumerative techniques arrive at an optimum solution by evaluating every single point of the finite or discretised infinite search space. However, this technique will be ineffective when using on a moderate size or less complex problem because it might be simply impossible to search all the points in the space.

Guided random search technique uses additional information about the search space to guide the search to potential regions of search space and this technique is based on enumerative methods. This can be further divided into two categories as single-point and multi-point search. Simulated annealing is a well-known example of a single point search technique and genetic algorithms are popular examples of multi-point search techniques. Figure 1.16. depicts the different search and optimisation techniques discussed above.

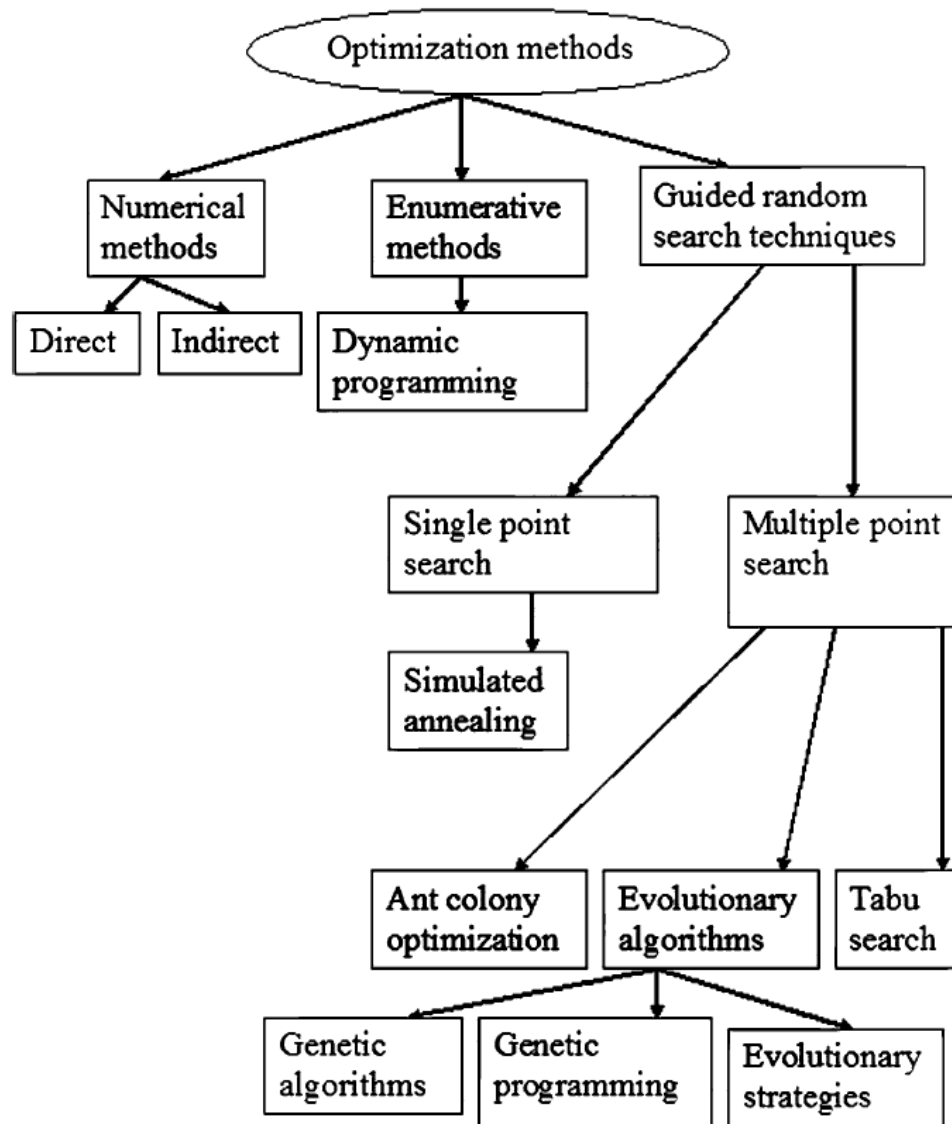


Figure 1.16 Different search and optimisation techniques [39]

#### 1.9.4 Parametric Design Process

Muñoz-Paniagua et al [40] has carried out a parametric design study on a nose shape of a high-speed train. The aim of the study was to represent the possible geometry as a design vector. A schematic representation of the optimisation scheme applied is shown in Figure 1.17. In this particular case, the number of parameters has been kept as low as possible. Also, limited range of each design variable was considered so that the design space could be reduced.

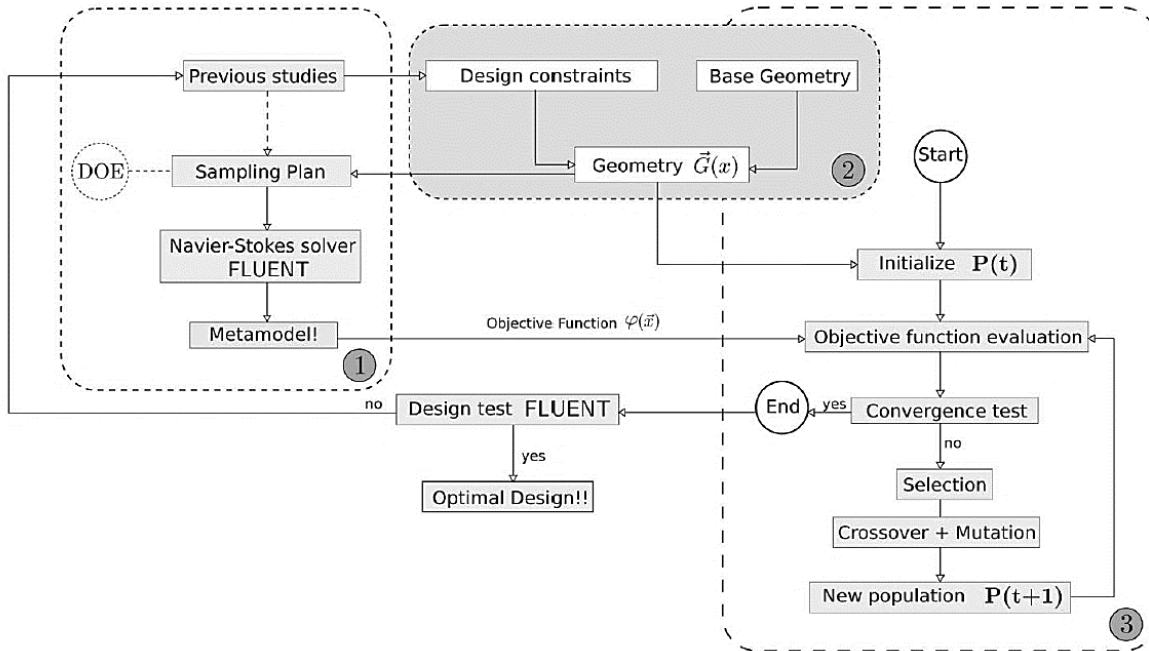


Figure 1.17 Schematic representation of the whole optimisation scheme

Various parametric techniques were taken into consideration such as potential flow equation combined with classical aerofoil parameterisation technique proposed by Guilmineau [41]. This was done to obtain a geometry of a primitive car shape. A slightly more sophisticated method of Hicks-Henne function methodology has been used to generate the train geometry [42]. The

$$G(x) = G_{base} + \sum_{i=1}^n w_i f_i \quad (1-8)$$

Hicks-Henne function is defined as:

$G_{base}$  is the baseline shape (a parabolic function) and  $w_i$  and  $f_i$  stands for weighting factor and the shape function respectively. This function is found to be quite limited as, only a limited range of different nose shapes are available, while the shapes obtained tend to be extremely simple in geometry.

After considering a number of techniques, the application of Bézier curves is proposed to generate the 3D high speed train nose as it was found to be simpler compared with Hicks-Henne function. Furthermore, the author states that the Bézier curves are coupled with underlying

polygon of control points and this simplifies the link between parameters and real design variables. The Bézier curve of degree  $n$  equation is given as:

$$\mathbf{C}(t) = \sum_{i=0}^n \binom{n}{i} (1-t)^{n-i} t^i \mathbf{P}_i \quad (1-9)$$

Where  $0 \leq t \leq 1$  is a parameter control and  $\mathbf{P}_i$  are the control points to be weighted. Set of control points  $P_0$  through to  $P_n$  are used to define a Bézier curve. The first and the last points are found to be end points of the curve while the intermediate control points are found to be situated away from the path of the actual curve. A quadratic curve is defined by three control points, while a cubic curve is defined using four control points. Once the control point's coordinates are defined, the Bézier curve can be easily generated.

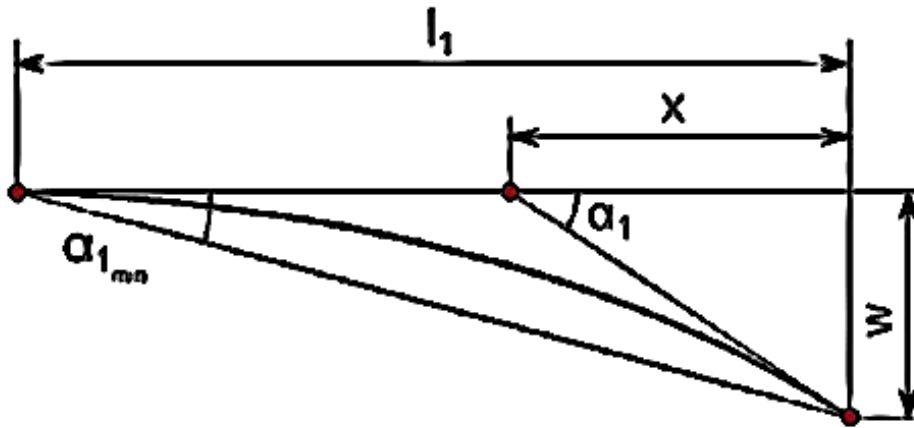


Figure 1.18 Roof shape representation using a quadratic Bézier curve. Outlined control polygon is also plotted. Red dots refer to control points [40]

Figure 1.18 illustrates the roof shape modelled using the quadratic Bézier curve defined using three points ( $P_1$ ,  $P_2$  and  $P_3$ ). The coordinates for  $P_1$  are already set as  $P_1$  is the connection point between nose and the train body profiles. Length  $l_1$ , Height  $h_1$  and Slope angle  $\alpha_1$  design variables were used to determine the coordinates for  $P_2$  and  $P_3$ .

The flexibility of the Bézier curve method is illustrated from Figure 1.19 as a using a high speed train model and the suitable fitting parameterisation variables.

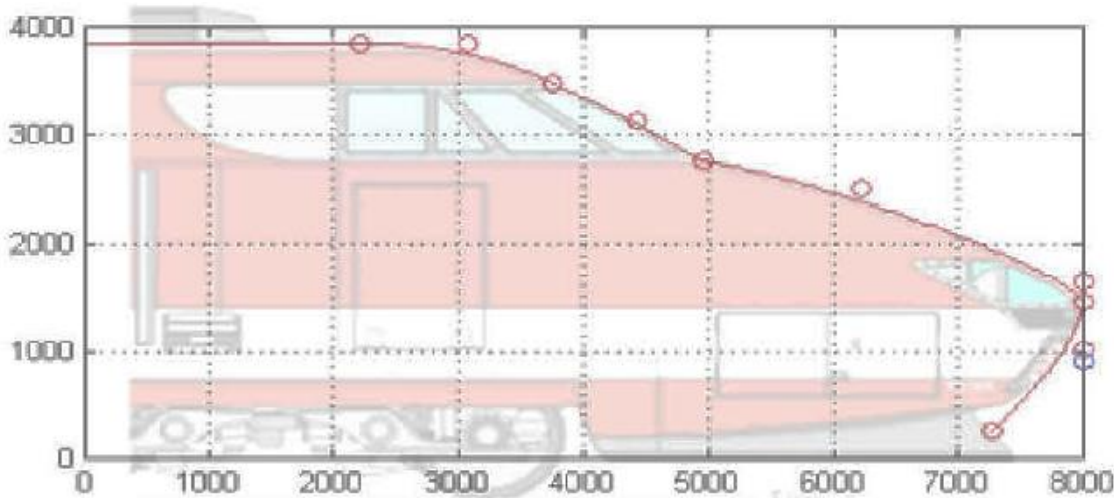


Figure 1.19 Roof shape representation using a quadratic Bézier curve. Outlined control polygon is also plotted. Red dots refer to control points [40]

## 1.10 Motivation

Truck-trailer units play a major role in transporting the goods inland. Around 70% of all goods are transported by trucks. These vehicle fleets mainly include articulated truck-trailer units. Truck-trailer units have high annual mileage and consume a great deal of fuel. Ever increasing fuel prices and environmental legislations have challenged truck-trailer designers to introduce more aerodynamically optimised and fuel efficient vehicles, while still adhering to legal design restrictions and designing for maximum load carrying capacity.

It is considered that the size of a truck-trailer unit directly influences the aerodynamic force acting on the vehicle. When these bluff bodied vehicles plough through the air, they generate pressure and velocity fields with considerable magnitudes. This in turn, generates aerodynamic forces such as drag, lift and side. Drag force acts opposite to the direction of travel and hence has a direct and a very strong influence on the fuel consumption of truck-trailer units. Add-on devices have proven to be popular to make the truck-trailer units more streamlined. However, the effectiveness of these devices depends on location, adjustment with respect to trailer dimensions, size and so on. Optimising the truck-trailer shape is considered to be the most effective and assured method for streamlining truck-trailers. However, the conventional truck-trailer design

process is known to be highly iterative where a significant number of experiments or CFD simulations are carried out involving a range of CAD or clay models. The CFD methods have been favoured over experimental methods in recent years as access and resources to wind tunnels are limited and have higher associated costs. Yet, the CFD methods are known to be tedious and very resource intensive. This creates the need for more robust and efficient design methodology where numerous models can be generated within a limited time frame. The proposed design methodology in this study is expected produce a cost effective and efficient design tool to replace the conventional design method.

Dimensions and the shape of truck-trailers have a considerable impact on the adverse forces acting on them. In the case of truck-trailer units, the oncoming flow usually separates at the leading edges of the truck and the trailer. This separation of flow creates circulating flow regions having low pressure air pockets above the surfaces of truck-trailer units and in the gap region between truck and the trailer. By controlling the boundary layer, it is possible to reduce the flow separation and this is expected to alter the forces such as drag, lift and side. Crosswinds can generate adverse pressure gradients on either side of truck-trailers causing instability thus increasing safety concerns. Significant flow separation occurs on windward edges around truck-trailer units and this phenomenon is more prominent in these boxed shaped vehicles. Even though research is carried out on truck-trailer aerodynamics, limited research is available on the effects of dimensions and the shapes of these vehicles and how they affect the flow field and resulting aerodynamic forces. This research considers both global and local flow parameters and studies the effects of truck-trailer shape on the resulting aerodynamic characteristics at both, straight headwind and crosswind scenarios.

The concept of developing a force prediction tool with respect to the design parameters in the geometric modelling methodology is expected to provide a much needed all-round solution for the truck-trailer design process. This is expected to be a viable alternative for time and resources intensive iterative design process. The final solution achieved at the end of this study is expected to be an accurate, robust, effective, easy to implement and advantageous tool considering the economic aspects without the need of numerical or experimental based studies.

## 1.11 Research Aims

The aim of this study is to propose an alternate truck-trailer design methodology and an aerodynamic force prediction tool considering both vehicle design and economical aspects. Based on the research motivation outlined in section 1.10, research aims are broken down into several sections as follows:

1. An alternative design methodology for bluff bodied truck-trailers and development of a novel aerodynamic force prediction tool, based on key truck-trailer dimensions at straight and crosswind profiles
2. Design capabilities of the proposed methodology to generate complex truck-trailer shapes and development of a novel aerodynamic force prediction tool, based on truck-trailer shapes at straight headwinds.
3. Development of a novel aerodynamic force prediction tool correlating both dimensional and shape effects considering crosswind profiles.

These aims cover both design and aerodynamic characteristics of truck-trailer units and will be quite useful in the pursuit of lower fuel consuming truck-trailer units with a lower environmental footprint. A comprehensive literature review is presented in the next chapter based on the three research aims listed above.

## CHAPTER 2

# LITERATURE REVIEW

---

This chapter highlights the existing experimental, numerical and analytical studies along with their knowledge gaps in the areas of geometric modelling techniques and optimisation, truck-trailer shape effects on aerodynamic characteristics and the flow behaviour and resulting aerodynamic phenomena at crosswinds. An extensive literature review has been presented which has been structured along the research aims mentioned in the previous chapter. Scope of research has been defined and the research objectives have been drawn based on the knowledge gaps discovered from the literature review.

## 2.1 Geometrical modelling techniques for road vehicle design optimisation

Rho et al [43] conducted an analytical study on applying a functional design method to road vehicle aerodynamic optimisation in the initial design stage. The authors investigated the concept of employing shape functions in order to control and alter aerodynamic shape parameters, as well as extracting geometric data via simple calculations. Each sector of the vehicle was categorised as a box model, which made it easy and efficient to represent and modify the details in the configurations. In addition to this, by categorising the vehicle sections, it made it possible to employ Bernstein polynomial curves to define complex 3D vehicle shapes by an accurate solution. This function carries the capabilities to remodel existing, as well as creating new vehicle shapes. Figure 2.1 depicts the box model which has each sector of the vehicle is categorised into simple rectangular boxes. The results found that aerodynamic performance can be predicted for vehicles whereby industries can employ this in order to achieve targets for low aerodynamic drag and fuel efficiency. The authors did not explore the possibilities of applying this design technique to model other vehicle shapes such as heavy duty vehicles where improving aerodynamic characteristics can provide significant financial gains.

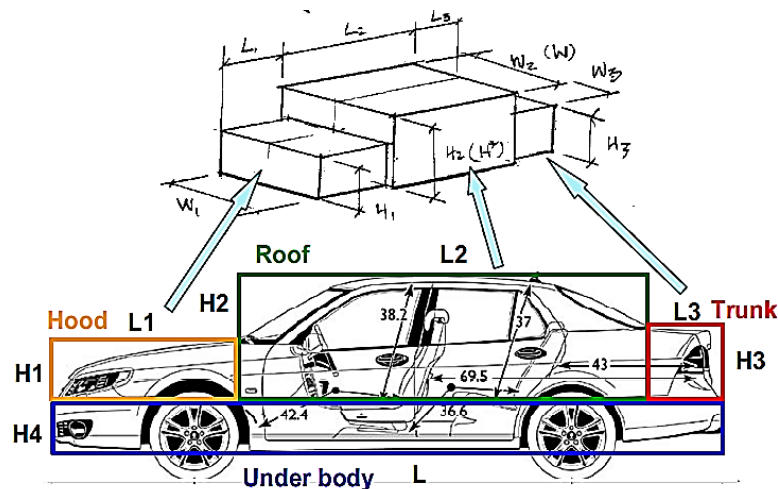


Figure 2.1 Box model category.

In 1998, Calkins et al [44] developed a novel design rule based tool for automobile systems design known as Automobile Design Support System (AutoDSS). This Knowledge-Based Engineering (KBE) tool enables users to create a virtual prototype before taking on the commitment to manufacture the product. The virtual prototype that is developed using this tool

will comprise of design rules, product model, and vehicle geometry, as well as all geometric and non-geometric characteristics. These non-geometric characteristics include materials, mass properties, stress and deflection characteristics, and so forth. The purpose of this tool was to enable design engineers to decrease for product cycle time, by examining and evaluating a wide range of design options, in good time, at increased levels of detail, and decrease the number of re-designs. This particular paper covered the phases, principles, laws, models and all aspects at which the developers implemented to create the tool, as well as taking the reader through the AutoDSS functions development to date. Figure 2.2 depicts one of the functions of the tool, known as the initializer, whereby the body type, dimensions and proportions database is employed via configuration boxes by sectioning the vehicle. At the time of the publication the researchers pointed out that the tool was still under development, however, when the tool was to be complete, it would vastly decrease the concept development stage from a time period of months to weeks.

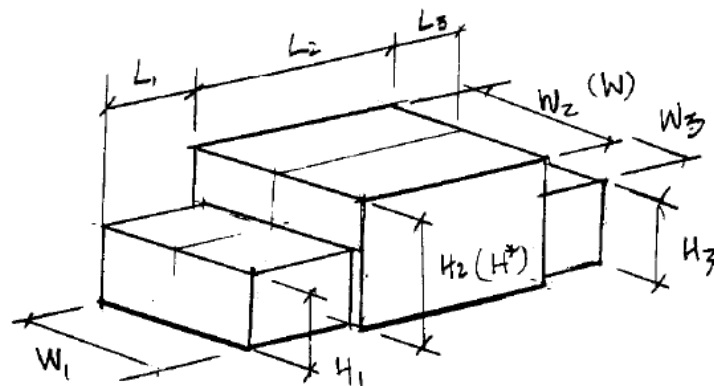


Figure 2.2 Vehicle Geometry: Configuration Boxes.

In addition to the previous review, Calkins and Su [45] also developed “CDaero”- a parametric aerodynamic drag prediction tool as a module for AutoDSS. This tool was developed using an equation solver known as TKSolver™ and was based on an algorithm developed by Motor Industry Research Association (MIRA). CDaero uses the features of the three-dimensional surface geometry control curves to predict the drag coefficient of the vehicle. There are 52 variables for the input feature values that are primarily determined from the vehicle geometry and are entered into the program. With 13 different components including the basic body and other components such as wheels and so forth, CDaero models the drag coefficient. The sum of

all these components obtains the total drag. This was evaluated and verified using five vehicles depicting an accuracy of between  $\pm 5\%$ , which could be improved.

Lietz [46] conducted an analytical study to optimise the aerodynamic shape of a pickup vehicle. The study integrates morphing, simulation and optimisation technologies into one process. This allows the aerodynamicist to optimise the shape of the vehicle and provide an in-depth understanding of design space around a given exterior. The 3D CAD geometry was designed and being simulated using a CFD setup in order to obtain the drag coefficient of the vehicle. Mesh morphing module integrated with the CFD solver was used to alter the geometry of the vehicle until a user defined drag coefficient value was achieved. A complex morphing technique was used which was capable of altering the complete vehicle shape as depicted in Figure 2.3. However, the proposed technique requires a CAD model of a vehicle designed using the conventional design techniques and is not capable of describing the shape of a vehicle.

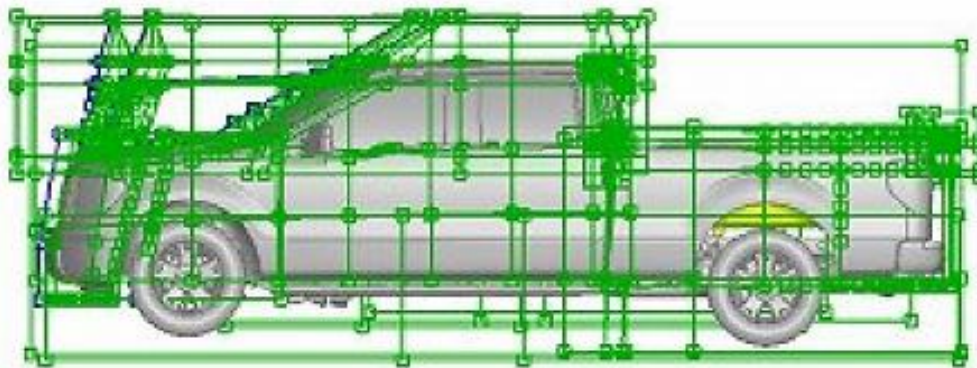


Figure 2.3 The pickup vehicle in the morphing process.

Singh [47] and Lundberg, et al [48] conducted out the study which aims to find a way of improving the fuel economy and reducing the CO<sub>2</sub> emissions of passenger vehicles using aerodynamic drag reduction techniques. An efficient method for vehicle shape optimisation has been developed using the recent advancements in neural network modelling techniques and evolutionary optimisation method. Five design parameters were chosen as roof drop, under body topography, diffuser angle, boat tailing and front wheel coverage as shown in Figure 2.4. The model with the least drag force was selected as the most optimum shape. The design changes

were limited from a minimum of 0 mm to a maximum of 107mm both in horizontal and vertical directions.

Parameter	Parameter Minimum (baseline) [mm]	Parameter Maximum [mm]
Roof drop	0	100
Underbody topography	0	107
Diffuser angle	0	100
Boat tailing	0	50
Front wheel coverage	0	60

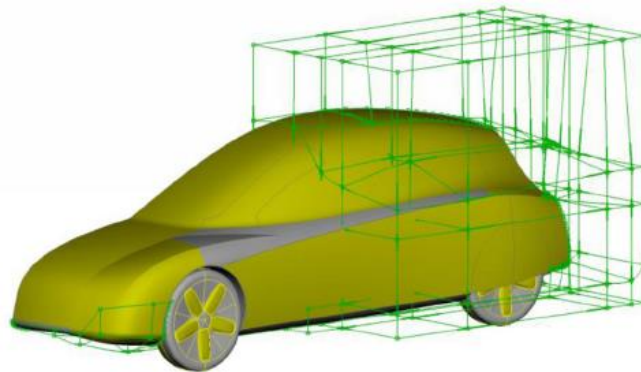


Figure 2.4 The design parameters and the morph boxes around the vehicle model.

The authors discovered that the change in front wheel coverage and boat tailing design parameters have a minimum impact on drag coefficient value whereas the roof drop, underbody topography and diffuser angle can have a substantial effect on changing the drag force coefficient. However, the maximum impact was seen at either the minimum or the maximum values in their respective design configuration. A 13% reduction in drag coefficient was achieved when the vehicle was at its optimal shape. However, the optimisation tool was only applied to a single geometrical shape and a limited number of design parameters were chosen which were tested within a limited design range. Limited information regarding the numerical study was provided with no information regarding a comparison of pressure and velocity distribution around the baseline and optimal design shape models.

Singh & Golsch [5] conducted a numerical study of down force optimisation for a racing car shape. The method was based on mesh morphing techniques to provide new designs for examination by morphing the CFD mesh of the existing design. A parametric study was

performed in order to improve the shape of a racing car to achieve maximum down force, appropriately, in this study a CAD design of a Pontiac from NASCAR was used. The parameters chosen in this study were offsets of the vehicle's nose, tail and roof. The CFD simulations were performed using the commercial software package Fluent. As a conclusion the authors mentioned that the morpher based CFD analysis can be considered a potentially powerful tool for design optimisation of racing cars.

A parametric design study was carried out along with a thorough fluid flow analysis by Singh [47]. Ansys fluent and the mesh work morpher were coupled with iSIGHT for an automatic exchange of data. Deck length, Roof edge length, roof edge height and deck height were chosen to be design variables as seen in Figure 2.5, and were altered automatically in order to achieve a specified drag coefficient. Once again, this technique could only be used to fine tune an existing CAD model.

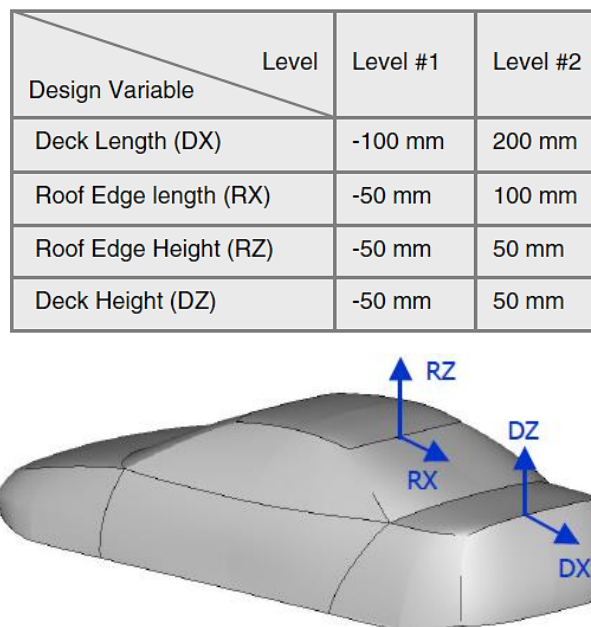


Figure 2.5 The design variables and levels and the 3D car model used for the study.

Koromilas et al [49], researched into developing a methodology for rapid aerodynamic development of vehicle themes, in the early stages of vehicle development. The study focused on developing designs for two-volume vehicle shapes and the standard surface template which was used as depicted from Figure 2.6. The initial design was generated using the Aerodynamic Shape

Development (ASD) program, an already established design tool. Drag estimation was done using nonlinear neural network program which was trained to evaluate aerodynamic drag force for respective geometric parameters.

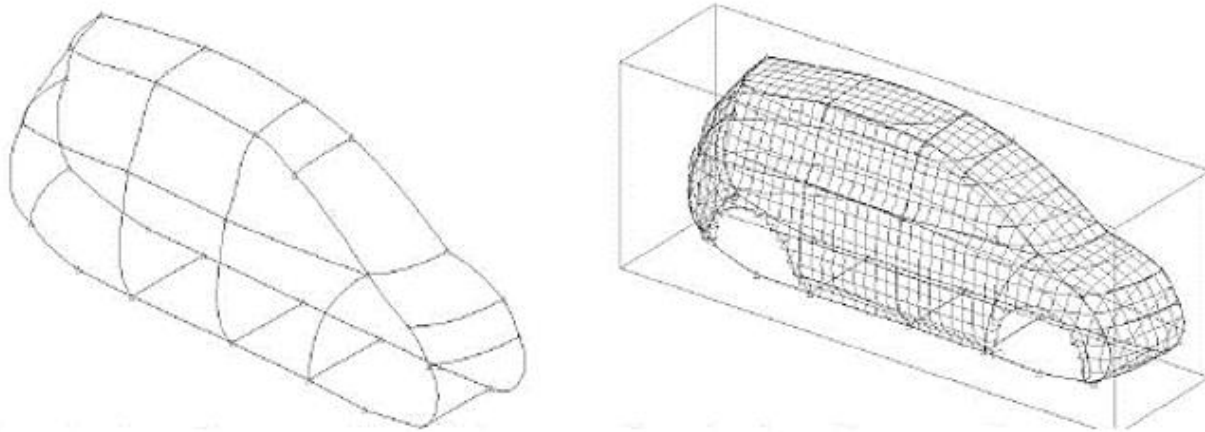


Figure 2.6 Standard template model generated using ASD for this study.

Sun, et al [9] conducted a study on shape optimisation of a SUV in the early development stage using a response surface method. Numerically, the authors of this study used commercial software PowerFLOW to carry out a detailed flow simulation of a SUV model under transient conditions. This was done to understand its performance and locate the regions for improvements. The upper-body design changes were made by determining the five parameters to characterise the design space and identify the optimal design with the least amount of simulations. Boat tailing, tumblehome, front taper 1, front taper 2 and grille angle were selected as parameters. Very limited information was provided regarding the 3D model generation and only two design changes for each geometric parameter was studied. Moreover, using the proposed methodology, it was unable to carry out significant design changes and could only be used to do slight design variations.

Ribaldone, et al [50] presented a multi objective optimisation methodology for external vehicle shape optimisation in view of reducing the design times and associated costs. Two design methodologies used by Centro Ricerche FIAT (CRF) method and Fiat Groups Automobiles (FGA) were discussed and the applications of these methods were presented. The vehicle design

optimisation was carried out using modeFrontier™ software. An iterative process was followed and a new geometry was generated for every iteration and analysed for its aerodynamics performance. Mesh morphing was used to alter the geometry and drag and lift forces were used as the objective functions. In total 11 geometrical parameters were chosen including “Middle Roof Z” and “Windscreen Top Z” which are shown in Figure 2.7.

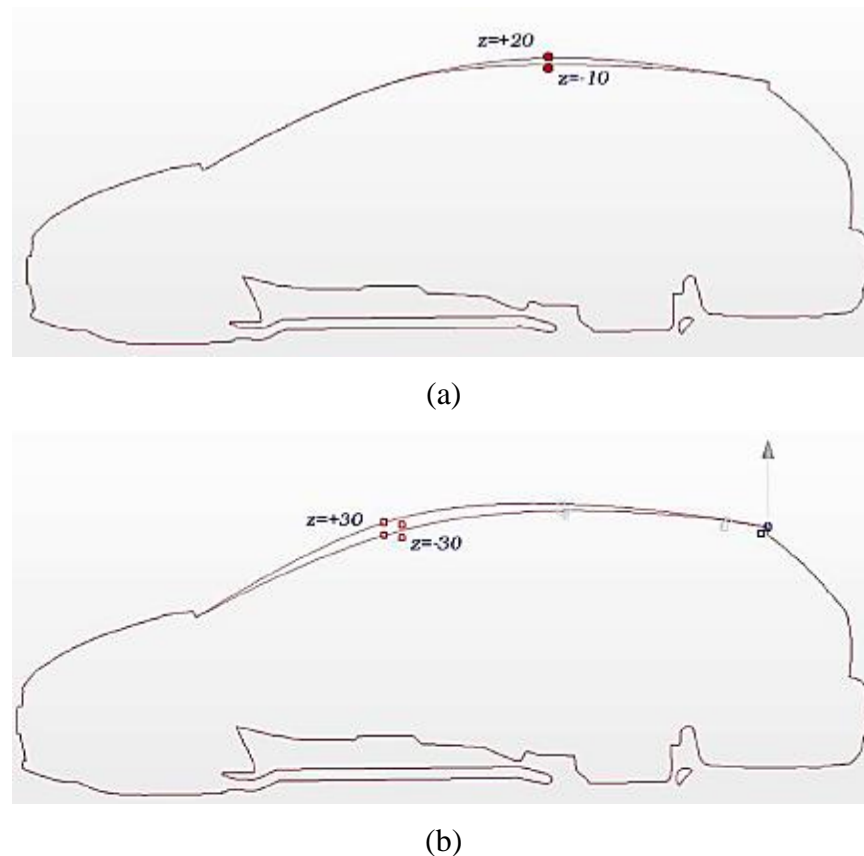


Figure 2.7 Upper and lower limits of Middle Roof Z (a) and Windscreen Top Z (b) design parameters.

Zhang, et al [51] carried out this study using a MIRA reference car model to develop an automated aerodynamic shape optimisation process. Three commercial software packages; Altair HyperMesh, HyperStudy and CD-adapco STAR-CCM+ were integrated in order to create the geometry, carry out the numerical analysis and develop the optimisation process. A DOE matrix with four design factors and thirty design levels were used and the base line geometry was morphed according to the DOE matrix. Windshield angle (W\_A), Rear window angle (R\_A), Departure angle (D\_A) and the Deck width (D\_W) were chosen as design variables and were

changed within the ranges  $28^\circ - 45^\circ$ ,  $30^\circ-40^\circ$ ,  $0^\circ - 15^\circ$  and 1.463m - 1.625m, respectively. Departure angle was identified as the most significant parameter when it comes to drag reduction. The morphing handles which were used to control D\_A is shown in Figure 2.8.

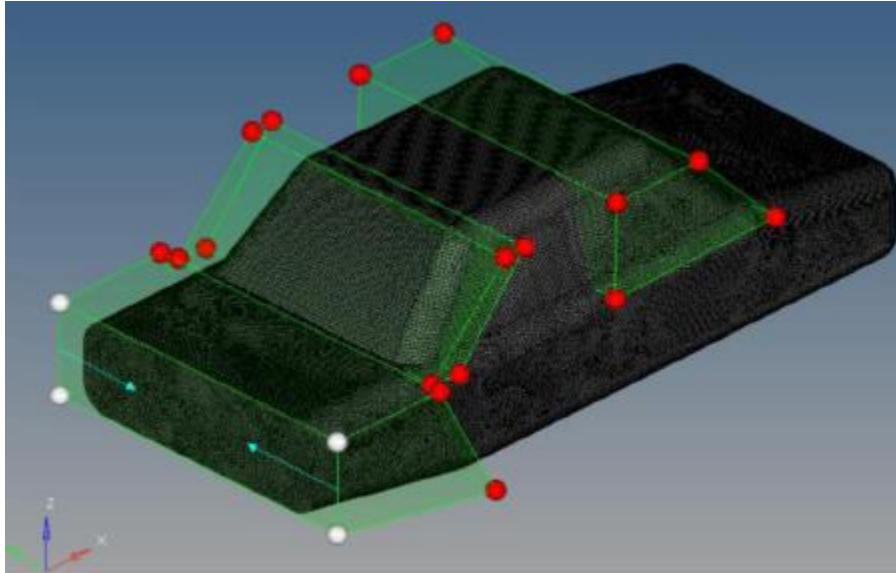


Figure 2.8 Handles correspond to D\_A design alteration.

Many other authors such as Gabbasa et al [52], Oktay Baysal [53] and Khondge & Sovani [54] also studied the vehicle design and optimisation techniques such as mesh morphing on various road and racing car shapes. All the studies have used an existing CAD model and defined the design parameters that should be altered. Drag force was used as the target criteria which should be reduced and the model with the least drag force was named as the most optimum design.

### 2.1.1 Summary of Literature regarding Geometrical Modelling Techniques

The literature review presented above mainly contains optimisation studies and almost all these optimisation studies were based on a preliminary CAD geometry. Mesh morphing technique was found to be one of the most widely used and was extensively applied for automobile shape optimisation. It was found that this technique is only capable of fine tuning an existing geometry. Significant design changes were not permitted and minimum design control is given to the user. Based on the literature review, there is a clear knowledge gap in developing mathematical based

geometric modelling techniques and exploring their potentials as a truck-trailer design tool. However, the functional design method used to describe a basic boxed shape car model provided a solid starting point to develop a design methodology for truck-trailer units.

## 2.2 Effect of Truck-Trailer Dimensions and Shape on Aerodynamic Forces

Wood [55] conducted a study to raise the awareness of the energy usage by the transportation industry. In this paper, numerous aerodynamic drag reduction research studies and a number of existing drag reduction technologies were discussed. It was noted that up to 16% of energy consumption is used to overcome drag force in transport systems. By reviewing existing data, it was claimed that up to 50% of energy was used by light ground vehicles to overcome aerodynamic drag force. However, it was seen from Figure 2.9 that around 60% of energy was used to overcome the drag force in the case of Heavy ground vehicles such as truck-trailer units.

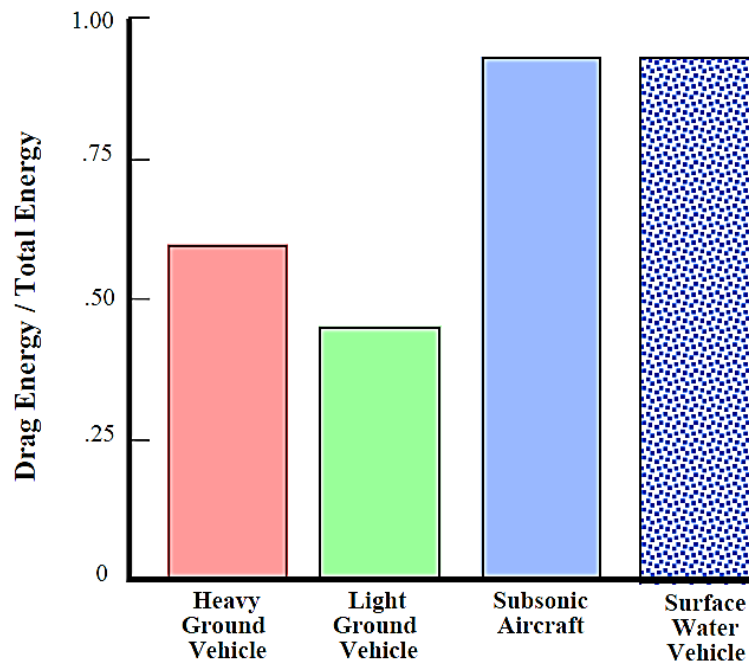


Figure 2.9 Energy consumed to overcome drag for ground, air, and water vehicles

Allan [56] carried out some of the earliest experimental research into reducing the drag by improving aerodynamic shape characteristics. The simplest and most effective method suggested by Allan was to round the leading edges of the truck-trailer units since the research proved that

rounding off sharp edges creates a significant positive impact on the drag reduction. Applying this research into the real-world situations was found to be quite limited as the scaled model that was used to undertake the study was extremely simplified. The model did not feature vital design features such as wheels and it was simply two boxes connected together to imply tractor and the trailer unit as depicted in Figure 2.10.

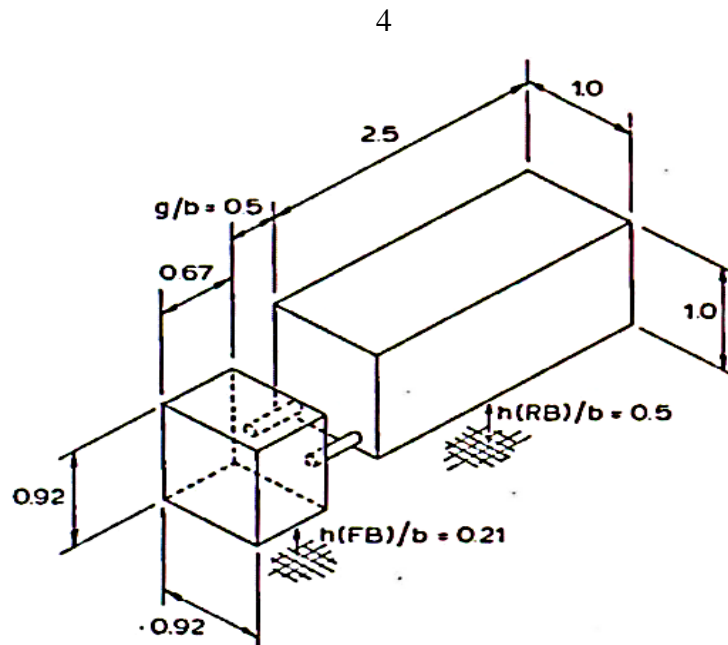


Figure 2.10 Simplified truck-trailer model used for wind tunnel experiments by Allan [76]

Östh & Krajnović [57] undertook a numerical study using Large Eddy Simulation (LES) to research the flow around a simplified truck-trailer model. The authors used four truck-trailer models that were created using similar dimensions as that of Allan [56]. It was conducted in this manner in order to explore the fundamental flow behaviours and the resulting drag coefficient when the models are being subjected to oncoming fluid flow. Two of the models were created with one having a sharp edge around the truck unit and the other with a rounded edge. The two other models were created again with sharp and rounded edges respectively, but with an increased truck-trailer gap width. By carrying out the analysis, authors noted that a rounded leading edge decreases the drag coefficient compared to the model with a sharp edge. The drag coefficient for the model with sharp edges was seen to increase from its original value as the truck-trailer gap was increased. These observations made by numerical studies were found to be in the same order of magnitude as the experimental results obtained by Allan. The results

depicted that there were strong flow separation and circulating flow regions at the top of the truck unit on the sharp edged model compared to the rounded edge model as seen from Figure 2.11. Once more, the model used was simplified to just two boxes in tandem connected by two rods. Therefore, the results obtained cannot be directly applied with the generic truck-trailer units. Moreover, the elimination of wheels from the model was expected to have a direct impact on the underbody flow and hence the flow characteristic exhibited at the rear of the model.

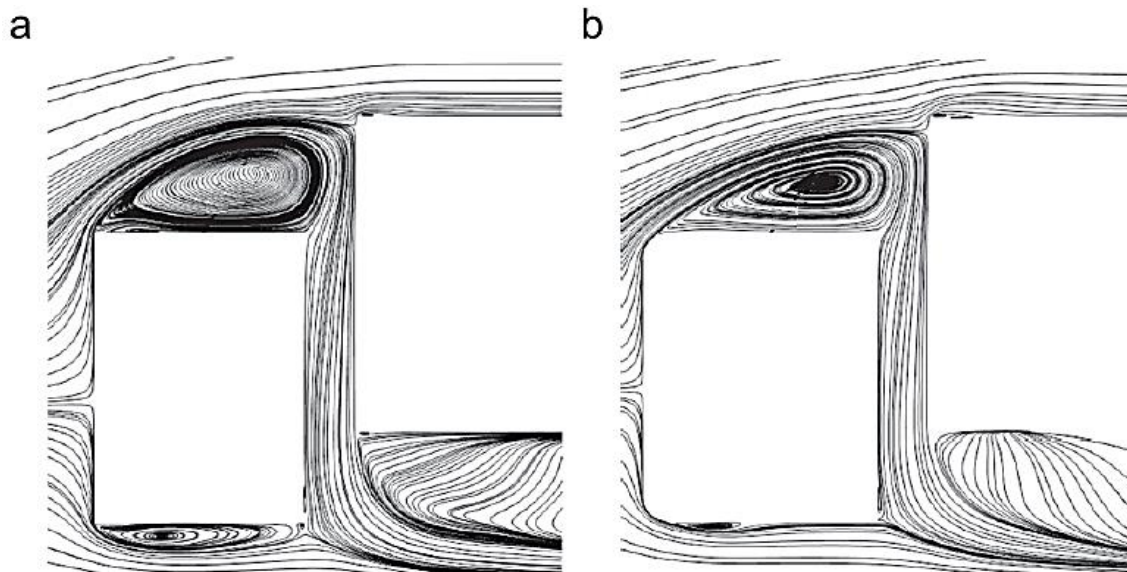


Figure 2.11 Velocity streamlines on top of the truck-trailer model projected along the symmetry plane. (a) Model 1 (small gap width, sharp edges). (b) Model 2 (small gap width, round edges).

Cooper [58] summarised the data collected by university of Maryland using an experimental study regarding truck-trailer drag force reduction techniques. Two models were generated with one having a square-cornered trailer unit and the other with a rounded corner with a 12 inch radius. It was found that just rounding the trailer front edges provides an 11.5% reduction in drag coefficient and the two models are shown in Figure 2.12.

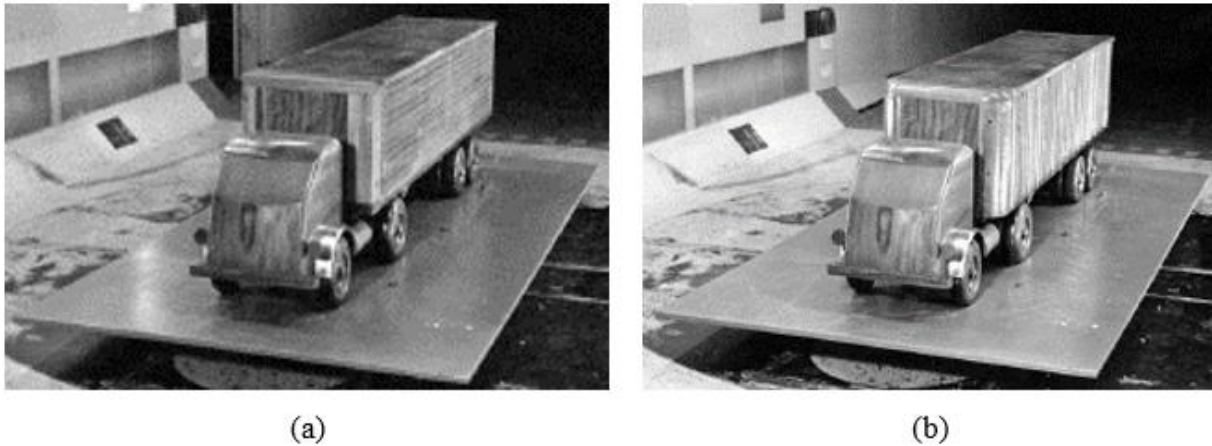
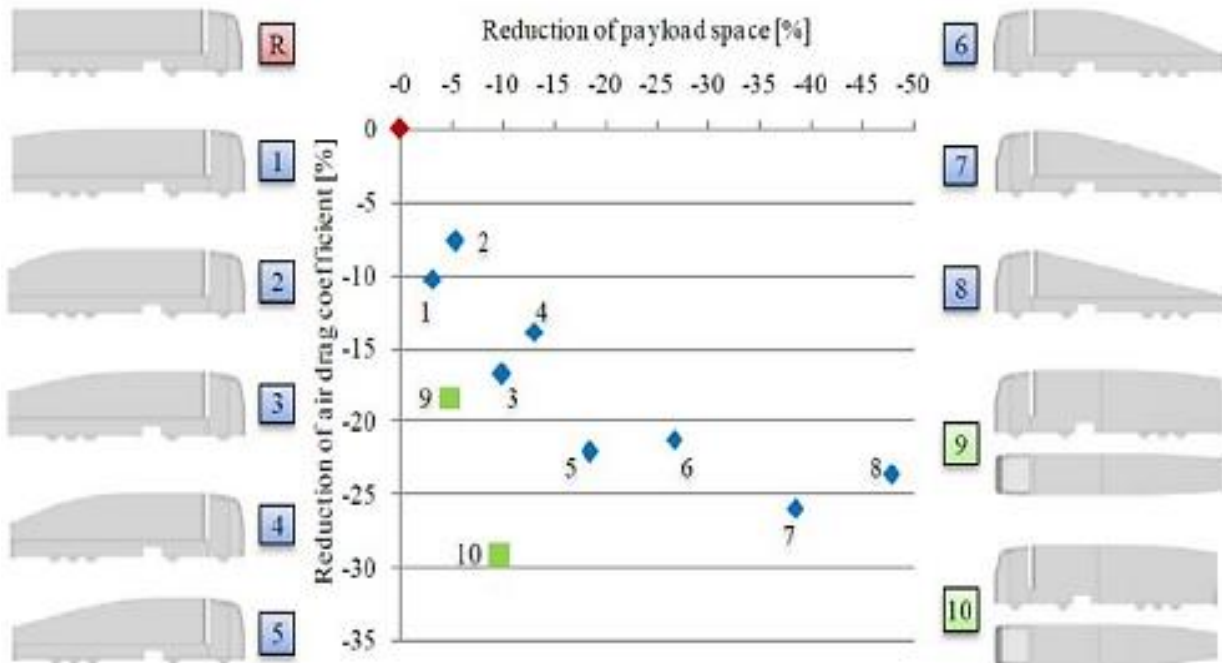


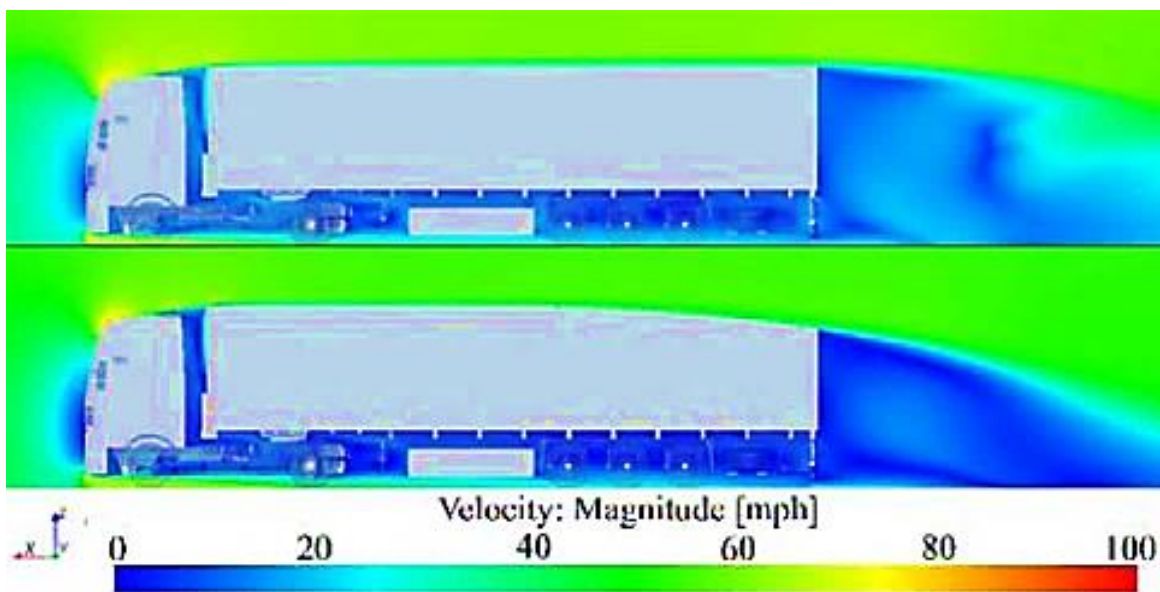
Figure 2.12 The trailer unit with square edges (a) and the trailer unit with rounded edges (b).

Hirz & Stadler [59], undertook a numerical investigation of aerodynamic characteristics of general modifications on the rear section of a trailer unit in regards to reducing the drag force thus the fuel consumption of truck-trailer units. Ten different truck-trailer models were generated with varying payload spaces in order to study the potential for drag reduction by altering the trailer end geometry. The flow analysis was carried out on ten models and the model that produced the least drag force was selected for further design optimisation and was named “model A”. When compared with the generic truck-trailer model, model A obtained a 15% reduction in aerodynamic drag force.

The baseline truck-trailer model was seen to be associated with a significant wake flow area behind the trailer unit due to its bluff shaped body. But, the aerodynamically optimised truck-trailer model was seen to guide the flow smoothly to the road surface at the rear resulting in a smaller wake flow region. However, it was found that the tapering feature used on trailers significantly affects the payload carrying capacity of the trailer units. The models and the data obtained from this study are shown in Figure 2.13.



(a)



(b)

Figure 2.13 Drag force reduction for ten different truck-trailer models with varying payload spaces (a) and the flow velocity for baseline truck-trailer and the optimised truck-trailer model A (b).

Burton et al [60] conducted an experimental study to quantify the drag reducing capability of number of add-on fuel saving devices including boat tails, side skirts, truck extenders, air dams and roof fairings. A 1/3 scale model of a typical truck-trailer model was used inside a close return type open jet wind tunnel to carry out this study. A four, 3 component Kistler force balance systems were used to measure force components drag, lift and side forces. The authors claimed that a 0.16 reduction in drag coefficient was achieved by just rounding off the trailer edges.

### **2.2.1 Use of Passive Add-On Devices to alter the Truck-Trailer Shape**

Rose [61] undertook an experimental investigation to analyse the effectiveness in drag reduction of passive add-on devices, such as a truck roof fairing, vortex stabiliser, trailer fairing and a simple air dam. A full scale truck-trailer model was used in a wind tunnel to carry out these studies. The passive add-on devices were tested both individually and in groups. It was claimed that by using a deflector, it was possible to achieve a 16% reduction in drag, simply by using a narrow bladed truck roof fairing device; and a 31% reduction in drag by using a wide bladed truck roof fairing device. Additionally, by using both the wide bladed deflector device and the air dam together, a 36% reduction in drag was achieved resulting in a 16% reduction in fuel consumption at a steady vehicle speed of 80 km/hour. Wonga et al [62] conducted experimental tests to investigate the drag reduction capabilities of truck roof mounted ducts, truck roof fairings, trailer corner vanes and truck-trailer gap sealer plates. The study claims that by using a truck mounted duct with a downward facing exit, a fairing on top of the truck mounted duct and curved sealer plates, it was possible to achieve a 30% reduction in drag force.

Wood et al [63, 64] studied three different drag reducing devices which would alter the flow profile in the gap region, rear of the trailer and the undercarriage of a truck-trailer unit. The designed add-on devices are as follows.

1. Cross flow vortex trap device (CVTD) for gap
2. Vortex strake device (VSD) for the base
3. Undercarriage flow device (UFD) for the undercarriage

These devices were tested under real life conditions where they have been used more than 85,000 miles within a time period of 20 months. It has been discovered that the devices offer a combined fuel saving of around 10% when a truck travels at 47.5 mph. This improvement in fuel economy correlates to an equivalent drag reduction of 30% with the corresponding drag coefficient of 0.45

Landman et al [65, 66] conducted experimental studies on three main types of add-on fuel saving devices, trailer skirts, gap sealers and boat tails. Three different trailer skirt designs were used named as practical skirt, extended skirt and full skirt to determine the effect of length of side skirt devices on drag reduction. A baseline model with no add-on devices and a model with all the add-on devices were used to define lower and upper limits of drag force experienced by the truck-trailer model. It was stated that the baseline model was associated with the highest wind average drag coefficients of 0.55 and 0.53 at 55 mph and 65 mph, respectively. The full side skirt model was found to provide an 18% reduction in drag force at 55 mph and was the most effective type of skirt device. Similarly, the gap seal and boat tail devices were respectively providing 7% and 10% reduction in drag experienced by the truck-trailer configuration. By using all the add-on devices studied, it was possible to reduce drag force by as much as 33%.

Asim and Gawad [67], conducted experimental studies to determine the effect of truck roof deflector on aerodynamic drag force. A 1/19<sup>th</sup> scale truck-trailer model was used while the truck unit was mounted with and without a truck roof fairing device. Two types of truck roof fairings were used with one being a flat sided, and the other being a curved truck roof fairing device. The results obtained from the study showed that the drag coefficient decreased by 10% compared with the baseline model when a flat sided truck roof fairing was being used. Additionally, a further 11% reduction in drag coefficient was achieved by using a rounded or curved truck roof fairing device.

Sulitka and Nozicka [68] carried out experimental and numerical studies to analyse the effects of base drag reduction on a trailer unit by using various side fairing designs and rear-end tapering profiles as depicted in Figure. A 1/15<sup>th</sup> truck-trailer model was used to perform the experimental study. Particle Image Velocimetry (PIV) flow visualization technique was employed for flow-field analysis in the wake downstream of the trailer unit and these experimental results were

compared to that of which was obtained by numerical studies. It was estimated that the contribution of semitrailer to the aerodynamic drag of a whole vehicle in the present form of truck-semitrailer unit, runs to some 15% when at straight winds. It was discovered that the optimum rear end tapering angle was at  $12^\circ$ . When the trailer is equipped with side skirts and with a full  $12^\circ$  rear-end tapering angle, the overall mean tangent drag coefficient was reduced by 12%.

Ortega et al [69] carried out investigations on the drag reduction capabilities of both commercially available and prototype drag reduction devices for class 8 truck-trailer models. The experiments were carried out using three full sized truck-trailer configurations while mounted with various side skirts, boat tail devices and gap filling devices. The most effective way of reducing the drag force was to reduce the truck-trailer gap. The fixed angle boat tails have reduced 0.047 from the drag coefficient and the largest reduction of 0.076 was achieved by using the optimum sized side skirt device.

Kazim and Filippone [70] analysed a range of passive add-on fuel saving devices to reduce the aerodynamic drag force. The realistic operating conditions of the truck-trailer units such as urban and long-haul driving conditions were taken into consideration prior to assessing the optimum use of add-on devices. The drag reduction capabilities of a range of add-on devices such as truck roof fairings, trailer-front fairing, truck and trailer side skirts, boat tails and gap splitters were explored. According to authors, the truck roof fairing device offers the most significant fuel savings followed by trailer –front fairings, which range from 1400 litres to 2600 litres annually. Furthermore, authors suggest that the add-on fuel saving devices have significantly improved performance when used in long-haul operations (LHDC) compared to urban operations (NEDC). The reason for this was that in urban operations, the fuel is mostly consumed upon acceleration as clearly seen in Figure 2.14.

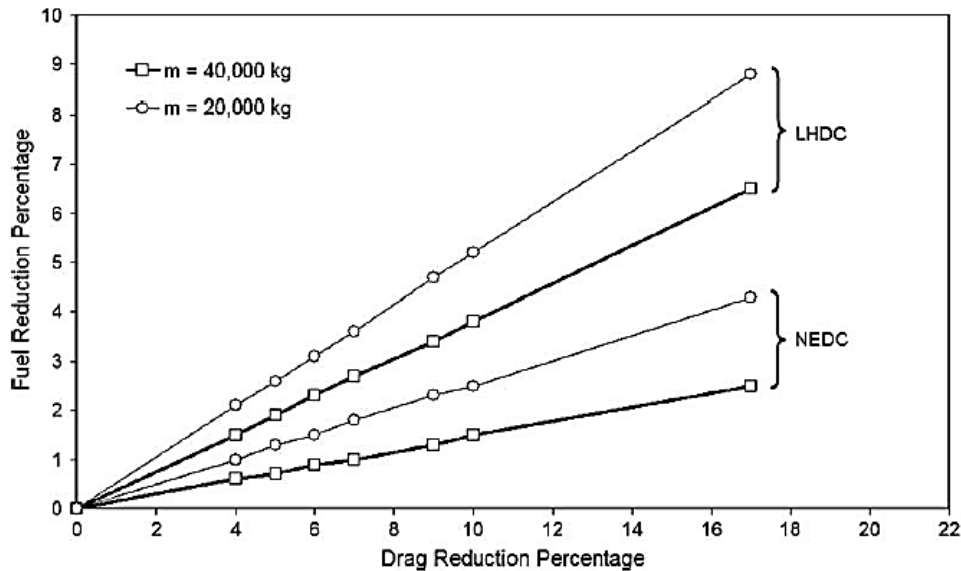


Figure 2.14 The fuel reduction percentage vs drag reduction percentage for different operation conditions for 40,000 kg and 20,000kg truck-trailer models.

Malinin [71] carried out numerical studies to investigate the effectiveness of several add-on fuel saving devices, such as truck roof fairing device and vortex generators. A dynamic foldable truck roof fairing and simple vortex generators were studied for effectiveness in reducing the drag while having minimum impact on basic truck-trailer operations, such as loading and un-loading. After undertaking numerical studies, the author stated that vortex generating devices are ineffective under head winds but provides a maximum of 14% drag reduction under side winds.

Wang et al [28] carried out numerical flow analysis to investigate the aerodynamics of a truck-trailer model focusing on the relationship of a truck roof deflector, trailer unit and the resulting drag force experienced by the vehicle. A modern truck-trailer model was used with two different trailer units with one trailer modelled to be taller than the other. The truck unit was modelled with an integrated fairing unit resembling one of the modern truck units. Two different heights for the top truck and the top trailer were used along with three different angles between the top of the truck unit and the fairing device as  $7^\circ$ ,  $14^\circ$  and  $24^\circ$ . By presenting the results obtained, the authors suggested that the conventional fixed truck roof fairing devices leads to an increase in drag force experienced by the truck-trailer configurations. However, the truck-trailer model used had rounded corners all around and these rounded corners had a significant impact on the flow

field, as demonstrated by Allan [56]. Therefore, any effects of the fairing unit on the resulting flow field could have been influenced by the rounded corners. Furthermore, micro level changes in the flow field such as flow reversal and friction effects were over looked.

Guo et al [88] undertook numerical and experimental investigations on aerodynamic drag reduction of commercial trucks based on external styling of a truck. The aim of this particular research was to study the influence of various truck shapes on aerodynamic drag, and various domes on aerodynamic characteristic. The findings discovered that the air flow around the truck would accelerate by increasing the curvature of the front truck. This also decreased the influence on the trailer as well as the high pressure regions windward, which was a key factor in reducing the drag force of the vehicle. Due to this model, the drag coefficient was reduced by 18.1%. Furthermore, it was also noted that the dome exhibited excellent drag reduction capabilities due to its curved design.

### **2.2.2 Summary of Literature regarding Effect of Truck-Trailer Dimensions and Shape on Aerodynamic Forces**

Much research has been carried out on truck-trailer models equipped with add-on devices. However, based on the literature presented in the above section, it is evident that the available literature regarding the dimensions and the shape of the truck-trailer units on the surrounding flow field and resulting aerodynamic forces are severely limited. The slightest geometrical change can affect the flow field in the vicinity of truck-trailers. This presents the need to isolate and study the dimensional and shape of truck and the trailer units separately. Limited research is available on the aerodynamic contribution of the truck unit as relatively less design limitations are imposed on truck units. Therefore, a thorough local flow analysis of pressure and velocity distribution with varying truck and trailer dimensions and shapes is needed to fill the knowledge gaps.

### 2.3 Effect of Crosswinds on Truck-Trailer Aerodynamic Forces

The side winds can affect the stability of the high sided vehicles such as truck-trailer units and can cause them to roll-over in extreme cases. Much research into understanding crosswind aerodynamics has been carried out [60,72,73,74] using both experimental and CFD means. Experimental studies were divided into two sections as real world operational tests [75] and wind tunnel tests.

Sterling, et al [76] explored the accuracy of using CFD based methods to predict the forces and moments experienced by a high sided lorry. Experiment investigations were performed and results obtained were compared with the CFD results to validate the accuracy. Experiments were performed using both scaled model in a wind tunnel and a full size model under normal operating conditions. Pressure tapping on side and top surfaces were used to obtain the surface pressure at both straight and crosswind conditions. The side force data were obtained between  $0^\circ$  yaw and  $90^\circ$  yaw at  $5^\circ$  intervals in the case of experiments and in  $10^\circ$  intervals for CFD studies. The authors have observed that the experimental data and the CFD data to be in excellent agreement across the full range of yaw angles. The side force data obtained is shown in Figure 2.15. This study reassures that CFD is an accurate tool to predict aerodynamic force such as side force experienced on a high sided vehicle under yaw conditions.

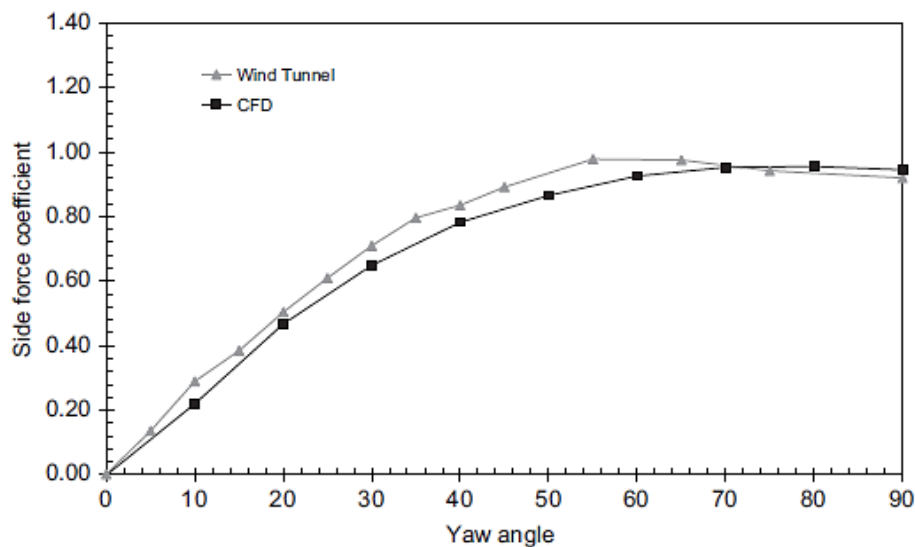


Figure 2.15 The side force coefficient with respect to yaw angle.

Nakashima et al, [77] studied the unsteady aerodynamics of a truck-trailer unit under crosswind conditions. The numerical simulations were performed using a LES code known as Front-Flow/red-Aero. The yaw angle range was set from  $0^\circ$  to  $45^\circ$  in  $5^\circ$  increments. Time-averaged side force coefficient obtained from the study is shown in Figure 2.16 and the side force is seen to increase sharply as the yaw angle increases.

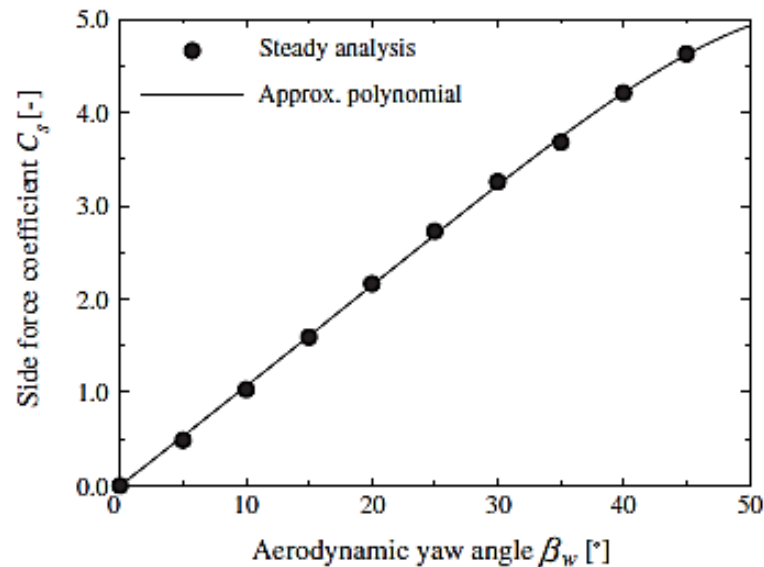


Figure 2.16 The side force coefficient with respect to yaw angle.

Mcarthur et al, [78] studied the unsteady wakes associated with truck-trailer units for yaw angles ranging from  $0^\circ$  to  $15^\circ$ . Number of add-on devices such as a deflector, skirts and boat tails were used and compared against the baseline model which consists of no add-on devices. Pressure taps were used on the trailer rear surface and they were connected to a dynamic pressure measurement system in order to obtain the surface pressure. The shift in pressure coefficient on the baseline trailer rear surface with respect to changing yaw is shown in Figure 2.17. The high pressure region at straightwind condition was seen to change to a low pressure region as the yaw angle increased.

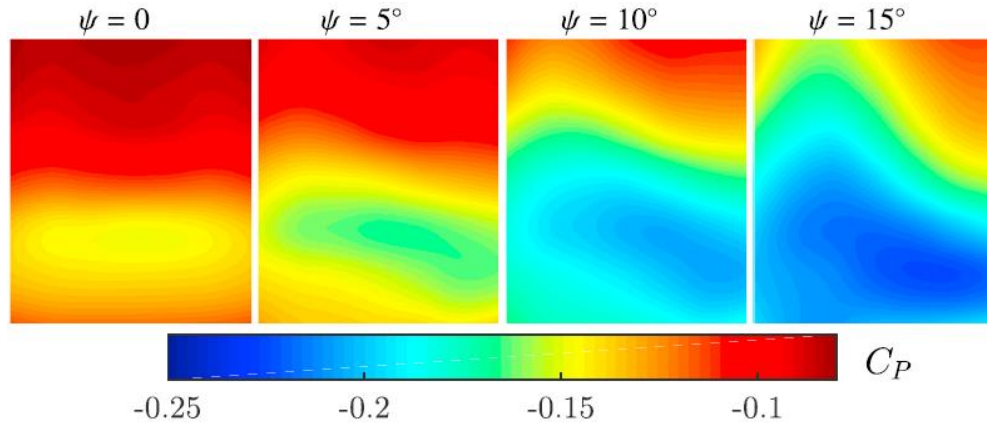


Figure 2.17 base pressure variations with the yaw angle.

Roy and Srinivasan [79] performed a three-dimensional near field flow analysis for axis and crosswind loadings to understand the air flow characteristics surrounding truck-trailer bodies. Numerical studies were performed on a generic truck-trailer geometry and a shape optimised truck-trailer geometry with design features such as a rounded front face and leading edges. The test results showed that when the shape modified truck-trailer model was subjected to a crosswind of a magnitude of 30 mph, it experiences a 30% reduction in drag compared to baseline model. It was calculated that this reduction in drag in turn, resulted in a 35% reduction in fuel consumption of the vehicle. Even though, the truck-trailer units in crosswind conditions were studied, the studied model was so simple such that it was not incorporated with key features such as a gap between the truck and the trailer that has a direct influence on the drag force experienced by the vehicle.

Experimental tests on various types of passive add-on devices were conducted by Cooper et al [80] and Cooper [32] using a 1/10<sup>th</sup> scale truck-trailer model and a full scale Navistar 9200 truck unit with a 40 ft. trailer unit. The passive devices that have been investigated include longer truck extenders, trailer side skirts, angled boat-tail plates and a truck roof fairing. The results obtained from the study suggest that it is possible to achieve an 18% reduction in drag by simply using a truck roof fairing device. By using both truck roof fairing device and truck side skirts, 23% reduction in drag was achieved. Further to this, the model was tested in a number of different yaw flow conditions, whereby the drag force coefficient is seen to increase along with the yaw flow angle. The drag reductions of the studied passive devices were seen to remain consistent

throughout increasing yaw conditions as shown from Figure 2.18. However, some of the devices that were used to carry out this study have practical limitations. The efficiency of boat tails depends on its length, and the effectiveness of extenders depends on how close they are to the road surface. Even though, these devices performed exceedingly well under experimental conditions they cannot be practically implemented on truck-trailer units because of their adverse effects on the day to day operations.

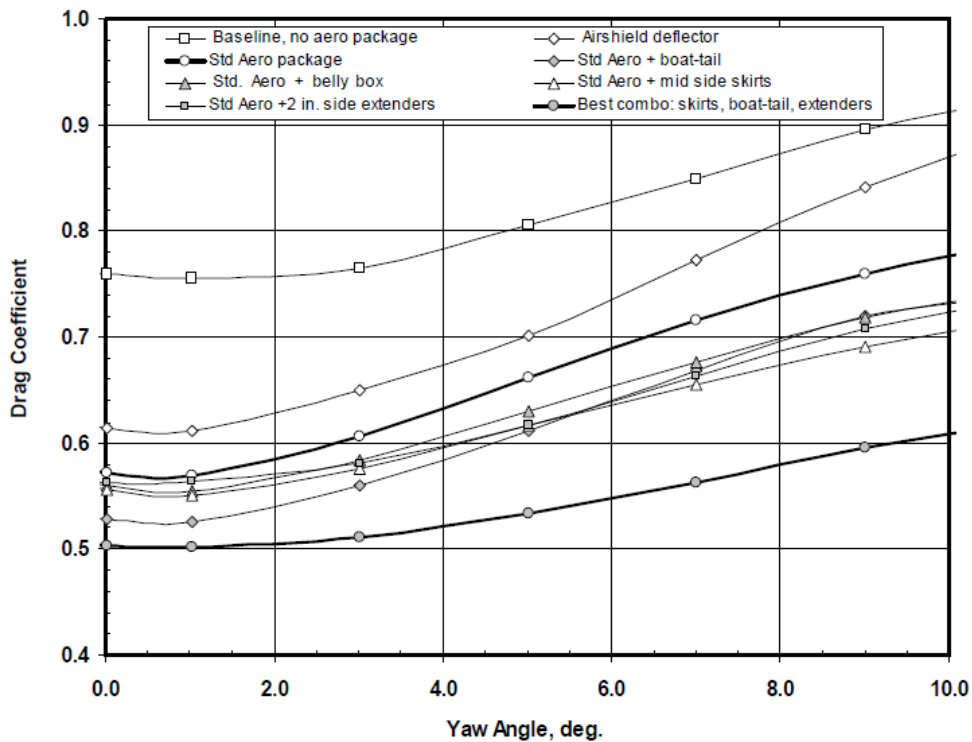


Figure 2.18 Drag coefficient for various configurations of add-on fuel saving devices.

Pevitt et al [81] conducted both experimental and numerical studies using the 1/10<sup>th</sup> scale Mack 600 class eight truck-trailer model to determine the aerodynamic impact of various fuel saving add-on devices. The aerodynamic drag force acting on the truck-trailer model was recorded and studied while mounted with front fairing, side fairing and gap filler devices. These devices were tested both individually and in groups, as well as under various upstream flow speeds from 40km/h to 120km/h through a range of yaw angles 0°, 5°, 10°, and 15°, which simulates crosswind flow conditions. The experimental and computational simulation results were found to be in good agreement with an average deviation of 3%. The results obtained indicate that by

using a truck roof fairing it is possible to achieve a 20% drag reduction over the baseline model at 0° yaw angle. Similarly, full skirting, part skirting and gap filling can reduce drag force by 30%, 24% and 24%, respectively. Furthermore, the data indicates that the full fairing provides the maximum drag reduction throughout the chosen range of yaw conditions, while the drag reduction capabilities of the truck roof fairing device was shown to decrease as the yaw angle increases, and became the least effective type of add-on device tested by authors as shown from Figure 2.19. Once again, no flow field analysis around the tested truck-trailer model was provided. The effect on having a truck roof fairing device on the flow field above the truck and trailer units was not provided. Furthermore, limited yaw flow angles were considered even though, truck-trailers quite often experience yaw flow conditions outside the chosen range in this study.

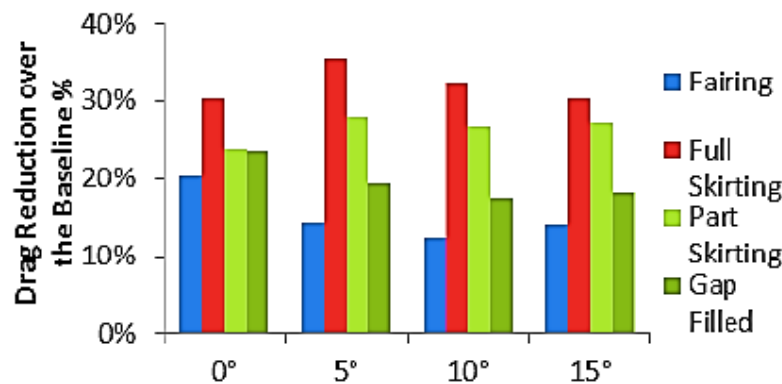


Figure 2.19 Percentage decrease of drag force over baseline model, for each add-on device under varying yaw conditions.

### 2.3.1 Summary of Literature regarding Effect of Crosswinds on Aerodynamic Forces acting on a Truck-Trailer Unit.

Based on the literature presented above, it is evident that more clarity is required on the flow field variations at crosswind flow scenarios. Limited research is available discussing the effects of truck-trailer shape at crosswinds. It is important to have a detailed analysis of pressure variations on individual surfaces to identify key truck-trailer surfaces to be improved to reduce adverse aerodynamic forces. A thorough local flow analysis of pressure and velocity distribution and forces acting on individual truck and trailer surfaces at crosswinds is required to fill the

knowledge gaps. Moreover, the lack of prediction tools available with respect to truck-trailer aerodynamic characteristics was evident throughout the literature review. Developing such a tool in conjunction with the geometrical modelling method could prove to be quite beneficial in this research area. Such a tool needs to correlate both dimensional and shape parameters at straight head wind and crosswind scenarios.

## 2.4 Scope of Research

Upon completing the literature review, it is clear that there is limited research exploring the potential of using geometrical modelling methods to design truck-trailer models. The conventional approach of creating a number of CAD or clay models to carry out numerical and experimental investigations was found to be the common practice. These methods turned out to be very time and resource consuming. The optimisation techniques such as mesh morphing, is not capable of being used as a mere design tool. Vast majority of vehicle aerodynamic research mainly focuses on refining the shape of road vehicles such as passenger transportation vehicles. Hence, one of the key areas of this research is to introduce a geometric modelling methodology that can be used for truck-trailer design.

Much research has been carried out to explore the potential of add-on fuel saving devices. In light of the above, the lack of published research on the geometrical and shape effects of truck-trailer units were minimal. This could be as a result of tightly controlled design regulations attached with these vehicles. As the slightest change in the truck or the trailer design will have a magnified effect on the flow field, it is vital to isolate these design changes and study their effects.

It was also identified that more clarity in the flow field behaviour is required at the crosswinds. Limited literature was carried out to analyse the flow field parameters and the forces experienced by the truck-trailer units with varying design changes for either truck or the trailer unit. The forces experienced by individual surfaces need to be analysed in detail.

Moreover, the lack of prediction tools available with respect to truck-trailer aerodynamic characteristics was evident throughout the literature review. Such a tool coupled with a suitable

geometrical modelling technique is expected to improve the truck-trailer design and optimisation process, by reducing time and resources which would normally be spent on numerical and experimental studies.

## 2.5 Research Objectives

The first aim explores the development of an alternative design methodology for bluff bodied truck-trailer unit, as well as the utilising a force prediction tool to predict aerodynamic forces. From this aim, the following objectives have been derived.

1. Develop a mathematical vehicle modelling methodology using shape functions to generate baseline truck-trailer geometry with varying dimensions.
2. Conduct an extensive flow field analysis in order to characterise the flow field around baseline truck-trailer unit to analyse the dimensional effects at straight and crosswinds conditions.
3. Quantify the variation of aerodynamic forces with flow angle and changing vehicle dimensions.

The second aim explores the capabilities of the proposed design methodology to generate complex truck-trailer shapes, as well as the development of an aerodynamic force prediction tool considering the shape of the truck-trailer. From this aim, the following objectives have been derived.

4. Develop a mathematical vehicle modelling technique using shape functions to generate truck-trailer geometries with varying shapes.
5. Conduct an extensive flow field analysis in order to isolate and characterise the flow field around varying truck-trailer shapes at straight wind conditions.
6. Quantify the variation of aerodynamic forces at straight headwind under changing truck-trailer shapes.

The third aim further improves the proposed aerodynamic force prediction tool considering vehicle shape and crosswinds. From this aim, the following objectives have been derived.

7. Conduct an extensive flow field analysis in order to characterise the flow field around varying truck-trailer shapes and crosswind angles.
8. Quantify the variation of aerodynamic forces at varying straight and crosswind conditions considering both dimensional and shape effects.

The next chapter presents the numerical methodology using CFD based techniques, employed in this study to achieve the above research objectives.

## CHAPTER 3

# NUMERICAL MODELLING OF THE TRUCK-TRAILER VEHICLE

---

Based on the research objectives identified in the previous chapter, advanced Computational Fluid Dynamics (CFD) techniques have been used to computationally simulate and solve the flow over the heavy duty vehicle. This chapter documents the CFD principles which provides an overview of the stages involved in conducting a numerical investigation. It includes the geometry and mesh, solver-settings, boundary conditions, turbulence modelling, discretization, convergence criteria, as well as the general flow map of the system for a valid comparison analysed later in the study.

### 3.1 Numerical Methodology

Computational Fluid Dynamics (CFD) based techniques have been used to carry out the presented numerical investigations. These numerical techniques make use of algorithms and governing equations. The numerical methodology comprises of three sectors. These are:

- Pre-processing
- Solver Execution
- Post-processing

### 3.2 Pre-Processing Stage of CFD

Pre-processing stage is where the designers can turn the truck-trailer designs to either 2D or 3D models in order to obtain the solution. The CAD truck-trailer model and the suitable sizes flow domain will be generated. Pre-processor can be divided into two categories as Geometry creation and Mesh generation. Once the geometry and the flow domain is generated, a suitable mesh can be generated using the meshing tool. In mesh generation, the geometry and the flow domain will be divided into a controllable number of elements or control volumes and the Navier-Stokes equations will be integrated from one mesh element to the other solving for velocity and pressure components. The mesh module in Ansys supports both 2D and 3D mesh elements with triangular, tetrahedral and hexahedral been some of the most common element types.

Once the mesh is generated and the boundary names are defined, the mesh can be imported to the Ansys Fluent solver module. The boundary conditions, initial flow parameters and solver setting can be defined in this stage prior to solving the flow field for a give truck-trailer geometry. The solver will carry out the calculations until the convergence is satisfied.

Once a solution is obtained, the post-processing module can be used to extract data. This includes contours, vectors, streamlines, data lines etc. These processes will be explained in details in the following sections.

### 3.2.1 Geometry Stage for Generic Truck-Trailer

Numerous truck-trailer models will be generated to complete this study and the models will be generated with the use of shape functions and Ansys design modeller. A baseline model will be generated with all the basic dimensions and key features for comparison purposes. Accurate and a realistic truck model was chosen in comparison to earlier studies [55] in order to prevent any inaccuracies such as flow escaping underneath the trailer due to a missing bridging section. These standard dimensions of the truck unit, trailer unit, wheels, ground clearance as well as the truck-trailer gap are typical of real vehicle [12] and are shown in Figure 3.1.

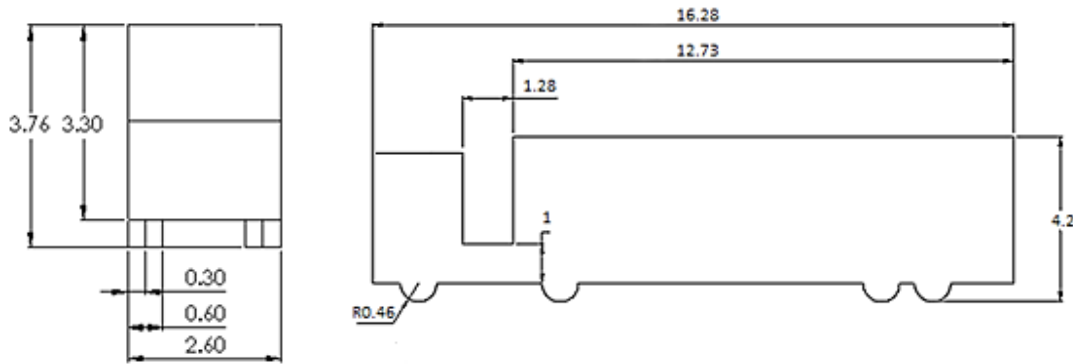


Figure 3.1 Dimensions for the baseline truck-trailer unit

The x, y and z coordinated of the baseline truck-trailer geometry will be obtained and used to generate the CAD geometry. A set of xyz coordinates will be obtained for a truck-trailer unit with a given maximum length height and a width. These coordinated will then be exported to Ansys design modeller to generate data points. Lines will be created by connecting the exported data points. Finally, the “skin” feature in Ansys design modeller will be used to connect the data lined and generate surfaces. Once all the surfaces are generated, the model can be used within a suitable mesh domain and then in numerical simulations. The capabilities of this process to produce complex geometries is illustrated from Figure 3.2.

DAF CF400 [82] truck model with a Don-Bur tear drop shaped trailer unit was used only in this instant to portray the capabilities of CAD modelling process to produce complex and detailed truck-trailer models. The shape functions to generate the xyz coordinates will precede the CAD modelling process. The model will be divided into number of profiles which outline the shape of the truck-trailer geometry. The modelling process starts with exporting the generated xyz points

for each profile into the Ansys design modeller tool as shown in A. The points for each profile will be connected to generate lines as depicted in B. The final stage is to use the “skin/loft” feature to generate surfaces in order to obtain the CAD model as shown in C. The same procedure will be used to generate the required truck-trailer geometries for this study.

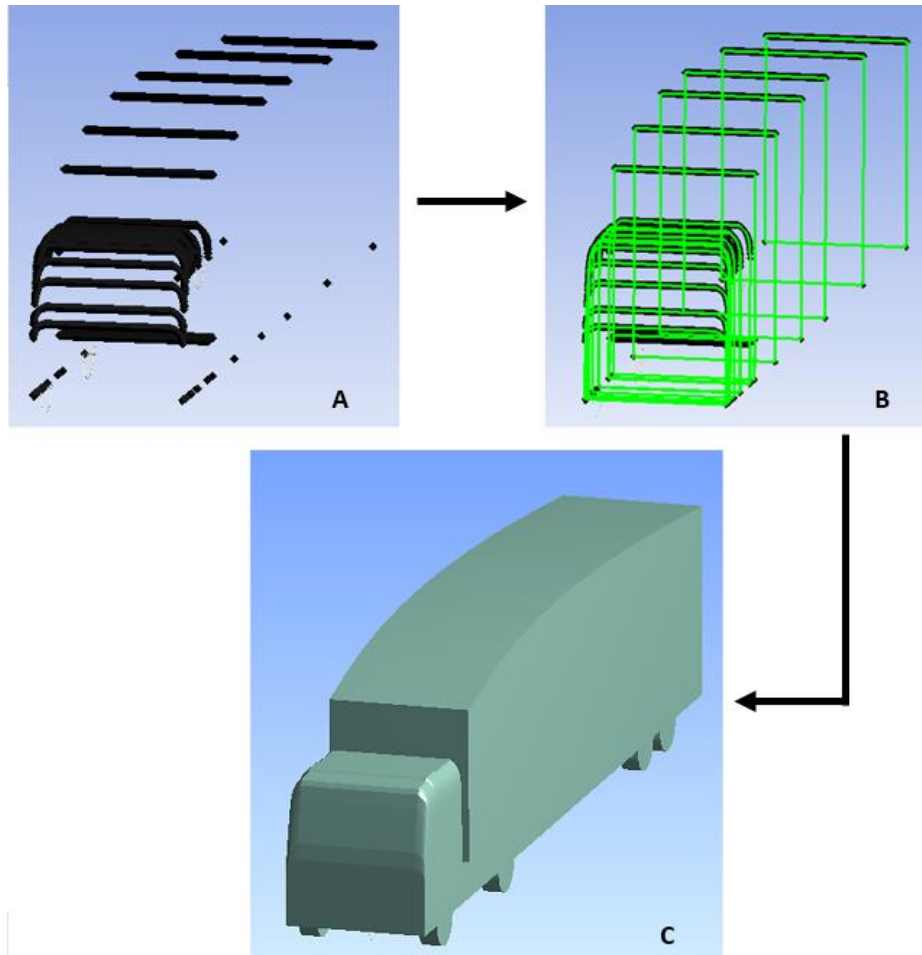


Figure 3.2 The DAF CF400 truck model with the Don-Bur trailer unit

### 3.2.2 Flow domain, Discretisation (meshing) and Mesh Independence Study

In order to minimise the near wall effects having an impact on the flow field around the truck-trailer geometry, [83] specifies the domain walls should be placed at a certain distance from the truck-trailer model. According to [83], the inlet surface should be placed at a distance of 5 times the overall length of the truck-trailer model, the outlet surface should be placed at a distance of 10 times the overall length of the truck-trailer model, the left and right sides should be located at

5 times the overall width of the truck-trailer model and the top surface should be located at 5 times the overall height of the truck-trailer model.

Having these instructions as a basic guideline, number of flow domain sizes were used to carry out a domain independence study in order to make sure that the size of the flow domain will not have an impact on the calculated flow field characteristics and forces. The drag force obtained for number of flow domains with varying sizes is listed in Table 3.1. It was evident that size of the flow domain profile 4 has the least effect on the calculated data hence been used to carry out this study.

Table 3.1 Domain independency

Domain profiles	Length of the domain (m)	Width of the domain (m)	Drag force (N)	Percentage difference (%)
1	137.5	200.0	3742.9	-
2	275.0	400.0	3676.9	1.8%
3	412.5	600.0	3632.8	1.2%
4	550.5	800.0	3626.7	0.2%

The cross-sectional blockage ratio for 4.2 m, 4.6 m and 4.8 m models were calculated based on flow domain cross sectional area of 20000 m<sup>2</sup>. The maximum blockage ratio for the models was calculated as 0.06%. As the calculated blockage ratio was much less than the 5% limit specified by Singh et al [15] no blockage corrections were necessary.

Mesh concentration and the level of refinement around the truck-trailer model have a significant impact on the output data accuracy from the CFD simulations. Therefore, the generated mesh was controlled in such a way that smaller mesh elements were deployed in the vicinity of the truck-trailer model to accurately capture the boundary layer phenomena. This mesh manipulation meant that the rectangular flow domain had to be divided into two sections. A small mesh domain was created to house the smaller mesh elements. The larger mesh domain sustained the coarse mesh in the area away from truck-trailer models. The generated flow domain was discretised using Ansys mesh module and mesh generated for this study is shown from Figure

3.3. It can be seen that the density and the size of the mesh elements vary depending on the location. Near the truck-trailer unit, a smaller and dense distribution of elements is employed to accurately capture the effects of geometry on the surrounding flow field. The mesh is seen to get much coarser further away from the truck-trailer unit, as the area of interest was reduced away from the truck-trailer unit. This method allowed an effective discretisation of flow domain that lead to an efficient use of available computer resources. The created mesh contained around 7,600,000 hybrid tetrahedral elements and hexahedron elements. As explained below, mesh independence study was carried out to make sure that the results obtained was independent from the number of elements in the mesh. And applied mesh controls meant that it was possible to concentrate around 75% of mesh elements to capture the flow domain altered by the truck-trailer geometry.

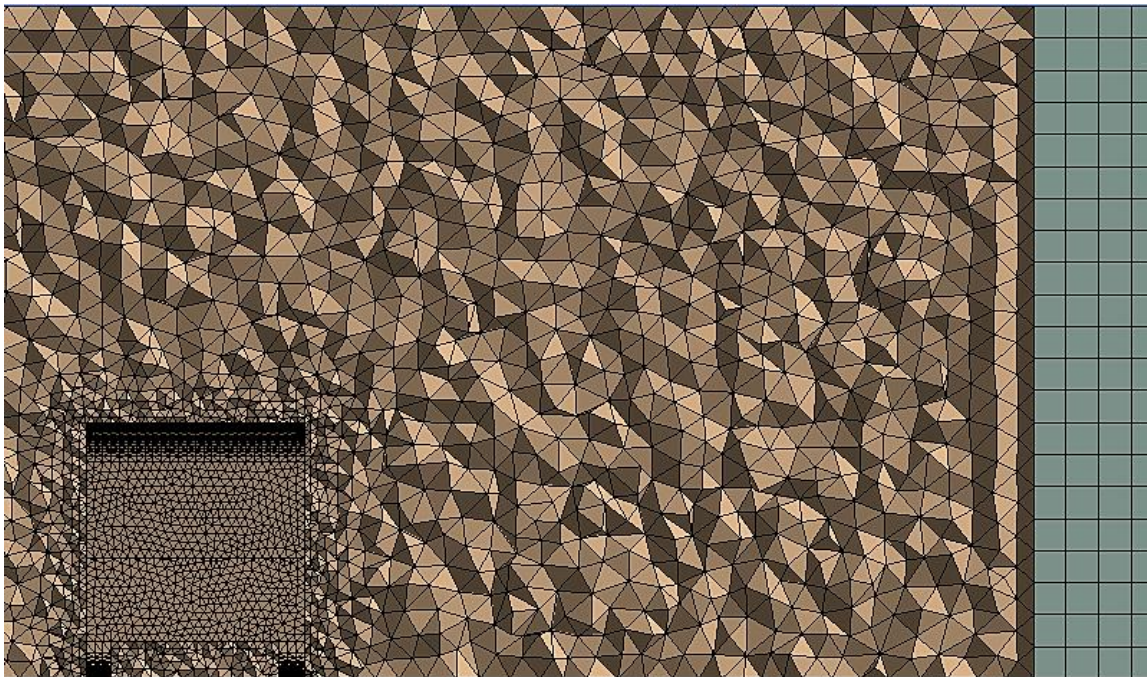


Figure 3.3 Mesh with inner section contained finer elements and the outer section consisted of much coarser elements

In order to ensure that the numerical simulations are not influenced by the meshing controls, a mesh independence study has been carried out. The mesh has been refined by simply dividing the flow domain into additional mesh elements and thus, enhancing the resolution of the simulation. The independence of the simulation from the mesh density has been judged by the

variation of the drag force coefficient ( $C_D$ ) values with number of elements. Four different mesh profiles with 1.9, 4.1, 7.6 and 16.3 million mesh elements were chosen to carry out the mesh independence testing. Figure 3.4 shows the mesh independence test results for the truck-trailer’s drag coefficient.

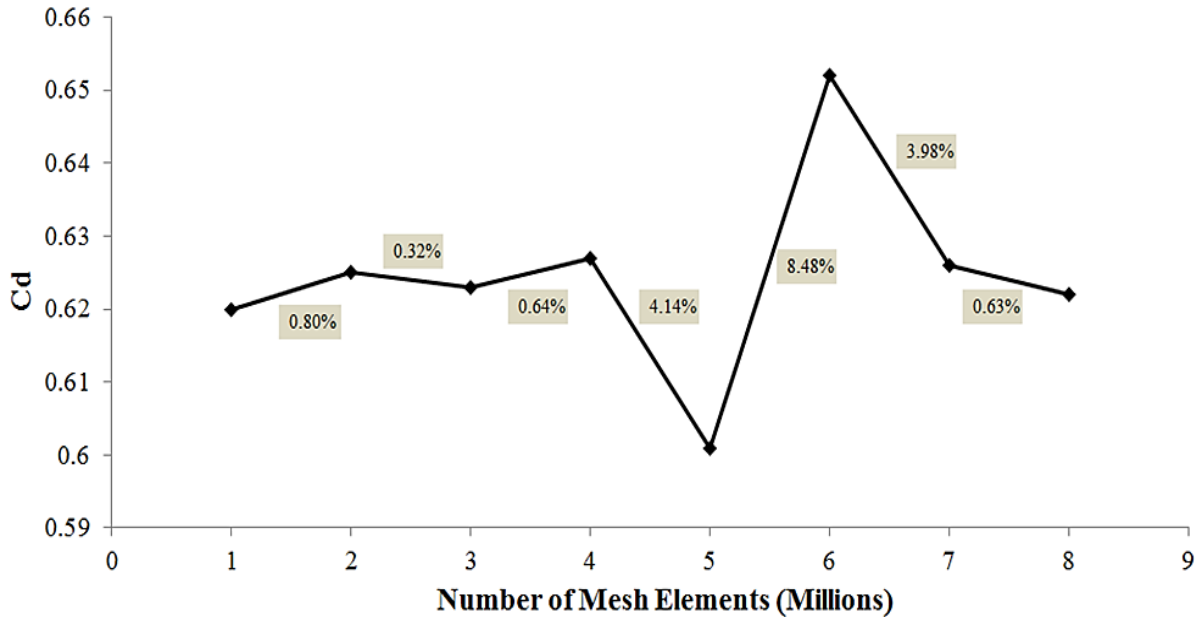


Figure 3.4 Mesh Independence test results

It can be seen that there are significant variations in the drag coefficient from 4-7 million mesh models. However, further increasing the mesh density to 8 million changes the drag coefficient of the truck-trailer unit negligibly (0.63%). Hence, the mesh model with 7 million mesh elements has been chosen in the present study for further analysis.

### 3.3 Solver Execution

ANSYS FLUENT has been used in this study to simulate the flow field around a vehicle model via finite volume methodology. This is used to solve a range of formulations such as Navier-Stokes for governing three dimensional, viscous, compressible fluid flow equations. The entire system for the Navier-Stokes equations comprises of continuity, momentum and energy, which are commonly established for their robustness during numerical simulations in order to determine various fluid dynamic phenomena within or around a body. ANSYS FLUENT uses

the finite volume method to solve the time-averaged Navier- Stokes equations, which consists of three stages; the formal integration of the governing equations of the fluid flow over all the control volumes of the flow domain. Followed by discretization, which involves the substitution of a variety of finite-difference-type approximations for the terms in the integrated equation that represents flow processes such as convection, diffusion and sources. This changes the integral equation into a system of algebraic equations, enabling it to then be solved in the third stage using iterative methods. The first stage of the process, the control volume integration, is the step that distinguishes the finite volume method from other CFD methods. The governing equations of fluid flow represents mathematical statements of the conservation laws of Physics.

### 3.3.1 Conservation of Mass

According to theory, the physical principle behind the continuity equation states [91]:

$$\begin{aligned} & \text{“Mass of the fluid flowing in the control volume – Mass of fluid out of the control volume} \\ & \quad = \text{Rate of change of mass with respect to time.”} \end{aligned}$$

Since the flow in this particular study is incompressible, the equation is as follows:

$$\text{div}(U) = 0$$

Where  $U$  is the time-averaged mean of the velocity vector magnitude.

### 3.3.2 Conservation of Momentum

The momentum equation is based on Newton’s second law of motion stating that the application of the net force onto the fluid particle is directly dependent on the mass and acceleration of the fluid element, given by [91]:

$$F = ma$$

The momentum equation is defined as:

*“Sum of all forces = Rate of change of Momentum”*

Two forces equate to the net force. These are forces that acts directly on the volumetric mass and acts at a distance, known as body forces defined as [91]:

$$\text{For x-direction:} \quad \rho f_x dx dy dz$$

$$\text{For y-direction:} \quad \rho f_y dx dy dz$$

$$\text{For z-direction:} \quad \rho f_z dx dy dz$$

The surface forces are directly applied on the surface and are caused by the pressure distribution introduced by the external fluid neighbouring the particles, as well as normal and shear stress distributions introduced by the external fluid on the surface via friction. The changing time rate of the deformation of the fluid element are related to these stresses.

Figure 3.5 shows pressure is always pushing directly into the fluid element while shear stress on the top surface is being applied in a tugging action. This will move the element in both positive and negative directions respectively. Front surface of the fluid element is subjected to the shear stress or the viscous stress and acts in the positive direction. However, the shear stress acting on the rear surface of the fluid element will act in the negative direction. The normal stress acts normal to the surface which in turn pulls the fluid element in a viscous action in turn delays the motion of the fluid element. The net force is the sum of all these body force and the surface forces.

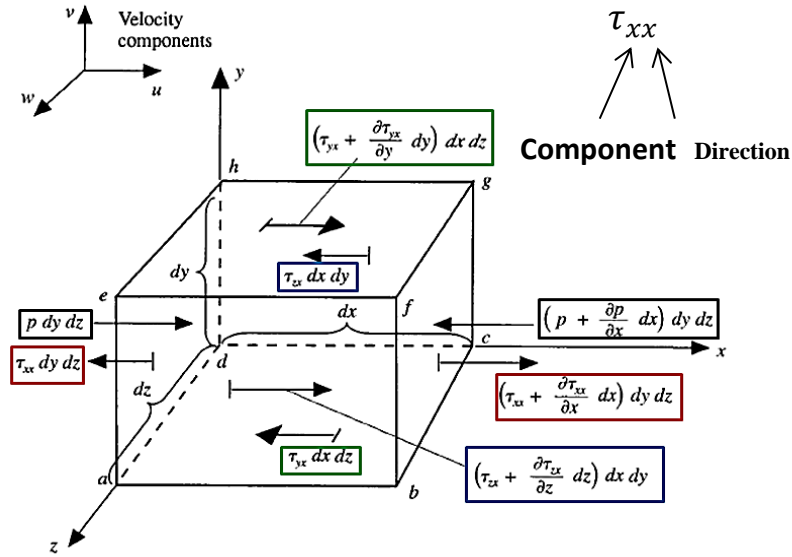


Figure 3.5 Forces Acting on the Fluid Element [91]

The mass is the matter within the control volume and is defined by:

$$\rho \cdot dx dy dz$$

Acceleration is the increase in velocity with respect to time and is defined by:

For x-direction:  $\frac{Du}{Dt}$

For y-direction:  $\frac{Dv}{Dt}$

For z-direction:  $\frac{Dw}{Dt}$

Therefore, through implementation and simplification the momentum equations can be governed.

The time-averaged momentum conservation is expressed as [91]:

$$\begin{aligned} & \frac{\partial(\rho U)}{\partial t} + \text{div}(\rho U U) = \\ & = -\frac{\partial P}{\partial x} + \mu \text{div}[\text{grad}(U)] + \left[ \frac{\partial(-\rho \overline{u'u'^2})}{\partial x} + \frac{\partial(-\rho \overline{u'v'})}{\partial y} + \frac{\partial(-\rho \overline{u'w'})}{\partial z} \right] \\ & \frac{\partial(\rho V)}{\partial t} + \text{div}(\rho V U) = \\ & = -\frac{\partial P}{\partial y} + \mu \text{div}[\text{grad}(V)] + \left[ \frac{\partial(-\rho \overline{u'v'})}{\partial x} + \frac{\partial(-\rho \overline{v'^2})}{\partial y} + \frac{\partial(-\rho \overline{v'w'})}{\partial z} \right] \end{aligned}$$

Velocity of the truck-trailer models are quite low and hence the compressibility effects of fluid can be safely ignored [84]. Hence a pressure based solver was used to simulate the flow around a truck-trailer model. The oncoming flow was considered to be steady and hence a steady state solver has been used throughout this study.

### 3.3.3 Turbulence modelling

In the present investigation, the continuity equation and momentum equation are solved along with two equation SST k- $\omega$  model for a steady turbulent flow. The primary reason behind choosing k- $\omega$  model is its ability in accurately modelling the wake regions and extreme pressure gradients between truck and the trailer and behind the trailer unit. SST k- $\omega$  is a two equation eddy-viscosity model that combines shear stress transport (SST) equation. The combination of SST makes the equation useable even in under low Reynolds number flows and provides accurate results even at the viscous-sub layer near the surface. Moreover, The SST formulation also switches to k- $\epsilon$  behaviour in the free-stream and thereby avoids the common k- $\omega$  problem that the model is too sensitive to the inlet free-stream turbulence properties [83].

### 3.3.4 Boundary Conditions

The numerical investigations have been carried out at the maximum allowed truck-trailer speeds on UK motorways which is 56mph. Therefore, the inlet velocity of the flow domain was taken as 25.034m/s. The magnitude of translational motion from Road and Walls was adjusted to match

the inlet flow speed and similar step have been taken with Wheels to control their rotational speeds. The pressure at the outlet was maintained at the zero-gauge static pressure. To simulate the straight headwind, the front surface of the flow domain was defined as a velocity inlet and the rear surface of the domain was defined as a pressure outlet. Slip flow condition was applied on left and right surfaces of the flow domain and top surface was set as symmetry. To simulate the crosswinds, front surface and the left surfaces of the flow domain were defined as a velocity inlet and the right surface and rear surface was defined as pressure outlets. The truck-trailer surfaces have been defined separately due to the convenience of isolating them to analyse the flow parameters and force components acting on them.

### **3.3.5 Solution methods setup**

The solution methods setup stage follows after boundary conditions. Mesh elements with high skewness magnitudes were expected around the tyre patch area of the wheels. To prevent these highly skewed elements adding instability to the solution, the SIMPLE (Semi-implicit Method for the Pressure-Linked Equation) pressure based segregated algorithm was used for pressure-velocity coupling [85]. The ‘Standard’ scheme was used for pressure interpolation and the ‘Second Order Upwind’ scheme was used to discretise the momentum equations to obtain higher accuracy flow variables at each cell face. The solver settings are specified to compute calculations and predictions for the flow fields as accurate as possible. The equation class in solver control, were set for continuity and momentum, with Green Gauss Node Based Second Order advection scheme using Navier-Stokes equations.

### **3.3.6 Convergence Criteria**

Reaching a converged solution is imperative given that a fully converged solution is known to provide reasonably accurate results. By default, the convergence criteria are set as 0.001 for continuity equation, x velocity, y velocity, z velocity and the turbulence parameters. Hence, as soon as the difference between two calculations (iterations) for all of the parameters mentioned above drops below 0.001 the solution is considered to be converged. However, in many

calculation this is not necessarily true and the convergence criterion alone is not regarded as a measure of convergence for the solution.

In this study, the convergence was studied by monitoring the variations in drag force, lift force and side force coefficient for each iteration. Once the drag, lift and side force coefficients were stable with minimal fluctuations, the solution was considered to be converged. It had been noticed that the solution converges around 2000 iterations as the variation between two drag force coefficients were negligible since all unsteady fluctuations had dampened.

### 3.4 Post-processing

Post-processing consists of the examination of the results obtained and revision of the model based on these results. These can be further elaborated into:

- Examine the results to view solution and extract useful data.
- Visualisation tools used to extract the overall flow pattern, separation, shocks, shear layers.
- Numerical reporting tools to calculate quantitative results like forces, moments, and average heat transfer co-efficient, flux balances, surface and volume integrated quantities.

Due to much improved processing power and graphics rendering capabilities on current computers, the leading CFD packages are now equipped with versatile data visualisation tools. These visualisation tools include vector plots, line and shaded contour plots, 2D and 3D surface plots, particle tracking, view manipulations, colour post – script output etc. More recently, the CFD packages also include the animation capturing tools for dynamic result display, and in addition to graphics, all codes produce trustworthy alphanumeric output and have data export facilities for further manipulation external to the codes. Figure 3.6 depicts a summary of implementing CFD into practice.

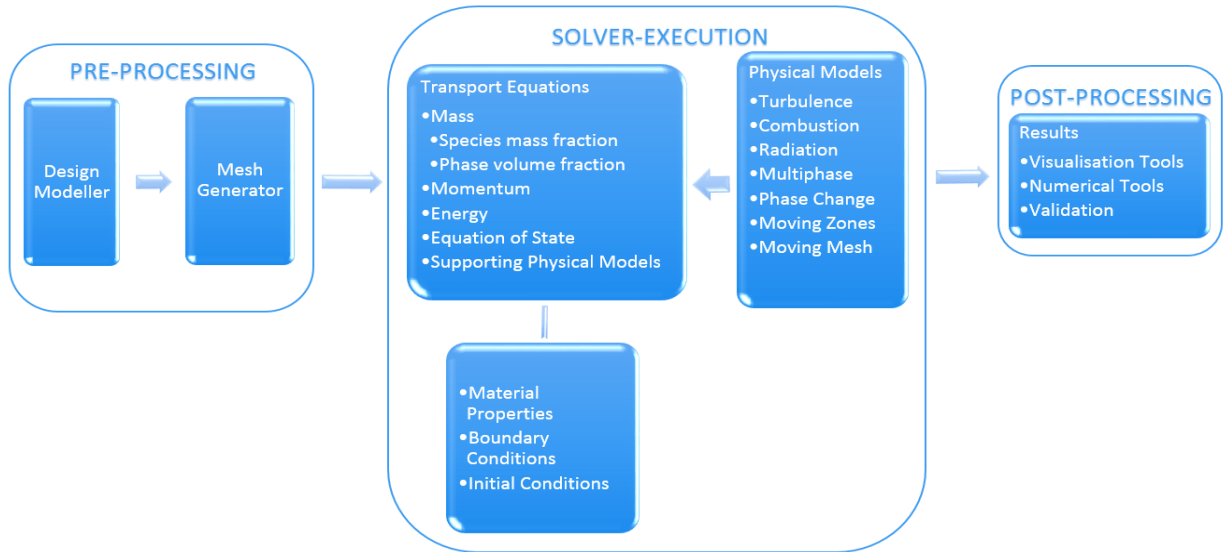


Figure 3.6: Summary of CFD process

### 3.5 Scope of the Numerical Investigations

There are numerous geometrical and flow related configurations involved during this study. In Chapter 4, the geometrical dimensions, length of 15.28m, 15.78m and 16.28m of the truck-trailer had been simulated with height of 4.4m, 4.6m and 4.8m. These are computed at straight headwind where  $\psi = 0^\circ$  and at crosswind where  $\psi = 45^\circ$ ,  $\psi = 30^\circ$ ,  $\psi = 45^\circ$ ,  $\psi = 60^\circ$ ,  $\psi = 75^\circ$  and  $\psi = 90^\circ$ . In Chapter 5, the maximum height and length of the truck-trailer with its shape coefficients had been simulated, where B1, B2, B5 and B6 are independently defined by three levels, 0.01, 0.05, and 0.1 at straight headwind where  $\psi = 0^\circ$ . In Chapter 6, the maximum height and length of the truck-trailer with its shape coefficients had been simulated, where B1, B2, B5 and B6 are independently defined by three levels, 0.01, 0.05, and 0.1 at crosswind where  $\psi = 45^\circ$ ,  $\psi = 30^\circ$ ,  $\psi = 45^\circ$ ,  $\psi = 60^\circ$ ,  $\psi = 75^\circ$  and  $\psi = 90^\circ$ .

Subsequently, from carrying out the numerical simulations for a number of truck-trailer combinations with changing geometrical and flow conditions, the results had been gathered and processed using the in-built Ansys post processing tool. Extensive and detailed discussions on the results are presented in the following chapters. The coming chapter discuss the variations in the flow and force characteristics when the total length, height, width at various crosswind profiles.

## CHAPTER 4

# AERODYNAMIC CHARACTERISATION METHODOLOGY FOR TRUCK-TRAILER UNITS BASED ON VEHICLE DIMENSIONS

---

Design alterations were identified as the key method of reducing the fuel consumption of truck-trailer units. Development of an alternate geometrical modelling method to be used as a truck-trailer design tool will be discussed and tested. The functionality of the developed geometric modelling tool will be showcased and validated using commercially established CAD software. The validated quantification tool will be used to generate a range of truck-trailer geometries with varying maximum height and lengths. The numerical simulation will be carried out to analyse the effect of dimensional characteristics such as length and height on the resulting flow field at straight and crosswind conditions. A prediction tool will be developed for predicting the drag, lift and side forces with respect to dimensional characteristics. The combination of geometrical modelling technique and the proposed prediction model are expected to be used in the early stages of the design process reducing both the design time and associated costs of producing number of models to be analysed.

## 4.1 Introduction into Geometric Modelling

In a nut shell, geometric modelling refers to a collection of methods used to define the shape and other geometric characteristics of an object. Geometric modelling is a key constituent of an area also known as computational geometry and extends beyond this to the newer fields of creating an elegant synthesis of solid geometry modelling using computers.

During the conventional vehicular design process, a scaled down clay model will be created including all the key characteristics of the parent vehicle model which is to be analysed. It is common practice to use a scaled down design model as it is much easier for designers to use and analyse. The model may only incorporate the details that are dictated by the required uses and the operations, to which the model will be subjected to. When the design analysis is carried out on the model, only essential information will be gathered with respect to the study objectives and if the scaled down model is highly detailed it is expected to respond and perform comparable to the full scale vehicle.

Geometric modelling technique has a strong substance combining with well-developed techniques from various fields such as vector calculus, matrix method, topology, analytic and descriptive geometry etc. and, is capable of constructing an accurate and a precise mathematical description of a real object and in this particular case a vehicular geometry. In early days, a simple 2D shape developed using geometrical modelling methods was an achievement. However, in the present day the industries demand both topologically and analytically complete 3D models which geometrical modelling techniques are more than capable of producing.

Three key aspects of geometric modelling has been identified and they are:

1. Representation – Use of shape functions to characterise a truck-trailer unit.
2. Design – Incorporating the key design parameters such as dimension and shape characteristics.
3. Rendering – Use of a CAD software package for generating 2D and 3D solid models.

Geometric modelling is a powerful tool and the primary purpose of it is to accurately represent and allow efficient and flexible manipulation of 3D objects. Representation is a key segment

which is involved at the very beginning of the modelling to the very end of the modelling process. The mathematical approximation will be performed to create a baseline geometric model from a real object.

The design process consists of manipulating the geometric model using geometric transformations, creating new shapes, editing the geometry, interrogating the model and even rendering it. It is important to do this step in order to satisfy chosen operational and aesthetic objectives. A range of variables that define the shape of a model will be manipulated to realise the design process.

Once the first two aspects; representation and design aspects are completed, the user should have an initial geometric model of a design and a manipulated design to suit the study objectives. By now the model should describe a physical shape of a designed geometry. As an image of a model is required to visually represent the model, the rendering provides necessary information to create visuals.

The computer graphics, computer aided design and computer aided manufacturing have been the driving forces behind the rapid development of geometric modelling schemes. Also, naturally the geometric modelling can be applied most effectively in these very areas.

## **4.2 Applicable Mathematical Techniques for Geometric Modelling**

There are several mathematical techniques that can be used in geometric modelling and the most crucial ones being vectors, linear algebra, matrix methods, determinants, set theory, polynomial interpolation and numerical approximation.

### **4.2.1 Vectors**

It is understood that Vectors are the most significant mathematical quantities, because they seem to fit the geometric intuition of displacement. Among the many advantages offered by Vectors, the most important has to be significantly reducing the need for a specific coordinate system. Therefore, using vectors enables the user to choose an appropriate coordinate system at the later

stages of the process when there is more information available to make a good decision rather than right at the beginning. Vectors also contain further geometrical information such as direction and magnitude. Vector operations allow us to readily determine perpendicularity or parallelism. These operations support algebraic operations while retaining geometric meaning. Last, but not least, Vector equations handle several component equations at once.

### 4.2.2 Matrix Methods

Next, matrix methods, the array of numbers that makes up a matrix can represent simply an orderly way of storing numbers pertinent to some problem or perhaps a set of polynomial equation coefficients. The rules of matrix algebra define the allowable operations in these arrays.

Another use of a matrix is an operator. Here, the matrix performs a geometric transformation on a set of points by operating on the position vectors that define these points. The rules of allowable operations are in turn governed by the rules of matrix algebra. This interpretation of a matrix as a geometric operator is the foundation of most geometric modelling computations.

### 4.2.3 Polynomial Interpolation

Upon a close examination of a polynomial interpolation, it can be seen that a great deal of practical numerical analysis depends on techniques called numerical interpolation. Using polynomials for interpolation is extremely advantageous, because they can be evaluated, differentiated, and integrated easily and all in a finite number of steps by using just the basic arithmetic operations of addition.

A polynomial of degree of  $n$  is a function of the form is shown in equation 4-1

$$f(x) = \alpha_0 + \alpha_1x + \dots + \alpha_nx^n \quad (4-1)$$

Polynomial interpolation is very sensitive to the choice of interpolation points. At appropriately chosen points, it produces an approximation differing very little from the best approximant by

polynomials of the same order. However, if the function to be approximated is badly behaved anywhere in the interval of approximation, then the approximation is poor everywhere. This global dependence on local properties can be avoided if piecewise polynomials are used. That is, by constructing a composite curve by fitting successive low-degree polynomial curves to successive groups of data points.

#### 4.2.4 Mathematical Vehicle Modelling Using Shape Functions

Rho et al [43], has carried out a study on shape functions in order to understand the capabilities of the technique to model the exterior shape of a vehicle geometry. In the past, 2D data were mainly used to define a vehicle shape but 3D CAD technology has slowly taken over. A set of number of discontinuous points are usually used to define a 3D CAD geometry. In order to define a somewhat complicated geometry, tens of millions of point will be created. However, Rho et al [43], have developed an efficient way of representing the 3D automobile geometry with less input data. To begin with, the vehicles were sectioned into separate parts and smoothly expressed in terms of Bernstein polynomial curves. Firstly, the vehicle geometry is broken into 3 to 4 different boxes as shown in Figure 4.1. Based on the classification by box, each box was divided into further small boxes as the study aims to represent the shape with functions.

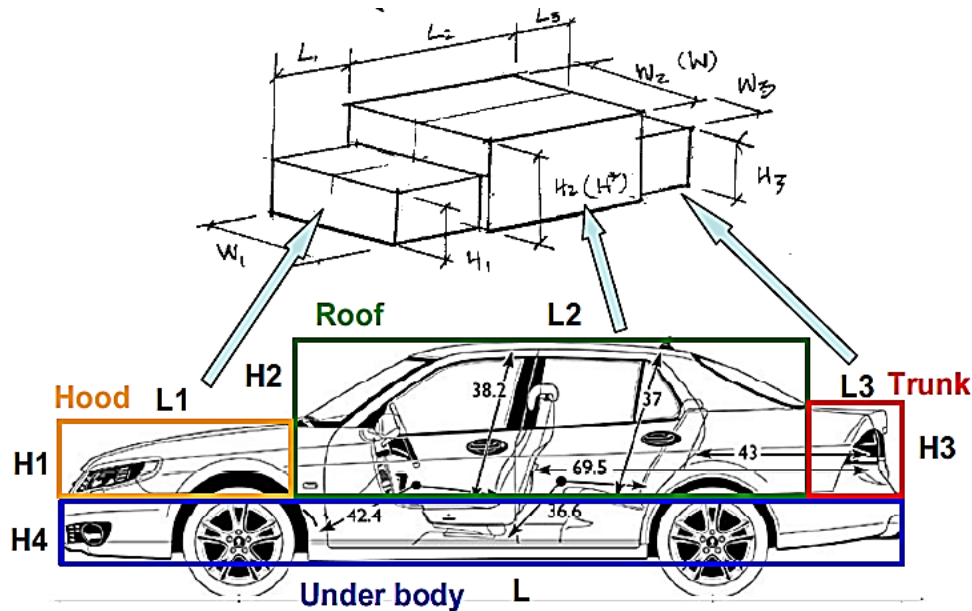


Figure 4.1 Vehicle model with box sections [43]

In order to represent the contour with a function a Bernstein polynomial has been modified. And the vehicle modelling function that freely modifies complex and various shapes has been defined in equation 4.2 [43].

$$F\left(\frac{x}{c}\right) = \left(\frac{x}{c}\right)^{n_1} \left(1 - \frac{x}{c}\right)^{n_2} S\left(\frac{x}{c}\right) + \left(1 - \frac{x}{c}\right) Y_1 + \frac{x}{c} Y_2 \quad (4-2)$$

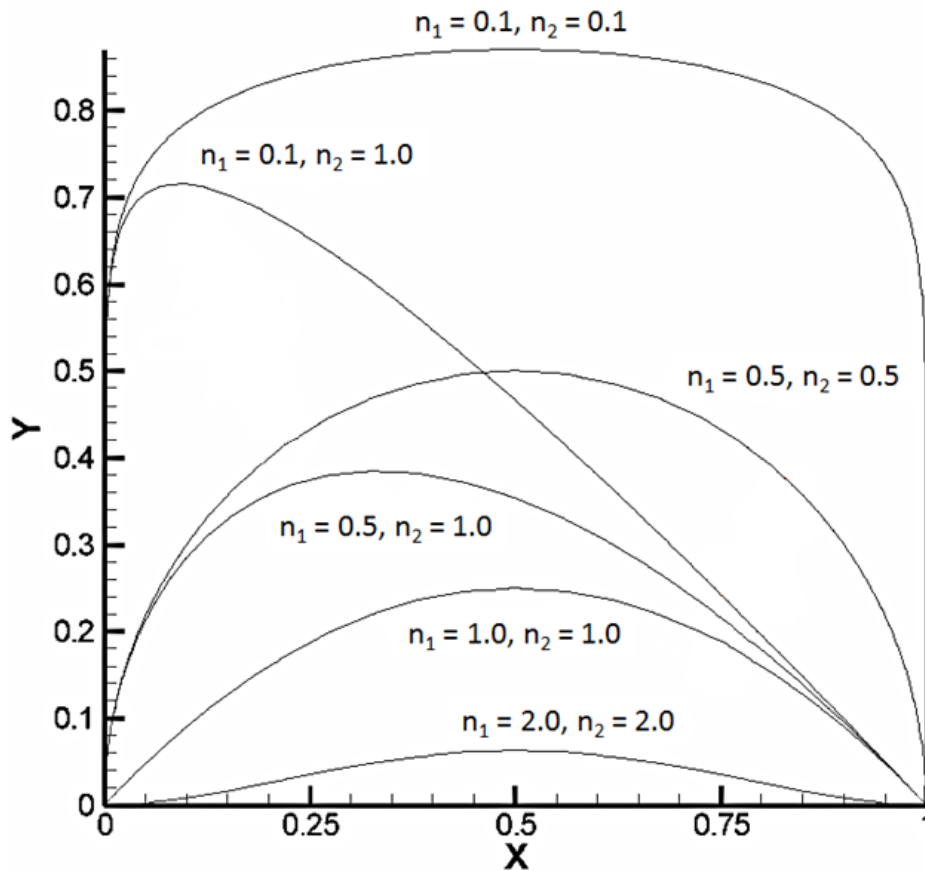


Figure 4.2 Modelling function for external shapes [43]

The length and the dimension of each section box was depicted in Figure 4.1. were represented using  $c$  and  $x$  respectively. The length of the function was non-dimensionalised giving a constant  $c$  while the height of the starting and the end points of the curves were controlled by  $(1 - x / c)$   $Y_1$  and  $(x / c)$   $Y_2$  respectively. Adjusting the curvature and changing the shape of the curves were done by altering the exponents  $n_1$  and  $n_2$  of the first term  $(x / c)^{n_1}$  and the second term  $(1 -$

$x/c$  n2. The characterisation of the functional section box shape was done using the third term  $S(x/c)$ .

Going forward with this approach number of section functions have been introduced to represent the complex contour curves of an automobile. Number of section functions were introduced to describe the shapes of hood, roof, truck, top view, under body so that the combination of these section functions produces the vehicle shape function. The vehicle shape function represented the complete overall vehicle shape. The section functions for hood and the trunk of an automobile is shown in equations 4-3 and 4-4 respectively.

$$S_{\text{Hood}}(x) = H \times \text{Min} \left\{ \left( \frac{x}{P} \right)^B, 1.0 \right\} \quad (4-3)$$

$$S_{\text{Trunk}}(x) = H \times \text{Min} \left\{ 1.0, \left[ \frac{1-x}{1-P} \right]^B \right\} \quad (4-4)$$

### 4.3 2D Representation of the Baseline Truck-Trailer Unit

By drawing the inspiration by the work carried out by Rho et al [43], the feasibility to apply the same design technique on truck-trailer modelling and shape optimisation was studied in the coming sections.

Combination of two shape functioned was used to represent the 2D baseline truck-trailer model. The complete truck-trailer geometry was separated into two sections as body and wheelbase. Then the body was further divided into three separate sections as the shape of the truck, bridge and the trailer unit as depicted in Figure 4.3. Two different shape functions were used to represent the full truck-trailer geometrical outline. First shape function was used to describe the truck, bridge and the trailer unit while the second was used to describe the wheelbase of the vehicle.

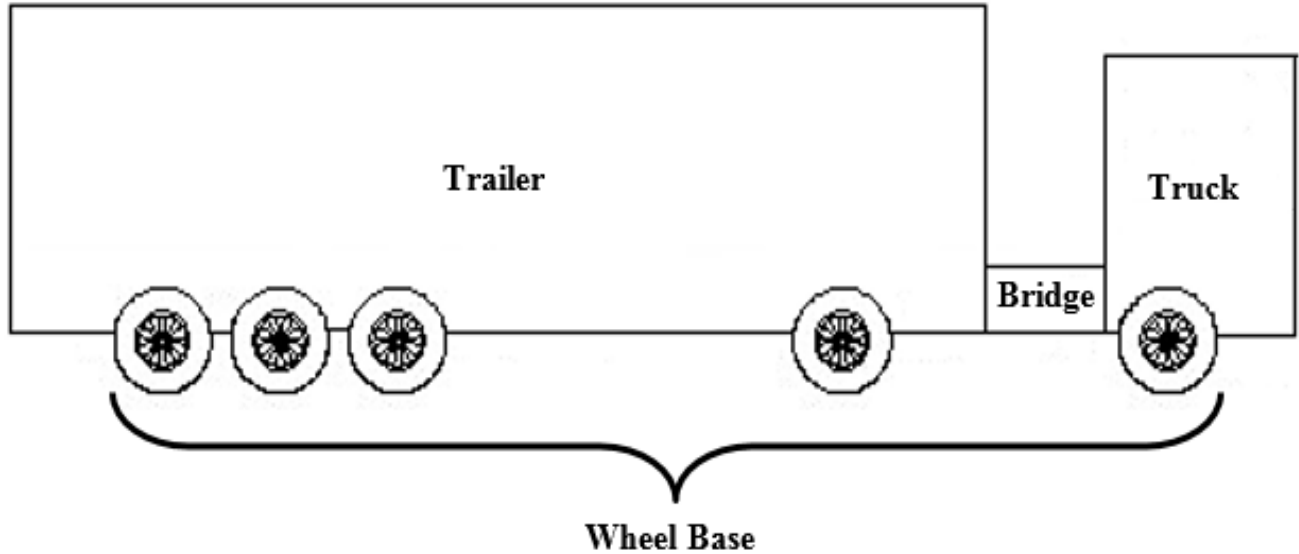


Figure 4.3 Sections of a truck-trailer unit

A single shape function was generated by combining the section functions shown in the equations 4-3 and 4-4 to represent a Truck, Bridge and Trailer sections of the vehicle. The sections were represented by the profiles which were generated along x and y axis using the shape function equation. This generated a 2D frontal profile for each of the truck, bridge and trailer sections and the single shape function to create these profiles is shown in equation 4-5.

$$S_{\text{Section}}(x) = H \times \text{Min} \left\{ \left( \frac{x}{P_1} \right)^{B_1}, 1.0, \left[ \frac{1-x}{1-P_2} \right]^{B_2} \right\} \quad (4-5)$$

Where  $S_{\text{Section}}$  is the section of the surface generated, x is the width of the section in a XY plane, H is the height of the profile in the y direction, P1 and P2 represents the end point and the starting point of the first profiles and the second profile respectively while coefficients B1 and B2 determine the gradients of the curves. Equation 4-5 has been used to define the first frontal profile of the truck-trailer unit, as shown in Figure 4.4.

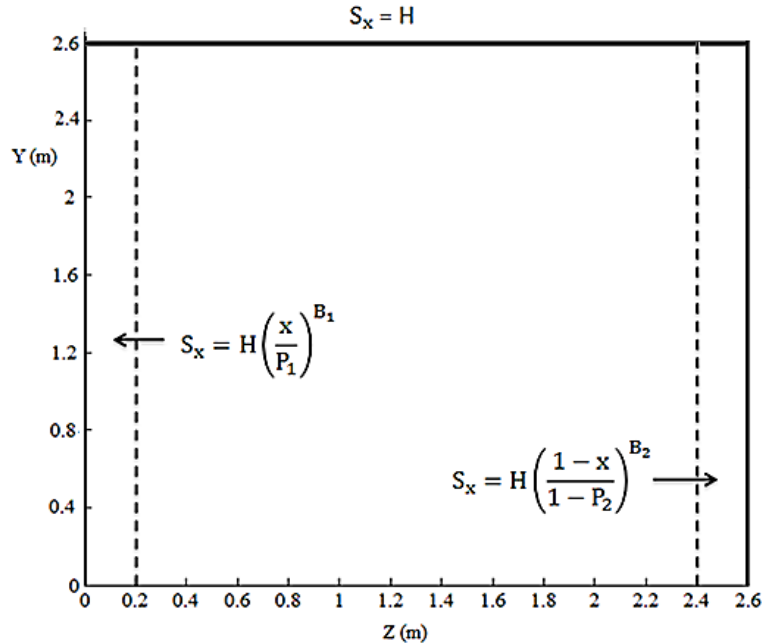


Figure 4.4 Very first profile of the truck unit

The first profile of the truck unit has a height of 2.6m and a width of 2.6m as this is the maximum width of the truck-trailer unit. Using the same methodology, a total of 13 profiles were used to represent the truck unit. Similarly, 4 profiles were generated to represent the bridge, connecting truck to the trailer unit and further 12 profiles to represent the trailer unit as shown in Figure 4.5.

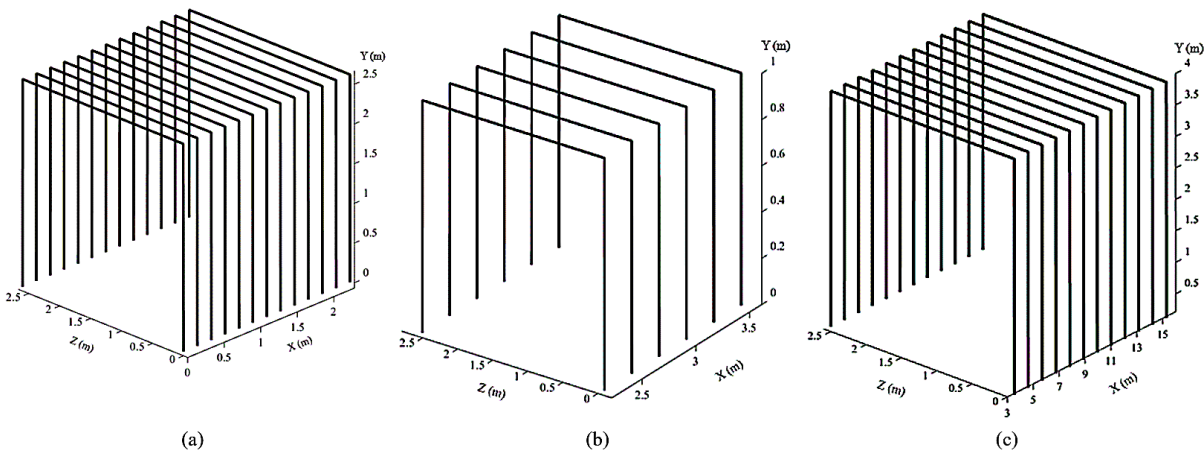


Figure 4.5 Section profiles on the YZ plane, positioned along the x direction to represent the truck (a), bridge (b) and the trailer unit (c).

The profiles were generated on the YZ plane and positioned along the x direction to achieve the complete profile of the truck-trailer model. This method permits the ability to manipulate the shape of the truck-trailer model in both the x direction as the surface profile of the top faces can be manipulated using the height and number of profiles been used along the x direction. The shape of the truck-trailer unit along the z direction can be altered using the B1 and B2 coefficients as they determine the gradients of the curvatures situated at the either end of a single profile.

It is possible to alter the shape function presented in equation 4-5 to generate profiles along the XY plane. This will provide further flexibility in changing the truck-trailer shape as this generates a 2D frontal profile for each of the truck, bridge and trailer sections along the z direction. The shape function to create these profiles is shown in equation 4-6.

$$S_{\text{Section}}(z) = H \times \text{Min} \left\{ \left( \frac{z}{P_1} \right)^{B_3}, 1.0, \left[ \frac{1-z}{1-P_2} \right]^{B_4} \right\} \quad (4-6)$$

Yet again the  $S_{\text{Section}}$  is the section of the surface generated, H is the height of the profile in the in the y direction, P1 and P2 represents the end point and the starting point of the first profiles and the second profile respectively. The coefficients B3 and B4 determine the gradients of the curves along the x direction and x represent the length of the section in XY plane.

A combination of profiles generated using  $S_{\text{Section}}(x)$  and  $S_{\text{Section}}(z)$  will provide profiles in both YZ plane and XY plane generating a wire frame model of a complete truck trailer model as depicted from Figure 4.6.

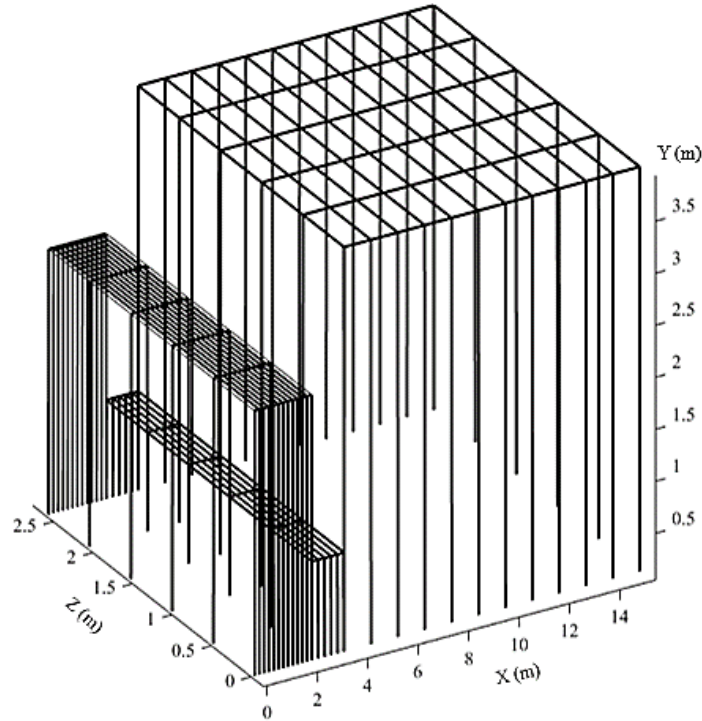


Figure 4.6 The generated 3D wireframe structure for a complete truck-trailer model.

Similarly, equation 4-7 has been developed to generate the wheel base for the truck-trailer unit, where  $K$  controls the vertical position of start and end points of the wheels,  $r$  is the wheel radius,  $x$  is the length dimension and  $w_c$  is the wheel centroid position.

$$S_{\text{Section}}(x) = K - \sqrt{r^2 - (x - w_c)^2} \tag{4-7}$$

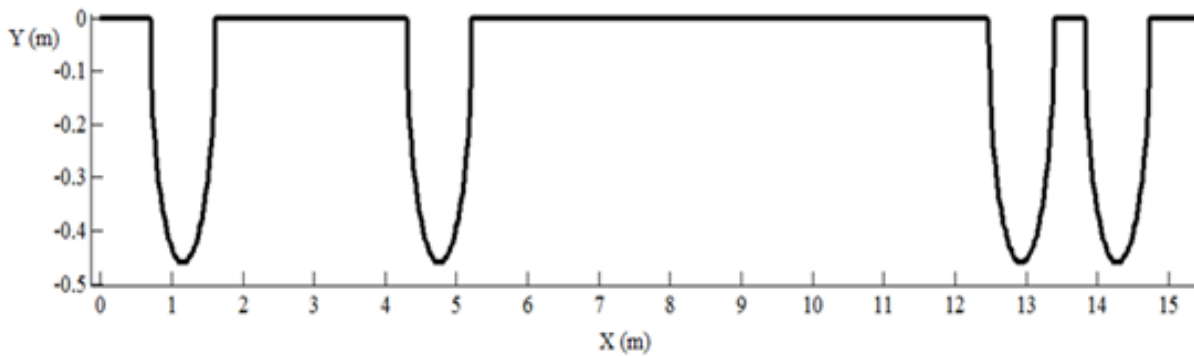


Figure 4.7 Profiles of the complete truck-trailer unit with wheelbase

Using equation 4-7 it is possible to generate 4 axles, 5 axles and 6 axles wheel base designs with various wheel diameters. The 4-axle wheelbase generated for this study is depicted from Figure 4.7.

The wheelbase profile generated using equation 4-5 was paired with the profiles generated using the shape function equation 4-6 to obtain the complete truck trailer profile as shown in Figure 4.8. The combination of the above developed shape functions has been used to generate the baseline truck-trailer unit, having width and length of 2.6m and 15.28 m respectively.

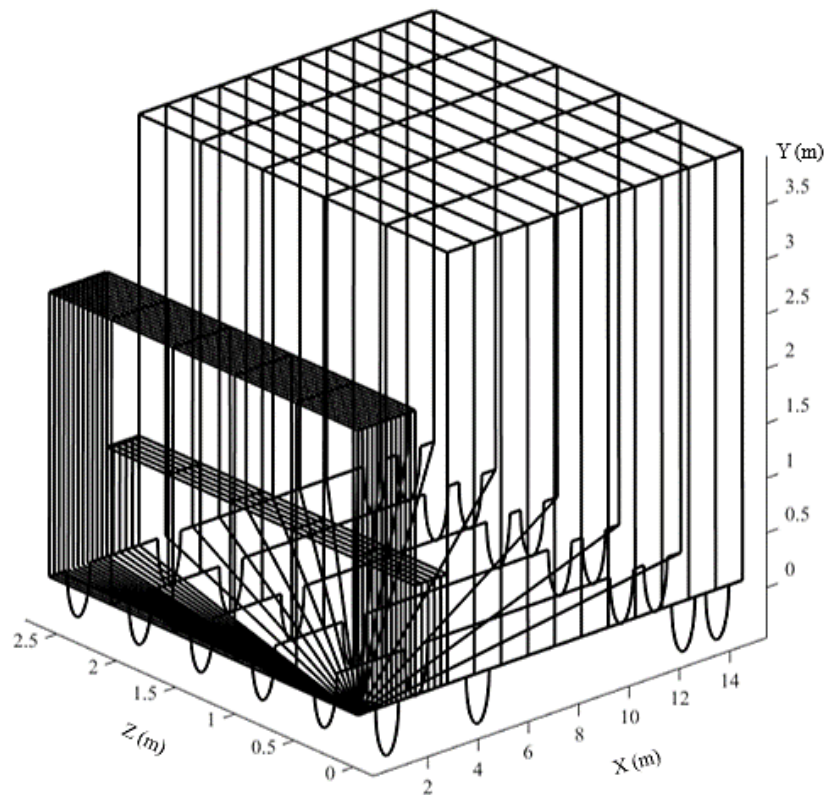


Figure 4.8 Complete truck trailer profile including the wheel base generated using the shape function equations.

#### 4.4 Solid Modelling of Baseline Truck-Trailer Model

Once the mathematical modelling techniques explained in the previous section is completed, X, Y and Z coordinate points for each truck-trailer profile were obtained. Once, the coordinate points were obtained, they were exported into a CAD software package in order to obtain a solid model. In this study, Ansys design modeller CAD software package was used to generate the geometry. The points obtained by solving the shape function equations were exported as data points. Once the data points are exported into the CAD package, individual profiles have been generated replicating the wireframe model obtained through the mathematical modelling process as shown in Figure 4.9.

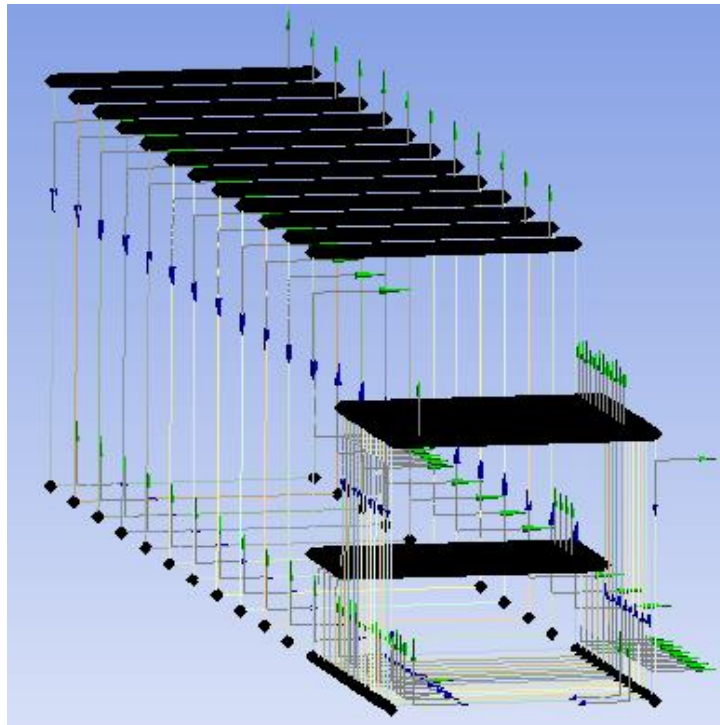


Figure 4.9 Profiles of the truck-trailer unit

When the wireframe model is generated using the CAD package, the loft feature has been used to combine the individual profiles together to generate a solid model which can then be meshed and numerically solved using a CFD software package to study the resulting aerodynamic effects.

To portray the capabilities of this design method a simple truck-trailer model with a 15.28m total length and a 4.4m trailer height was designed and shown in Figure 4.10. The capabilities of this proposed design methodology to accurately model and generate complex truck-trailer shapes has been illustrated in the coming chapters.

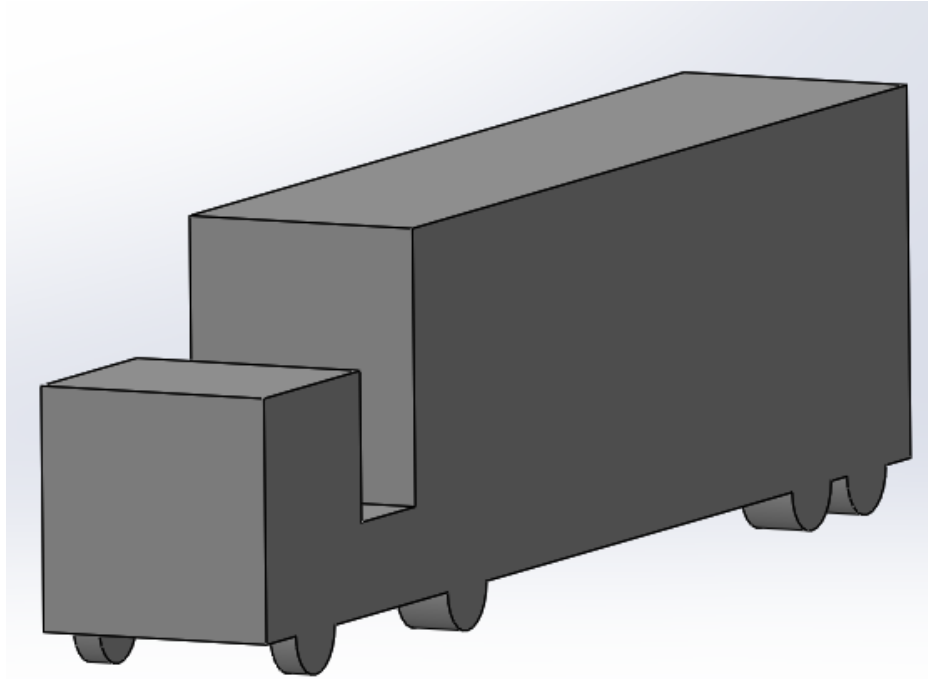


Figure 4.10 CAD model of the baseline truck-trailer model with a 15.28m length and 4.4m trailer height.

#### 4.5 3D Representation of the Baseline Truck-Trailer Unit

A simple truck-trailer unit was used as the baseline model in order to validate the proposed design methodology and the resulting aerodynamic parameters. In order to carry out the baseline data analyses, a generic truck-trailer configuration has been generated as depicted in Figure 4.11. This illustrates the dimensions specified for the model as well as the baseline solid model imported into the numerical setup. Once the baseline geometry is generated, a steady state CFD simulations will be carried out and the corresponding results will be discussed in the following sections.

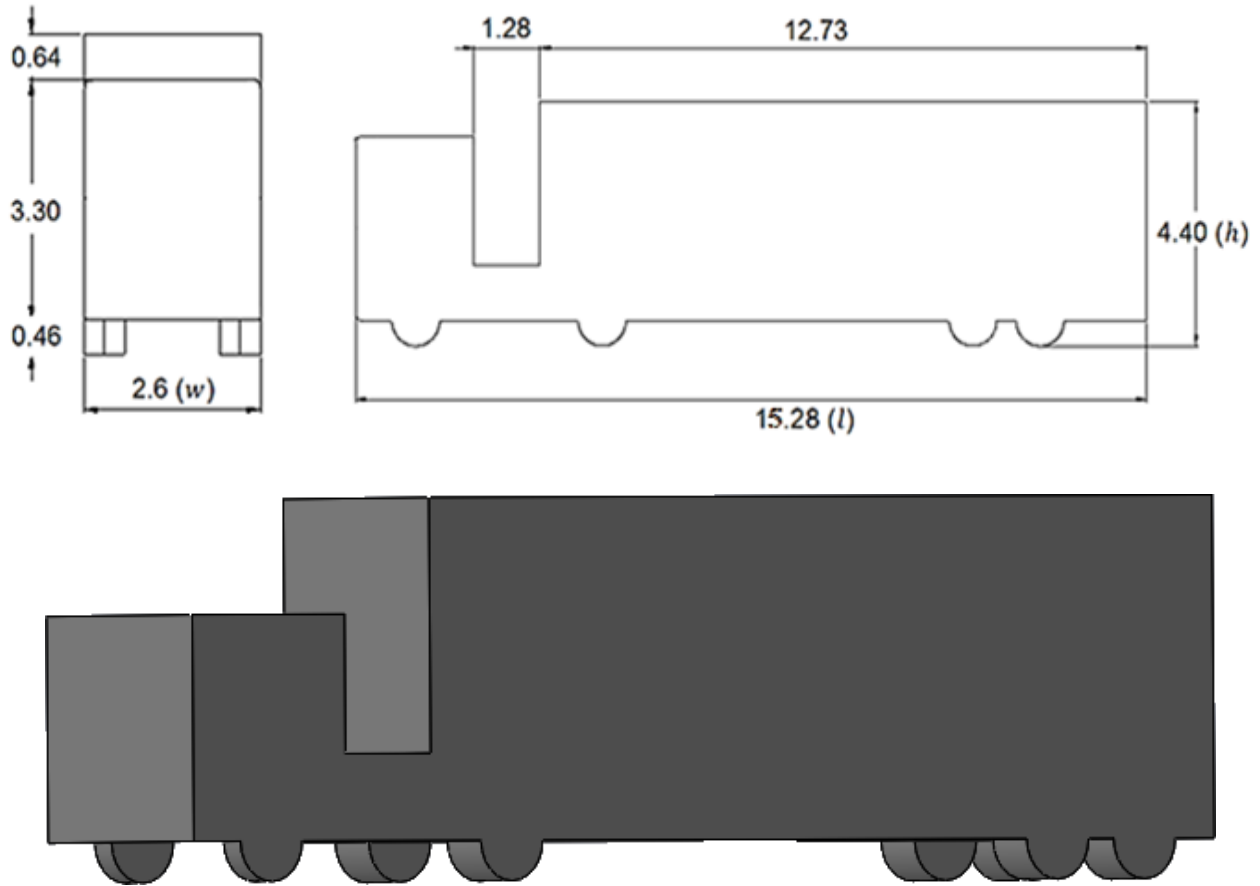


Figure 4.11 The baseline truck-trailer configuration with a total length of 15.28m and a height of 4.4m.

#### 4.6 Validation of the CFD Code and Proposed Design Methodology

Prior to starting the simulation process, it is vital to validate the CFD code to make sure that accurate and reliable data can be obtained. In order to validate the CFD code the widely used technique is to compare the CFD data with experimental data obtained at the exact same conditions.

The CFD predicted aerodynamic coefficients have been verified against the experimental data obtained by Coleman and Baker [34] for a truck-trailer unit with different dimensions to the one considered in this particular study. The numerical study carried out to compare the aerodynamic coefficient obtained by CFD against the aerodynamic coefficient obtained by Coleman and Baker in order to verify the reliability of the CFD model. Lift coefficient ( $C_L$ ) and side

coefficient ( $C_S$ ) data have been recorded for a range of yaw angles ( $\psi$ ) at a constant inlet flow velocity of 16.6m/s. Figure 4.12 ( a and b) depicts the variation in  $C_S$  and  $C_L$  at various yaw angles. It can be clearly seen that  $C_S$  values obtained using CFD simulations are quite low at smaller yaw angles, which then increases proportionally. This trend observed in CFD data is in-line with the published experimental data recorded by Coleman and Baker [34]. Furthermore, the  $C_L$  values rise gradually with the yaw angle, until it reaches  $40^\circ$ , depicting the peak of the  $C_L$ . When the yaw angle reaches  $40^\circ$ , the  $C_L$  then decreases as the flow angle continues to increase. The trend appears to follow a sinusoidal waveform since when the yaw angle reaches  $80^\circ$ , the  $C_L$  once again begins to rise. It can be seen that the CFD predicted results follows a similar trend to that of the experimental data. In both data sets, the highest  $C_L$  values are recorded at  $40^\circ$ , which subsequently begin to decline until the lowest  $C_L$  values are obtained at  $80^\circ$ . The obtained CFD data has been discovered to be in reasonable agreement with the experimental data with respect to the trends, standard error of estimate and the Chi Square between the experimental and numerical data. Standard error of estimate and the Chi Square have been calculated to be approximately 10% and 0.99 respectively. Hence, the numerical results obtained using CFD depict no significant difference to the experimental data. This confirms that the CFD setup used to obtain the data for the current work predicts the aerodynamic force to a reasonable accuracy.

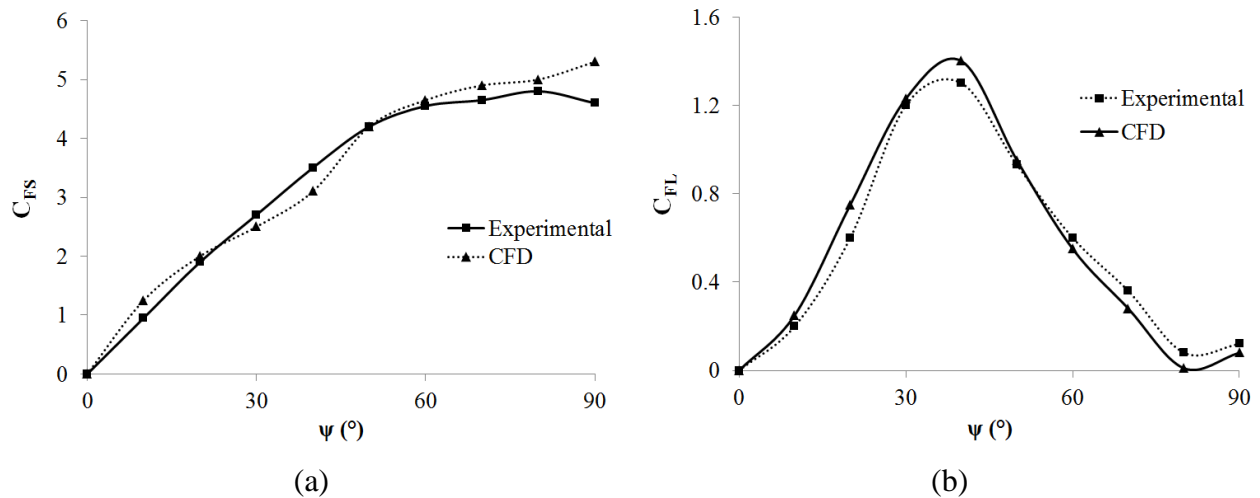


Figure 4.12 Comparison of aerodynamic coefficients at various yaw angles (a) Side coefficient ( $C_S$ ) (b) Lift coefficient ( $C_L$ )

## 4.7 Validation of the Proposed Design Methodology using the Baseline Truck-Trailer Model.

The proposed design methodology was used to generate the baseline truck-trailer geometry using the dimensions shown in Figure 4.12. Validation of the design methodology was carried out using CFD to solve the surrounding flow field of this baseline geometry. This section is expected to conclude the geometrical modelling section by illustrating that a truck-trailer geometry can be obtained and solve for its flow field using CFD. The flow field characteristics of the baseline model is explained in detail from the following sections.

A through flow analysis was carried out as the data obtained from this section was regarded as the reference data throughout this chapter to isolate the change in height and length effects on the resulting flow field.

### 4.7.1 Pressure Distribution on Key Surfaces of the Baseline Truck-Trailer Unit

Investigation of flow behaviour in the vicinity of the truck-trailer unit is essential as it provides important insight into the response of the vehicle's flow field to variations in the vehicle shape and on coming flow profile. In the present study, these variations are characterised by change in flow angle about the yaw (vertical,  $y$ ) axis, change in trailer length and trailer height. A study of the pressure distribution has been carried out to gain an understanding of this aerodynamic behaviour. In order to analyse the pressure field in depth, the pressure distribution on key surfaces of the vehicle have been analysed. These pressure values have been represented in non-dimensional form, as coefficient of pressure ( $C_p$ ), which can be expressed as:

$$C_p = \frac{P - P_\infty}{0.5 \rho V_\infty^2} \quad (4-8)$$

Where  $P$  is the local static pressure (in Pa),  $P_\infty$  is the static pressure at free-stream location (upstream the model where there is no disturbance in the pressure field; in Pa),  $\rho$  is air density (in  $\text{kg/m}^3$ ),  $V_\infty$  is the free-stream flow velocity magnitude (in m/s). In the present study,  $P_\infty$  has been considered as the ambient atmospheric pressure of 101325Pa,  $\rho$  has been specified as  $1.225\text{kg/m}^3$

and  $V_\infty$  has been considered the same as the flow velocity at the inlet of the flow domain. The analysis presented in this section has been carried out to see the flow field effects of baseline truck-trailer model.

#### 4.7.2 Pressure Distribution on the Front Face of the Truck

The front face of the truck unit is a key surface on the vehicle as it experiences the highest pressure as it comes to direct contact with the oncoming flow. This makes the front surface one of the dominant contributors to the overall pressure drag acting on the vehicle. Therefore, a detailed analysis of the variations in the pressure on this face is crucial for a better understanding of the aerodynamic behaviour of the model. In this section, the pressure distribution on the front face of the truck has been discussed.

Figure 4.13 depicts the distribution of coefficient of pressure ( $C_p$ ) on the front face of the truck unit at straight head wind, ( $\psi = 0^\circ$ ). Front face has been divided into four sections using a horizontal and a vertical centreline for analysis purposes as depicted from Figure 4.13. It can be seen that a circular high pressure region is concentrated at the centre of the face having a diameter of about 55% of the surface width. This is also known as the point of stagnation pressure and the highest pressure in the entire vehicle exists in this region. This is due to the fact that the oncoming air perpendicular to the face come to rest after colliding on the front surface converting kinetic energy into pressure in the process. From the centre, the flow accelerates towards the peripheral edges of the surface and separates away. Consequently, the pressure coefficient is seen to decrease from a maximum of 0.9 at the centre of the face to a minimum of -0.1 close to edges. It is also noted that the bottom half of the front face has a higher concentration of high pressure compared to the top half and the pressure distribution is not symmetrical about the horizontal centreline.

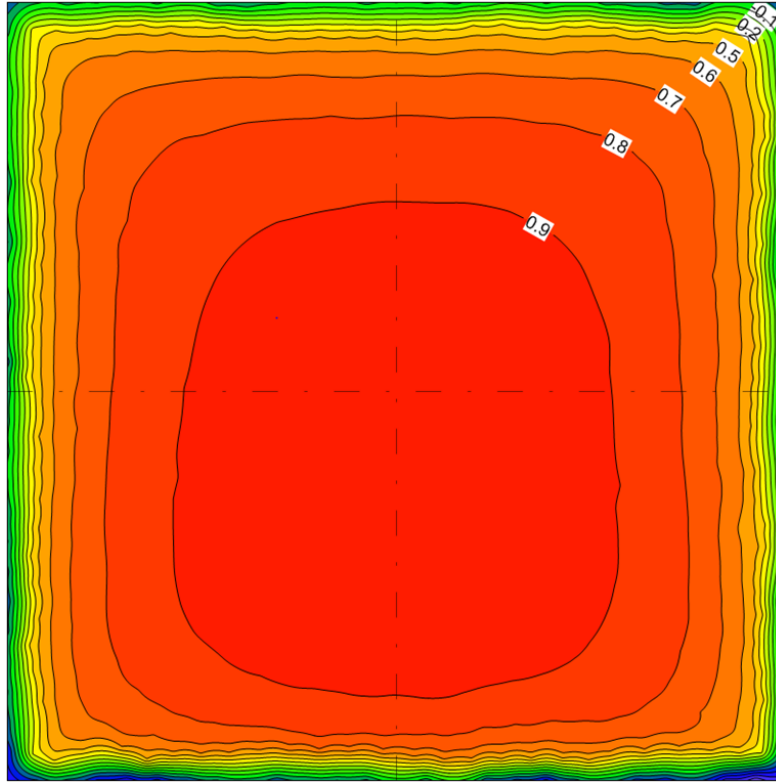


Figure 4.13 Distribution of coefficient of pressure ( $C_p$ ) on the front face of the truck unit with a 15.28m trailer length and 4.4m height.

### 4.7.3 Pressure Distribution on the Rear Face of the Truck

Figure 4.14 depicts the distribution of coefficient of pressure on the rear face of the truck unit at straight head wind. The highest  $C_p$  of 0.2 is seen to exist near the bottom edge of the face and the  $C_p$  is seen to decrease towards the bordering edges reaching a lowest  $C_p$  of -0.5. Low pressure regions are seen to occupy more than 2/3 of the rear truck face and compared to the front truck face shown in Figure 4.13, the reduction in highest pressure is around 77.7%. The low pressure is a result of flow separation at the top leading edge of the face and the consequent flow recirculation region generated in between the truck-trailer gap region.

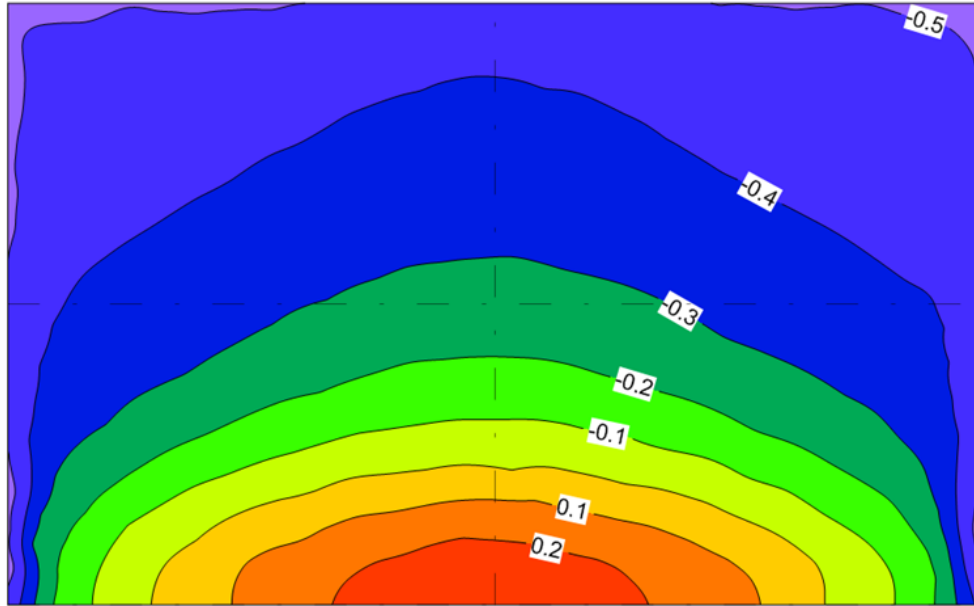


Figure 4.14 Distribution of coefficient of pressure ( $C_p$ ) on the rear face of the truck unit with a 15.28m trailer length and 4.4m height.

#### 4.7.4 Pressure Distribution on the Front Face of the Trailer

Figure 4.15 depicts the distribution of coefficient of pressure on the front face of the trailer unit. The pressure distribution is symmetrical about the vertical centreline of the surface mainly as a result of straight head wind condition. Some of the oncoming flow on top of the truck unit is seen to strike the top 10% of the face generating a high pressure region having a  $C_p \Rightarrow 0.4$ . Immediately after this high pressure region, the pressure gradually decreases towards the bottom edge of the face. Two identical low-pressure regions of  $C_p = -0.4$  are seen on either side of the vertical centre line of the face. After the low pressure region on the middle of the face, pressure gradually starts to increase towards the bottom of the face. Near the bottom edge of the face the  $C_p$  increases to 0.2 matching the pressure that was observed on rear truck face depicted in Figure 4.14. This high pressure region is due to the circulating air in the gap region coming into contact and getting trapped by the rear truck, top bridge and front trailer faces.

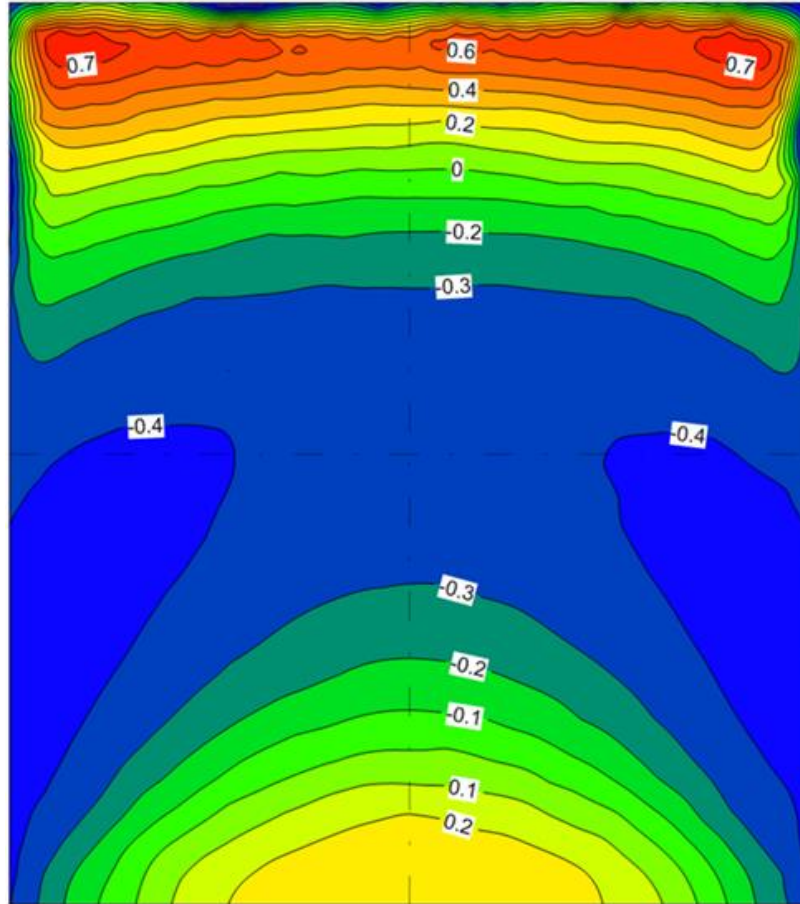


Figure 4.15 Distribution of coefficient of pressure ( $C_p$ ) on the front face of the trailer unit with a 15.28m trailer length and 4.4m height.

#### 4.7.5 Pressure Distribution on the Rear Face of the Trailer

Figure 4.16 depicts the distribution of coefficient of pressure on the rear face of the trailer unit. The pressure distribution is fairly symmetrical about the vertical centreline of the surface but the low pressure area at the bottom of the surface is seen to lean towards the left edge. Negative  $C_p$  values are obtained throughout the rear trailer face, as a result of being located next to the low pressure wake region behind the vehicle. The highest  $C_p$  is obtained as -0.115, whereas the lowest  $C_p$  is obtained to be -0.225. At headwind flow conditions, the flow separate at the top leading edge of the trailer unit. A wake flow region is generated next to the rear face of the trailer unit exhibiting negative pressure. It is also evident that a highly non uniform pressure distribution exists on this face, where the average  $C_p$  is measured at -0.17.

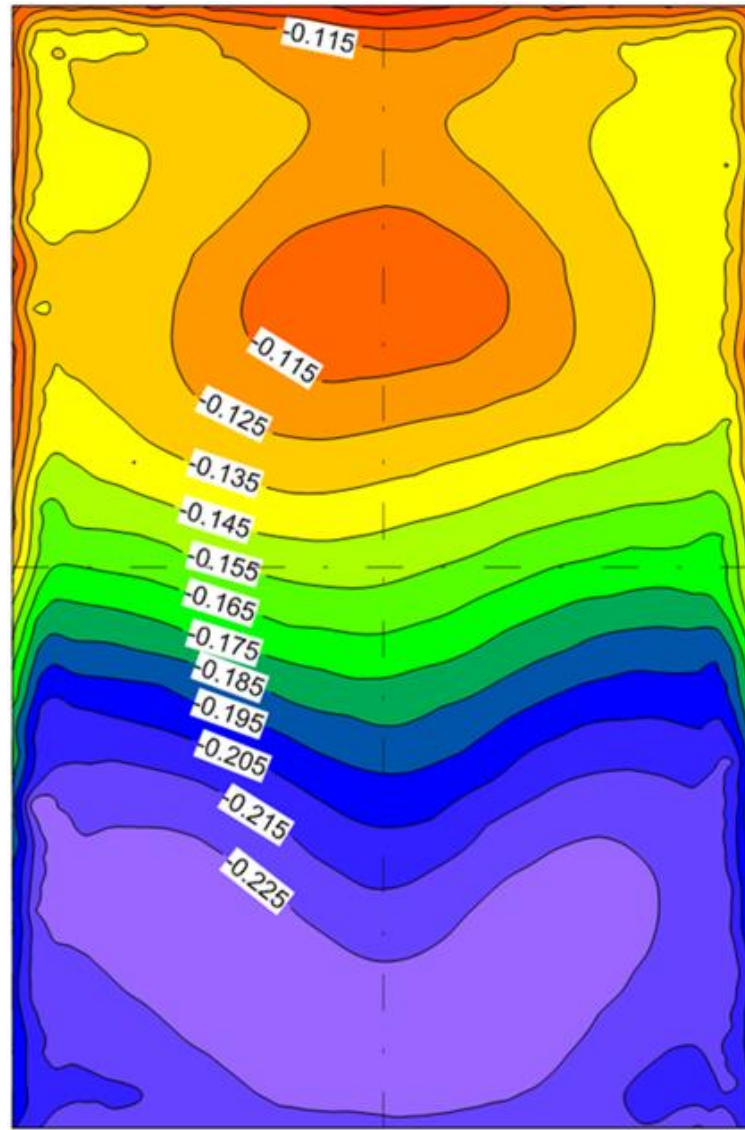


Figure 4.16 Distribution of coefficient of pressure ( $C_p$ ) on the rear face of the trailer unit with a 15.28m trailer length and 4.4m height.

#### 4.7.6 Velocity Distribution Around the Baseline Truck-Trailer Unit

The flow velocity around the truck-trailer model is depicted from Figure 4.17. The velocity fields around the truck-trailer units are highly non uniform. Low velocity regions are seen to exist in front of the truck unit, on the top of the truck unit and in the truck-trailer gap and in the wake region behind the trailer unit. The oncoming flow slows down upon coming into contact with front truck face, creating the first low velocity area as a result. The flow separates at the top

leading edge of the truck unit generating a flow circulation bubble on the top truck face. Part of the separated flow is seen to flow on top of the trailer unit while some of the flow is seen to move into the truck-trailer gap region. The most significant low velocity area is formed behind the trailer unit. This is due to the flow separation that occurs on the rear leading trailing edge of the trailer unit. The airflows underneath and top of the truck-trailer unit is expected to form multiple flow circulation zones at the rear of the trailer. This is evident as the velocity at the centre of the wake region is seen to be 7m/s. However, immediately after the velocity is seen to reduce to 5m/s and 3m/s before increasing gradually after.

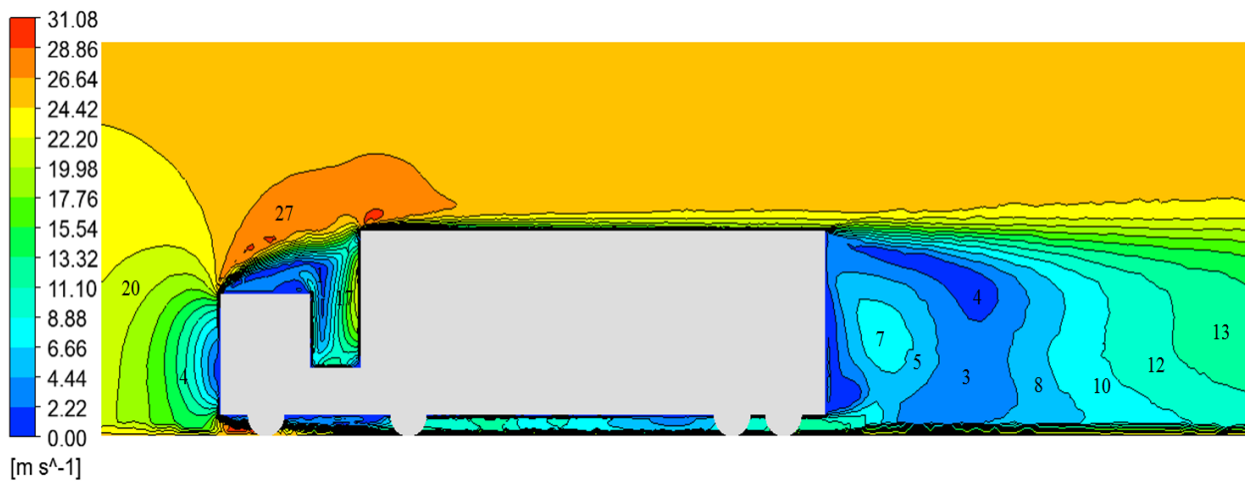


Figure 4.17 Velocity fields around the baseline truck-trailer unit 15.28m long (Side view)

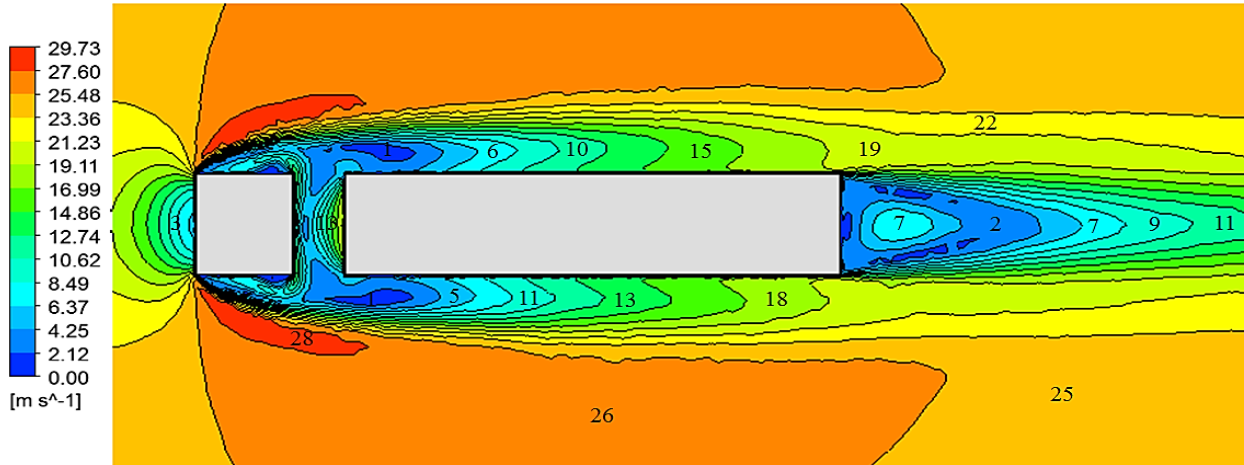


Figure 4.18 Velocity fields around the baseline truck-trailer unit 15.28m long (Top view)

Figure 4.18 depicts the top view of velocity fields around the baseline truck-trailer unit. It is seen that the flow velocity distribution on either side of the vehicle is symmetrical along the horizontal centre line. The flow is seen to separate at either side of the truck unit giving rise to a low velocity region close to the vehicle. This low velocity region extends well past the truck-trailer gap region generating two low velocity circulation flow regions with a maximum velocity magnitude of 1m/s. However, as the flow gets re-attached on the sides of the vehicle the velocity is seen to be recovering to a maximum of 19m/s close to the rear trailer region. This effect is shown from Figure 4.19.

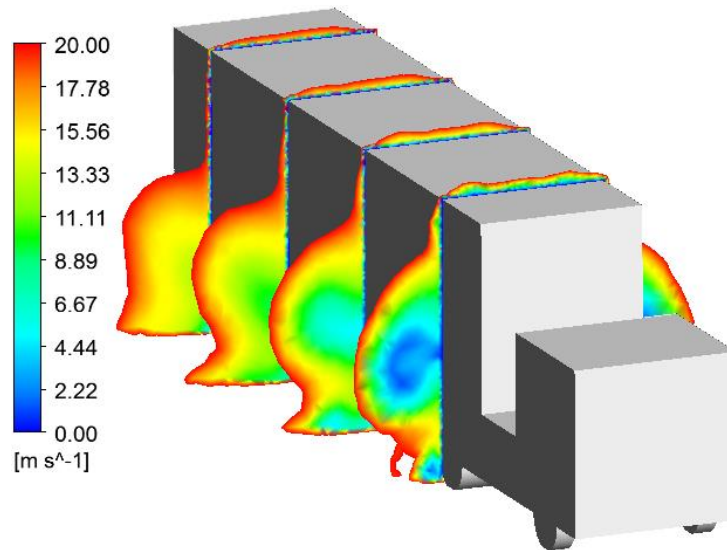


Figure 4.19 Velocity magnitude displayed in XY-planes along the trailer unit

Figure 4.20 shows the flow streamlines around the front section of the baseline truck-trailer vicinity and in the gap region. The oncoming flow in the x direction is seen to separate on the either side of the truck unit. The flow field is seen to be symmetrical along the horizontal centre line of the truck-trailer unit. The separated flow is seen to generate four circulation regions and they have been named as A, B, C and D. The most prominent circulation region is denoted by A and this was observed to occur near the right hand side surface of the truck unit. Circulation region B occurs on the left and hand side face of the truck unit opposite to circulation region A. This is seen to be of reduced size and less prominent compared to A. Two more circulation regions are generated on either side of the gap region and are denoted as C and D. They are both smaller in magnitude and size compared to A and B.

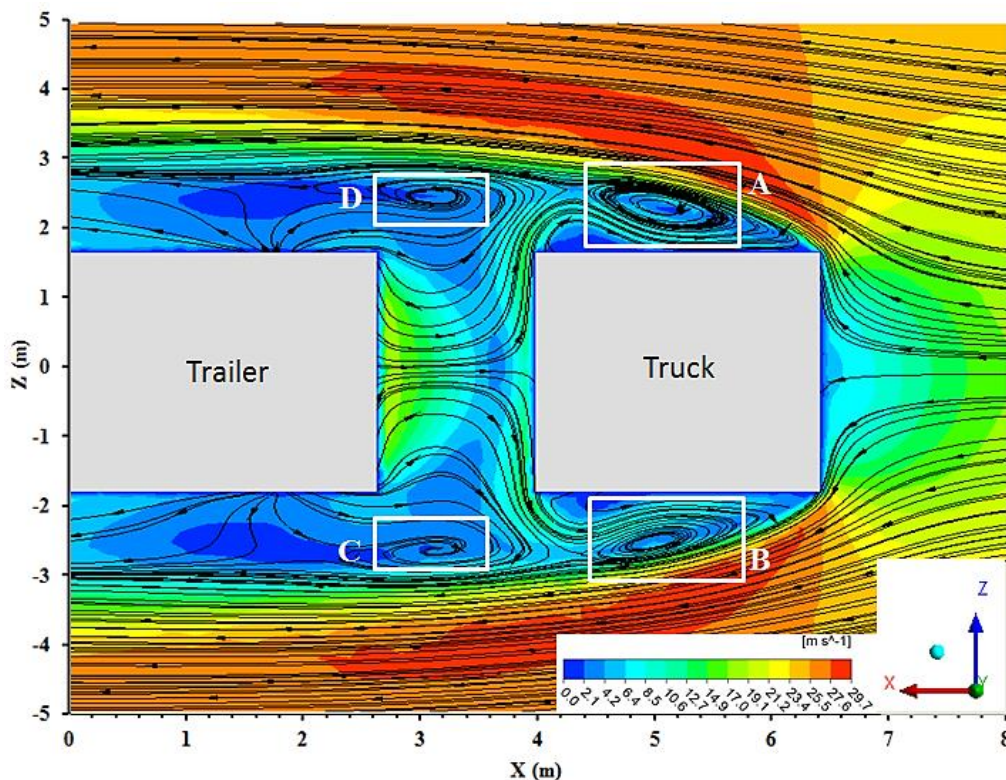


Figure 4.20 The streamline patterns of the flow field in the front section of the baseline truck-trailer vicinity and in the gap region

The flow field at the rear of the trailer unit is depicted using streamline patterns in Figure 4.21. The flow is seen to separate at the leading trailer edge generating a wake region consist of low pressures and velocities. The under carriage flow is seen to escape into the wake region from the bottom of the rear trailer edge. Whilst some of this flow continues to travel in the direction of the upstream flow (x direction), some seen to travel towards the rear trailer face before moving up and joining the high velocity flow at the top of the flow field. This generate two flow recirculation zones at the rear of the truck-trailer unit denoted by A and B. The separation point for the under carriage flow is denoted by C.

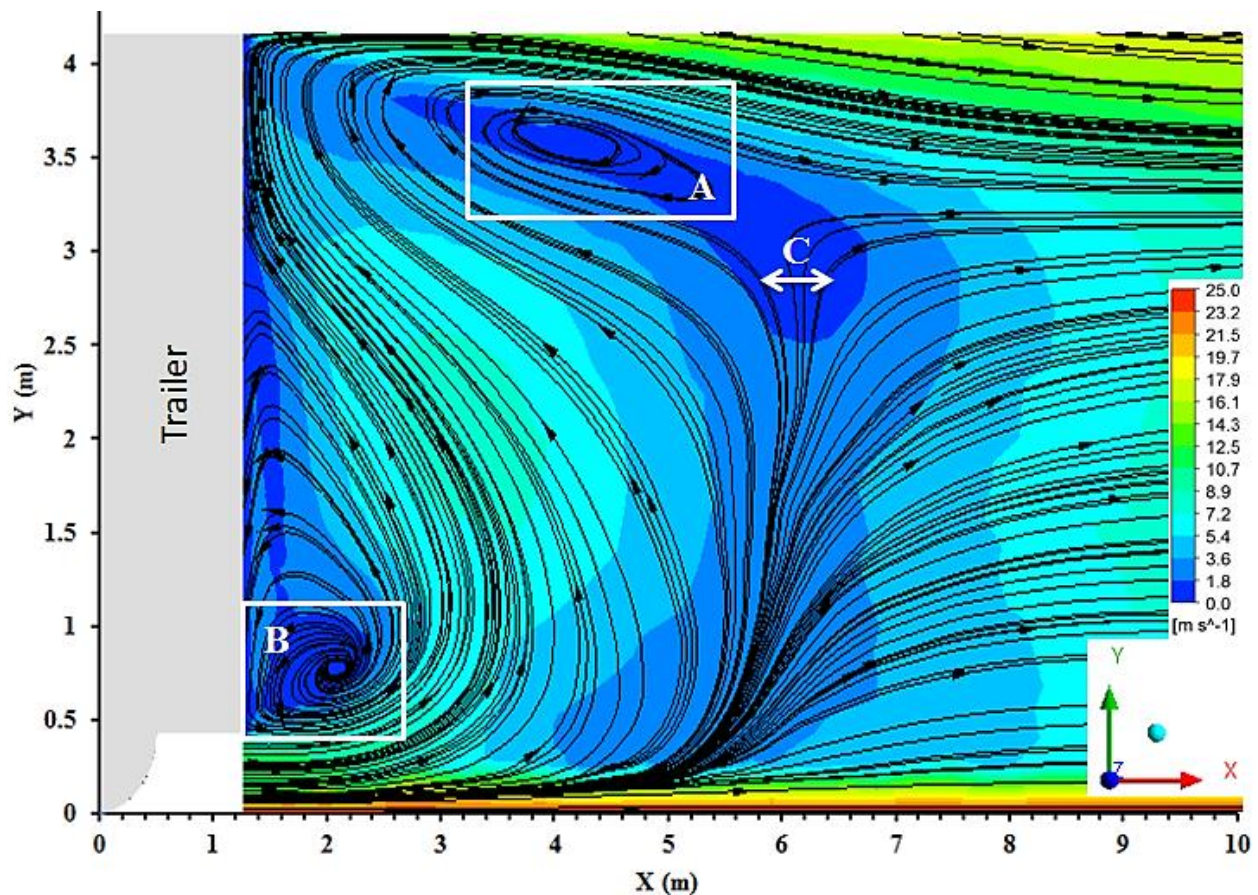


Figure 4.21 Streamline patterns of the flow field at the rear of the baseline truck-trailer model

## 4.8 Effect of crosswinds on the Pressure Distribution on Key Surfaces of the Truck-Trailer Unit

A significant contribution of this study is to understand the aerodynamic forces acting on a truck-trailer unit. The crosswinds can significantly alter the flow profiles around the truck-trailer units. The flow will separate at alternate locations around the vehicle surfaces, shifting wake flow regions in the process. Similarly, the pressure profiles on individual truck-trailer surfaces will vary, changing the magnitudes of drag, lift and side forces acting on the vehicles.

Consideration of the angle between the wind velocity relative to the truck-trailer unit and direction of truck-trailer velocity is vital when calculating wind induced forces and moments. This is further illustrated in Figure 4.22.

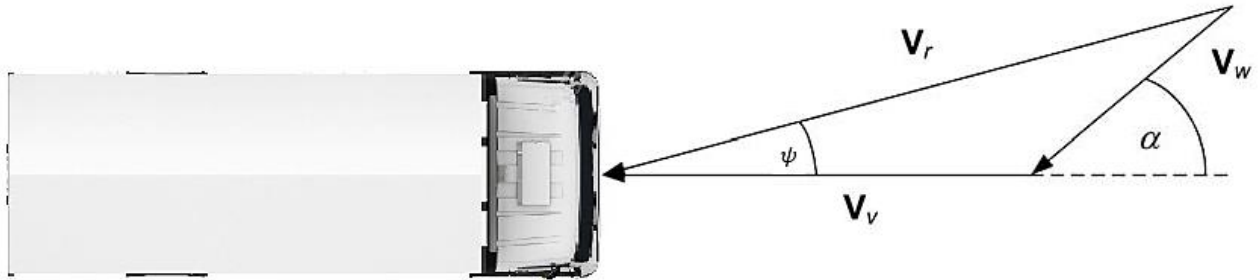


Figure 4.22 Formation of relative wind velocity with respect to the vehicle by considering the wind velocity  $V_w$ , velocity of the truck-trailer unit  $V_v$ , direction of the wind  $\alpha$ , wind velocity relative to truck-trailer  $V_r$  and the yaw flow angle  $\psi$ .

After studying the Figure, it is possible to ascertain the following equations:

$$V_r = \sqrt{V_w^2 + V_v^2 + 2V_wV_v\cos(\alpha)} \quad (4-9)$$

$$\psi = \cot^{-1} \left\{ \frac{V_v + V_w\cos(\alpha)}{V_w\sin(\alpha)} \right\} \quad (4-10)$$

Here,  $V_w$  is the wind velocity,  $V_v$  is the velocity of the truck-trailer unit, direction of the wind is given by  $\alpha$ , wind velocity relative to truck-trailer is denoted by  $V_r$  and the yaw flow angle is denoted by  $\psi$ . When the crosswind angle and magnitude, the velocity of the wind close to the truck-trailer unit is a direction function of its speed. In this case, it was assumed that the truck-trailer unit is moving in a straight line.

Number of yaw flow profiles were used in this section of the study ranging  $0^\circ$  to  $90^\circ$ . Alteration in pressure fields on the key surfaces of the baseline geometry will be compared with the pressure fields generated under straight headwind.

#### 4.8.1 Pressure Distribution on the Front Face of the Truck

The front face of the truck unit experiences the highest pressures as it comes to direct contact with the oncoming flow and contribute to the aerodynamic forces significantly. In this section, the pressure distribution on the front face of the truck has been discussed for crosswind angles of  $0^\circ$ ,  $30^\circ$ ,  $60^\circ$  and  $90^\circ$ .

Figure 4.23 depicts the distribution of coefficient of pressure ( $C_p$ ) on the front face of the truck at various relative flow angles considered in the present study. Figure 4.23(a) corresponds to  $\psi = 0^\circ$ , where it is expected that the head-on wind will get separated from the peripheral edges of the front face of the truck. Hence, it can be seen in the Figure that there is a relatively low pressure region present at the periphery of the front face. As the yaw angle increases, and the flow is expected to approach the truck from the left side in the Figures, it is expected that the separation will now take place from the left hand side edges of the front face, which is clearly visible in Figure 4.23(b) for  $\psi = 30^\circ$ . Further increase in the yaw angle to  $60^\circ$  and  $90^\circ$  are expected to significantly decrease the pressure on the front face of the truck, as the flow is no longer directly approaching this surface and due to heavy separation around the edges. A very non-uniform pressure distribution can be seen in Figures 4.23(d), with pressure decreasing rapidly as the yaw angle increases to  $90^\circ$ .

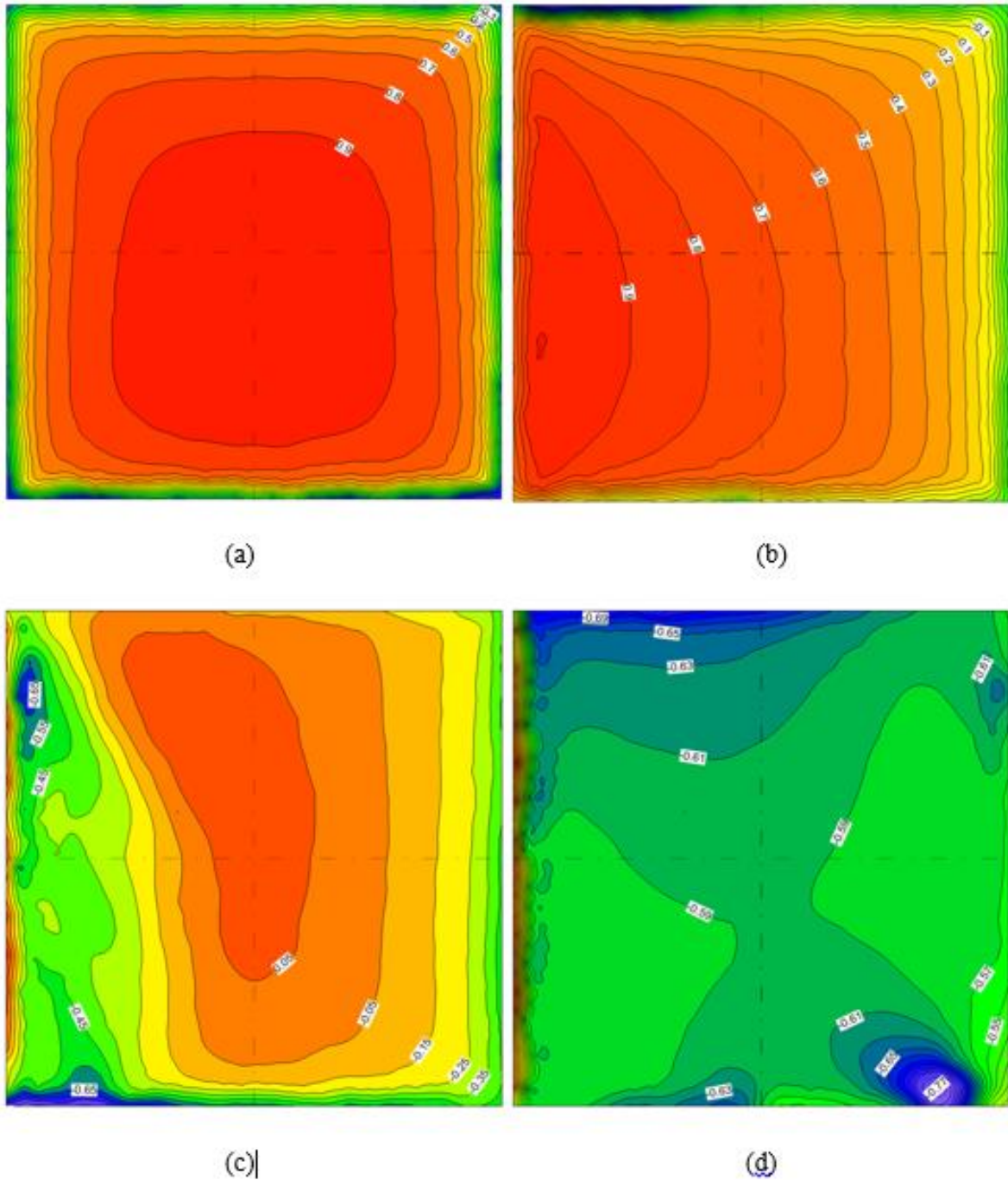


Figure 4.23 Variations in coefficient of pressure ( $C_p$ ) on the front face of the 15.28m truck unit when the trailer height is 4.4m at yaw flow angles ( $\psi$ ) of (a)  $0^\circ$  (b)  $30^\circ$  (c)  $60^\circ$  (d)  $90^\circ$ .

## 4.8.2 Pressure Distribution on the Rear Face of the Truck

Figure 4.24 depicts the distribution of coefficient of pressure ( $C_p$ ) on the rear face of the trailer at various relative flow angles considered in the present study. Figure 4.24(a) corresponds to  $\psi = 0^\circ$ , where the flow is head-on to the truck's frontal face. At this particular flow angle, the contribution of the rear surface of the trailer towards the aerodynamic drag force is due to the negative pressure. The flow is expected to separate at the top trailing edge of the truck and the flow is not approaching the rear surface of the trailer directly. Highly non uniform pressure distribution is seen on Figure (b-d). As the yaw angle increases, and the flow is expected to approach the truck from the right side in the Figures, it is expected that the separation will now take place from the right hand side edges of the front face, which is clearly visible in Figure 4.24 (d) for  $\psi = 90^\circ$ . As the yaw angle is changed to  $30^\circ$ ,  $60^\circ$  average pressure coefficient is seen to decrease to -0.54 and -0.78 respectively. However, as the yaw angle was further increased to  $90^\circ$ , the pressure coefficient on the truck rear face is seen to increase back up to -0.35. Also it was noted that, when the flow angle changes from  $60^\circ$  to  $90^\circ$ , the high pressure region of the face shift from left hand in former to right hand side in latter case.

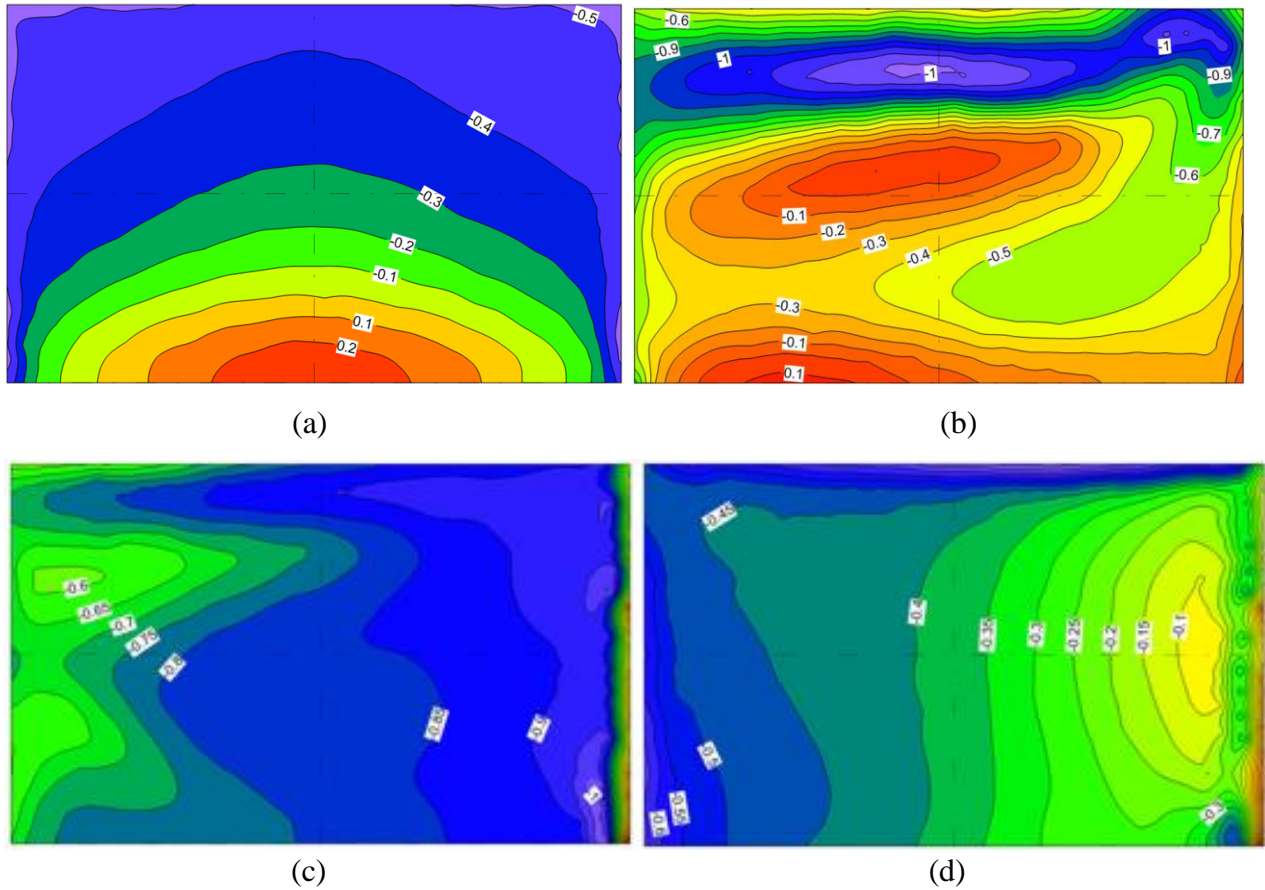


Figure 4.24 Variations in coefficient of pressure ( $C_p$ ) on the rear face of the 15.28m truck unit when the trailer height is 4.4m at flow angles ( $\psi$ ) of (a)  $0^\circ$  (b)  $30^\circ$  (c)  $60^\circ$  (d)  $90^\circ$ .

### 4.8.3 Pressure Distribution on the Front Face of the Trailer

Figure 4.25 depicts the distribution of coefficient of pressure ( $C_p$ ) on the front face of the truck at various relative flow angles considered in the present study. Figure 4.25 (a) shows the pressure coefficient on the front trailer face when  $\psi = 0^\circ$ . The high pressure areas exist close to the top and the bottom leading edges of the trailer front face. The separated flow going past the truck unit come into contact on the front trailer face and come to rest. This in turn reduces the velocity of the flow generating a high pressure area on the top 10% of the trailer face where a highest pressure coefficient of 0.7 exists. The middle of the face is largely dominated by low pressures as a result been close to the truck-trailer gap region. A relatively high pressure region is seen at the bottom of the face due to recirculating flow in the gap region coming into contact with the

surface. As the yaw angle increases, and the flow is expected to approach the trailer from the left side in the Figures and the flow separation will take place from the left hand side edges of the front face. The lowest pressure of  $-0.52$  is seen when the  $\psi = 90^\circ$ . Again the pressure fields on trailer front is seen to be quite uniform at increasing flow angles.

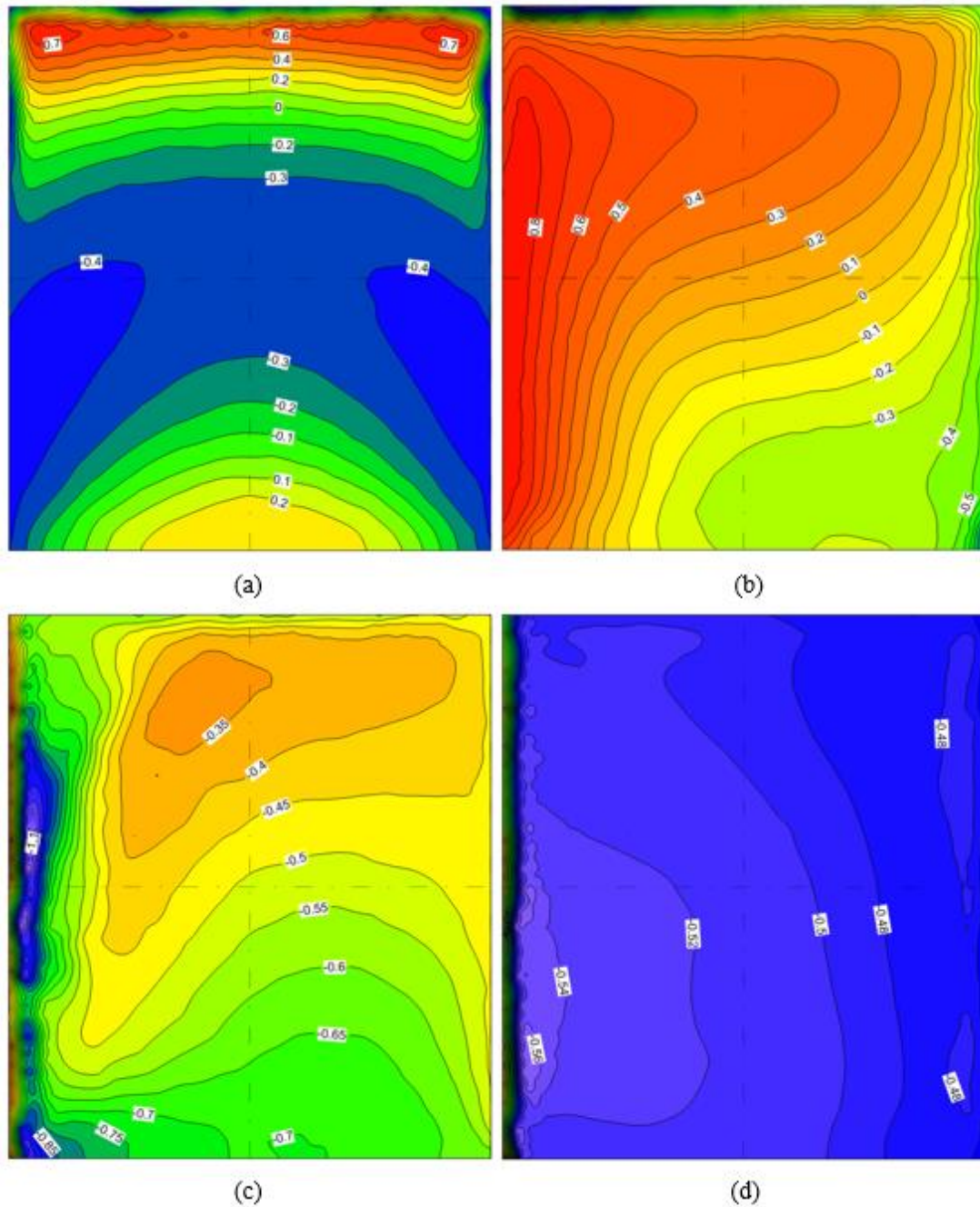
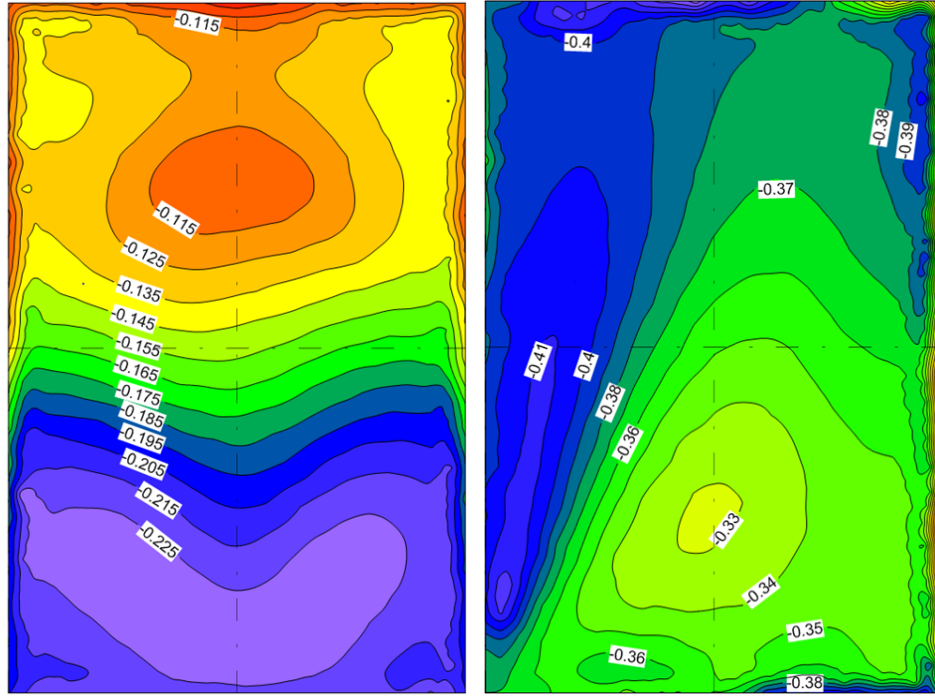


Figure 4.25 Variations in coefficient of pressure ( $C_p$ ) on the front face of the 15.28m trailer unit when the trailer height is 4.4m at flow angles ( $\psi$ ) of (a)  $0^\circ$  (b)  $30^\circ$  (c)  $60^\circ$  (d)  $90^\circ$ .

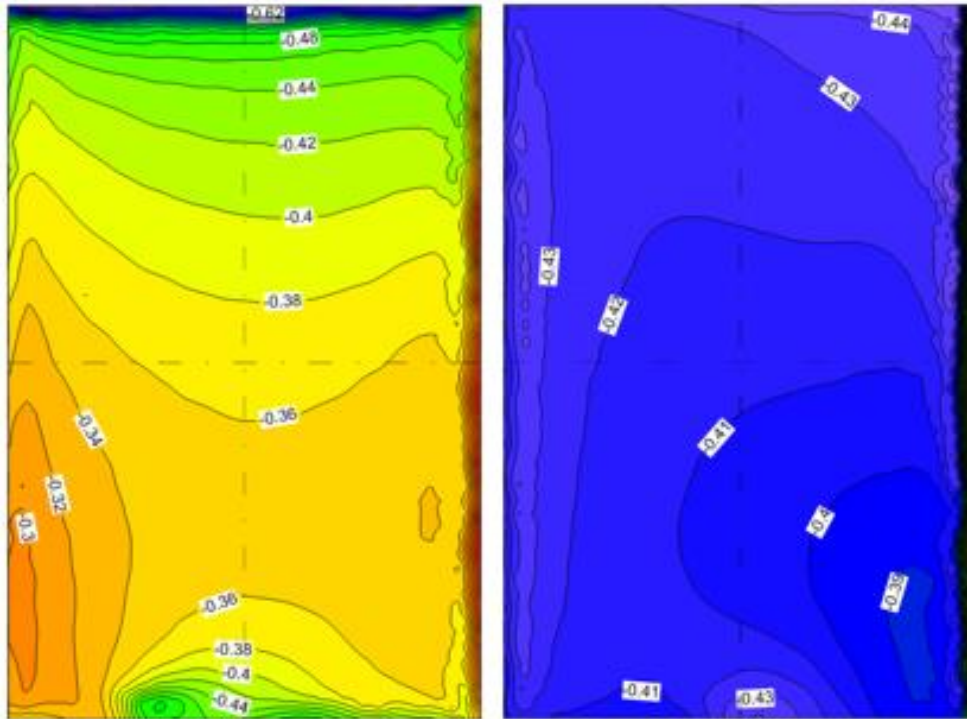
#### 4.8.4 Pressure Distribution on the Rear Face of the Trailer

Figure 4.26 depicts the distribution of coefficient of pressure on the rear face of the trailer at various relative flow angles considered in the present study. Figure 4.26 (a) corresponds to  $\psi = 0^\circ$ , where the flow is head-on to the truck's frontal face. At this particular flow angle, the contribution of the rear surface of the trailer towards the aerodynamic drag force comes because of negative pressure, as the flow is not approaching the rear surface of the trailer directly. It can also be seen that the pressure distribution is highly non-uniform, where the average pressure coefficient has been measured to be  $-0.17$ . Increasing the angle of attack to  $30^\circ$ , in Figure 4.26 (b), it can be seen that as the flow is now approaching from the right side in the Figure, the flow separation is taking place at the right peripheral edge of the trailer's rear face. The average pressure on the surface is still low ( $C_P = -0.37$ ). Further increasing the yaw angle to  $60^\circ$  and  $90^\circ$ , it can be seen that the flow separation on the right edge of the trailer's rear surface increases. This in turn results in an additional decrease in the pressure on the trailer rear face as seen in Figure 4.26 (c-d).



(a)

(b)



(c)

(d)

Figure 4.26 Variations in coefficient of pressure ( $C_p$ ) on the rear face of the 15.28m trailer unit when the trailer height is 4.4m at flow angles ( $\psi$ ) of (a)  $0^\circ$  (b)  $30^\circ$  (c)  $60^\circ$  (d)  $90^\circ$ .

#### 4.8.5 Pressure Distribution on the Windward Face of the Vehicle

The side faces of the truck-trailer unit are important in the overall flow field analysis of the vehicle. This is because these faces are the largest faces on the surface of the entire vehicle. Moreover, the left side has greater significance due to the fact that this face experiences the impact of the larger portion of the oncoming free stream flow at higher angles, in the present study.

Figure 4.27 shows the distribution of coefficient of pressure on the left side surface of the truck-trailer at various relative flow angles considered in the present study. Entire side face of the vehicle can be divided into two sections for simplicity; one being the truck section and the other being trailer section, both connected together by the bridge. Figure 4.27 (a) corresponds to  $\psi = 0^\circ$ , where it is expected that the head-on wind will get separated from the leading edges of the front face of the truck and the trailer, which is expected to re-attach to the solid surfaces somewhere downstream. Hence, it can be seen in the Figure that there is a low pressure region present near the front of the truck unit (right end in the Figure) with  $C_P \leq -0.6$ , where the flow gets separated from the surface of the truck, causing lower pressure. This pressure is seen to increase to  $\geq -0.35$  near the back end of the truck, where the flow gets re-attached to the surface of the truck. Similarly, in the case of trailer, non-uniformity in pressure distribution is seen in the front half of this face. This non-uniformity in the pressure field can be attributed to the separation of the flow as it passes beyond the leading vertical edges of the trailer. The front end of the trailer region is seen to have a  $C_P$  value of  $-0.35$  or less. The middle and the back end of the trailer depict  $C_P$  of  $-0.1$ , which is substantially higher than at the front end of the trailer. This relatively higher pressure region in the middle and the back of the trailer can be attributed to the re-attachment of the flow to the surface of the trailer.

In Figure 4.27 (b), where the relative flow angle changes to  $30^\circ$ , it is expected that as the flow is approaching the truck-trailer model at an angle, the flow separation will take place from the edges of the right side surface predominantly. Hence, the lowest pressure points are observed to be on the periphery of the right surface of the truck-trailer. Moreover, as  $\psi = 30^\circ$ , higher pressure is expected at the front section of the truck surface, while the pressure is expected to decrease gradually towards the back end of the trailer surface. Combining these two observations, it can

be clearly seen in Figure 4.27 (b-c) that a high value of  $C_P$  (around 0.5 and 0.9 respectively) exists near the leading edges of both the truck and the trailer. This pressure is seen to gradually decrease to a very small value near the back end of the trailer ( $C_P = 0.1$  or less in both case).

Further increasing the yaw angle to  $90^\circ$ , Figure 4.27 (d) depicts that there is a symmetrical distribution of pressure on the entire left face of the vehicle, as expected, as the flow is now approaching the vehicle totally from its side; hence the separation is only from the peripheral edges of the right surface. The pressure is highest in the centre of the right surface, while it decreases outwards (towards the peripheral edges).

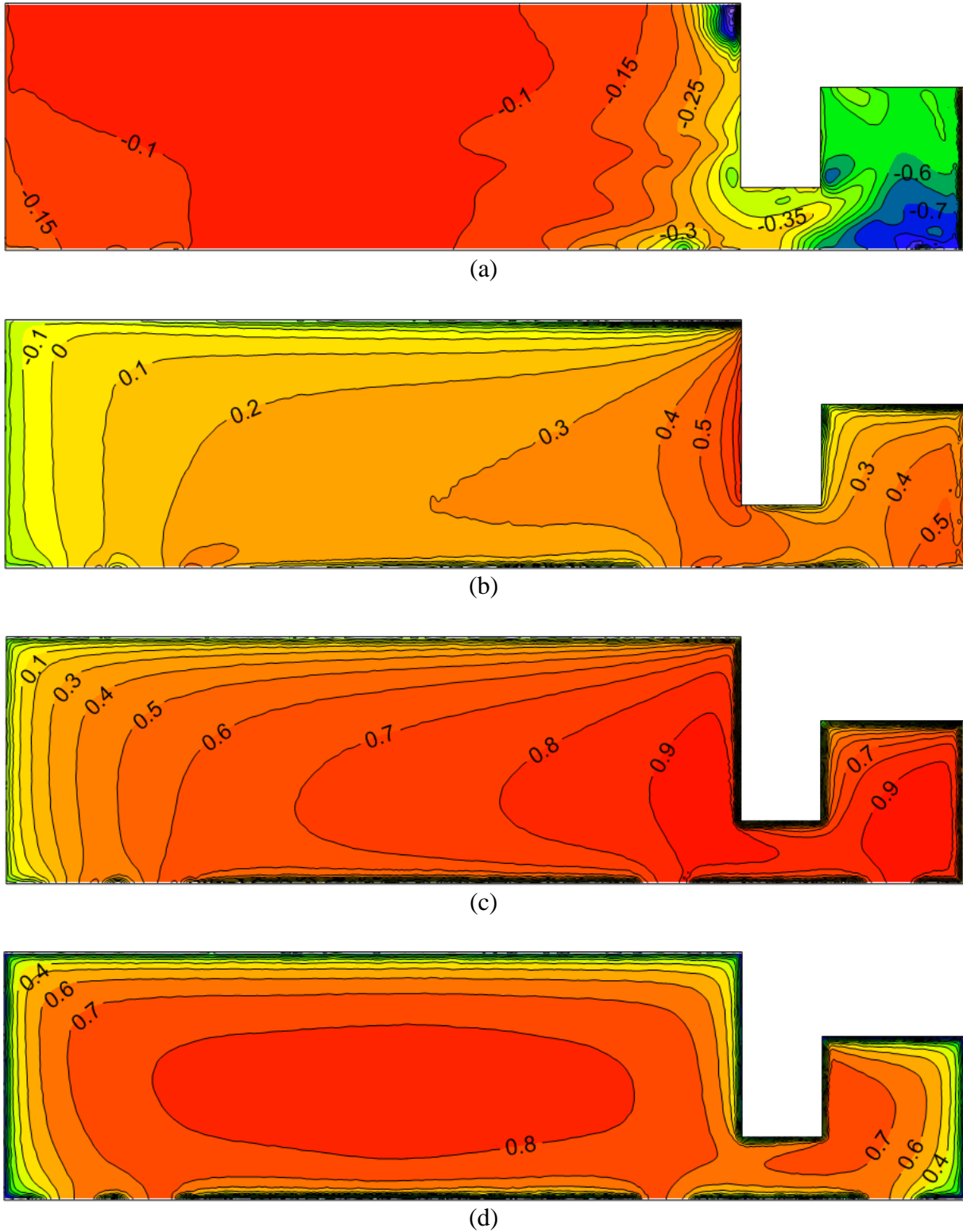


Figure 4.27 Variations in coefficient of pressure on the left face of the truck-trailer unit at a relative flow angle ( $\psi$ ) of (a)  $0^\circ$  (b)  $30^\circ$  (c)  $60^\circ$  (d)  $90^\circ$ .

#### 4.8.6 Velocity Distribution on the Leeward Side of the Baseline Truck-Trailer Unit at Crosswinds

Drastic increase in lift force and side force can introduce instabilities to truck-trailer unit making them unstable and prone to roll over accidents. The simulations were set for yaw angles ranging from  $0^\circ \leq \psi \leq 90^\circ$  in  $15^\circ$  increments. However, the results evaluated in this section are for  $0^\circ$ ,  $30^\circ$ ,  $60^\circ$  and  $90^\circ$  only. At straight head wind condition ( $\psi = 0^\circ$ ), the flow gets separated on the vertical side edges of the truck and the trailer unit giving rise to two flow circulating regions that exist on either side of the vehicle. This is depicted in Figures 4.19 and 4.28 (a) as the two circulation regions are clearly visible on the latter. The diameter of each circulation region is seen to be around 1m.

Figure 4.28 (b) shows the flow streamlines within a contour of velocity magnitude when the yaw angle is  $30^\circ$ , where the flow is flowing from Z direction. At this yaw angle the flow is fully separated hence generating three circulation regions as depicted from (b). According to Coleman and Baker [34], for low turbulence flow this vortex pair is evident between  $0^\circ - 40^\circ$ . A flow recirculation area of significant size (almost 7 meters) is seen on the leeward side of the trailer unit.

From Figure 4.28 (b-c), it can be seen that after  $40^\circ$  yaw, the flow on the trailer unit is completely separated resulting in fairly uniform pressure fields on top of the trailer and leeward face of the trailer unit. Large wake regions are seen to generate on the leeward side of the truck-trailer unit while the most prominent wake region is associated with the  $90^\circ$  yaw model. In this case, the windward side of the truck-trailer had transformed into a stagnation pressure region as shown in Figure 4.28 (d). At  $60^\circ$  and  $90^\circ$  yaw angles, the width of the wake region from the leeward side of the vehicle is approximately 15m and 40m respectively.

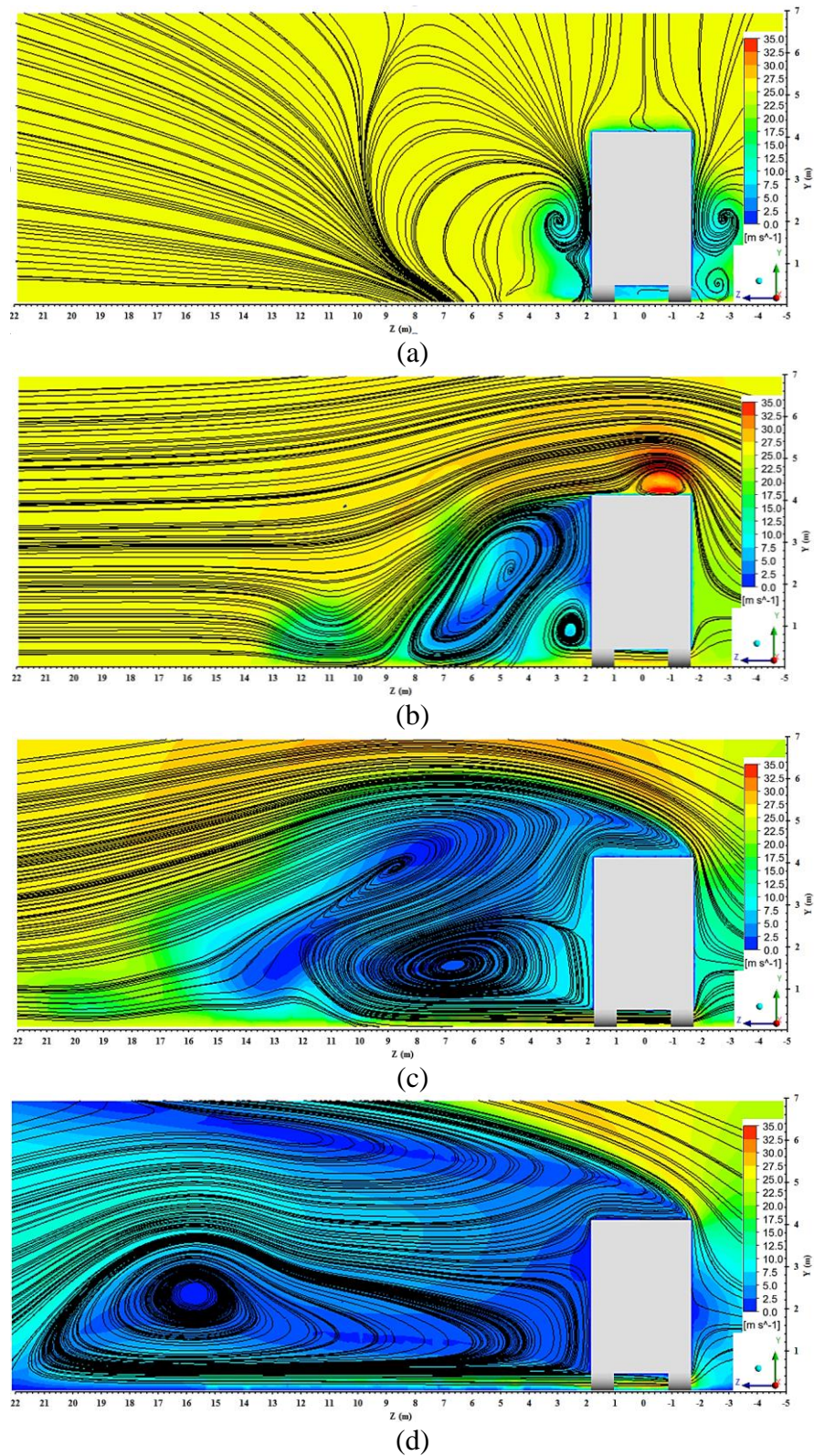


Figure 4.28 The streamlines along the baseline truck-trailer cross section at 7.64m from the front truck face when  $\psi = 0^\circ$  (a),  $\psi = 30^\circ$  (b),  $\psi = 60^\circ$  (c) and  $\psi = 90^\circ$  (d).

### 4.9 Flow Field Characteristics at Varying Trailer Heights.

A single truck unit will be used to pull a variety of trailer units with varying shapes and sizes. The minimum height of a trailer unit in UK is 4m while the maximum being 4.9m. Height of a trailer unit can vary anywhere between 4.0m and 4.9m. For this study, three different trailer heights were used; 4.4m, 4.6m and 4.8m. However, the discussion presented in this section only consider the 4.4m height and 4.8m height models.

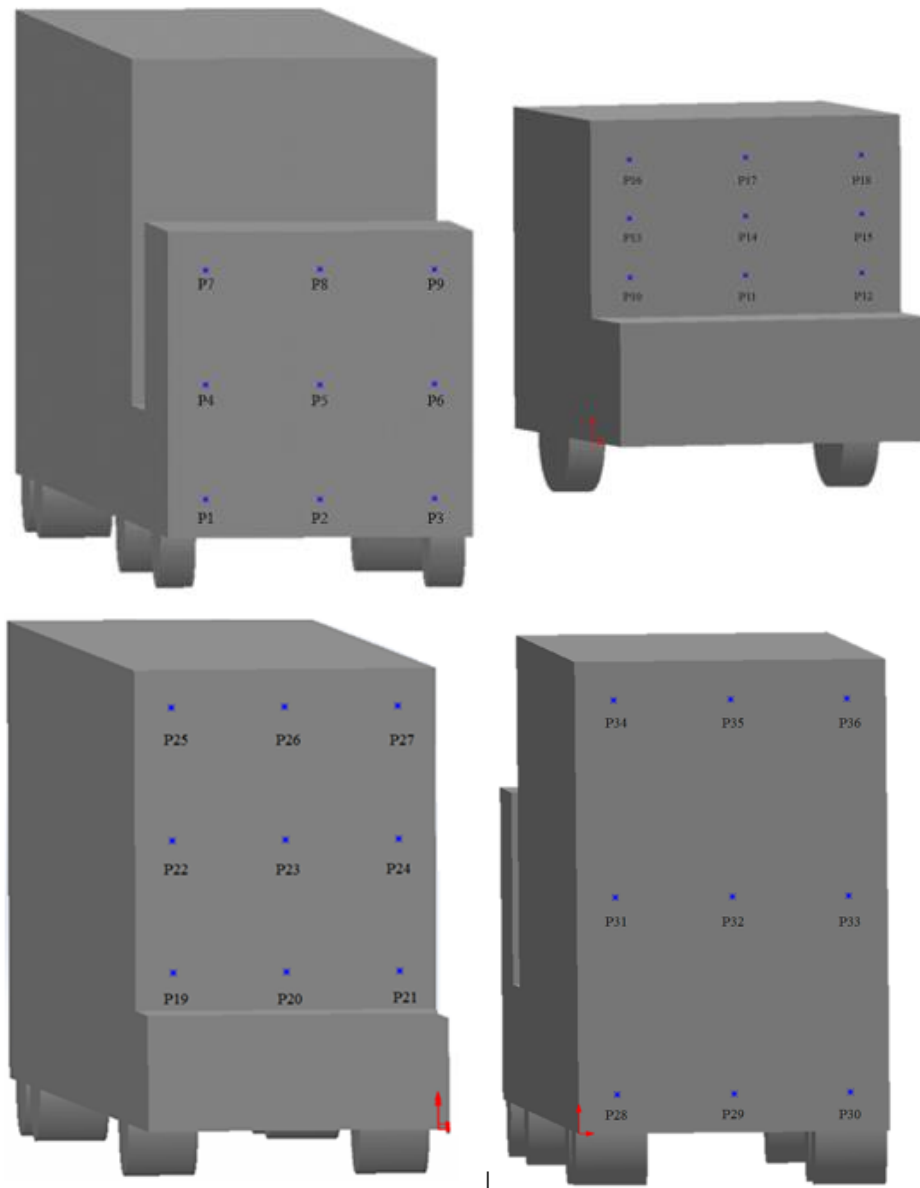


Figure 4.29 Truck-trailer geometry with 36 data points

Numerous points were generated on the truck-trailer surfaces as shown in Figure 4.29. These points are used to explain the non-uniformity of the pressure distribution on the key truck-trailer surfaces. A point cloud containing 36 points were generated and they were systematically distributed in groups of 9 on truck front, truck rear, trailer front and trailer rear surfaces. Figure 4.29 depicts the distribution of points 1 - 9 on the front truck face. Similarly, points 10 - 18 are distributed on the truck rear, points 19 - 27 are distributed on the trailer front and 28 - 36 are distributed on the trailer rear surface.

Figure 4.30 depicts the variation in pressure coefficient on the front truck face as the trailer height changes from 4.4m to 4.8m. The change in trailer height is expected to have a minimal effect on the front truck surface. It is seen that, when the trailer height is increased to 4.8m, the average pressure coefficient from P1 to P9 is decreases by 0.53%. This is due to the oncoming flow accelerating towards the wake regions behind the truck unit which is now increased in size due to height in trailer size. For both cases, maximum pressure of around 0.9 is recorded at P5 which is located at the centre of the surface. The pressure is seen to decrease to around 0.76, 0.75, 0.68, 0.67 at P1, P3, P7, P8 respectively at four corners where the separation occurs. On the top right side of front truck face, at P9 the pressure is seen in increase by 1.1% as the trailer height increases.

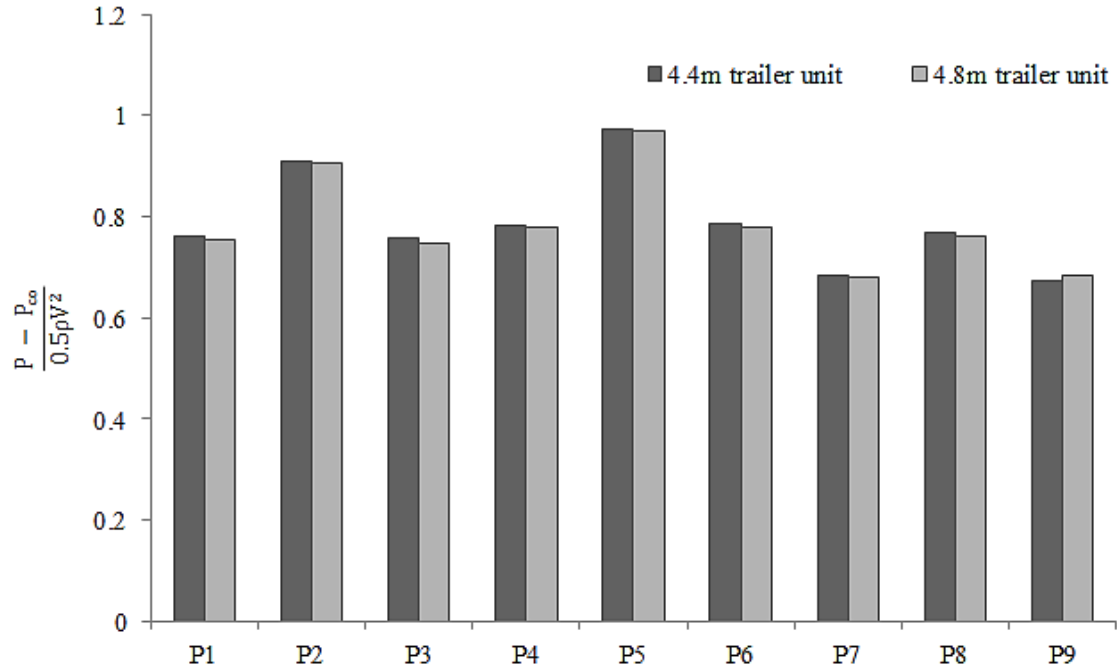


Figure 4.30 Variation in pressure coefficient on the front truck surface with varying trailer heights.

Figure 4.31 depicts the variation in pressure coefficient on the rear truck face as the trailer height changes from 4.4m to 4.8m. As the trailer height increases, a significant variation is seen in pressure fields on the rear truck surface in contrast to the front truck face. When the trailer height is 4.4m, the rear surface of the truck unit is seen to experience negative pressures except at P11 where the pressure is 0.04. However, when the trailer height is increased to 4.8m, the pressure at P10, P11 and P12 is obtained as 0.01, 0.35 and 0.0002 respectively. As the height of the trailer increases, the pressure at P13, P14, P15, P16, P17 and P18 is seen to decrease by 13.6%, 2.1%, 11.5%, 23.3%, 31.4% and 27.1% respectively. Hence, it is possible to say that there is a significant drop in pressure on the rear truck face as the trailer height increases from 4.4m to 4.8m.

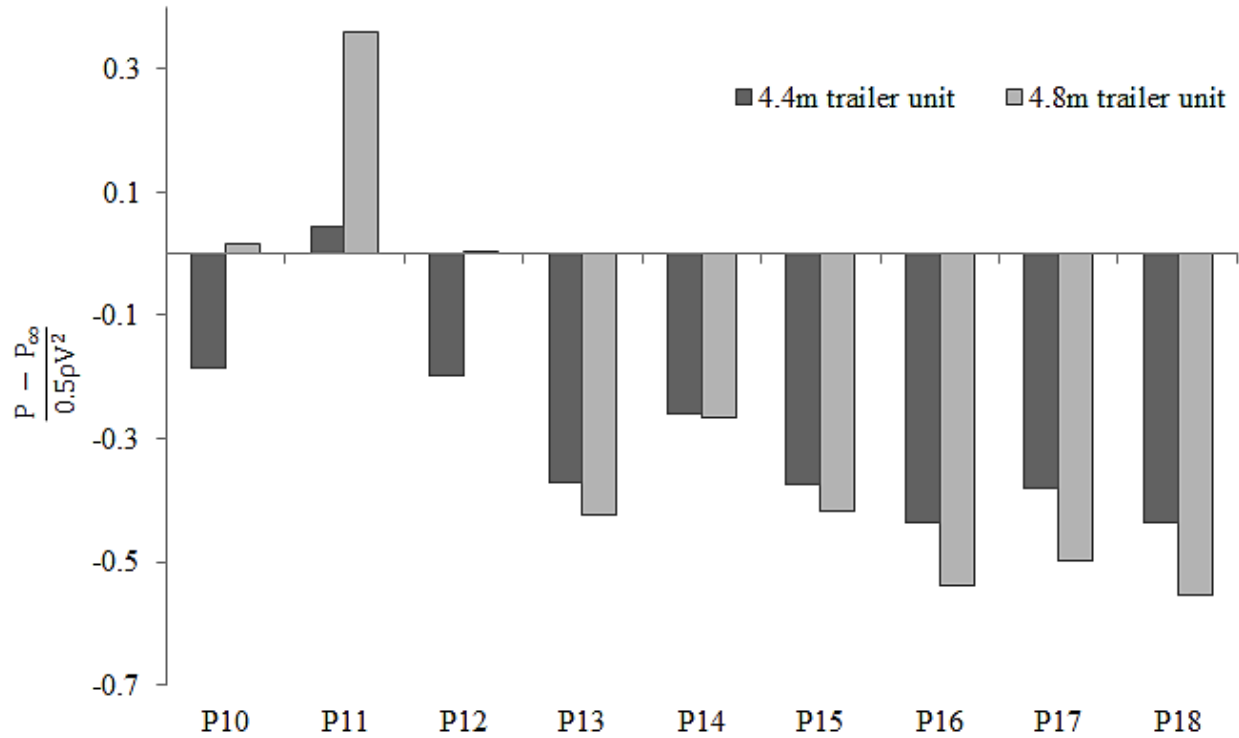


Figure 4.31 Variation in pressure coefficient on the rear truck surface with varying trailer heights

Figure 4.32 depicts the variation in pressure coefficient on the front trailer face as the trailer height changes from 4.4m to 4.8m. In the case of 4.4m model, P19 and P21 is seen to have low pressure of -0.26 and -0.25 respectively whilst, P20 has a high pressure value of 0.16. Along the horizontal centre line of the face the pressure is seen to be relatively low as P22, P23, P24 are associated with -0.41, -0.36 and -0.40 respectively. The upper section of the surface is associated with high pressures as a result of oncoming flow impinging on the surface. This is evident as the static pressure at P25, P26 and P27 are 0.50, 0.31, 0.48 respectively. On the contrary, the pressure on the front trailer surface is seen to increase significantly as the trailer height increases to 4.8m. The negative pressure regions on P19, and P21 have increased to 0.14 and 0.12, whilst the pressure on P20 has increased to 0.56. The static pressure on P22, P24, P25, P26 and P27 have increased by 20.5%, 18.6%, 88.8%, 221.1% and 90.1 respectively. It was also noted that as the trailer height increases, on the middle of the surface the pressure is seen to decrease. Upon increasing the height, the pressure on P23 decreases by 7.1%.

The increased trailer height from 4.4m to 4.8m generates a secondary stagnation pressure region close to the top leading edge of the front trailer face. This can be seen on P25, P26 and P27 on Figure 4.32. This adverse pressure region forces the oncoming flow towards the bottom edge of the front trailer face giving rise to a strong and concentric flow circulation within the truck-trailer gap region. The low pressure which exists in the flow circulation region has increased the velocity of the flow particle in the vicinity of the rear truck face. Hence, low pressure coefficient values were observed on the rear truck face for 4.8m high truck-trailer model with comparison to 4.4m high truck-trailer model.

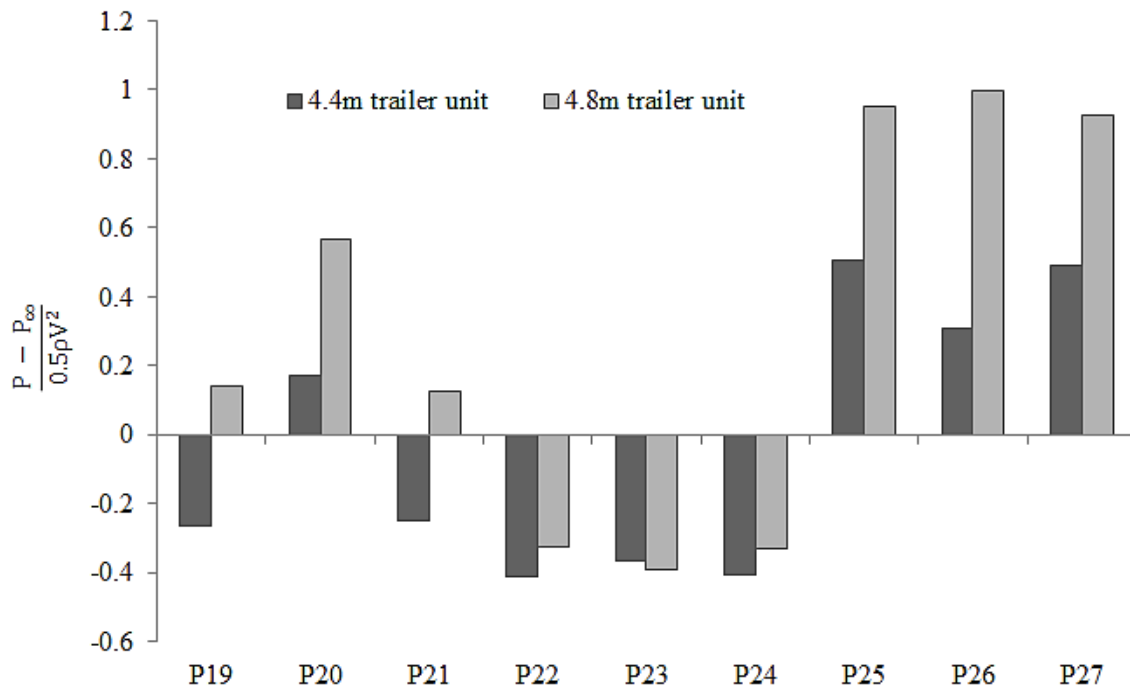


Figure 4.32 Variation in pressure coefficient on the front trailer surface with varying trailer heights

Figure 4.33 depicts the variation in pressure coefficient on the rear trailer face as the trailer height changes from 4.4m to 4.8m. As the height increases, an average pressure drop of 2.8% on the rear trailer surface is observed compared to the 4.4m height model. In comparison with 4.4m height model, the pressure drop on P28, P29, P30, P31, P32, P34 and P35 is seen to be 2.9%,

4.5%, 3.5%, 4.1%, 3.0%, 4.7% and 7.0% respectively whilst the pressure on P33 and P36 increases by 2.4% and 2.1% respectively.

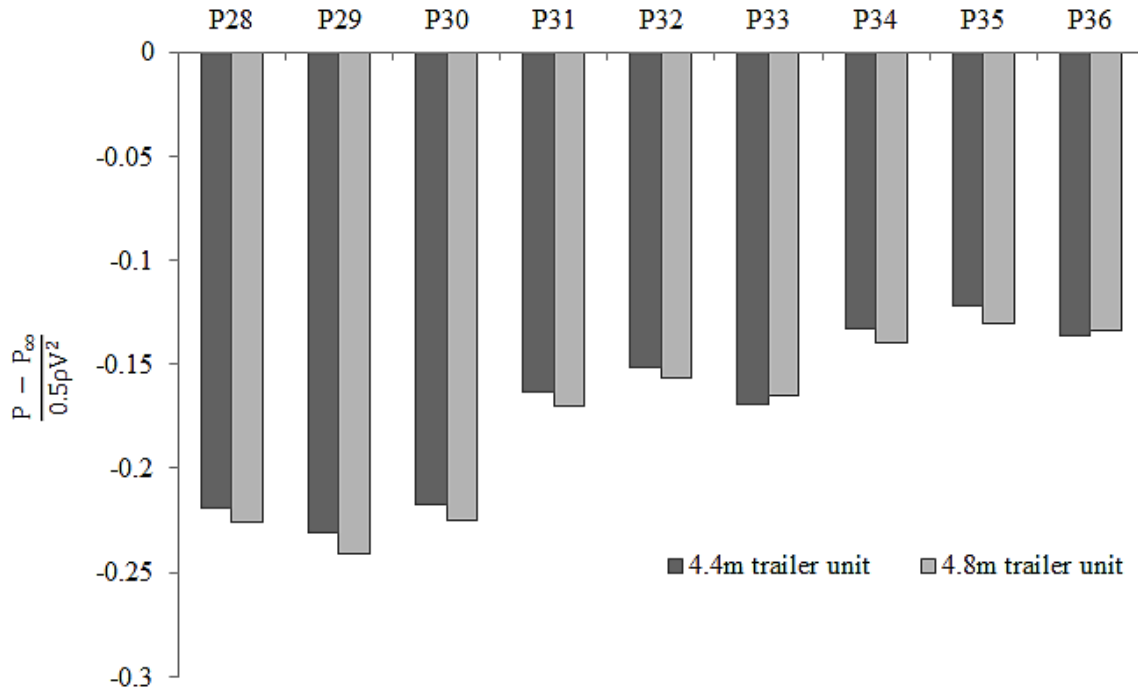


Figure 4.33 Variation in pressure coefficient on the rear trailer surface with varying trailer heights

#### 4.10 Flow Field Characteristics at Varying Trailer Lengths.

The maximum length of the truck-trailer units has been limited by the regulations due to operational and safety concerns. From a road haulage point of view, longer the trailer unit more goods can be transported. However, limited work has been carried out to evaluate the aerodynamic characteristics of operating truck-trailer units of various lengths. This section is dedicated to study the change in pressure on key truck-trailer surfaces as the length of the trailer changes from 15.28m to 16.28m. The height of the trailer unit was maintained at the lowest height with was considered in this study which is 4.4m.

Figure 4.34 depicts the variation in pressure coefficient on the front truck face as the trailer length changes from 15.28m to 16.28m. The change in trailer length is expected to have a minimal effect on the front truck surface. It is seen that, when the trailer length is increased to 16.28m, the average pressure coefficient from P1 to P9 is decreases by 0.05%. In terms of truck-trailer aerodynamics this can be considered as a negligible difference in pressure as an infinitesimal change in static pressure will have minute effect on overall vehicle dynamics.

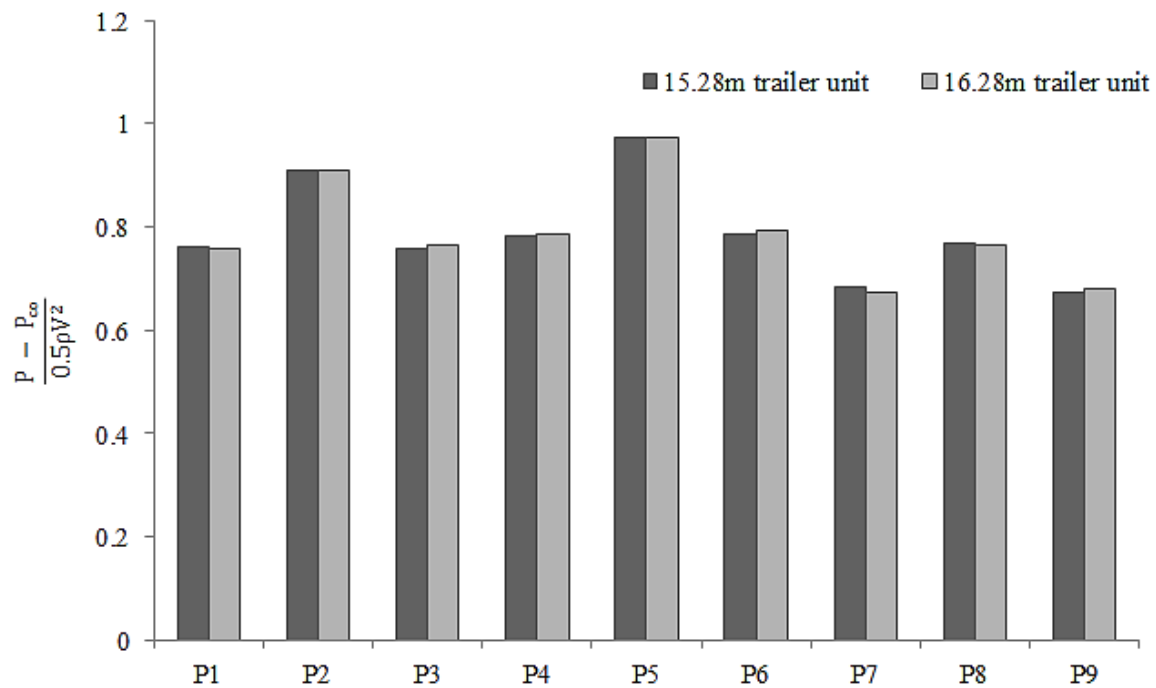


Figure 4.34 Variation in pressure coefficient on the front truck surface with varying trailer lengths

Figure 4.35 depicts the variation in pressure coefficient on the rear truck face as the trailer length changes from 15.28m to 16.28m. It is seen that increasing the length of the trailer unit does not significantly affect the static pressure acting on the rear truck surface. Positive pressure is only seen at P11 and this is further increased by 28.5% as the length of the trailer increases to 16.28%. However, along points P10, P12, P13, P14, P15, P16, P17 and P18 an average pressure drop of 0.8% is discovered as a result of the increase in trailer length.

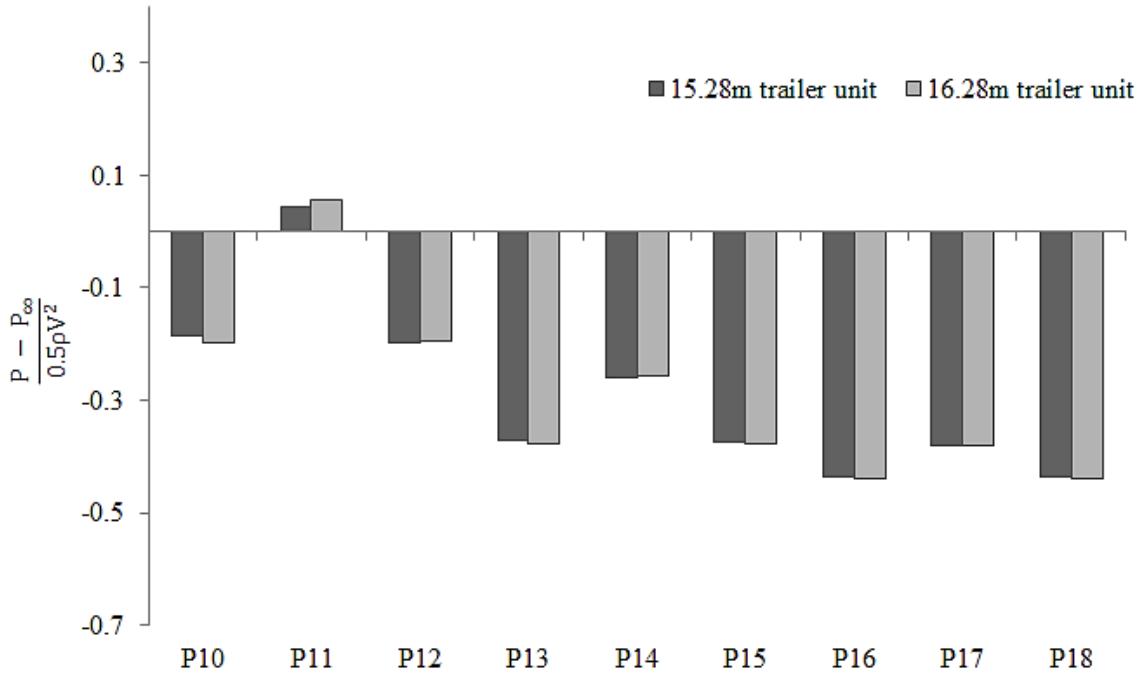


Figure 4.35 Variation in pressure coefficient on the rear truck surface with varying trailer lengths

Figure 4.36 depicts the variation in pressure coefficient on the front trailer face as the trailer length changes from 15.28m to 16.28m. The pressure profiles on both models look exactly the same except the magnitude changes in pressure at various points. As the length of the trailer increases to 16.28m the pressure is seen to increase on P19, P21, P22, P26, and P27 by 2.8%, 1.8%, 0.2%, 8.4% and 7.1% respectively. A 1.1%, 1.0%, 1.0% and 1.3% drop in pressure is seen on P20, P23, P24 and P25 respectively. As the length increases the average pressure on the front trailer surface is seen to rise by approximately 2%.

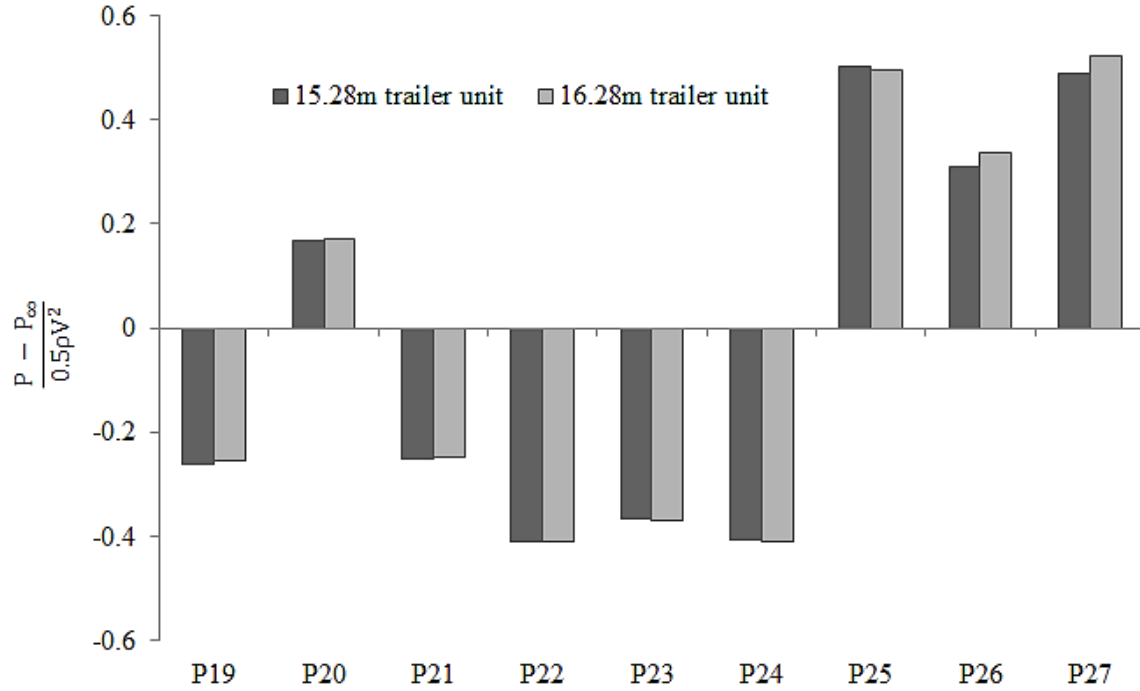


Figure 4.36 Variation in pressure coefficient on the front trailer surface with varying trailer lengths

Figure 4.37 depicts the variation in pressure coefficient on the rear trailer face as the trailer length changes from 15.28m to 16.28m. It is seen that on points P28 to P33 the pressure decreases and on points P34 to P36 the pressure increases. The decrease in pressure in comparison to 15.28m model on points P28, P29, P30, P31, P32 and P33 is 4.3%, 5.2%, 5.4%, 16.7%, 15.2% and 12.6% respectively. The increase in pressure in comparison to 15.28m model on points P34, P35 and P36 is 13.6%, 22.0% and 13.3% respectively. On average the pressure has decreased by 1.18% on the entire rear trailer surface.

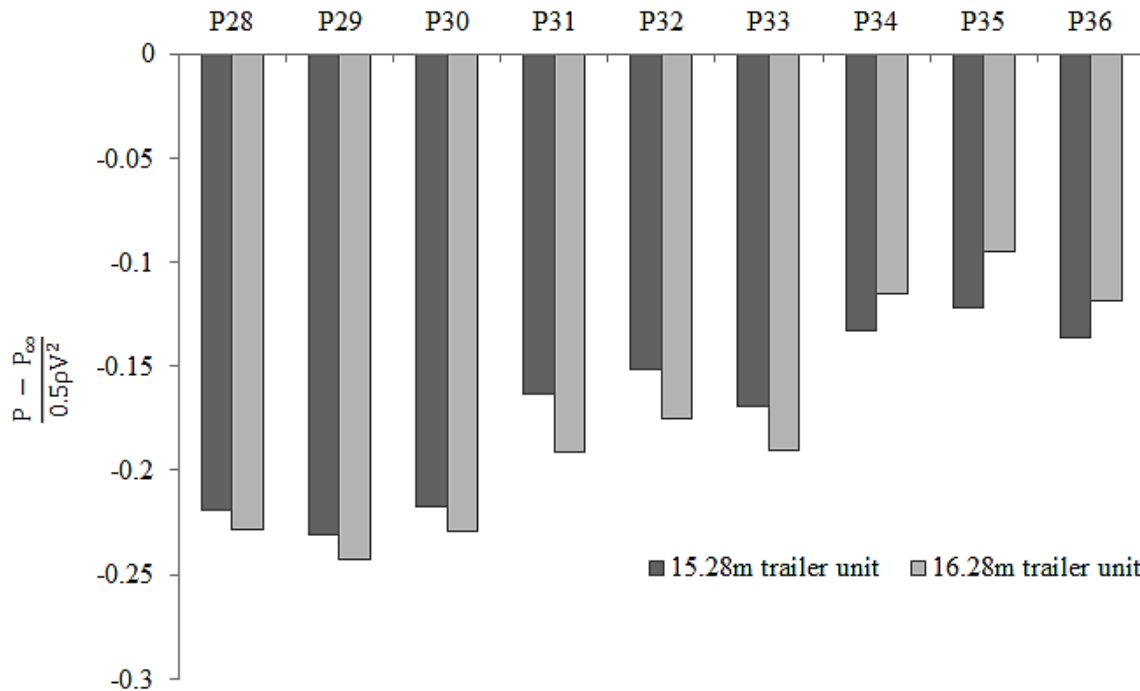


Figure 4.37 Variation in pressure coefficient on the rear trailer surface with varying trailer.

By carrying out these analysis, it was observed that increasing the height of the trailer unit has a more prominent effect on the truck-trailer aerodynamics than increasing the length of the truck-trailer unit. It was found that increasing the height of the trailer unit had a substantial effect on the pressure distribution on the rear truck, front trailer and rear trailer surfaces. Increasing the length of the trailer unit had a minute effect on truck surfaces and mostly affected the pressure distribution on the rear trailer surface.

#### 4.11 Overall Variation of Aerodynamic Forces with the Effect of Truck-Trailer Dimensions and Crosswind Angles

The pressure and velocity variations were expected to make a direct impact on the aerodynamic forces acting on a truck-trailer unit such as drag, lift and side forces. In the previous section, the effect of trailer height and length on the pressure and velocity fields were discussed. The force variations on the truck-trailer unit upon the height and length variation will be discussed in the coming section.

### 4.11.1 Effect of Truck-Trailer Height on Aerodynamic Forces at Various Crosswind Flow Profiles

The effects on the pressure fields around the truck-trailer model as the geometry and crosswind angle changes has been studied in sections 4.8 and 4.9 respectively. Any fluctuations in the pressure fields can influence the overall forces acting on the truck-trailer units. As was seen in the previous sections, even the slightest change in the geometrical and crosswind angles have a significant effect on the resulting pressure fields. The crosswind velocity magnitude was maintained at 25.03m/s throughout the yaw range.

Figure 4.38 shows the variation in drag force on the 15.28m long truck-trailer model having 4.4m, 4.6m and 4.8m trailer heights at various cross flow angles. It can be seen that at 0° yaw angle, the drag force experience by 4.4m truck-trailer unit is 3086N, whereas the force experience by 4.6m and 4.8m models become 3476N and 3870N respectively. When the trailer height increased from 4.4m to 4.8m the drag force acting on the vehicle increased by approximately 25%. The maximum drag force obtained at 15° yaw angle for 4.4m, 4.6m and 4.8m high truck trailer models were 5268N, 5350N and 5658N respectively. Beyond 45° yaw angle, minute variations in drag force is seen for 4.6m and 4.8m models and the 4.4m high truck-trailer model is seen to associate with higher drag forces compared to latter two models. It can be observed that the drag force is negative for 75° and 90° yaw flow angles as the force is acting in the opposite direction to the truck-trailer motion.

The increase in height generates a large stagnation flow region on the windward side of the trailer unit. This increased high pressure region comprising slow moving flow deflects the fast moving air molecules on the out edge of this region towards the front of the truck-trailer unit. This alters the symmetry of the fast moving air flow in the truck-trailer gap region altering the pressure acting on the truck and trailer faces. As a result, when the trailer height increased from 4.4m to 4.8m, the pressure acting on the front and rear truck surfaces are reduced. Moreover, the increase in trailer height has also increased the pressure acting on the front trailer face and reduced the pressure acting on the rear trailer face. These pressure variations are causing the 4.4m high truck-trailer unit to be associated with higher drag force values at both 60° and 75° yaw flow conditions.

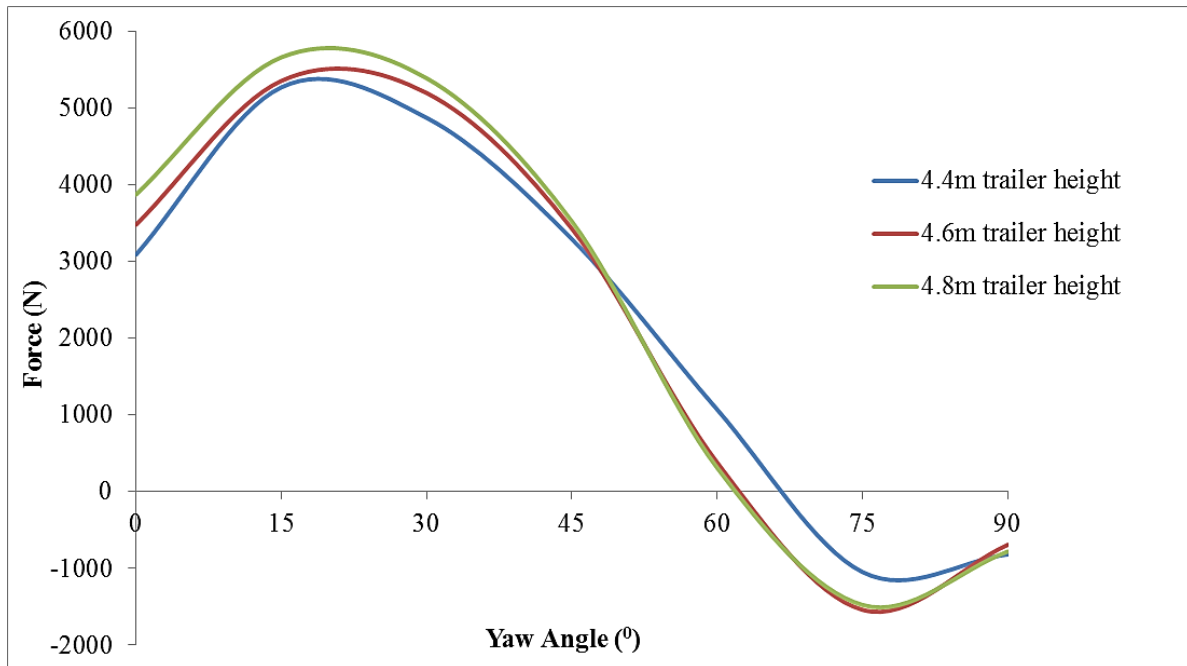


Figure 4.38 Drag force experienced by 15.28m truck-trailer configuration at 4.4m, 4.6m and 4.8m trailer heights at changing yaw angles.

Figure 4.39 shows the variation in lift force on the 15.28m long truck-trailer model having 4.4m, 4.6m and 4.8m trailer heights at various cross flow angles. It can be seen that at  $0^\circ$  yaw angle a negative lift force is exerted on the truck-trailer unit at all trailer heights. The maximum lift force of 7902N is experienced by 4.4m trailer model as the lift is seen to increase from  $\psi = 0^\circ$  to  $30^\circ$ , and then decreases to a minimum of -850N at  $\psi = 90^\circ$  which is experienced by the 4.6m vehicle model. The trend in the lift force is seen to be somewhat symmetrical about the  $90^\circ$  yaw angle. Once again a minute variation in the lift force is seen between 4.6m and 4.8m models from  $\psi = 0^\circ$  to  $90^\circ$ . Relatively high lift force experienced by 4.4m high truck-trailer model is due to relatively high velocities that exists due to undisturbed flow on top of the trailer unit.

The high lift force seen observed on the figure comes as a result of faster moving air directly on top of the trailer unit. When the height of the trailer unit increased to 4.8m, the oncoming flow obstruction is also increased specifically at higher yaw flow conditions. This increases the pressure acting on the top the trailer unit, reducing predominantly the lift force experienced by the trailer unit.

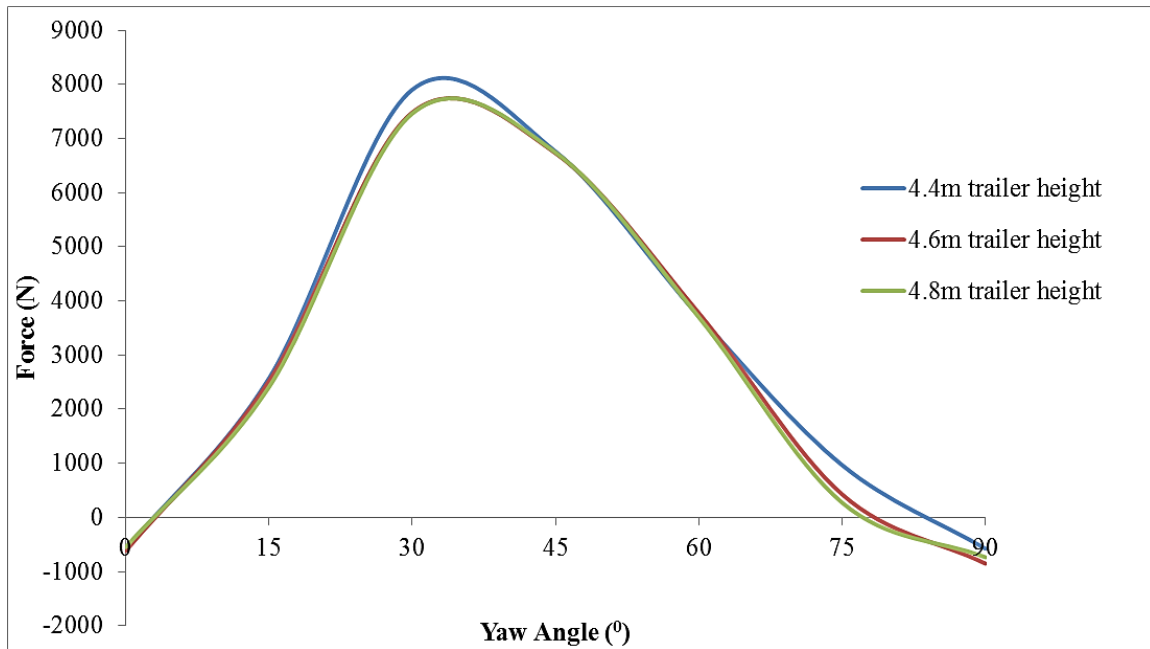


Figure 4.39 Lift force experienced by 15.28m truck-trailer configuration at 4.4m, 4.6m and 4.8m trailer heights at changing yaw angles.

Figure 4.40 shows the variation in side force on the 15.28m long truck-trailer model having 4.4m, 4.6m and 4.8m trailer heights from  $\psi = 0^\circ$  to  $90^\circ$ . The side force is seen to be positive throughout the range of flow angles investigated. The lowest side force was obtained when the flow is parallel to the vehicle axis and a remarkable increase is observed in the side force even at small deviation from this parallel position. The side force for all the models is seen to increase to around 9000N when the flow angle increases from  $0^\circ$  to  $15^\circ$ . The maximum side force of 24267N, 26560N, 27946N are experienced by 4.4m, 4.6m and 4.8m models respectively when the crosswind angle is  $60^\circ$ .

It is observed that when the height of the trailer unit increased from 4.4m to 4.8m, the side force experienced by the truck-trailer model increases respectively. As the yaw angle increase from  $0^\circ$  to  $90^\circ$ , the pressure acting on the windward side of the truck-trailer unit increases. And high static pressures are observed on the 4.8m truck-trailer model due to significantly more flow coming to rest on the increased surface areas.

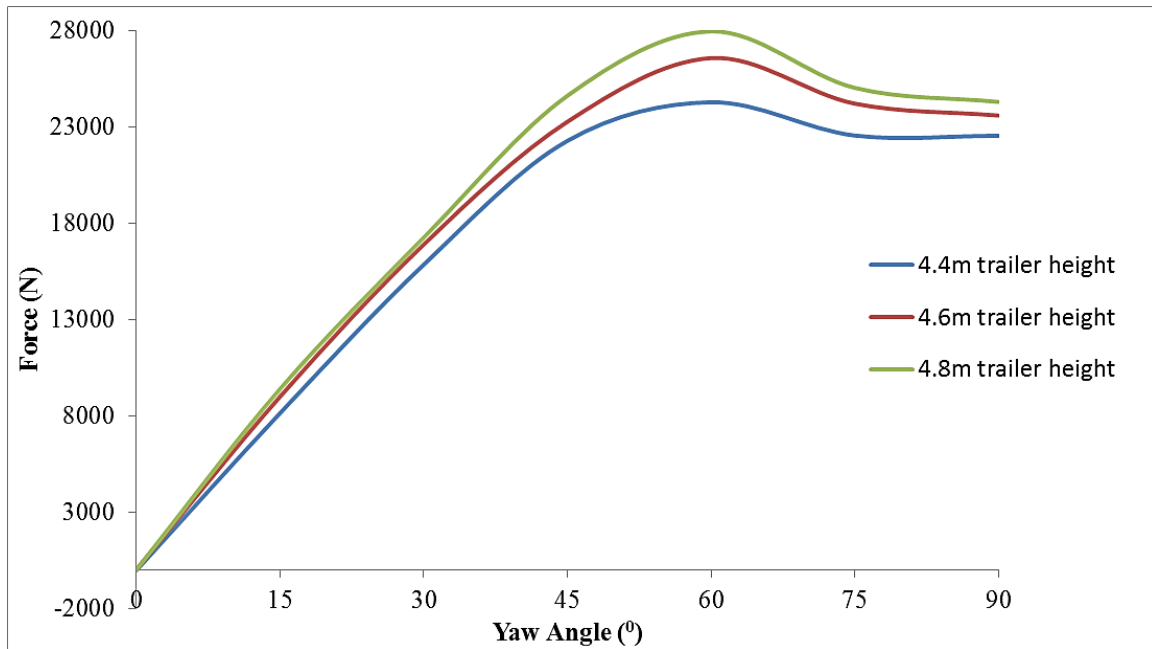


Figure 4.40 Side force experienced by 15.28m truck-trailer configuration at 4.4m, 4.6m and 4.8m trailer heights at changing yaw angles.

#### 4.11.2 Effect of Truck-Trailer Length on Aerodynamic Forces at Various Crosswind Flow Profiles

Changing length of the trailer unit on the pressure distribution around a truck-trailer unit is been discussed in the section 4.10. How the changing trailer length affect the drag force, lift force and the side force has been studied in this section.

Figure 4.41 shows the variation in drag force on the 4.4m high truck-trailer model having 15.28m, 15.78m and 16.28m trailer lengths from  $\psi = 0^\circ$  to  $90^\circ$ . At straight headwind the drag force experienced by the truck-trailer model with a 15.28m trailer model is seen to be 3086N. As the trailer length increases to 15.78m and 16.28m, the drag force is seen to increase by 0.71% and 3.1% respectively compared to the 15.28m truck-trailer model. The maximum drag force is seen to attain when  $\psi = 15^\circ$  before gradually decreasing where negative drag forces are seen from  $\psi = 75^\circ$  to  $\psi = 90^\circ$ . The highest positive drag force of 5295N is experienced by the 16.28m truck-trailer model when  $\psi = 15^\circ$  whilst, the highest negative drag force of -1379N is experienced by the 15.78m truck-trailer model when  $\psi = 75^\circ$ . The drag force is seen to vary

throughout the crosswind flow range showing no real pattern while the drastic drag force variations are seen to occur beyond  $\psi = 45^\circ$ .

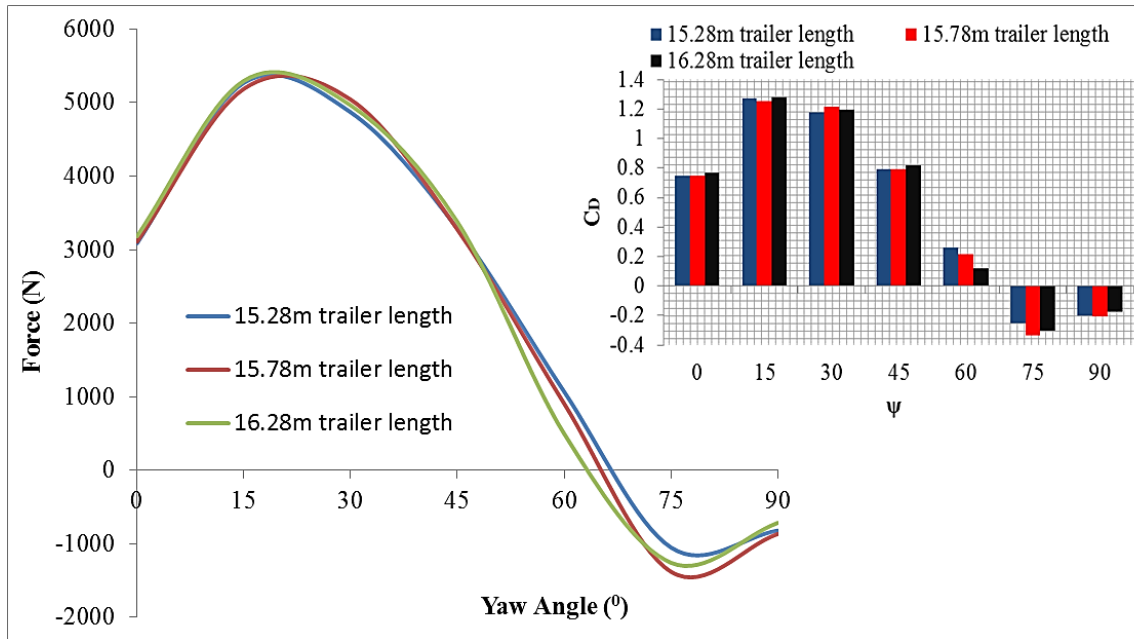


Figure 4.41 Drag force experienced by 4.4m high truck-trailer configuration at 15.28m, 15.78m and 16.28 trailer lengths at changing yaw angles.

Figure 4.42 shows the variation in the lift force on the 4.4m high truck-trailer model having 15.28m, 15.78m and 16.28m trailer lengths from  $\psi = 0^\circ$  to  $90^\circ$ . The lift force is seen to increase rapidly until the  $\psi = 30^\circ$  before rapidly decrease towards  $\psi = 90^\circ$ . Negative lift force is only seen when the  $\psi = 0^\circ$  and  $\psi = 90^\circ$ . The lift force acting on the 15.78m truck-trailer model is seen to be relatively low compared to 15.28m and 16.28m truck-trailer models. A highest positive lift force value is obtained at 15.28m truck-trailer unit when the  $\psi = 30^\circ$ , whilst the lowest negative lift force was attained at 16.28m truck-trailer model when the  $\psi = 90^\circ$ . Having a high positive lift force values can introduce instabilities to truck-trailer units raising safety concerns. According to the data presented from Figure 43, it is evident that the introduction of crosswind has a considerable effect on the lift forces experienced by the truck-trailer units.

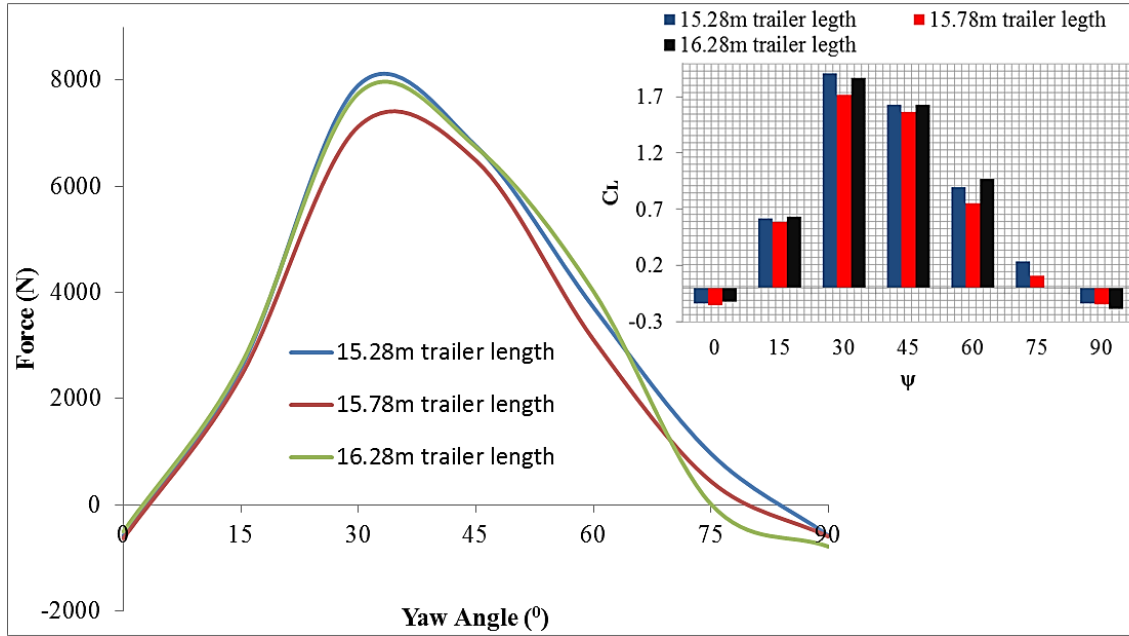


Figure 4.42 Lift force experienced by 4.4m high truck-trailer configuration at 15.28m, 15.78m and 16.28 trailer lengths at changing yaw angles.

Figure 4.43 shows the variation in the side force on the 4.4m high truck-trailer model having 15.28m, 15.78m and 16.28m trailer lengths from  $\psi = 0^\circ$  to  $90^\circ$ . The side force is seen to increase until when  $\psi = 60^\circ$  and then decrease a little for  $\psi = 75^\circ$  and  $\psi = 90^\circ$ . The lowest side force was obtained when  $\psi = 0^\circ$  as expected and the highest side force is obtained when the  $\psi = 60^\circ$  for all the models. The model with 16.28m length trailer unit is associated with the highest side force values at all crosswind angles followed by the 15.78m model and 15.28m model. For  $\psi = 15^\circ$ ,  $30^\circ$ ,  $45^\circ$ ,  $60^\circ$ ,  $75^\circ$  and  $90^\circ$  the increase in side force upon increasing the trailer length from 15.28m to 16.28m, was found to be 4.2%, 10.5%, 7.0%, 12.2%, 9.9% and 8.4% respectively. The findings clear suggest that the alterations to the truck-trailer length by increasing the trailer length results in higher side forces throughout the crossflow range.

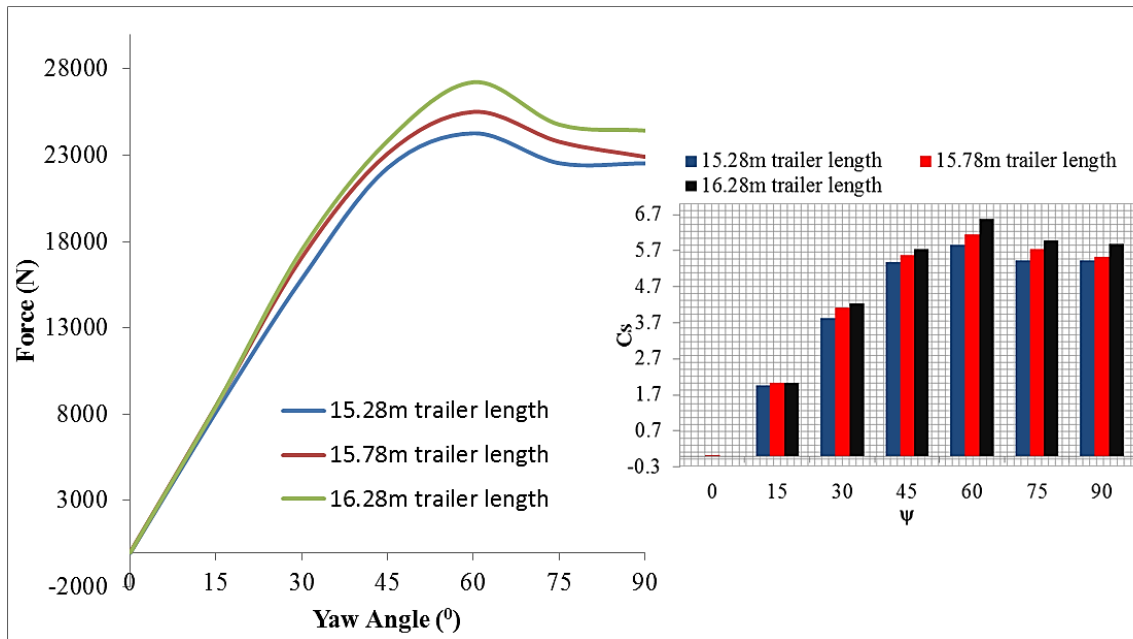


Figure 4.43 Side force experienced by 4.4m high truck-trailer configuration at 15.28m, 15.78m and 16.28 trailer lengths at changing yaw angles.

#### 4.12 Development of Semi-Empirical Prediction Models for the Aerodynamic Coefficients of a Truck-Trailer Unit

As discussed earlier, the aerodynamic coefficients are influenced by the vehicle's dimension, as well as the relative flow angle. The values of the aerodynamic coefficients obtained under known conditions, from CFD predictions, have been used to develop novel semi-empirical correlations between the dimensions of the vehicle, flow angle, and the aerodynamic coefficient, where these correlations are similar to Baker [87], but for a flexible truck-trailer unit rather than a rigid bus. Based on its behaviour, drag coefficient ( $C_D$ ) of a truck-trailer unit can be characterised by its length ( $l$ ) and height ( $h$ ). These dimensions have been converted to non-dimensional form using the vehicle's width ( $w$ ). As the variations in the aerodynamic coefficients have been shown earlier to be non-linear in nature, the Evolutionary non-linear optimisation model has been incorporated to optimise the coefficients in equations (1-3) for a truck-trailer unit [86]. Moreover, an advanced statistical process, known as multiple regression analysis, has been used to estimate the relationship between truck-trailer's geometrical characteristics and its aerodynamic coefficients.

### 4.12.1 Developing the Drag Coefficient Equation

A through flow analysis in the vicinity of truck-trailer units with various maximum lengths (l), maximum heights (h) and maximum width (w) was carried out in sections 4.7 to 4.11. Further, a compressive data set of the forces experienced by various truck-trailer configurations with varying above mentioned dimensioned was obtained using CFD means. This data set was used to develop semi-empirical prediction equations to predict drag force coefficient. Baker [89] has carried out experimental investigations to observe the effect of crosswinds on high sided vehicles and the resulting stability issues. In the process he has developed three prediction models to obtain drag, lift and side force coefficients of a high sided vehicles. These equations were obtained using empirical methods using the results obtained from experimental studies. Equation (4-11) represents the relationship of the drag coefficient with respect to the crosswind flow angle proposed by Baker [89]:

$$C_D = -0.25 (1 + 2. \sin(3. \psi)) \quad (4-11)$$

Baker has used a constant -0.25 to represent the drag force coefficient corresponding to zero-degree flow angle. Constant 2 was used as a constant to be obtained from the curve fitting techniques and 3 was used as a constant to represent drag coefficient under crosswind angles. Number of limitations and shortcomings were observed in the proposed equation (4-11) by Baker [89]. The most significant was the fact that the equation was only applicable for the specific vehicle tested. Further to this, it was evident that the equation was incapable of considering the effects of key vehicle dimensions such as length and height into account before predicting the drag force. Therefore, a more widely applicable and an accurate prediction model was required in order to predict the drag force on a truck-trailer model. The same equation was expressed as:

$$C_D = A (1 + B. \sin(C. \psi)) \quad (4-12)$$

In this study, A is allocated to represent the drag force coefficient at zero yaw angle, 'B' is maintained as a constant and 'C' is represented as a function of length, height, width and

crosswind angle. Coefficient ‘C’ is expected to depend on the vehicle’s geometrical parameters and the flow angle to predict the drag force coefficient.

According to Baker, the drag force coefficient incorporates both straight and crosswind effects.

$$C_D = C_{D\psi=0} + C_{D\psi\neq 0} \quad (4-13)$$

At straight headwinds the equation will provide a constant ‘A’ and at crosswinds the equation will be a combination of ‘B’, ‘C’ and ‘ $\psi$ ’ as shown below :

$$C_{D\psi=0} = A \quad (4-14)$$

$$C_{D\psi\neq 0} = B \cdot \sin(C \cdot \psi) \quad (4-15)$$

It was identified that to correct the shortcomings of the equation (4-11), the drag coefficient should be represented as a function of dimensional parameters in order to incorporate the effects of key dimensions such as length, height and width of a truck-trailer unit. Additionally, when the yaw angle is zero (straight headwind), the drag coefficient should depend entirely on length, height and width of a given truck-trailer model. Since, the coefficients proposed by Baker [89] in equation (4-11) were replaced by ‘A’, ‘B’ and ‘C’ they could be represented as a function of dimensional parameters; length, height and width. In this particular instance, the coefficient ‘A’ and ‘C’ were represented as functions of length, height and width parameters as shown below. The coefficient ‘B’ was maintained as a constant similar to Baker.

$$A = A\left(\frac{l}{w}, \frac{h}{w}\right) \quad (4-16)$$

$$C = C\left(\frac{l}{w}, \frac{h}{w}, \psi\right) \quad (4-17)$$

The coefficient A will be used to calculate the drag force coefficient when the crosswind angle is zero based on dimensional parameters.

Figure 4.44 depicts the variation in drag coefficient with changing truck-trailer heights and lengths under straight headwind. It is clear the trend in data illustrates that the drag coefficient increases almost linearly as the height of the truck-trailer unit increases as expected. This increase was a result of increased truck-trailer frontal cross sectional area due to height increase. Data also illustrates that the drag coefficient increases as the length of the truck-trailer unit increases.

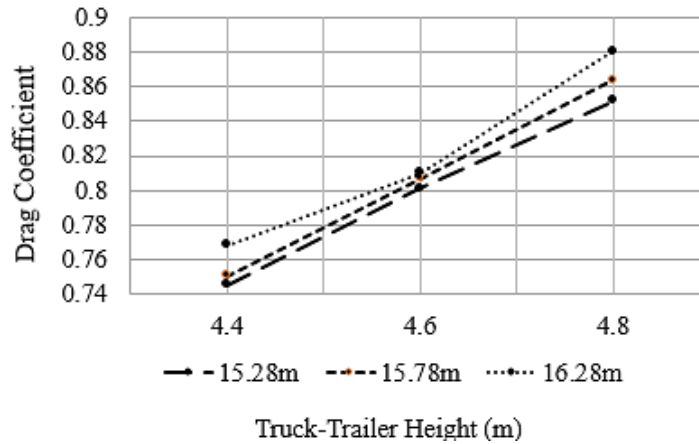


Figure 4.44 The drag coefficient for truck-trailer models with changing maximum heights changing maximum lengths at 0° yaw angle.

Upon examining the data trend of increasing drag coefficient with respect to increasing height and length of the truck-trailer models, the following functional form was used to predict the drag coefficient at straight headwinds. This equation was used to replace the constant ‘A’ specified in Bakers equation.

$$A = C_1 \left(\frac{l}{w}\right)^a \cdot \left(\frac{h}{w}\right)^b \tag{4-18}$$

Here,  $C_1$ ,  $a$  and  $b$  were constants that will vary in order to match the data trend which was observed on CFD data set.

Figure 4.45 illustrates the variation in drag coefficient at various truck-trailer heights, lengths and crosswind conditions. By examining the Figure, it is observed that the drag force decreases as the crosswind flow angle increases and this was the case for 4.4m, 4.6m and 4.8m high truck-

trailer models. For the 15.28m long truck-trailer model, at 15° and 75° yaw angles, the drag force is seen to decrease from 4.4m high model to 4.6m high model before increasing at 4.8m high model. A gradual decrease in drag coefficient was observed at 45° yaw from 4.4m high model to 4.8m high model. For the 15.78m long truck-trailer model, at 15° and 75° yaw angles, the drag force is seen to increase from 4.4m high model to 4.6m high model before decreasing at 4.8m high model. An initial decrease in drag coefficient is observed from 4.4m high model to 4.6m high model, before increasing at 4.8m high model at 45° yaw. For 16.28m truck-trailer model, at 15° yaw, the drag coefficient was seen to increase slightly from 4.4m height to 4.6m height before sharply decreasing at 4.8m high model. Drag coefficient is seen to decrease from 4.4m model to 4.8m model at 45° yaw. At 75° yaw, the drag force was seen to increase gradually from 4.4m high model to 4.8m high model.

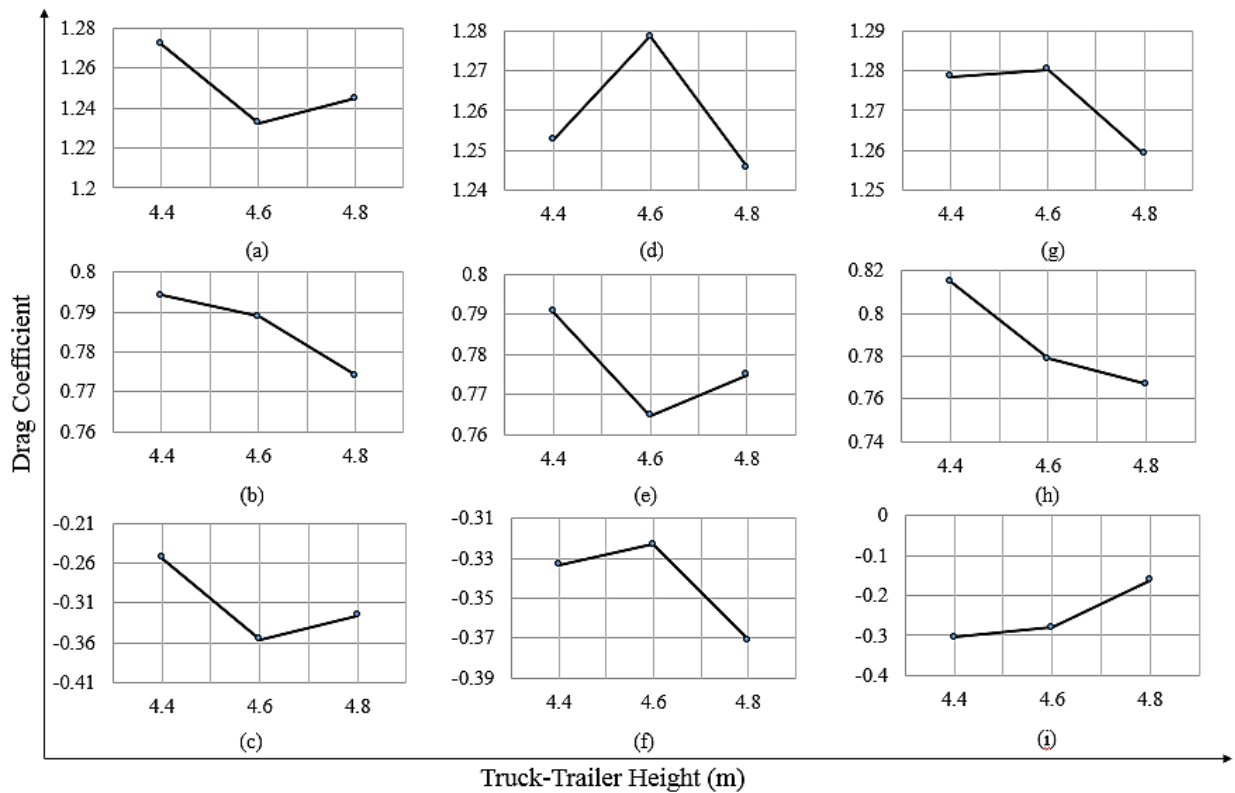


Figure 4.45 The drag coefficient for truck-trailer models with changing maximum heights, when length is 15.28m for 15°(a), 45°(b) and 75°(c) crosswind flow, 15.78m for 15°(d), 45°(e) and 75°(f) crosswind flow and 16.28m length for 15°(g), 45°(h) and 75°(i) crosswind flow.

By examining the Figure 4.46, it is observed that the drag coefficient decreases as the crosswind flow angle increases and this was the case for 15.28m, 15.78m and 16.28m long truck-trailer models. At a constant high of 4.4m, the drag coefficient is seen to decrease from 15.28m length model to 15.78m length model before increasing back at 16.28m length model under 15°, 45° and 75° yaw angles. At a constant height of 4.6m, the drag coefficient is seen to increase from 15.28m model to 16.28m model at both 15° and 75° yaw angles. However, at 45° yaw, the drag is seen to decrease from 15.28m to 15.78m model, before increasing back at 16.28m model. At a constant height of 4.8m, the drag in seen to increase slightly from 15.28m model to 15.78m model before sharply increasing at 16.28m model. At 45° yaw angle, the drag coefficient is seen to increase from 15.28m model to 15.78m model before sharply decreasing at 16.28m model. At 75° yaw angle, the drag is seen to decrease from 15.28m model and 15.78m model before increasing back at 16.28m model.

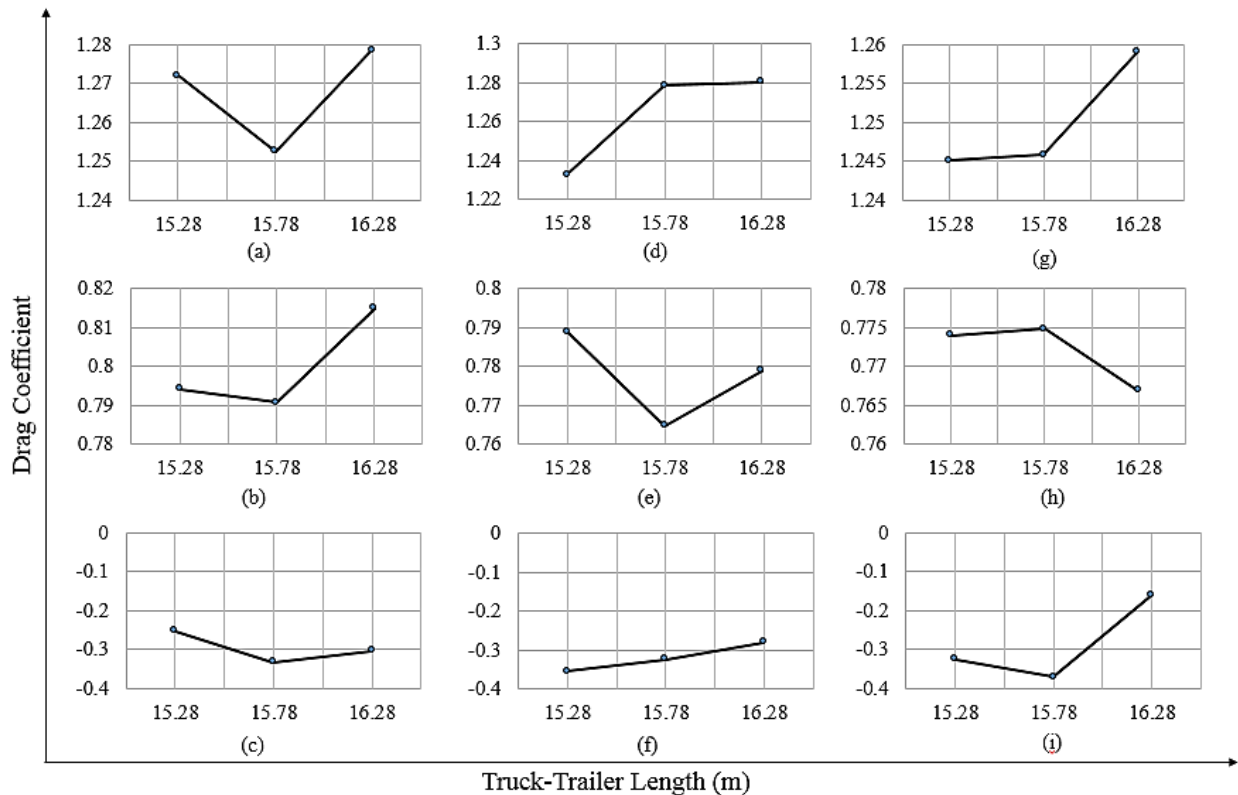


Figure 4.46 The drag coefficient for truck-trailer models with changing maximum lengths, when height is 4.4m for 15°(a), 45°(b) and 75°(c) crosswind flow, 4.6m for 15°(d), 45°(e) and 75°(f) crosswind flow and 4.8m length for 15°(g), 45°(h) and 75°(i) crosswind flow.

After examining the data trend with respect to increasing height and length of the truck-trailer model and the yaw angle, following functional form was used to predict the drag coefficient at crosswinds incorporating dimensional characteristics. This equation was used to replace the constant ‘C’ specified in Bakers equation.

$$C_{D \text{ (Crosswind)}} = C_2 \cdot \sin \left( \frac{C_3 \cdot \left(\frac{h}{w}\right)^c}{\left(\frac{l}{w}\right)^d} \cdot \psi \right) \quad (4-19)$$

Here,  $C_2, C_3, c$  and  $d$  were constants that will vary in order to match the data trend which was observed on CFD data set. The constant  $B$  in equation (4-12) has been replaced with  $C_2$  in this occasion. The final drag force coefficient obtained combining equation (4-18) and (4-19) can be represented in following equation:

$$C_D = 0.101 \left(\frac{l}{w}\right)^{0.820} \cdot \left(\frac{h}{w}\right)^{0.011} + \left( 0.792 \cdot \sin \left( \frac{8.387 \left(\frac{h}{w}\right)^{0.010}}{\left(\frac{l}{w}\right)^{0.506}} \cdot \psi \right) \right) \quad (4-20)$$

Figure 4.47 depicts the correlation between the predicted values of the aerodynamic drag coefficients, and those obtained from CFD. It can be clearly seen that the predicted values agree reasonably well with those obtained from CFD. The standard error of estimate has been calculated to be around 15%. Hence, equation (4-20), developed for characterising the aerodynamic drag coefficient in terms of the vehicle’s dimensions and the relative flow angle, is well capable of predicting the drag coefficients for truck-trailer units of various sizes, for different flow conditions.

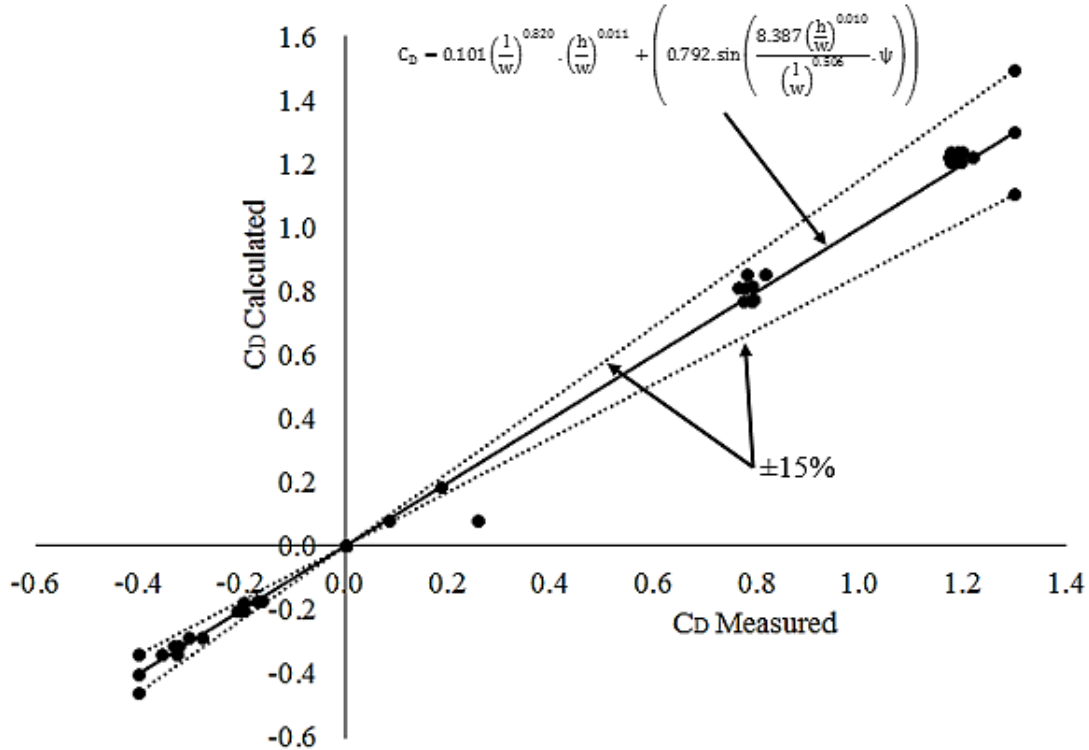


Figure 4.47 Correlation between aerodynamic drag coefficient measured from CFD and calculated by the new methodology for various vehicle geometries and relative flow angles.

### 4.12.2 Developing the Lift Coefficient Equation

Once again Baker has incorporated both straight and crosswind effects into the lift force coefficient prediction tool.

$$C_L = C_{L\psi=0} + C_{L\psi\neq 0} \tag{4-21}$$

At straight headwinds the equation will provide a constant ‘A’ and at crosswinds the equation will be a combination of ‘B’, ‘C’ and ‘ $\psi$ ’ as shown below:

$$C_{L\psi=0} = A \tag{4-22}$$

$$C_{L\psi\neq 0} = B \cdot \sin(C \cdot \psi) \tag{4-23}$$

Figure 4.48 depicts the variation in lift coefficient with changing truck-trailer heights and lengths under straight headwind. Unlike drag force coefficient, a direct trend was not observed for the lift force coefficient. The lift coefficient is seen to decrease from 4.4m to 4.6m and increase gradually at 4.8m, for 15.28m and 16.28m length truck-trailer models. Linear increase in lift coefficient is seen throughout the height range for 15.78m length model as depicted in Figure 4.48 (a). Decrease in lift coefficient is seen between 15.28m to 15.78m length models at heights 4.4m and 4.8m before increasing at 16.28m long model. A gradual decrease in lift coefficient is observed throughout the length range for 4.6m height model as seen in Figure 4.48 (b).

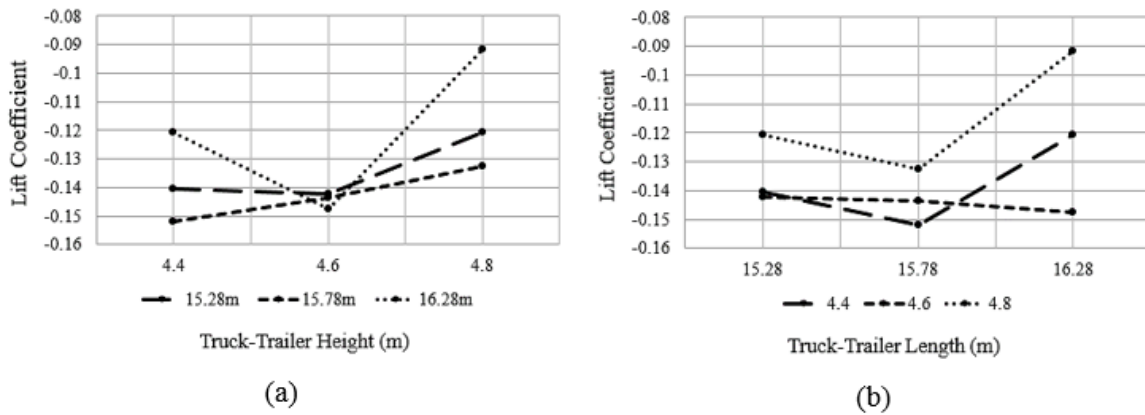


Figure 4.48 The lift coefficient for truck-trailer models with changing maximum heights (a) and changing maximum lengths (b) at 0° yaw angle.

Upon examining the data trend, decreasing lift coefficient with respect to increasing truck-trailer height, and decreasing and then increasing nature of lift coefficient with respect to the truck-trailer length were observed. The constant ‘A’ in equation (4-22) has been replaced with equation (4-24) in this occasion. Hence, the following functional form was chosen to predict the lift coefficient at straight head winds with no crosswind present.

$$A = \frac{C_1}{\left(\frac{l}{w}\right)^a \left(\frac{h}{w}\right)^b} \tag{4-24}$$

Here,  $C_1$ ,  $a$  and  $b$  were constants that will vary in order to match the data trend which was observed on CFD data set.

Figure 4.49 illustrates the variation in lift coefficient at various truck-trailer heights, lengths and crosswind conditions. By examining the Figure, it is observed that the lift force decreases as the height of the truck-trailer unit increases and this trend is seen throughout the data range. For the 15.28m long truck-trailer model at heights of 4.4m, 4.6m and 4.8m, the lift coefficient is seen to increase from 15° to 45° yaw and then decrease at 75° yaw. Once more, this trend has been observed throughout the data range. Almost liner decrease in lift coefficient as the height increases was seen for 15.28m model at 15° and 45° yaw angles and the 16.28m model at 75° yaw angle. Relatively high lift coefficients were obtained at 45° yaw angle for all models.

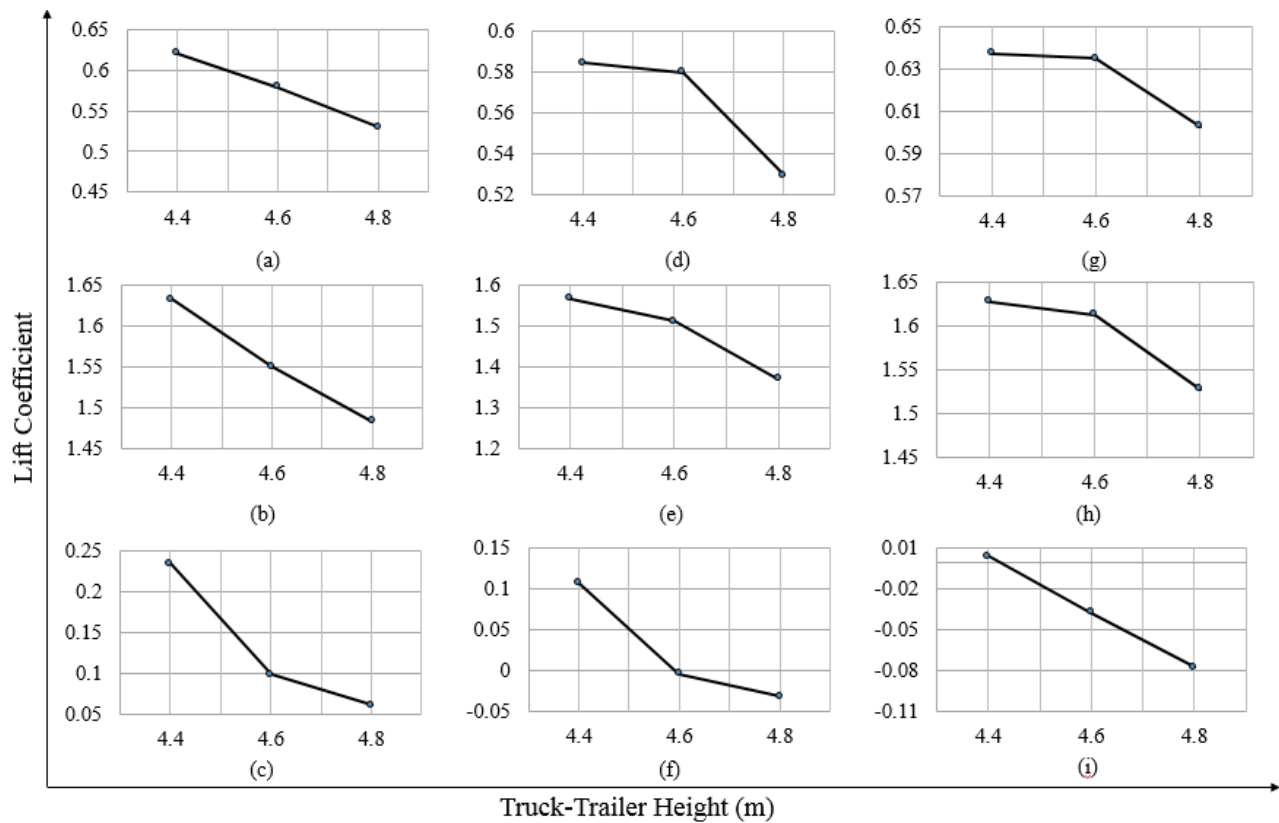


Figure 4.49 The lift coefficient for truck-trailer models with changing maximum heights, when length is 15.28m for 15°(a), 45°(b) and 75°(c) crosswind flow, 15.78m for 15°(d), 45°(e) and 75°(f) crosswind flow and 16.28m length for 15°(g), 45°(h) and 75°(i) crosswind flow.

By examining the Figure 4.50, it is observed that the lift coefficient decreases from 15.28m length model to 15.78m length model for all the cases except the 4.6m height model at 15° yaw, where a slight increase in lift coefficient was observed. At a yaw angle of 75°, the lift coefficient is seen to decrease as the length increases for 4.4m, 4.6m and 4.8m high truck-trailer models.

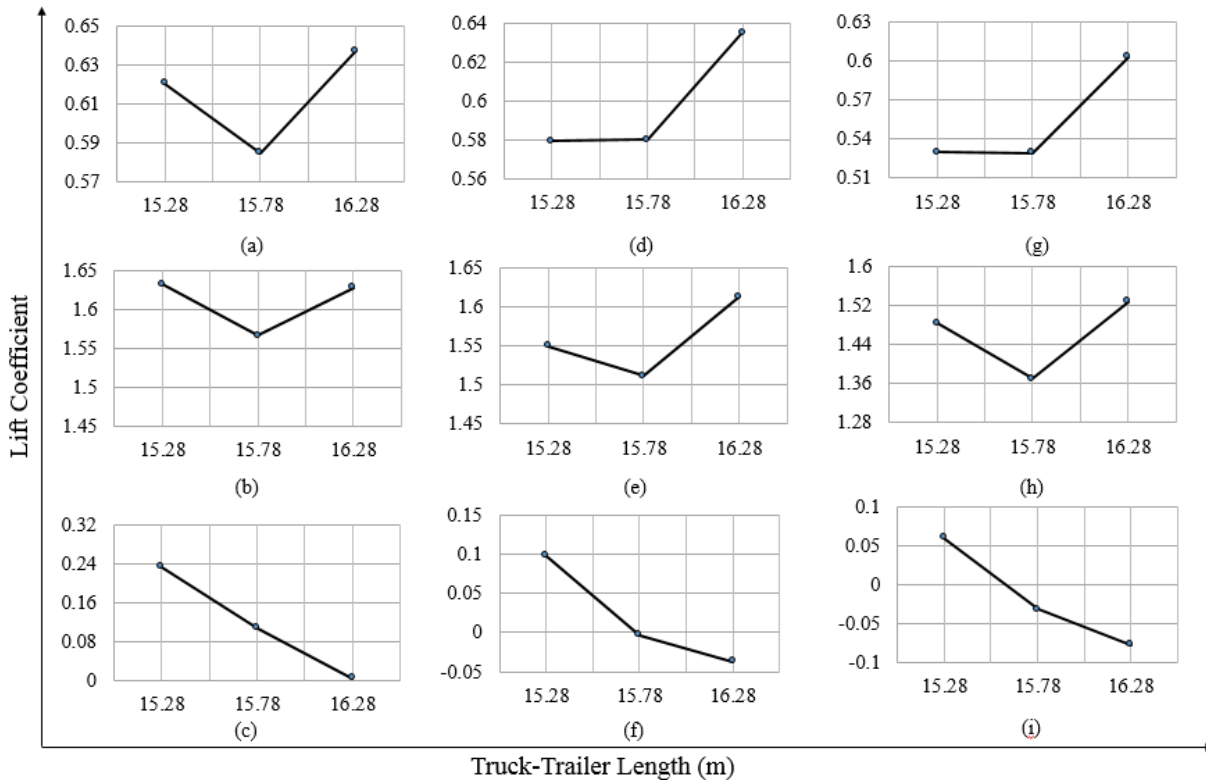


Figure 4.50 The lift coefficient for truck-trailer models with changing maximum lengths, when height is 4.4m for 15°(a), 45°(b) and 75°(c) crosswind flow, 4.6m for 15°(d), 45°(e) and 75°(f) crosswind flow and 4.8m length for 15°(g), 45°(h) and 75°(i) crosswind flow.

Once more, observing the data trend for the lift coefficient for increasing height and length of the truck-trailer model and the yaw angle, following functional form was used to predict the lift coefficient at crosswinds incorporating dimensional characteristics. In this instant, constant ‘B’ in equation (4-23) has been replaced with equation (4-25) and constant ‘C’ was maintained as a constant provided by the curve fitting technique. As the lift force is not directly affected by the dimensional parameters and crosswind angle, the functional form of ‘ $\psi$ ’ had to be changed to ‘ $\psi^e$ ’ as shown in equation (4-19) in order to achieve a better accuracy with the CFD data.

$$B = \left( \frac{C_2}{\left(\frac{l}{w}\right)^c \left(\frac{h}{w}\right)^d} \right) \quad (4-25)$$

$$C = C_3 = \text{Constant} \quad (4-26)$$

$$\psi = \psi^e \quad (4-27)$$

Here,  $C_2, C_3, c, d$  and  $e$  were constants that will vary in order to match the data trend which was observed on CFD data set. The final lift force coefficient obtained combining equation (4-25) and (4-28), can be represented in following equation:

$$C_L = \frac{-0.488}{\left(\frac{l}{w}\right)^{0.502} \left(\frac{h}{w}\right)^{0.657}} + \left( \frac{4.891}{\left(\frac{l}{w}\right)^{0.408} \left(\frac{h}{w}\right)^{1.787}} \cdot \sin(2.82 \cdot \psi^{0.210}) \right) \quad (4-28)$$

Figure 4.51 depicts the correlation between the predicted values of the aerodynamic lift coefficients, and those obtained from CFD. It can be clearly seen that the predicted values agree reasonably well with those obtained from CFD. The standard error of estimate has been calculated to be around 15%. Hence, equation (4-28), developed for characterising the aerodynamic lift coefficient in terms of the vehicle's dimensions and the relative flow angle, is well capable of predicting the lift coefficients for truck-trailer units of various sizes at different flow conditions.

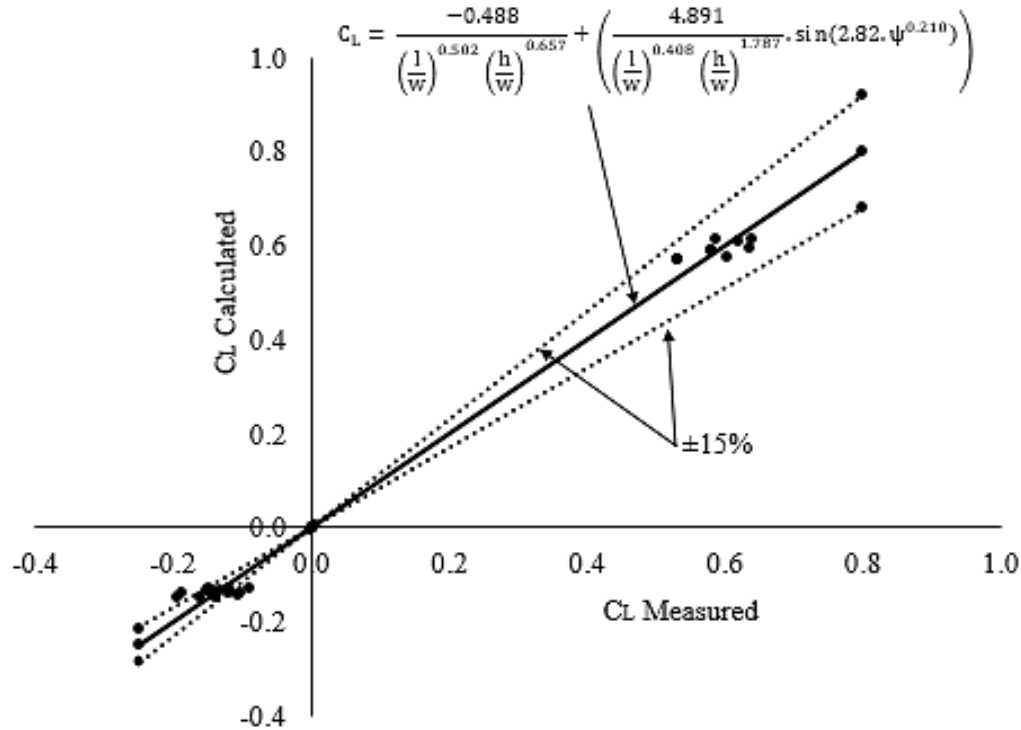


Figure 4.51 Correlation between aerodynamic lift coefficient measured from CFD and calculated by the new methodology for various vehicle geometries and relative flow angles.

### 4.12.3 Developing the Side Coefficient Equation

Baker has eliminated the straight wind effects from the side force prediction model as it was only capable of capturing the crosswind effects as depicted from equation (4-29).

$$C_S = 3.84(\psi^{0.382}) \tag{4-29}$$

$$C_S = C_{S\psi=0} + C_{S\psi \neq 0} \tag{4-30}$$

When the at straight headwind conditions the side force coefficient will be zero:

$$C_{S\psi=0} = 0 \tag{4-31}$$

Hence the side force prediction equation will become:

$$C_S = C_{S_{\psi \neq 0}} \quad (4-32)$$

In this study, the crosswinds the prediction equation will be a combination of 'B', 'C' and ' $\psi$ ' as shown below and the constant 'A' will not be incorporated assuming that at straight headwind condition, the side force coefficient will be zero.

$$C_{S_{\psi \neq 0}} = B \cdot \sin(C \cdot \psi) \quad (4-33)$$

When developing side force coefficient prediction model, the straight wind factor has been completely ignored. This is because at straight head wind, the flow characteristics on either side of the truck-trailer unit tend to be highly symmetrical and therefore, the side force was observed to be negligible.

Figure 4.52 depicts side force coefficient  $15^\circ$ ,  $45^\circ$  and  $75^\circ$  yaw angles for 4.4m, 4.6m and 4.8m high truck-trailer units at (a) 15.28m, 15.78m (b) and 16.28m (c) lengths. It is identified for all three cases, side force coefficient increases from  $15^\circ$  and  $45^\circ$  then rises slightly between  $45^\circ$  and  $75^\circ$ . However, in the case of truck-trailer unit with 16.28m length, the height of 4.8m depicts a fall in side force coefficient between these crosswind angles. Additionally, there are slight side force coefficient variations between the models at crosswind angles  $15^\circ$  and  $45^\circ$ . The truck-trailer unit with 15.78m length depicts minimal variations throughout the crosswind angles. Maximum variations in side force coefficient are seen between crosswind angles of  $45^\circ$  and  $75^\circ$  for the truck-trailer unit with a length of 16.28m

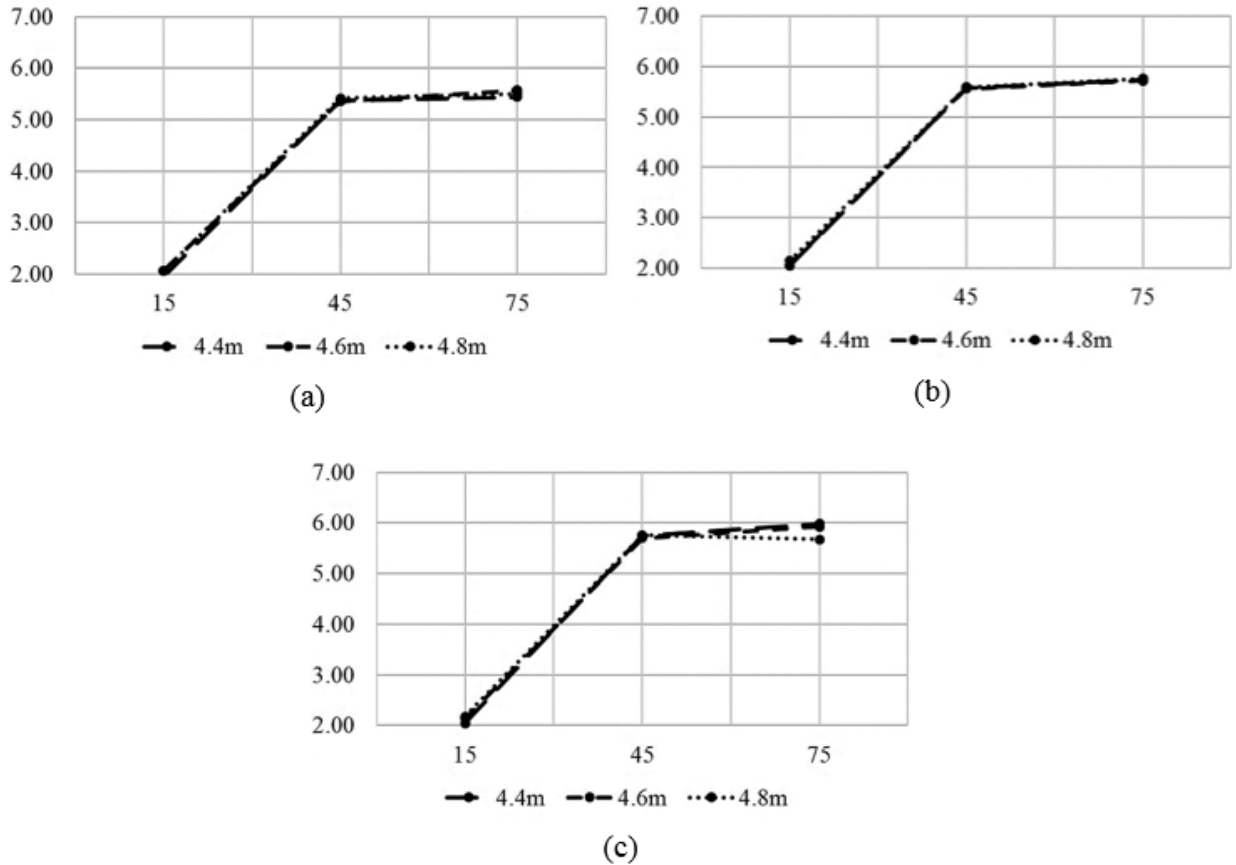


Figure 4.52 Side force coefficient 15°, 45° and 75° yaw angles for 4.4m, 4.6m and 4.8m high truck-trailer units at (a) 15.28m, (b) 15.78m and (c) 16.28m lengths.

Figure 4.53 depicts side force coefficient at 15°, 45° and 75° yaw angles for 15.28m, 15.78m and 16.28m long truck-trailer units at (a) 4.4m, (b) 4.6m and (c) 4.8m heights. It is identified for all three cases, side force coefficient increases from 15° and 45° then remains fairly consistent between 45° and 75°. Additionally, there are minimal side force coefficient variations between the models at crosswind angles 15° and 45°. The truck-trailer unit with 4.8m height depicts minimal variations throughout the crosswind angles. Maximum variations in side force coefficient are seen between crosswind angles of 45° and 75° for the truck-trailer unit with a height of 4.4m.

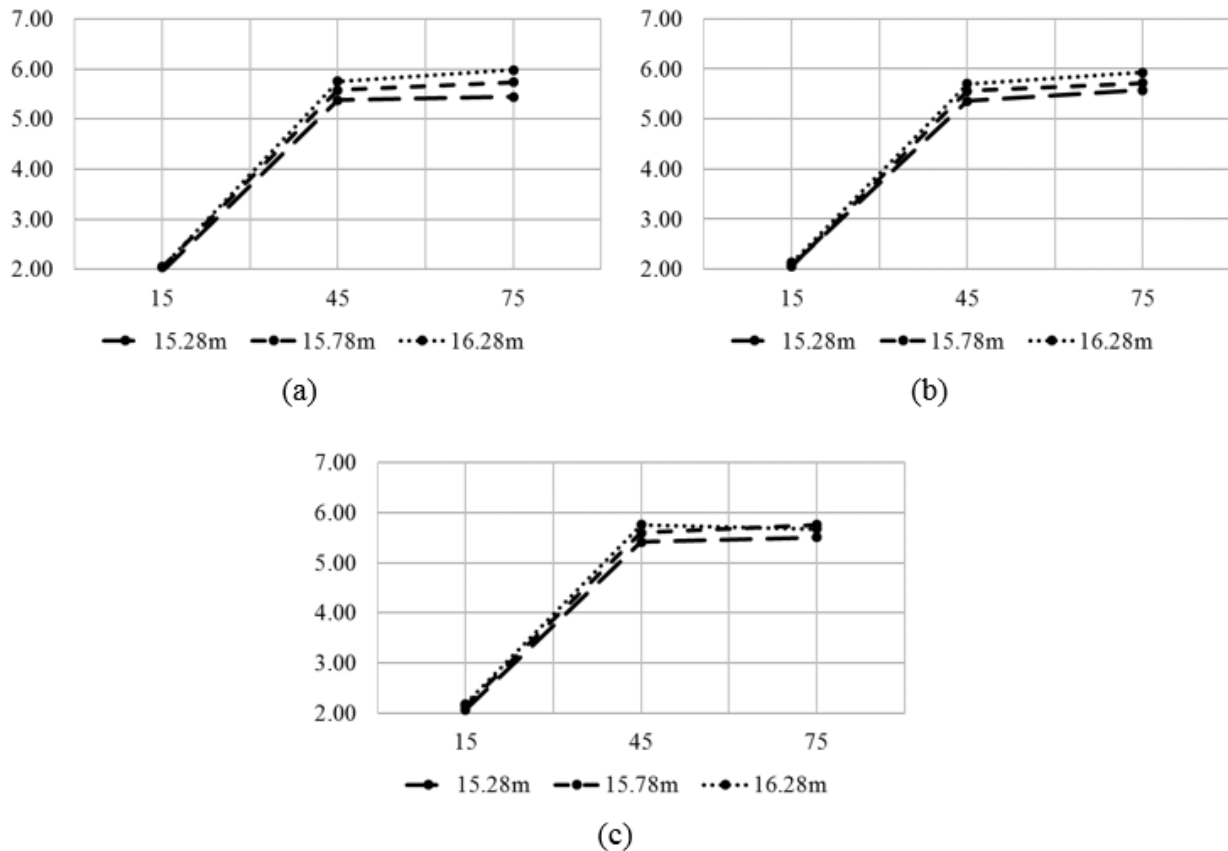


Figure 4.53 Side force coefficient 15°, 45° and 75° yaw angles for 15.28m, 15.78m and 16.28m long truck-trailer units at (a) 4.4m, (b) 4.6m and (c) 4.8m heights.

Figure 4.54 illustrates the variation in side force coefficient at various truck-trailer heights, lengths and crosswind conditions. By examining the Figure, it is observed that the side force coefficient on 15.28m length model increases from 4.4m to 4.6m truck-trailer height, before decreasing at 4.8m height model at 15° and 75° yaw angles. Whereas, at 45° yaw angle, side force coefficient has a vice versa effect. The side force coefficient at 15.78m length model, decreases from 4.4m to 4.6m truck-trailer height before increasing at 4.8m for 45° and 75° yaw angles. Whereas, at 15° yaw angle, side force coefficient is seen to increase throughout. The side force coefficient at 16.28m length model, increases throughout truck-trailer heights at 15° yaw angle. At 45° yaw angle, side force coefficient is seen to decrease from 4.4m to 4.6m truck-trailer height before increasing at 4.8m. At 75° yaw angles, side force coefficient is seen to decrease throughout the truck-trailer heights.

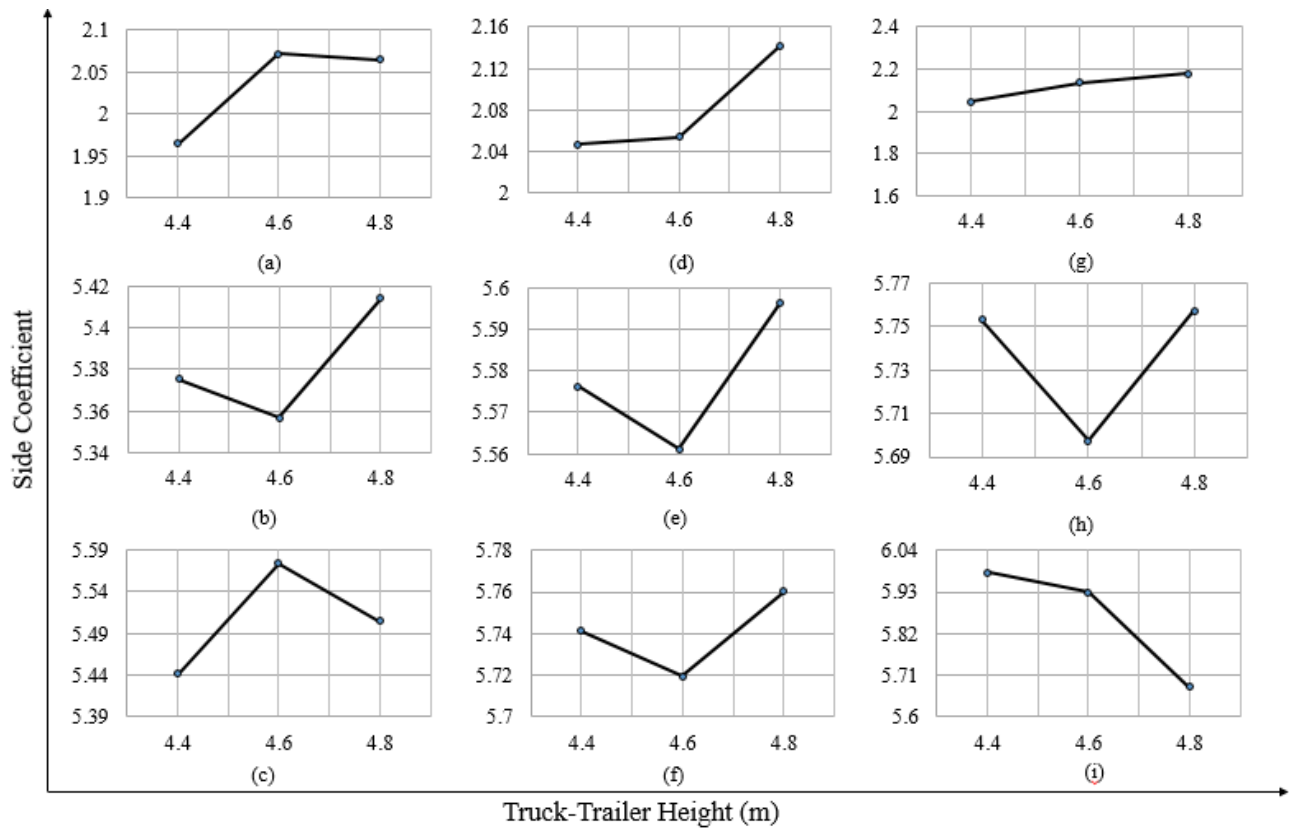


Figure 4.54 The side force coefficient for truck-trailer models with changing maximum heights, when length is 15.28m for 15°(a), 45°(b) and 75°(c) crosswind flow, 15.78m for 15°(d), 45°(e) and 75°(f) crosswind flow and 16.28m length for 15°(g), 45°(h) and 75°(i) crosswind flow.

By examining the Figure 4.55, it is observed for the 4.4m height model, side coefficient at 15° yaw angle increases sharply from 15.28m length model to 15.78m length model, prior to remaining at a constant at the 16.28m length model. At 45° and 75° yaw angle, side force coefficient is seen to continuously increase throughout each models. For the 4.6m height model, side coefficient at 15° yaw angle decreases from 15.28m length model to 15.78m length model, prior to increasing at the 16.28m length model. At 45° and 75° yaw angle, side force coefficient is seen to continuously increase throughout each models. For the 4.8m height model, side coefficient at 15° and 45° yaw angle is seen to continuously increase throughout each models. At 75° yaw angle however, side force coefficient increases sharply from 15.28m length model to 15.78m length model, prior to decreasing at the 16.28m length model.

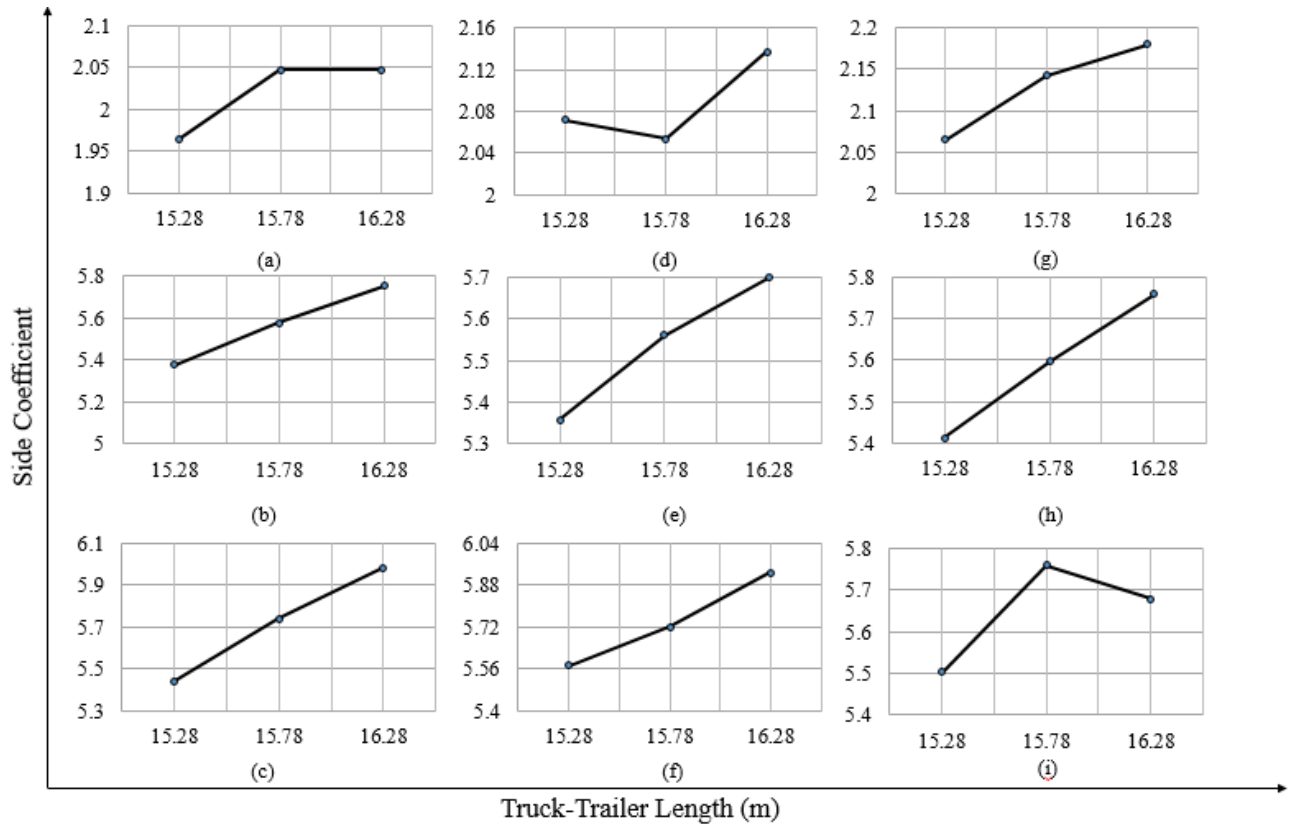


Figure 4.55 The side coefficient for truck-trailer models with changing maximum lengths, when height is 4.4m for 15°(a), 45°(b) and 75°(c) crosswind flow, 4.6m for 15°(d), 45°(e) and 75°(f) crosswind flow and 4.8m length for 15°(g), 45°(h) and 75°(i) crosswind flow.

Once more, observing the data trend for the side force coefficient for increasing height and length of the truck-trailer model and the yaw angle, proposed functional form was used to predict the side force coefficient at crosswinds. In this instant, constant ‘B’ in equation (4-33) has been replaced with equation (4-34) and constant ‘C’ in this case was maintained as a constant provided by the curve fitting techniques. Equation (4-34), depicts the proposed functional form for ‘B’:

$$B = \left( C_1 \left( \frac{l}{w} \right)^a \left( \frac{h}{w} \right)^b \right) \tag{4-34}$$

Upon studying the CFD data obtained for the side force coefficient, following functional form was used to predict the side coefficient at crosswinds incorporating dimensional characteristics only at crosswinds.

$$C_S = \left( 2.669 \left( \frac{l}{w} \right)^{0.442} \left( \frac{h}{w} \right)^{0.115} \sin(1.319 \cdot \psi) \right) \quad (4-35)$$

Figure 4.56 depicts the correlation between the predicted values of the aerodynamic side force coefficients, and those obtained from CFD. Once again, it can be clearly seen that the predicted values agree very well with those obtained from CFD. The standard error of estimate has been calculated to be around 15%. Hence, equation (4-35), developed for characterising the aerodynamic side force coefficient in terms of the vehicle’s dimensions and the relative flow angle, is well capable of predicting the side force coefficients for truck-trailer units of various sizes at different flow conditions.

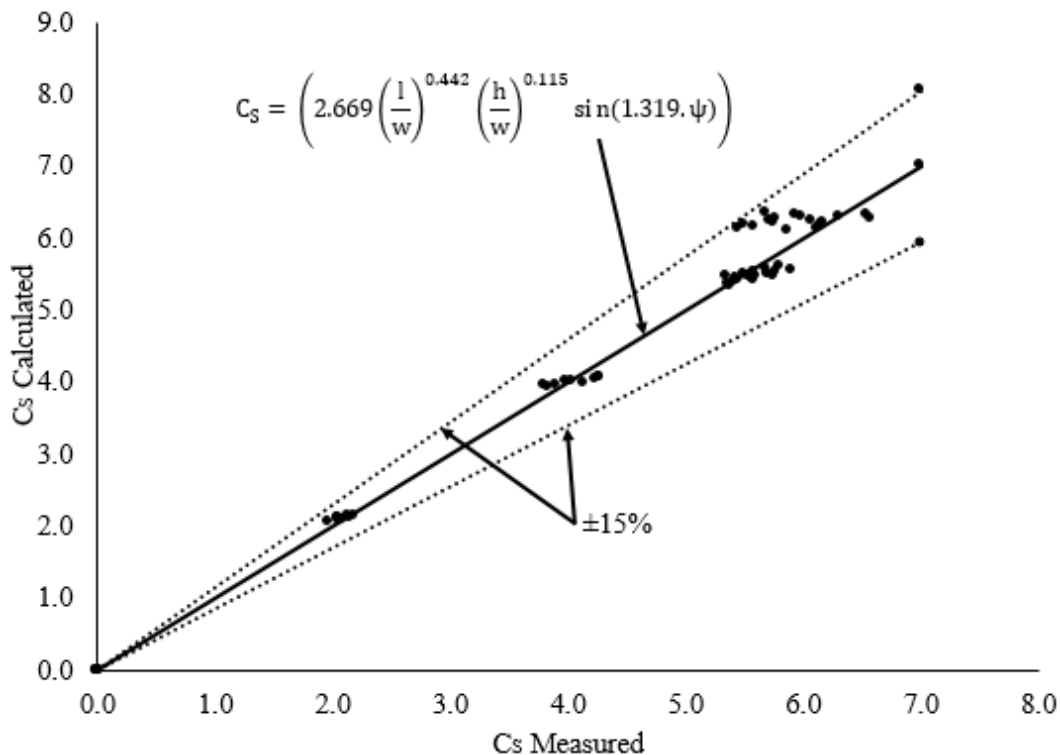


Figure 4.56 Correlation between aerodynamic side force coefficient measured from CFD and calculated by the new methodology for various vehicle geometries and relative flow angles.

#### 4.12.4 Further Validation of the Proposed Prediction Techniques

A further validation study was carried out to further establish the accuracy and the performance of the proposed design method. Number of truck-trailer geometrical configurations at various crosswind angles were generated and simulated using the CFD means. Identical simulation setting was applied in order to eliminate any discrepancies affecting the data accuracy. The width of the models was maintained at a constant of 2.6m throughout the range. The generated geometrical configurations are listed in Table 4.1 as illustrated below.

Table 4.1 Further validation of drag force coefficient (a), lift force coefficient (b), side force coefficient (c) using CFD and prediction model

Truck-Trailer Height	Truck-Trailer Length	Crosswind Angle	Measured Drag Coefficient	Calculated Drag Coefficient	Percentage Difference
4.3	15.28	15	1.17	1.06	9.4%
4.5	15.28	30	1.19	1.21	1.7%
4.7	15.28	75	-0.37	-0.34	8.1%
4.4	15.53	45	0.794	0.793	0.13%

(a)

Truck-Trailer Height	Truck-Trailer Length	Crosswind Angle	Measured Lift Coefficient	Calculated Lift Coefficient	Percentage Difference
4.3	15.28	15	0.622	0.680	9.3%
4.5	15.28	15	0.618	0.621	0.5%
4.7	15.28	15	0.561	0.569	1.4%
4.4	15.53	15	0.622	0.650	4.5%

(b)

Truck-Trailer Height	Truck-Trailer Length	Crosswind Angle	Measured Side Coefficient	Calculated Side Coefficient	Percentage Difference
4.3	15.28	15	1.852	2.056	11.1%
4.5	15.28	30	3.894	3.934	1.1%
4.7	15.28	45	5.371	5.365	0.1%
4.4	15.53	60	6.148	6.134	0.2%

(c)

### 4.13 Summary

An alternate design methodology capable of improving the efficiency of the conventional truck-trailer design process was proposed. It was revealed that by using the proposed geometrical modelling technique, it was possible to design a generic truck-trailer model. The validation of the design methodology was completed by generating a 3D geometry of the baseline truck-trailer unit using Ansys Design Modeller CAD tool. Number of truck-trailer units with changing dimensions such as length, height and width were generated using the proposed design methodology. Extensive CFD based aerodynamic analyses have been carried out using the generated truck-trailer models at both headwind and crosswind scenarios to analyse the dimensional effects on the resulting flow field. The stagnation pressure region was located at the front of the truck unit at straight headwind. However, the pressure on the front face was seen to reduce as the crosswind flow angle increases. Flow separation around the periphery of the truck-trailer surfaces was identified as a significant contributor for the non-uniform pressure distribution observed on the truck and trailer surfaces. As a result, high pressure regions on the windward sides were observed to shift towards the leeward sides as the crosswind angle increases. At 90° crosswind flow angle, negative pressure coefficients were observed on the entire truck-trailer faces situated perpendicular to the flow such as front and rear truck-trailer faces. Increasing the height of the trailer unit from 4.4m to 4.8m has a significant influence on the pressure distribution of the rear truck surface and both front and rear trailer surfaces. Decreased pressure regions were observed on large areas of the truck rear surface as the trailer height increased. However, a significant increase in pressure on the front trailer face was recorded as the height increased. This is due to the kinetic energy loss of oncoming flow as a result of adverse pressure gradients generated by the increased surface area of the front trailer unit. The increased height has also caused a slight reduction in pressure on the trailer rear face. Highest drag force is seen on the 4.8m high truck-trailer model up to a crosswind angle of 45° and thereafter, the 4.4m high truck-trailer model is associated with the highest drag force. As the trailer height increased, the side force was also seen to increase throughout the crosswind flow range. It was discovered that increasing the trailer length from 15.28m to 16.28m has minimal effect on the pressure distribution on both front and rear truck faces and front trailer face. However, a slight reduction in surface pressure was observed on the rear trailer face as the trailer

length increased to 16.28m. Using data gathered during the analysis stage, a force prediction methodology has been developed. The prediction methodology has been validated against the CFD data and was proven to be capable of predicting drag, lift and side forces at both straight and crosswind profiles with a reasonable accuracy.

## CHAPTER 5

# AERODYNAMIC CHARACTERISATION METHODOLOGY FOR TRUCK-TRAILER UNITS BASED ON VEHICLE SHAPES

---

Altering the shape of the truck-trailer units has proved to be a popular method of making them more streamlined and efficient. Considerable amount of numerical and experimental work has been carried out to explore the potential of shape modification on truck-trailer aerodynamic improvements and resulting aerodynamic gains. Due to several constrictions such as the pay load capacity and legal requirements, significant shape modifications to the trailer has proven counterproductive. However, the top leading edge and the trailing edge of the truck-trailer units were identified as the two main areas which need to be improved in order to make the truck-trailer units more streamlined. The effects of changing the shape of the truck-trailer unit to its surrounding flow field is analysed and quantified in this chapter. Numerous truck-trailer models were generated with various shapes and the respective surrounding flow field is analysed in this chapter. The geometrical modelling tool developed in the previous chapter will be improved and used to obtain various truck-trailer geometries with changing shape. The models were analysed using the data gathered from steady state simulations at a constant headwind velocity. This approach was vital in order to isolate the resulting effects of the shape of the truck-trailer on the aerodynamic performance parameters such as drag, lift and side forces. A semi-empirical prediction model developed in the previous chapter will be further improved by incorporating the elements that define various shapes.

## 5.1 Mathematical Modelling Technique to Modifying Truck-Trailer Shapes

The key advantage of employing mathematical methods when designing a truck-trailer model is that it eases the generation of numerous models with various shapes. This helps to produce models with a quantified shape and hence when reproducing a design, a highly accurate duplicate of the original model can be made. Furthermore, the design time will be considerably reduced and this in turn will result in substantial financial gains.

The shape function which will be used to define a truck-trailer shape is given in equations 5-1, 5-2 and 5-3. The truck, bridge and the trailer unit will be defined using designated shape function equation for individual sections as shown below.

$$S_{\text{Truck}}(x) = H \times \text{Min} \left\{ \left( \frac{x}{P_1} \right)^{B_1}, 1.0, \left[ \frac{x_E - x}{x_E - P_2} \right]^{B_2} \right\} \quad (5-1)$$

$$S_{\text{Bridge}}(x) = H \times \text{Min} \left\{ \left( \frac{x_B - x}{x_B - P_1} \right)^{B_3}, 1.0, \left[ \frac{x_E - x}{x_E - P_2} \right]^{B_4} \right\} \quad (5-2)$$

$$S_{\text{Trailer}}(x) = H \times \text{Min} \left\{ \left( \frac{x_B - x}{x_B - P_1} \right)^{B_5}, 1.0, \left[ \frac{x_E - x}{x_E - P_2} \right]^{B_6} \right\} \quad (5-3)$$

Each equation defines a section of the truck-trailer unit and each function defines first, second and third sections of the profile as illustrated from Figure 5.1. The profiles will be generated on the XY plane. The height is denoted by H, position along x axis is denoted by x, end of the first profile and beginning of the third profile is denoted by P1 and P2 respectively. The x position at the start of the curve and end of the curve is denoted by  $x_B$  and  $x_E$  respectively and the coefficient that determines the gradient of each curve is denoted using B1, B2, B3, B4, B5 and B6.

## 5.2 2D Representation of the Baseline Truck-Trailer Unit

Changing B1 to B6 coefficients will consecutively alter the gradient on each curve. This will change the shape of the front and rear leading edges of truck, bridge and trailer units. The bridge geometry on truck-trailer units are not subjected to any shape alterations. Therefore, in this study, B3 and B4 coefficients which are responsible for the bridge geometry are maintained as zero. The value of B1, B2, B5, B6 coefficients are changed to 0.01, 0.05 and 0.1 in order to obtain a range of different truck-trailer shapes. When B1 = 0, B2 = 0, B5 = 0 and B6 = 0 the baseline geometry was obtained and this was discussed in chapter 4. Figure 5.1a and 5.1b depicts the truck-trailer shapes obtained when {B1, B2, B5, B6} = 0 and when {B1, B2, B5, B6} = 0.1 respectively.

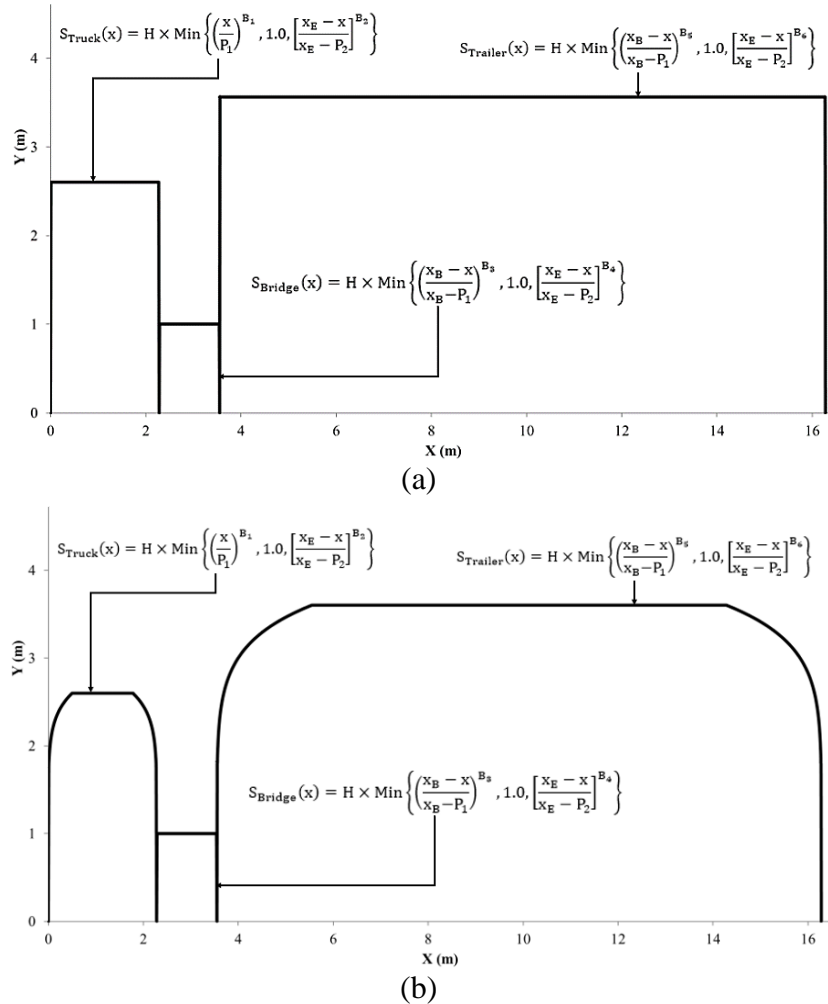


Figure 5.1 Baseline truck-trailer model when {B1, B2, B5, B6} = 0 (a) and when {B1, B2, B5, B6} = 0.1 (b)

Since the baseline model was already discussed and analysed in chapter 4, three values 0.01, 0.05 and 0.1 have been chosen as B1, B2, B5 and B6 coefficients. Figure 5.2 shows the varying truck-trailer shapes as each of the B1, B2, B5 and B6 coefficients were 0.01, 0.05 and 0.1.

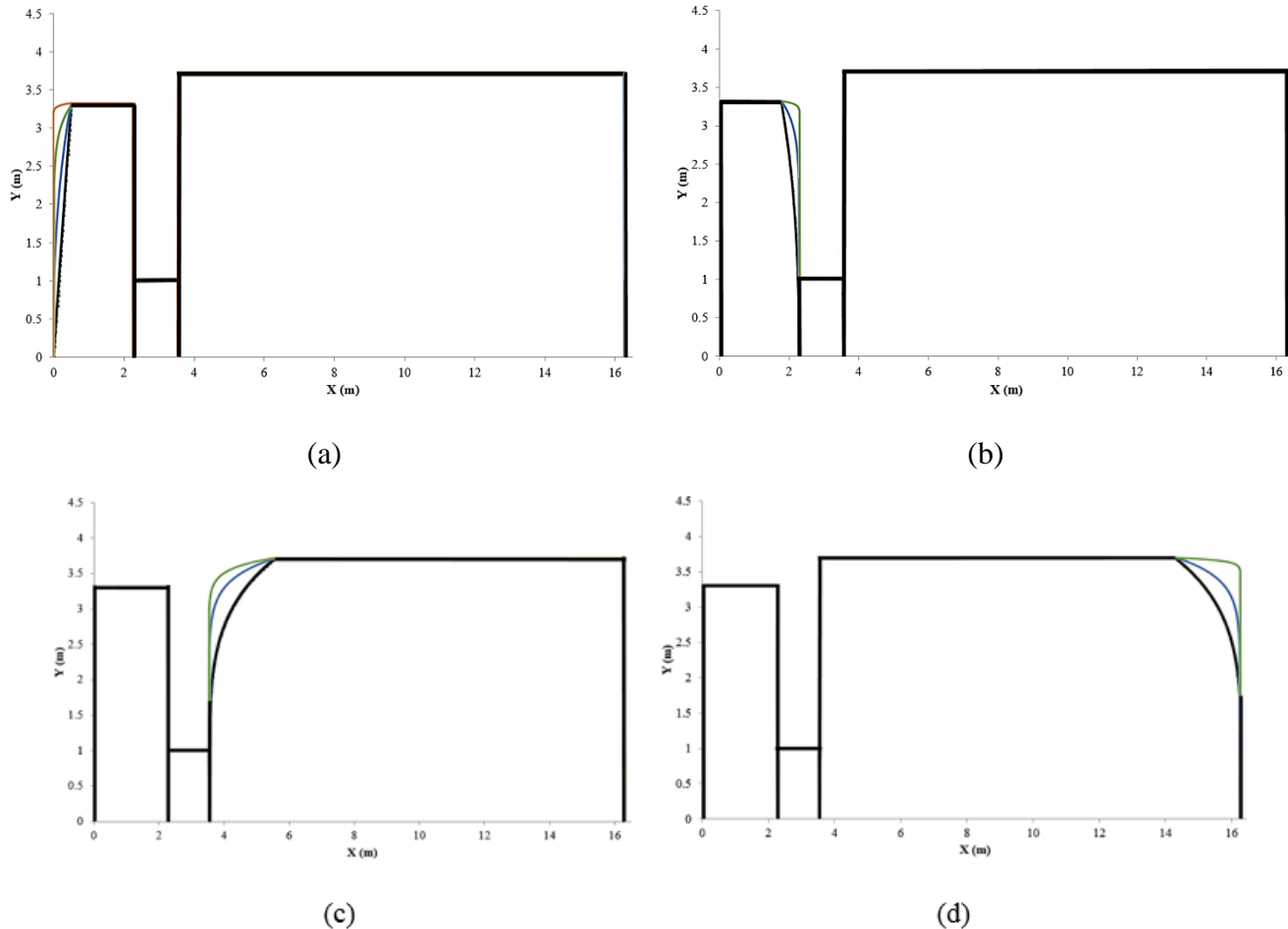


Figure 5.2 Varying B1 and B2 coefficient of 0.01, 0.05, 0.1 to obtain changing truck shapes (a-b) and varying B5 and B6 coefficient of 0.01, 0.05, 0.1 to obtain changing trailer shapes (c-d)

### 5.3 3D Representation of the Baseline Truck-Trailer Unit

Once more, a combination of profiles generated using  $S_{\text{Section}}(x)$  and  $S_{\text{Section}}(z)$  were in both XY plane and YZ plane respectively generating a wire frame model of a complete 3D truck trailer model as depicted from Figure 5.3. The points obtained through the wire frame model will be used in a CAD software to obtain the 3D CAD model of the truck-trailer unit.

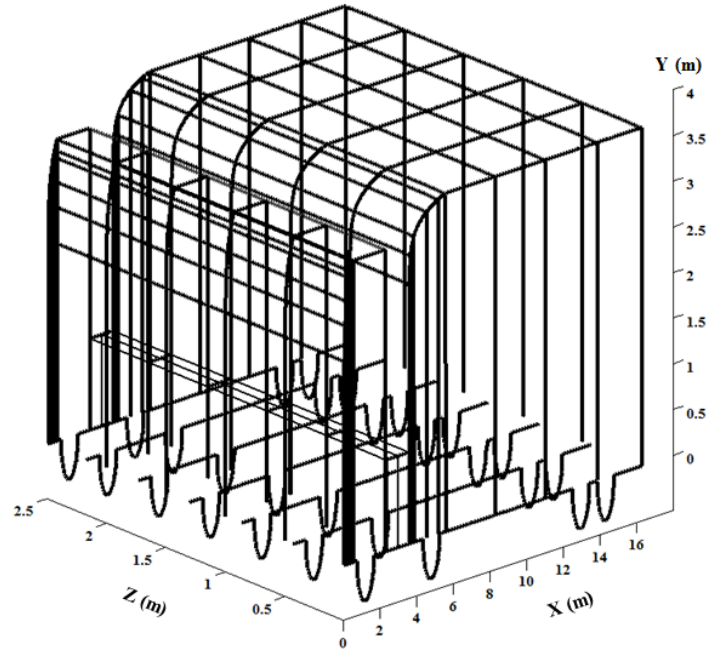


Figure 5.3 The generated 3D wireframe structure for a complete truck-trailer model with shape alterations.

#### 5.4 Full Factorial Truck-Trailer Unit Design Configurations

A full factorial design analysis was carried out to study the effects of B1, B2, B5 and B6 factors on the drag, lift and side forces. Varying the levels of B coefficients between 0.01, 0.05 and 0.1 were altered each time to study the interaction between geometrical factors and the resulting aerodynamic forces. With four B coefficients and three different levels for each coefficient, a total of 81 possible geometrical shapes were obtained. Appendix A-1 lists the geometrical configurations considered for this study.

#### 5.5 Effect of B1 on the truck-trailer unit aerodynamic characteristics

In order to analyse the effect of B1 on aerodynamic performance of truck-trailer unit, three B1 values of 0.01, 0.05, 0.1 were used. The B2, B5 and B6 coefficients were maintained at 0.01 while the B1 values were changed. The resulting geometric shape modification is illustrated from Figure 5.4. Straight headwind flow condition was used having a constant velocity of 25.03m/s from the inlet.

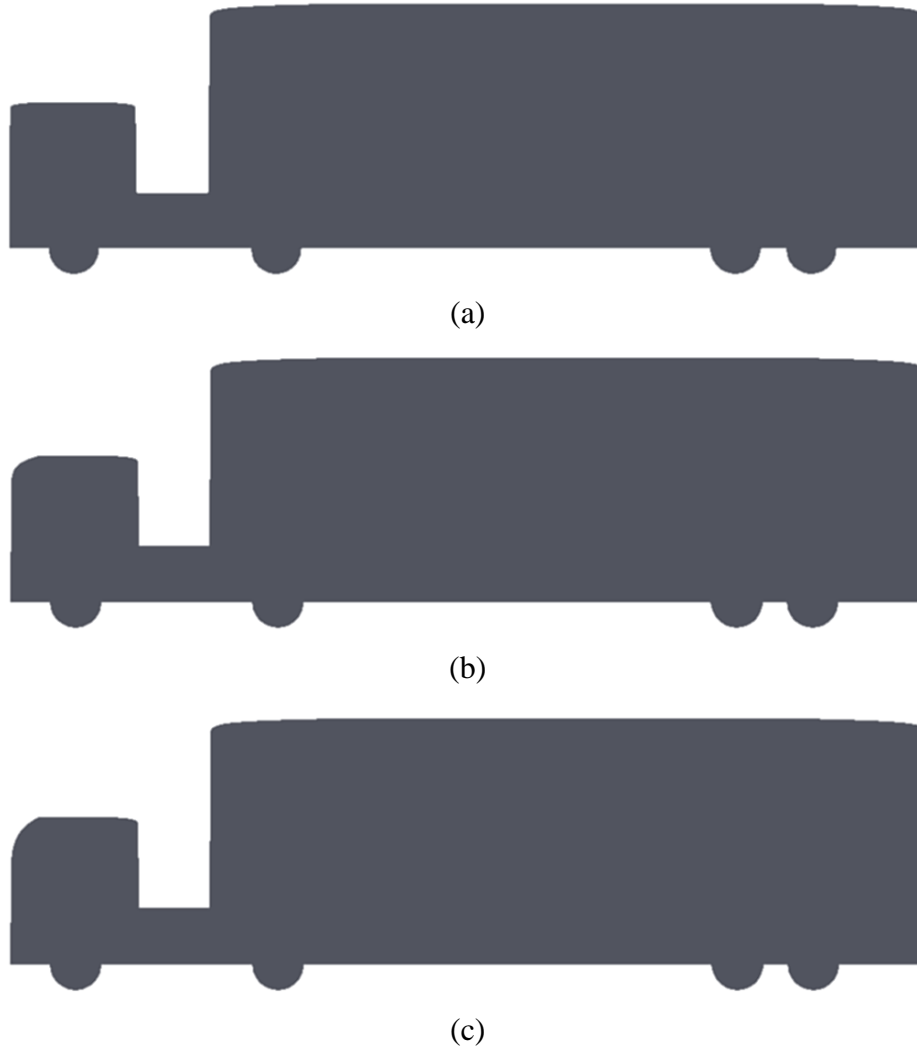
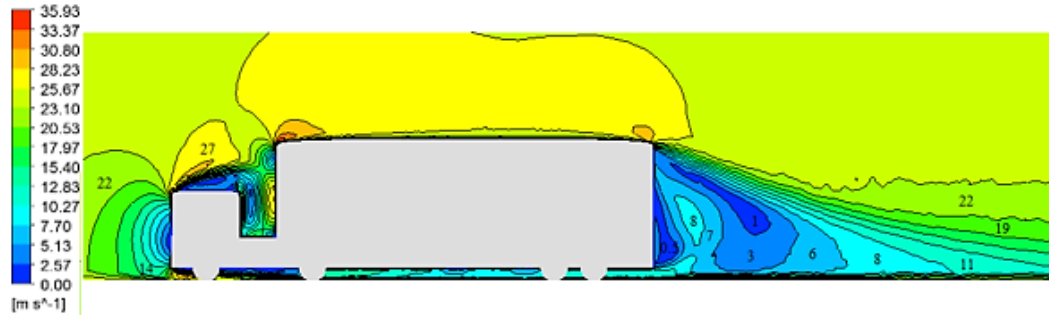


Figure 5.4 Truck-trailer unit with changing B1 coefficients (a)  $B1 = 0.01$  (b)  $B1 = 0.05$  (c)  $B1 = 0.1$

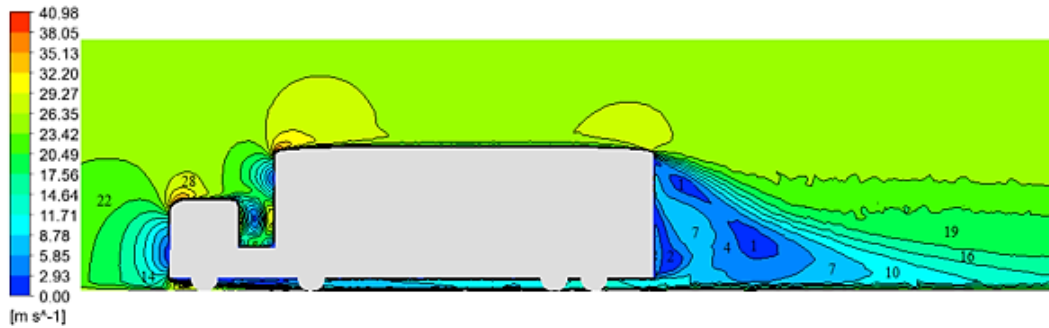
### 5.5.1. Velocity Distribution around the Truck-Trailer Unit with Changing B1 Values.

The velocity distribution around the truck-trailer unit at  $B1 = 0.01$ ,  $0.05$  and  $0.1$  whilst maintaining  $B2$ ,  $B5$ ,  $B6$  at a constant value of  $0.01$  is depicted from Figure 5.5. It can be clearly seen that having a  $B1$  value of  $0.01$  leads to flow separation on top of the truck unit. The separated flow is seen to generate a wake region with low velocity which continues into the truck-trailer gap region. This subsequently leads to low velocity flow on top of the truck unit and the trailer unit. Upon changing  $B1$  to  $0.05$  and  $0.1$ , the flow velocity on the truck unit increases

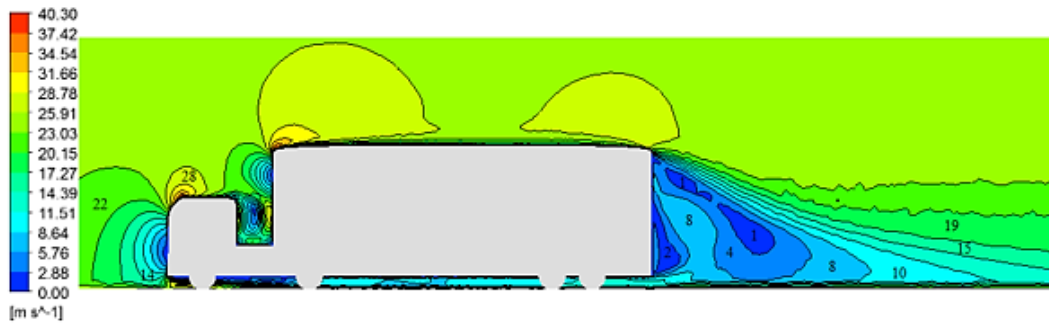
and completely eradicates the low velocity wake flow region on top of the truck unit. In fact, the increasing curvature on the top leading edge of the truck unit is seen to increase the flow velocity on top of the trailer unit accordingly.



(a)



(b)



(c)

Figure 5.5 Velocity fields around the Truck-trailer units with changing B1 coefficients.

Figure 5.6 depicts the truck unit with the top leading edge profile of  $B1 = 0.1$  and the six data lines ranging from  $L1_F$  to  $L6_{BR}$  where the velocity in the streamwise direction was recorded. The velocity data will be obtained and compared for models  $B1 = 0.01$ ,  $B1 = 0.05$  and  $B1 = 0.1$  in order to understand the effects of B1 on the flow field in the vicinity of truck unit. Data lines  $L1_F$

and  $L4_T$  were positioned along the mid plane of the truck unit while the former was positioned at the start of the curved surface and the latter at the end of the curved surface. Data lines  $L2_{BL}$  and  $L3_{TL}$  were positioned on the left side of the truck and the data lines  $L5_{TR}$  and  $L6_{BR}$  on the right side of the truck (viewing from front elevation) at the beginning and the end of the curved surface.

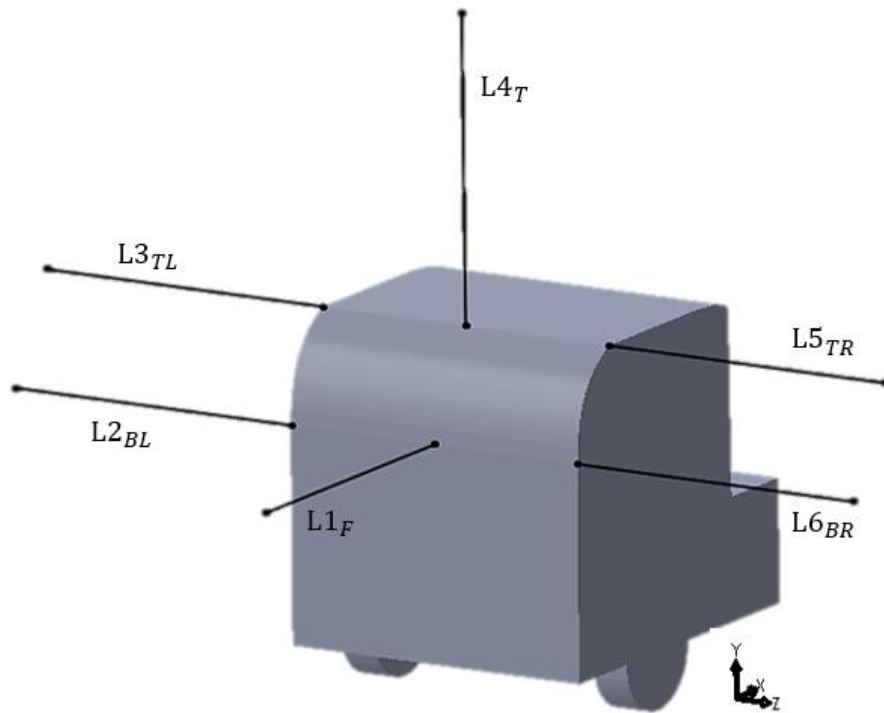


Figure 5.6 Data line locations around the top leading edge of the truck unit when  $B1 = 0.1$

Figure 5.7 depicts velocity distribution along data line  $L1_F$  that was positioned at the front of the truck unit. The data line extends from the origin to  $-4\text{m}$  in the negative  $X$  direction while air flows in the positive  $X$  direction towards the front face of truck unit. Velocity data have been obtained for  $B1$  values  $0.01$ ,  $0.05$  and  $0.1$  and it is evident that as the flow is approaching front of the truck, velocity decreases to zero for all the models. Further away from front truck face, free stream flow velocity of  $25.03\text{m/s}$  is observed. Velocity variation between  $0.01$ ,  $0.05$  and  $0.1$  models are seen to be negligible beyond  $4\text{m}$  from the negative  $X$  direction. The  $B1 = 0.1$  model maintains highest velocity while  $B1 = 0.01$  model is associated with lowest flow velocity. Highest velocity variations are depicted between  $X = 0$  to  $X = -2.5$  from front truck face.

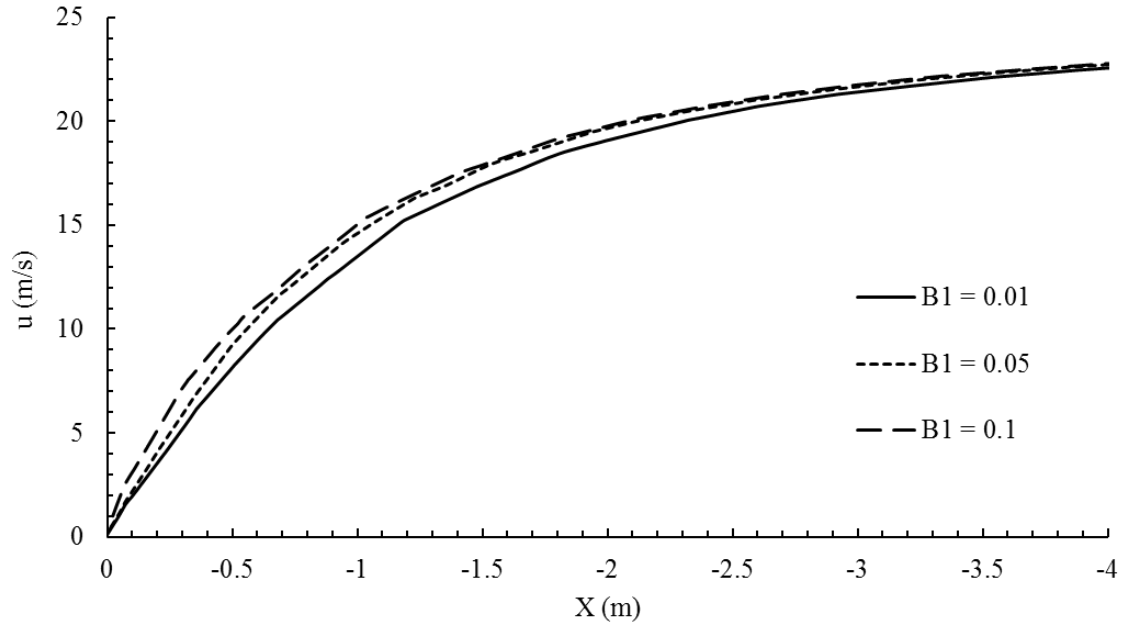


Figure 5.7 The x direction velocity plotted along the data line L1<sub>F</sub>

Figure 5.8 depicts velocity distribution along data lines L2<sub>BL</sub> and L6<sub>BR</sub> which have been positioned on the left and right sides of the truck unit respectively, at the beginning of curved leading edge surface. The L2<sub>BL</sub> data line extends from the truck left surface (-1.3m) to -3m in the negative Z direction. The velocity is seen to be around 25m/s at 1.7m from the left truck surface before decreasing to zero at truck surface as result of no-slip boundary condition and stationary surface. Upon examining Figure 5.8, it is evident that at the beginning of the curved surface the velocity variation between 0.01, 0.05 and 0.1 model are minimal. Between -1.7m and -1.5m, the 0.01 model is seen to have the highest velocity of 19.2 m/s while 0.1 model has the lowest velocity of 17.5m/s. However, between -1.5m and -1.3m, 0.1 model has the highest velocity of 11.8m/s and 0.05 model has the lowest velocity of 9.3m/s.

The L6<sub>BR</sub> data line extends from the truck right surface (1.3m) to 3m in the positive Z direction. Once more, the velocity is seen to be around 25m/s at 1.7m from the left truck surface before decreasing down to zero at truck surface as result of no-slip boundary condition and stationary surface. The velocity variations between three models on this occasion is observed to be minute and the 0.1 model is seen to have the highest velocity while the 0.01 model is associated with the lowest velocity. At any point the maximum difference between the highest and lowest velocities is found to be 9.6%.

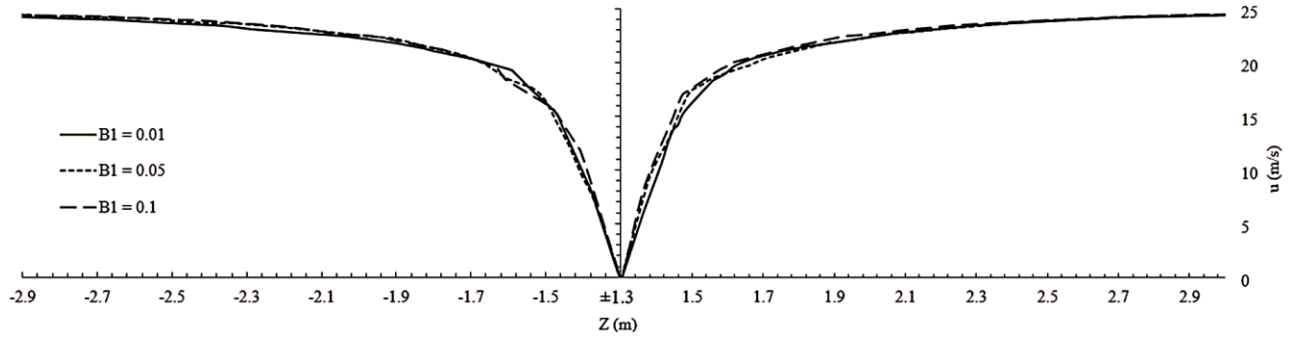


Figure 5.8 The x direction velocity plotted along the data lines L2<sub>BL</sub> (left) and L6<sub>BR</sub> (right)

Figure 5.9 depicts velocity distribution along data lines L3<sub>TL</sub> and L5<sub>TR</sub> which have been positioned on the left and right sides of the truck unit respectively, at the end of curved leading edge surface. It is clearly seen that, at the end of the curved surface there are significant velocity variations between all three truck-trailer models. The free stream velocity of 25m/s is observed for 0.1 model at a distance of 0.3m from the left truck face while 0.05 model and 0.01 model behave the same way at 0.4m and 0.8m respectively. Increased flow velocity in the vicinity of the 0.1 model is due accelerating flow as a result of the curvature of the front leading edge. A maximum flow velocity of 6.5m/s in the opposite direction can be seen at a distance of 0.06m from the left surface of truck unit for the 0.01 model and this is due to flow separation as result of the sharp leading edge.

The L5<sub>TR</sub> data line extends from the truck right surface (1.3m) to 3m in the positive Z direction. The velocity data observed in this occasion is seen to be very similar to what was observed on the L3<sub>TL</sub> data line positioned on the opposite side truck surface. At a distance of 1.9m from the right side surface of truck unit, a free stream velocity of 25m/s is observed for 0.01, 0.05 and 0.1 models. The free stream velocity for 0.1 model is observed at a distance of 0.18m from the right truck face, while for 0.05 model and 0.01 model the distances are 0.3m and 0.5m respectively. Once again, a maximum flow velocity of 5.5m/s in the opposite direction can be seen at a distance of 0.07m from the right surface of the truck unit for the 0.01 model and this is due to flow separation as result of the sharp leading edge.

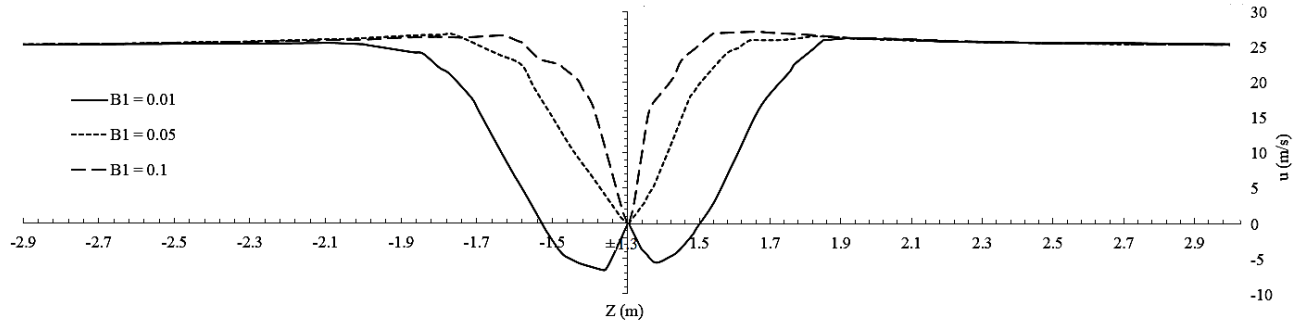


Figure 5.9 The x direction velocity plotted along the data line L3<sub>TL</sub> (left) and L5<sub>TR</sub> (right)

Velocity distribution along the L4<sub>T</sub> data line situated on top of the truck unit immediately after the curved leading edge is shown in Figure 5.10. It can be seen that flow velocity increases sharply in the boundary layer for all three models. Separated flow is exhibited on the top truck surface of the 0.01 model, with a maximum velocity of 3m/s in the opposite direction. The highest flow velocity of 38.5m/s is seen for the 0.1 model at a height of 2.6m from the top surface of the truck while at same height, 0.05 model has a flow velocity of 34.8m/s.

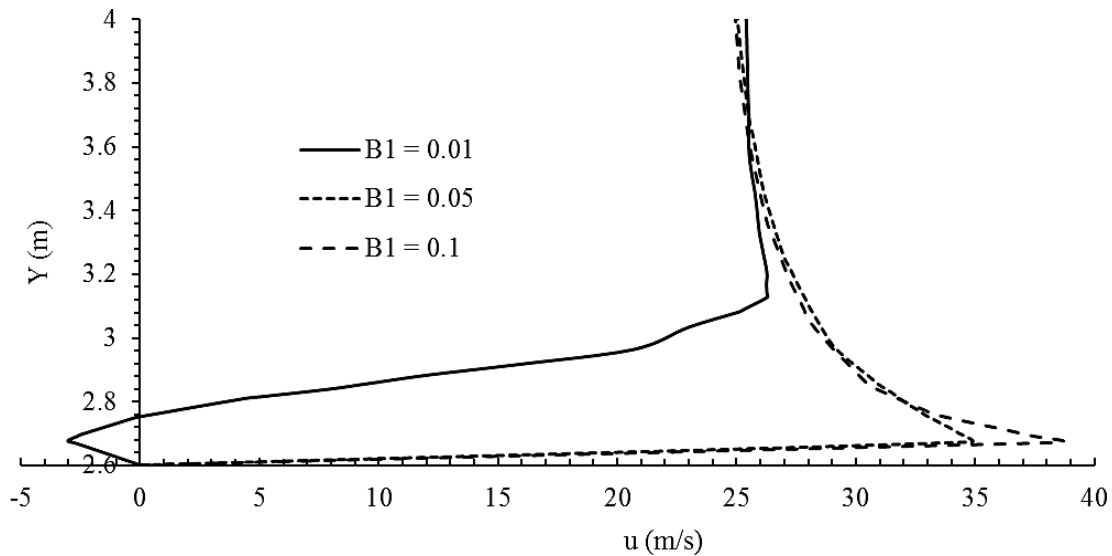


Figure 5.10 The x direction velocity plotted along the data line L4<sub>T</sub>

The velocity profiles in the wake region on top of the truck unit, when  $B1 = 0.01$  at various distances from the front face is shown in Figure 5.11. The area of the wake region is seen to increase towards the rear face of the truck unit. At a distance of 0.75m from the front face of the truck unit, the height of the wake region was found to be 2.84m from the truck roof. When the distance from truck front face increased to 1.15m and 1.55m, the height of the wake regions is seen to increase up to 2.92m (3.0%) and 2.97m (4.5%) respectively. A maximum axial flow velocity of 3.6m/s in the opposite direction can be seen at a distance of 0.75m from the front face of the truck unit. At a distance of 1.15m and 1.55m from the front face of the truck unit this axial flow velocity in the opposite direction is seen to increase up to 3.9m/s (8.3%) and 4.9m/s (36%) respectively.

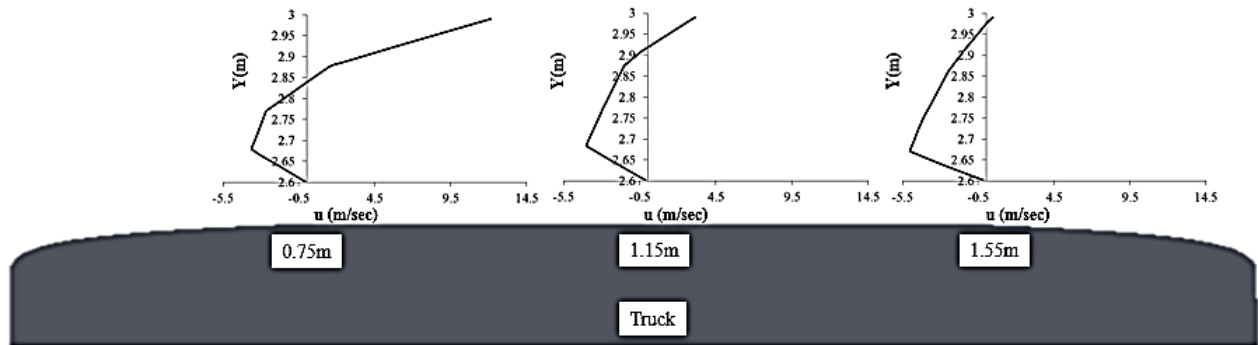


Figure 5.11 Axial flow velocity profiles at various distances from the top leading edge of the truck unit when  $B1 = 0.01$

The velocity profiles on top of the truck unit, when  $B1 = 0.1$  at various distances from the front face is shown in Figure 5.12. It can be seen that, there is no axial flow in the opposite direction indicating that flow circulation does not take place and the subsequent wake flow area is not exhibited on top of the truck unit. For all the velocity profiles, the axial velocity is seen to increase linearly up to a height of 2.67m from the truck roof before attaining a stable flow velocity. The first velocity profile located at a distance of 0.75m from the front face of the truck unit is incorporated with the highest velocities with a maximum velocity of 30.7m/s at a height of 2.77m. The velocity profile located at a distance of 1.15m from the front face of the truck unit has a maximum axial flow velocity of 27m/s at a height of 2.86m. The lowest axial flow velocities are associated with the velocity profile which is located at 1.55m from the front of the

truck unit and the maximum axial flow velocity is recorded as 24.5m/s at a height of 2.9m from the roof of the truck, which is 20% lower than the first velocity profile.

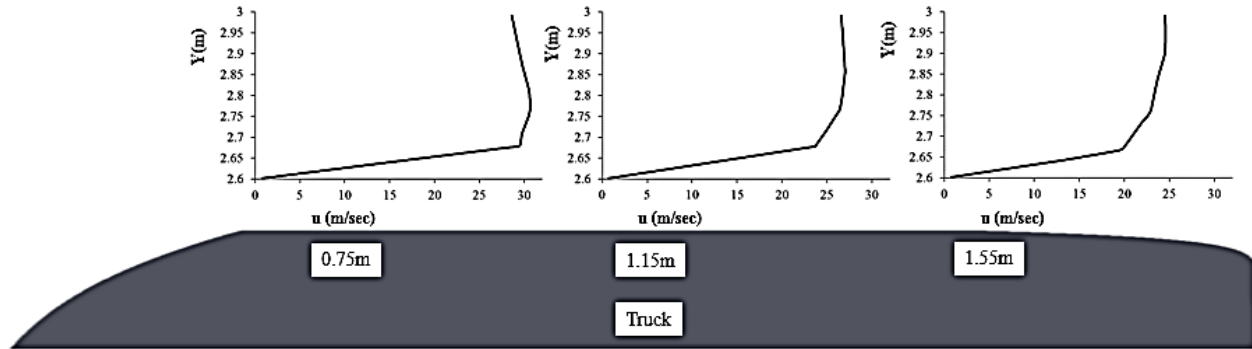


Figure 5.12 Axial flow velocity profiles at various distances from the top leading edge of the truck unit when  $B1 = 0.1$

### 5.5.2. Pressure Distribution around the Truck-Trailer Unit with Changing $B1$ Values.

The coefficient of pressure around the truck-trailer unit when  $B1 = 0.01, 0.05$  and  $0.1$  whilst maintaining  $B2, B5, B6$  at a constant  $0.01$  is depicted from Figure 5.13. Upon examining the Figure, it is evident that increasing the curvature of the leading edge of the truck unit has a significant effect on the stagnation pressure region located at the truck front. Area of the high pressure region ( $C_p = 0.9$ ) is seen to decrease gradually from  $B1 = 0.01$  to  $B1 = 0.1$  as a result of flow escaping to top of the truck unit over the curved surface. The low pressure recirculation region on truck roof ( $C_p = -0.5$ ) is only observed for  $B1 = 0.01$  model and is completely eliminated for  $B1 = 0.05$  and  $0.1$  models. The low pressure region in the truck-trailer gap has been increased from  $-0.3$  to  $-0.7$  as  $B1$  increases along with the high pressure air stagnation region on the front face of trailer unit.

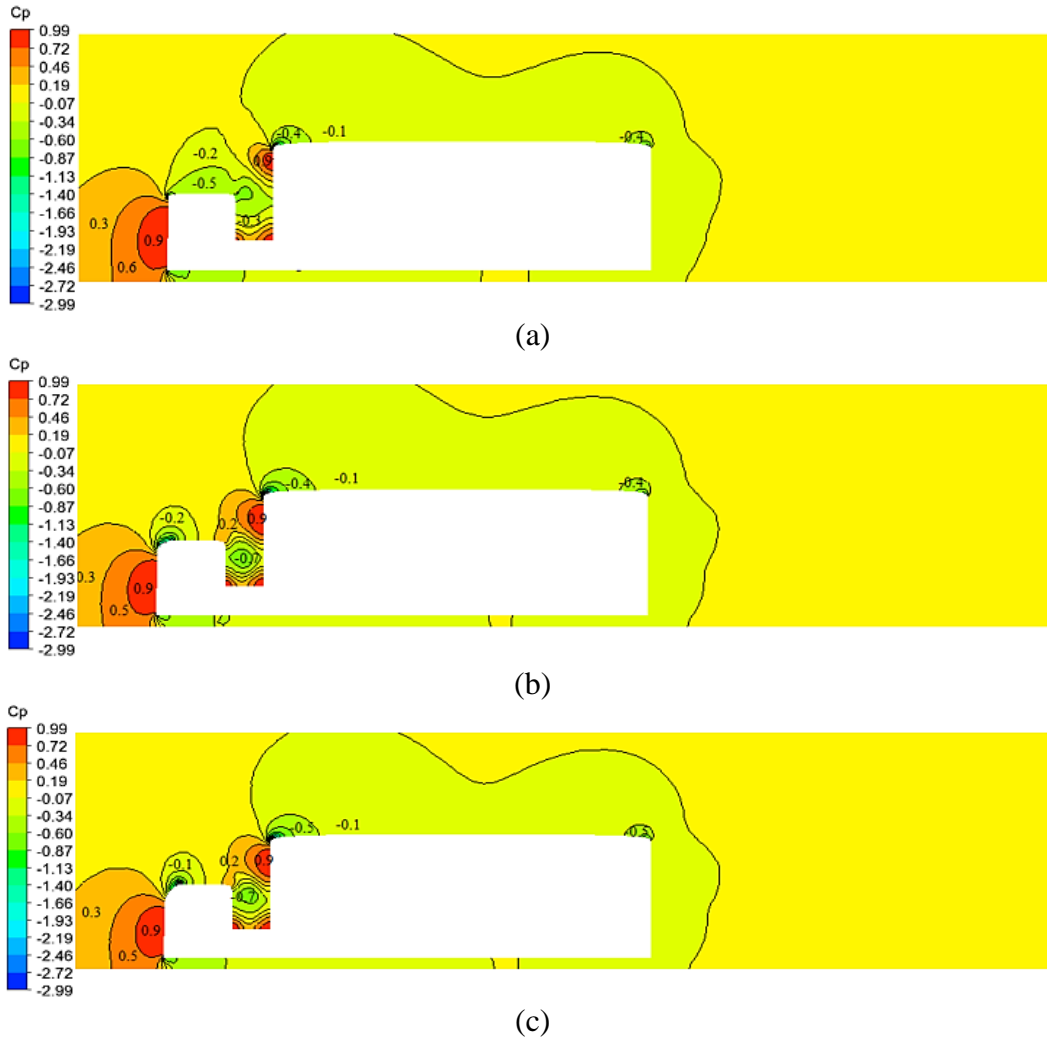


Figure 5.13 Coefficient of pressure around the Truck-trailer units with changing B1 coefficients.

### 5.5.3. Pressure Distribution on the Truck-Trailer Unit with Changing B1 Values

A data line positioned along the symmetry line of the truck-trailer unit as seen from Figure 5.14, has been used to investigate the pressure distribution on truck-trailer models at various B1, B2, B5 and B6 coefficients and 0.01, 0.05, 0.1 levels. TRU-F, TRU-T, TRU-R, BRI, TRA-F, TRA-T and TRA-R denotes the truck front, truck top, truck rear, bridge, trailer front, trailer top and trailer rear faces respectively.

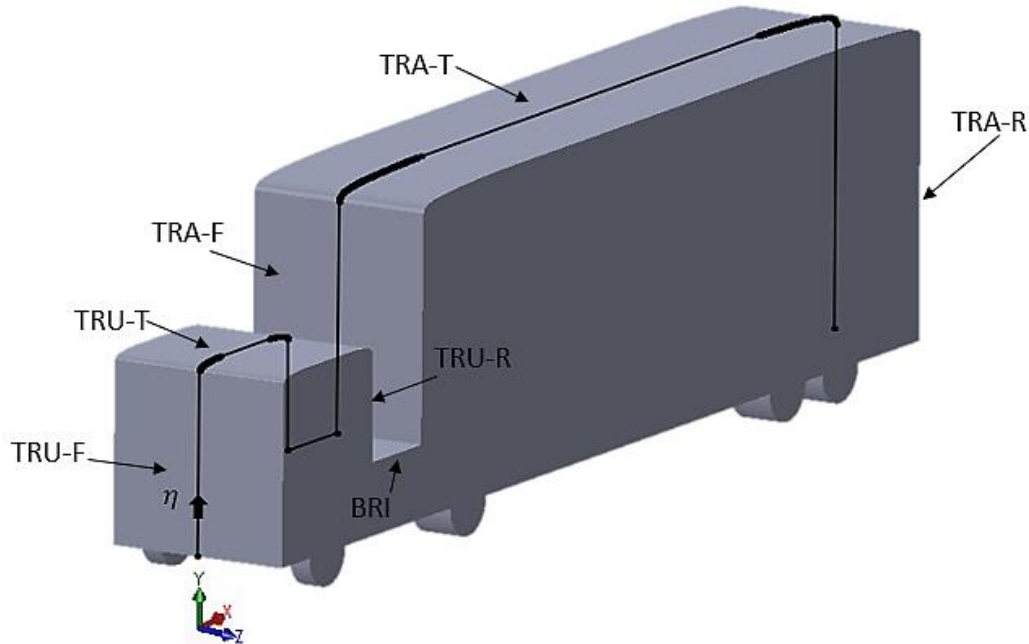


Figure 5.14 Coordinate  $\eta$  is used to plot pressure coefficient around the truck-trailer unit along the symmetry line starting at bottom front truck face and ending at bottom rear trailer face.

The pressure coefficient ( $C_p$ ) plotted over the truck-trailer unit along the symmetry line with changing  $B1$  coefficients is depicted from Figure 5.15. The pressure along the symmetry line is observed to have a highest pressure of 0.99 when  $B1 = 0.01$  and a lowest pressure of -2.48 when  $B1 = 0.05$ . It is observed that the varying  $B1$  shape coefficients only influence the pressure profiles on the truck-trailer geometry up to  $\eta = 0.50$ . Moreover, after  $\eta = 0.13$ , a reasonably identical pressure distribution is seen for both  $B1 = 0.05$  and  $B1 = 0.1$  geometries. The lowest pressure of -1.55 has been recorded on the truck front face when the  $B1 = 0.05$  and this is approximately 122% lower than  $B1 = 0.01$  geometry. This low pressure region is seen to extend to the middle of the truck top surface and transform into a positive pressure region on the truck top surface. The positive pressure region on the truck top surface is only seen to exist for  $B1 = 0.05$  and  $B1 = 0.1$  geometries. The top half of the truck rear surface is seen to be associated with negative pressure while the bottom half of the surface is associated with positive pressure. This positive pressure continues on to the bridge while a maximum pressure of 0.81 is seen to exist towards the rear of the bridge surface. Significant pressure fluctuations are seen on the trailer front surface. Highest pressure of 0.98 is recorded on  $B1 = 0.01$  model and the lowest pressure of -2.48 is recorded on  $B1 = 0.05$  model. For  $B1 = 0.01$  model, the positive pressure distribution is

seen to spread along 45% of the symmetry line while on models  $B1 = 0.05$  and  $B1 = 0.1$ , the positive pressure on the trailer front surface is seen to spread along approximately 60% of the symmetry line. The pressure on the trailer top surface and trailer rear surface are seen to be negative along the symmetry line and pressure fluctuations between three  $B1$  geometries are seen to be mostly identical.

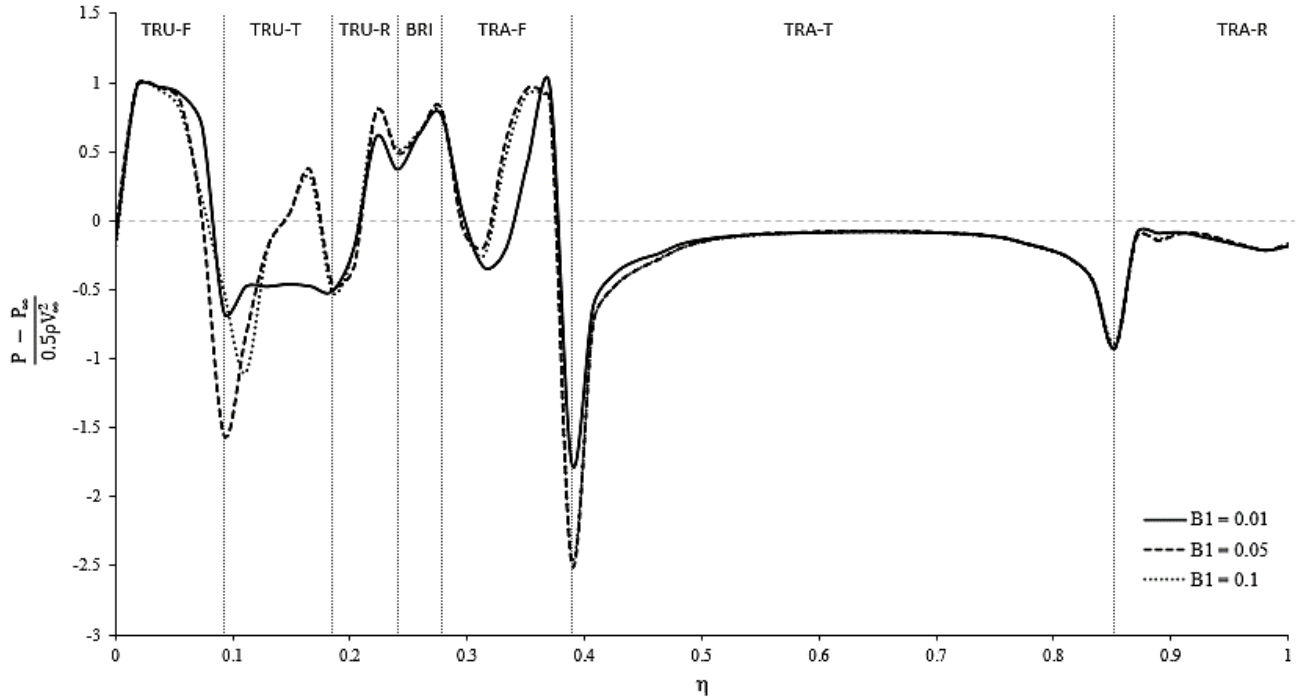
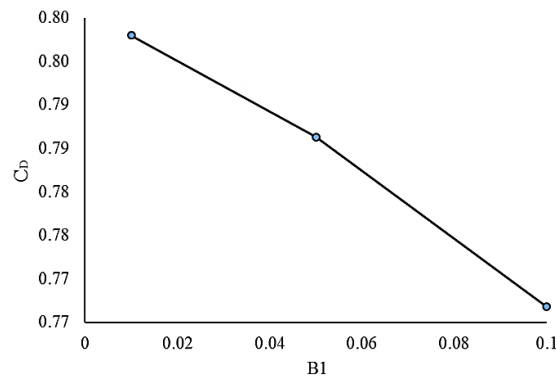


Figure 5.15 The pressure coefficient ( $C_p$ ) plotted over the truck-trailer unit along the symmetry line with changing  $B1$  coefficients.

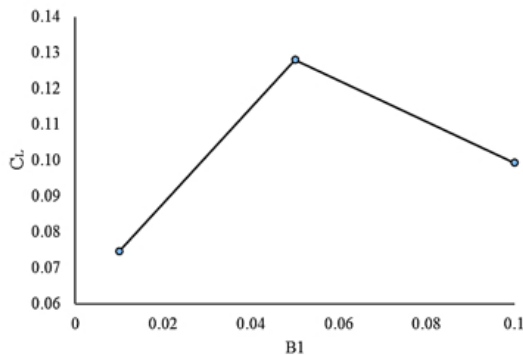
#### 5.5.4. Effects of Changing $B1$ Values on Aerodynamic Forces

The effects on velocity fields and pressure fields around a truck-trailer geometry upon changing the  $B1$  shape coefficient have been discussed in the above sections. The behaviour of flow and the resulting pressure gradients most certainly influence the overall forces acting on a truck-trailer model. As seen in the previous sections, even a slightest alteration to a truck-trailer geometry has a significant effect on the pressure fields throughout the vehicle model.

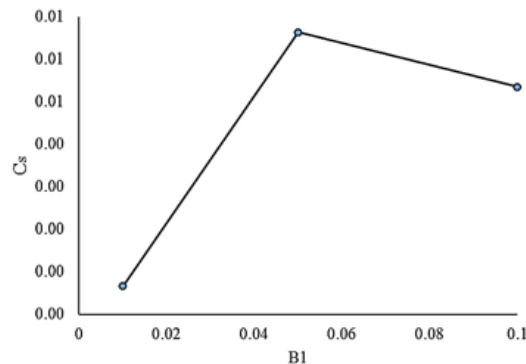
Figure 5.16 depicts the drag, lift and side force coefficients experienced by the truck-trailer unit when the B1 shape coefficient changes from 0.01, 0.05 to 0.1. The drag force coefficient data is presented on Figure 5.16 (a). It is evident that when  $B1 = 0.01$  the truck-trailer is associated with the maximum drag coefficient which is 0.8. As the B1 increases to 0.1, the drag coefficient decreases by 3.8% to 0.77. Almost linear reduction in drag force coefficient can be seen as the B1 shape coefficient increases. The lift force coefficient data is presented from Figure 5.16 (b) and the minimum lift is accompanied by  $B1 = 0.01$  model which is 0.07 and the height lift is associated with  $B1 = 0.05$  model which is an 85% increase to 0.13. However, it can be seen that when B1 increases to 0.1, the lift force decreases by 23% to 0.1. The side force coefficient data is presented from Figure 5.16 (c) and is seen to have insignificant variation between a minimum of 0.0007 and a maximum of 0.006. This is to be expected as the study was conducted at straight headwind flow conditions.



(a)



(b)



(c)

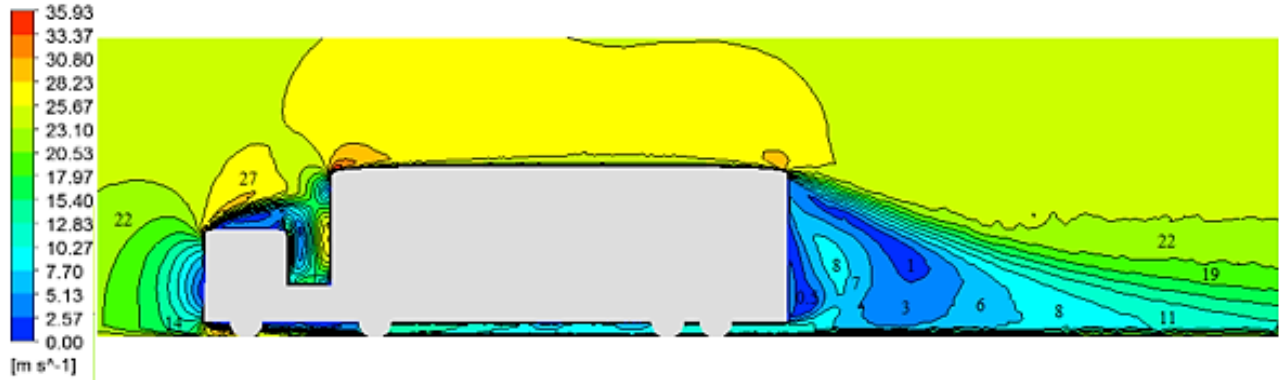
Figure 5.16 The drag force (a), lift force (b) and side force (c) coefficients for the truck-trailer geometry when  $B1 = 0.01$ ,  $B1 = 0.05$  and  $B1 = 0.1$  at straight headwind.

## **5.6 Effect of B2 on the truck-trailer unit aerodynamic characteristics**

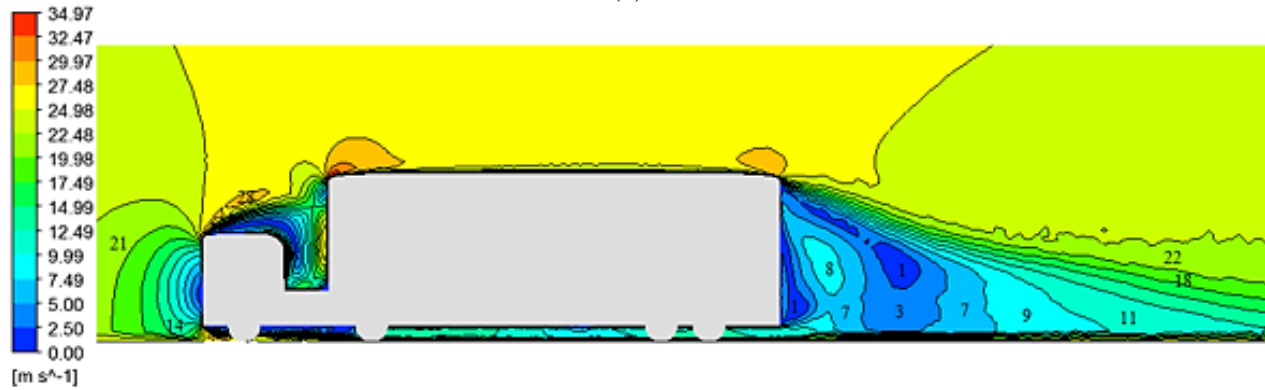
In order to analyse the effect on B2 on aerodynamics performance of truck-trailer unit, three B2 values of 0.01, 0.05, 0.1 were used for analysis purposes. The B1, B5 and B6 coefficients were maintained at 0.01 while the B2 values were changed.

### **5.6.1. Velocity Distribution around the Truck-Trailer Unit with Changing B2 Values.**

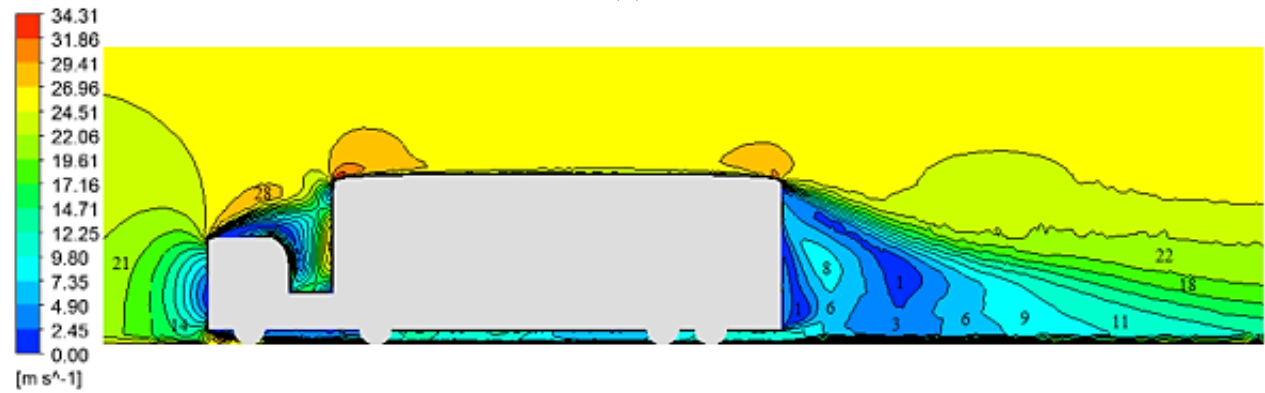
The velocity distribution around the truck-trailer unit when  $B2 = 0.01, 0.05$  and  $0.1$  whilst maintaining B1, B5, B6 values at a constant 0.01 is depicted from Figure 5.17. It can be clearly seen that having a B1 value of 0.01 leads to flow separation on top of the truck unit. The separated flow is seen to generate a wake region with low velocity which continues into the truck-trailer gap region. This subsequently leads to low velocity flow on top of the truck unit and the trailer unit. Upon changing B2 to 0.05 and 0.1, the flow velocity on the truck unit increases and completely eradicates the low velocity wake flow region. In fact, the increasing curvature on the top leading edge of the truck unit is seen to increase the flow velocity on top of the trailer unit accordingly.



(a)



(b)



(c)

Figure 5.17 Velocity fields around the Truck-trailer units with changing B2 coefficients.

Figure 5.18 depicts the truck unit with the top trailing edge profile of  $B2 = 0.1$  and the six data lines ranging from  $L7_R$  to  $L12_{BR}$  where the velocity in the streamwise direction was recorded. The velocity data will be obtained and compared for models  $B2 = 0.01$ ,  $B2 = 0.05$  and  $B2 = 0.1$  in order to understand the effects of  $B2$  on the flow field in the vicinity of truck unit. Data lines  $L10_T$  and  $L7_R$  were positioned on the symmetry plane of the truck unit. The former was

positioned at the start of the curved surface and the latter at the end of the curved surface. Data lines  $L8_{BL}$  and  $L9_{TL}$  were positioned on the left side of the truck and the data lines  $L12_{BR}$  and  $L11_{TR}$  on the right side of the truck (viewing from rear elevation) at the beginning and the end of the curved surface. The data lines will be used to gain an understanding of flow velocity in the vicinity of changing B2 shape profiles.

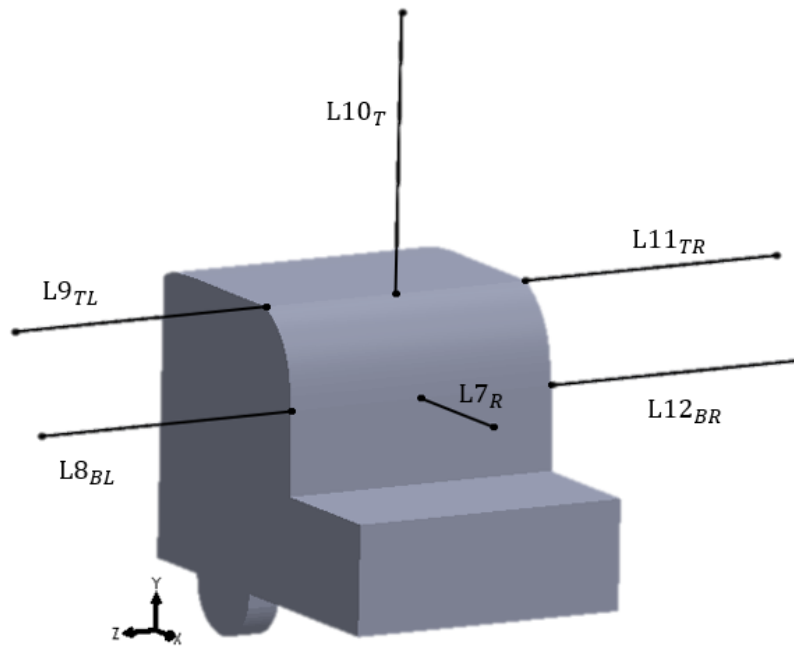


Figure 5.18 Data line locations around the top trailing edge of the truck unit when  $B2 = 0.1$

Figure 5. 19 depicts velocity distribution along data line  $L7_R$  which was positioned at the rear of the truck unit and the end of the curved surface. The data line starts from the truck rear surface and extends 3.5m towards the truck-trailer gap region. Velocity data have been obtained for  $B2$  values 0.01, 0.05 and 0.1 and it is evident that there are significant velocity variations between three models. Due to low pressure flow recirculation conditions in the truck-trailer gap region, the flow velocity is seen to be in the negative  $x$  direction. The maximum flow velocities have been obtained near to the centre of the data line for all models. This is due to the fact that the centre of  $L7_R$  data line is also situated in close proximity to the centre of flow circulating area in the gap region. The maximum velocity of 4.8m/s is observed for  $B2 = 0.01$  model followed by

4.1m/s and 3.3m/s, which is 14.5% and 31.2% less than the maximum velocity for  $B2 = 0.1$  and  $B2 = 0.05$  models, respectively.

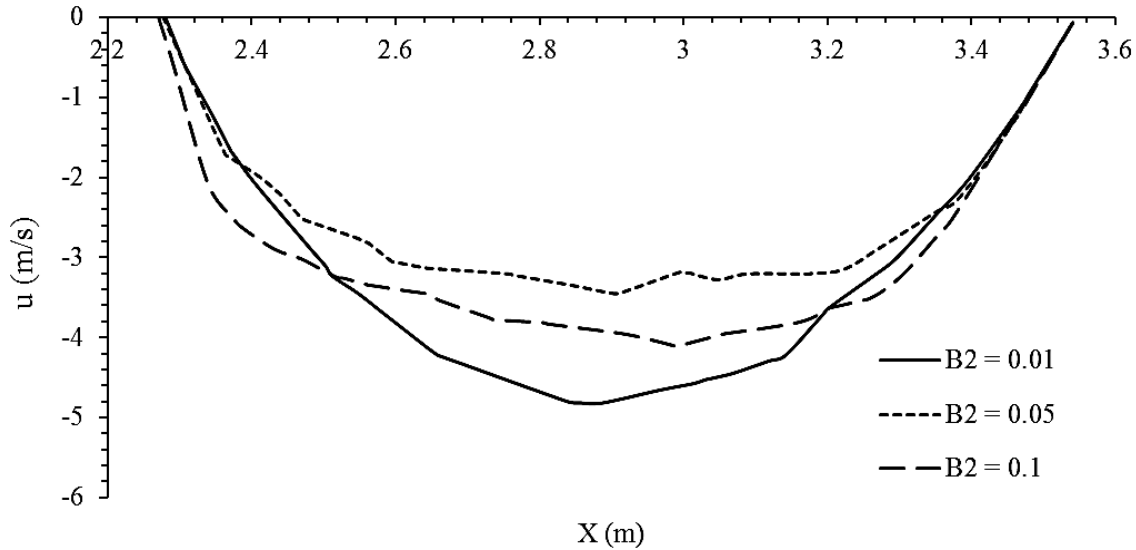


Figure 5.19 The x direction velocity plotted along the data line L7<sub>R</sub>

Figure 5.20 depicts velocity distribution along data lines L8<sub>BL</sub> and L12<sub>BR</sub> which have been positioned on the left and right sides of the truck unit respectively, at the end of curved leading edge surface. The L8<sub>BL</sub> data line extends from truck left surface (1.3m) to 3m in the positive Z direction (viewing from rear elevation). A similar trend in velocity fluctuation can be seen for all three models where at the surface of the truck unit velocity is zero due to no slip boundary condition. The flow is seen to travel in positive X direction for up to 0.3m from truck left surface for all models, where the velocity is seen to increase for up to around 1.8m/s before gradually decreasing to around 0.1m/s. In the case of  $B2 = 0.01$  model, the flow is seen to travel in opposite direction (negative -X direction) from 1.6m to 1.9m having a peak velocity of 1.6m/s. Likewise, for the model  $B2 = 0.05$ , the flow is seen to travel in the opposite direction from 1.6m to 1.7m with a much lower peak velocity of 0.6m/s. It has been noted that there is no flow travelling in the opposite direction in model  $B2 = 0.1$ , however it was found that after the flow separation on  $B2 = 0.01$  and  $0.05$  models, the velocity recovery is much quicker and free stream velocity is observed before the  $B2 = 0.1$  model.

Data line L12<sub>BR</sub> which has been positioned on the right side of the truck unit at the end of curved leading edge surface extends from truck left side surface (1.3m) to 3m in the negative Z direction (viewing from rear elevation). A similar trend in velocity fluctuation can be seen for all three models as previously observed on the data line L7<sub>BR</sub> which has been mirrored on the left side truck face (viewing from rear elevation). The flow is seen to travel in positive X direction for up to 0.3m from truck left side surface for all models, where the velocity is seen to increase for up to around 2.5m/s before gradually decreasing to around 0.8m/s. In the case of B2 = 0.01 model, the flow is seen to travel in opposite direction (negative -X direction) from 1.7m to 1.9m having a peak velocity of 0.7m/s. Likewise, for the model B2 = 0.05, the flow is seen to travel in the opposite direction from 1.6m to 1.7m with a much lower peak velocity of 0.3m/s. It has been noted that there is no flow travelling in the opposite direction in model B2 = 0.1

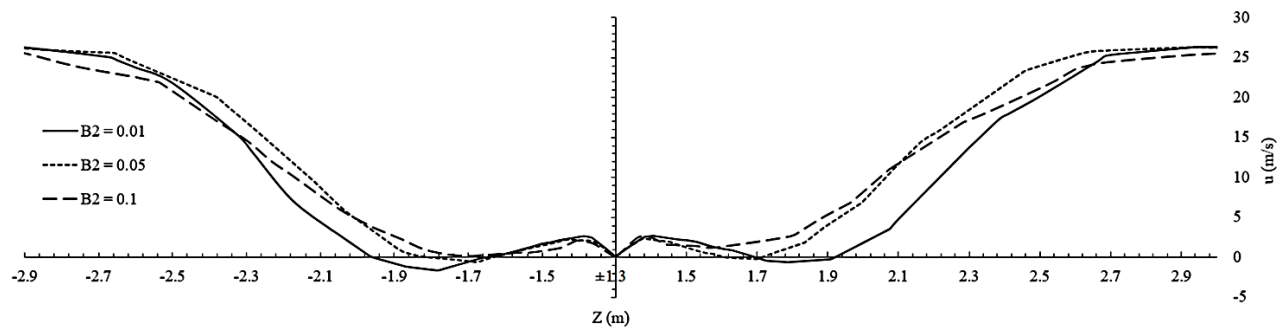


Figure 5.20 The x direction velocity plotted along the data lines L8<sub>BL</sub> (left) and L12<sub>BR</sub> (right)

Figure 5.21 depicts velocity distribution along data lines L9<sub>TL</sub> and L11<sub>TR</sub> which have been positioned on the left and right sides of the truck unit respectively, at the beginning of the curved leading edge surface. Once again, the data line L9<sub>TL</sub> extends from truck left surface (1.3m) to 3m in the positive Z direction (viewing from rear elevation). Significant variations in flow velocity can be seen for all three truck trailer models between 1.39m and 2.4m of the data line. Flow reversal is observed for all three models near the left truck surface. Model B2 = 0.05 has the highest flow velocity of 8.9m/s in opposite direction and the flow reversal region extends 0.5m away from the left truck surface. The minimum flow velocity of 6.8m/s in the opposite direction is exhibited on B2 = 0.1 model, and the flow reversal region extends 0.2m from the left truck surface. Therefore, by changing B2 from 0.05 to 0.1, a 60% reduction in flow reversal region can

be achieved. After the flow reversal regions, the velocity recovery is seen to be much quicker with  $B2 = 0.1$  where the free stream velocity is observed hence, preceding  $B1 = 0.01$  and  $B1 = 0.05$  models.

Data line L11<sub>TR</sub>, has been positioned on the right side of the truck unit at the beginning of the curved leading edge surface. This extends from truck right side surface (1.3m) to 3m in the negative Z direction (viewing from rear elevation). Substantial variations in flow velocity can be seen for all three truck trailer models between 1.36m and 2.4m of the data line. Flow reversal is observed for all three models near the right side truck surface. Model  $B2 = 0.05$  has the highest flow velocity of 8.6m/s in opposite direction and the flow reversal region extends 0.3m away from the right truck surface. The minimum flow velocity of 7.4m/s in the opposite direction is exhibited on  $B2 = 0.01$  model, and the flow reversal region extends 0.3m from the right side truck surface.

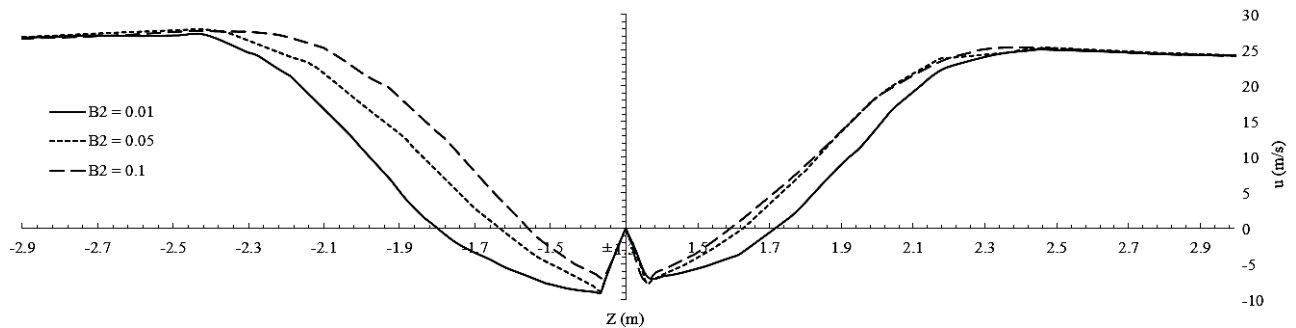


Figure 5.21 The x direction velocity plotted along the data lines L9<sub>TL</sub> (left) and L11<sub>TR</sub> (right)

Velocity distribution along the L10<sub>T</sub> data line situated on top of the truck unit at the beginning of curved edge is shown in Figure 5.22. The start of the data line is situated on the truck top surface (2.6m) and extends 5m upwards in the positive Y direction. It is shown that the trend in velocity between  $B2 = 0.05$  and  $B2 = 0.1$  models are seen to be largely similar with minimal variations. The separation and resulting flow reversal regions are seen on all three models with the maximum flow velocity of 11.6m/s in the opposite direction being exhibited on the  $B2 = 0.1$  model. The minimum flow velocity in the reversal region is seen on  $B2 = 0.01$  model and this was recorded as 3.6m/s, a reduction of 68% compared to former model. However, for  $B2 = 0.01$  model, the recirculation region extends up to 0.4m from the truck top surface while for  $B2 = 0.1$

model the recirculation region extends only up to 0.3m from truck top surface. The free stream velocity is observed for all three models at a height of about 3.5m from the top truck surface.

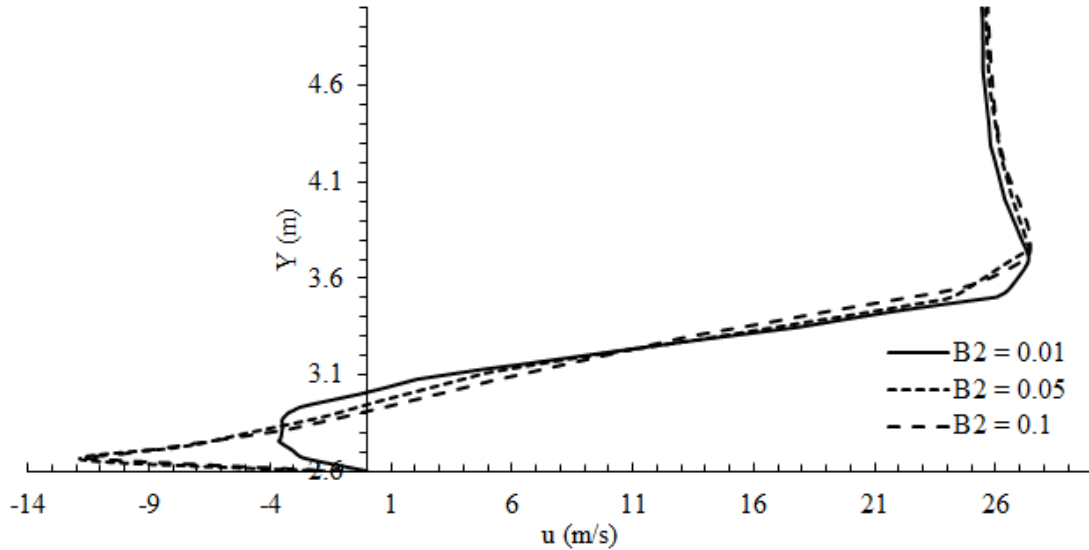
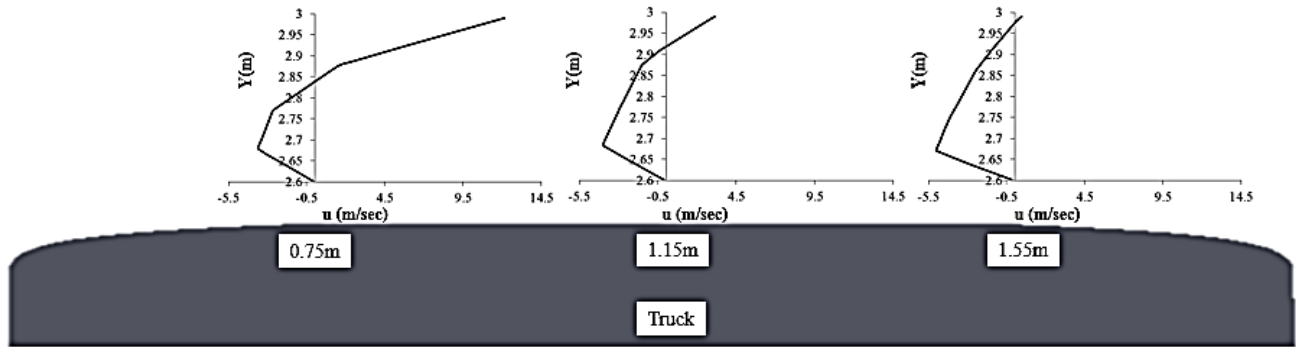


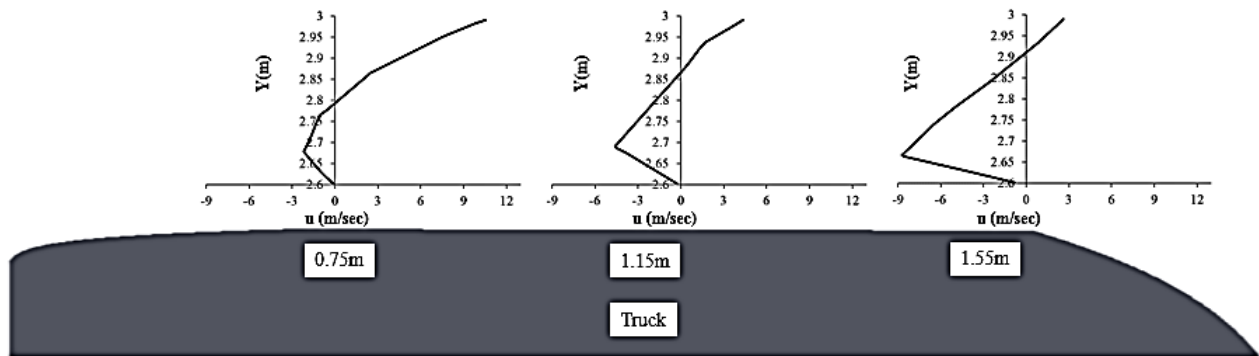
Figure 5.22 The x direction velocity plotted along the data line L10r

The velocity profiles in the wake flow circulation region on top of the truck unit when  $B2 = 0.01$  and  $B2 = 0.1$  is shown from Figure 5.23. Three equally spaced data lines were generated at 0.75m, 1.15m and 1.55m from the front face of the truck unit. Each line started at 2.6m (the top surface) and ended at the vertical height of 3m from the top truck surface. The velocity on the  $B1 = 0.01$  model has already been discussed from Figure 5.11, since when the B coefficient is 0.01, the shape of the model stays the same throughout. Reversed flow due to separation can be observed in both (a) and (b) with a maximum flow velocity of 5m/s is recorded on the data line located at 1.55m from the front truck surface for  $B2 = 0.01$  model. For the same model, minimum flow velocity of 3.6m/s is observed on the data line located 0.75m from the front truck surface. Also for  $B2 = 0.01$  model, the height of the flow reversal region is seen to increase towards the rear of the truck unit. The maximum velocity in the opposite direction for  $B2 = 0.1$  model on the 0.75m data line is seen to be 2.18m/s, and this is a 40% reduction compared to the  $B2 = 0.01$  model. However, the maximum velocity recorded in the wake region on the data line located 1.55m was 8.7m/s and this is a considerable 74% increase compared to the  $B2 = 0.01$  model. The height of the wake region is seen to decrease for the model  $B2 = 0.1$  compared to  $B2$

= 0.01 model. A 1.4%, 1.7% and 2.3% reduction in the height of the wake region can be seen for 0.75m, 1.15m and 1.55m data lines, respectively. The increased reversed flow velocity and the wake region height is due to the extended influence of the high velocity flow recirculation region in the truck-trailer gap region on the truck top surface.



(a)



(b)

Figure 5.23 Axial flow velocity profiles at various distances from the top leading edge of the truck unit when  $B2 = 0.01$  (a) and  $B2 = 0.1$  (b).

### 5.6.2. Pressure Distribution around the Truck-Trailer Unit with Changing $B2$ Values.

The coefficient of pressure around the truck-trailer unit when  $B2 = 0.01, 0.05$  and  $0.1$  whilst maintaining  $B1, B5, B6$  at a constant  $0.01$  is depicted from Figure 5.24. In all three cases, the highest pressure coefficient depicted is  $0.9$  while the lowest pressure coefficient depicted is  $-0.5$ . The front face of the truck exhibits high pressure coefficient signifying that pressure is stagnant. Further to this, the distribution of mid-range pressure coefficient depicted at the top of the truck

elongates into the truck-trailer gap while depicting stagnant pressure on the front face of the trailer and low pressure coefficient at the top face of the trailer, both in the B5 location. Additionally, a small region of mid-range pressure can be found at the B6 location. It is clear that altering B2 has a predominant effect at the top of truck and at the truck-trailer gap. The pressure coefficient at the top of the truck is -0.5, which elongates much more prominently in the case of (a). Pressure coefficient slightly higher at the top of the truck is -0.2, which distributes into the truck-trailer gap, whereas in (b) and (c) this region, manifests across and beyond the entire length trailer unit. Further to this, in the base corners of the truck-trailer gap, pressure coefficient is higher for cases (a) and (c) than for case (b) and at the top front of the trailer, there is a region where the pressure coefficient falls for cases (b) and (c).

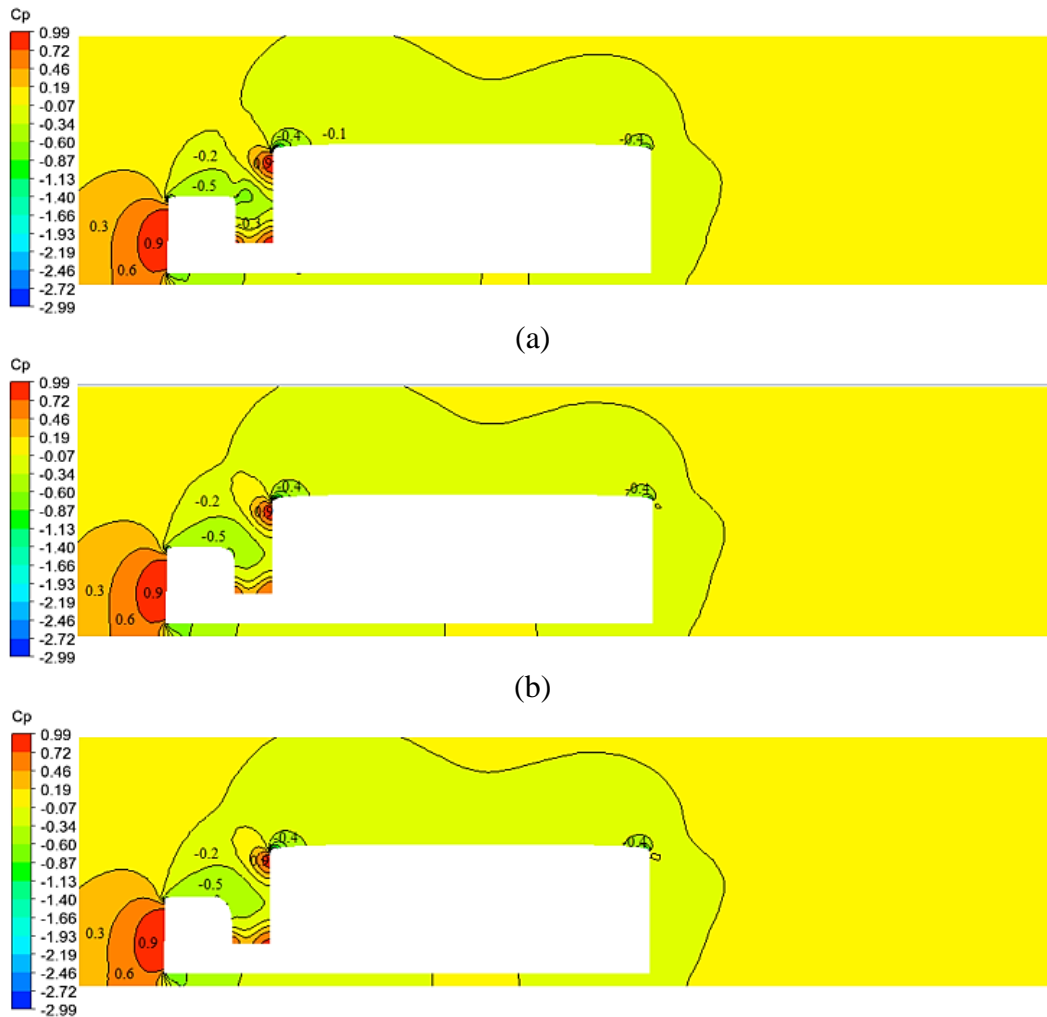


Figure 5.24 Coefficient of pressure around the Truck-trailer units with changing B2 coefficients.  
 (a)  $B_2 = 0.01$  (b)  $B_2 = 0.05$  (c)  $B_2 = 0.1$

The pressure coefficient plotted over the truck-trailer unit along the symmetry line with changing B2 coefficients is depicted from Figure 5.25. Maximum pressure coefficient of 1.05 and a minimum pressure coefficient of -1.74 were observed on the data line for B2 = 0.01 model. It was observed that varying B2 shape coefficients have a significant influence on the pressure magnitudes on the truck-trailer geometry up to  $\eta = 0.38$ . Thereafter, negligible pressure variation is seen for all three models up until the trailer rear face where a slight pressure variation is seen between B2 = 0.01 model and B2 = 0.05 and 0.1 models. The lowest pressure of -0.66 was exhibited on the truck-front face when B2 = 0.01, compared to 0.55 and 0.59 for B2 = 0.05 and B2 = 0.1 models, respectively. The positive pressure region continues into the truck-top surface starting from  $\eta = 0.09$  up to  $\eta = 0.11$  for models B2 = 0.05 and 0.1 while the pressure stays negative throughout for B2 = 0.01 model. For B2 = 0.01 model, the pressure on the truck-top face is seen to have relatively low pressure at the front and high pressure towards the rear while the opposite is seen to be true for B2 = 0.05 and 0.1 models. The lowest pressure of -0.71 was obtained towards the rear of truck-top surface for B2 = 0.05 model, a reduction of 9.2% and 10.7% compared to B2 = 0.01 and B2 = 0.1 models, respectively. The top half of the truck rear surface is seen to be associated with negative pressure while the bottom half of the surface is associated with positive pressure for B2 = 0.01 model while for both B2 = 0.05 and 0.1 models the low pressure regions are seen to extend for approximately  $2/3$  along the truck rear surface. The bridge surface is seen to have high pressures for all three models while the height being 0.72 for B2 = 0.01 model. Minimal pressure fluctuations are seen on the trailer front surface for three truck-trailer models and pressure is seen to change from positive at the bottom of the surface to negative towards the middle of the surface. Pressure is seen to increase in the vicinity of the stagnation region before rapidly reducing to negative pressure towards the top edge of the surface. The pressure on the trailer top surface and trailer rear surface are seen to be negative along the symmetry line. Also, pressure fluctuations between three B2 geometries are seen to be mostly identical except at the end of trailer-rear surface where the lowest pressure of -1.04 was recorded on the B2 = 0.1 model which is a 15% reduction compared to the B2 = 0.01 model with a pressure coefficient of -0.9 at the same location.

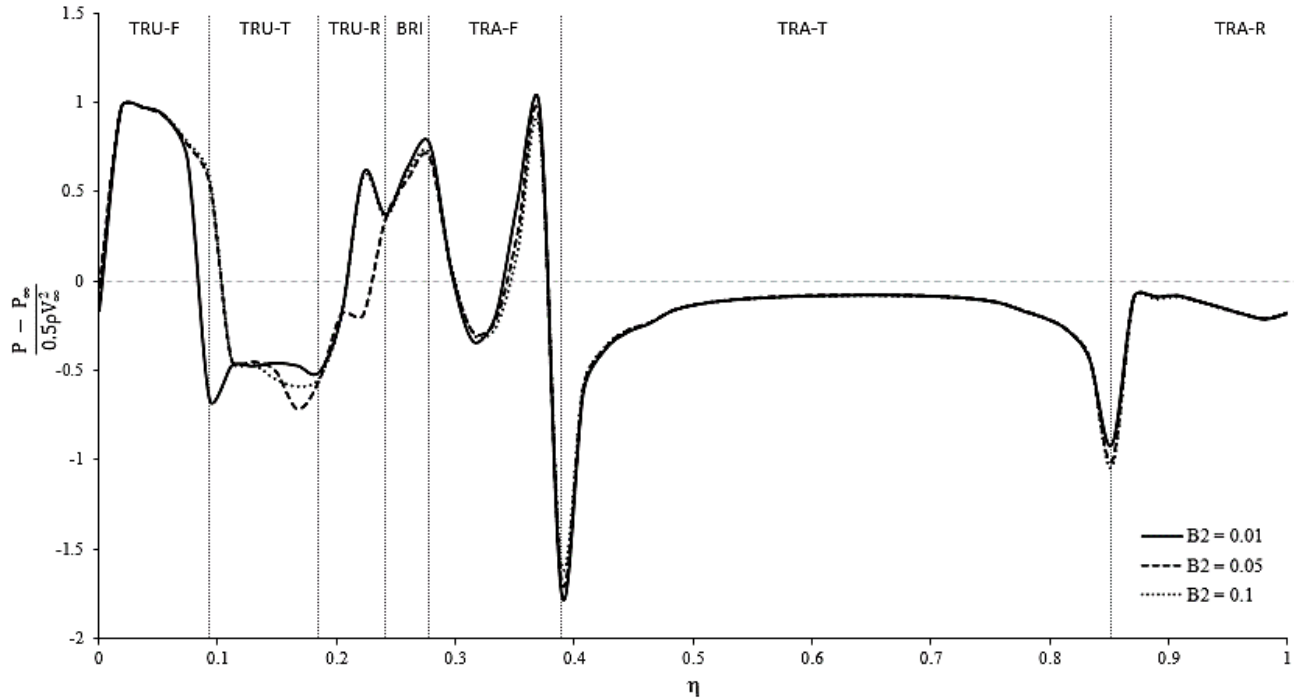
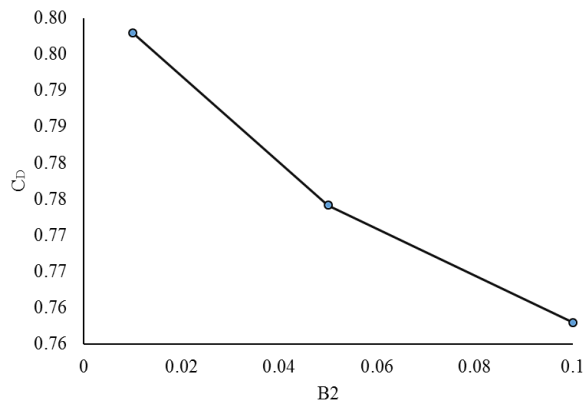


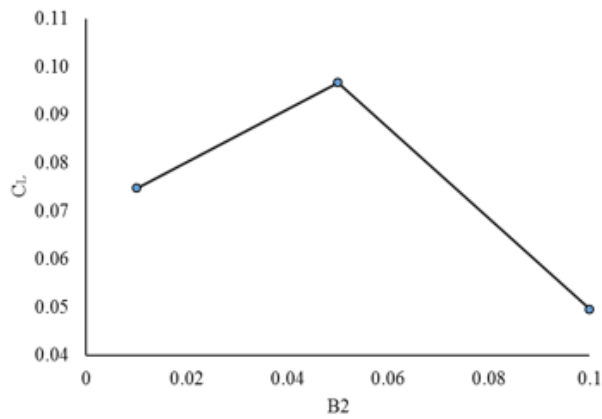
Figure 5.25 The pressure coefficient ( $C_p$ ) plotted over the truck-trailer unit along the symmetry line for changing  $B_2$  coefficients.

### 5.6.3. Effects of Changing $B_2$ Values on Aerodynamic Forces

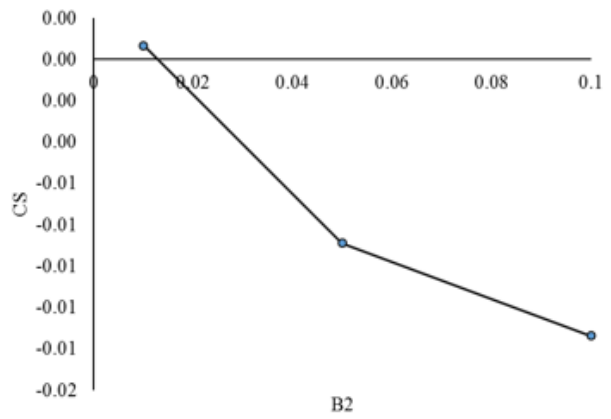
The effects on velocity fields and pressure fields around a truck-trailer geometry upon changing the  $B_2$  shape coefficient have been discussed in the above sections. Figure 5.26 depicts the drag, lift and side force coefficients experienced by the truck-trailer unit when the  $B_2$  shape coefficient changes from 0.01, 0.05 to 0.1. The drag force coefficient data is presented from Figure 5.26 (a) and it can be clearly seen that a maximum drag coefficient of 0.8 is associated with  $B_2 = 0.01$  model. When  $B_2 = 0.05$ , the drag coefficient is seen to decrease by 3.7% to 0.77 and upon further increasing the  $B_2$  shape coefficient to 0.1, the drag coefficient is seen to decrease further 1.3% to 0.76. The lift force coefficient data is presented from Figure 5.26 (b) and a minimum lift of 0.05 is seen to be associated with  $B_2 = 0.1$  model and a maximum lift of 0.1 is associated with  $B_2 = 0.05$  model which is an increase of 100%. The side force coefficient data is presented from Figure 5.26 (c) and is seen to have negligible variation between a minimum of -0.013 and a maximum of 0.0007. This is to be expected as the study was conducted at straight headwind flow conditions.



(a)



(b)



(c)

Figure 5.26 The drag force (a), lift force (b) and side force (c) coefficients for the truck-trailer geometry when  $B2 = 0.01$ ,  $B2 = 0.05$  and  $B2 = 0.1$  at straight headwind.

## 5.7 Effect of B5 on the truck-trailer unit aerodynamic characteristics

In order to analyse the effect of B5 on aerodynamics performance of truck-trailer unit, three B5 values of 0.01, 0.05, 0.1 were used for analysis purposes. The B1, B2 and B6 coefficients were maintained at 0.01 while the B5 values were changed.

### 5.7.1 Velocity Distribution around the Truck-Trailer Unit with Changing B5 Values

Velocity distribution around the truck-trailer unit when  $B5 = 0.01, 0.05$  and  $0.1$  whilst maintaining B1, B2, B6 at a constant 0.01 is depicted from Figure 5.27. In all three cases, velocity is very low at the front face of the truck with flow separation at the top front of the truck, top front of the trailer and the top rear of the trailer. Altering B5, has a negligible effect on velocity magnitude in the truck-trailer gap. In the case of (b) and (c), velocity magnitude is higher at the top front of the truck and at the top front of the trailer than that exhibited in (a). In the case of (a), there is a region of higher velocity magnitude that begins at the top front of the trailer, which distributes across the trailer length. In cases of (b) and (c), higher velocity magnitude begins at the top front of the truck, which in the case of (b) propagates across the truck and trailer length, and in the case of (c) manifests beyond the vehicle in the domain. Additionally, velocity magnitude appears to increase at the top front and top rear of the trailer as B5 increases. Due to this, the recirculation region within the wake increases in its distribution behind the trailer.

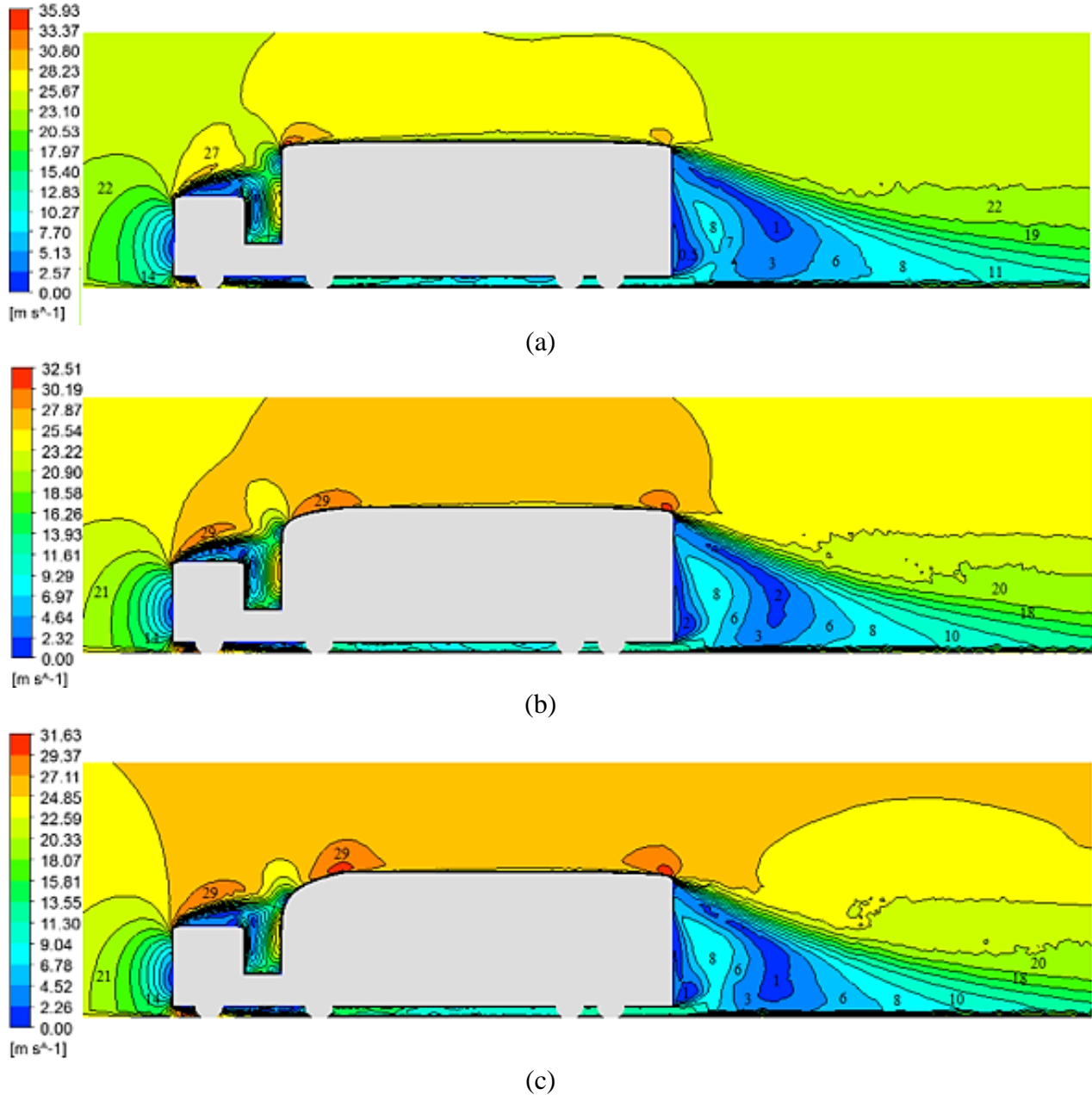


Figure 5.27 Velocity fields around the Truck-trailer units with changing B5 coefficients.

Figure 5.28 depicts the trailer unit with the top leading edge profile of  $B5 = 0.1$  and the six data lines ranging from L13<sub>F</sub> to L18<sub>BR</sub> where the velocity in the streamwise direction was recorded. The velocity data will be obtained and compared for models  $B5 = 0.01$ ,  $B5 = 0.05$  and  $B5 = 0.1$  in order to understand the effects of the geometric coefficient  $B5$ , on the flow field in the vicinity of the trailer unit. Data lines L13<sub>F</sub> and L16<sub>T</sub> were positioned along the mid plane of the trailer unit while the former was positioned at the start of the curved surface, latter was at the end of the

curved surface. Data lines L14<sub>BL</sub> and L15<sub>TL</sub> were positioned on the left side of the trailer and the data lines L17<sub>TR</sub> and L18<sub>BR</sub> on the right side of the trailer (viewing from front elevation) at the beginning and the end of the curved surface.

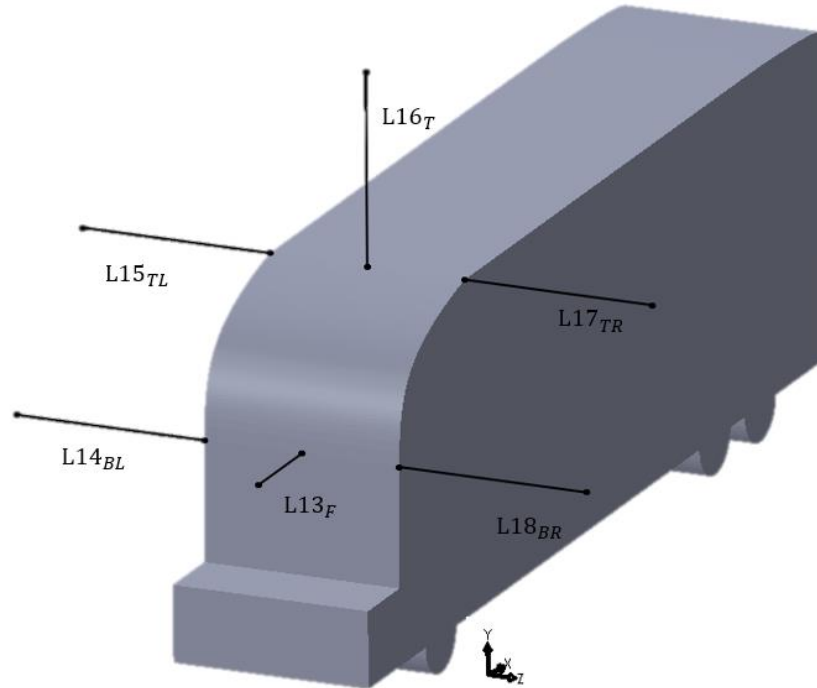


Figure 5.28 Data line locations around the top leading edge of the trailer unit when  $B5 = 0.1$ .

Figure 5.29 depicts velocity distribution along data line L13<sub>F</sub> which was positioned at the front of the trailer unit. The data line starts at 2.3m away from the trailer front surface and ends at 3.55m which is the surface of the trailer front. Velocity data have been obtained for  $B5$  values 0.01, 0.05 and 0.1 and it is evident that as the flow is approaching front surface of the trailer, velocity decreases to zero for all the models. The velocity profiles obtained along the data line for three models are seen to behave uniquely over the set distance. The highest velocities for all three models are seen in reverse flow conditions. Maximum flow velocity of 3.6m/s is recorded 1.2m upstream to the trailer front surface for the model  $B5 = 0.01$  while for  $B5 = 0.05$  and  $B5 = 0.1$  maximum velocities of 0.82m/s and 2.4m/s are seen in the opposite direction, respectively. Velocity in the reversed direction from 2.3m to 2.8m on the data line is seen for  $B5 = 0.01$  model. The model  $B5 = 0.05$  has lowest reversed flow velocity magnitudes which occurred from 2.4m up to the trailer front surface. The reversed flow has been observed along the entire length of the data line, for  $B5 = 0.1$  model. In both  $B5 = 0.1$  and  $B5 = 0.01$  models a high velocity

magnitude in the reverse flow region is visible while  $B5 = 0.01$  inhibits the most prominent variation in velocity varying from  $-3.6\text{m/s}$  to  $0.56\text{m/s}$  peak to peak.

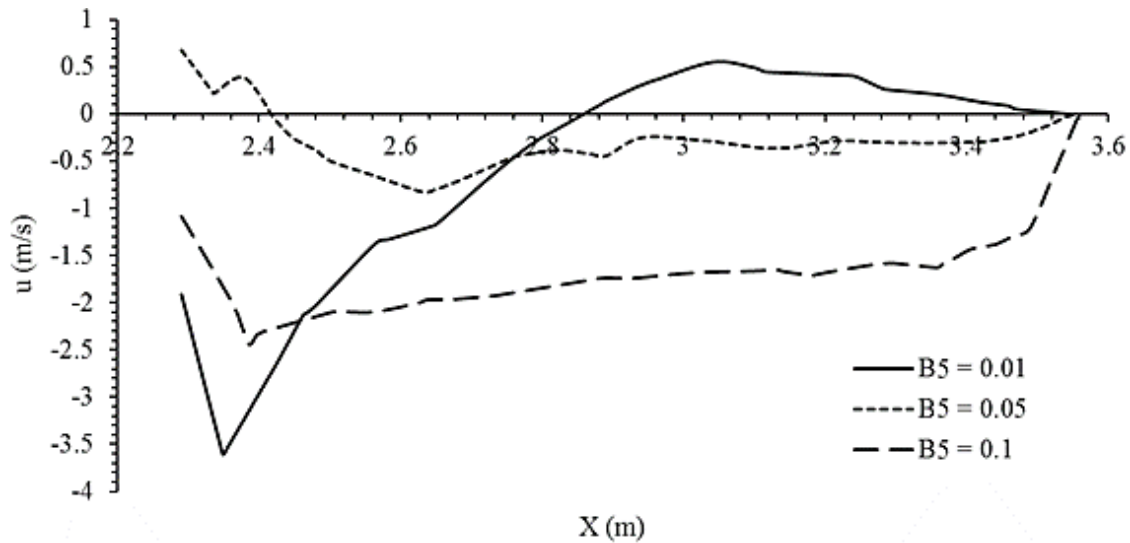


Figure 5.29 The x direction velocity plotted along the data line L13<sub>F</sub>.

Figure 5.30 depicts velocity distribution along data lines L14<sub>BL</sub> and L18<sub>BR</sub> which have been positioned on the left and right sides of the truck unit respectively, at the beginning of curved leading edge surface. The L14<sub>BL</sub> data line extends from the trailer left surface ( $-1.3\text{m}$ ) to  $-3\text{m}$  in the negative Z direction. A rapid linear increase in flow velocity is observed for all three models from the trailer left surface up to  $0.7\text{m}$  away from the surface with a maximum velocity of  $12.6\text{m/s}$  is recorded in the vicinity of  $B5 = 0.01$  model while a minimum velocity of  $7.1\text{m/s}$  is recorded for  $B5 = 0.1$  model. The free stream velocity of  $25\text{m/s}$  is observed for all three models at a distance of  $1.2\text{m}$  from the trailer left surface. Model  $B5 = 0.01$  is observed to have the highest velocity of all three models up to  $0.23\text{m}$  away from the trailer left surface. After  $0.23\text{m}$ ,  $B5 = 0.05$  model is seen to exhibit the highest velocity throughout the set distance. Minimum flow velocity has largely been recorded for the  $B5 = 0.1$  model over other two models.

Data line L18<sub>BR</sub> has been positioned on the right side of the trailer unit at the end of the curved leading edge surface. Once more, the data line extends from truck right side surface ( $1.3\text{m}$ ) to  $3\text{m}$  in the positive Z direction. A similar trend in the velocity fluctuation is seen for all three models.

Overall, highest flow velocities along the data line was observed for  $B5 = 0.01$  model and once more, the free stream velocity is observed before other two models at a distance of 1.05m from the right side trailer surface. For most of the data line low flow velocity values were obtained for the  $B5 = 0.1$  model with free stream velocity being observed at a distance of 1.17m from the trailer right side surface.

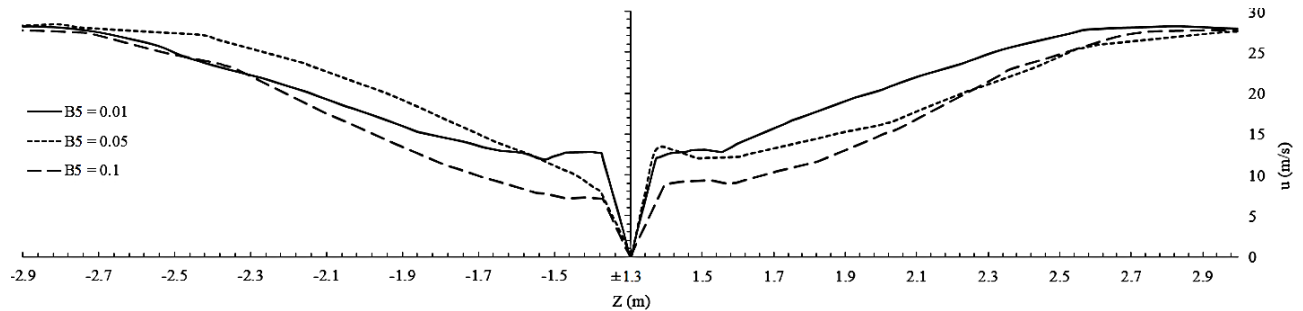


Figure 5.30 The x direction velocity plotted along the data lines L14<sub>BL</sub> (left) and L18<sub>BR</sub> (right)

Figure 5.31 depicts velocity distribution along data lines L15<sub>TL</sub> and L17<sub>TR</sub> which have been positioned on the left and right sides of the truck unit respectively, at the end of the curved leading edge surface. It is seen that, at the end of the curved surface there are visible velocity variations between all three truck-trailer models. The free stream velocity is observed for all three models at a distance of around 0.2m from the left trailer surface. Once again, a linear increase in flow velocity is observed for all three models in the vicinity of the left trailer surface. This occurs for a distance of 0.06m, 0.11m and 0.09m for  $B5 = 0.01$ ,  $B5 = 0.05$  and  $B5 = 0.1$  models respectively from the trailer left surface. In this flow regions, the highest velocity was observed for  $B5 = 0.01$  model with a maximum velocity of 23m/s and the lowest velocity is observed for  $B5 = 0.05$  model with a maximum velocity of 20m/s. After the initial increase in the velocity of  $B5 = 0.01$  model it continues to increase towards the free stream velocity in a steady manner, whereas the other two models appeared to do this in somewhat erratic manner.

Data line L17<sub>TR</sub> has been positioned on the right side of the trailer unit at the end of the curved leading edge surface. The data line extends from truck right side surface (1.3m) to 3m in the Z direction.  $B5 = 0.01$  model is seen to have a highest flow velocity in the vicinity of the trailer

right side surface while the  $B5 = 0.05$  model is associated with the lowest velocities. The free stream velocity is observed first for model  $B5 = 0.01$  at a distance of 0.14m from the right trailer surface followed by  $B5 = 0.1$  model which was 0.17m away from trailer right side surface. In contrast, for  $B5 = 0.05$  model free stream velocity is observed 0.44m from the trailer right side surface.

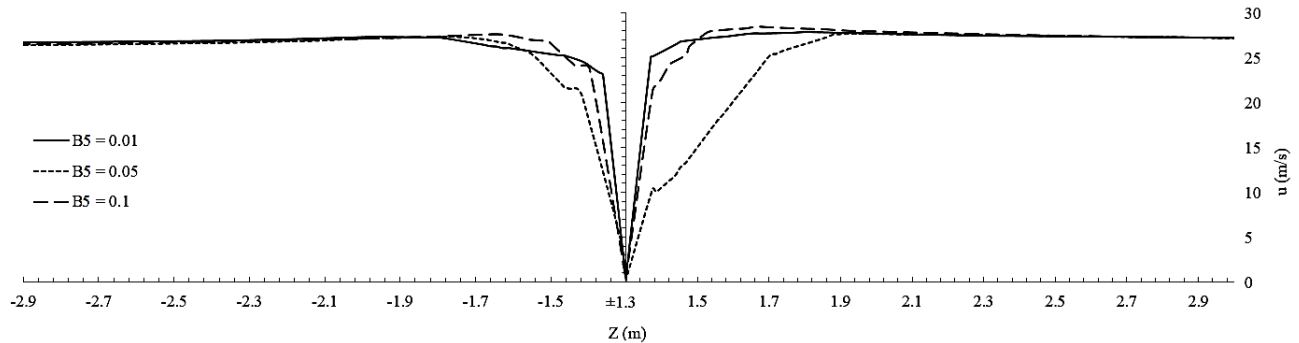


Figure 5.31 The x direction velocity plotted along the data lines L15<sub>TL</sub> (left) and L17<sub>TR</sub> (right)

Velocity distribution along the L16<sub>T</sub> data line situated on top of the trailer unit immediately after the curved leading edge is shown in Figure 5.32. The start of the data line is located on top of the trailer top surface (4.34m) and extends in positive Y direction up to 5m as illustrated from Figure 5.28. Flow velocity can be seen to increase in a linear manner in the boundary layer and minute velocity variations between the three models are observed. For the  $B5 = 0.01$  model, minute variations in the velocity were observed from a height of a 0.26m upwards from the top trailer surface, whereas for  $B5 = 0.05$  and 0.1 models this was observed from much lower heights of 0.08m and 0.09m, respectively. It is also evident that as the  $B5$  coefficient increases, the velocity on the data line increases with the maximum velocity of 31m/s recorded for  $B5 = 0.1$  model at a height of 0.09 from the trailer top surface.

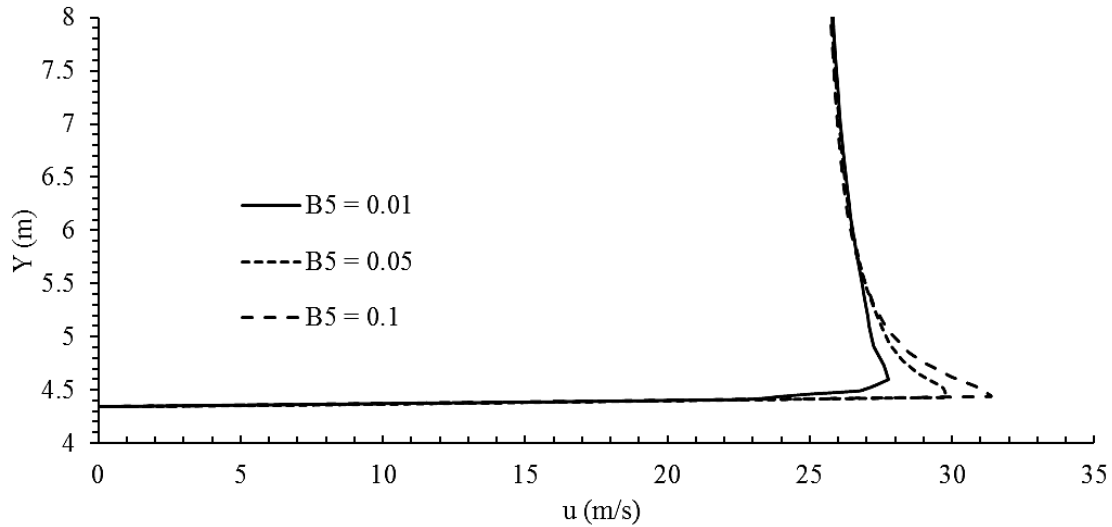
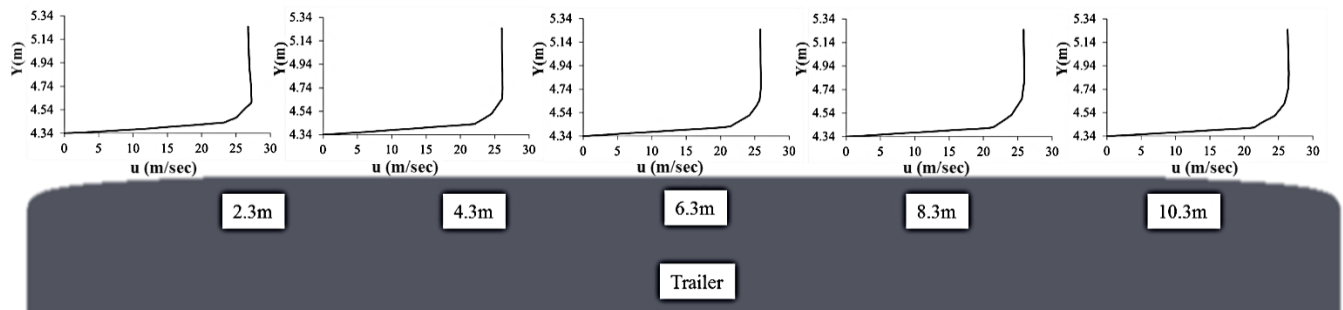


Figure 5.32 The x direction velocity plotted along the data line L16r.

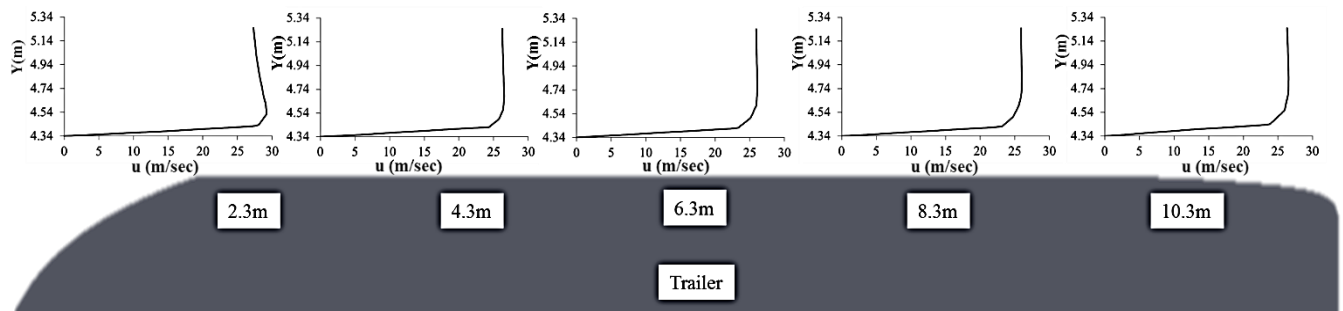
The velocity on top of the trailer unit is plotted along five equally spaced data lines that extend from the trailer top surface to 5.3m vertically towards the free stream region as depicted from Figure 5.33. For both models, the velocity is observed to be in the direction of the free stream flow (positive X direction) and hence no flow separation is observed. For  $B5 = 0.01$  model, maximum velocity of 27.3m/s was observed on the first data line followed by 26.1m/s for the second data line, 25.8m/s for the third data line, 25.9m/s for the fourth data line and lastly 26.4m/s for the fifth data line. The velocity trend was noticed to fluctuate over the length of the trailer top surface. Over this length the velocity fluctuates from high velocity to low velocity and back to high velocity with their respective locations being front, middle and rear of the trailer top surface. A reduction in velocity of 5.5% is seen from front to middle and an increase of 2.3% is seen from middle to rear.

For  $B5 = 0.1$  model maximum velocity of 29.2m/s was observed on the first data line followed by 26.5m/s for the second data line, 26.1m/s for the third data line, 26.0m/s for the fourth data line and lastly 26.5m/s for the fifth data line. In this case, the overall trend in velocity was observed as, increased velocity at the beginning of the top trailer surface with lowest velocity area located (reduction of 10.1%) at about 4/5 of the trailer length from the front leading edge and increased velocity towards the rear of the surface (Increase of 2% compared to the lowest point).

It is observed that increasing B5 from 0.01 to 0.1 increases the overall velocity on top of the trailer unit. A 7% increase in maximum velocity can be seen on the first data line followed by a 1.5% increase on the second data line, 0.8% increase on the third data line, 0.3% on the fourth data line and 0.2% increase on the fifth data line when B5 is increased from 0.01 to 0.1.



(a)



(b)

Figure 5.33 Axial flow velocity profiles at various distances from the top leading edge of the trailer unit when B5 = 0.01 (a) and B5 = 0.1 (b).

### 5.7.2 Pressure Distribution around the Truck-Trailer Unit with Changing B5 Values.

The coefficient of pressure around the truck-trailer unit when B5 = 0.01, 0.05 and 0.1 whilst maintaining B1, B2, B6 at a constant 0.01 is depicted from Figure 5.34. In all three cases, the highest pressure coefficient depicted is 0.9 while the lowest pressure coefficient depicted is -0.5. High pressure coefficient is depicted at the front face of the truck and pressure coefficient in the

mid-range at the top of the truck elongates into the truck-trailer gap. Pressure coefficient in the mid-range is identified at the top rear of the trailer for all three cases, however (b) and (c) depicts slightly higher pressure coefficient at the top rear of the trailer. It can be seen that altering B5 has a predominant effect at the top of truck, in the truck-trailer gap and at the top of the trailer. Pressure coefficient at the top of the truck is -0.5, which elongates into the truck-trailer gap. In the base corners of the truck-trailer gap and at the top front of the trailer, high pressure coefficient is exhibited for all three cases, however (a) appears to show higher pressure coefficient than (b) and (b) appears to show higher pressure coefficient than (c). This means the pressure coefficient decreases as the B5 radius increases. Further to this, at the top front of the trailer in the case of (a), a small region of low to mid-range pressure coefficient can be seen distributed at a short distance over the trailer top surface. In the case of (b), there is simply only a shallow area of mid-range pressure coefficient which is distributed and elongated over the trailer top over a distance slightly higher than that of (a). Further to this, in the case of (c), pressure coefficient in the mid-range is exhibited further along the top of the trailer and is a smaller area than that of (b), with slightly lower pressure coefficient within this region.

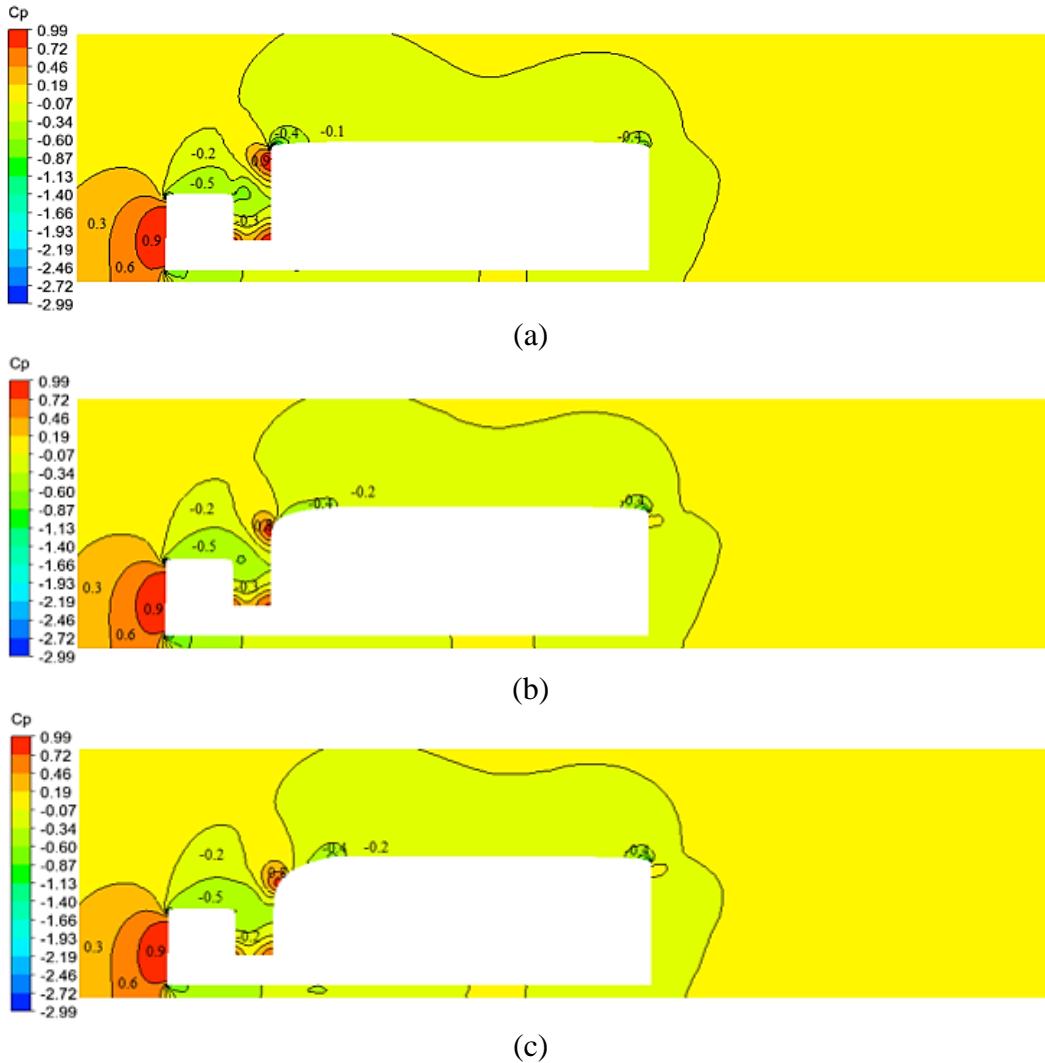


Figure 5.34 Coefficient of pressure around the Truck-trailer units with changing B5 coefficients.

The pressure coefficient plotted over the truck-trailer unit along the symmetry line with changing B5 coefficients is depicted from Figure 5.35. Maximum pressure coefficient of 0.98 and a minimum pressure coefficient of -1.74 were observed on the data line for B5 = 0.01 model. It was observed that varying B5 shape coefficients have a significant influence on the pressure magnitudes of a considerable area of truck-trailer geometry as the pressure is seen to vary between  $\eta = 0.1$  to  $\eta = 0.55$ . Negligible pressure variation is seen for all three models between  $\eta = 0$  to  $\eta = 0.1$  and  $\eta = 0.55$  to  $\eta = 0.1$ . However, a slight pressure variation is seen between B5 = 0.01 model and B5 = 0.05 and 0.1 models at the beginning of the trailer rear face. Negligible pressure variations on the truck-front face is observed between the B5 models. Lowest pressure

of -0.65 was exhibited at the start of the truck-top face when  $B5 = 0.01$  despite the fact that  $B5 = 0.05$  model is associated with the overall lowest pressure on truck-top face. Negative pressure is seen to exist throughout the truck-top surface and this is seen to continue to the truck-rear surface. Pressure on the start of the truck-rear face is seen to be negative from  $\eta = 0.18$  to  $\eta = 0.21$  before becoming positive with a highest pressure of 0.6 at  $\eta = 0.23$  for  $B5 = 0.01$  model. The high pressure region at the bottom of the truck-rear surface is seen to continue well in to the truck-trailer bridge surface. High positive pressure is seen to exist on the bridge surface with a maximum pressure of 0.77 at  $\eta = 0.27$  for  $B5 = 0.01$  model and a minimum pressure of 0.51 at the same  $\eta$  location for  $B5 = 0.1$  model. On the lower regions, for  $2/3$  of the trailer front face, the pressure variations for three  $B5$  models are seen to be largely similar while closer to the top leading edge of the trailer front face ( $\eta = 0.35$  to  $\eta = 0.39$ ), the pressure is seen to differ significantly. Lowest pressure of 0.47 was observed for the  $B5 = 0.1$  model where highest pressure of 0.97 was recorded for  $B5 = 0.01$  model. High pressure is seen to exist at the beginning of the trailer top surface for both  $B5 = 0.05$  and  $B5 = 0.1$  models whereas, negative pressure is seen to exist in the case of  $B5 = 0.01$  model. This is due to the drastic reduction in the flow separation region at the beginning of the trailer top surface due to the increased curvature of the trailer leading edge. After the initial high pressure region at the beginning, the pressure is seen to reduce and low pressure is seen to exist throughout the trailer top surface and trailer rear surface.

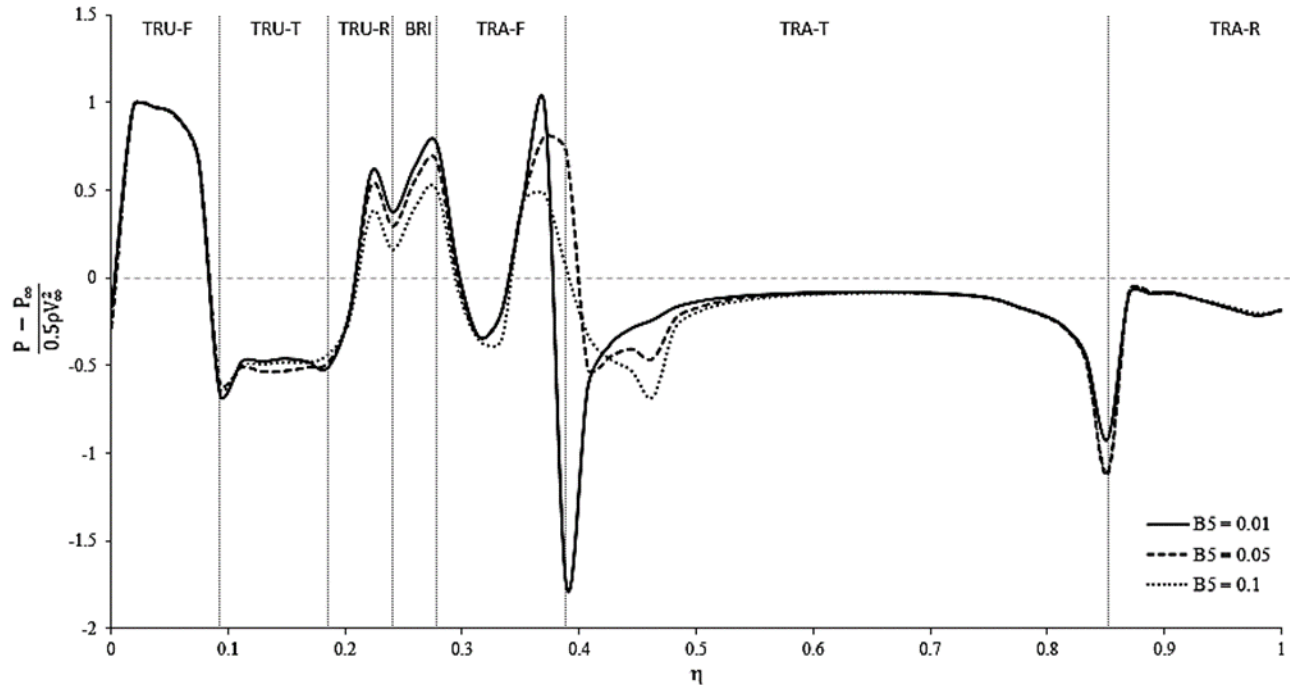


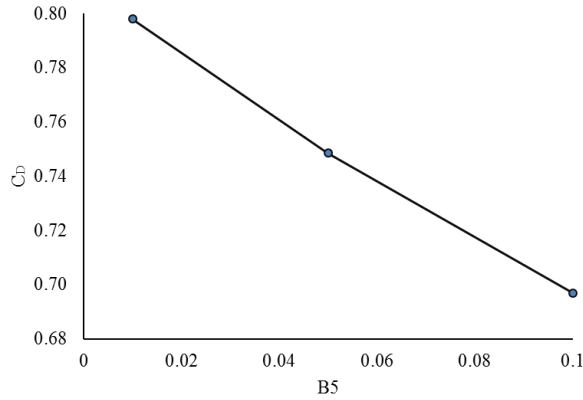
Figure 5.35 The pressure coefficient ( $C_p$ ) plotted over the truck-trailer unit along the symmetry line for changing  $B_5$  coefficients.

### 5.7.3 Effects of Changing $B_5$ Values on Aerodynamic Forces

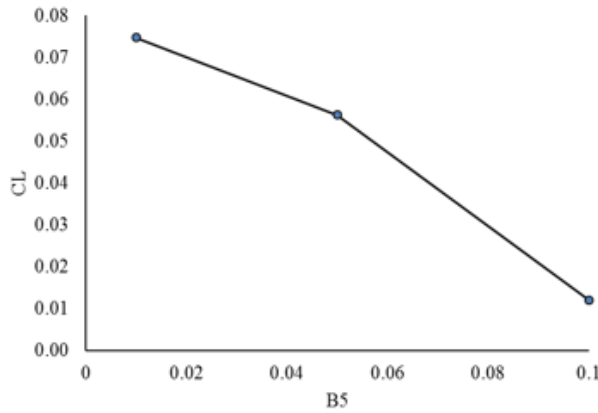
Figure 5.36 depicts the drag, lift and side force coefficients experienced by the truck-trailer unit when the  $B_5$  shape coefficient changes from 0.01, 0.05 to 0.1. The drag force coefficient data is presented from Figure 5.36 (a) and it can be clearly seen that a maximum drag coefficient of 0.8 is associated with  $B_5 = 0.01$  model. When  $B_5 = 0.05$ , the drag coefficient is seen to decrease by 6.25% to 0.75 and upon further increasing the  $B_5$  shape coefficient to 0.1, the drag coefficient is seen to decrease further 6.6% to 0.70.

The lift force coefficient data is presented from Figure 5.36 (b) and the maximum lift coefficient of 0.07 is observed on  $B_5 = 0.01$  model. When  $B_5 = 0.05$  the lift coefficient is seen to reduce by 14.3% to 0.06, and for the  $B_5 = 0.1$  model the lift is seen to decrease even further to 0.01 and this is seen as a further reduction of 83%.

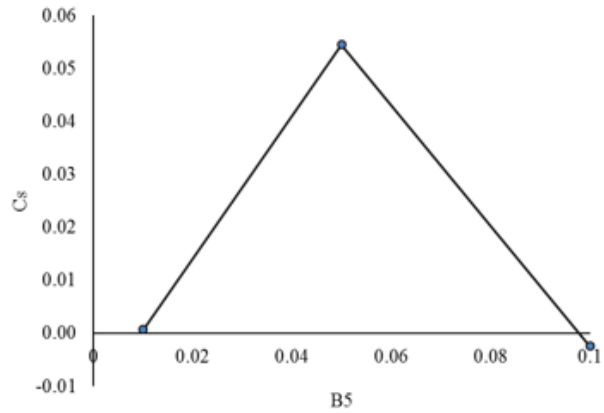
The side force coefficient data is presented from Figure 5.36 (c) and is seen to have negligible variations between a minimum of -0.002 and a maximum of 0.05. Once again, this is to be expected as the study was conducted at straight headwind flow conditions.



(a)



(b)



(c)

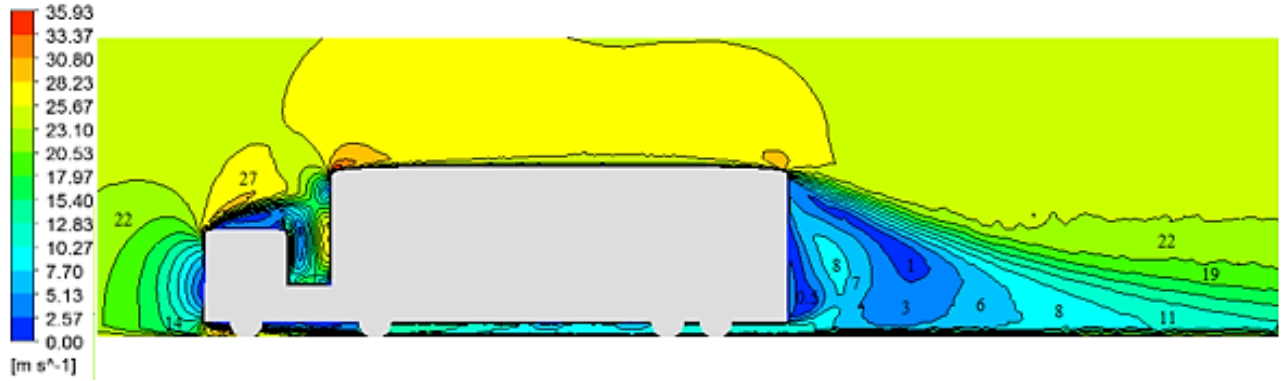
Figure 5.36 The drag force (a), lift force (b) and side force (c) coefficients for the truck-trailer geometry when  $B5 = 0.01$ ,  $B5 = 0.05$  and  $B5 = 0.1$  at straight headwind

## 5.8 Effect of B6 on the truck-trailer unit aerodynamic characteristics

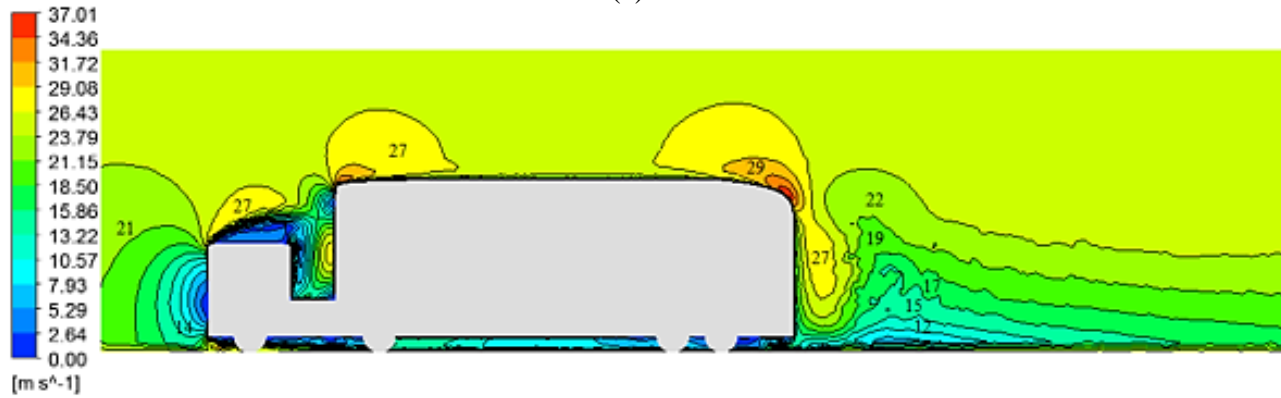
In order to analyse the effect on B6 on aerodynamics performance of a truck-trailer unit, three B6 values of 0.01, 0.05, 0.1 were used for analysis purposes. The B1, B2 and B5 coefficients were maintained at 0.01 while the B6 values were changed.

### **5.8.1 Velocity Distribution around the Truck-Trailer Unit with Changing B6 Values**

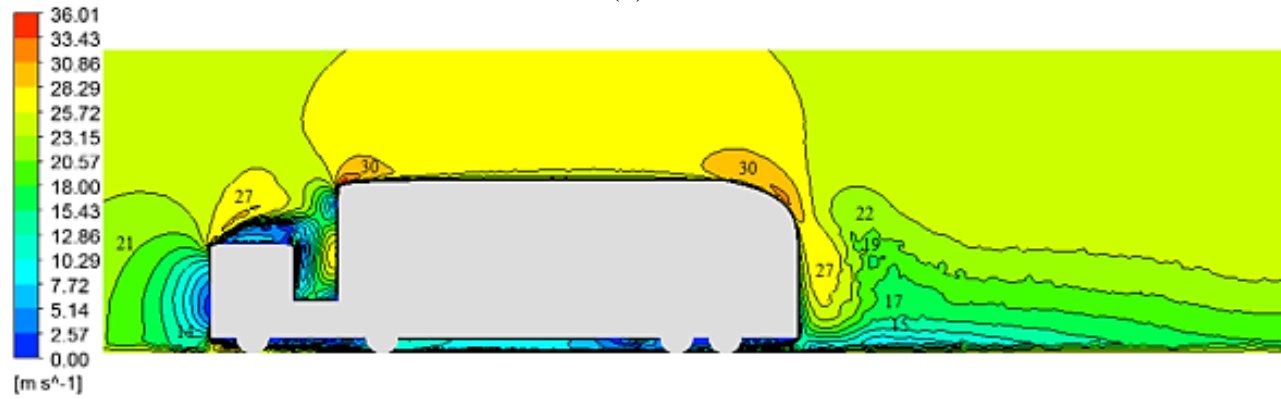
Velocity distribution around the truck-trailer unit when  $B6 = 0.01, 0.05$  and  $0.1$  whilst maintaining  $B1, B2, B5$  at a constant  $0.01$  is depicted from Figure 5.37. Low velocity magnitude can be exhibited at the front face of the truck with flow separation at the top front of the truck, top front of the trailer and the top rear of the trailer. Altering  $B6$  appears to have no effect on velocity magnitude in the truck-trailer gap. In the case of (a), there is a region of high velocity magnitude that begins at the top front of the trailer, which distributes across the trailer length with small regions of higher velocity at the top front and top rear of the trailer. Case (b), there are only two regions at the top front and top rear of the trailer that exhibits regions of high velocity magnitude, one of which continues to flow behind the trailer. Case (c) appears to behave similar to (a) in that, high velocity magnitude begins at the top front of the truck, which propagates across the length of the trailer, however, in this case, this distribution of velocity magnitude continues behind the trailer. Behind the trailer for cases (b) and (c), it can be seen that altering  $B6$  has resulted in a significant velocity magnitude increase.



(a)



(b)



(c)

Figure 5.37 Velocity fields around the Truck-trailer units with changing B6 coefficients.

(a)  $B6 = 0.01$  (b)  $B6 = 0.05$  (c)  $B6 = 0.1$

Figure 5.38 depicts the trailer unit with the top trailing edge profile of  $B6 = 0.1$  and six data lines ranging from L19<sub>R</sub> to L24<sub>BR</sub> where the velocity in the streamwise direction was recorded. The velocity data will be obtained and compared for models  $B6 = 0.01$ ,  $B6 = 0.05$  and  $B6 = 0.1$  in order to understand the effects of  $B6$  on the flow field in the vicinity of the truck unit. Data lines

L22<sub>T</sub> and L19<sub>R</sub> were positioned on the symmetry plane of the truck unit. The former was positioned at the start of the curved surface and the latter at the end of the curved surface. Data lines L20<sub>BL</sub> and L21<sub>TL</sub> were positioned on the left side of the trailer and the data lines L23<sub>BR</sub> and L24<sub>TR</sub> on the right side of the trailer (viewing from rear elevation) at the beginning and the end of the curved surface. The data lines will be used to gain an understanding of flow velocity in the vicinity of changing B6 shape profiles.

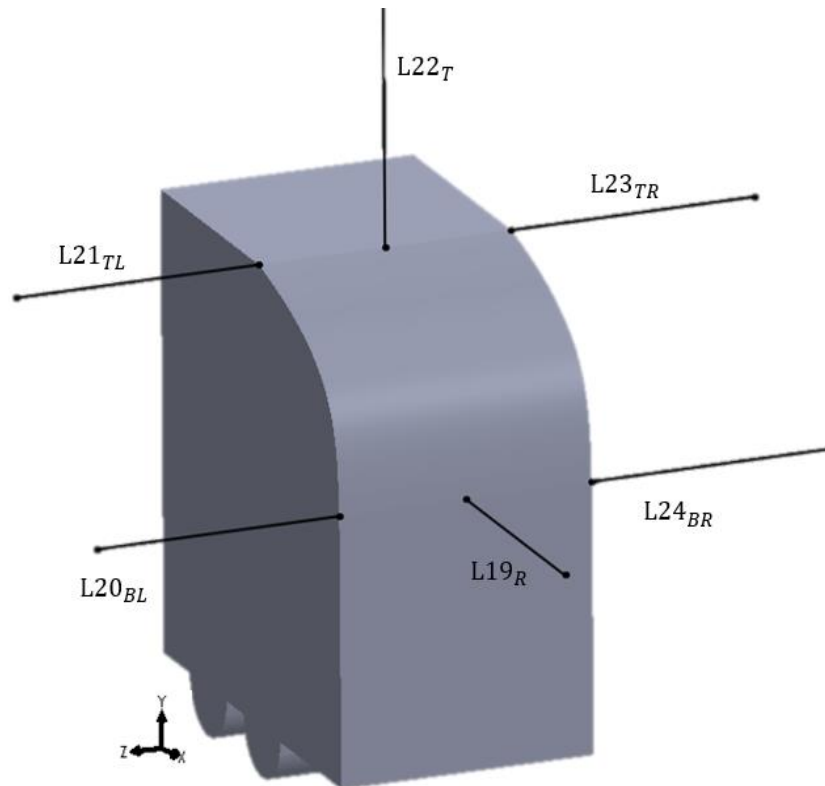


Figure 5.38 Data line locations around the top leading edge of the trailer unit when  $B6 = 0.1$ .

Figure 5.39 depicts the velocity distribution along data line L19<sub>R</sub> which was positioned at the rear of the trailer unit and the end of the curved surface. The data line starts from the trailer rear surface and extends 40m towards the trailer rear wake region. Velocity data have been obtained for B6 values 0.01, 0.05 and 0.1 and significant velocity variations between  $B6 = 0.01$  model and  $B6 = 0.05$  and  $B6 = 0.1$  models have been detected. The lowest flow velocities throughout the B6 range is seen for  $B6 = 0.01$  model and this remains the case for the full length of the data line.

Flow is seen to travel towards the trailer rear surface from a distance of 18.5m. This signifies the flow reversal and a maximum velocity of 5.8m/s in the opposite direction is recorded at this region. After the flow reversal region, the velocity is seen to increase steadily in the free stream direction while a maximum velocity of 23m/s is recorded at 40m away from the trailer rear surface. No flow reversal was observed for  $B6 = 0.05$  and  $B6 = 0.1$  models and a similar trend in velocity increase is observed for both these models while the highest velocity throughout was recorded on the  $B6 = 0.1$  model.

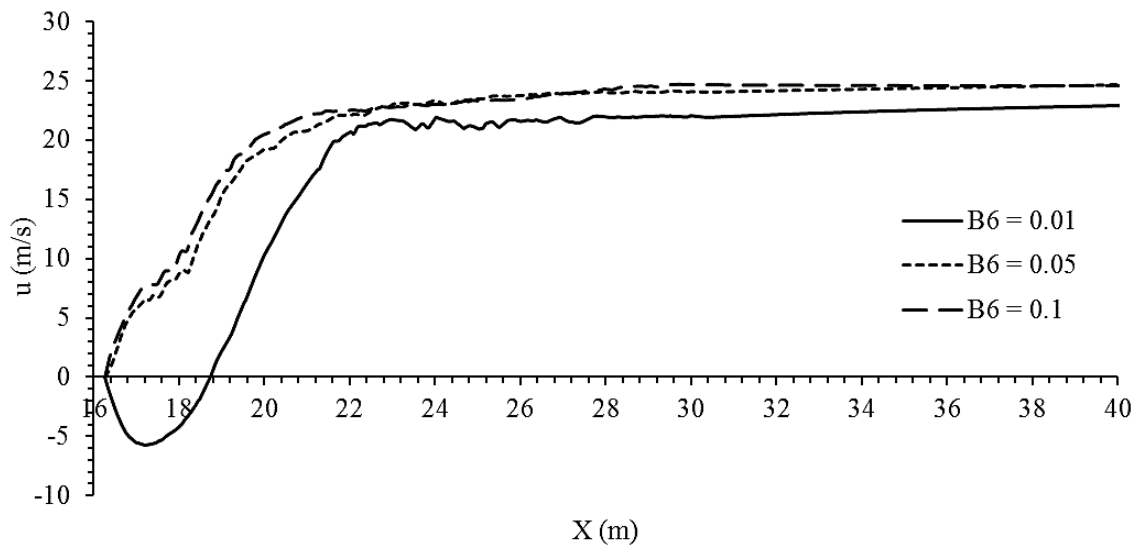


Figure 5.39 The x direction velocity plotted along the data line L19<sub>R</sub>.

Figure 5.40 depicts velocity distribution along data lines L20<sub>BL</sub> and L24<sub>BR</sub> which have been positioned on the left and right sides of the trailer unit respectively, at the end of curved leading edge surface. The L20<sub>BL</sub> data line extends from trailer left surface (1.3m) to 5m in the positive Z direction (viewing from rear elevation). A similar trend in velocity fluctuation can be seen for  $B6 = 0.05$  and  $B6 = 0.1$  models along the full length of the data line. Close to the trailer surface the velocity is seen to increase in a linear manner for all the models. The highest velocity of 24.5m/s was recorded on  $B6 = 0.1$  model at a distance of 0.15m from the trailer left side surface followed by 23.5m/s for  $B6 = 0.05$  model at the same location. On the contrary, the lowest velocity of 20.6m/s was recorded for the  $B6 = 0.01$  model once again at the same location. However, at a distance of 0.5m from the trailer left side surface, the flow velocity decreases for  $B6 = 0.05$  and  $B6 = 0.1$  models while the highest velocity is seen to be associated with  $B6 = 0.01$  model.

Furthermore, it shows the free stream velocity of 25m/s is observed for all three B6 models at a distance of 2.8m from the trailer left side surface.

Data line L24<sub>BR</sub> has been positioned on the right side of the trailer unit at the end of curved leading edge surface. This data line extends from trailer left side surface (1.3m) to 5m in the negative Z direction (viewing from rear elevation). A similar trend in velocity fluctuation can be seen for B6 = 0.05 and B6 = 0.1 models along the full length of the data line. Close to the trailer surface, the velocity is seen to increase in a linear manner for all the models. The highest velocity of 25.3m/s was recorded on B6 = 0.05 model at a distance of 0.15m from the trailer right side surface followed by 23.8m/s for B6 = 0.05 model on the same location. The lowest velocity of 21.1m/s was recorded on the B6 = 0.01 model once again at the same location. However, at a distance of 0.48m from the trailer left side surface, the flow velocity decreases for B6 = 0.05 and B6 = 0.1 models while the highest velocity is seen to be associated with B6 = 0.01 model. It was perceived, that the free stream velocity of 25m/s is observed for all three B6 models at a distance of 2.9m from the trailer left side surface. The overall minimum flow velocity of 20.3m/s was seen on the B6 = 0.05 model at a distance of 1.0m from the trailer surface and the greatest fluctuation in velocity between minimum and a maximum was also noted on the B6 = 0.05 model.

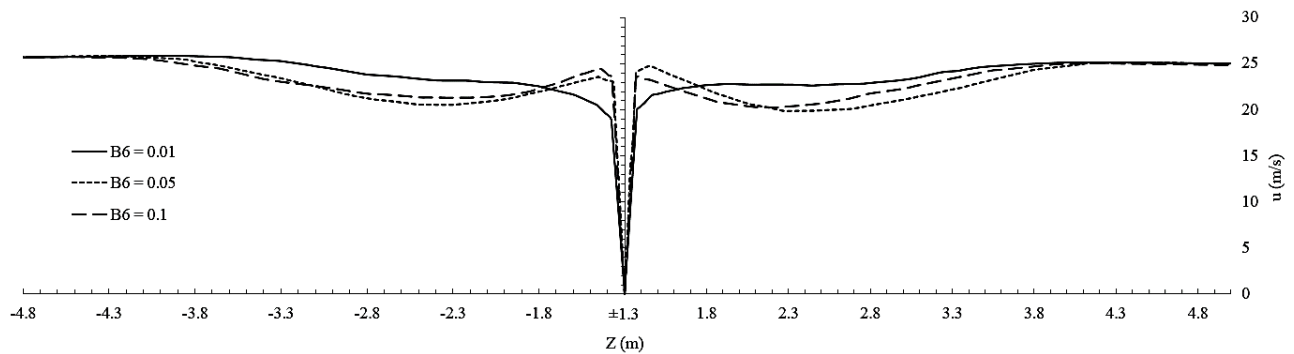


Figure 5.40 The x direction velocity plotted along the data lines L20<sub>BL</sub> (left) and L24<sub>BR</sub> (right)

Figure 5.41 depicts velocity distribution along data lines L21<sub>TL</sub> and L23<sub>TR</sub> which have been positioned on the left and right sides of the trailer unit respectively, at the beginning of the

curved leading edge surface. Once again, the data line extends from trailer left side surface (1.3m) to 3m in the positive Z direction (viewing from rear elevation). Minute variations in flow velocity is seen for all three truck-trailer models with free stream flow velocities existing in close proximity to the trailer left side surface. In comparison, the lowest velocities are seen on the data line for  $B6 = 0.01$  model while the highest velocities are recorded on the  $B6 = 0.1$  model.

Figure 5.41 also depicts the velocity distribution along the  $L23_{TR}$  data line, which has been positioned on the right side of the trailer unit at the beginning of the curved leading edge surface. The data line extends from trailer right surface (1.3m) up to 5m in the negative Z direction (viewing from the rear elevation). Minute variations in flow velocity is seen for all three truck-trailer models with free stream flow velocities existing in close proximity to the trailer right side surface. Steady non fluctuating velocities are seen to exist on the  $B6 = 0.01$  model. Up to 0.6m from the trailer right side surface, the  $B6 = 0.05$  model is seen to have the highest flow velocities. Lowest velocities are seen to exist on  $B6 = 0.1$  model for up to 0.43m from the trailer right surface and subsequently exhibiting highest flow velocities along the remainder of the data line.

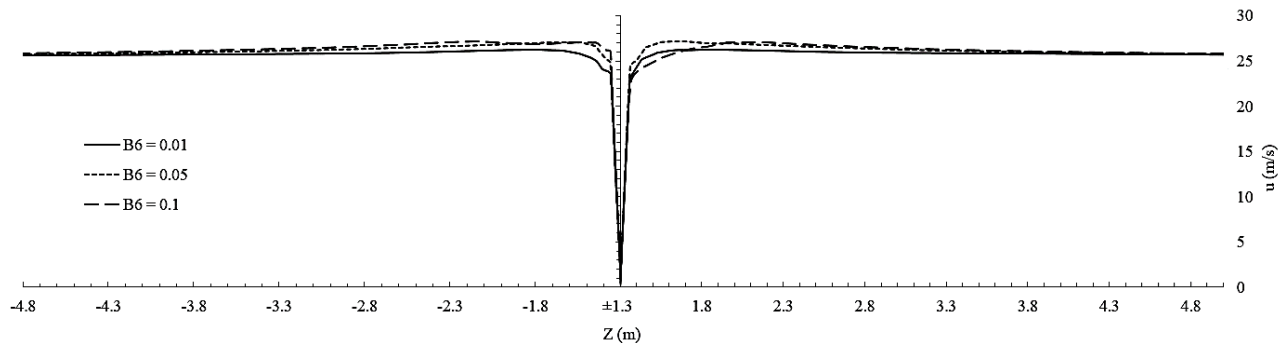


Figure 5.41 The x direction velocity plotted along the data lines  $L21_{TL}$  (left) and  $L23_{TR}$  (right)

Velocity distribution along the  $L22_T$  data line situated on top of the trailer unit at the beginning of the curved edge is shown in Figure 5.42. The start of the data line is situated on the trailer top surface (4.34m) and extends 3.6m upwards in the positive Y direction. Once again, the overall trend in velocity at the beginning of the curved edge for all truck-trailer models is seen to be

largely similar. However, significant variations in velocity between the models have been observed. A maximum flow velocity of 30m/s is recorded for  $B6 = 0.1$  model at a height of 0.38m from the trailer top surface. At the same location, a velocity of 28.9 m/s was recorded for the  $B6 = 0.05$  model and this is a 3.6% reduction in velocity when compared to  $B6 = 0.1$  model. The lowest maximum velocity of 26.7 m/s was observed for  $B6 = 0.01$  model again at a height of 0.38m from the trailer top surface which is a 11% reduction in velocity compared to  $B6 = 0.1$  model. It is evident from the Figure that increasing the  $B6$  coefficient and the curvature of the trailing rear edge of the trailer unit increases the flow velocity on top of the trailer unit.

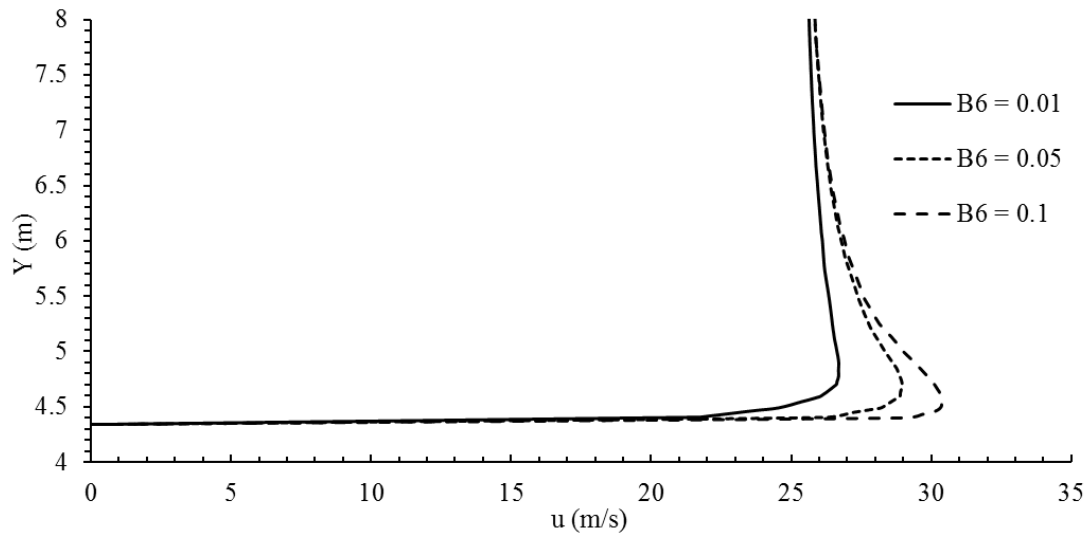


Figure 5.42 The x direction velocity plotted along the data line L22<sub>T</sub>.

The velocity on top of the trailer unit is plotted along five equally spaced data lines that extends from the trailer top surface to 5.3m vertically towards the free stream region as shown in Figure 5.43. For both models the velocity was observed to be in the direction of the free stream flow. For  $B6 = 0.01$  model a maximum velocity of 27.3m/s was observed on the first data line followed by 26.1m/s for the second data line, 25.8m/s for the third data line, 25.9m/s for the fourth data line and lastly 26.4m/s for the fifth data line. Similar to  $B5$  model the overall trend in velocity was observed to be fluctuating from the front of the trailer top surface to the rear. Over the length of top surface of the trailer unit, the velocity fluctuates from high velocity to low velocity and back to high velocity with their respective locations being front, middle and rear of the trailer top surface. A reduction in velocity of 5.5% is seen from front to middle and an increase of 2.3% is seen from middle to rear.

For the  $B6 = 0.1$  model, a maximum velocity of 27.3m/s was observed on the first data line followed by 26.2m/s for the second data line, 26m/s for the third data line, 26.4m/s for the fourth data line and lastly 29m/s for the fifth data line. In comparison with the  $B6 = 0.01$  model, an 0.38% increase in velocity for the second data line, 0.77% increase in velocity for the third data line, 2.0% increase in velocity for the fourth data line and a 9.8% increase in velocity for the fifth data line was observed.

The overall trend in velocity was observed to be similar to that of B5 models. Over the length of the top surface of trailer unit, the velocity fluctuates from high velocity at the front of the trailer unit to low velocity in the middle of trailer unit back to high velocity towards the rear of the trailer unit. A 2.3% increase on velocity was discovered from middle of the trailer to the end of the trailer in case of  $B6 = 0.01$  model whereas a 11.5% increase in velocity was noted for  $B6 = 0.1$  model for the same distance.

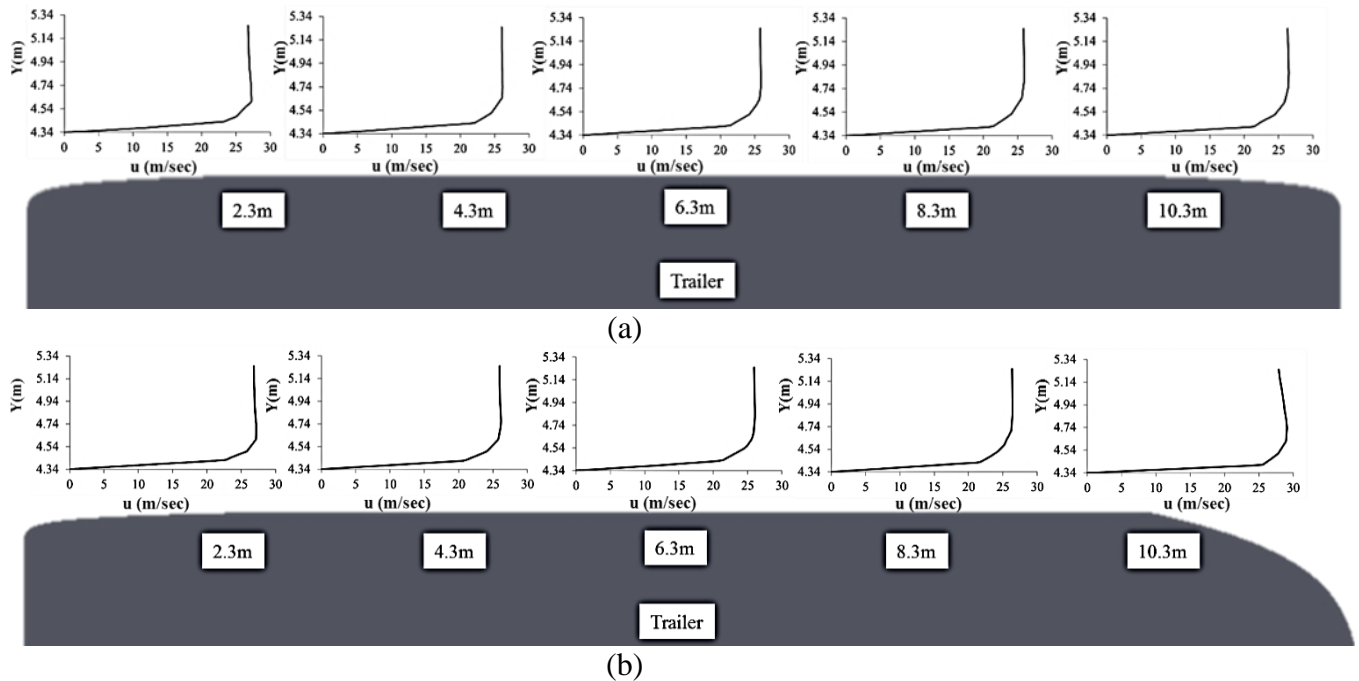


Figure 5.43 Axial flow velocity profiles at various distances from the top leading edge of the trailer unit when  $B6 = 0.01$  (a) and  $B6 = 0.1$  (b).

### 5.8.2 Pressure Distribution around the Truck-Trailer Unit with Changing B6 Values.

The coefficient of pressure around the truck-trailer unit when  $B6 = 0.01, 0.05$  and  $0.1$  whilst maintaining  $B1, B2, B5$  at a constant  $0.01$  is depicted from Figure 5.44. In all three cases, the highest pressure coefficient depicted is  $0.9$  while the lowest pressure coefficient depicted is  $-0.5$ . It can be seen that high pressure coefficient is distributed across the front face of the truck and mid-range pressure coefficient is distributed at the top of the truck which elongates into the truck-trailer gap. Additionally, in the  $B5$  location, stagnant pressure on the top front face of the trailer and low pressure coefficient at the top face of the trailer is identified. Furthermore, pressure coefficient in the mid-range from the top front of the trailer manifests over and beyond the length of the trailer. It is evident that altering  $B6$  has a predominant effect at the top rear and the rear face of the trailer. Figure (a) below depicts a small region with mid-range pressure coefficient identified at the top rear of the trailer. In the case of (b), lower pressure coefficient is exhibited within this mid-range pressure coefficient region, which begins further upstream of the trailer than that depicted in (a) and propagates down the rear face of the trailer. In cases for (b) and (c), high pressure coefficient regions are depicted behind the trailer and the bottom rear of the trailer.

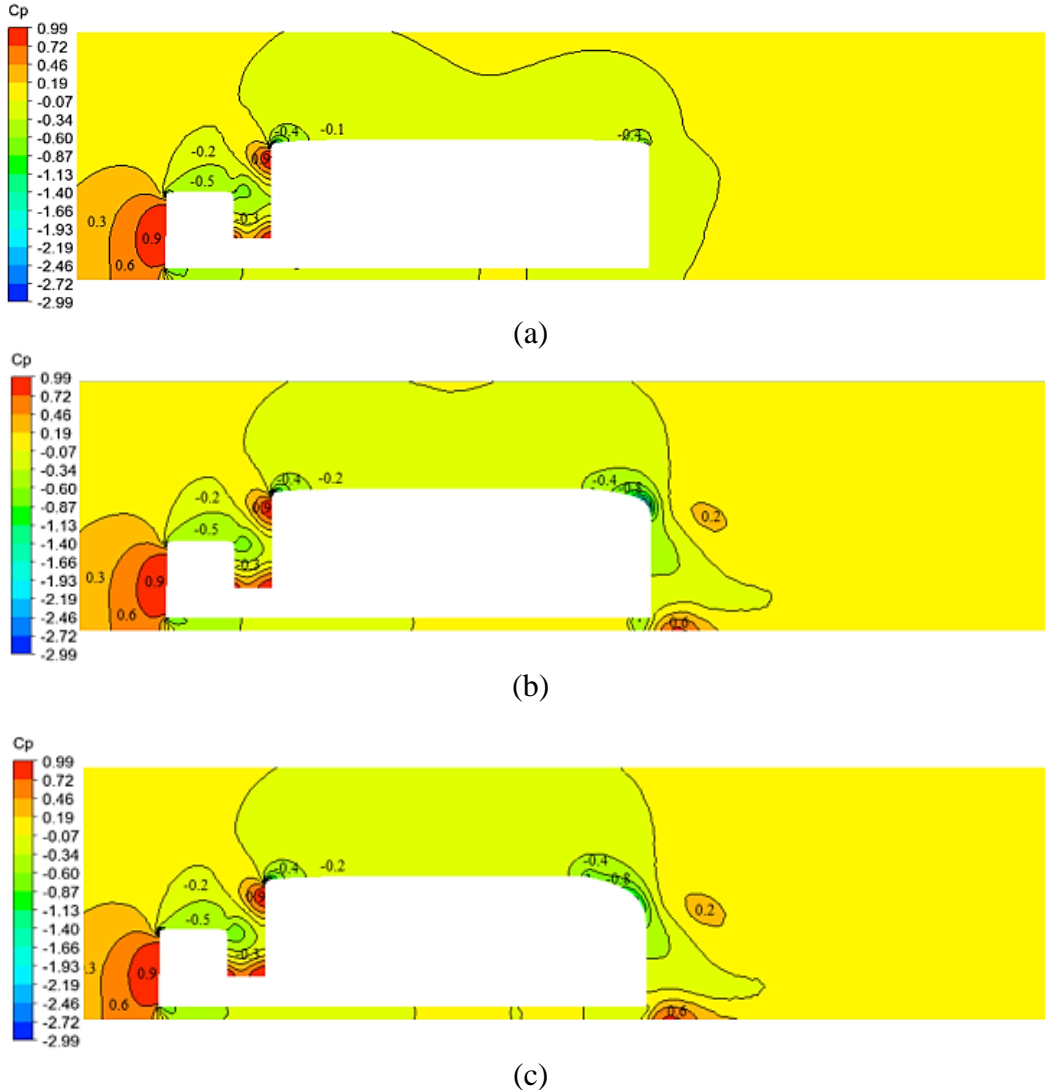


Figure 5.44 Coefficient of pressure around the truck-trailer units with changing B6 coefficients. (a) B6 = 0.01 (b) B6 = 0.05 (c) B6 = 0.1.

The pressure coefficient plotted over the truck-trailer unit along the symmetry line with changing B6 coefficients is depicted from Figure 5.45. Maximum pressure coefficient of 1.0 and a minimum pressure coefficient of -1.96 were observed on the data line for B6 = 0.05 model. It was observed that varying B6 shape coefficients result in sharp variations in pressure at the rear of the trailer unit between  $\eta = 0.66$  and  $\eta = 1$  but the effects are not seen to spread towards the front of the truck-trailer unit. Hence, insignificant pressure variations were noticed from  $\eta = 0$  to  $\eta = 0.66$  and the pressure profiles in this region has already been discussed in Figure 5.34. The lowest pressure of -1.96 was recorded between  $\eta = 0.66$  and  $\eta = 1$  region for B6 = 0.05 model

while highest pressure of -0.9 was observed on the  $B6 = 0.01$  model. These pressure variations are seen at the very end of the trailer top surface and beginning of trailer rear surface.

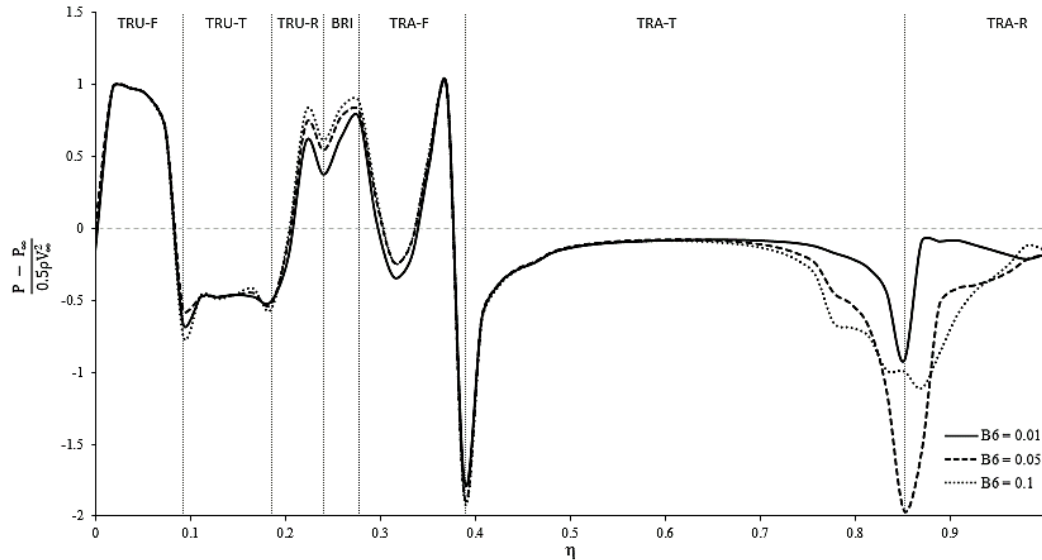


Figure 5.45 The pressure coefficient ( $C_p$ ) plotted over the truck-trailer unit along the symmetry line for changing  $B6$  coefficients.

### 5.8.3 Effects of Changing $B6$ Values on Aerodynamic Forces

Figure 5.46 depicts the drag, lift and side force coefficients experienced by the truck-trailer unit when the  $B6$  shape coefficient changes from 0.01, 0.05 to 0.1. At  $B6 = 0.01$  the minimum drag coefficient of 0.8 was observed. The drag force then is seen to increase to a maximum of 1.22 for the model  $B6 = 0.05$  before decreasing to 1.19 for the model  $B6 = 0.1$ . A 52% increase in drag was observed between minimum and the maximum drag models. Overall, the drag force experienced by the truck-trailer model is seen to increase significantly when the  $B6$  shape coefficient increases.

The lift force coefficient data is presented from Figure 5.46 (b) and the minimum lift coefficient of 0.07 was observed for  $B6 = 0.01$  model. A maximum lift of 0.52 was seen for the  $B6 = 0.05$  model before a slightly reduced lift of 0.5 was recorded for  $B6 = 0.1$  model.

The side force coefficient data is presented from Figure 5.46 (c) and is seen to have negligible variation between a minimum of -0.003 and a maximum of 0.03. Once again, this is to be expected as the study was conducted at straight headwind flow conditions.

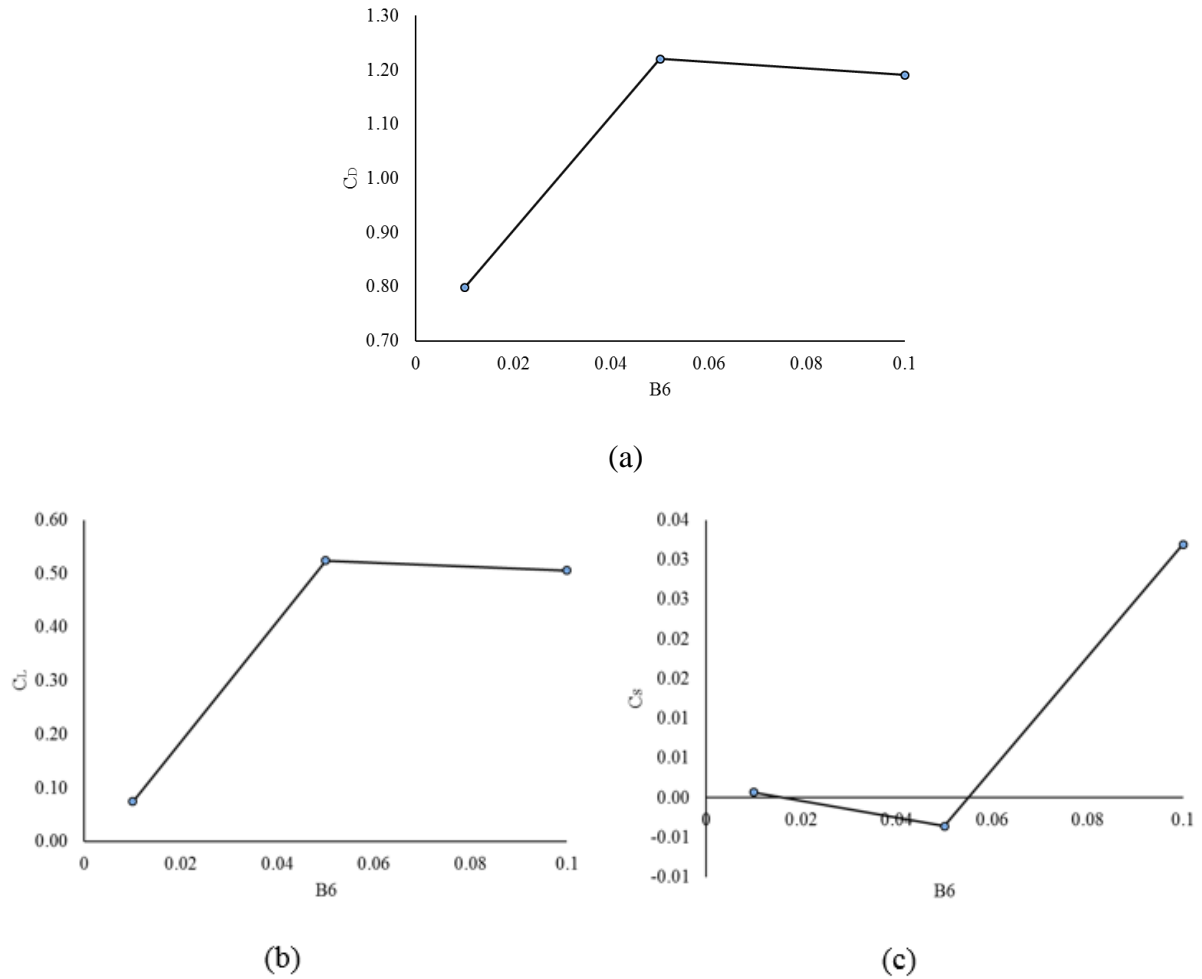


Figure 5.46 The drag force (a), lift force (b) and side force (c) coefficients for the truck-trailer geometry when  $B_6 = 0.01$ ,  $B_6 = 0.05$  and  $B_6 = 0.1$  at straight headwind.

## 5.9 Optimum Truck-Trailer Model

Full factorial design method was used to produce a total of 81 different truck-trailer geometries with changing B1, B2, B5 and B6 coefficients with each individual coefficient changing from 0.01, 0.05 and 0.1. Each of the truck-trailer geometry was allocated a case number from 1 - 81 due to convenience when portraying the drag force associate with each of B1, B2, B5 and B6 combination. In this study, drag force has been used as the performance parameter to decide the optimum aerodynamic shape of a truck-trailer unit as lower the drag force, more aerodynamically optimum the vehicle shape is considered to be.

The form drag is a result of the variations in pressure fields and this is expected to influence the magnitude of overall drag force. Changing B shape coefficients are seen to have a considerable effect on pressure fields around the truck-trailer units and this has been discussed previously. Using the drag force data portrayed in Figure 5.47, it is possible to see the variation of drag force for various B shape coefficients. The drag force is seen to vary considerably between a maximum of 5562N and a minimum of 3065N. The minimum drag force was observed for number 12 truck trailer configuration with B1 = 0.01, B2 = 0.05, B5 = 0.1 and B6 = 0.01 whereas the maximum drag force was observed for number 30 truck-trailer configuration having B1 = 0.1, B2 = 0.1, B5 = 0.01 and B6 = 0.05.

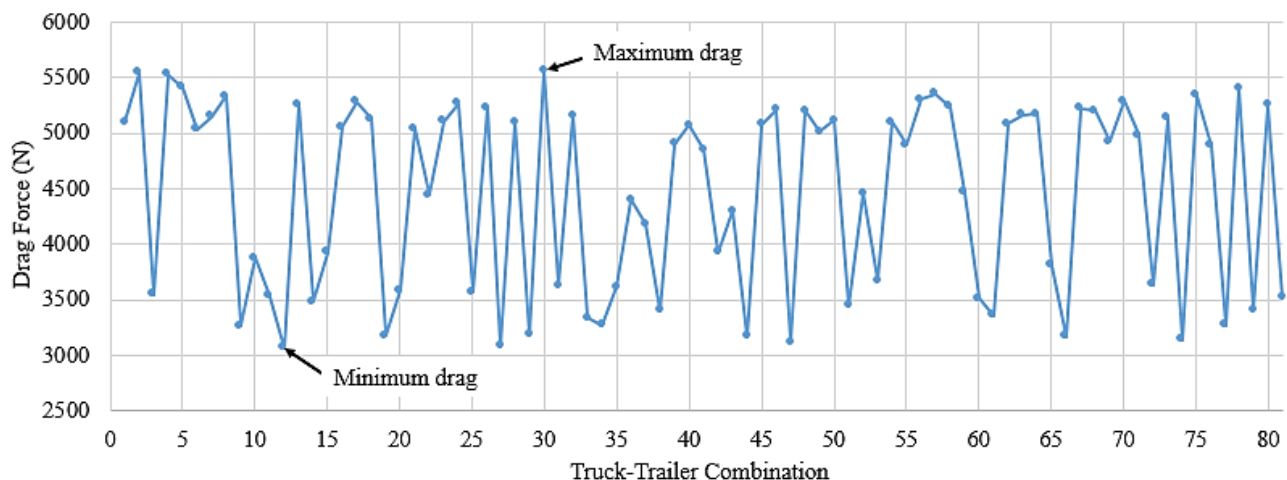


Figure 5.47 Variations in drag force for various truck-trailer combinations with varying B1, B2, B5 and B6 coefficients.

The surfaces which are placed perpendicular to the oncoming flow are thought to be the key contributors to the aerodynamic drag force experienced by a truck-trailer unit [90]. Hence, the drag force acting on truck front, truck rear, trailer front and trailer rear faces for maximum and minimum truck-trailer configurations are tabulated in Table 5-1. The lowest drag forces of 1313N and 273N on the truck front and truck rear surfaces, respectively are seen to be associated with the truck-trailer combination with the highest drag force. However, in the case of maximum drag force truck-trailer configuration, high drag forces of 1056N and 2611N are seen to be associated with trailer front and trailer rear surfaces giving a combined drag force of 3667N just for the trailer unit. In the case of lowest drag truck-trailer configuration, a much reduced total drag force of 407N is experienced by the trailer unit. The truck-trailer configuration that produced the maximum drag force is contributed by mainly the trailer unit, specifically due to the shape at top leading edge and trailing edge profiles  $B5 = 0.01$  and  $B6 = 0.05$ . The reasons being,  $B5 = 0.01$  profile is seen to generate a stagnation pressure region close to the top leading edge of the trailer front surface. Meanwhile,  $B6 = 0.05$  profile gives rise to a larger wake flow region in the vicinity of trailer rear surface giving rise to a high drag force on the trailer unit

Table 5.1 Variations in drag force for various truck-trailer combinations with varying  $B1$ ,  $B2$ ,  $B5$  and  $B6$  coefficients

Truck-Trailer Surface	12 <sup>th</sup> truck-trailer configuration	30 <sup>th</sup> truck-trailer configuration
	(Minimum drag force)	(Maximum drag force)
	(N)	(N)
Truck Front	1695	1313
Truck Rear	540	273
Trailer Front	-372	1056
Trailer Rear	779	2611

The minimum drag force and the maximum drag force was recorded on 12<sup>th</sup> and 30<sup>th</sup> truck-trailer configurations respectively. Figure 5.48 illustrates the pressure distribution on truck front surface and truck rear surface for minimum drag model (a,c) and maximum drag model (b,d).

Aerodynamic drag force was calculated in the direction of the free stream flow. The oncoming flow comes to a rest at the front surface of the truck unit generating a stagnation pressure region. It is observed, that on the front surface of the minimum drag model (a), high pressure spreads on a larger area compared to the maximum drag model (b). As a result of the high pressure exerted on the truck front face, a resulting force of 1659N is recorded for (a) compared to 1313N of force recorded on (b). The B1 coefficients for (a) and (b) are 0.01 and 0.1 providing a smaller curvature of the leading edge for the (a) truck unit and a greater curvature at the leading edge for the (b) truck unit respectively. When the curvature of the leading edge is 0.1, the stagnation pressure region is reduced as the flow is moved to the truck top surface with minimal obstruction resulting in relatively low force been exerted on the truck front surface.

The truck rear surface for minimum drag truck-trailer model and maximum drag truck-trailer model is shown from (c) and (d), respectively. A relatively low pressure is seen throughout the surface for model (c) while the maximum pressure of 0.21 is located towards the bottom of the surface and a minimum pressure of -0.73 is located towards the top of the surface. In comparison to surface (c), higher pressures are observed for surface (d) with a maximum pressure coefficient of 1 was seen at the bottom of the surface, a minimum pressure coefficient of -1.1 was observed towards the top of the surface. However, at the top edge of the surface a high pressure region of 0.21 was observed. The overall pressure on surface (d) was higher than surface (c). The higher pressures near the top and bottom end of surface (c) is a result of the circulated flow in the truck-trailer gap region coming into contact with the truck rear surface. Hence, the pressure profiles on the truck rear surface in both cases are seen to be heavily influenced by the flow behavior in the gap region. As a result of low pressures that exists on surface (c), a force of 540N was recorded on the surface whereas a force of 273N was recorded for surface (d).

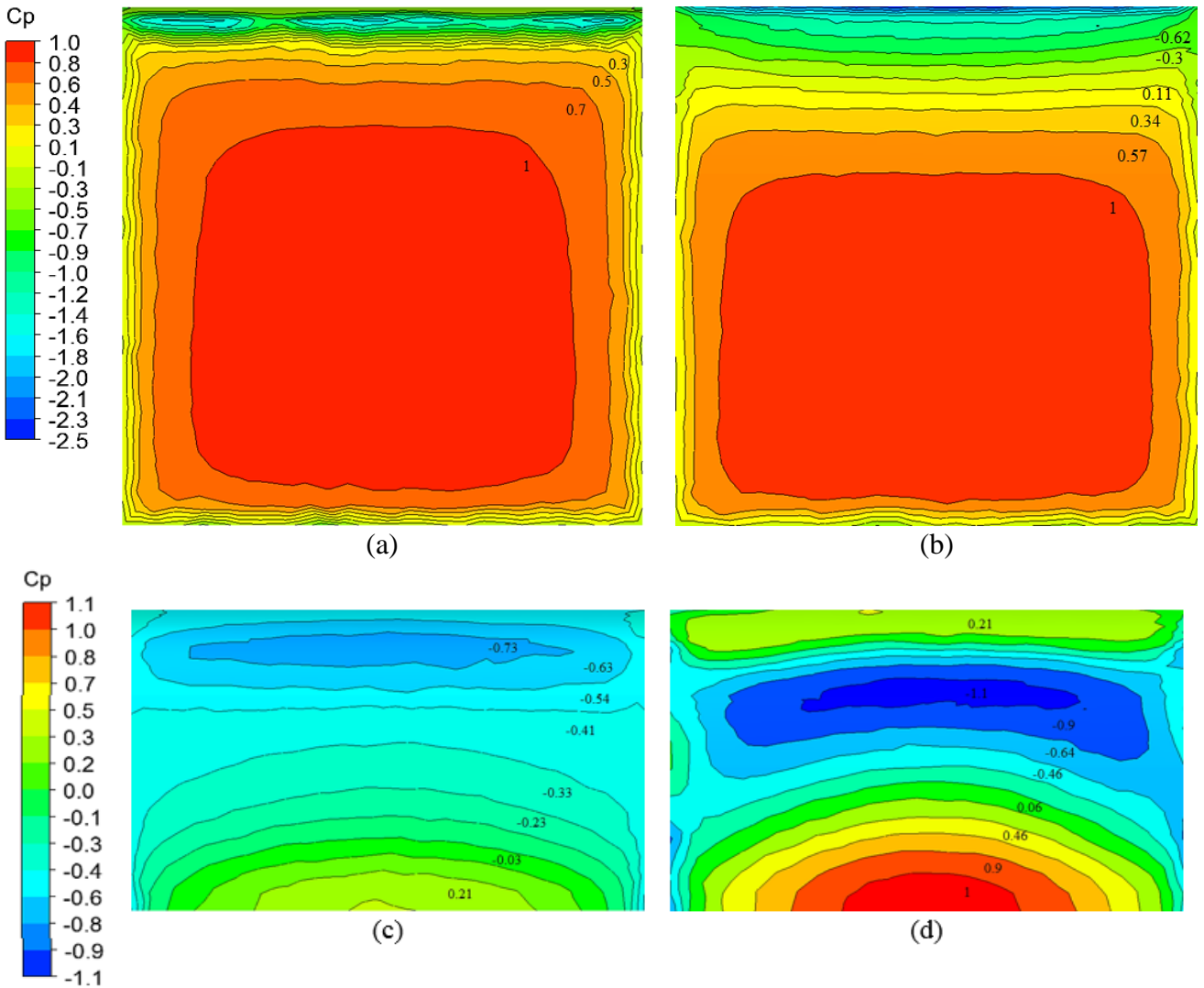


Figure 5.48 Pressure Coefficient of the (a) minimum drag model on the Truck-Front surface (b) maximum drag model of the Truck-Front surface (c) minimum drag model of the Truck-Rear surface (d) maximum drag model of the Truck-Rear surface.

Figure 5.49 illustrates the pressure distribution on trailer front surface and trailer rear surface for minimum drag model (a, c) and maximum drag model (b, d). The flow going past the truck unit is seen to be impinging on the top half of the trailer front surface resulting in a high pressure region. The circulating flow in the gap region is seen to contribute to the high pressure region which exists near the bottom edge of the trailer front surface. The highest pressure is seen on the trailer front surface of maximum drag model. Here, a maximum pressure coefficient of 1 is seen to cover approximately half the trailer front surface and while the minimum pressure of -2.9 is seen

to exist on the top edge of the surface due to acceleration of flow towards the trailer top surface. Relatively low pressures are seen to exist on most of the trailer front surface of the minimum drag model. Maximum pressure coefficient of 0.78 is observed at the middle of top half of the surface and a minimum pressure coefficient of -0.47 was seen at the top leading edge of the surface. The low pressure at (a) is seen to occur as a result of  $B5 = 0.1$  as this provided the maximum leading edge curvature compared to (b) where  $B5 = 0.01$  has the smallest leading edge curvature profile. Due to this high pressure, the highest force of 1056N was recorded for (b) and a drag force of -372N was obtained for (a). The negative drag signifies the force acting in the opposite direction to the direction of flow.

The trailer rear surface for minimum drag truck-trailer model and maximum drag truck-trailer model is shown from (c) and (d), respectively. Significant variations in pressure magnitudes are observed on both (c) and (d) with the lowest pressures seen to exist on the trailer rear face for the maximum drag truck-trailer model. Here, the lowest pressure coefficient of -1.9 is observed in the vicinity of the top trailing edge and a highest pressure of -0.1 is observed close to the bottom trailing edge of the surface. Conversely, the lowest pressure coefficient on (c) was found as -0.21 and the highest pressure was found as -0.08 on the top half of the trailer rear surface. In comparison, the low pressure region which was observed close to the bottom trailer edge on surface (c) had moved closer to top trailer edge on surface (d). High pressures that exist on the trailer rear surface for the minimum drag model is found to produce a force of 779N while the low pressures that exist on the same surface for the maximum drag model is seen to produce a significantly increased force of 2611N.

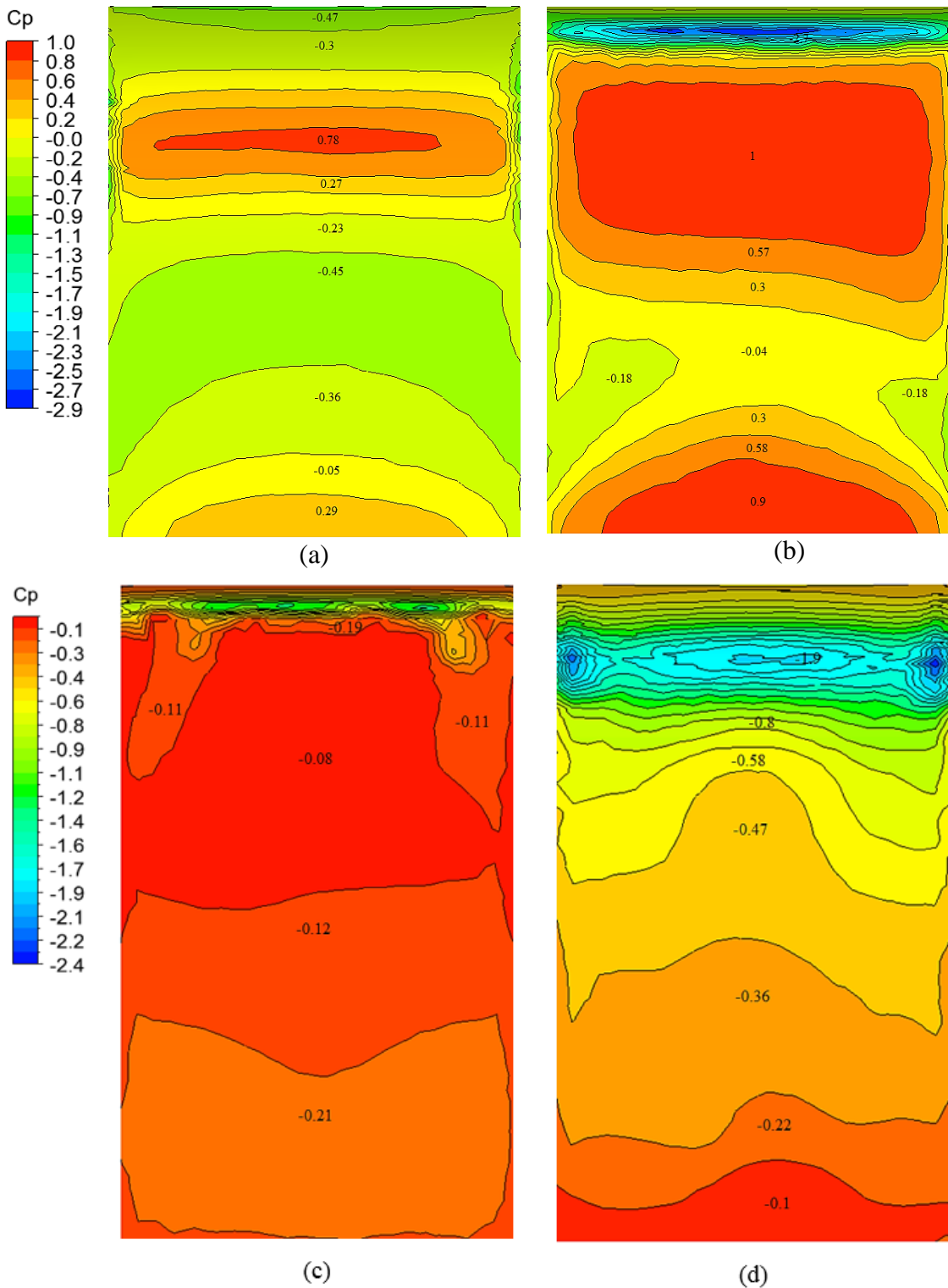


Figure 5.49 Pressure Coefficient of the (a) minimum drag model on the Trailer-Front surface (b) maximum drag model of the Trailer-Front surface (c) minimum drag model of the Trailer-Rear surface (d) maximum drag model of the Trailer-Rear surface.

The pressure variations of key surfaces that directly contribute towards the aerodynamic drag force of the maximum and minimum drag models were discussed previously. Figure 5.50 depicts the coefficient of pressure plotted along the symmetry line of the truck-trailer models which were associated with the minimum and the maximum drag force. Upon observing the Figure, clear variations in pressure are seen for both models. No variations in the pressure distribution is seen on the truck front surface up to  $\eta = 0.03$  for both models. However, between  $\eta = 0.03$  and  $\eta = 0.08$ , the highest pressure coefficients and between  $\eta = 0.08$  and  $\eta = 0.09$ , the lowest pressure coefficients were observed for minimum drag model. The pressure is seen to fluctuate on top of the truck top surface with the highest peak of 0.19 and lowest valley of -1.09 is recorded for the maximum drag model. Compared to the maximum drag model, minimum pressure fluctuations on the truck top surface were seen on the minimum drag model. Considerably high pressures compared to minimum drag model is seen between  $\eta = 0.19$  and  $\eta = 0.37$  spreading over truck rear, bridge and trailer front surfaces on the maximum drag model. At the top leading edge of the trailer front and trailer top surfaces (between  $\eta = 0.37$  and  $\eta = 0.42$ ), a steep reduction in pressure on maximum drag model is seen in comparison to minimum drag model where the pressure is seen to plummet to a minimum of -2.48 at the leading edge. At this point, the highest pressure coefficient of 0.08 was recorded for the minimum drag model. Low pressures are seen throughout the trailer top and trailer rear surfaces. At the start of the trailer top surface, between  $\eta = 0.38$   $\eta = 0.42$  the minimum drag model is seen to have higher pressures, with the maximum pressure being 0.08. On the rear half of the trailer top surface, the minimum drag model is seen to be associated with a higher pressure compared to the maximum drag model. At the top trailing edge, the lowest pressure of -1.82 is recorded for maximum drag model while the highest pressure of -1.16 was recorded for the minimum drag model. The minimum drag model is observed to be associated with higher pressures over the maximum drag model on the trailer rear surface. This effect is seen for around 87% of the trailer rear surface from top trailer edge towards the bottom trailing edge.

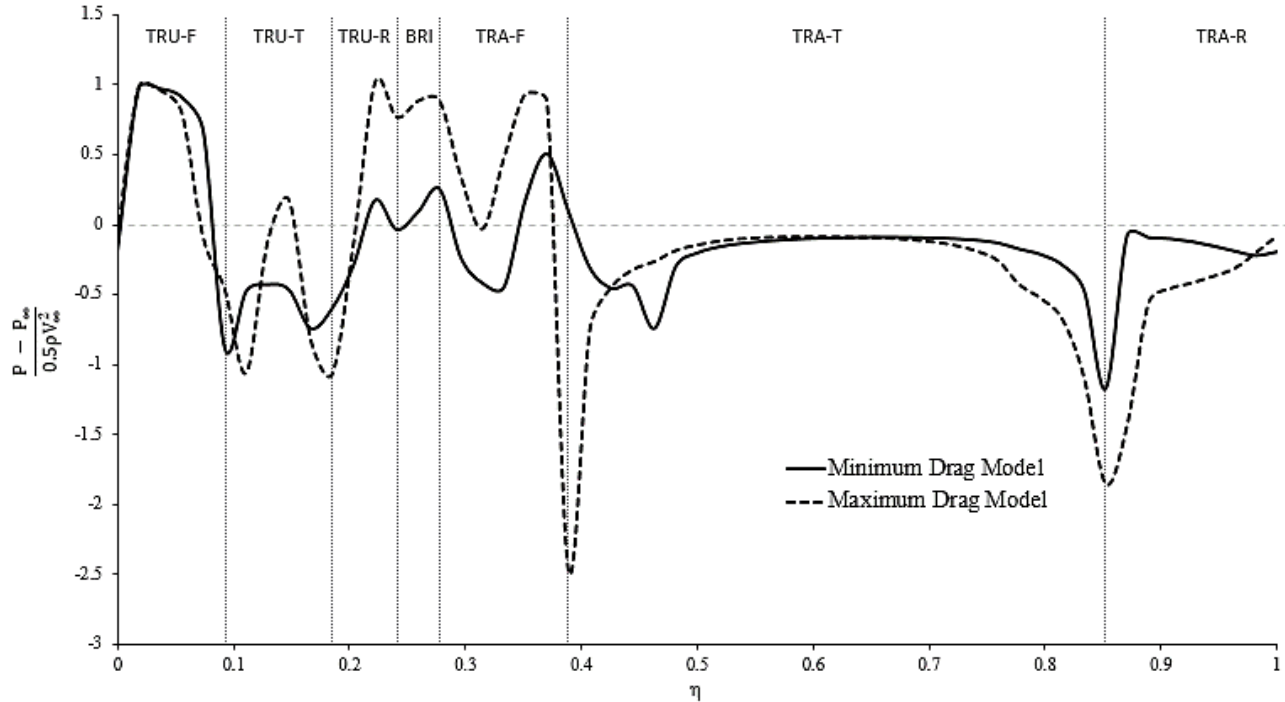


Figure 5.50 The pressure coefficient ( $C_p$ ) plotted over the truck-trailer unit along the symmetry line for minimum and maximum drag truck-trailer models.

## 5.10 Development of Semi-Empirical Prediction Models for Drag and Lift Aerodynamic Coefficients for Changing Truck-Trailer Shapes

The changing aerodynamic coefficients with respect to the truck-trailer dimensions and development of a semi-empirical prediction model for resulting aerodynamic force was discussed previously in chapter 4. In this section, development of a novel semi-empirical prediction model which correlates B1, B2, B5 and B6 shape coefficients with resulting aerodynamic coefficients is discussed. The developed prediction models are only expected to produce drag and lift coefficients as the effect of side force was neglected due to the absence of crosswind flow profiles. The effect of B1, B2, B5 and B6 coefficients and resulting aerodynamic characteristics on and around a truck-trailer unit were well documented in the previous sections. The prediction model is expected to replicate the computational data with a reasonable level of accuracy. Again, the Evolutionary non-linear optimisation model has been combined along with

multiple regression analysis to estimate the truck-trailer shape geometrical characteristics and resulting drag and lift aerodynamic coefficients.

### 5.10.1 Developing the Drag Coefficient Equation

The drag coefficient equation in chapter number 4 was represented in the following form correlating the length, height, width and crosswind flow angle.

$$C_D = A (1 + B \cdot \sin(C \cdot \psi)) \quad (5-4)$$

However, the prediction model developed in this section will be correlating the B1, B2, B5 and B6 shape coefficients in order to predict the drag force coefficients. In order to achieve this, the force coefficients should be presented as functions of proposed shape coefficients.

$$C_D = C_D(B_1, B_2, B_5, B_6) \quad (5-5)$$

The proposed drag force coefficient prediction equation will be in a specific form so; it is capable of predicting the drag force coefficient when all the value of B shape coefficients reduces down to zero.

$$C_D = C_{D_{B_1, B_2, B_5, B_6=0}} \cdot C_{D_{B_1, B_2, B_5, B_6 \neq 0}} \quad (5-6)$$

Here, the B1, B2, B5, B6 = 0 will be represented by

$$C_{D_{B_1, B_2, B_5, B_6=0}} = A \quad (5-7)$$

And B1, B2, B5, B6 ≠ 0 will be represented as B

$$C_{D_{B_1, B_2, B_5, B_6 \neq 0}} = B \quad (5-8)$$

Hence:

$$C_D = A \cdot B \quad (5-9)$$

Figure 5.51 depicts drag force coefficients for the truck-trailer geometry for changing B coefficients to (a) 0.01; (b) 0.05; (c) 0.1. The first column (a), consist of changing B1, B2, B5 and B6 coefficients one at a time, while the remaining respective B coefficients of the truck-trailer model are maintained at a constant value of 0.01. The second column (b), consist of changing B1, B2, B5 and B6 coefficients one at a time, while the remaining respective B coefficients of the truck-trailer model are maintained at a constant value of 0.05. The third column (c), consist of changing B1, B2, B5 and B6 coefficients one at a time, while the remaining respective B coefficients of the truck-trailer model are maintained at a constant value of 0.1. It can be seen that in the case of changing B1, B2, B5 coefficients while the remaining of the respective coefficients are maintained at 0.01, drag force almost linearly decreases. In the case of B6 coefficient varying while the respective coefficients remain at 0.01, drag coefficient increases from  $B6 = 0.01$  to  $B6 = 0.05$ , prior to slightly decreasing. Observing the trend through (b), it is noticed that drag coefficient at all varying B coefficients, significantly increases from  $B = 0.01$  to  $B = 0.05$ . However, from  $B = 0.05$  to  $B = 0.1$ , the case of varying B1 coefficient shows a decrease in drag coefficient, whereas in the cases of varying B2 and B5 coefficients, drag coefficient increases and in the case of varying B6 coefficient, drag coefficient attains at a constant. It is noticed in (c), all the varying B coefficients increase in drag coefficient from  $B = 0.01$  to  $B = 0.05$ . However, in the cases for varying B1, B2 and B5, drag coefficient increases even further from  $B = 0.05$  to  $B = 0.1$  and varying B6 leads to a very slight increase in drag coefficient.

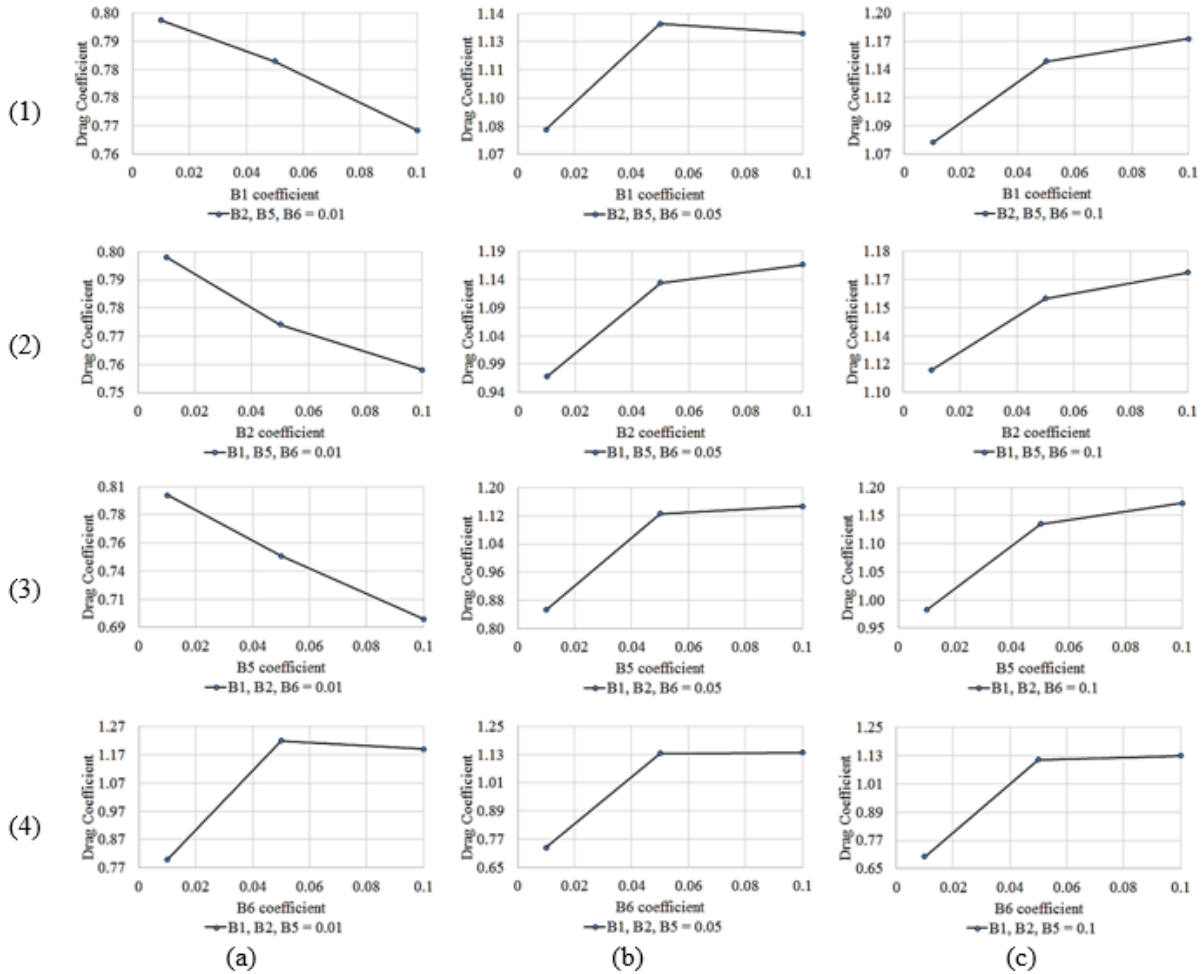


Figure 5.51 The drag force coefficients for the truck-trailer geometry for changing B coefficients.

Here, ‘A’ has been defined as a constant value which represent the drag force coefficient when B1, B2, B5 and B6 are all equal to zero as represented in equation (5-10). By studying the CFD data obtained for the drag force coefficient, following functional form was used to represent ‘B’ which incorporates the shape characteristics defined by B shape coefficients.

$$B = \left( \frac{1 + \frac{B_6^a}{C_1}}{1 + B_1^b + B_2^c + B_5^d} \right) \tag{5-10}$$

After evaluating the data set for drag force coefficient, the final drag coefficient prediction equation was obtained which has been characterised by B1, B2, B5 and B6 shape coefficients. This equation can be illustrated as:

$$C_D = 0.55 \left( \frac{1 + \left( \frac{B_6^{0.461}}{0.329} \right)}{1 + B_1^{1.781} + B_2^{1.730} + B_5^{9.862}} \right) \quad (5-11)$$

Figure 5.52 depicts the correlation between the predicted values of the aerodynamic drag force coefficients, and those obtained from CFD. Once again, it can be clearly seen that the predicted values agree very well with those obtained from CFD. The standard error of estimate has been calculated to be around 15%. Hence, equation (5-11), developed for characterising the aerodynamic drag force coefficient in terms of the proposed truck-trailer shape parameters is well capable of providing accurate predictions in place of CFD data.

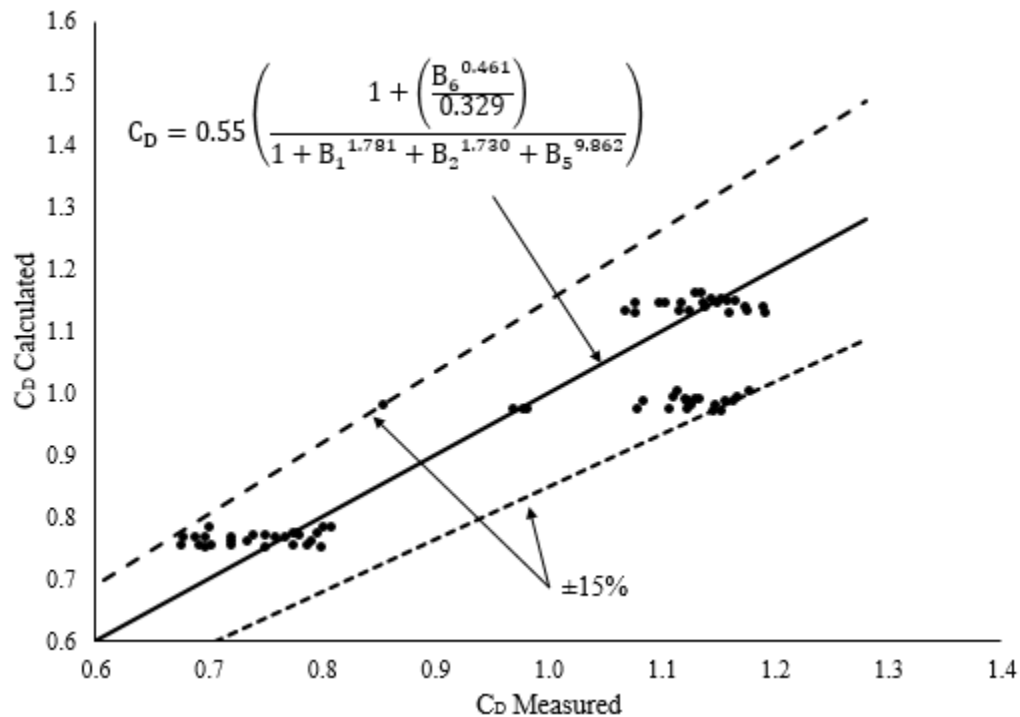


Figure 5.52 Correlation between aerodynamic drag force coefficient measured from CFD and calculated by the new methodology for various truck-trailer geometries.

### 5.10.2 Developing the Lift Coefficient Equation

Similar to the previous section, the prediction model developed in this section will be correlating B1, B2, B5 and B6 shape coefficients in order to predict the lift force coefficients. To achieve this, the force coefficients should be presented as functions of proposed shape coefficients.

$$C_L = C_L(B_1, B_2, B_5, B_6) \quad (5-12)$$

The proposed lift force coefficient prediction equation will be in a specific form so that it is capable of predicting the lift coefficient when the value for all the B shape coefficients reduce down to zero.

$$C_L = C_{L_{B_1, B_2, B_5, B_6=0}} \cdot C_{L_{B_1, B_2, B_5, B_6 \neq 0}} \quad (5-13)$$

Here, the B1, B2, B5, B6 = 0 will be represented by

$$C_{L_{B_1, B_2, B_5, B_6=0}} = A \quad (5-14)$$

And B1, B2, B5, B6 ≠ 0 will be represented as B

$$C_{L_{B_1, B_2, B_5, B_6 \neq 0}} = B \quad (5-15)$$

Therefore, the final lift force equation should be in the form of:

$$C_L = A \cdot B \quad (5-16)$$

Figure 5.53 depicts lift force coefficients for the truck-trailer geometry for changing B coefficients to (a) 0.01; (b) 0.05; (c) 0.1. The first column (a), consist of changing B1, B2, B5 and B6 coefficients one at a time, while the remaining respective B coefficients of the truck-trailer model are maintained at a constant value of 0.01. The second column (b), consist of changing B1, B2, B5 and B6 coefficients one at a time, while the remaining respective B coefficients of the truck-trailer model are maintained at a constant value of 0.05. The third column (c), consist of changing B1, B2, B5 and B6 coefficients one at a time, while the

remaining respective B coefficients of the truck-trailer model are maintained at a constant value of 0.1. It can be seen that in the case of changing B1 and B2 coefficients whilst the remaining of the respective coefficients maintain at 0.01, lift coefficient linearly increases from B1, B2 = 0.01 to B1, B2 = 0.05 then decreases from B1, B2 = 0.05 to B1, B2 = 0.1. However, in the case of changing B6 coefficient whilst the remaining of the respective coefficients maintain at 0.01, lift coefficient continuously decreases. Observing the trend through (b), it is noticed that lift coefficient at all varying B coefficients, significantly increases from B = 0.01 to B = 0.05. However, from B = 0.05 to B = 0.1, the case of varying B1, B2 and B5 coefficients show a decrease in lift coefficient, whereas in the case of varying B6 coefficient, lift coefficient slightly increases. It is noticed in (c), lift coefficient increases linearly from B1, B5, B6 = 0.01 to B1, B5, B6 = 0.05 for cases where B1, B5 and B6 are changing and the remaining B coefficients maintain at 0.1. In the case of changing B2 and the remaining B coefficients attain 0.1, lift coefficient linearly decreases from B2 = 0.01 to B2 = 0.05. From B = 0.05 to B = 0.1, cases for changing B1 and B5 coefficients, lift coefficient decreases whereas cases for changing B2 and B6, lift coefficient increases.

Once more, ‘A’ has been defined as a constant value which represent the lift force coefficient when B1, B2, B5 and B6 are all equal to zero. By studying the CFD data obtained for the lift force coefficient, following functional form was used to represent ‘B’ which incorporates the shape characteristics defined by B shape coefficients.

$$B = \left( \frac{1 + \frac{B_6^a}{C_1} \cdot C_2}{1 + \left(\frac{B_1^b}{C_3}\right) + \left(\frac{B_2^c}{C_4}\right) + \left(\frac{B_5^d}{C_5}\right)} \right) \quad (5-17)$$

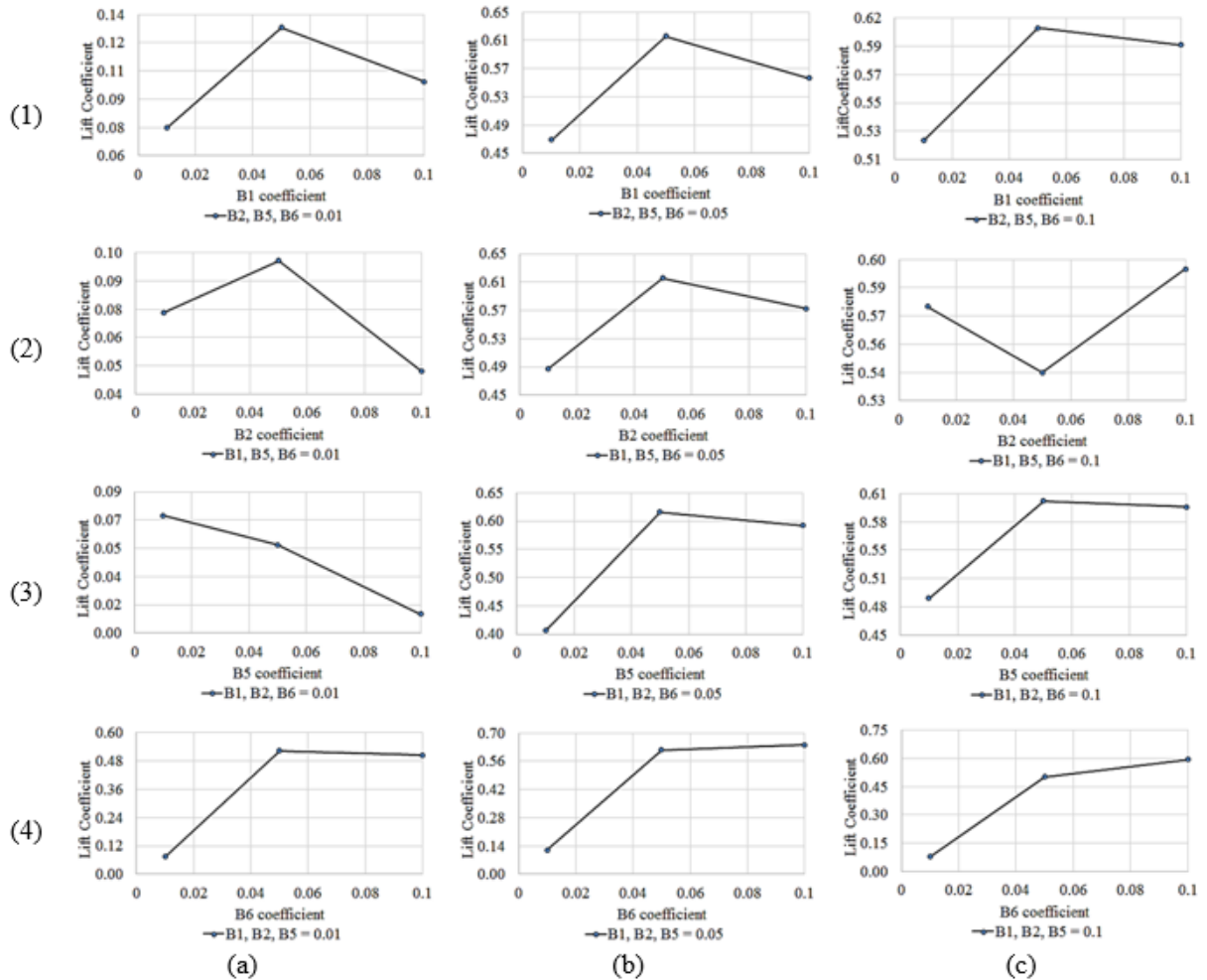


Figure 5.53 Lift force coefficients of the truck-trailer geometry with changing B coefficients to (a) 0.01; (b) 0.05; (c) 0.1

After evaluating the data set for lift force coefficient, the final form of the lift coefficient prediction equation was obtained which has been characterised by B1, B2, B5 and B6 shape coefficients. This equation can be illustrated as:

$$C_L = -0.13 \left( \frac{1 - \left( \left( \frac{2.538(B_6^{0.579})}{0.390} \right) \cdot 3.097 \right)}{1 + \left( \frac{B_1^{0.352}}{8.536} \right) + \left( \frac{B_2^{1.993}}{1.117} \right) - \left( \frac{B_5^{1.399}}{0.755} \right)} \right) \quad (5-18)$$

Figure 5.54 depicts the correlation between the predicted values of the aerodynamic lift force coefficients, and those obtained from CFD. Once again, it can be clearly seen that the predicted values agree very well with those obtained from CFD. The standard error of estimate has been calculated to be around 15%. Hence, equation (5-18), developed for characterising the aerodynamic lift force coefficient in terms of the proposed truck-trailer shape parameters is well capable of providing accurate predictions in place of CFD data.

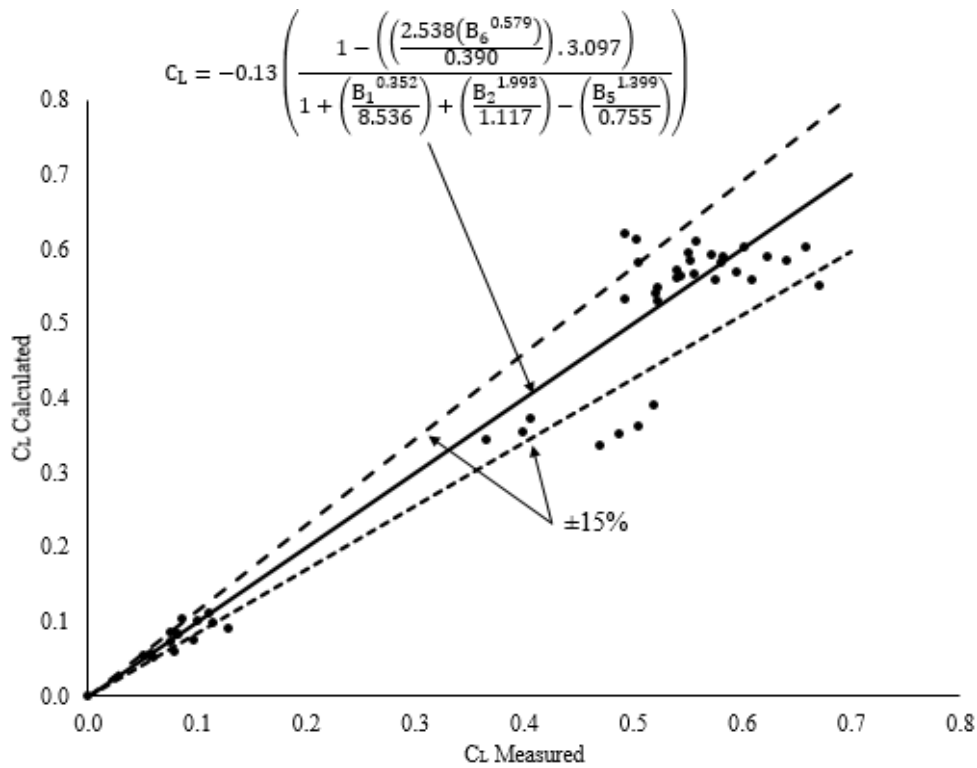


Figure 5.54 Correlation between aerodynamic drag force coefficient measured from CFD and calculated by the proposed prediction methodology for various truck-trailer geometries.

## 5.11 Summary

The capabilities of using the proposed geometrical modelling methodology to generate truck-trailer geometries with varying shapes have been explored. Truck top leading and trailing edges and trailer top leading and trailing edges were chosen as the key areas for design alterations using the proposed design methodology. Each edge profile was changed between three different levels and the corresponding truck-trailer CAD models were prepared for numerical simulations. Extensive CFD based aerodynamic analysis had been carried out using the generated truck-trailer models at straight headwind condition to analyse the shape effects on the resulting flow field. Increasing B1 shape coefficient from 0.01 to 0.1 has completely eliminated the flow recirculation region at the top of the truck unit and increased the oncoming flow velocity towards the truck-trailer unit. The B1 shape modification has significantly affected the pressure on the front half of the truck-trailer unit while pressure variations on the rear half of the truck-trailer unit were marginal. Increasing B2 shape coefficient from 0.01 to 0.1 has not had a significant effect on the overall flow field in the vicinity of the truck-trailer unit. However, at  $B2 = 0.1$ , the shape alteration has had a positive impact on the flow circulation region at the truck-trailer gap by directing more structured flow and reducing the circulation. Increasing B5 shape coefficient from 0.01 to 0.1 was observed to significantly increase the flow velocity on top of the trailer unit. This was due to the reduction of stagnation pressure region near the top leading edge of the trailer unit. Increasing B6 shape coefficient from 0.01 to 0.1 has reduced the wake flow region situated behind the trailer rear face by directing flow from top of the trailer unit into the wake flow region. This in turn has increased the pressure on the rear trailer surface and the surrounding flow regions. It was also noted that as the values of B1, B2 and B5 shape coefficients increased from 0.01 to 0.1, the drag force respectively decreased and the opposite was true for the B6 shape coefficient. Using the data gathered in the analysis stage, a force prediction methodology has been developed. The prediction methodology was validated against the CFD data and was proven to be capable of predicting drag, lift and side forces at straight headwind for varying truck-trailer shapes with a reasonable accuracy.

## CHAPTER 6

# DEVELOPMENT OF A MATHEMATICAL MODEL TO PREDICT AERODYNAMIC FORCES BASED ON TRUCK-TRAILER SHAPE PARAMETERS AT CROSSWIND CONDITIONS

---

The effects of altering the shape of leading and trailing edges of both truck and trailer units, and the corresponding effects on the surrounding flow regions at straight head wind condition were analysed and quantified from the previous chapter. However, the high-sided truck-trailer units are also subjected to aerodynamic crosswinds. The crosswinds are capable of introducing significant alterations to the flow field in the vicinity of a truck-trailer unit affecting aerodynamics characteristics and giving rise to safety concerns. In this chapter, the effects of changing the shape of leading and trailing edges of both truck and trailer units and the resulting effects on the surrounding flow field at various crosswind flow angles were analysed using both qualitative and quantitative means. Using the information gathered during the analysis, a prediction model is developed which is capable of accurately predicting the aerodynamic performance indicators such as drag, lift and side force coefficients for various truck-trailer shapes at various crosswind flow angles.

## 6.1 Introduction into the effect of crosswinds on the truck-trailer unit

Truck-trailer units are extremely prone to the disturbances caused by crosswinds and is a major safety issue. Truck-trailer accidents due to overturning or getting blown across lanes are a common occurrence throughout the UK under powerful crosswinds. The aerodynamic side force is generated due to the pressure difference between windward and leeward faces. As a truck-trailer unit consists of two separate bodies and a gap between the truck unit and the trailer unit, the cross flow structure is considerably more complex when compared to a single body vehicle.

## 6.2 Flow field in the vicinity of a Truck-trailer unit at crosswinds

The introduction of crosswinds, significantly change the flow structure in the vicinity of a truck-trailer unit. This in turn alters the aerodynamic forces acting on a truck-trailer unit introducing adverse effects on the economy and stability. In this chapter the effects of crosswinds on a truck-trailer unit with changing B1, B2, B5 and B6 shape coefficients is discussed. However, overall length and the height of the truck-trailer geometry has been fixed at 16.28m and 4.8m, respectively meanwhile crossflow was modelled at 15°, 30°, 45°, 60°, 75° and 90° angles. Prior to analysing the effect of changing truck-trailer geometries under crosswinds it is important to obtain the general overview of the flow field alterations under crosswinds. Figure 6.1 depicts the variations in crosswind flow velocity in the vicinity of the truck-trailer model at (a)  $\psi = 30^\circ$ , (b)  $\psi = 60^\circ$  and (c)  $\psi = 90^\circ$ . It can be seen from (a) that relatively less flow separation occurs resulting in a wake flow region seen at  $\psi = 30^\circ$ . Higher velocities such as 25m/s, 23m/s and 20m/s are seen close to the windward faces of the truck-trailer unit while the wake region is seen to comprise of low velocities of 1m/s to 4m/s in the immediate vicinity of the model on the leeward side. It can be seen from (b) that when the cross-flow is  $\psi = 60^\circ$ , velocity magnitude is comparatively lower than when the crossflow is  $\psi = 30^\circ$  approaching the windward direction at the trailer. On the leeward side of the trailer, although velocity magnitude is fairly low, even lower velocities manifests from the front of the trailer on the leeward side towards the rear of the trailer. This region of low velocity has elongated comparatively greater than that depicted when the crossflow is  $\psi = 30^\circ$ . When the crossflow is  $\psi = 30^\circ$ , the velocity magnitude of 1 m/s is situated at the rear of the trailer, whereas, when the crossflow is  $\psi = 60^\circ$ , the velocity magnitude of 1m/s is situated at a distance away from the trailer almost in line with the leeward side of the

trailer. It can be seen from (c) that when the crosswind is  $\psi = 90^\circ$ , even lower velocity magnitude on the windward side propagates along the length of the trailer at the windward side. Velocity magnitude has reached 1 m/s in proximity of the central region of the windward side of the trailer. This implies the flow has reached a stagnant zone. On the leeward side of the trailer the velocity at the truck propagates to merge with the wake region of the trailer, which has manifested itself to be even greater than when the crosswind is  $\psi = 60^\circ$ .

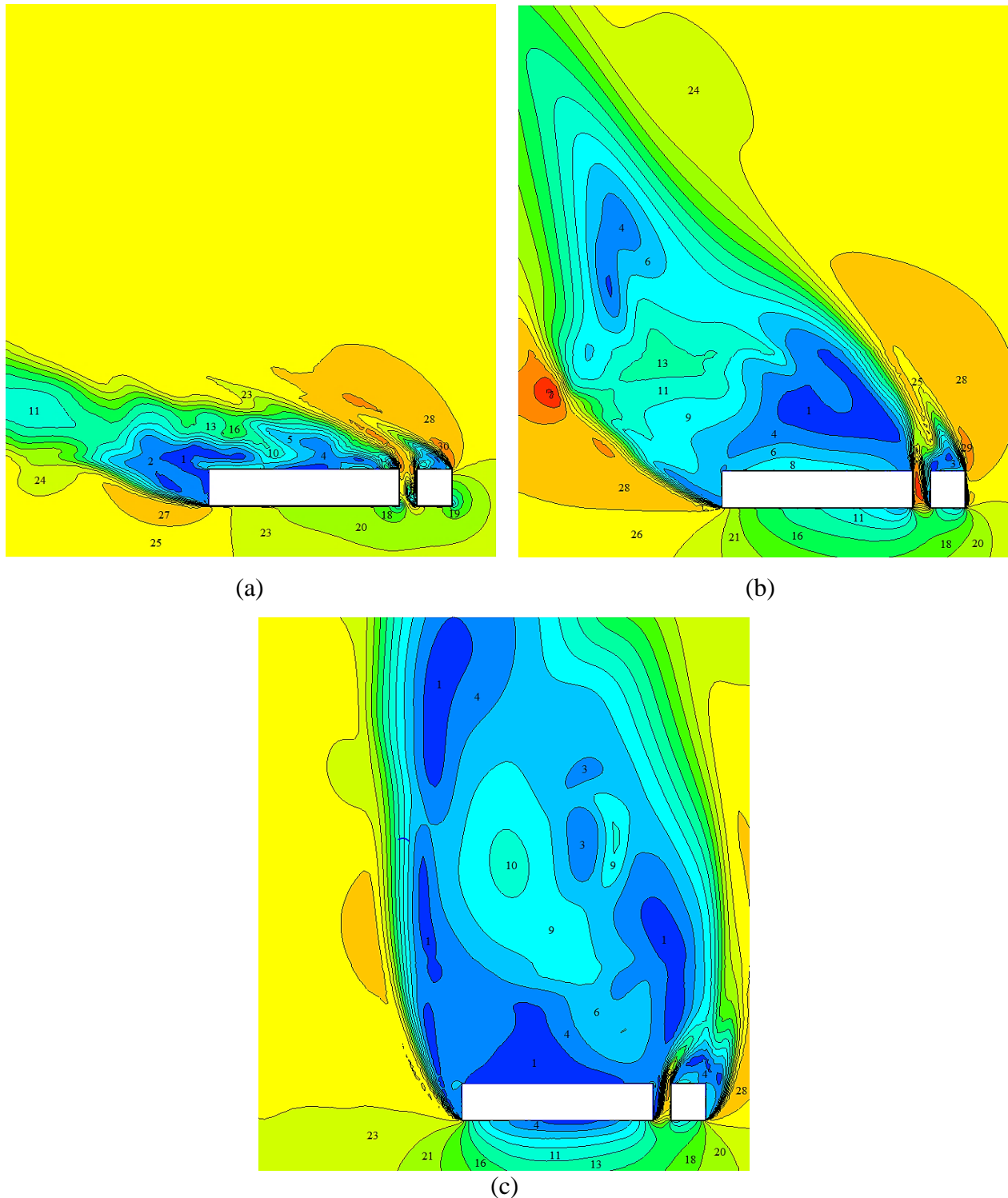


Figure 6.1 Variations in flow velocity in the vicinity of the truck-trailer model at yaw flow angles ( $\psi$ ) of (a) 30° (b) 60° and (c) 90°.

The velocity profiles on the leeward side of the truck-trailer unit at  $\psi = 30^\circ$ ,  $\psi = 60^\circ$  and  $\psi = 90^\circ$  are depicted from Figure 6.2 on a plane located at  $\frac{x}{l} = 0.5$ . At  $\psi = 30^\circ$  the smallest flow circulation region is observed at (a) and this area is seen to extend up to  $\frac{z}{w} = 2.5$ . Three distinctive flow recirculation zones are observed close to the leeward side of the trailer unit where the flow is seen to move towards the trailer. A slightly more extended flow recirculation region is seen when  $\psi = 60^\circ$ , where the region extends up to  $\frac{z}{w} = 4$ . In this case, the circulation zones have reduced to two where one was observed towards the top of the trailer unit and the other towards the bottom of the trailer unit. Once more, the circulation flow is seen to move towards the leeward trailer surface and impinge on the surface. The bottom circulation region is seen to be much more prominent than the top circulation region. The flow circulation region extends from the leeward trailer surface considerably at  $\psi = 90^\circ$  to a distance of  $\frac{z}{w} = 7$ . In this case, a single circulation zone is seen to exist on the leeward side of the trailer unit. Yet again, the flow in the circulation region is seen to move towards the trailer surface. The flow circulation occurs due to flow separation over the sharp edges around the truck-trailer unit. The shear action between the fast moving fluid layer on top the trailer unit and the slow moving separated flow causes flow circulation and the energy is transferred from the fast moving fluid layer into the circulation regions to keep the flow rotating.

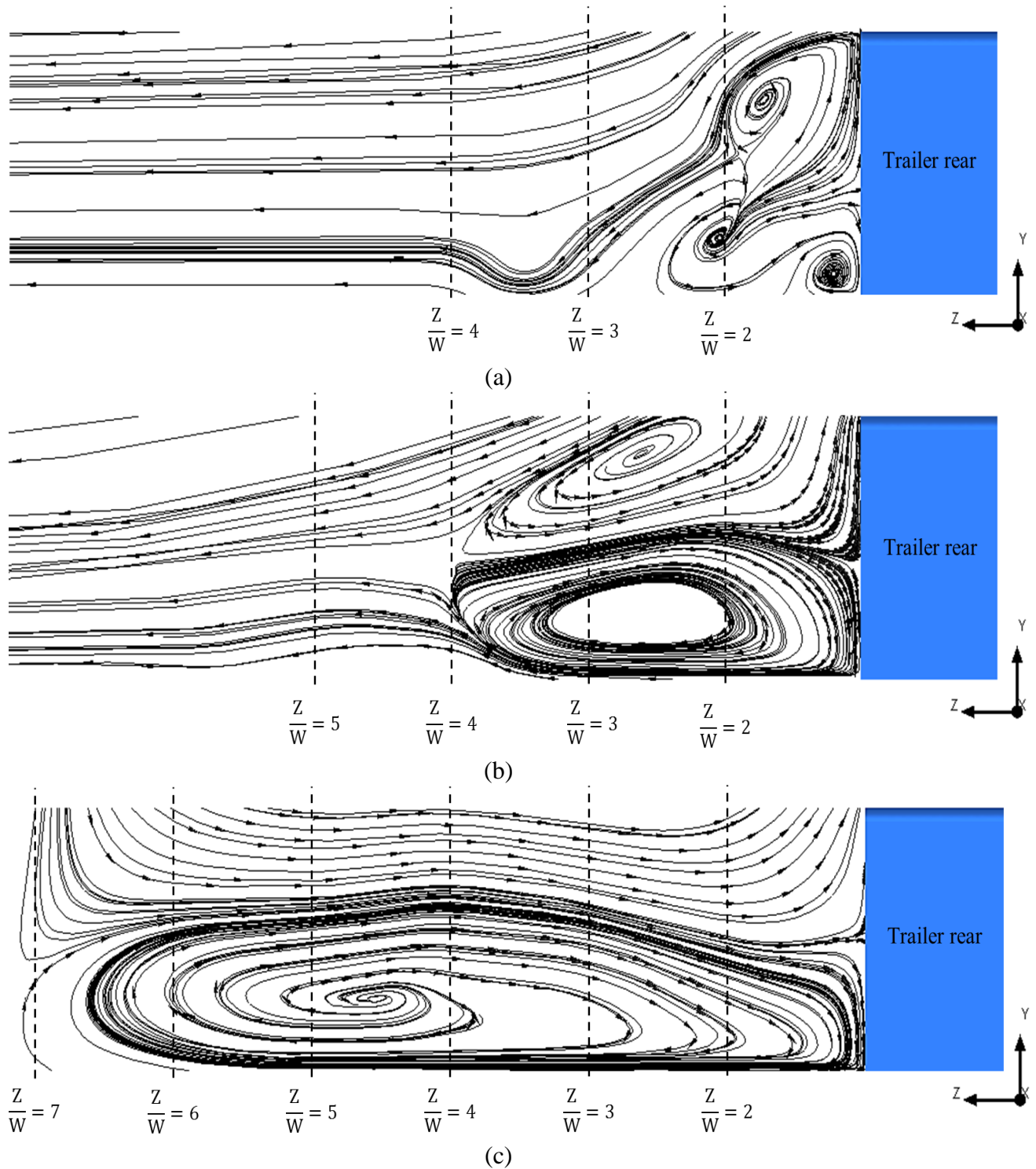


Figure 6.2 Velocity streamlines on the leeward side of the truck-trailer model at yaw flow angles ( $\psi$ ) of (a)  $30^\circ$  (b)  $60^\circ$  and (c)  $90^\circ$ .

### 6.3 Effect of B1 on the truck-trailer unit performance under crosswinds

The effects of crosswinds on the flow field around the baseline truck-trailer unit has been discussed in detail in chapter 4. The front face of the truck unit is a key contributor to aerodynamic drag force as it comes into direct contact with the oncoming flow generating the largest stagnation pressure region throughout the pressure spectrum. The  $C_P$  variations on the key truck-trailer surfaces including the truck front face at various B shape coefficients has been discussed in chapter 5. This section will discuss the  $C_P$  variation on the front face of the truck unit when  $B1 = 0.01$  and  $B1 = 0.1$  at yaw angles  $30^\circ$ ,  $60^\circ$  and  $90^\circ$  as shown in Figure 6.3 (a) Figure 6.3 (b) and Figure 6.3(c), respectively. In both cases, it can be seen that the stagnation pressure region has moved towards the windward side and then the  $C_P$  is gradually seen to decrease towards the leeward side of the truck front surface. At  $\psi = 30^\circ$ , the flow is expected to directly impact the truck front surface closer to the left edge and hence pressure distribution is expected. A highly concentrated low pressure region with  $C_P = -2.4$  is seen closer to the top leading edge at (a). When the shape of the leading edge profile is changed from  $B1 = 0.01$  to  $B1 = 0.1$  as shown in (b), a relative increase in pressure at the top edge of the truck face is observed where  $C_P$  has increased up to  $-1.6$ . However, the shape change is seen to reduce  $C_P$  in the top 1/3 area of the truck front surface having a more prominent effect on the surface pressure profile. Figure 6.3 (c) and (d) corresponds to  $B1 = 0.01$  at  $\psi = 60^\circ$  and  $B1 = 0.1$  at  $\psi = 60^\circ$ , respectively. It is quite evident that as yaw angle increases to  $60^\circ$ , the positive pressure regions have been completely diminished and are non-existent. This is due to the shear layer separation at the windward edge of the truck front surface producing low pressures. The highest pressure of  $C_P = -0.03$  is seen on the centre of the surface for both  $B1 = 0.01$  and  $B1 = 0.1$  models while a low pressure region is seen just after the flow separation point for the latter model. Figure 6.3 (e) and (f) corresponds to  $B1 = 0.01$  and  $B1 = 0.1$  both at  $\psi = 90^\circ$ , respectively. Largely similar pressure distribution is seen for both B models with slight variations closer to the leeward edge of the surface. At  $\psi = 90^\circ$ , the stagnation pressure region is expected to shift on to the windward side of the truck unit while a separation bubble is expected on the truck front surface with reversing flow taking place across the surface from leeward side to windward side. As a result, the lowest pressure on the truck front surface has been observed at  $\psi = 90^\circ$ .

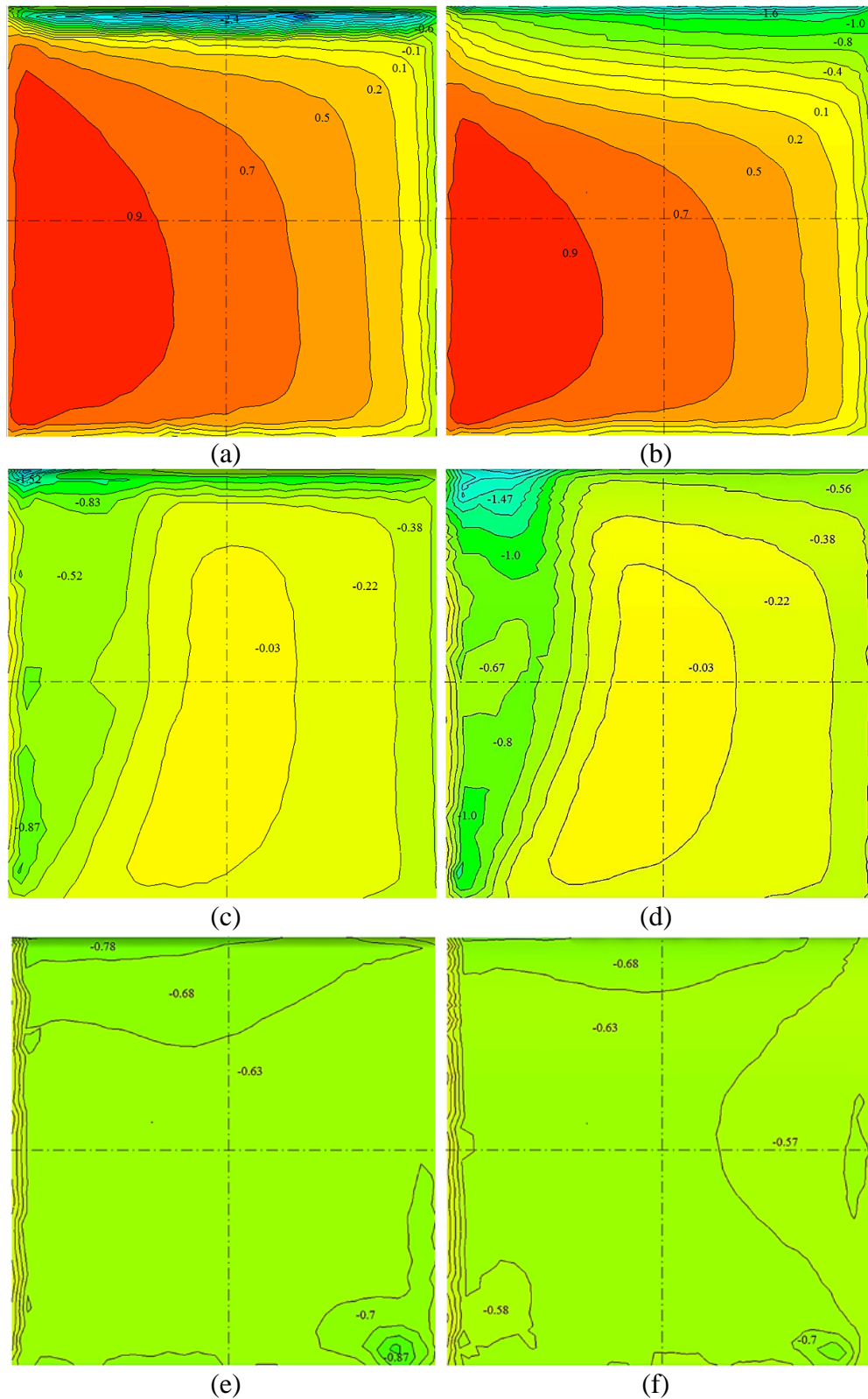


Figure 6.3 Variations in coefficient of pressure ( $C_p$ ) on the front face of the truck unit with  $B1 = 0.01$  (left) and  $B1 = 0.1$  (right), where  $\psi = 30^\circ$  (top);  $\psi = 60^\circ$  (middle);  $\psi = 90^\circ$  (bottom).

It is evident from the above section that under crosswind conditions, the pressure distribution on the truck front face becomes highly asymmetrical. This effect is expected on all the truck-trailer surfaces and is known to significantly alter the aerodynamic forces experienced by the truck-trailer unit. Therefore, quantification of the asymmetrical pressure distribution is necessary to understand the pressure unbalance on key truck-trailer surfaces as the vehicle is subjected to various crossflow operating conditions. Moreover, it was important to capture the changes in pressure distribution on a surface for changing B shape profiles.

In order to achieve this, the selected truck-trailer surfaces were divided in to two sections as windward and leeward side as demonstrated in Figure 6.4. A vertical data line was positioned along the centre of windward side and another was positioned along the centre of leeward side extending from bottom of the surface to the top of the surface. Figure 6.4 depicts the schematics of the setup on truck front surface for both  $B1 = 0.01$  and  $B1 = 0.1$  models. The average pressure coefficient data were obtained for each line and this is expected to provide accurate information to quantify the pressure variations under crossflow conditions.

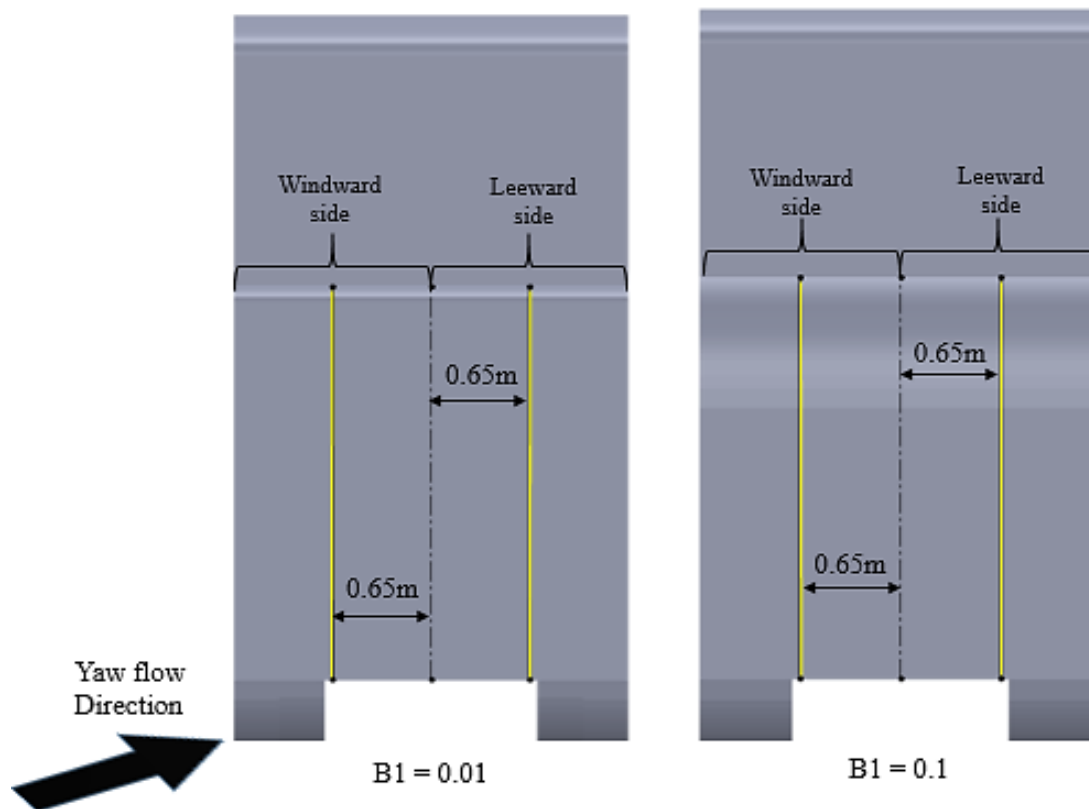


Figure 6.4 The data lines (Highlighted) position on either side of truck front surface which will be used to extract average pressure coefficient data.

Figure 6.5 demonstrates the average pressure coefficient on the truck front surface for  $B1 = 0.01$  and  $B1 = 0.1$  models from  $\psi = 15^\circ$  to  $\psi = 90^\circ$  in  $15^\circ$  degree increments. Truck front surface is seen to experience positive pressures up to  $\psi = 45^\circ$  and negative pressure between  $\psi = 60^\circ$  and  $\psi = 95^\circ$ . Highest average  $C_P$  of 0.73 is observed on the windward side of the  $B1 = 0.01$  truck surface at  $\psi = 15^\circ$  and this is seen to reduce by 13.7% as the shape of the surface changes to  $B1 = 0.1$ . Lowest average  $C_P$  of -0.91 was recorded on the windward side at  $\psi = 75^\circ$  for  $B1 = 0.1$  model. Up to  $\psi = 45^\circ$ , higher pressures were seen on the windward side compared with the leeward side. However, from  $\psi = 60^\circ$  onwards the opposite was seen to be true, where the leeward side was observed to be experiencing higher pressures than the windward side. At  $\psi = 15^\circ$ , a 24.6% decrease in average  $C_P$  from windward side to leeward side was observed for the  $B1 = 0.01$  model while for  $B1 = 0.1$  model, a 31.7% decrease from windward side to leeward side was recorded. At  $\psi = 30^\circ$ , a 52.4% decrease in average  $C_P$  from windward side to leeward

side was observed for the  $B1 = 0.01$  model while for  $B1 = 0.1$  model, a 61.1% decrease from windward side to leeward side was recorded. At  $\psi = 45^\circ$ , a 91.1% decrease in average  $C_P$  from windward side to leeward side was observed for the  $B1 = 0.01$  model while for  $B1 = 0.1$  model, a 111.1% decrease from windward side to leeward side was recorded. The pressure difference on either sides of the front surface is seen to increase as the yaw angle increases and when the shape coefficient is changed from  $B1 = 0.01$  to 0.1 the pressure difference consequently increases. At  $\psi = 60^\circ$ , a 60% increase in average  $C_P$  from windward side to leeward side was observed for the  $B1 = 0.01$  model while for  $B1 = 0.1$  model, a 61.5% increase from windward side to leeward side was recorded. At  $\psi = 75^\circ$ , a 40% increase in average  $C_P$  from windward side to leeward side was observed for the  $B1 = 0.01$  model while for  $B1 = 0.1$  model, a 40.6% increase from windward side to leeward side was recorded. At  $\psi = 90^\circ$ , a 3% increase in average  $C_P$  from windward side to leeward side was observed for the  $B1 = 0.01$  model while for  $B1 = 0.1$  model, a 3.3% increase from windward side to leeward side was recorded. The pressure difference on either sides of the front surface is seen to decrease as the yaw angle increases from  $60^\circ$  to  $90^\circ$ . When the shape coefficient is changed from  $B1 = 0.01$  to 0.1, the pressure difference consequently shows a slight increase.

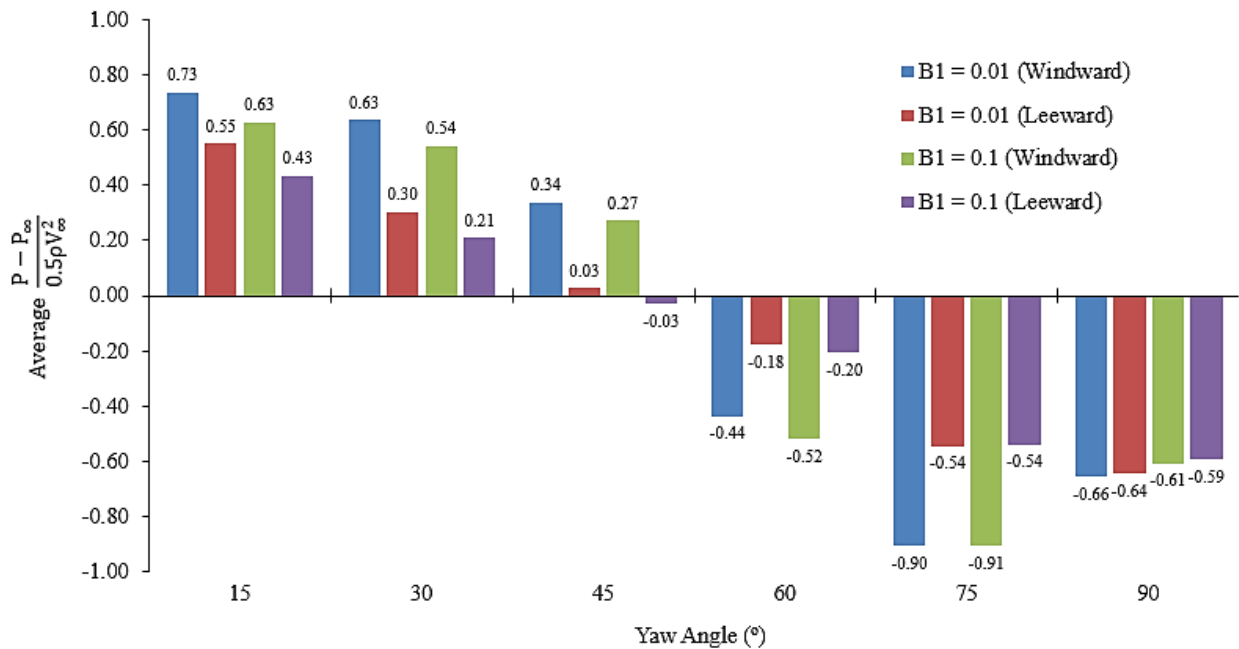


Figure 6.5 The average pressure coefficient on the truck front surface for  $B1 = 0.01$  and  $B1 = 0.1$  models from  $\psi = 15^\circ$  to  $\psi = 90^\circ$ .

Truck front surface is crucial when analysing the aerodynamic force acting on a truck-trailer unit as this surface comes into direct contact with the oncoming flow. The force acting on a surface is expected to vary as a result of disparities in the pressure profiles. Therefore, it is of great interest to see how the variations in pressure on the truck front surface affect the force acting on the surface. Figure 6.6 depicts the forces acting on the truck front surface for  $B1 = 0.01$  and  $B1 = 0.1$  models between  $\psi = 15^\circ$  and  $\psi = 90^\circ$ . The force calculated normal to the surface is shown from (a) and it is evident that as yaw angle increases the force acting normal to the surface decreases. This trend can be seen to exhibit from  $\psi = 15^\circ$  to  $\psi = 75^\circ$ . From here to  $\psi = 90^\circ$  the forces acting on the surface begins to rise. Highest positive force of 1490N and negative force of -1902N has been recorded at  $\psi = 15^\circ$  and  $\psi = 75^\circ$ , respectively for  $B1 = 0.01$  model where a negative (sign of) value indicates the direction of force. It can be seen that the  $B1 = 0.1$  model initially exhibits lower forces than the  $B1 = 0.01$  model up to  $\psi = 75^\circ$ , from which it rises above the  $B1 = 0.01$  model to  $\psi = 90^\circ$ . Correlating Figure 6.5 with Figure 6.6, it can be clearly identified that the force increases and decreases proportionally with pressure. When the pressure decreases from  $\psi = 15^\circ$  to  $\psi = 75^\circ$ , force also decreases depicting  $B1 = 0.01$  with lower pressures. Additionally, when the pressure increases from  $\psi = 75^\circ$  to  $\psi = 90^\circ$ , force also increases depicting in this instance  $B1 = 0.1$  with higher pressure and force. A reduction in force of 18.6% from  $B1 = 0.01$  at  $\psi = 15^\circ$  is observed. This difference in force correlates with the 13.7% and 21.8% reduction in pressure for windward and leeward sides from  $B1 = 0.01$  model to  $B1 = 0.1$  model. The force calculated in the positive Y direction for the truck front surface is shown in (b). Significantly higher forces were observed for the  $B1 = 0.01$  model compared to  $B1 = 0.1$  model for all yaw angles except when  $\psi = 75^\circ$ , where in that case the force value obtained was almost the same magnitude. Mostly, the front truck surface is not expected to be associated with vertical forces with such magnitudes but in this instant, the curved surface extended on to the truck top surface providing high vertical pressure magnitudes. Increases in shear layer separation is expected at the top leading edge of  $B1 = 0.01$  truck model generating lower pressure at the top of the truck front surface. Also, when the leading edge profile is  $B1 = 0.1$ , the shear layer separation is delayed and flow stays attached. This in turn reduces the pressure forces and increases viscous forces. The resulting force reduction for  $B1 = 0.1$  model is quite evident as seen in (b). The force calculated in the positive Z direction for the truck front surface is shown in (c). Minimal force variations

between the two models can be observed and the magnitude of the force is observed to be quite low.

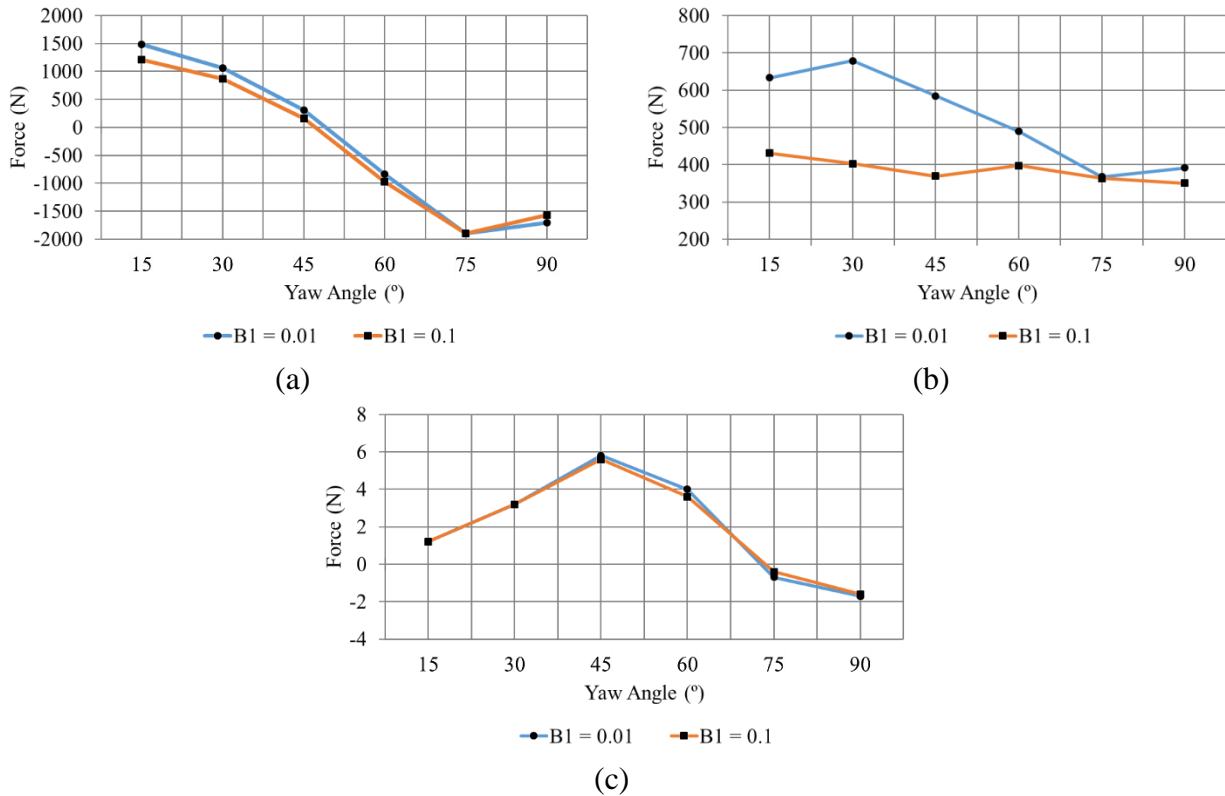


Figure 6.6 The force acting on the truck front surface in the positive X direction (a) positive Y direction (b) and positive Z direction (c) for B1 = 0.01 and B1 = 0.1 models from  $\psi = 15^\circ$  to  $\psi = 90^\circ$ .

#### 6.4 Effect of B2 on the truck-trailer unit performance under crosswinds

Truck rear surface is located next to the truck-trailer gap region where complex and highly asymmetrical flow structures are exhibited under crosswind conditions. The recirculating wake flow structure in the gap region when  $\psi=0^\circ$  is seen to change significantly at crosswinds and act as a passage for the flow to move from windward side to leeward side of the vehicle as seen in Figure 6.1. This will affect the pressure distribution on the truck rear surface and  $C_p$  variation on the truck rear surface when  $B2 = 0.01$  and  $B2 = 0.1$  at yaw angles  $30^\circ$ ,  $60^\circ$  and  $90^\circ$  as shown in Figure 6.7 (a) Figure 6.7 (b) and Figure 6.7 (c), respectively. The highest pressures of around 0.4 is seen when  $\psi = 30^\circ$  and the lowest pressures of around -0.9 was observed when  $\psi = 60^\circ$ . At  $\psi$

=  $30^\circ$ , comparatively higher pressures are seen across the  $B2 = 0.1$  model. In both models, there are high pressure regions existing at bottom left side of the surface. For  $B2 = 0.1$ , this region of high pressure is much more prominent and elongated across the bottom than that depicted in  $B2 = 0.01$ . It can also be seen that pressure decreases uniformly towards the top of the surface with a low pressure region concentrated on the top right of the surface. In the case  $B2 = 0.01$ , the general overall trend of pressure being found to decrease towards the top of the surface, also exists. However, the pressure appears to fluctuate in some areas. Further to this, low pressure region is distributed along the top of the surface, which remains slightly higher than that depicted in  $B2 = 0.1$ . At  $\psi = 60^\circ$ , the positive  $C_P$  regions have completely disappeared. As the  $B2$  increased to 0.1, the pressure is seen to further reduce, near the top edge  $C_P$  was observed to be -1.13. It was also observed that when  $B2 = 0.01$ , low pressures exist on the windward side and high pressures exist on the leeward side. However, in the case of  $B2 = 0.1$  model, low pressures are seen to exist towards the top of the surface while the higher pressures are seen to exist towards the bottom of the surface. At  $\psi = 90^\circ$ , a slight increase in pressure was observed on both models. A more uniform pressure distribution is exhibited in  $B2 = 0.01$  model and a low pressure region extending along the length of the top edge has been observed. In  $B2 = 0.1$  model, the low pressure region is concentrated on top right side of the surface.

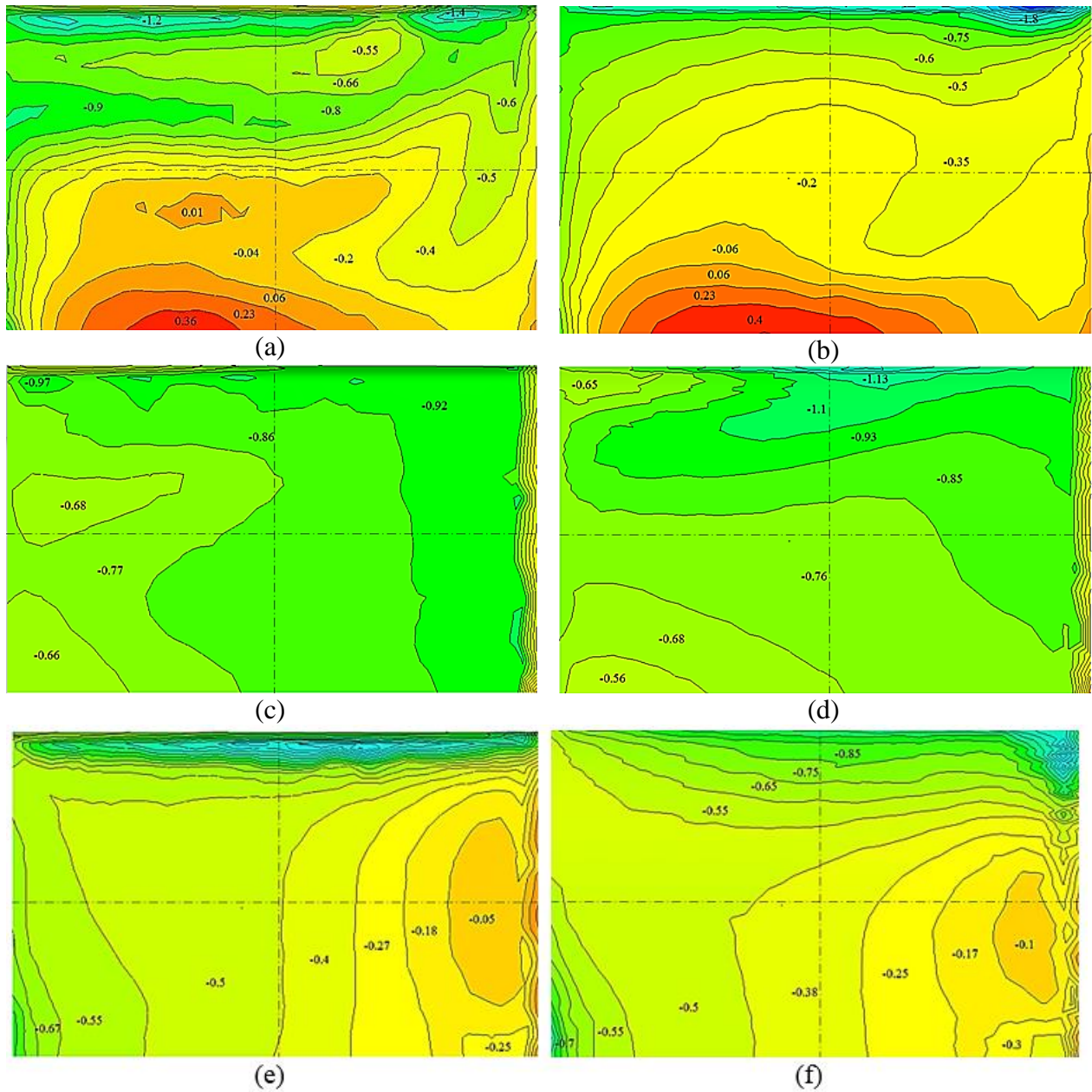


Figure 6.7 Variations in coefficient of pressure ( $C_p$ ) on the rear face of the truck unit with  $B_2 = 0.01$  (left) and  $B_2 = 0.1$  (right), where  $\psi = 30^\circ$  (top);  $\psi = 60^\circ$  (middle);  $\psi = 90^\circ$  (bottom).

Figure 6.8 demonstrates the average pressure coefficient on the truck rear surface for  $B_2 = 0.01$  and  $B_2 = 0.1$  models from  $\psi = 15^\circ$  to  $\psi = 90^\circ$  in  $15^\circ$  degree increments. Once more, two data lines were generated on the windward and leeward sides of the surface and average  $C_p$  was calculated on each line. At a first glance, it is evident that the negative  $C_p$  exists on the truck rear surface throughout the full yaw range. The highest pressure of  $-0.19$  is observed at  $\psi = 15^\circ$  and  $\psi$

= 30° for B2 = 0.01 and B2 = 0.1 model, respectively whereas, the lowest pressure of -0.91 was observed for B2 = 0.01 model when  $\psi = 60^\circ$ . Between  $\psi = 30^\circ$  and  $\psi = 75^\circ$  the leeward side is seen to be subjected to higher pressures compared to windward side. At  $\psi = 15^\circ$ , a pressure reduction of 26.3% is observed from the windward side to the leeward side for B2 = 0.01 model. However, on the B2 = 0.1 model, a  $C_p$  of -0.23 is observed for both sides. When  $\psi = 30^\circ$ , a 27% increase in pressure is observed from windward side to leeward side for B2 = 0.01 model. For B2 = 0.1 model, a considerably high 40.6% pressure increase was observed. When  $\psi = 45^\circ$ , a 20.8% increase in pressure is observed from windward side to leeward side for B2 = 0.01 model and for B2 = 0.1 model, 32.8% increase in pressure was recorded. At  $\psi = 60^\circ$  the pressure difference between windward and leeward sides seem to reduce but highest negative pressures are observed at this yaw angle. In this case a 14.3% increase in pressure is observed from windward side to leeward side for B2 = 0.01 model and for B2 = 0.1 model, 6% increase in pressure was recorded. At  $\psi=75^\circ$ , a 21.7% increase in pressure is observed from windward side to leeward side for B2 = 0.01 model and for B2 = 0.1 model, 31.6% increase in pressure was recorded. However, at  $\psi = 90^\circ$  the trend was seen to behave inversely as 85.7% reduction in pressure is observed from the windward side to the leeward side for B2 = 0.01 model and for B2 = 0.1 model a reduction of 48.5% is observed.

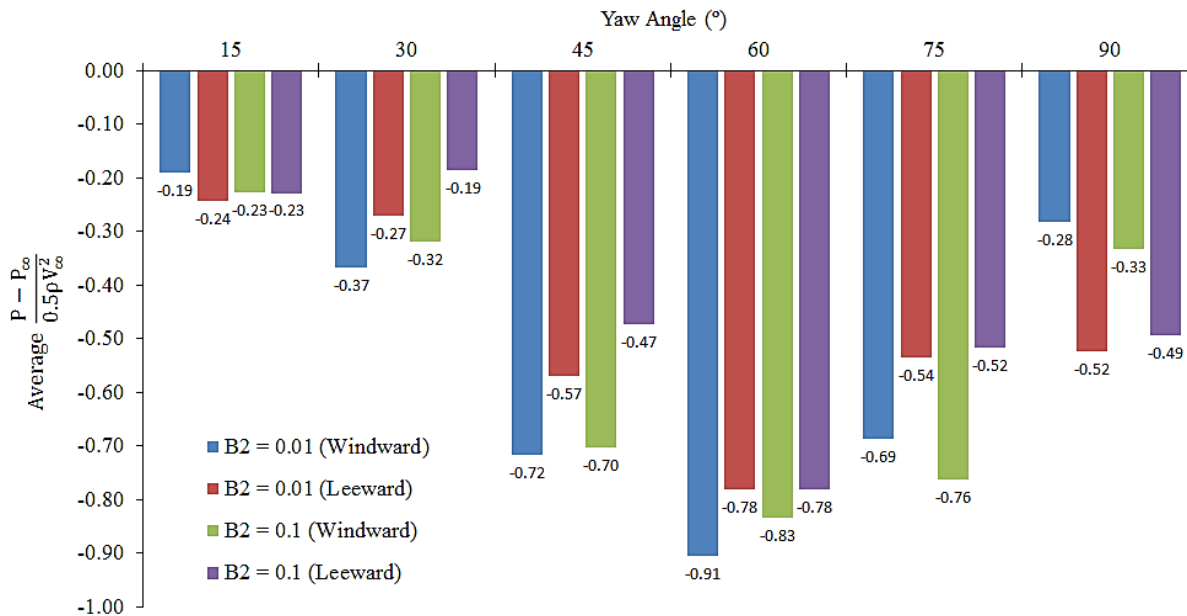


Figure 6.8 The average pressure coefficient on the truck rear surface for B2 = 0.01 and B2 = 0.1 models from  $\psi = 15^\circ$  to  $\psi = 90^\circ$

The aerodynamics around a truck-trailer unit is complicated as it is made of two separate bodies (truck and the trailer units) connected in tandem. Therefore, when calculating aerodynamic forces such as drag, lift and side, truck and the trailer units individually contribute to the overall net forces. The force acting on the truck front face has been discussed from Figure 6.6 and the force acting on truck rear surface for  $B2 = 0.01$  and  $B2 = 0.1$  models at various yaw angles is depicted in Figure 6.9. The force acting in the positive x direction to the truck rear surface is shown in (a). Generally, the force is seen to increase from a minimum of 385N at  $\psi = 15^\circ$  to a maximum of 1355N at  $\psi = 60^\circ$  before decreasing to around 740N when  $\psi = 90^\circ$ . The rear truck surface for  $B2 = 0.01$  model is seen to experience higher forces throughout the yaw flow range. Only significant differences in force, between  $B2 = 0.01$  and  $B2 = 0.1$  models were seen when  $\psi = 30^\circ$  and  $\psi = 45^\circ$  calculated as 20% and 8.6%, respectively and minute force variations were seen for rest of the yaw flow angles. Force calculated in the positive Y direction for the truck rear surface is shown in (b). The force seems to increase continuously throughout the yaw flow range for  $B2 = 0.1$  model experiencing both the minimum force of 191N when  $\psi = 15^\circ$  and a maximum force of 486N when  $\psi = 90^\circ$ . It is also observed that up to  $\psi = 60^\circ$ ,  $B2 = 0.1$  model is subjected to higher forces than  $B2 = 0.01$  model and vice versa for  $\psi = 75^\circ$  and  $\psi = 90^\circ$ . The force calculated in the positive Z direction for the truck rear surface is shown in (c). Once more, minimal force variations between the two models have been observed and the magnitude of the forces obtained throughout the yaw range is seen to be quite low.

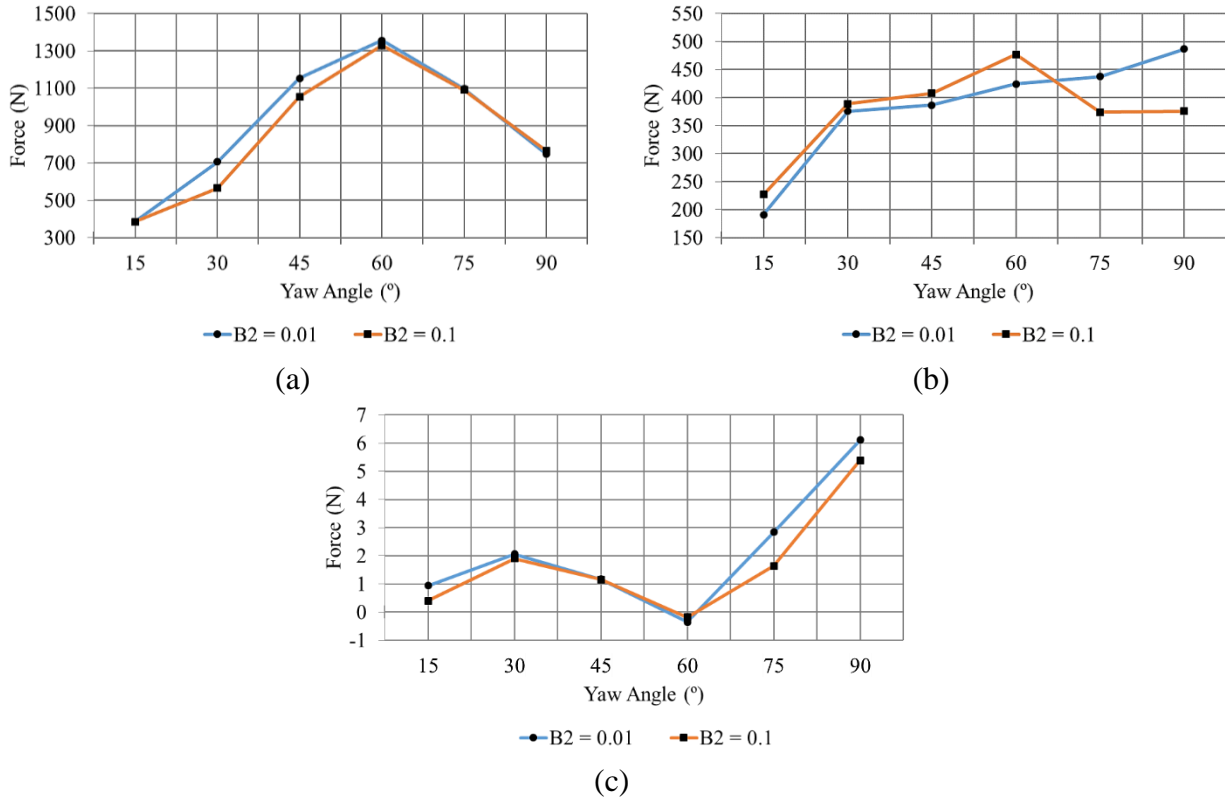


Figure 6.9 The force acting on the truck rear surface in the positive X direction (a) positive Y direction (b) and positive Z direction (c) for B2 = 0.01 and B2 = 0.1 models from  $\psi = 15^\circ$  to  $\psi = 90^\circ$

## 6.5 Effect of B5 on the truck-trailer unit performance under crosswinds

Naturally, the trailer unit is greater in height compared to the truck unit. This means the trailer unit also comes directly in contact with the oncoming flow generating a significant stagnation pressure towards the top edge on the trailer front face as shown in Figure 5.49. However, at crosswinds this is expected to change. In a similar fashion to above section, this section will discuss the  $C_p$  variation on the front face of the trailer unit when B5 = 0.01 and B5 = 0.1 at yaw angles  $30^\circ$ ,  $60^\circ$  and  $90^\circ$  as shown in Figure 6.10. Figures 6.10 (a) and (b) corresponds to B5 = 0.01 at  $\psi = 30^\circ$  and B5 = 0.1 at  $\psi = 30^\circ$ , respectively. At a first glance, it can be seen that in both cases stagnation pressure region has moved towards the windward side and then the  $C_p$  is gradually seen to decrease towards the leeward side of the trailer front surface. At  $\psi = 30^\circ$ , it is expected that some of the oncoming flow to directly impact the trailer front surface closer to the

windward side causing asymmetrical pressure distribution throughout the surface. A highly concentrated low pressure region with  $C_p = -2.3$  is seen closer to the top leading edge at (a). When the shape of the leading edge profile is changed from  $B5 = 0.01$  to  $B5 = 0.1$  as shown in (b), a relative increase in pressure around the top edge of the trailer face is observed where  $C_p$  has increased up to  $-0.65$ . Figures 6.10 (c) and (d) corresponds to  $B5 = 0.01$  at  $\psi = 60^\circ$  and  $B5 = 0.1$  at  $\psi = 60^\circ$ , respectively. Once again, as yaw increases to  $60^\circ$ , the positive pressure regions are non-existent. This is due to the shear layer separation at the windward edge of the trailer front surface producing low pressures. The highest  $C_p = -0.50$  and  $-0.62$  is seen on the centre of the surface for both  $B5 = 0.01$  and  $B5 = 0.1$  models respectively. Two small clusters of  $C_p = -0.55$  are noticed closer to windward and leeward sides on the latter model. There is a 52.2% increase in  $C_p$  value of (c) in the low pressure region existing near the top edge compared with (a). Similarly, the low pressure region on Figure (c) seems to be eliminated once the profile change occurs ( $B5 = 0.1$  model). Figure 6.10 (e) and (f) corresponds to  $B5 = 0.01$  and  $B5 = 0.1$  at  $\psi = 90^\circ$  respectively. Both models share some similarities close to the windward side however, the latter model has a relatively higher  $C_p = -0.44$  at the centre of the trailer. It has been noticed that on the  $B5 = 0.01$  model,  $C_p$  variation exists across the surface of the trailer whereas on the  $B5 = 0.1$  model, a very large portion of the trailer surface has a uniform  $C_p$  value of  $-0.44$ .

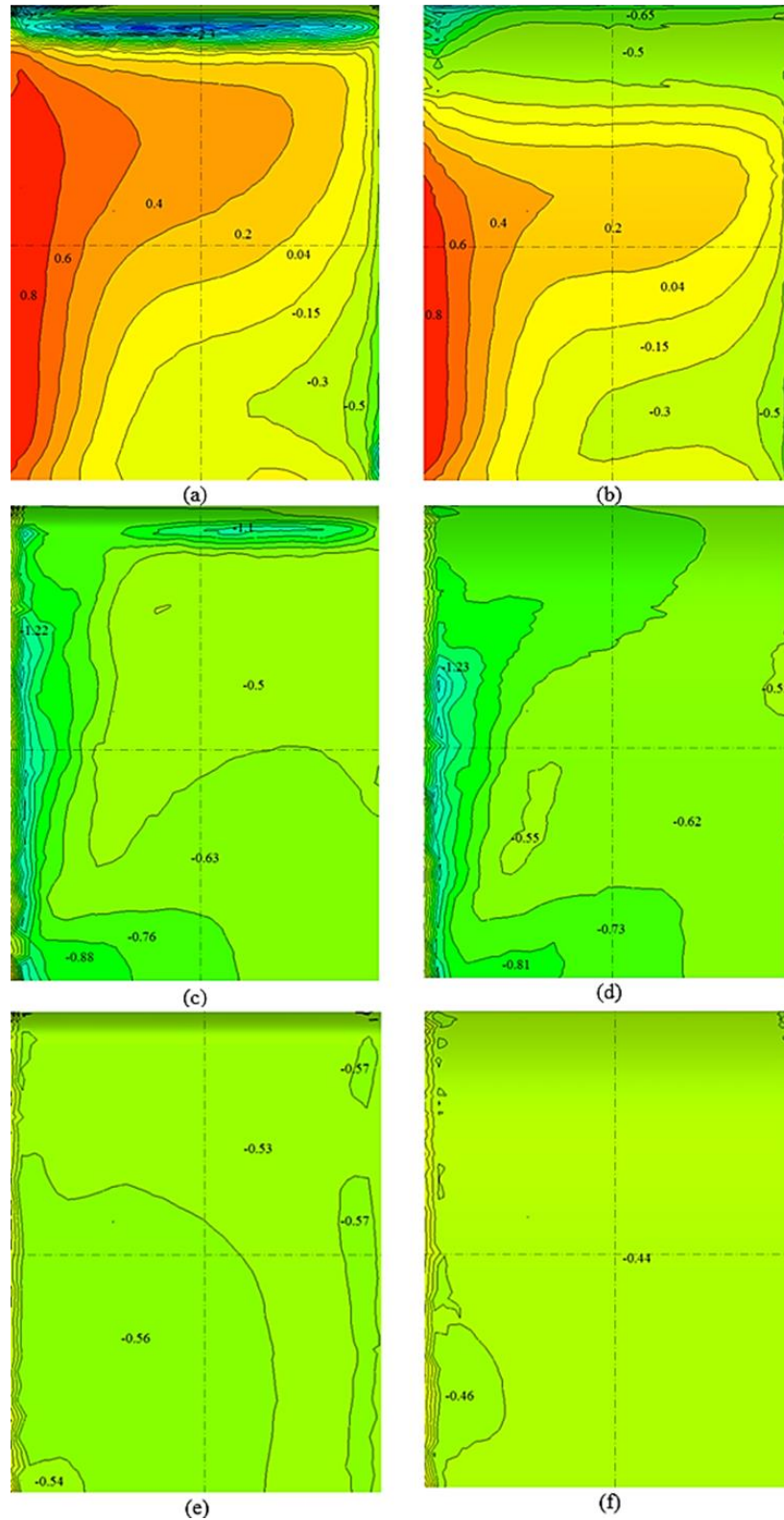


Figure 6.10 Variations in coefficient of pressure (CP) on the front face of the trailer unit with  $B_5 = 0.01$  (left) and  $B_5 = 0.1$  (right), where crosswind flow is  $30^\circ$  (top);  $60^\circ$  (middle);  $90^\circ$  (bottom).

The trailer unit is a key contributor to aerodynamic forces experienced by a truck-trailer unit. They are mostly bluff bodies with high-sided surfaces all around influencing the drag force and side force affecting the fuel economy and stability, respectively. The overall pressure distribution has been discussed in previous section and the pressure asymmetry has been quantified in this section. Figure 6.11 shows the average  $C_p$  distribution on the windward and leeward sides of the trailer front surface for  $B5 = 0.01$  and  $B5 = 0.1$  models for a range of yaw angles. A maximum positive average  $C_p$  of 0.34 was recorded on the leeward side for  $B5 = 0.01$  model and a maximum negative average  $C_p$  of -0.71 was recorded on the windward side of  $B5 = 0.1$  model. Positive  $C_p$  was observed on the trailer front faces for both vehicle models at  $\psi = 15^\circ$  and in both cases the leeward side was perceived to have higher pressure than the windward side. This difference was found to be 54.5% and 47.0% for  $B5 = 0.01$  and  $B5 = 0.1$  models, respectively. When the leading edge of the trailer unit was changed from  $B5 = 0.01$  to  $B5 = 0.1$  the windward pressure is seen to decrease by 22.7% and the leeward pressure is seen to decrease by 26.5%. When  $\psi = 30^\circ$ , the windward sides were discovered to be associated with positive pressures and leeward sides were seen to have negative pressures. A pressure difference of 0.23 is seen between the windward and leeward side for  $B5 = 0.01$  model and a difference of 0.16 is seen for  $B5 = 0.1$  model. From  $\psi = 30^\circ$  onwards, negative pressures are observed on the trailer front face for both truck-trailer models. When  $\psi = 45^\circ$ , a 78.3% increase in pressure is observed on the windward side compared to leeward side for  $B5 = 0.01$  model and for  $B5 = 0.1$  model, 30.5% increase in pressure was recorded. When the leading edge of the trailer unit was changed from  $B5 = 0.01$  to  $B5 = 0.1$  the windward pressure is seen to decrease by 56.5% and the leeward pressure is seen to decrease by 14.6%. When  $\psi = 60^\circ$ , a 7.7% increase in pressure is observed on the leeward side compared to windward side for  $B5 = 0.01$  model and for  $B5 = 0.1$  model, 8.4% increase in pressure was recorded. As the leading edge profile changed to  $B5 = 0.1$ , the windward pressure is seen to decrease by 9.2% and the leeward pressure is seen to decrease by 8.3%. When  $\psi = 75^\circ$ , an 18.1% increase in pressure is observed on the leeward side compared to windward side for  $B5 = 0.01$  model and for  $B5 = 0.1$  model, 14.9% increase in pressure was recorded. As the leading edge profile changed to  $B5 = 0.1$ , the windward pressure is seen to decrease by 1.5% and the leeward pressure is seen to decrease by 5.5%. When  $\psi = 90^\circ$ , a 3.5% increase in pressure is observed on the leeward side compared to windward side for  $B5 = 0.01$  model and for  $B5 = 0.1$  model, 4.4% increase in pressure was recorded.

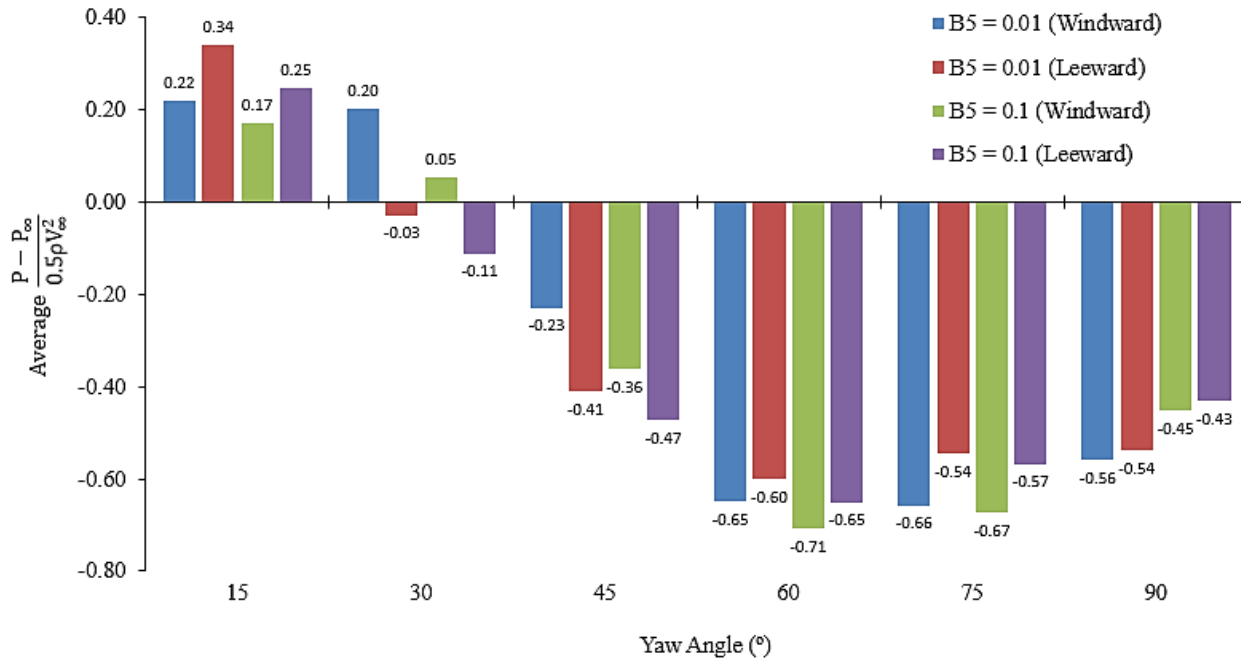


Figure 6.11 The average pressure coefficient on the trailer front surface for B5 = 0.01 and B5 = 0.1 models from  $\psi = 15^\circ$  to  $\psi = 90^\circ$ .

Figure 6.12 depicts the forces acting on the trailer front surface for B5 = 0.01 and B5 = 0.1 models between  $\psi = 15^\circ$  and  $\psi = 90^\circ$ . The overall trend in measured forces seems to match that of which was observed for the truck front face depicted from Figure 6.6. The force acting in the positive X direction is shown from (a). Here, a maximum force in positive X direction was obtained as 877N and a maximum force in the negative X direction was obtained as -2399N. When  $\psi = 15^\circ$  and  $\psi = 30^\circ$ , B5 = 0.01 model was seen to experience 37.4% and 58.5% higher forces than B2 = 0.1 model, respectively. However, between  $\psi = 30^\circ$  and  $\psi = 75^\circ$  the latter model is associated with higher forces. Moreover, it was observed that after  $\psi = 30^\circ$ , forces for both models were acting in the negative X direction. The force acting in the positive Y direction is shown from Figure (b). A significant variation in force experienced by two models were observed for  $\psi = 15^\circ, 30^\circ, 45^\circ$  where the B5 = 0.01 model was having 120%, 66.9% and 22.8%, more force, respectively. This increased force in positive Y direction was caused by the low pressure region which exists in the vicinity of the trailer leading edge. The force calculated in the positive Z direction for the trailer front surface is shown in (c). Once more, minimal force variations between the two models have been observed.

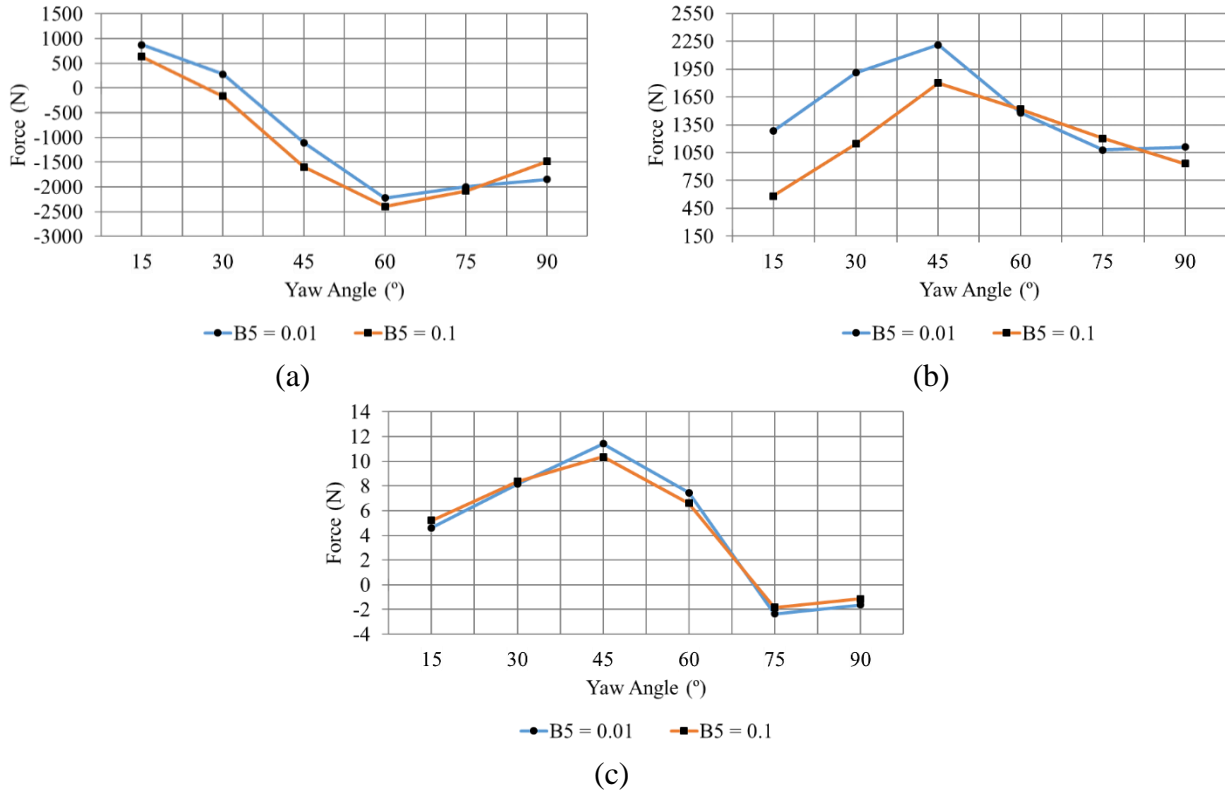


Figure 6.12 The force acting on the trailer front surface in the positive X direction (a) positive Y direction (b) and positive Z direction (c) for B5 = 0.01 and B5 = 0.1 models from  $\psi = 15^\circ$  to  $\psi = 90^\circ$ .

## 6.6 Effect of B6 on the truck-trailer unit performance under crosswinds

The most significant wake flow region exists in the vicinity of the trailer rear surface. This low pressure, circulating flow region is expected to have a significant impact on the pressure distribution and the force exerted on the trailer rear surface. The  $C_P$  variation on the trailer rear surface when B6 = 0.01 and B6 = 0.1 at yaw angles  $30^\circ$ ,  $60^\circ$  and  $90^\circ$  is shown in Figures 6.13 (a), 6.13 (b) and 6.13 (c), respectively. Negative  $C_P$  is seen throughout the trailer rear surface for both truck-trailer models at all yaw angles. At  $\psi = 30^\circ$ , a low  $C_P$  region of -1.3 is seen closer to the top trailing edge of the trailer unit for B6 = 0.01 model, and this has been eradicated upon increasing the rear trailer edge profile to B6 = 0.1. The lowest  $C_P$  of -1.3 and the highest  $C_P$  of -0.28 are both obtained from B6 = 0.01 model. The highest pressure region is seen to exist closer to bottom edge of the trailer rear surface followed by a region of  $C_P = -0.34$  which seems to

occupy a significant area on the bottom half of the surface. In  $B6 = 0.1$  model, the highest pressure region with  $C_P = -0.34$  is seen to confine mainly to bottom left area of the surface as shown from (b). The trend in  $C_P$  continues when  $\psi = 60^\circ$ , as once more, the lowest  $C_P$  of  $-0.64$  is observed near the top trailing edge and the highest  $C_P$  of  $-0.32$  is observed near the windward edge of the trailer rear surface on  $B6 = 0.01$  model. When  $\psi = 60^\circ$ , two low  $C_P$  areas were observed where one elongated along the top trailer edge and the other is concentrated closer to bottom trailer edge of the surface as depicted from (c). For  $\psi = 30^\circ$  and  $\psi = 60^\circ$ , the pressure is seen to increase closer to the top trailer edge once the  $B6$  is changed from  $0.01$  to  $0.1$  and the pressure distribution is observed to become more uniform. Minimal pressure variations are seen when  $\psi = 90^\circ$  between the model but the highest pressure is observed on the  $B6 = 0.1$  model.

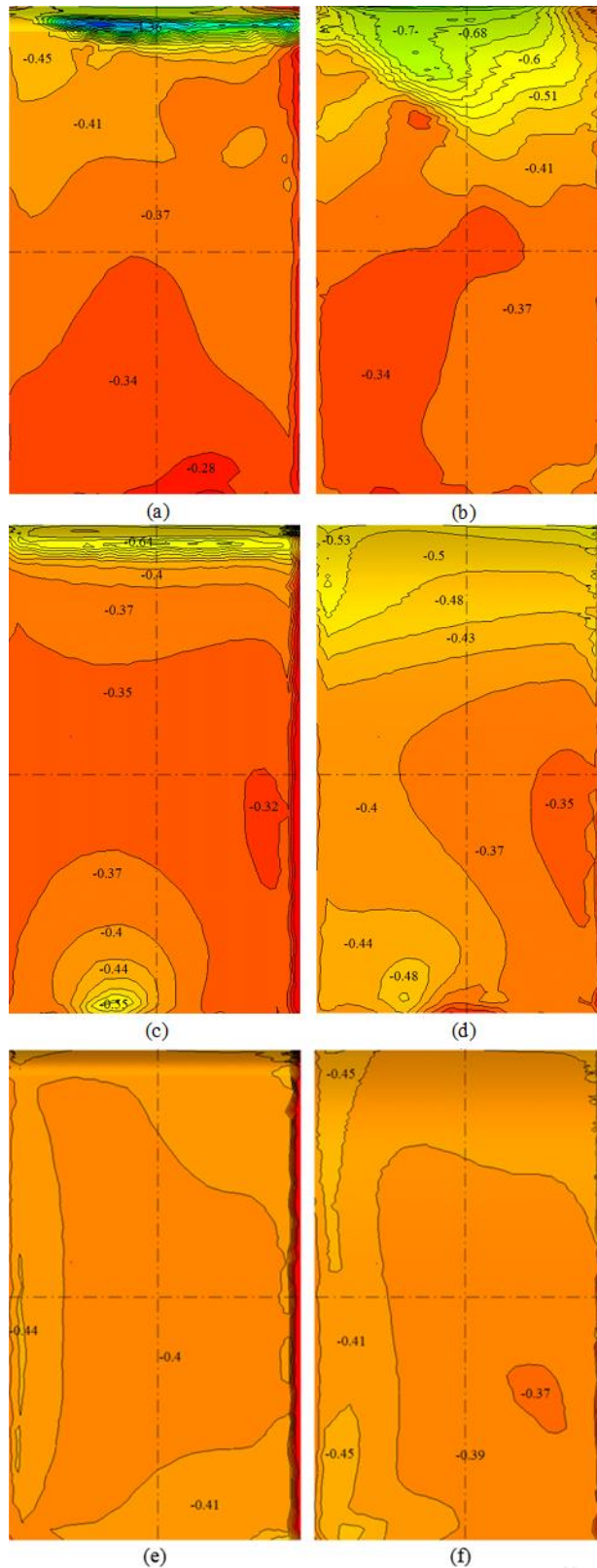


Figure 6.13 Variations in coefficient of pressure (CP) on the rear face of the trailer unit with  $B_6 = 0.01$  (left) and  $B_6 = 0.1$  (right), where crosswind flow is 30° (top); 60° (middle); 90° (bottom).

Figure 6.14 below displays the average pressure coefficient ( $C_p$ ) on the rear surface of the trailer unit for models  $B6 = 0.01$  and  $B6 = 0.1$  models with varying yaw angles ( $\psi$ ) starting from  $\psi = 15^\circ$  to  $\psi = 90^\circ$  in  $15^\circ$  degree increments. Furthermore, two data lines were created on the windward and leeward sides of the surface and as a result an average  $C_p$  value was generated for each line for each condition. Upon close examination, it is immediately noted that only negative  $C_p$  exists on the rear surface of the trailer unit. The highest recorded  $C_p$  value is  $-0.24$  at  $\psi = 15^\circ$  for  $B6 = 0.01$  model whereas  $B6 = 0.1$  model has a highest  $C_p$  value of  $-0.26$  at  $\psi = 15^\circ$ . Interestingly, the lowest value was recorded at  $\psi = 15^\circ$  from  $B6 = 0.1$  model, windward line. It seems the most variation between the models and windward/leeward conditions are seen at  $\psi = 15^\circ$ . An overall decrease of  $104.17\%$  of  $C_p$  (windward to leeward) is noticed from  $B6 = 0.01$  model to  $B6 = 0.1$  model. A decrease of  $41.67\%$  of  $C_p$  is noticed from Windward to Leeward side of model  $B6 = 0.01$ . Inversely, a  $C_p$  increase of  $46.94\%$  is noticed from windward to leeward side on  $B6 = 0.1$  model. Across the rest of the yaw angles the variation seems to be minimal in comparison. When  $\psi = 30^\circ$ , a constant pressure of  $-0.38$  is observed from windward side to leeward side for  $B2 = 0.01$  model. Also, for  $B2 = 0.1$  model, a  $4.76\%$  pressure increase was observed. When  $\psi = 45^\circ$ , a  $6.67\%$  increase in pressure is observed from windward side to leeward side for  $B2 = 0.01$  model and for  $B2 = 0.1$  model,  $4.17\%$  increase in pressure was recorded. At  $\psi = 60^\circ$  the pressure change trend seems to change as there is a pressure decrease of  $8.33\%$  from windward to leeward side on  $B6 = 0.01$  model and similarly a pressure decrease of  $10\%$  for  $B6 = 0.1$  model. At  $\psi = 75^\circ$ , the overall pressure values both model models seem to be low, lowest being  $-0.32$  for both models and highest being  $-0.29$  for  $B6 = 0.01$  model. A pressure decrease of  $10.34\%$  and  $6.67\%$  is noticed from windward to leeward side for  $B6 = 0.01$  and  $B6 = 0.1$  models respectively. At  $\psi = 90^\circ$  the overall pressure has decreased with lowest being  $-0.41$  and highest being  $-0.40$  for both models. Interestingly, a  $2.44\%$  increase in pressure is seen from windward to leeward side for  $B6 = 0.01$  model while a decrease of  $2.5\%$  in pressure is seen for  $B6 = 0.1$  model. As mentioned before, with the exception of  $\psi = 15^\circ$ , for the rest of the yaw angles the difference in pressure change is very minimal in terms of percentage.

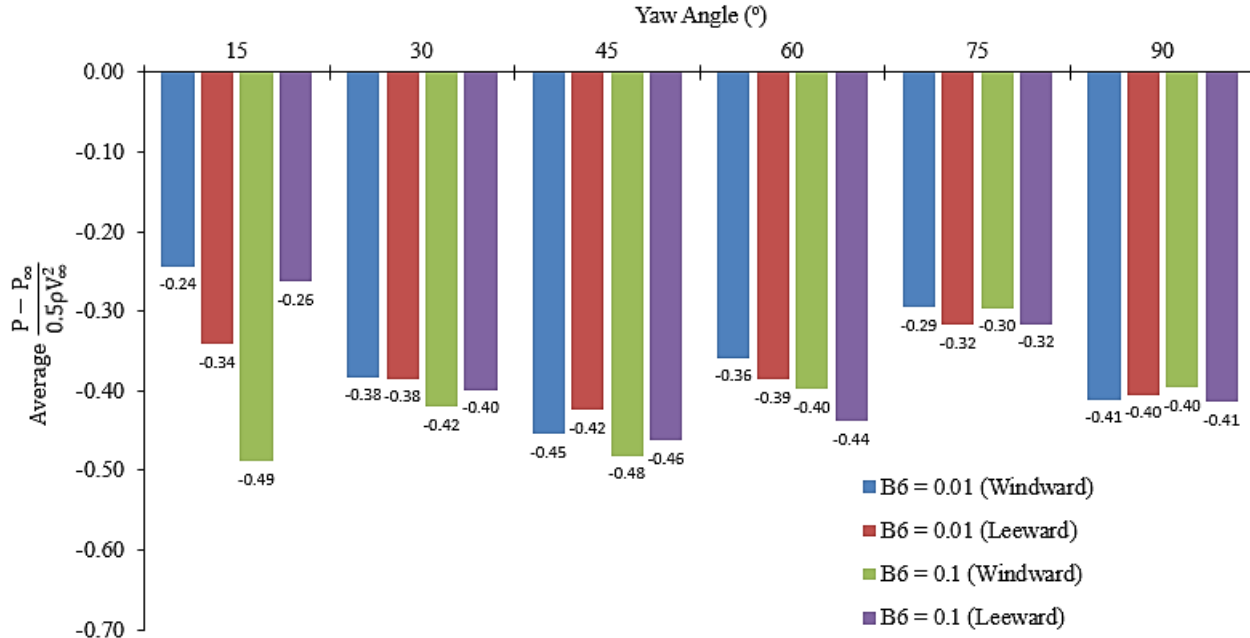


Figure 6.14 The average pressure coefficient on the trailer front surface for B6 = 0.01 and B6 = 0.1 models from  $\psi = 15^\circ$  to  $\psi = 90^\circ$ .

Figure 6.15 below shows the forces acting on the trailer rear surface for B6 = 0.01 and B6 = 0.1 models between  $\psi = 15^\circ$  and  $\psi = 90^\circ$ . In general, both models seem to loosely share the same behaviour, sometimes even exactly the same values. The force acting in the positive X direction is shown by (a). Both models experienced their respective maximum force values of 2060N and 1943N at  $\psi = 45^\circ$ , B6 = 0.1 and B6 = 0.01 models respectively. It is important to note, for both models after the peak point the force began to decline to their respective minimum values at  $\psi = 75^\circ$  before once again increasing up to around 1800N at  $\psi = 90^\circ$ . The force acting in the positive Y direction is shown from Figure (b). At  $\psi = 15^\circ$ , B6 = 0.1 model experiences 37% more force than B6 = 0.01 model, exact force values being 1945N and 1227N respectively. Interestingly, from  $\psi = 30^\circ$  onwards B6 = 0.1 model experiences less force compared to B6 = 0.01 model. At  $\psi = 75^\circ$ , B6 = 0.1 model experiences 21% less force compared to B6 = 0.01 model. Moreover, similarly to Figure (a) at  $\psi = 90^\circ$  both models converge by experiencing very similar forces, between 855-865N. The force calculated in the positive Z direction for the trailer front surface is shown in (c). Unlike before, both models seem to be acting in the negative Z direction for the complete range of  $\psi = 15-90^\circ$ . At  $\psi = 15^\circ$ , B6 = 0.1 experiences 86% more force when compared

to  $B_6 = 0.01$  model. From  $\psi = 30^\circ$  to  $60^\circ$  both models show similar trend in the force experienced.

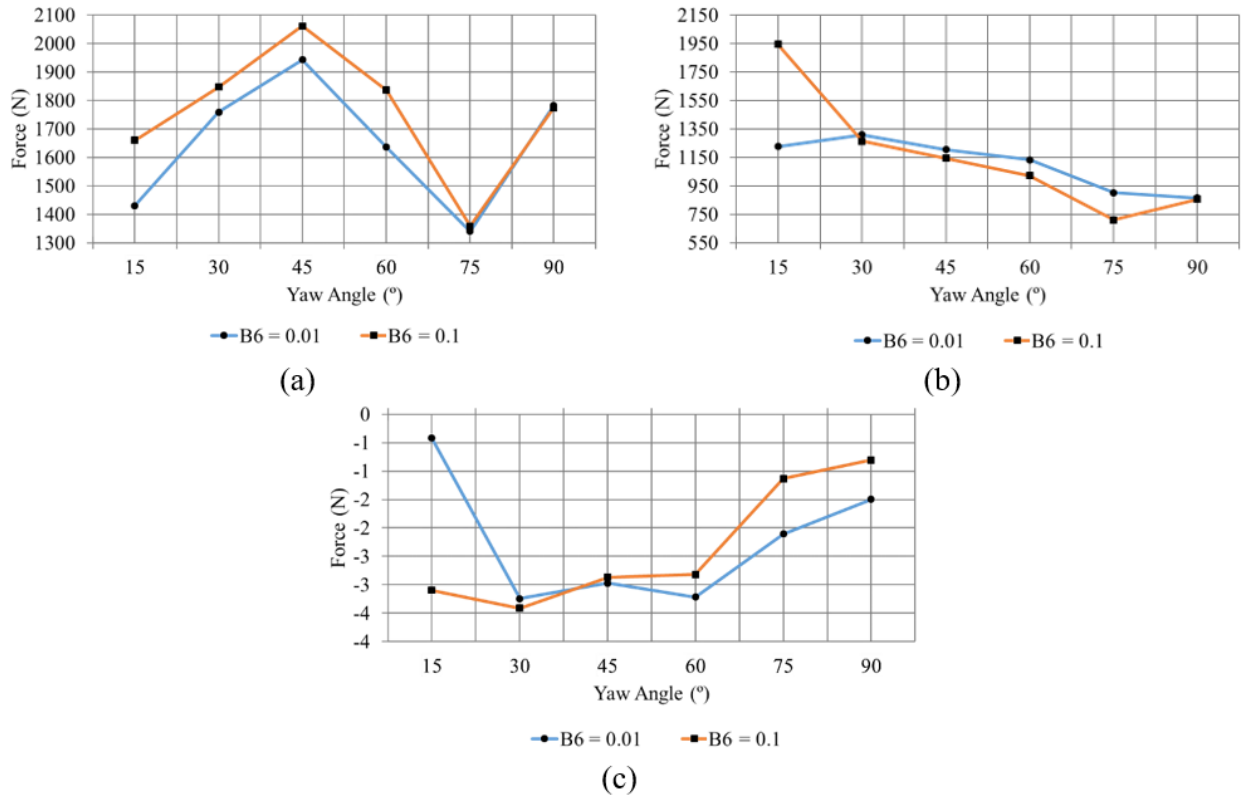


Figure 6.15 The force acting on the trailer rear surface in the positive X direction (a) positive Y direction (b) and positive Z direction (c) for  $B_6 = 0.01$  and  $B_6 = 0.1$  models from  $\psi = 15^\circ$  to  $\psi = 90^\circ$

## 6.7 Pressure variations on windward, top and leeward surfaces of truck-trailer unit with changing B coefficient at a constant crosswind angle of $60^\circ$

The maximum side force applied on the truck-trailer takes place when the airflow is directed at a  $60^\circ$  yaw angle towards the vehicle. Pressure distribution of three surfaces are looked at in detail, windward surface, the top surface and the leeward surface of the truck-trailer. Figure 6.16 below shows the windward surface of the truck-trailer unit being subjected to a crosswind profile acting at a  $60^\circ$  yaw angle. To begin with, all the profiles  $B_1 - B_6$  were set at 0.01 as standard. These profiles were individually changed to 0.1 one at a time whilst the rest remained at 0.01. Figure

(a) shows that towards the front of the truck unit high pressure areas exist as confirmed by pressure coefficient 0.95. This pressure is seen to exist at the middle edge of the trailer unit before gradually decreasing towards the top rear corner of the trailer unit. Figure (b) shows profile change  $B1 = 0.1$  which seems to show a negligible effect on the pressure distribution. Figure (c) shows profile change  $B2 = 0.1$  which once again seemed to have made no significant changes to the pressure distribution. Figure (d) shows profile change  $B5 = 0.1$  which clearly enlarges the area of the high pressure regions on the truck unit and elongates pressure regions on the trailer unit towards the rear. Figure (e) shows profile change  $B6 = 0.1$  and in comparison shows minimal transformation of pressure distribution when compared with Figure (a).

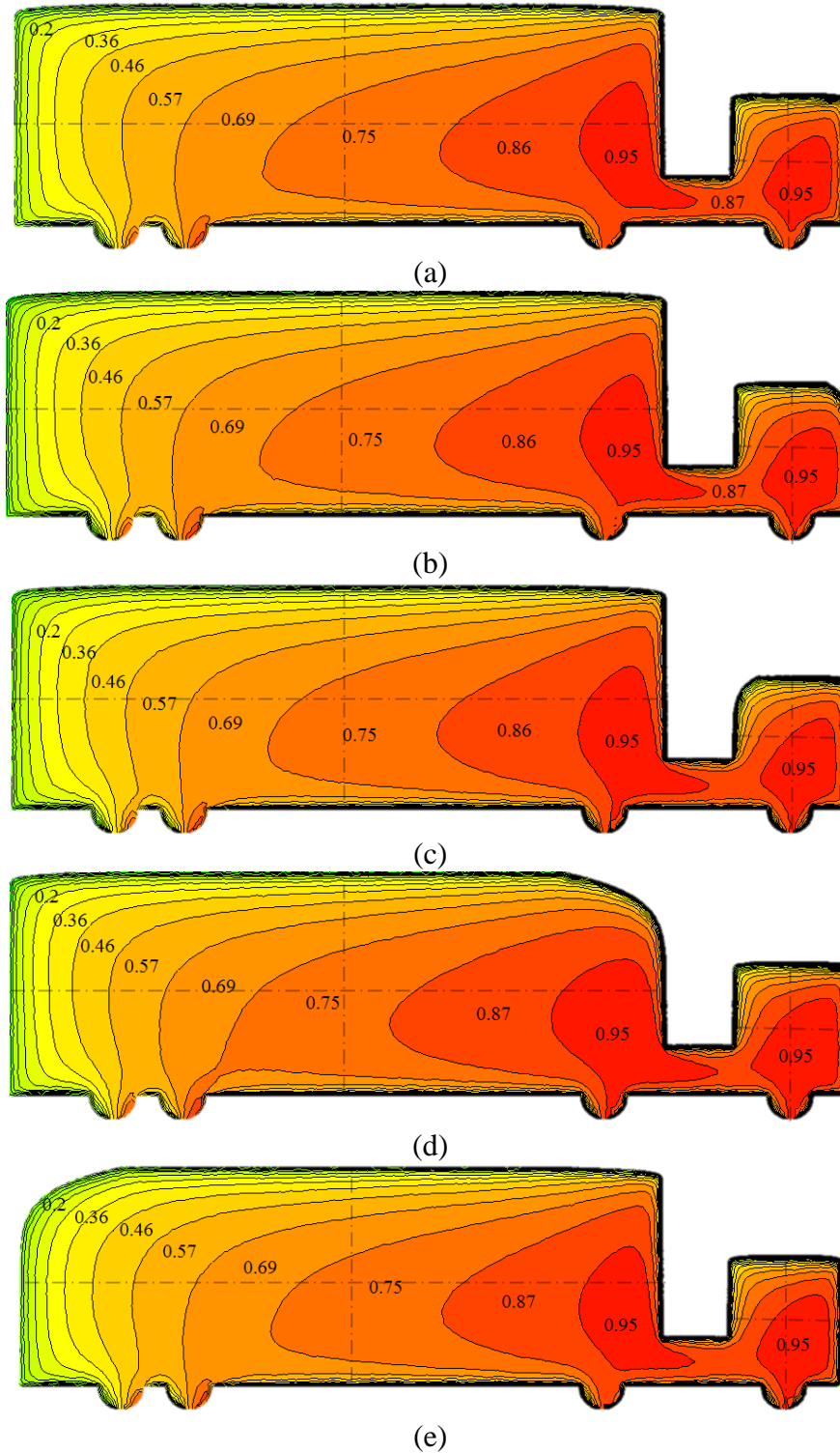


Figure 6.16 Variations in coefficient of pressure ( $C_p$ ) on windward side of the truck-trailer unit with changing B profiles. (a)  $B_1, B_2, B_5, B_6 = 0.01$  (b)  $B_1 = 0.1$ , (c)  $B_2 = 0.1$ , (d)  $B_5 = 0.1$ , (e)  $B_6 = 0.1$  at  $\psi = 60^\circ$

Figure 6.17 shows variations in  $C_P$  on top surface of the truck-trailer unit with changing B profiles when  $\psi = 60^\circ$ . The model when all B shape coefficients were set to 0.01 is depicted from (a). Significant pressure variations are seen on top of the truck unit where minimal variations are seen to exist on the top trailer surface. Significant area of increased  $C_P$  of -0.39 was seen on the truck unit and the minimum pressure was observed in the vicinity of windward side where the pressure was seen to decrease to  $C_P = -1.5$ . As B1 changed from 0.01 to 0.1, the pressure is seen to increase near the truck leading edge as seen from (b). The  $C_P = -0.39$  pressure region has decreased in size and the pressure towards the rear of the trailer top surface has decreased with  $C_P$  being decreased to -0.63. Increasing B2 = 0.1 is only seen to have a minimal effect on the truck top surface. However, as a result, the  $C_P = -0.66$  pressure region on the trailer top surface has significantly increased and was seen to elongate up to top trailing edge of the trailer unit. Upon increasing B5 = 0.1,  $C_P$  is seen to reduce up to -0.67 on the front of the trailer top surface where an even lower pressure region of  $C_P = -0.8$ , close to the leading edge has appeared. Increasing B6 = 0.1 has increased the pressure in B6 region on top the trailer surface and  $C_P$  is maintained at -0.66 for the most of trailer top surface as shown in (e). Interestingly, as the B6 increased, the area of  $C_P = -0.39$  high pressure region to top of the truck surface was seen to increase.

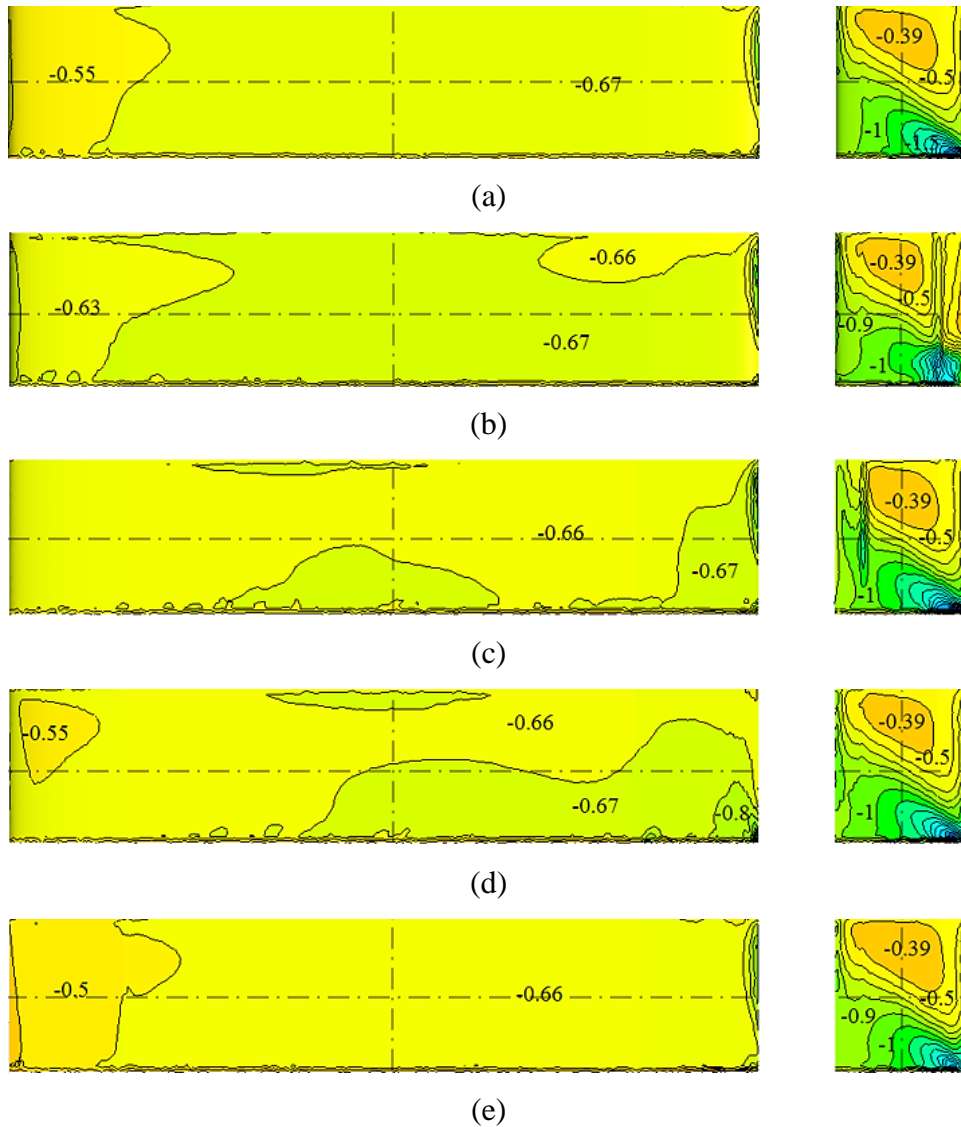


Figure 6.17 Variations in coefficient of pressure ( $C_P$ ) on top surface of the truck-trailer unit with changing B profiles. (a)  $B_1, B_2, B_5, B_6 = 0.01$  (b)  $B_1 = 0.1$ , (c)  $B_2 = 0.1$ , (d)  $B_5 = 0.1$ , (e)  $B_6 = 0.1$  at  $\psi = 60^\circ$ .

Figure 6.18 depicts the variations in  $C_P$  on leeward surface of the truck-trailer unit with changing B profiles when  $\psi = 60^\circ$ . As expected, negative  $C_P$  distribution is seen throughout the geometric configurations and the lowest  $C_P$  are seen on the truck leeward surface and in between rear two trailer wheels. Relatively higher  $C_P$  is observed in the trailer surface. Once again, the model when all B shape coefficient were set to 0.01 is depicted from (a). The lowest pressure regions of  $C_P = -0.72$  is seen near the truck trailing edge and the highest  $C_P$  is seen near the rear edge of the

trailer. When the B2 shape coefficient is increased to 0.1 as shown in (b), the low pressure area on the truck leeward surface is seen to decrease and pressure on the trailer surface is seen to decrease in general as the  $C_P = -0.6$  area is seen to get replaced by  $C_P = -0.61$  region. Changing the B2 coefficient from 0.01 to 0.1 seems to further increase the low  $C_P$  region of  $-0.76$ , which is seen to elongate towards the front of the truck unit. Also, a high  $C_P$  region of  $-0.57$  is seen to develop at the front of the trailer unit with a relative pressure increase throughout is observed as seen from (c). Upon increasing B5 and B6 coefficients to 0.1, visible  $C_P$  increase on the leeward trailer surface is observed and this is depicted from (d) and (e). The former is seen to have minimal impact on the truck  $C_P$  distribution while the latter is seen to affect the  $C_P$  distribution significantly while further increasing the  $C_P$  on the trailer surface where a  $C_P = -0.54$  region is seen near the trailer front.

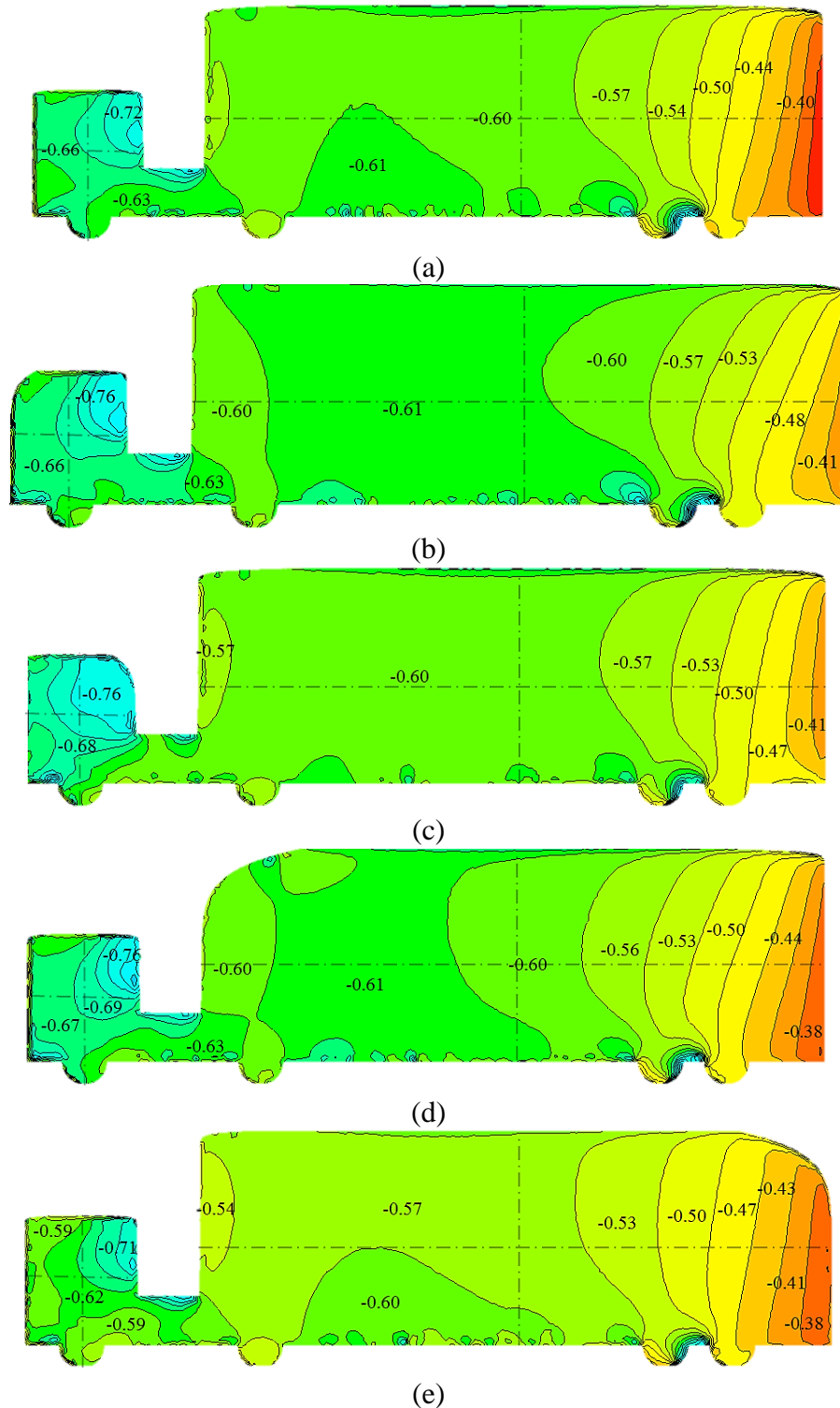


Figure 6.18 Variations in coefficient of pressure ( $C_p$ ) on leeward surface of the truck-trailer unit with changing B profiles. (a)  $B_1, B_2, B_5, B_6 = 0.01$  (b)  $B_1 = 0.1$ , (c)  $B_2 = 0.1$ , (d)  $B_5 = 0.1$ , (e)  $B_6 = 0.1$  at  $\psi = 60^\circ$ .

Pressure distribution on the windward and leeward surfaces determines the force acting on each of the surfaces. The combined force on each surface is known as the side force and is known to affect the stability of a truck-trailer model. In this case the force acting on windward surface for B1, B2, B5, B6 = 0.01, B1 = 0.1, B2 = 0.1, B5 = 0.1, B6 = 0.1 models, from  $\psi = 15^\circ$  to  $\psi = 90^\circ$  is calculated and depicted from Figure 6.19. In this study, the force was calculated in the direction of the inlet flow which was in positive Z direction and was compared with the B1, B2, B5, B6 = 0.01 configuration (standardised model) to be observed the influence of geometrical shape effects on the force. It can be seen that force increases with the crosswind angle. At  $\psi = 15^\circ$ , negative force is observed for all the models which represents the force acting in the opposite direction. The highest force in the opposite direction of 460.3N was observed for B6 = 0.1 model and the lowest force of 184.1N was recorded on B1 = 0.1. After  $\psi = 15^\circ$ , all the forces acting at various crosswind angles are in the positive direction. At  $\psi = 30^\circ$ , it can be seen that forces acting on B1, B2, B5, B6 are less than the standardised model, where the variations are -0.3%, -2.1%, -1.9%, -2.1%, respectively. At  $\psi = 45^\circ$ , force acting on the standardised model and B1 has no variations, however, force acting on B5 incurs an increase of 1.8%. Additionally, forces acting on B2 and B6 have decreased by 0.5% and 1.4%, respectively. At  $\psi = 60^\circ$ , it can be seen that forces acting on B1, B2, B5, B6 are less than the standardised model, where the variations have decreased by 1.3%, 5.1%, 2.2%, 0.7%, respectively. At  $\psi = 75^\circ$ , B1, B2 and B6 models are greater than the standardised model by 3.3%, 2.1% and 0.4, respectively while, B5 decreases by 1.7%. At  $\psi = 90^\circ$ , force acting on B1 has a slight increase of 0.2% over the standardised model, whereas, force acting on B2, B5 and B6 has decreased by 0.4%, 1.4% and 1.3%, respectively.

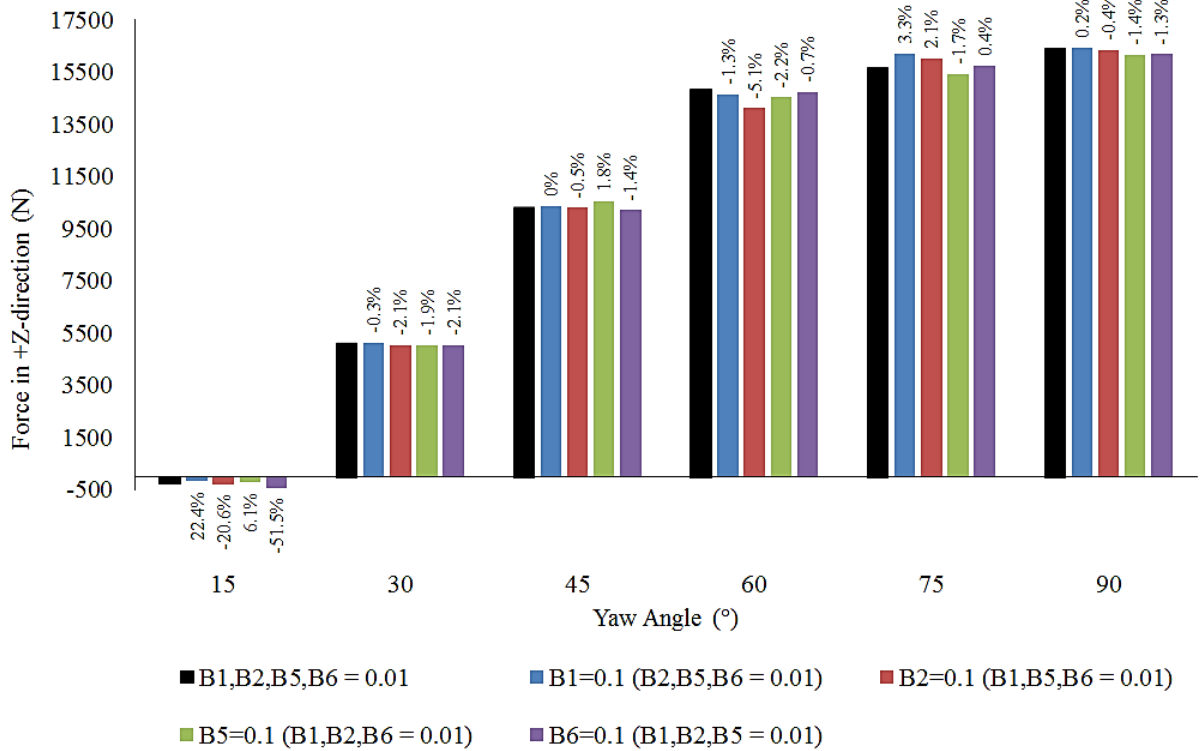


Figure 6.19 The force acting on the windward vehicle surface in the positive Z direction for B1, B2, B5, B6 = 0.01, B1 = 0.1, B2 = 0.1, B5 = 0.1, B6 = 0.1 models, from  $\psi = 15^\circ$  to  $\psi = 90^\circ$ .

Force acting on leeward surface for B1, B2, B5, B6 = 0.01, B1 = 0.1, B2 = 0.1, B5 = 0.1, B6 = 0.1 models, from  $\psi = 15^\circ$  to  $\psi = 90^\circ$  is calculated and depicted from Figure 6.20. It can be seen that forces acting on all models are positive throughout the crosswind range. The highest force is depicted at  $\psi = 45^\circ$ , while the lowest force is acting at  $\psi = 90^\circ$ . At  $\psi = 15^\circ$ , B1, B2 and B5 are greater than the standardised model by 0.16%, 0.17% and 1.6%, respectively while, B6 identifies a significantly lower force with a reduction of 6.8%. At  $\psi = 30^\circ$ , B2 shows an increase of 1.5% against the standardised model while B1, B5 and B6 show a considerable fall in force by 1.9%, 3.8% and 6.3%, respectively. At  $\psi = 45^\circ$ , there are marginal increases in force on B1 and B2 against the standardised model of 0.4% and 0.5%, while B5 and B6 shows a decrease of 0.9% and 1.2%, respectively. At  $\psi = 60^\circ$ , there are no variations in force between B5 and the standardised model, however, B1 and B2 increases by 3.8% and 1.2% respectively, while B6 decreases by 5.8%. At  $\psi = 75^\circ$ , B5 depicts a 2.8% increase whereas, B1, B2 and B6 decreases significantly by 7.8%, 10.6% and 8.1%, respectively. These are the highest variation recorded

throughout this data range. At  $\psi = 90^\circ$ , it can be seen that forces acting on B1, B2, B5, B6 are less than the standardised model, where the variations have decreased by 2.5%, 0.6%, 5.9%, 6.3%, respectively. Throughout the crosswind range, the B6 model reveals the most significant amount of decrease against the standardised model.

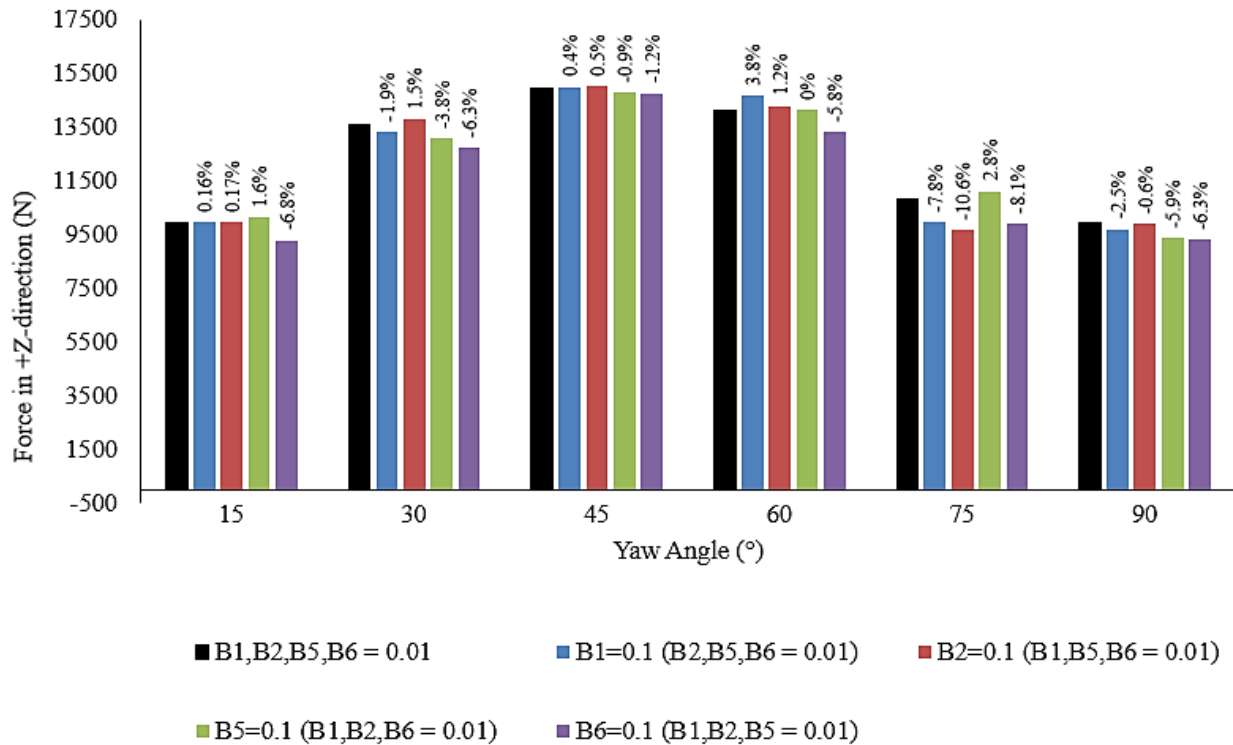


Figure 6.20 The force acting on the leeward vehicle surface in the positive Z direction for B1, B2, B5, B6 = 0.01, B1 = 0.1, B2 = 0.1, B5 = 0.1, B6 = 0.1 models, from  $\psi = 15^\circ$  to  $\psi = 90^\circ$ .

## 6.8 The Aerodynamic Forces Experienced by Truck-Trailer Models with Varying B Coefficients and Crosswind Angles.

Figure 6.21 below shows the total drag force experienced by the truck-trailer unit for all four configurations B1, B2, B5 and B6 with varying magnitudes and yaw angles. The configurations are examined/alterred one at a time, during this the remaining configurations are all set to 0.01 magnitude by default. At a first glance all four graphs look quite similar in their trends. However, it is easy to make the mistake of observing that all three lines show minimal variation between each other. This is due to the wide scale required accommodate the minimum and maximum values on the drag force axis. Also, for all four graphs shortly after  $\psi = 60^\circ$ , the

direction of the drag force reverses. When Figure (a), which is based on the front leading edge of the truck is examined closely, at  $\psi = 15^\circ$  the maximum drag force is 4920N from  $B1 = 0.01$  and this is 4% higher than both other variants. At  $\psi = 60^\circ$ , the minimum drag force of 200N is experienced by the truck-trailer by  $B1 = 0.01$  model. Figure (b) which is based on the trailing edge of the truck can be seen to follow a similar trend as (a), maximum and minimum drag force of 4926N from  $B2 = 0.1$  and 200N from  $B2 = 0.01$  respectively. Unlike (a), beyond  $\psi = 60^\circ$  an increased spread of drag force is noticed. Figure (c) which is based on the leading edge of the trailer, shows a maximum and minimum drag force of 4920N from  $B5 = 0.01$  and 182N from  $B5 = 0.1$  respectively. A wide range of drag force between the three magnitudes are seen at  $\psi = 45^\circ$  and  $\psi = 90^\circ$ . Figure (d) is based on the trailing edge of the trailer. The maximum and minimum drag force of 5146N from  $B6 = 0.05$  and 200N from  $B6 = 0.01$ . To summarise, a maximum drag force of 182N is achieved by  $B5 = 0.1$  which is the trailer leading edge and the minimum drag force of 5146N is achieved by  $B6 = 0.05$  which is the trailing edge of the trailer.

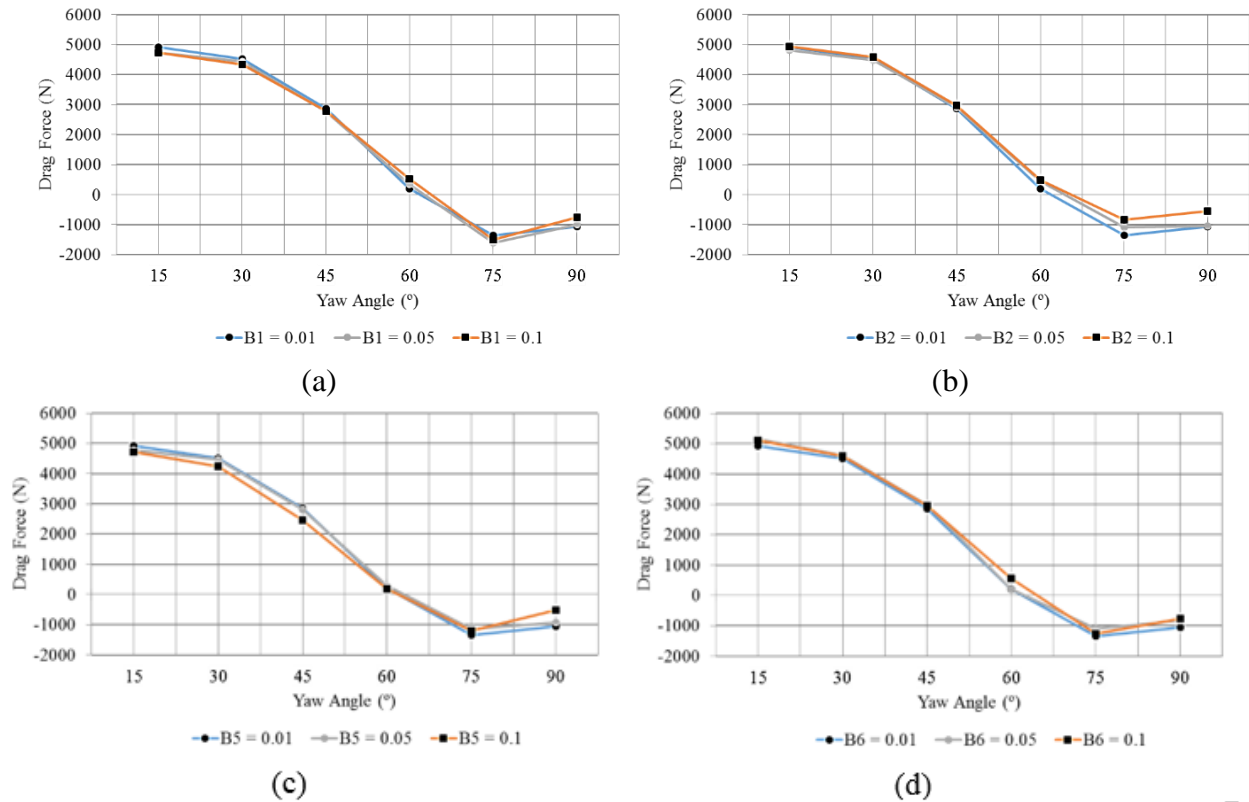


Figure 6.21 Truck-trailer drag force acting for various  $B1$ ,  $B2$ ,  $B5$ ,  $B6$  configurations with varying magnitudes from  $\psi = 15^\circ$  to  $\psi = 90^\circ$ .

Figure 6.22 depicts truck-trailer lift force acting on various B1, B2, B5, B6 configurations with varying magnitudes from  $\psi = 15^\circ$  to  $\psi = 90^\circ$ . It can be seen that the trend is the same for all B configurations where the maximum lift force was observed at  $\psi = 30^\circ$  and minimum lift force was observed at  $\psi = 90^\circ$ . It is noted that after  $\psi = 75^\circ$  the lift force acts in the negative direction. Again, due to the wide scale of the maximum and minimum force, the variations are not very obvious to see. In the case of (a), a maximum positive lift force of 8048N was recorded on B1 = 0.01 whereas, maximum negative lift force of 1155N occurs when B1 = 0.05. The maximum variation occurs at  $\psi = 30^\circ$  between B1 = 0.01 and B1 = 0.1 models, which was calculated to be 7.4%. The minimum variation occurs at  $\psi = 75^\circ$ , between B1 = 0.05 and B1 = 0.1, which was calculated to have 2.7%. In the case of (b), the maximum positive lift force of 8048N was recorded on B2 = 0.01 whereas, maximum negative lift force of 1305N occurs when B2 = 0.1. The maximum variation occurs at  $\psi = 90^\circ$  between B2 = 0.05 and B2 = 0.1 models, which was calculated to be 61%. The minimum variation occurs at  $\psi = 60^\circ$ , between B2 = 0.01 and B2 = 0.1, which was calculated to have 0.6%. In the case of (c), the maximum positive lift force of 8048N was recorded on B5 = 0.01 whereas, maximum negative lift force of 969N occurs when B5 = 0.1. The maximum variation occurs at  $\psi = 30^\circ$  between B5 = 0.01 and B5 = 0.1 models, which was calculated to have 12%. The minimum variation occurs at  $\psi = 60^\circ$ , between B5 = 0.01 and B5 = 0.05, which was calculated to have 1.7%. In the case of (d), once more, the maximum positive lift force of 8048N was recorded on B6 = 0.01 whereas, maximum negative lift force of 918N occurs when B6 = 0.01. The maximum variation occurs at  $\psi = 15^\circ$  between B6 = 0.01 and B6 = 0.05 models, which was calculated to have 47.2%. The minimum variation occurs at  $\psi = 45^\circ$ , between B6 = 0.05 and B6 = 0.1, which was calculated to have 2.2%.

To summarise, it is evident that when the B coefficients = 0.01, highest lift force was observed, however where the B coefficients = 0.1, predominantly lower lift force values were observed. For this reason, it can be considered that B coefficient = 0.1 produces the most desirable lift force Figures.

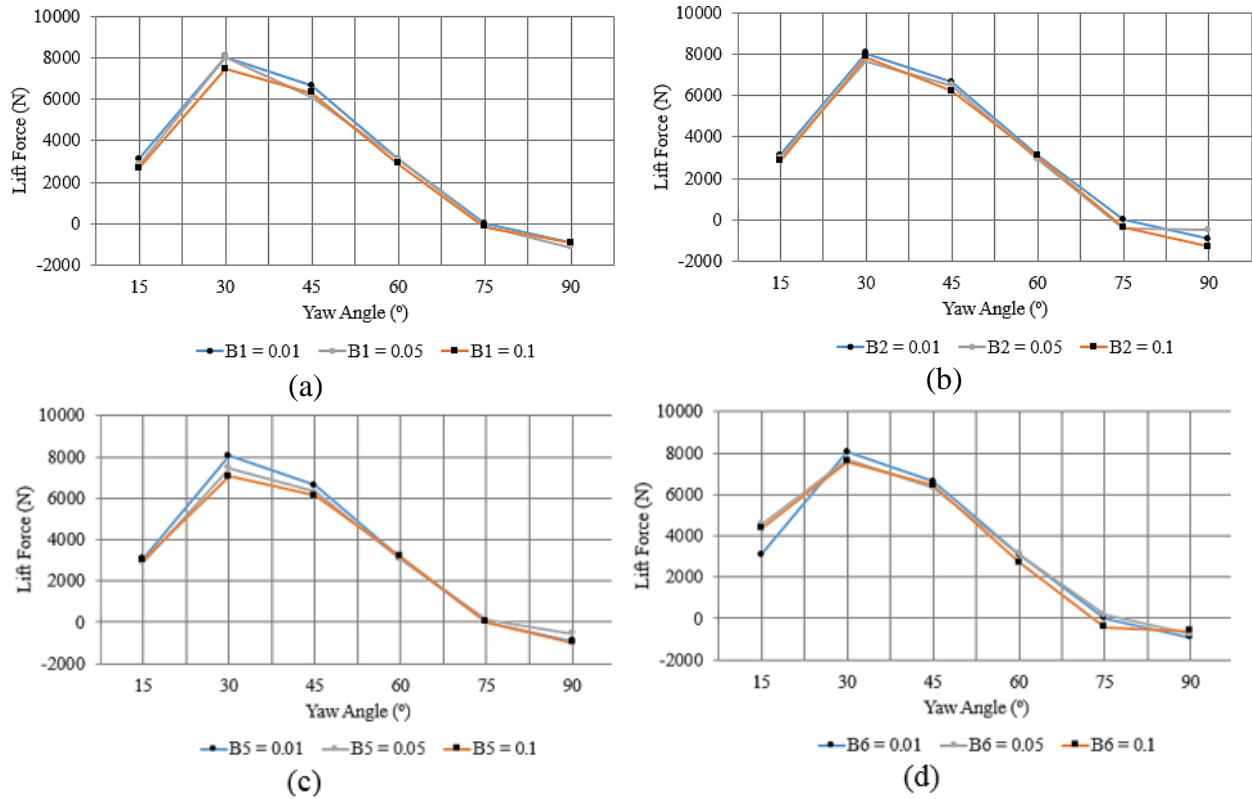


Figure 6.22 Truck-trailer lift force acting on various B1, B2, B5, B6, configurations with varying magnitudes from  $\psi = 15^\circ$  to  $\psi = 90^\circ$ .

Figure 6.23 depicts truck-trailer lift force acting on various B1, B2, B5, B6, configurations with varying magnitudes from  $\psi = 15^\circ$  to  $\psi = 90^\circ$ . It can be seen that the trend is the same for all B configurations where the maximum side force was observed at  $\psi = 60^\circ$  and minimum lift force was observed at  $\psi = 15^\circ$ . Once more, variations are not very obvious due to the wide scale of the maximum and minimum force. In the case of (a), the maximum side force of 29642N was recorded on B1 = 0.1 whereas, minimum side force of 9984N occurs when B1 = 0.01. The maximum variation occurs at  $\psi = 75^\circ$  between B1 = 0.05 and B1 = 0.1 models, which was calculated to have 2.6%. The minimum variation occurs at  $\psi = 15^\circ$ , between B1 = 0.05 and B1 = 0.1, which was calculated to have 0.3%. In the case of (b), the maximum side force of 29578N was recorded on B2 = 0.05 whereas, minimum side force of 9939N occurs when B2 = 0.1. The maximum variation occurs at  $\psi = 75^\circ$  between B2 = 0.01 and B2 = 0.1 models, which was calculated to have 3%. The minimum variation occurs at  $\psi = 15^\circ$ , between B2 = 0.01 and B2 = 0.1, which was calculated to have 0.4%. In the case of (c), the maximum side force of 29298N

was recorded on  $B5 = 0.01$  whereas, minimum side force of 9984N occurs when  $B5 = 0.01$ . The maximum variation occurs at  $\psi = 30^\circ$  between  $B5 = 0.01$  and  $B5 = 0.1$  models, which was calculated to have 3.4%. The minimum variation occurs at  $\psi = 75^\circ$ , between  $B5 = 0.01$  and  $B5 = 0.05$ , which was calculated to have 0.1%. In the case of (d), once more, the maximum side force of 29849N was recorded on  $B5 = 0.05$  whereas, minimum side force of 9075N occurs when  $B5 = 0.1$ . The maximum variation occurs at  $\psi = 60^\circ$  between  $B6 = 0.05$  and  $B6 = 0.1$  models, which was calculated to have 5%. The minimum variation occurs at  $\psi = 45^\circ$ , between  $B6 = 0.01$  and  $B6 = 0.05$ , which was calculated to have 0.5%.

To summarise, it is evident that maximum side force is achieved when the B coefficients = 0.01, while the lowest side force is achieved where the B coefficients = 0.1. For this reason, it can be considered that B coefficient = 0.1 provides the most desirable side force performance for vehicle stability.

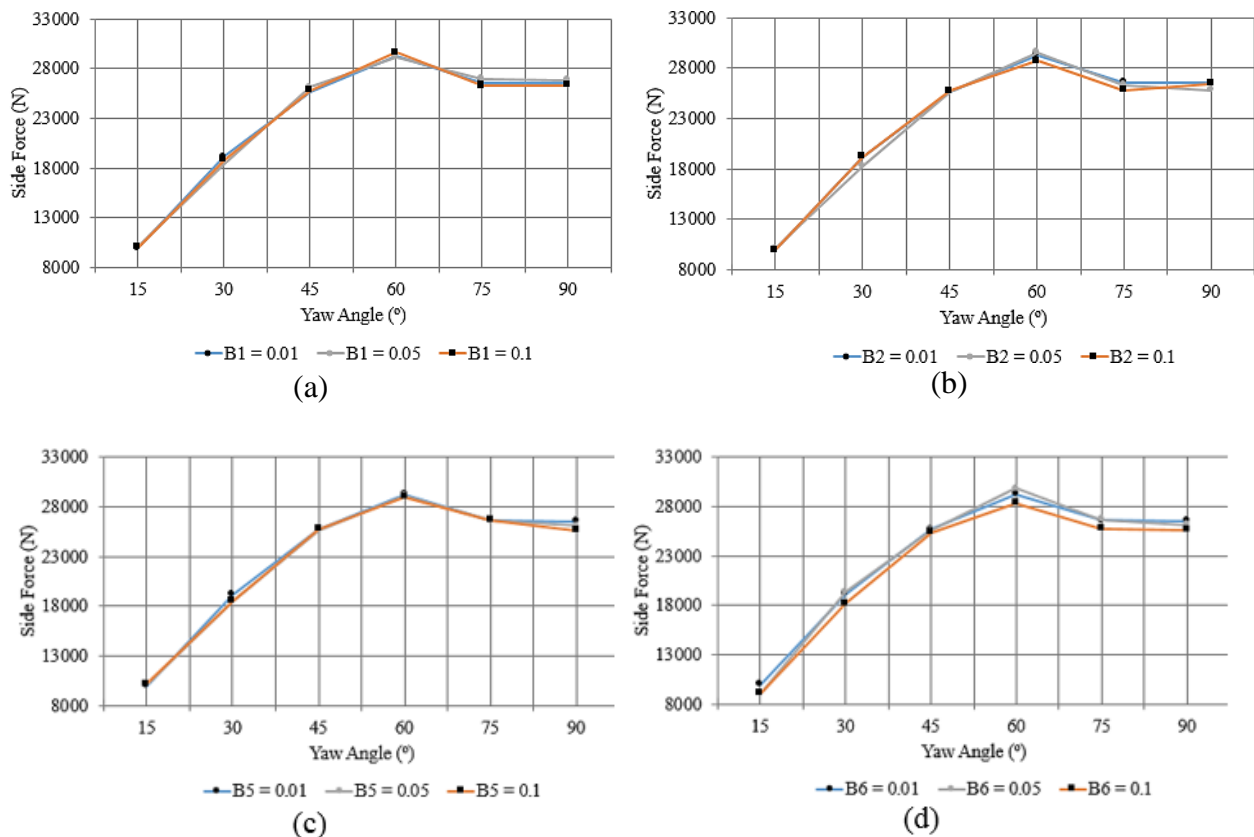


Figure 6.23 Truck-trailer side force acting on various B1, B2, B5, B6, configurations with varying magnitudes from  $\psi = 15^\circ$  to  $\psi = 90^\circ$ .

## 6.9 Development of Semi-Empirical Prediction Models for Drag, Lift and Side Aerodynamic Coefficients considering Shapes Effects at Varying Crosswind Angles

In Chapter 4, the effects of truck-trailer dimensions, such as length, height and width at varying yaw angles was studied. In Chapter 5, the effects of truck-trailer shape coefficients, such as B1, B2, B5 and B6 at straight headwind was studied. This chapter has studied the effects of truck-trailer shape coefficients, such as B1, B2, B5 and B6 at crosswinds. A semi-empirical equation has been developed in this chapter based on B shape coefficients and the crosswind flow angles. This prediction model integrates the aerodynamics force coefficients with truck-trailer shape coefficients at varying crosswind angles. The prediction model replicates the computational data with reasonable accuracy. In this case, evolutionary non-linear optimisation model has been coupled with multiple regression analysis techniques to estimate the truck-trailer shape characteristics and resulting drag, lift and side aerodynamic coefficients.

### 6.9.1 Developing the Drag Coefficient Equation

The prediction model developed in this section will be correlating B1, B2, B5 and B6 shape coefficients and the crosswind flow angles in order to predict the drag force coefficients. To achieve this, the drag force coefficient is represented as functions of proposed shape coefficients and the crosswind angles.

$$C_D = C_D(B_1, B_2, B_5, B_6, \psi) \quad (6-1)$$

Here, three coefficients are defined as 'A', 'B' and 'C' to represent the drag coefficient when B shape coefficient and crosswind flow angle is zero, shape characteristics, and the crosswind flow characteristics, respectively.

$$C_D = A(B + C) \quad (6-2)$$

Figure 6.24 below shows the variation in drag coefficient produced when the B1, B2, B5 and B6 shape coefficient values were altered between 0.01, 0.05 and 0.1 independently, while the rest

were kept at 0.01. The crosswind flow angle for this set of results were set at 15° degrees. For (a), B1 coefficient was selected as the variable that will change and it was noticed that from 0.01 to 0.05 there was a sharp decrease in drag coefficient. From 0.05 to 0.1, a slight reduction was noticed. B2 coefficient is depicted from (b) and as previously, from 0.01 to 0.05 a sharp reduction in drag coefficient was noticed. However, from B2 = 0.05 to 0.1, an increase in drag coefficient was seen at an almost identical rate of change. Figure (c) shows that, when B5 coefficient increases from 0.01 to 0.05 a reduction in drag coefficient was seen. Additionally, when B5 changes from 0.05 to 0.1 drag coefficient continues to decrease further at a reduced rate. It was seen from (d), as B6 coefficient increases from 0.01 to 0.05, the drag coefficient increased at a sharp rate and from 0.05 to 0.1 the drag coefficient decreased slightly.

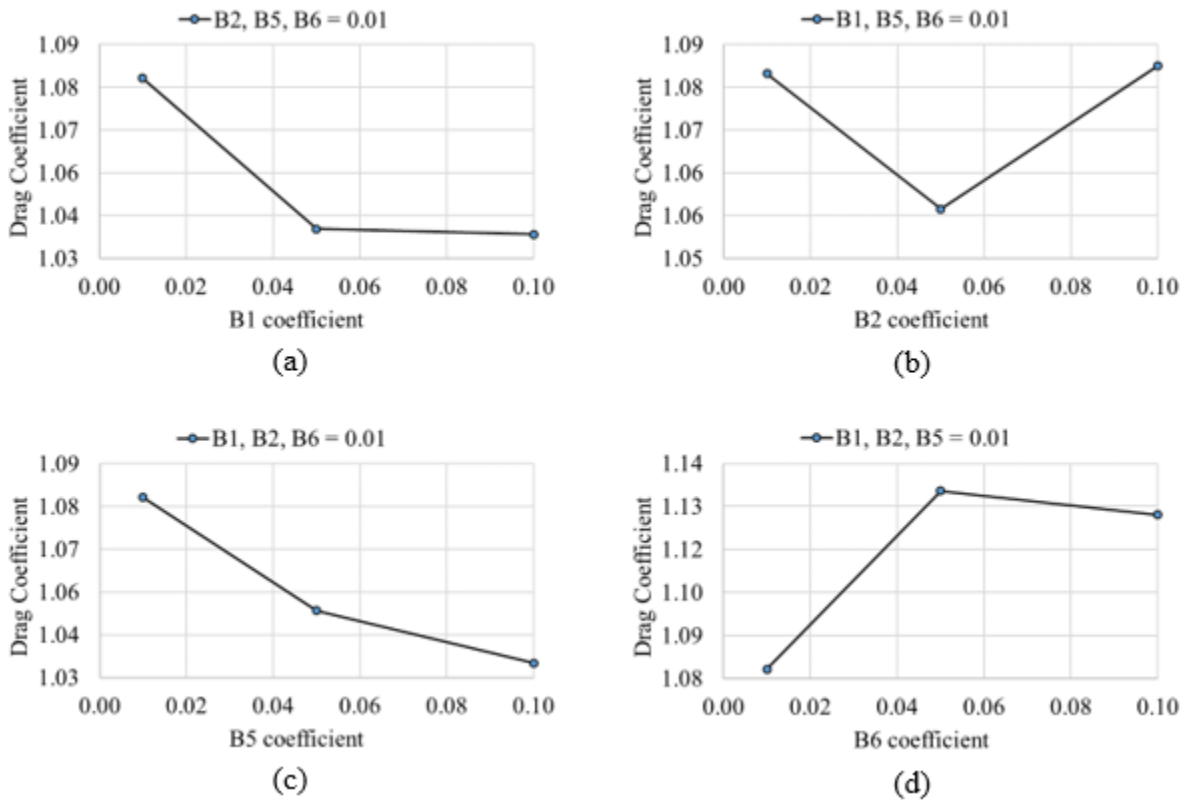


Figure 6.24 Drag force coefficient for varying (a) B1, (b) B2, (c) B5 and (d) B6 shape coefficients at 15° yaw angle.

Figure 6.25 below shows the variation in drag coefficient produced when the B1, B2, B5 and B6 coefficient values were altered between 0.01, 0.05 and 0.1 independently, while the rest were

kept at 0.01. The crosswind flow angle for this set of results were set at 45° degrees. For (a), B1 coefficient B1 was selected as the variable that will change, it was noticed that from 0.01 to 0.05, there was a sharp decrease in drag coefficient. From 0.05 to 0.1 a slight increase in drag coefficient was noticed. B2 coefficient was depicted from (b), from 0.01 to 0.05 a sharp increase in drag coefficient was noticed. In addition, from 0.05 to 0.1 drag coefficient was seen to continue to increase at almost the same rate. Figure (c) showed that, when B5 coefficient increased from 0.01 to 0.05, a slight reduction in drag coefficient was seen, when B5 changes from 0.05 to 0.1 a sudden decrease drag coefficient was seen. It can be seen from (d), as B6 coefficient increased from 0.01 to 0.05 the drag coefficient increased at a sharp rate and from 0.05 to 0.1 the drag coefficient decreased slightly, very similar to (d) from Figure 6.25 with crosswind flow angle 15°.

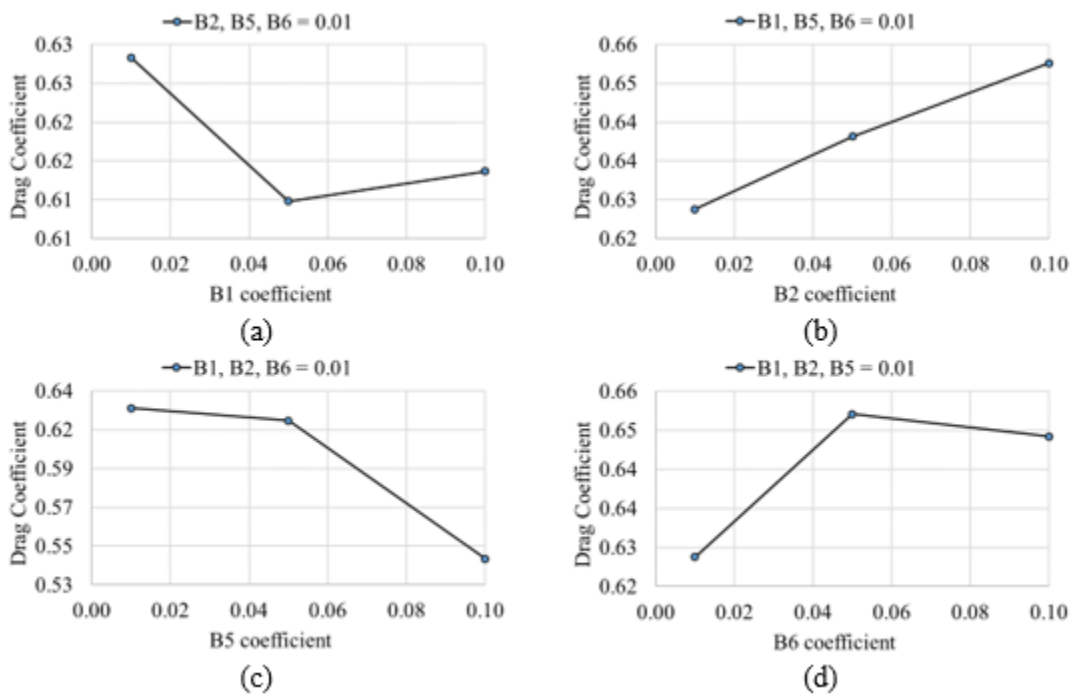


Figure 6.25 Drag force coefficient for varying (a) B1, (b) B2, (c) B5 and (d) B6 shape coefficients at 45° yaw angle.

Figure 6.26 below shows the variation in drag coefficient produced when the B1, B2, B5 and B6 coefficient values were altered between 0.01, 0.05 and 0.1 independently while the rest were kept at 0.01. The crosswind flow angle for this set of results were set at 75° degrees. For (a),

coefficient B1 was selected as the variable that will change, it was noticed that from 0.01 to 0.05 there was a sharp decrease in drag coefficient. From 0.05 to 0.1 an increase in drag coefficient was noticed albeit at a lower rate. B2 was chosen for (b), from 0.01 to 0.05 a sharp increase in drag coefficient was noticed furthermore, from 0.05 to 0.1 drag coefficient was seen to continue to increase at almost the same rate. This almost seemed to mimic the behaviour of (b) from Figure 6.26. Figure (c) showed that when B5 coefficient increased from 0.01 to 0.05 a significant increase in drag coefficient was seen, when B5 increased from 0.05 to 0.1 a slight decrease drag coefficient was seen. It was seen from (d), as B6 coefficient increased from 0.01 to 0.05 the drag coefficient increased at a sharp rate and from 0.05 to 0.1 the drag coefficient decreased, albeit at a slightly reduced rate.

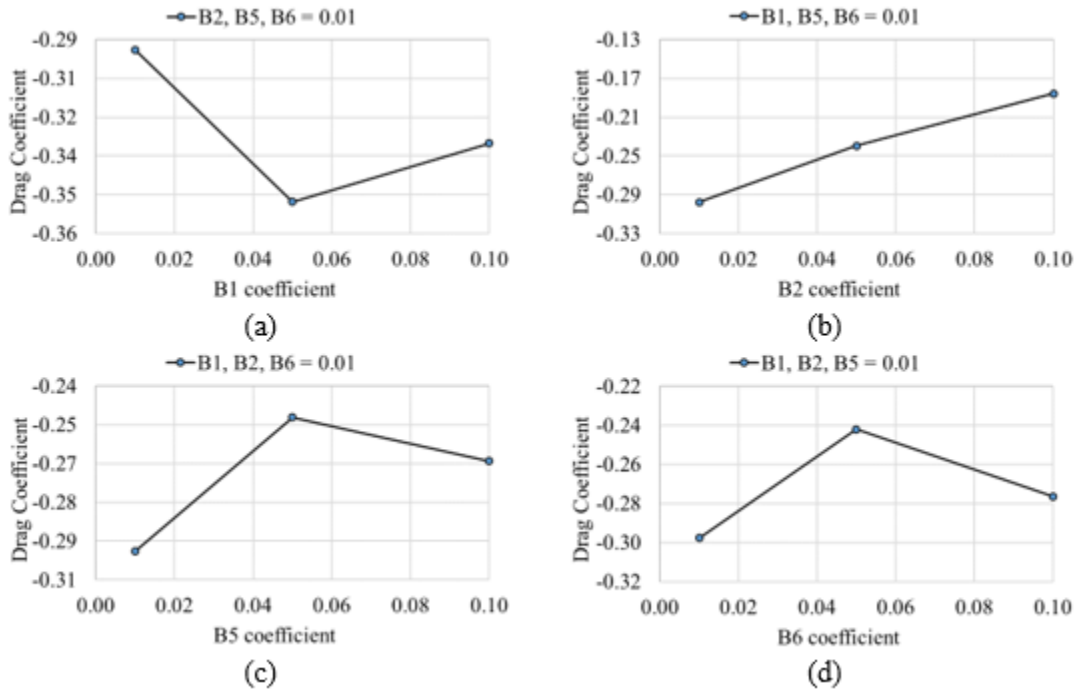


Figure 6.26 Drag force coefficient for varying (a) B1, (b) B2, (c) B5 and (d) B6 shape coefficients at 75° yaw angle.

When the yaw angles were taken into consideration the following was deduced. All three (a) Figures showed that for B1 coefficient, when the crosswind yaw angle was 15°, 45° and 75° drag force showed a sharp decrease when B1 coefficient increased from 0.01 to 0.05. However, when

B1 increased from 0.05 to 0.1 both 45° and 75° models showed a sharp increase in drag force, whereas 15° model showed a slight decrease in drag force. All three (b) Figures showed that, when B2 coefficient increased from 0.01 to 0.1 both 45° and 75° models showed perpetual increase in drag force. However, 15° model showed a sharp decrease in drag force when B2 increased from 0.01 to 0.05 while a rapid increase in drag force was seen when B2 increased from 0.05 to 0.1. All three (c) Figures showed that as B5 coefficient increased from 0.01 to 0.1 both 15° and 45° models showed a perpetual decrease in drag force. However, for 75° model as B5 coefficient increased from 0.01 to 0.05 drag force showed a sharp increase and as B5 increased from 0.05 to 0.1 a slight decrease in drag force was seen. All three (d) Figures showed that as B6 coefficient increased from 0.01 to 0.1 all three 15°, 45° and 75° models behaved in the same manner. When B6 increased from 0.01 to 0.05 drag force showed a rapid increase and from B6 = 0.05 to 0.1 drag force decreased. A sharper decrease was seen for 75° model, meanwhile 15° and 45° only showed a slight decrease.

By studying the CFD data obtained for the drag force coefficient, following functional form was used to represent coefficients ‘B’ and ‘C’ which incorporates the shape characteristics defined by B shape coefficients and the crosswind characteristics. The coefficients ‘A’, ‘B’ and ‘C’ are represented as:

$$A = C_{D_{B1,B2,B6,\psi=0}} \quad (6-3)$$

$$B = \left( \frac{1 + \left(\frac{B_6^a}{C_1}\right) \cdot C_2}{1 + \frac{B_1^b}{C_3} + B_2^c + C_4 B_5^d} \right) \quad (6-4)$$

Coefficient ‘C’ is represented as:

$$C = \left( C_5 \cdot \sin \left( \frac{C_6 \psi^e}{C_7} \right) \right) \quad (6-5)$$

After evaluating the data set for drag force coefficient, the final form of the drag coefficient prediction equation was obtained which has been characterised by B1, B2, B5 and B6 shape coefficients and the crosswind flow angle. This equation can be illustrated as:

$$C_D = 0.55 \left( \frac{1 + \left( \frac{B_6^{1.062}}{0.991} \right) \cdot 1.166}{1 + \left( \frac{B_1^{0.307}}{1.051} \right) + (B_2^{1.758}) - (0.298B_5^{1.965})} \right) + 0.676 \cdot \sin \left( \frac{0.973\psi^{0.837}}{0.268} \right) \quad (6-6)$$

Figure 6.27 depicts the correlation between the predicted values of the aerodynamic drag force coefficients, and those obtained from CFD. Once again, it can be clearly seen that the predicted values agree very well with those obtained from CFD. The standard error of estimate has been calculated to be around 15%. Hence, equation (6-6), developed for characterising the aerodynamic drag force coefficient in terms of the proposed truck-trailer shape parameters is well capable of providing accurate predictions in place of CFD data.

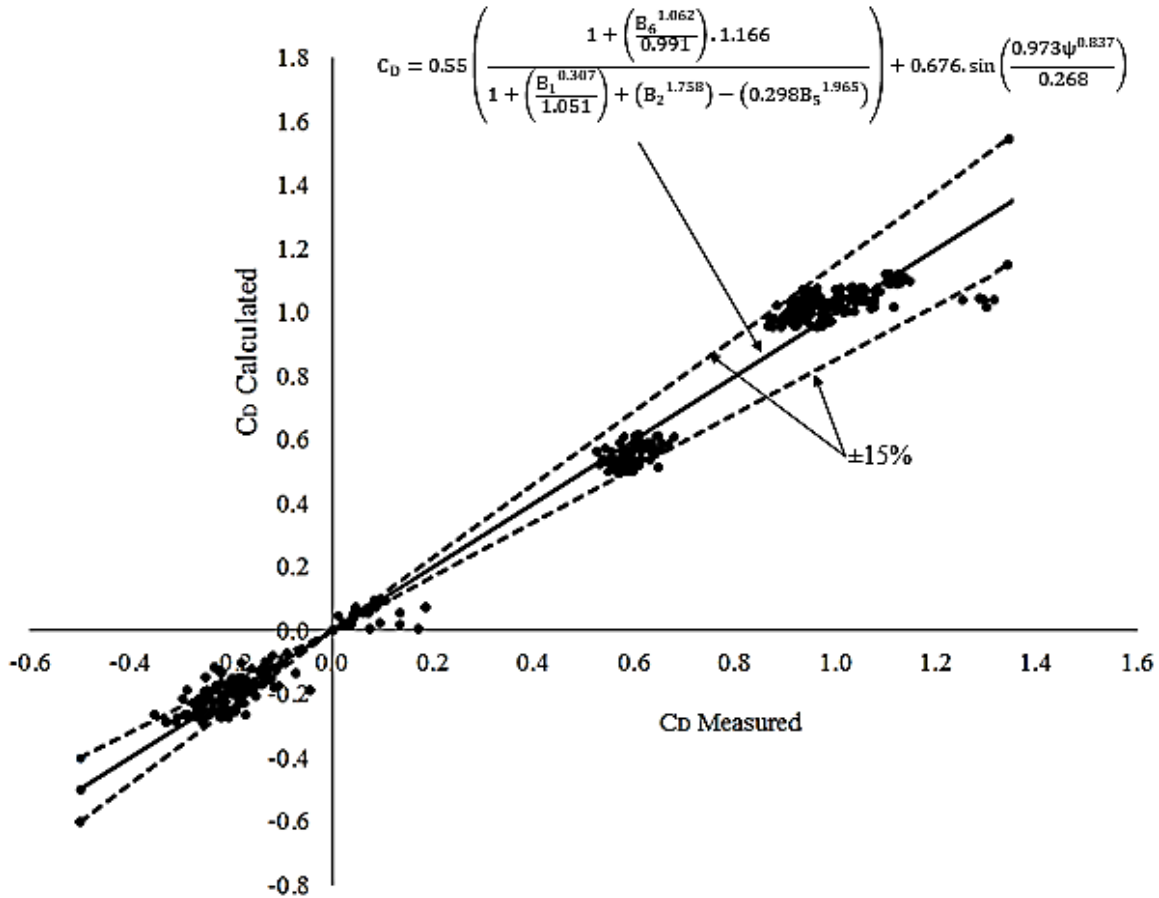


Figure 6.27 Correlation between aerodynamic drag force coefficient measured from CFD and calculated by the proposed prediction methodology for various truck-trailer geometries.

### 6.9.2 Developing the Lift Coefficient Equation

The prediction model developed in this section will be correlating the B1, B2, B5 and B6 shape coefficients and the crosswind flow angles in order to predict the lift force coefficients. In order to achieve this, the lift force coefficient is represented as functions of proposed shape coefficients and crosswind angle.

$$C_L = C_L(B_1, B_2, B_5, B_6, \psi) \quad (6-7)$$

Once more, three coefficients are defined as ‘A’, ‘B’ and ‘C’ to represent the lift coefficient when B shape coefficients and crosswind flow angles are zero, shape characteristics and the crosswind flow characteristics, respectively.

$$C_L = A(B + C) \quad (6-8)$$

Figure 6.28 depicts the lift force coefficient for varying (a) B1, (b) B2, (c) B5 and (d) B6 shape coefficients at 15° yaw angle where the remaining B coefficients were fixed at 0.01. The maximum lift coefficient was observed in the case of B6 = 0.05, while the minimum lift coefficient was observed in the case of B1 = 0.05. It was seen when B1, B2, B5 = 0.01 to 0.05, lift coefficient decreased however when B6 = 0.01 to 0.05, lift coefficient decreased. Further to this, when B2, B5, B6 = 0.05 to 0.1, lift coefficient gradually declined whereas, in the case for B6, lift coefficient increased. It was noticed that the effect of lift coefficient had a higher rate of change in cases where B5 and B6 coefficients were varying. Meanwhile, the change in lift coefficient was more linear in the cases when B1 and B2 coefficient were varying.

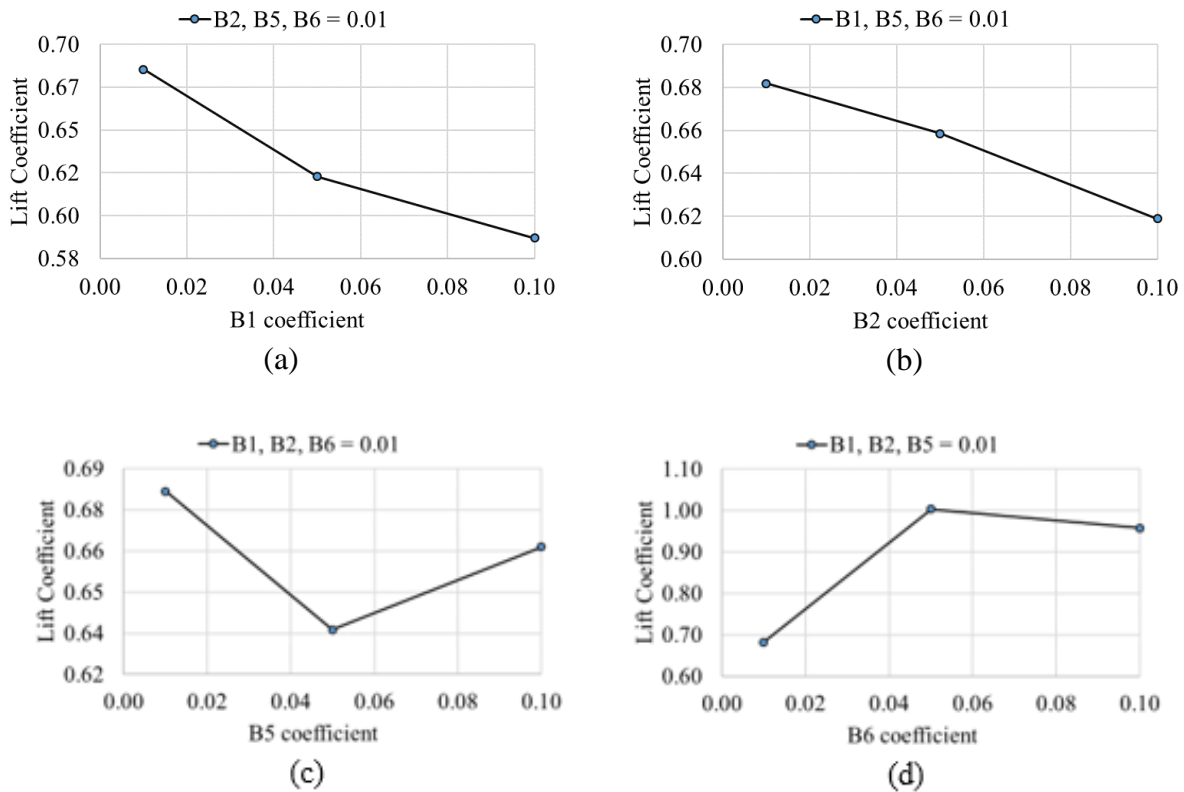


Figure 6.28 Lift Force Coefficient for varying (a) B1, (b) B2, (c) B5 and (d) B6 shape coefficients at 15° yaw angle.

Figure 6.29 depicts the lift force coefficient for varying (a) B1, (b) B2, (c) B5 and (d) B6 shape coefficients at 45° yaw angle where the remaining B coefficients were fixed at 0.01. The maximum lift coefficient was observed in the case of B6 = 0.01, while the minimum lift coefficient was observed in the case of B1 = 0.01. It was observed that when B1, B2, B5, B6 = 0.01 to 0.05, lift coefficient decreased however this reduction was much steeper in the cases on varying B1 and more gradual in the cases of varying B2 and B5. When B1, B2, B5, B6 = 0.05 to 0.1, lift coefficient increases in cases for B1 and B6 and decreases in cases for B2 and B5. It was noticed that the trend for varying B5 was opposing to that at B2, while B1 and B6 appeared somewhat the same.

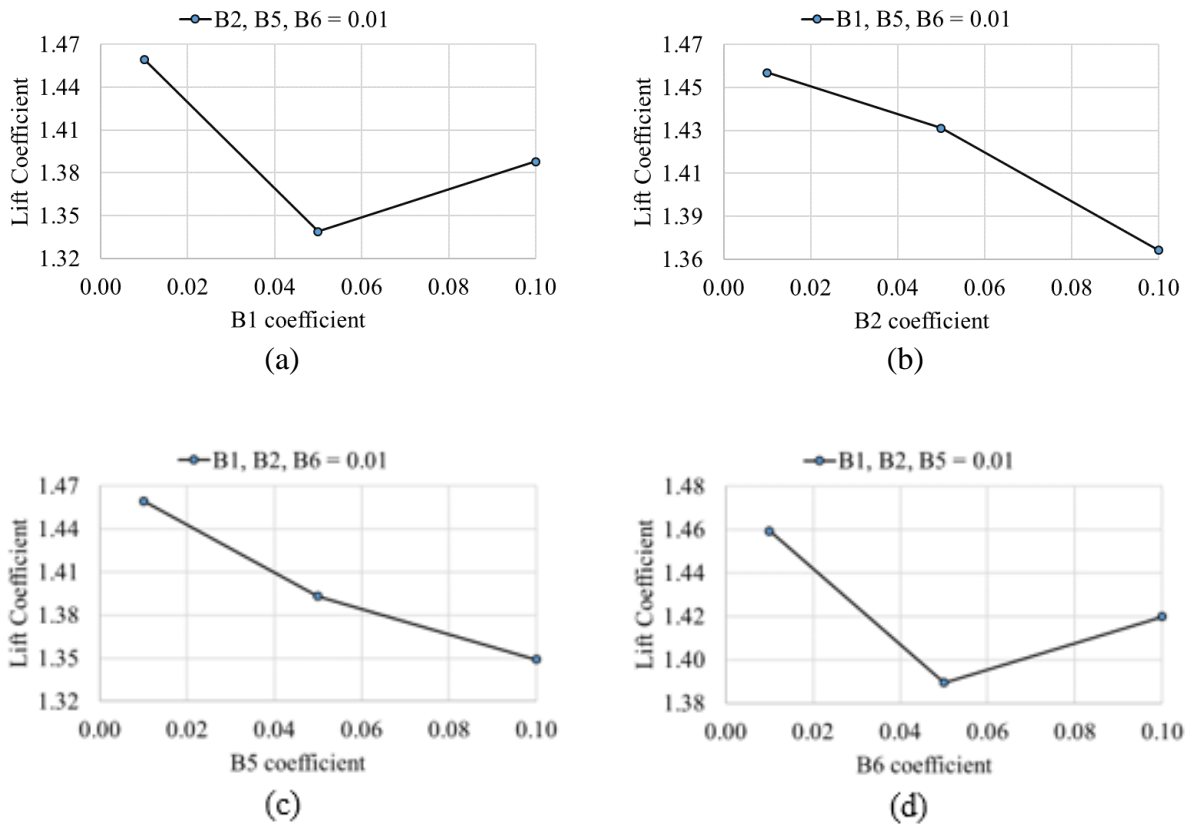


Figure 6.29 Lift Force Coefficient for varying (a) B1, (b) B2, (c) B5 and (d) B6 shape coefficients at 45° yaw angle.

Figure 6.30 depicts the lift force coefficient for varying (a) B1, (b) B2, (c) B5 and (d) B6 shape coefficients at 75° yaw angle where the remaining B coefficients were fixed at 0.01. The

maximum lift coefficient was observed in the case of  $B_6 = 0.05$ , while the minimum lift coefficient was observed in the case of  $B_6 = 0.1$ . It was seen that when  $B_1, B_2 = 0.01$  to  $0.05$ , lift coefficient sharply decreased, whereas when  $B_5, B_6 = 0.01$  to  $0.05$  lift coefficient increased. When  $B_1, B_5, B_6 = 0.05$  to  $0.1$ , lift coefficient decreased sharply for varying  $B_5$  and  $B_6$ , while very slightly for varying  $B_1$ . In addition to this, when  $B_2 = 0.05$  to  $0.1$ , lift coefficient slightly increased.

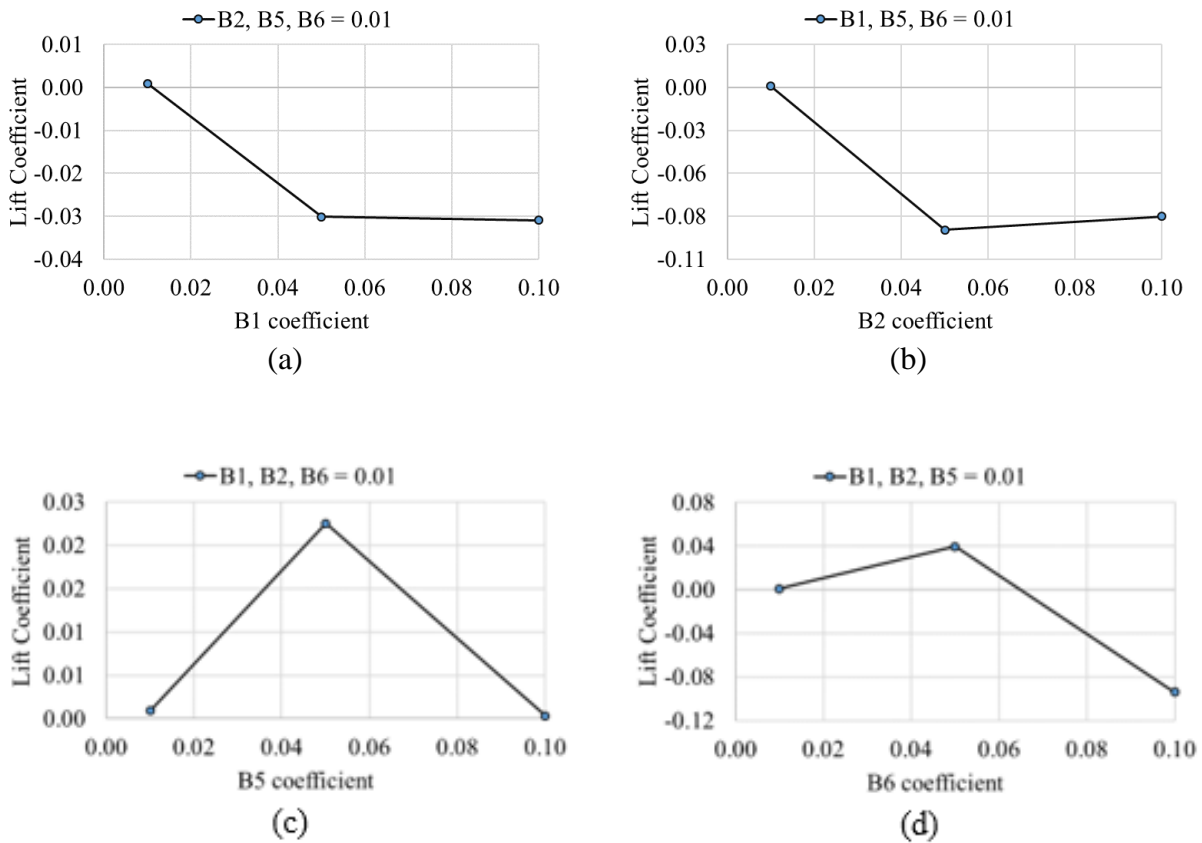


Figure 6.30 Lift Force Coefficient for varying (a) B1, (b) B2, (c) B5 and (d) B6 shape coefficients at 75° yaw angle.

Overall, when  $B_1$  was varying at various crosswind angles, the effect of lift force coefficient decreased for  $B_1 = 0.01$  to  $0.05$  through all the yaw angles. When  $B_1 = 0.05$  to  $0.1$ , lift coefficient decreases during 15° yaw angle and increased significantly during 45° and slightly during 75°. When  $B_2$  is varying at various crosswind angles, the effect of lift force coefficient almost linearly decreased throughout  $B_2 = 0.01$  to  $0.1$  at yaw angles 15° and 45°. This linearity

was more prominent at 15° than at 45°. Moreover, at 75° yaw angle, lift coefficient decreased from B2 = 0.01 to 0.05, which then slightly increased when B2 = 0.1. Observing varying B5 shape coefficients, lift force coefficient varied throughout for 45° yaw angle in an almost linear manner. When B5 = 0.01 to 0.5 in the case of 15°, lift coefficient decreased considerably and increased significantly during yaw angle of 75°. When B5 = 0.05 to 0.1, there was an abrupt increase in lift coefficient during 15° yaw angle and an abrupt decrease at 75° yaw angle. Further to this, lift coefficient increase when B6 = 0.01 to 0.05 at 15° and 75° yaw angles whereas during 45°, lift coefficient decreased considerably. When B6 = 0.05 to 0.1, lift coefficient decreased slightly during 15° and significantly during 75° while increases at 45°.

By studying the CFD data obtained for the lift force coefficients, following functional form was used to represent coefficients ‘B’ and ‘C’ which incorporates the shape characteristics defined by B shape coefficients and the crosswind characteristics. The coefficients ‘A’, ‘B’ and ‘C’ are represented as:

$$A = C_{L, B1, B2, B6, \psi=0} \quad (6-9)$$

$$B = \left( \frac{1 + \left( \frac{C_1(B_6^a)}{C_2} \right) \cdot C_3}{1 + \frac{C_4(B_1)^b}{C_5} + \frac{C_6(B_2)^c}{C_7} + \frac{C_8(B_5)^d}{C_9}} \right) \quad (6-10)$$

And coefficient ‘B’ is represented as:

$$C = \left( C_{10} \cdot \sin(C_{11} \psi^e) \right) \quad (6-11)$$

After evaluating the data set for lift force coefficient, the final form of the lift coefficient prediction equation was obtained which has been characterised by B1, B2, B5 and B6 shape coefficients and the crosswind flow angle. This equation can be illustrated as:

$$C_L = -0.13 \left( \frac{1 + \left( \frac{0.251B_6^{1.517}}{1.434} \right) \cdot 1.1}{1 + \left( \frac{1.235B_1^{-1.332}}{1.515} \right) + \left( \frac{1.2B_2^{1.978}}{0.123} \right) - \left( \frac{0.95B_5^{2.12}}{0.762} \right)} \right) - 6 \cdot \sin(2.88\psi^{0.313}) \quad (6-12)$$

Figure 6.31 depicts the correlation between the predicted values of the aerodynamic lift force coefficients, and those obtained from CFD. It was observed that the predicted values agreed very well with those obtained from CFD. The standard error of estimate was calculated to be around 15%. Hence, equation (6-12), developed for characterising the aerodynamic lift force coefficient in terms of the proposed truck-trailer shape parameters is capable of providing accurate predictions in place of CFD data.

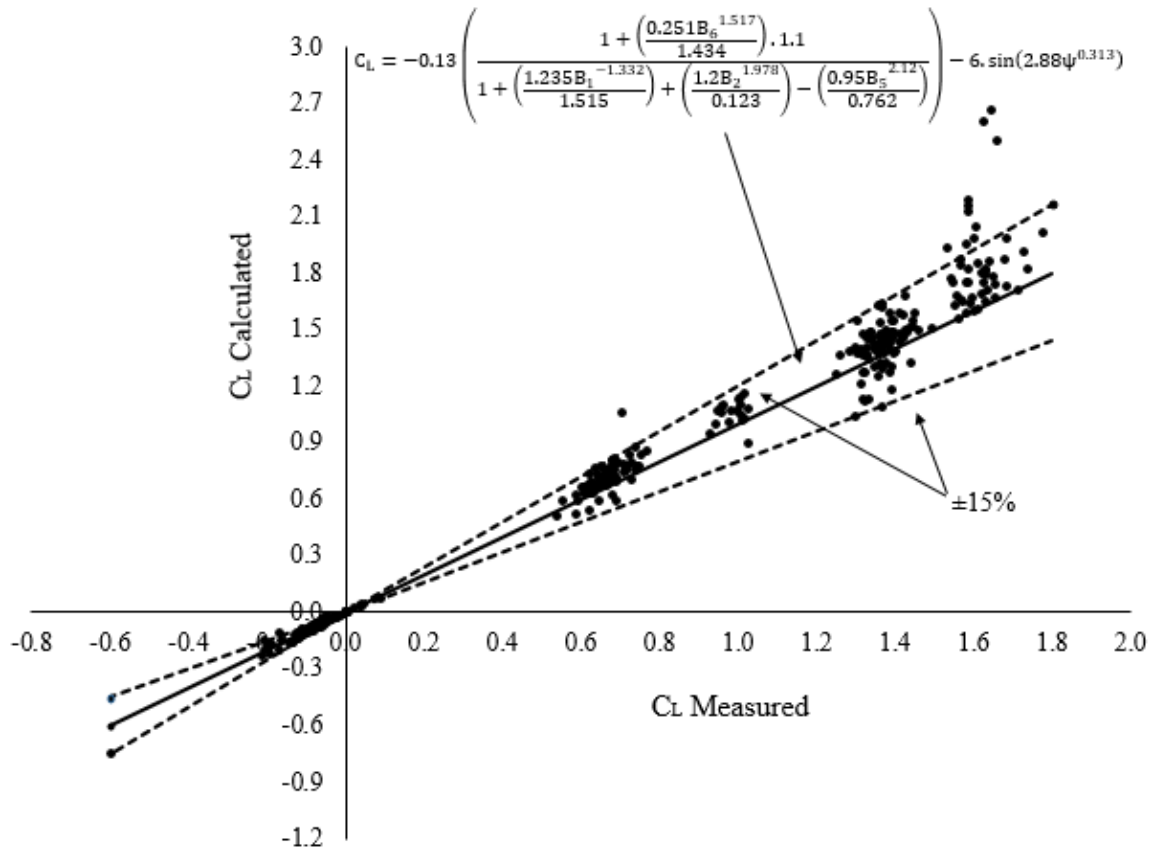


Figure 6.31 Correlation between aerodynamic lift force coefficient measured from CFD and calculated by the proposed prediction methodology for various truck-trailer geometries.

### 6.9.3 Developing the Side Coefficient Equation

The prediction model developed in this section will be correlating the B1, B2, B5 and B6 shape coefficients and the crosswind flow angle in order to predict the side force coefficients. In order to achieve this, the side force coefficient is represented as functions of B1, B2, B5, B6 shape coefficients and crosswind angle.

$$C_S = C_S(B_1, B_2, B_5, B_6, \psi) \quad (6-13)$$

In this particular instance, only two coefficients were defined to represent shape characteristics and the crosswind flow characteristics. This was done based on the assumption that at zero crosswinds, the side force coefficient is zero. Coefficients ‘A’ and ‘B’ in this case represent the shape characteristics and the crosswind flow characteristics, respectively as depicted from equation (6-14).

$$C_S = A + B \quad (6-14)$$

Figure 6.32 depicts the side force coefficient for truck-trailer units when the B1, B2, B5 and B6 coefficient varies between the values of 0.01, 0.05 and 0.1 at 15° yaw angle. Observing (a) it was seen that the side force coefficient increased from B1 = 0.01 to 0.05 before decreasing at B1 = 0.1. At (b), the side force coefficient was seen to increase from B2 value of 0.01 to 0.05 before decreasing to the minimum side coefficient value at B2 = 0.1. A steady increase in the side force coefficient was seen at (c) when the B5 shape coefficient value increased from 0.01 to 0.1. Lastly, the side force coefficient was seen to decrease sharply when B6 value increased from 0.01 to 0.05 and followed by further decrease at B6 = 0.1.

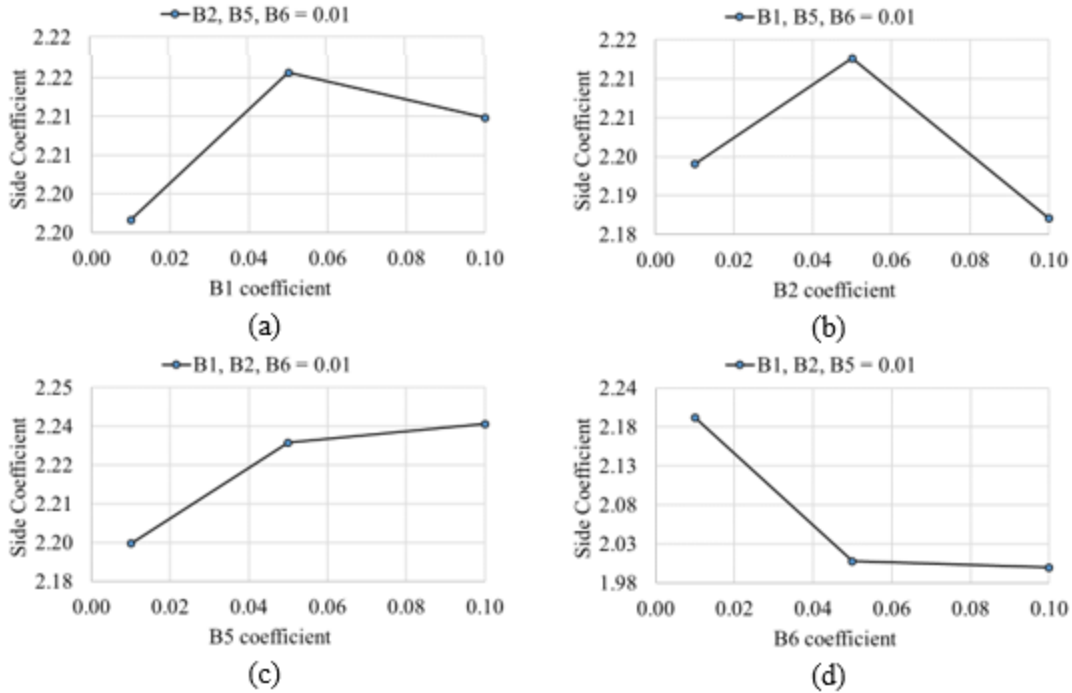


Figure 6.32 Side force coefficient for varying (a) B1, (b) B2, (c) B5 and (d) B6 shape coefficients at 15° yaw angle.

Figure 6.33 depicts the side force coefficient for truck-trailer units when the (a) B1, (b) B2, (c) B5 and (d) B6 coefficients varied between the values of 0.01, 0.05 and 0.1 at 45° yaw angle. Observing (a) it was seen that the side force coefficient increases from B1 = 0.01 to 0.05 before decreasing at B1 = 0.1. At (b), the side force coefficient was seen to decrease from B2 value of 0.01 to 0.05 before increasing to a maximum side coefficient value at B2 = 0.1. A decrease in the side force coefficient was seen at (c) when the B5 shape coefficient value increased from 0.01 to 0.05 before increasing at B5 = 0.1. Almost linear decrease in the side force coefficient was seen at (d) when the B5 shape coefficient value increased from 0.01 to 0.1.

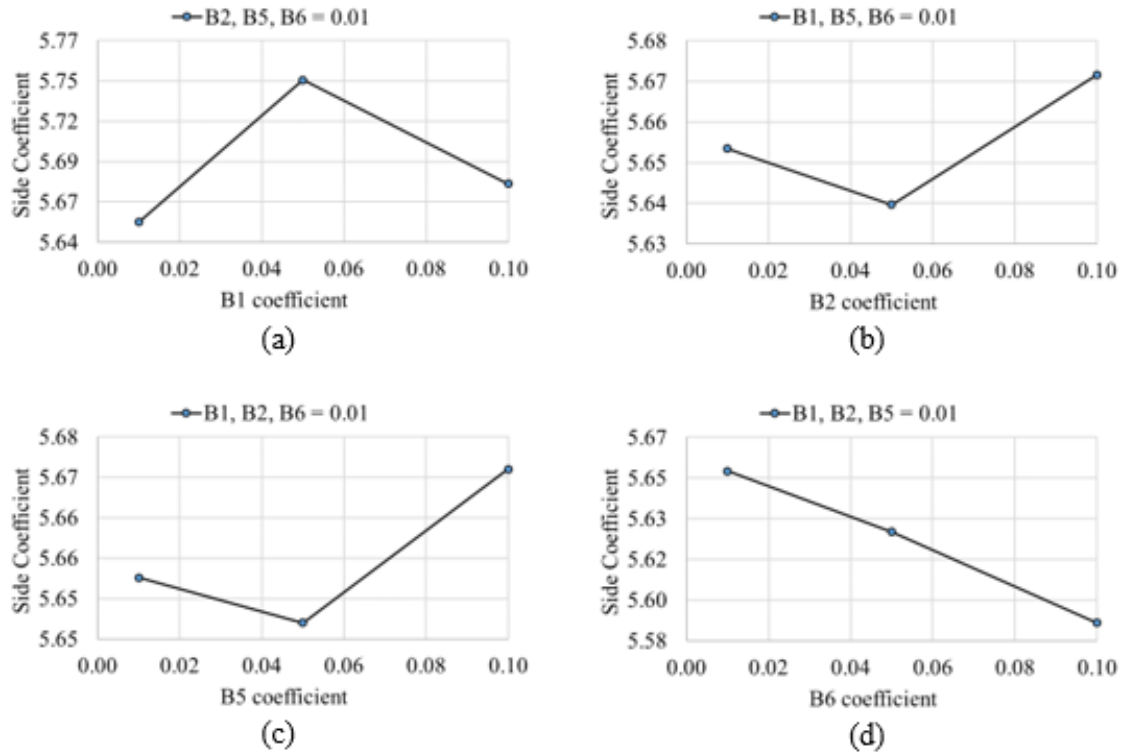


Figure 6.33 Side force coefficient for varying (a) B1, (b) B2, (c) B5 and (d) B6 shape coefficients at 45° yaw angle.

Figure 6.34 depicts the side force coefficient for truck-trailer units when the B1, B2, B5 and B6 coefficient varied between the values of 0.01, 0.05 and 0.1 at 75° yaw angle. Once again, looking at (a), it was seen that the side force coefficient increased from B1 = 0.01 to 0.05 before decreasing at B1 = 0.1. Almost a linear decrease in the side force coefficient was seen at (b) when B2 shape coefficient values increased from 0.01 to 0.1. Whereas, a steady increase in side force coefficient was observed for (c) when B5 coefficient value increased from B5 = 0.01 to 0.1. At (d), the side force coefficient was seen to increase slightly from B6 = 0.01 to 0.05, before decreasing sharply at B6 = 0.1.

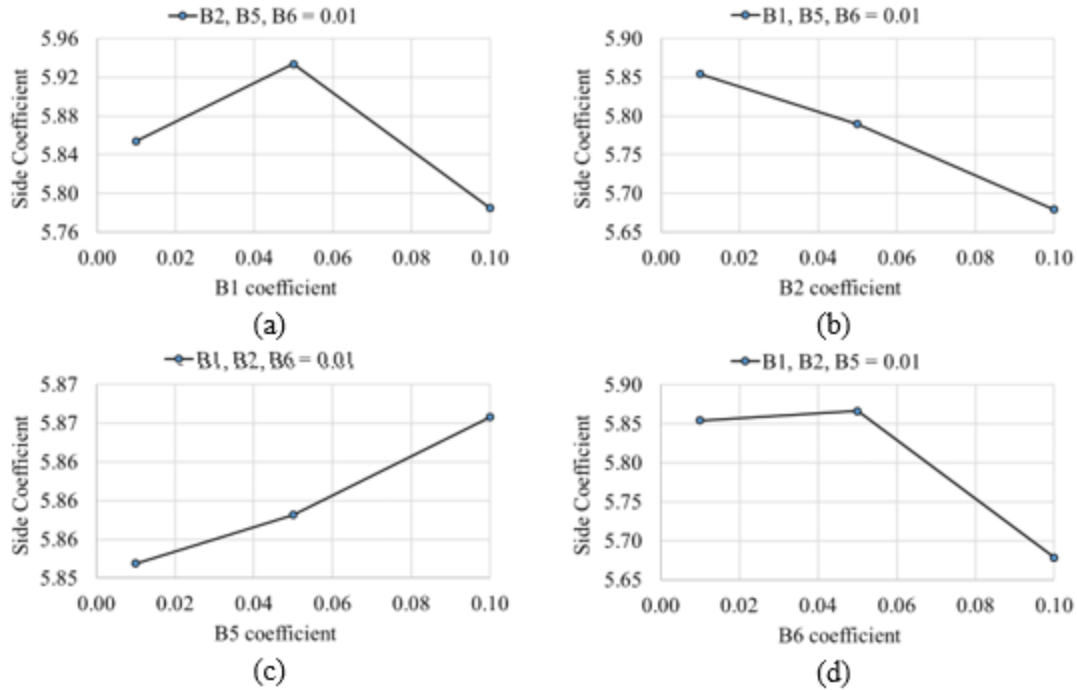


Figure 6.34 Side force coefficient for varying (a) B1, (b) B2, (c) B5 and (d) B6 shape coefficients at 75° yaw angle.

The changing crosswind angles were seen to have an effect on the side force coefficients observed at truck-trailer units with varying B shape coefficients. The side force coefficient acting on the truck-trailer units were seen to increase as the yaw angle increased from 15° to 75°. The side force coefficient trend observed as the B1 coefficient increased was seen to be very similar throughout the crosswind flow range. At B2 shape coefficient, completely opposite trend in side force coefficient was seen at 15° and 45° yaw angles followed by a complete decrease in side force throughout the B2 range at 75° yaw. A steady increase in side force coefficient was observed at both 15° and 75° yaw angles for B5 coefficient, whereas at 45° yaw, the side force coefficient was seen to decrease and then increase at B5 = 0.1. For B6 coefficient, the side force was seen to decrease at 15° and 45° yaw angles. However, at 75° yaw angle, the side force was seen to increase slightly before decreasing rapidly.

By studying the CFD data obtained for the lift force coefficients, following functional form was used to represent coefficients ‘A’ and ‘B’ which incorporates the shape characteristics defined by

B shape coefficients and the crosswind characteristics. The coefficients ‘A’ and ‘B’ are represented as:

$$A = \left( \frac{1 + \left(\frac{B_6^a}{C_1}\right) \cdot C_2}{1 + B_1^b + B_2^c + B_5^d} \right) \quad (6-15)$$

And coefficient ‘B’ is represented as:

$$B = \left( C_3 \cdot \sin\left(\frac{C_4 \Psi^e}{C_5}\right) \right) \quad (6-16)$$

After evaluating the data set for side force coefficient, the final form of the side force coefficient prediction equation was obtained which has been characterised by B1, B2, B5 and B6 shape coefficients and the crosswind flow angle. This equation can be illustrated as:

$$C_s = \left( \frac{1 - \left(\frac{B_6^{-1.191}}{3.877}\right) \cdot 2.549}{1 + (B_1^{6.722}) + (B_2^{8.192}) + (B_5^{-5.108})} \right) + 6.472 \cdot \sin\left(\frac{9.88\Psi^{1.1}}{7.465}\right) \quad (6-17)$$

Figure 6.35 shows the correlation between the predicted values of the aerodynamic side force coefficients, and those obtained from CFD. Once again, it can be clearly seen that the predicted values agree very well with those obtained from CFD. The standard error of estimate has been calculated to be around 15%. Hence, equation (6-17), developed for characterising the aerodynamic side force coefficient in terms of the proposed truck-trailer shape parameters is well capable of providing accurate predictions in place of CFD data.

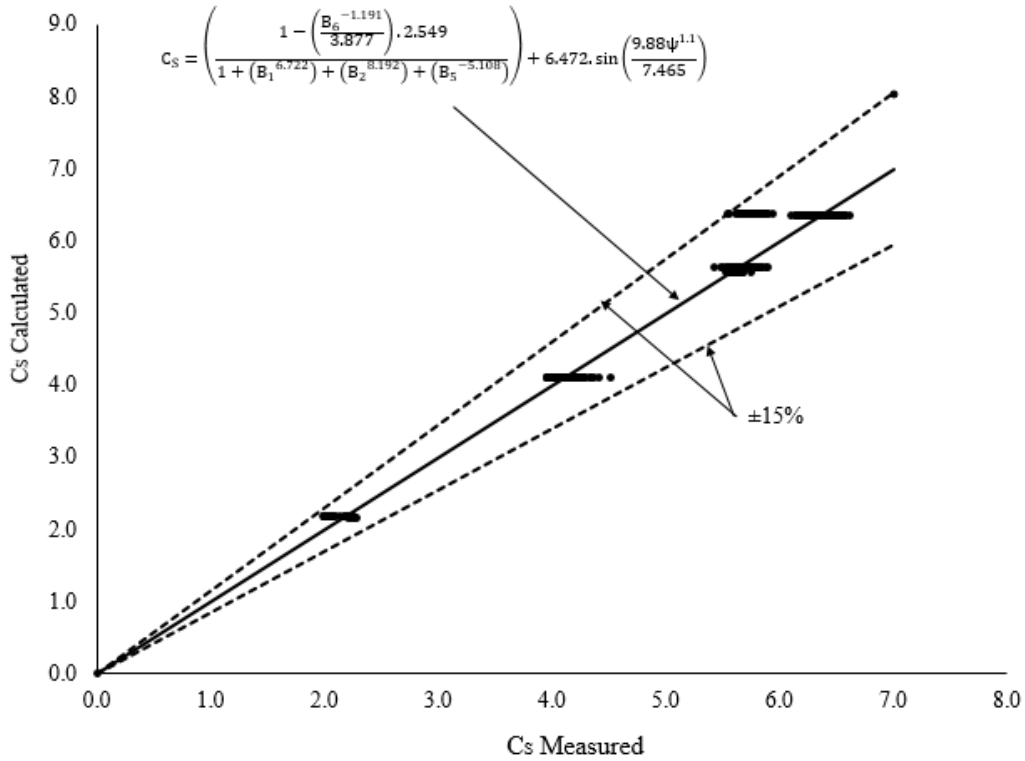


Figure 6.35 Correlation between aerodynamic side force coefficient measured from CFD and calculated by the proposed prediction methodology for various truck-trailer geometries.

## 6.10 Summary

The effects of changing truck-trailer shape on the resulting aerodynamic characteristics have been analysed under crosswinds. Significant flow separation is seen around truck-trailer units under crosswind flow conditions and the resulting flow circulation regions on the leeward side of the vehicles were observed to increase with the yaw angle. The pressure acting on the front-truck, rear-truck, front-trailer and rear-trailer surfaces are seen to reduce significantly with increasing yaw angle. Increasing B1 shape coefficient from 0.01 to 0.1 generates low average pressure on the front surface of the truck throughout all crosswind angles. Negative pressure was observed on the rear surface of the truck throughout all crosswind angles. Between  $\psi = 30^\circ$  and  $\psi = 75^\circ$ , the leeward side was seen to exhibit higher pressures in comparison with the windward side. High pressure was observed on the front trailer surface for both  $B_5 = 0.01$  and  $B_5 = 0.1$  shape profiles at  $\psi = 15^\circ$ . After  $\psi = 15^\circ$ , negative pressure was observed on the trailer front surface for both cases. For the rear surface of the trailer, negative pressure was depicted

throughout all crosswind angles. Furthermore, when B6 was increased from 0.01 to 0.1 the pressure was seen to further decrease on the trailer rear surface for majority of the crosswind profiles. Significant variations in forces acting on individual truck-trailer surfaces under crosswinds were observed. Changing the B1, B2, B5 and B6 shape coefficients were seen to have an effect on the forces experienced by truck-trailer units. Drag force experienced by truck-trailer units were seen to decrease with increasing crosswind angles. Certain B shape parameters were seen to have more of an effect on the overall drag, lift and side forces than others. It was discovered that when B1 = 0.01, the front surface of the truck was subjected to higher forces in the positive x-direction and positive y-direction throughout the crosswind range. This was also made evident on the rear surface of the truck for B2 = 0.01 for force in the positive x-direction, however for the positive y-direction, B2 = 0.1 exhibit higher forces. Additionally, when B5 = 0.01, the front surface of the trailer was subjected to higher forces in the positive x-direction and positive y-direction throughout the crosswind range. When B6 = 0.1, high force is exhibited in the positive x-direction for the trailer rear surface. Using the data gathered in the analysis stage, a force prediction methodology has been developed. The prediction methodology has been validated against the CFD data and was proven to be capable of predicting drag, lift and side forces at both straight and crosswind profiles. The developed prediction methodology is capable of predicting aerodynamic forces considering both yaw angle and shape parameters with a reasonable accuracy.

## CHAPTER 7

# CONCLUSIONS

---

Given the results attained from the conducted numerical studies regarding geometric modelling methodologies and aerodynamic prediction techniques in the previous chapters, a thorough, detailed and critical analysis have been presented. This chapter summarises, concludes and highlights the findings, achievements and contributions of this research study as well as evaluating and making recommendations to future work.

## 7.1 Research Problem Synopsis

Truck-trailer units are bluff-bodied vehicles specially designed to carry high-pay loads over long distances at any given time predominantly on the motorway. This means these commercial vehicles are exposed to operating under motorway speeds of approximately 56mph. Rising fuel costs and mounting truck-trailer safety have become a significant concern in the commercial goods industry. Hence, improving the fuel economy and operational stability of the commercial vehicle has gained considerable attention in research as well as in industry.

Over the years, many research studies have investigated ways in which improvements can be made to the fuel economy and safety of truck-trailer vehicles. Drag and side forces have a direct influence of the fuel economy and the operational stability of truck-trailer vehicles. Extensive literature review has been carried out in this regard. The findings identified that researchers have developed and used various techniques and methods to achieve this. This involves both active and passive externally mounted add-on devices. Some of the commonly used are moving surface boundary-layer control; pneumatic blower; cab roof fairing; side skirts; boat tails; and vortex generators. Although these devices have been proven to be effectively favourable in manipulating aerodynamic forces, there are many operational implications that in turn reduces the effectiveness of these devices over time. Literature also suggested that changing the shape of truck-trailer units are an effective means of achieving the same goal. However, the operational restrictions such as the maximum pay-load carrying capacity and legislative design restrictions, mean that little research has been carried out in significantly optimising the truck-trailer shape making them more streamline and stable.

Shape optimising can be achieved through experimentation and numerically, via CFD. Even though experimental and numerical investigations have been proven to be invaluable in studying aerodynamic characteristics, there are issues that are beyond control in conducting the investigations. For example, experimental investigations require many resources such as large wind tunnels, models, instrumentation, while the accuracy and effectiveness of numerical investigations depends on computational power, available software and licenses.

From published literature, a comprehensive and critical review have been carried out, enabling the aims and objectives to formulate for pursuing the present research study. The following

presents these aims and objectives with the achievements and contributions of the discoveries obtained during the presented research study.

## 7.2 Research Aims and Achievements

The aims of the thesis defined from an extensive literature review in this area are as follows:

**Research Aim # 1: Development of a mathematical model to predict aerodynamic forces based on basic truck-trailer geometrical parameters and a range of crosswind angles.**

**Achievement # 1:** This sector of study investigated existing geometric modelling methodologies. Using the knowledge gained from that which is existing, a geometric modelling methodology has been developed. This is applicable in defining the outline of a truck-trailer unit, taking the basic truck-trailer geometrical design parameters, such as maximum length, height and width into consideration. This methodology has been employed initially to generate a 2D outline, followed by a 3D wireframe, then finally a solid CAD model of the truck-trailer unit, which had been used as the baseline model. The baseline model was numerically validated against the experimental results obtained by Coleman and Baker [34]. This validation proved that the developed geometric modelling methodology was working and the numerical setup was in good agreement.

Using the validated numerical results, detailed qualitative and quantitative critical analysis had been comprehensively carried out to understand the flow structure and behaviour of pressure and velocity fields around the truck-trailer unit. Qualitative analysis has been used to describe the coefficient of pressure contours on key baseline truck-trailer surfaces at various crosswind angles. This is followed by the velocity contours in the vicinity of the truck-trailer unit. Quantitative analysis has been carried out using the coefficient of pressure to study the effect of change in height and length at both, straight headwind and crosswind scenarios. Based on these results and findings, the first semi-empirical prediction model has been developed to accurately predict the aerodynamic drag, lift and side force coefficients at straight headwind and crosswind scenarios.

**Research Aim # 2: Development of a mathematical model to predict aerodynamic forces based on truck-trailer shape parameters at straight headwind conditions.**

**Achievement # 2:** This sector of the study investigates the shape of the truck-trailer unit by introducing a similar geometrical modelling methodology as that previously developed. In this case, four new shape coefficients have been introduced, namely, B1, B2, B5, B6. These shape coefficients are capable of independently altering the shape of the truck and trailer geometries. Once more, the proposed methodology was tested and has proven to be capable of generating a 2D outline, followed by a 3D wireframe, then a solid CAD model of the truck-trailer unit with shape modifications. Each B coefficient had been defined by three levels: 0.01, 0.05, and 0.1, which in turn increased the gradient of the curvature of the top leading and trailing edges of the truck and the trailer. Given this, 81 configurations had been obtained using full-factorial method retaining the maximum length and height.

Qualitative analysis had been carried out to investigate the variations of velocity magnitude and coefficient of pressure in vicinity and on key surfaces of truck-trailer models, respectively. Further to this, quantitative analysis had been carried out using axial flow velocity, coefficient of pressure and variations in aerodynamic forces to capture the effects of changing B coefficients. Based on these results and findings, the second semi-empirical prediction model has been developed to accurately predict the aerodynamic drag, lift and side force coefficients when provided with the respective B1, B2, B5 and B6 shape coefficients at straight headwind scenario.

**Research Aim # 3: Development of a mathematical model to predict aerodynamic forces based on truck-trailer shape parameters at various cross wind conditions.**

**Achievement # 3:** This sector of the study combines the truck and trailer shape configurations with various crosswind profiles from 15° to 90° in increments of 15°. This combination is used to analyse the change in aerodynamic flow field characteristics of various truck-trailer shapes. Qualitative analysis had been carried out to investigate the variations of velocity magnitude contour, velocity magnitude streamlines and coefficient of pressure contour at various crosswind flow profiles.

Further to this, quantitative analysis had been carried out for each changing B coefficient at each crosswind profile. The coefficient of pressure had been analysed to determine the pressure asymmetry on windward and leeward sides. Additionally, forces experienced by each of the key surfaces had been investigated to determine the contribution to the overall aerodynamic forces. Based on these results and findings, the third semi-empirical prediction model has been developed to accurately predict the aerodynamic drag, lift and side force coefficients when provided with the B1, B2, B5, B6 shape coefficients and crosswind profiles. This final semi-empirical prediction model incorporates the effect of change in shape coefficients and crosswinds, to predict the respective aerodynamic force coefficients.

### 7.3 Thesis Conclusions

A comprehensive study has been carried out to support the existing literature regarding the truck-trailer shape optimisation and to provide novel additions in developing an efficient and accurate methodology for designing truck-trailer units. It introduces three semi-empirical force prediction tools by considering the effect of dimensions, shape and operational characteristics. The main conclusions from each aspect of this research study are summarised as follows:

**Research Objective # 1: To develop a mathematical vehicle modelling methodology using shape functions to generate 3D truck-trailer geometry.**

**Conclusion # 1:** From the investigations carried out regarding the basic geometric modelling methodologies, this aspect of the study concludes that it is possible to streamline the design process for truck-trailer units by a means of developing and employing a geometric modelling tool. It can be concluded that the truck, bridge and trailer unit can be generated independently using shape functions. A separate shape function was developed to define a 4-axle wheelbase. This had been integrated with truck, bridge and trailer to give a complete 2D profile for a truck-trailer unit. The number of 2D profiles were combined to generate a 3D wireframe for a truck-trailer unit, which provided a cloud of x, y and z points. These points were exported into a CAD software in order to obtain a complete 3D solid model of a truck-trailer unit.

**Research Objective # 2: To carry out an extensive flow field analysis in order to characterise the flow field around baseline truck-trailer unit.**

**Conclusion # 2:** This aspect of the study has validated the proposed developed geometric modelling methodology and the numerical setup against the experimental data, which was found to be in good agreement. Extensive and detailed flow field analysis had been carried out on the baseline model, which concluded that stagnation pressure region occurs on the front truck surface and towards the top edge of the trailer surface. Additionally, low pressure regions occur on the bottom half of the trailer front surface as well as on the truck and trailer rear surfaces. Further to this, flow separation occurs around the sharp edges given rise to wake regions, altering the pressure distribution of the truck-trailer unit. The findings also showed that as the crosswind angle increases, the pressure on the truck and trailer front and rear surfaces decreases and the pressure on the windward side surface increases. Additionally, increasing the trailer height incurs in a pressure decrease on the truck front and rear as well as the trailer rear surfaces, while the pressure on the trailer front surface incurs in an increase. Further to this, increasing the trailer length has less impact on pressure distribution than increasing the height, which is more predominant on the trailer rear surface. It was discovered that maximum drag force acting in the direction of the flow incurs between  $15^\circ$  and  $30^\circ$  yaw angle while above  $60^\circ$ , drag force acts in the opposite direction showing that increasing the trailer height also increases the drag force. Additionally, as the yaw angle increases, lift force is high at lower trailer height and side force is high at high trailer height. The results revealed that increasing trailer length significantly affects the drag force after  $45^\circ$  yaw angle. Additionally, there are no clear trends occurring in lift force with respect to the trailer length. Furthermore, side force increases with the trailer length and this variation is more significant above  $15^\circ$  yaw angle.

**Research Objective # 3: To quantify the variation of aerodynamic forces with flow angle and changing vehicle dimensions.**

**Conclusion # 3:** Based on the findings regarding the basic geometric modelling methodologies, this aspect of the study concludes with the first semi-empirical prediction model at straight headwind and crosswind scenarios. This semi-empirical model is capable of accurately predicting the

drag, lift and side force coefficients based on the length, height, width of the truck-trailer model and the operating yaw angle.

**Research Objective # 4: To develop a mathematical vehicle modelling technique using shape functions to generate 3D truck-trailer geometry with varying shapes.**

**Conclusion # 4:** Four different shape coefficients capable of independently altering the shape of the truck and trailer geometries was introduced, namely B1, B2, B5, B6. These B coefficients were defined by three distinct levels, namely, 0.01, 0.05, and 0.1. These levels affect the curvature gradient at the top leading and trailing edges of the truck and the trailer. This geometric modelling methodology once more was used to create numerous 2D profiles, which were combined to generate a 3D wireframe for a truck-trailer unit. Similar to previous, the x, y and z coordinate points of the 3D wireframe model was extracted. However, in this case the model incorporated shape information. The 3D wireframe model was then exported into a CAD software in order to obtain a complete 3D solid model of a truck-trailer unit with the modifications to the shape to the truck-trailer unit.

**Research Objective # 5: To carry out an extensive flow field analysis in order to characterise the flow field around varying truck-trailer shapes.**

**Conclusion # 5:** Extensive and detailed flow field analysis had been carried out on the truck-trailer model with the independent effect of shape coefficients B1, B2, B5 and B6. The results conclude that increasing the B1 shape coefficient from 0.01 to 0.1 causes the velocity magnitude to increase closer to the truck-trailer model. This occurs in the vicinity of end curve profile at either sides of the vehicle model and on the truck unit. Additionally, the flow separation region on top of the truck unit and subsequent flow reversal becomes eliminated. Further to this, the effect of modifying the B1 coefficient effects the coefficient of pressure on the truck-trailer surfaces up to the leading edge of the trailer unit. It was also found that as B1 increases the drag force experienced by the model decreases. The lift force and side force increases from B1 = 0.01 to B1 = 0.05 and decreases from B1 = 0.05 to B1 = 0.1. The findings revealed that increasing the B2 shape coefficient from 0.01 to 0.1 decreases the recirculating flow velocity in the truck and

trailer gap region and has no effect on the flow separation occurring on the truck unit. Additionally, change in coefficient of pressure significantly affects the pressure distribution on the truck unit. Further to this, increasing B2 also causes the drag force acting on the model to decrease. The lift force and side force increase from  $B2 = 0.01$  to  $B2 = 0.05$  and decrease from  $B2 = 0.05$  to  $B2 = 0.1$ . The discoveries exposed that increasing B5 increases the flow velocity on top of the trailer unit. Additionally, the B5 shape coefficient affects the pressure distribution on the truck-trailer unit from the truck rear surface to the trailer rear surface. Further to this, increasing B5 also causes the drag force and lift force acting on the model to decrease. The side force increases from  $B5 = 0.01$  to  $B5 = 0.05$  and decreases from  $B5 = 0.05$  to  $B5 = 0.1$ . The outcomes depicted that increasing B6 increases the velocity on top of the trailer unit and reduces the flow recirculation by guiding flow with increased velocity into that region. Additionally, similar to that found in B5, the B6 shape coefficient affects the pressure distribution on the truck-trailer unit from the truck rear surface to the trailer rear surface, however the most significant pressure variations are on the trailer rear surface. Further to this, increasing B6 also causes the drag force and lift force acting on the model to increase from  $B6 = 0.01$  to  $B6 = 0.05$  and slightly decrease from  $B6 = 0.05$  to  $B6 = 0.1$ . However, the side force slightly decreases from  $B6 = 0.01$  to  $B6 = 0.05$  and significantly increases from  $B6 = 0.05$  to  $B6 = 0.1$ . This concludes that out of 81 configurations, the model with  $B1 = 0.01$ ,  $B2 = 0.05$ ,  $B5 = 0.1$  and  $B6 = 0.01$  shape coefficients experienced the least drag force, hence considered to be the optimum.

**Research Objective # 6: To quantify the variation of aerodynamic forces at straight headwind under changing truck-trailer shapes.**

**Conclusion # 6:** From the findings, this aspect of the study concludes with the second semi-empirical prediction model at straight headwind scenarios. This semi-empirical model is capable of accurately predicting the drag, lift and side force coefficients based on the B1 and B2 truck shape coefficients as well as B5 and B6 trailer shape coefficients.

**Research Objective # 7: To carry out an extensive flow field analysis in order to characterise the flow field around varying truck-trailer shapes and crosswind angles.**

**Conclusion # 7:** From the findings, this aspect of the study analysed the truck front, truck rear, trailer front and trailer rear faces for B1, B2, B5 and B6 shape coefficients. The B shape coefficients have varying effects in pressure distribution on key truck-trailer surfaces at crosswinds. The asymmetric pressure distribution between the windward and leeward sides were computed on the key surfaces at the full range of yaw angles. The results conclude that the truck front surface of both models where  $B1 = 0.01$  and  $B1 = 0.1$ , from yaw angle of  $15^\circ$  to  $45^\circ$ , have higher pressure on the windward side than the leeward side. From  $45^\circ$  onwards, opposing pressure effects occurs. Where forces are concerned in the x-direction, there is a decrease as the yaw angle increases. When reaching  $45^\circ$ , the surface incurs force in negative direction followed by an increase after  $75^\circ$ . Between the two model, highest pressure is incurred on the  $B1 = 0.01$ . Where forces are concerned in the y-direction, there are considerable variations between the two models until the yaw angle reaches  $75^\circ$ . Where forces are concerned in the z-direction, there are negligible variations between the two models. The findings revealed that the truck rear surface of both models where  $B2 = 0.01$  and  $B2 = 0.1$ , for yaw angle of  $15^\circ$  and  $90^\circ$ , has higher pressure on the windward side than the leeward side. However, opposing pressure effects are incurred from  $30^\circ$  to  $75^\circ$ . Where forces are concerned in the x-direction, there is an increase from  $15^\circ$  to  $60^\circ$  with higher forces for  $B2 = 0.01$  model. Following on from here, there is an almost linear decrease with negligible variation between the two models. Where forces are concerned in the y-direction, the  $B2 = 0.01$  model increases throughout the range of yaw angle, however this model incurs in lower forces than the  $B2 = 0.1$  model. Where forces are concerned in the z-direction, there are negligible variations between the two models. The discoveries exposed that the trailer front surface of both models where  $B5 = 0.01$  and  $B5 = 0.1$ , for yaw angle of  $15^\circ$  has higher pressure on the leeward side; for  $30^\circ$  and  $45^\circ$  there are higher pressures on the windward side; and from  $60^\circ$  to  $90^\circ$  the leeward side has higher pressure. Where forces are concerned in the x-direction, there is a decrease as the yaw angle increases. When reaching  $30^\circ$ , the surface incurs force in a negative direction where the maximum force occurs at  $60^\circ$ . Where forces are concerned in the y-direction, there are considerable variations between the two models until the yaw angle reaches  $60^\circ$ . Where forces are concerned in the z-direction, there are negligible variations between the two models. The outcomes of the trailer rear depicted that at a yaw angle of  $15^\circ$ , when  $B6 = 0.01$  the windward side has higher pressure whereas when  $B6 = 0.1$ , there is higher pressure on the leeward side. For  $30^\circ$  and  $45^\circ$ , the leeward side has higher pressure for

both models. Additionally, for  $60^\circ$  and  $75^\circ$  the windward side has higher pressure for both models. At a yaw angle of  $90^\circ$ , when  $B6 = 0.01$  the leeward side has higher pressure whereas when  $B6 = 0.1$ , there is higher pressure on the windward side. The force acting in the z-direction was calculated for left surface of the vehicle. The variations in pressure was studied on the top surface of the vehicle and right surface of the vehicle at a yaw angle of  $60^\circ$ , for changing  $B1$ ,  $B2$ ,  $B5$  and  $B6$  coefficients from 0.01 to 0.1. Modifying  $B1$  and  $B2$  shape coefficients were seen to affect the variance of pressure coefficient on the truck unit more prominently than the variance of pressure coefficient on the trailer unit. Modifying  $B5$  and  $B6$  shape coefficients were seen to affect the variance of pressure coefficient on the trailer unit more prominently than the variance of pressure coefficient on the truck unit. Moreover, highest force acting on the windward face was recorded for when  $B1 = 0.1$  at  $75^\circ$  yaw angle, while the lowest force acting on the windward face was recorded for when  $B2 = 0.1$  at  $15^\circ$  yaw angle. Additionally, highest force acting on the leeward face was recorded for when  $B2 = 0.1$  at  $45^\circ$  yaw angle, while lowest force acting on the leeward face was recorded for when  $B6 = 0.1$  at  $90^\circ$  yaw angle. Overall, it is concluded the maximum drag force of 182N is achieved when  $B5=0.1$  and the minimum drag force of 5146N is achieved when  $B6=0.05$ . Also, highest lift force occurs when the B coefficients = 0.01, while lower lift forces predominantly occurs where the B coefficients = 0.1. Furthermore, maximum side force is achieved when the B coefficients = 0.01, while the lowest side force is achieved when the B coefficients = 0.1.

**Research Objective # 8: To quantify the variation of aerodynamic forces at varying crosswind angles under changing truck-trailer shapes.**

**Conclusion # 8:** From the findings, this aspect of the study concludes with the third semi-empirical prediction model at both straight headwind and crosswind scenarios. This semi-empirical model is capable of accurately predicting the drag, lift and side force coefficients based on the  $B1$  and  $B2$  truck shape coefficients,  $B5$  and  $B6$  trailer shape coefficients and the operating yaw angle.

## 7.4 Thesis Contribution

The contributions of this research are summarised below in which novelties of this research are described:

**Contribution # 1:** The first major contribution of this study is the development of a geometric modelling methodology, which defines the 2D outline of a truck-trailer. This in turn enables one to generate a 3D wireframe and finally a solid CAD model with decreased resources and design time. Having CFD tools available along with good agreement with the experimental data has allowed the author to carry out this investigation. The pressure and velocity variations on and surrounding the truck-trailer unit have been investigated over a wide range of the flow conditions. The effects of truck-trailer dimensional parameters such as the length, height and width of the truck-trailer unit on the flow parameters have been closely studied. Given this, a semi-empirical equation has been developed that has the potential to significantly reduce costs associated with the truck-trailer design process. This is since the equation can accurately predict the aerodynamic performance characteristics, such as the drag, lift and side force coefficients by considering the dimensional parameters, such as the length, height and width at both, straight headwind and crosswind conditions.

**Contribution # 2:** The second major contribution of this study is introducing shape coefficients to the geometric modelling methodology. This in turn enables one to generate a 3D wireframe and finally a solid CAD model with independent modification to the truck and trailer units. The pressure, velocity and force variations on and surrounding the truck-trailer unit have been investigated at straight headwind conditions. The effects of truck-trailer shape parameters determined by B1, B2, B5 and B6 on the flow parameters have been studied in extensive detail. Given this, another semi-empirical equation has been developed that has can accurately predict the aerodynamic performance characteristics, such as the drag, lift and side force coefficients by considering the shape parameters, determined by the B shape coefficient at straight headwind conditions.

**Contribution # 3:** The pressure, velocity and force variations on and surrounding the truck-trailer unit have been investigated at crosswind conditions. The effects of truck-trailer shape parameters determined by B1, B2, B5 and B6 on the flow parameters have been studied at various crosswinds in extensive detail. The third major contribution of this study is introducing the final semi-empirical equation, which is capable of accurately predicting the aerodynamic performance characteristics, such as the drag, lift and side force coefficients. This is by considering the shape parameters such as

B1, B2, B5 and B6 coefficients at both straight headwind and crosswind conditions. Using this prediction model, it is possible to predict the aerodynamic force coefficients for any given truck-trailer shape at crosswind angles without pursuing either experimental or numerical investigations.

### **Supervisor Contributions**

Professor Rakesh Mishra supervised the author throughout the PhD journey and suggested the idea of pursuing this research project in the field of truck-trailer units using Computational Fluid Dynamics. Professor Mishra contributed throughout this research with his ideas, insights and technical knowledge.

## **7.5 Recommendation for Future Work**

The main goal of this research is to develop a geometric modelling methodology for designing a truck-trailer unit, as well as a tool that accurately predicts aerodynamic performance parameters such as drag, lift and side forces with minimal effort, cost and resources. After considering the concluded remarks outlined in the previous sections, there is significant potential for growth in this particular area of geometric modelling methodology for truck-trailer units and predictive aerodynamic techniques. The main areas identified for further work are summarised below.

**Recommendation # 1:** Due to the haulage capacity, the truck-trailer operators are using a wide range of add-on devices. The presented geometric modelling methodology however, does not take the profiles of the add-on devices into account. This can be improved by developing a separate non-dimensionalised shape function for each type of add-on device, which could be incorporated into the proposed geometric modelling methodology as required.

**Recommendation # 2:** The predictive aerodynamic techniques aforementioned has only taken a maximum operating speed of 56mph. However, the truck-trailer units often operate at within city limits adhering to speeds such as 30mph and 40mph. The predictive aerodynamic technique can be further improved by also taking the operating speed into considering.

**Recommendation # 3:** The presented study considers straight headwind and crosswind flow profiles under steady conditions. It is recommended to investigate the presented study under transient conditions over various crosswind profiles. Using the results from this study, there is potential to develop a tool that can accurately predict aerodynamic moments, such as yawing, rolling and pitching, as well as forces, such as drag, lift and side.

---

## REFERENCES

---

- [1] Department for Transport; Office of Rail Regulation; Department of Energy and Climate Change Report (2011). UK
- [2] Lawrence David. (2004). Fuel-saving semi-trailers: an independent report. The definitive guide to truck and trailer aerodynamics. Produced by Lawrence David Ltd. Based on research carried out by MIRA.
- [3] Climate Action - European Commission. (2018). 2020 climate & energy package - Climate Action - European Commission. [online] Available at: [https://ec.europa.eu/clima/policies/strategies/2020\\_en](https://ec.europa.eu/clima/policies/strategies/2020_en) [Accessed 31 May 2018].
- [4] Mccallen, R., Couch, R., Hsu, J., Browand, F., Hammache, M., Leonard, A., . . . Zilliac, G. (1999). Progress in Reducing Aerodynamic Drag for Higher Efficiency of Heavy Duty Trucks (Class 7-8). doi:10.2172/771211
- [5] Singh, R., & Golsch, K. (2005). A Downforce Optimisation Study for a Racing Car Shape. SAE Technical Paper Series. doi:10.4271/2005-01-0545
- [6] Hucho, W. (1998). Aerodynamics of road vehicles: From fluid mechanics to vehicle engineering. Warrendale, PA: Society of Automotive Engineers.
- [7] Dyke, M. V. (2012). An album of fluid motion. Stanford, California: The Parabolic Press.
- [8] Vlachopoulos, J. (1982). Fundamentals of fluid mechanics. Hamilton, Ont.: Dept. of Chemical Engineering, McMaster University.
- [9] Sun, S., Chang, Y., Fu, Q., Zhao, J., Ma, L., Fan, S., . . . Friz, H. (2014). Aerodynamic Shape Optimisation of an SUV in early Development Stage using a Response Surface Method. SAE International Journal of Passenger Cars - Mechanical Systems, 7(4), 1252-1263. doi:10.4271/2014-01-2445

- [10] Alvarez, A., Arnold, F.R., (1961). A study of the aerodynamic characteristics of a high lift device based on rotating cylinder flap, Technical Report, Stanford University, Stanford, USA.
- [11] Favre, A., (1938). Contribution à l'étude expérimentale des mouvements hydrodynamiques à deux dimensions, Ph.D. Thesis, University of Paris, France.
- [12] Singh, S., Rai, L., Puri, P. and Bhatnagar, A. (2005). 'Effect of moving surface on the aerodynamic drag of road vehicles'. Proceedings of the Institution of Mechanical Engineers, Part D: Journal of Automobile Engineering, Volume 219, Part 2, pp. 127-134
- [13] Modi, V.J., Fernando, M.S.U.K., Yokomizo, T. (1991). 'Moving Surface Boundary Layer Control: Studies with Bluff Bodies and Application'. American Institute of Aeronautics and Astronautics .Vol 29 (9) 1400-1406
- [14] Modi, V.J., Fernando, M.S.U.K., Yokomizo, T. (1991). 'Moving Surface Boundary Layer Control as applied to two-dimensional and three-dimensional bluff bodies'. Journal of Wind Engineering and Industrial Aerodynamics. Vol 38 83-92
- [15] Modi, V. J. (1997). Moving Surface Boundary-Layer Control: A Review, Journal of Fluids and Structures 11 627 – 663
- [16] Malviya, V., Mishra, R., Fieldhouse, J.D. (2008). Comparative computational analysis of drag-reducing devices for tractor-trailers. In: Proceedings of Computing and Engineering Annual Researchers' Conference 2008: CEARC'08. University of Huddersfield.
- [17] Modi, V.J., Ying, B., Yokomizo, T. (1992). Effect of momentum injection on the aerodynamics of several bluff bodies. Journal of Wind Engineering and Industrial Aerodynamics. 41-44 713-714.

- [18] Robson, S.E and Ahmed, N.A.(2004). 'Drag reduction on bluff bodies using a rotation device', 15th Australasian Fluid Mechanics Conference, The University of Sydney, Sydney, Australia. PP 13-17
- [19] Buckley, F.T. & Marks, C.H. (1979). Feasibility of active boundary layer control methods for reducing aerodynamic drag on tractor trailer trucks. *Journal of Industrial Aerodynamics* .4 133-148.
- [20] Agarwal, R.K. (2013). Computational Study of Drag Reduction of Models of Truck-Shaped Bodies in Ground Effect by Active Flow Control. SAE Technical Paper
- [21] Malviya, V., Mishra, R., & Fieldhouse, J. (2009). CFD Investigation of a Novel Fuel-Saving Device for Articulated Tractor-Trailer Combinations. *Engineering Applications of Computational Fluid Mechanics*, 3(4), 587-607. doi:10.1080/19942060.2009.11015293
- [22] Krishna, M.V. & Ram, C.V. (2011). Adjustable roof fairing for truck aerodynamics. Society of Automotive Engineers.
- [23] Jing, C., Yun-zhu, W., Deng-feng, W., Wei-gang, X., Gui-Jin, W. (2010). Research on Aerodynamic Drag Reduction of Heavy Commercial Vehicle. 2nd International Conference on Computing Engineering and Technology. 191-194
- [24] Marks, C.H., Buckley, F.T., Walston, W.H. (1976). 'An Evaluation of the Aerodynamic Drag Reductions Produced by Various Cab Roof Fairings and a Gap Seal on Tractor-Trailer Trucks'. SAE Technical Paper.
- [25] Bayraktar, I., Baysal, O., Bayraktar, T. (2004). Computational Parametric Study on External Aerodynamics of Heavy Trucks. *The Aerodynamics of Heavy Vehicles: Trucks, Buses, and Trains, Lecture Notes in Applied and Computational Mechanics* . 19 , 485-501.

- [26] Das, P., Tsubokura, M., Matsuuki, T., Oshima, N., Kitoh, K. (2013). Large eddy simulation of the flow-field around a full-scale heavy-duty truck. 5th BSME International Conference on Thermal Engineering. *Procedia Engineering* 56 , 521-530
- [27] Dominy, R.G. (1997). 'Fuel saving by the optimized use of cab roof fairings for typical articulated vehicle operating cycles'. *Proceedings of the Institution of Mechanical Engineers, Part D: Journal of Automobile Engineering*, Volume 211, Part 3, pp. 219-226
- [28] Wang, M., Li, Q., Wang, D., Yang, C., Zhao, J., Wen, G. (2009). The air deflector and the drag: A case study of low drag cab styling for a heavy truck. *IEEE 10th International Conference*. 1025-1030.
- [29] Ali, I.S. & Mahmood, A.A. (2013). Improvement of Aerodynamics Characteristic of Heavy Trucks. 3rd International Conference on Trends in Mechanical and Industrial Engineering. Kuala Lumpur (Malaysia).
- [30] Chowdhury, H., Moria, H., Ali, A., Khan, I., Alam, F., Watkins, S. (2013). A study on aerodynamic drag of a semi-trailer truck. 5th BSME International Conference on Thermal Engineering. *Procedia Engineering* 56, 201-205
- [31] Hucho, W., & Sovran, G. (1993). Aerodynamics of Road Vehicles. *Annual Review of Fluid Mechanics*, 25(1), 485-537. doi:10.1146/annurev.fl.25.010193.002413
- [32] Cooper, K. (2003). *Truck Aerodynamics Reborn - Lessons from the Past*. Society of Automotive Engineers.
- [33] Håkansson, C., & Lenngren, M. J. (2010). CFD analysis of aerodynamic trailer devices for drag reduction of heavy duty trucks. Göteborg: Chalmers University of Technology

- [34] Coleman, S., & Baker, C. (1990). High sided road vehicles in cross winds. *Journal of Wind Engineering and Industrial Aerodynamics*, 36, 1383-1392. doi:10.1016/0167-6105(90)90134-x
- [35] Batista, M., & Perkovič, M. (2014). A simple static analysis of moving road vehicle under crosswind. *Journal of Wind Engineering and Industrial Aerodynamics*, 128, 105-113. doi:10.1016/j.jweia.2014.02.009
- [36] Peddiraju, P., Papadopoulos, A., & Singh, R. (2009). CAE frame work for aerodynamic design development of automotive vehicles. 3rd ANSA &  $\mu$ ETA International Conference.
- [37] Linfield, K. W., & Mudry, R. G. (2008). Pros and Cons of CFD and Physical Flow Modeling. Airflow Sciences Corporation.
- [38] Malik, M. R. & Bushnell, D. M. (2012). Role of Computational Fluid Dynamics and Wind Tunnels in Aeronautics R&D. NASA TP-2012-217602.
- [39] Bandyopadhyay, S., & Saha, S. (2013). Similarity Measures. *Unsupervised Classification*, 59-73. doi:10.1007/978-3-642-32451-2\_3
- [40] Muñoz-Paniagua, J., García, J., Crespo, A., & Krajnovic, S. (2008.). Aerodynamic Optimisation of the ICE 2 High-Speed Train Nose using a Genetic Algorithm and Metamodels. *Proceedings of the First International Conference on Railway Technology: Research, Development and Maintenance*. doi:10.4203/ccp.98.165
- [41] Guilmineau, E., & Chometon, F. (2007). Experimental and Numerical Analysis of the Effect of Side Wind on a Simplified Car Model. *SAE Technical Paper Series*. doi:10.4271/2007-01-0108

- [42] Lee, J., & Kim, J. (2007). Approximate optimisation of high-speed train nose shape for reducing micropressure wave. *Structural and Multidisciplinary Optimisation*, 35(1), 79-87. doi:10.1007/s00158-007-0111-9
- [43] Rho, J.H., Ku, Y.C., Lee, D.H., Kee, J.D., & Kim, K.Y. (2009). Application of Functional Design Method to Road Vehicle Aerodynamic Optimisation in Initial Design Stage. SAE International.
- [44] Calkins, D.E., Su, W., & Chan, W.T. (1998). A Design Rule Based Tool for Automobile System Design. SAE Technical Paper, 1-12.
- [45] Calkins, D.E. & Su, W. (1998). Cdaero – A Parametric Aerodynamic Drag Prediction Tool. SAE Technical Paper, 1-9.
- [46] Lietz, R.L. (2011). Vehicle Aerodynamic Shape Optimisation. SAE International.
- [47] Singh, R. (2003). Automated Aerodynamic Design Optimisation Process for Automotive Vehicle. SAE Technical Paper Series. doi:10.4271/2003-01-0993
- [48] Lundberg, A., Hamlin, P., Shankar, D., Broniewicz, A., Walker, T., & Landström, C. (2015). Automated Aerodynamic Vehicle Shape Optimisation Using Neural Networks and Evolutionary Optimisation. *SAE International Journal of Passenger Cars - Mechanical Systems*, 8(1). doi:10.4271/2015-01-1548
- [49] Koromilas, C., Harris, C., Sumantran, V., Pachon, L., & Zeng, S. (2000). Rapid Aerodynamic Development of Two-Volume Vehicle Shapes. SAE Technical Paper Series. doi:10.4271/2000-01-0488
- [50] Ribaldone, E., Puri, I. D., Cogotti, F., Pizzoni, R., & Gautero, M. (2011). Optimizing the External Shape of Vehicles at the Concept Stage: Integration of Aerodynamics and

- Ergonomics. SAE International Journal of Engines, 4(2), 2622-2628. doi:10.4271/2011-37-0014
- [51] Zhang, Y., Ding, W., & Zhang, Y. (2014). Aerodynamic Shape Optimisation Based on the MIRA Reference Car Model. SAE Technical Paper Series. doi:10.4271/2014-01-0603
- [52] Gabbasa, A., Jawad, B. A., & Koutsavdis, E. (2012). CFD-Based Shape Optimisation for Optimal Aerodynamic Design. SAE International Journal of Passenger Cars - Electronic and Electrical Systems, 5(1), 227-237. doi:10.4271/2012-01-0507
- [53] Baysal, O. (1999). Aerodynamic Shape Optimisation: Methods and Applications. SAE Technical Paper Series. doi:10.4271/1999-01-5500.
- [54] Khondge, A., & Sovani, S. (2012). An Accurate, Extensive, and Rapid Method for Aerodynamics Optimisation: The 50:50:50 Method. SAE Technical Paper Series. doi:10.4271/2012-01-0174
- [55] Wood, R. M. (2004). Impact of Advanced Aerodynamic Technology on Transportation Energy Consumption. SAE Technical Paper Series. doi:10.4271/2004-01-1306.
- [56] Allan, J. (1981). Aerodynamic drag and pressure measurements on a simplified tractor-trailer model. Journal of Wind Engineering and Industrial Aerodynamics, 9(1-2), 125-136. doi:10.1016/0167-6105(81)90083-0
- [57] Östh, J., & Krajnović, S. (2012). The flow around a simplified tractor-trailer model studied by large eddy simulation. Journal of Wind Engineering and Industrial Aerodynamics, 102, 36-47. doi:10.1016/j.jweia.2011.12.007
- [58] Cooper, K. R. (2004). Commercial Vehicle Aerodynamic Drag Reduction: Historical Perspective as a Guide. The Aerodynamics of Heavy Vehicles: Trucks, Buses, and Trains

Lecture Notes in Applied and Computational Mechanics, 9-28. doi:10.1007/978-3-540-44419-0\_2

- [59] Hirz, M., & Stadler, S. (2013). A New Approach for the Reduction of Aerodynamic Drag of Long-Distance Transportation Vehicles. SAE International Journal of Commercial Vehicles, 6(2), 453-458. doi:10.4271/2013-01-2414
- [60] Burton, D., McArthur, D., Sheridan, J., Thompson, M. (2013). Contribution of Add-On Components to the Aerodynamic Drag of a Cab-Over Truck-Trailer Combination Vehicle. SAE 2013 Commercial Vehicle Engineering Congress. 6(2) , 477-485
- [61] Rose, M.J. (1981). 'Commercial vehicle fuel economy - The correlation between aerodynamic drag and fuel consumption of a typical truck'. Journal of Wind Engineering and Industrial Aerodynamics, Volume 9, Part 1-2, pp. 89-100
- [62] Wong, H.Y., Cox, R.N., Rajan, A. (1981). 'Drag reduction of trailer-tractor configuration by aerodynamic means'. Journal of wind engineering and industrial aerodynamics. Volume 9, pp.101-111
- [63] Wood, R. and Bauer, S. (2003). Simple and Low-Cost Aerodynamic Drag Reduction Devices for Tractor-Trailer Trucks , in International Truck & Bus Meeting & Exhibition, Ft. Worth (TX), USA: Society of Automotive Engineers (SAE), p. 18
- [64] Wood, R. (2010). A discussion of a heavy truck advanced aerodynamic trailer system. SOLUS – Solution and Technologies LLC
- [65] Landman, D., Wood, R., Seay, W., Bledsoe, J. (2009). Understanding Practical Limits to Heavy Truck Drag Reduction. SAE International Journal of Commercial Vehicles.
- [66] Landman, D., Cragun, M., McCormick, M., Wood, R. (2011). "Drag Reduction of a Modern Straight Truck. SAE International Journal of Commercial Vehicles.

- [67] Azim, A.F.A. &Gawad, A.F.A. (2001). Effect of different parameters of the drag coefficient for commercial vehicles. Proceeding of 9th international conference on Aerospace Science and Aviation Technology, Cairo, Egypt.
- [68] Sulitka, M. & Nožička, J. (2004). Aerodynamic devices to reduce the base and under body drag of semitrailer unit. Engineering, Division of Fluid Dynamics and Thermodynamics, Technická 4, 166 07 Praha 6, Czech Republic.
- [69] Ortega, J., Salari, K., Brown, A., Schoon, R. (2013). Aerodynamic drag reduction of class 8 heavy vehicles: a full-scale wind tunnel study. Lawrence Livermore National Laboratory, U.S. Department of Energy
- [70] Mohamed-Kassim, Z. &Filippone, A. (2010). Fuel saving on a heavy vehicle via aerodynamic drag reduction. Transportation Research Part D. 15 275-284
- [71] Malinin, L., Borovkov, A., Voynov, I., Pyak, B., Pyak, V. (2010). Modelling of efficiency of aerodynamic devices on a tractor-trailer. International Journal of Aerodynamics. 206-219
- [72] Suzuki, M., Tanemoto, K., & Maeda, T. (2003). Aerodynamic characteristics of train/vehicles under cross winds. Journal of Wind Engineering and Industrial Aerodynamics, 91(1-2), 209-218. doi:10.1016/s0167-6105(02)00346-x
- [73] Diedrichs, B., Sima, M., Orellano, A., & Tengstrand, H. (2007). Crosswind stability of a high-speed train on a high embankment. Proceedings of the Institution of Mechanical Engineers, Part F: Journal of Rail and Rapid Transit, 221(2), 205-225. doi:10.1243/09544409jrtr126
- [74] Chiu, T., & Squire, L. (1992). An experimental study of the flow over a train in a crosswind at large yaw angles up to 90°. Journal of Wind Engineering and Industrial Aerodynamics, 45(1), 47-74. doi:10.1016/0167-6105(92)90005-u

- [75] Saltzman, E.J. & Meyer, R.R. Jr. (1999). A Reassessment of Heavy-Duty Truck Aerodynamic Design Features and Priorities. NASA/TP-1999-206574, National Aeronautics and Space Administration and Dryden Flight Research Center, Edwards, California
- [76] Sterling, M., Quinn, A., Hargreaves, D., Cheli, F., Sabbioni, E., Tomasini, G., . . . Morvan, H. (2010). A comparison of different methods to evaluate the wind induced forces on a high sided lorry. *Journal of Wind Engineering and Industrial Aerodynamics*, 98(1), 10-20. doi:10.1016/j.jweia.2009.08.008
- [77] Nakashima, T., Tsubokura, M., Vázquez, M., Owen, H., & Doi, Y. (2013). Coupled analysis of unsteady aerodynamics and vehicle motion of a road vehicle in windy conditions. *Computers & Fluids*, 80, 1-9. doi:10.1016/j.compfluid.2012.09.028
- [78] McArthur, D., Burton, D., Thompson, M., & Sheridan, J. (2018). An experimental characterisation of the wake of a detailed heavy vehicle in cross-wind. *Journal of Wind Engineering and Industrial Aerodynamics*, 175, 364-375. doi:10.1016/j.jweia.2018.01.033
- [79] Roy, S. and Srinivasan, P.S. (2000). External Flow Analysis of a Truck for Drag Reduction. Society of Automotive Engineers
- [80] Cooper, K. and Leuschen, J. (2005). 'Model and Full-Scale Wind Tunnel Tests of Second-Generation Aerodynamic Fuel Saving Devices for Tractor-Trailers (2005-01-3512)', in 2005 SAE Commercial Vehicle Engineering Conference, Rosemont (IL), USA
- [81] Pevitt, C., Chowdury, H., Moriaand, H. and Alam, F (2012) 'A Computational Simulation of Aerodynamic Drag Reductions for Heavy Commercial Vehicles', 18th Australian Fluid Mechanics Conference, Launceston, Australia. 3-7

- [82] DAF Trucks Limited. (n.d.). Retrieved May 12, 2018, from <http://www.daf.co.uk/SpecsheetsMedia//TSGBEN016F8699XAAA201529.PDF>
- [83] Regert, T., & Lajos, T. (2007). Description of flow field in the wheelhouses of cars. *International Journal of Heat and Fluid Flow*, 28(4), 616-629. doi:10.1016/j.ijheatfluidflow.2007.04.017
- [84] Peng, J., Wang, T., Yang, T., Sun, X., & Li, G. (2018). Research on the Aerodynamic Characteristics of Tractor-Trailers with a Parametric Cab Design. *Applied Sciences*, 8(5), 791. doi:10.3390/app8050791
- [85] Gilkeson, C., Thompson, H., Wilson, M., Gaskell, P., & Barnard, R. (2009). An experimental and computational study of the aerodynamic and passive ventilation characteristics of small livestock trailers. *Journal of Wind Engineering and Industrial Aerodynamics*, 97(9-10), 415-425. doi:10.1016/j.jweia.2009.06.004
- [86] Lasdon, L. S., Fox, R. L., & Ratner, M. W. (1973). Nonlinear Optimisation Using the Generalized Reduced Gradient Method. doi:10.21236/ad0774723
- [87] Baker, C. (1988). High sided articulated road vehicles in strong cross winds. *Journal of Wind Engineering and Industrial Aerodynamics*, 31(1), 67-85. doi:10.1016/0167-6105(88)90188-2
- [88] Guo, P., Hu, X.J., Zhu, Y.Y., Fu, Q., Wang, X.Y., Fan, S.J., Fan, Q.Y. (2013). Investigation on Aerodynamic Drag Reduction of Commercial Truck Based on External Styling of Cab. *Applied Mechanics and Materials*. 307, 186-191
- [89] Baker, C. (1986). A simplified analysis of various types of wind-induced road vehicle accidents. *Journal of Wind Engineering and Industrial Aerodynamics*, 22(1), 69-85. doi:10.1016/0167-6105(86)90012-7

- [90] Sendanayake, I., Asim, T., & Mishra, R. (2017). Development of Novel Vehicle Design Modelling Functions for Quantifying Vehicles' Shapes. *International Journal of Research, Science, Technology & Management*, 7 (2). pp. 26-31. ISSN 2455-2240
- [91] Anderson, J.D. and Wendt, J. (1995). *Computational fluid dynamics*. Vol. 206.: Springer.
- [92] Barnard, R.H (2009). *Road Vehicle Aerodynamic Design, An Introduction*, Third Edition. Hertfordshire, England: MechAero Publishing.

# APPENDICES

## A-1 Full Factorial Geometrical Configurations

Various truck-trailer geometrical configurations generated for this study

Parameter	B1 Coefficient	B2 Coefficient	B5 Coefficient	B6 Coefficient
1	0.1	0.01	0.05	0.05
2	0.01	0.01	0.01	0.05
3	0.1	0.05	0.01	0.01
4	0.05	0.1	0.01	0.05
5	0.01	0.01	0.01	0.1
6	0.05	0.01	0.01	0.05
7	0.1	0.05	0.01	0.05
8	0.05	0.05	0.1	0.1
9	0.05	0.05	0.1	0.01
10	0.05	0.05	0.01	0.05
11	0.05	0.1	0.1	0.01
12	0.01	0.05	0.1	0.01
13	0.1	0.05	0.1	0.1
14	0.1	0.01	0.01	0.01
15	0.05	0.01	0.01	0.1
16	0.1	0.1	0.1	0.05
17	0.1	0.01	0.01	0.05
18	0.1	0.1	0.1	0.1
19	0.1	0.1	0.1	0.01
20	0.05	0.05	0.01	0.01
21	0.05	0.1	0.1	0.05
22	0.01	0.05	0.1	0.05
23	0.01	0.05	0.05	0.1
24	0.01	0.01	0.05	0.1
25	0.05	0.01	0.01	0.01
26	0.05	0.1	0.1	0.1
27	0.01	0.1	0.1	0.01
28	0.05	0.01	0.1	0.05
29	0.05	0.01	0.1	0.01
30	0.1	0.1	0.01	0.05

31	0.01	0.01	0.01	0.01
32	0.1	0.1	0.05	0.1
33	0.05	0.05	0.05	0.01
34	0.01	0.1	0.05	0.01
35	0.05	0.1	0.01	0.01
36	0.05	0.01	0.05	0.05
37	0.05	0.1	0.01	0.1
38	0.01	0.01	0.05	0.01
39	0.01	0.05	0.05	0.05
40	0.05	0.01	0.05	0.1
41	0.01	0.05	0.1	0.1
42	0.05	0.01	0.1	0.1
43	0.1	0.05	0.01	0.1
44	0.01	0.01	0.1	0.01
45	0.1	0.01	0.1	0.1
46	0.05	0.05	0.1	0.05
47	0.1	0.01	0.1	0.01
48	0.01	0.01	0.1	0.05
49	0.1	0.01	0.05	0.1
50	0.05	0.05	0.05	0.05
51	0.01	0.1	0.01	0.01
52	0.01	0.05	0.01	0.05
53	0.1	0.1	0.05	0.01
54	0.1	0.01	0.1	0.05
55	0.01	0.1	0.1	0.1
56	0.05	0.1	0.05	0.05
57	0.1	0.1	0.05	0.05
58	0.01	0.01	0.05	0.05
59	0.1	0.1	0.01	0.1
60	0.05	0.1	0.05	0.01
61	0.1	0.05	0.1	0.01
62	0.1	0.05	0.1	0.05
63	0.1	0.01	0.01	0.1
64	0.05	0.05	0.05	0.1
65	0.01	0.1	0.05	0.05
66	0.1	0.01	0.05	0.01
67	0.01	0.1	0.01	0.1
68	0.05	0.1	0.05	0.1
69	0.01	0.1	0.1	0.05
70	0.1	0.05	0.05	0.1
71	0.01	0.1	0.05	0.1

72	0.1	0.1	0.01	0.01
73	0.1	0.05	0.05	0.05
74	0.01	0.05	0.05	0.01
75	0.01	0.05	0.01	0.1
76	0.01	0.01	0.1	0.1
77	0.05	0.01	0.05	0.01
78	0.05	0.05	0.01	0.1
79	0.1	0.05	0.05	0.01
80	0.01	0.1	0.01	0.05
81	0.01	0.05	0.01	0.01

# LIST OF PUBLICATIONS

---

Malviya, V., Asim, T., Sendanayake, I., & Mishra, R. (2018). Development of a Novel Characterisation Methodology for the Aerodynamic Coefficients of a Tractor–Trailer Unit Based on Relative Flow Angles and Vehicle Dimensions. *Arabian Journal for Science and Engineering*, 1-19.

Sendanayake, I., Asim, T., & Mishra, R. (2017). Development of novel vehicle design modelling functions for quantifying vehicles' shapes. *International Journal of Research, Science, Technology & Management*, 7(2), 26-31.

Mishra, R., Albarzenji, D., Shrawasti, S., Sendanayake, I., & Pradhan, S. (2015). Flow diagnostics.

Asim, T., Sendanayake, I., & Mishra, S. (2013). Numerical Analysis of Atherosclerosis and Aneurysm in Carotid Bifurcations using Computational Fluid Dynamics.

Sendanayake, I., Asim, T., & Mishra, R. (2013). Effects of Cab Deflector Height on the Aerodynamic Drag for Heavy Commercial Vehicles. University of Huddersfield.

Asim, T., Sendanayake, I., Mishra, R., Zala, K., & Ubbi, K. (2013). Effects of a Moving Surface Boundary Layer Control Device (MSBC) on the Drag Reduction in Heavy Commercial Vehicles.